



Skolkovo Institute of Science and Technology

Skolkovo Institute of Science and Technology

EFFECTS OF TECHNOLOGICAL REGIMES ON STRUCTURAL
PERFORMANCE OF PULTRUDED PROFILES

Doctoral Thesis

by

Aleksandr Vedernikov

DOCTORAL PROGRAM IN MATHEMATICS AND MECHANICS

Supervisor

Alexander Safonov, Assistant Professor

Moscow – 2022

© Aleksandr Vedernikov 2022

I hereby declare that the work presented in this thesis was carried out by myself at Skolkovo Institute of Science and Technology, Moscow, except where due acknowledgement is made, and has not been submitted for any other degree.

Candidate (Aleksandr Vedernikov)

Supervisor (Assistant Professor Alexander Safonov)

Abstract

This Ph.D. thesis studies the effects of technological regimes on the structural performance of pultruded profiles which are widely used in the construction sector, bridge and bridge deck engineering. Several manufacturing issues are to be solved to further promote the application of pultruded structural profiles. The objective of this work is to study the possibility of increasing the profitability of the pultrusion process while maintaining the structural performance of the manufactured composite profiles. To solve this problem, the experimental and numerical studies of pultruded flat laminates and L-shaped structural profiles were conducted at the Laboratory of Composite Materials and Structures of the Center for Materials Technologies (Skolkovo Institute of Science and Technology, Moscow, Russia).

An experimental investigation of pultruded glass fiber/epoxy-vinyl resin L-shaped profiles of $75 \times 75 \times 6$ mm was performed to understand the relationships between pulling speed and structural performance. Profiles were pultruded using a Pultrex Px500-6T machine at three different pulling speeds: 200, 400, and 600 mm/min. Based on the results of differential scanning calorimetry and data from thermocouples embedded within the profiles, the evolution of the thermochemical parameters (i.e., temperature, degree of curing, and cure rate) of the advancing material during the pultrusion process were determined. Furthermore, the evolutions of the spring-in angle were analyzed through a 90-day experiment. Cross-sections of the profiles, cut perpendicular to the pulling direction, were studied using an optical microscope to evaluate the number, size, and location of the cracks and delaminations. Tensile, compressive, flexural, in-plane shear, and interlaminar shear properties of the pultruded profiles were determined using a testing machine, in accordance with the corresponding ASTM standards, and the relationships between these properties and the pulling speed were analyzed. The results show that changes in the pulling speed influence the shape distortions, and the microstructural and mechanical properties of the composite due to the polymerization peak being shifted beyond the die block exit. Higher pulling speeds result in increased spring-in angles, more pronounced delaminations, higher variations and in substantially impaired mechanical properties.

An experimental investigation of pultruded glass fiber/epoxy-vinyl resin-based 150×3.5 mm flat laminates was performed to better understand the influence of high pulling speeds on mechanical characteristics and morphology of pultruded composites. Four different pulling speeds of 200, 600, 1000, and 1400 mm/min were utilized to manufacture the composites. The morphology of produced flat laminates was studied with the use of optical and scanning electron microscopy. The flexural and interlaminar shear properties were determined both for 0° and for 90° fiber orientations. The observed difference in the mechanical characteristics of flat laminates can be explained by the presence of bubbles, longitudinal voids, and matrix cracks, and by an increase in their density and dimensions with an increase in pulling speed. It was demonstrated that high pulling speeds make it possible to increase pultrusion output at least by the factor of 1.7, without compromising mechanical performance of produced profiles, as compared to their counterparts

produced at regular speed.

A numerical model was developed to predict the occurrence of spring-in in 75×75×6 mm L-shaped profiles manufactured at various pulling speeds. The model was built in ABAQUS software suite with user subroutines UMAT, FILM, USDFLD, HETVAL, and UEXPAN. The 2D approach was used to describe the thermochemical and mechanical behavior via the modified Cure Hardening Instantaneous Linear Elastic (CHILE) model. The developed model was validated in two experiments conducted within a 6-month interval, using glass fiber/vinyl ester resin L-shaped profiles reinforced with unidirectional glass fiber rovings and fabrics, and manufactured at pulling speeds of 200, 400, and 600 mm/min. Spring-in predictions obtained with the proposed numerical model fall within the experimental data range. Numerical simulation results were used to analyze the possibility of reducing the spring-in with the help of a post-die cooling tool or by reducing the chemical shrinkage of the resin.

The influence of aluminum hydroxide $\text{Al}(\text{OH})_3$ flame retardant additive and zinc stearate $\text{Zn}(\text{C}_{18}\text{H}_{35}\text{O}_2)_2$ internal release agent on the cure kinetics of vinyl ester pultrusion resin and pulling speed of pultrusion was also analyzed. In particular, the neat resin composition, the composition containing $\text{Al}(\text{OH})_3$, the composition containing $\text{Zn}(\text{C}_{18}\text{H}_{35}\text{O}_2)_2$, and the composition with both $\text{Al}(\text{OH})_3$ and $\text{Zn}(\text{C}_{18}\text{H}_{35}\text{O}_2)_2$ were analyzed experimentally, with the use of differential scanning calorimetry (DSC), at the heating rates of 5, 7.5, and 10 K/min. To characterize the cure kinetics, 16 kinetic models were tested, and their performances were compared. To analyze the influence of the processing parameters and additives on the curing behavior of resin compositions, a numerical simulation of pultrusion of a flat laminate profile at different heating temperatures (115 and 125 °C) and pulling speeds (600 and 1000 mm/min) for all four compositions was performed. Besides, the curing times were determined for all compositions under isothermal conditions at 115, 120, 125, and 130 °C, using the 600 mm long die block, and the maximum pulling speeds were calculated. It was demonstrated, that ignoring the effects of certain processing additives may result in a significant difference between the predicted and experimental values of cure degree obtained at the die exit. Thus, the predicted pulling speeds for a specified set of compositions can differ at least by a factor of 1.7. Therefore, the influence of processing additives must be taken into account when choosing pulling speed and predicting the outcomes of pultrusion manufacturing.

Shape memory behavior of unidirectional glass fiber/epoxy-based pultruded flat laminates of 150×3.5 mm was also investigated and shape memory performance of polymer composites and cured resin specimens was evaluated. Moreover, the shape memory performance of composite specimens during shape memory cycling was determined, and the shape fixity and shape recovery ratios for cured resin specimens were evaluated. Tensile, compression, flexural, and interlaminar shear properties of the cured resin and composite specimens with 0° and 90° fiber orientations were measured. To lay the foundation for further studies on the simulation and

optimization of the pultrusion process, the resin cure kinetics, thermomechanical and thermophysical properties of the cured resin were analyzed.

Chapter 1 describes the motivation for this Ph.D. project. The pultrusion manufacturing process is explained and its technological challenges are formulated. Scientific articles tackling these issues are briefly reviewed, their limitations are emphasized and unresolved research gaps are outlined. Overall structure of the Ph.D. thesis is presented. Subsequently, the mathematical model of the pultrusion process, containing main governing equations, is presented in Chapter 2. Further on, Chapter 3 discusses the main results presented in the articles that have been published in the course of this Ph.D. project. These publications are presented in Chapters 4–11. Finally, Chapter 12 concludes this Ph.D. thesis highlighting the main findings and setting-up future research possibilities for scholars and practitioners working in pultrusion.

Journal Publications

1. **A. Vedernikov**, L. Gemi, E. Madenci, Y. O. Özkılıç, Ş. Yazman, S. Gusev, A. Sulimov, J. Bondareva, S. Evlashin, S. Konev, I. Akhatov, A. Safonov. *Effects of high pulling speeds on mechanical properties and morphology of pultruded GFRP composite flat laminates*. Composite Structures. 2022. doi:10.1016/j.compstruct.2022.116216.
2. **A. Vedernikov***, K. Minchenkov*, S. Gusev, A. Sulimov, P. Zhou, C. Li, G. Xian, I. Akhatov, A. Safonov. *Effects of the pre-consolidated materials manufacturing method on the mechanical properties of pultruded thermoplastic composites*. Polymers. 2022. doi:10.3390/polym14112246. * - equal contribution.
3. K. Minchenkov*, **A. Vedernikov***, Y. Kuzminova, S. Gusev, A. Sulimov, A. Gulyaev, A. Kreslavskaya, I. Prosyanyoy, G. Xian, I. Akhatov, A. Safonov. *Effects of the quality of pre-consolidated materials on the mechanical properties and morphology of thermoplastic pultruded flat laminates*. Composites Communications. 2022. doi:10.1016/j.coco.2022.101281. * - equal contribution.
4. P. Zhou, C. Li, Y. Bai, S. Dong, X. Guijun, **A. Vedernikov**, I. Akhatov, A. Safonov, Q. Yue. Durability study on the interlaminar shear behavior of glass-fibre reinforced polypropylene (GFRPP) bars for marine applications. Construction and Building Materials. 2022. doi:10.1016/j.conbuildmat.2022.128694.
5. **A. Vedernikov**, F. Tucci, P. Carlone, S. Gusev, S. Konev, D. Firsov, I. Akhatov, A. Safonov. *Effects of pulling speed on structural performance of L-shaped pultruded profiles*. Composite Structures. 2021. doi:10.1016/j.compstruct.2020.112967.
6. R. Korotkov*, **A. Vedernikov***, S. Gusev, O. Alajarmeh, I. Akhatov, A. Safonov. *Shape memory behavior of unidirectional pultruded laminate*. Composites Part A: Applied Science and Manufacturing. 2021. doi:10.1016/j.compositesa.2021.106609. * - equal contribution.

7. **A. Vedernikov***, A. Safonov*, F. Tucci, P. Carlone, I. Akhatov. *Modeling spring-in of L-shaped structural profiles pultruded at different pulling speeds*. Polymers. 2021. doi:10.3390/polym13162748. * - equal contribution.
8. O. Alajarmeh, X. Zeng, T. Aravinthan, T. Shelley, M. Alhawamdeh, A. Mohammed, L. Nicol, **A. Vedernikov**, A. Safonov, P. Schubel. *Compressive behaviour of hollow box pultruded FRP columns with continuous-wound fibres*. Thin-Walled Structures. 2021. doi:10.1016/j.tws.2021.108300.
9. K. Minchenkov, **A. Vedernikov**, A. Safonov, I. Akhatov. *Thermoplastic pultrusion: A review*. Polymers. 2021. doi:10.3390/polym13020180.
10. **A. Vedernikov**, Y. Nasonov, R. Korotkov, S. Gusev, I. Akhatov, A. Safonov. *Effects of additives on the cure kinetics of vinyl ester pultrusion resins*. Journal of Composite Materials. 2021. doi:10.1177/00219983211001528.
11. F. Tucci*, **A. Vedernikov***. *Design criteria for pultruded structural elements*. Encyclopedia of Materials: Composites. 2021. doi:10.1016/B978-0-12-819724-0.00086-0. * - equal contribution.
12. **A. Vedernikov**, A. Safonov, F. Tucci, P. Carlone, I. Akhatov. *Pultruded materials and structures: A review*. Journal of Composite Materials. 2020. doi:10.1177/0021998320922894.

Conference Proceedings

1. **A. Vedernikov**, A. Safonov, F. Tucci, P. Carlone, I. Akhatov. *Analysis of spring-in deformation in L-shaped profiles pultruded at different pulling speeds: Mathematical simulation and experimental results*. ESAFORM 2021 - 24th International Conference on Material Forming. 2021. doi:10.25518/esaform21.4743.
2. **A. Vedernikov**, A. Safonov, I. Akhatov. *Modelling and experimental validation of thermoset resin curing during pultrusion*. IOP Conference Series: Materials Science and Engineering. 2021. doi:10.1088/1757-899x/1129/1/012011.
3. **A. Vedernikov**, F. Tucci, A. Safonov, P. Carlone, S. Gusev, I. Akhatov. *Investigation on the shape distortions of pultruded profiles at different pulling speed*. Procedia Manufacturing. 2020. doi:10.1016/j.promfg.2020.04.107
4. **A. Vedernikov**, A. Safonov, S. Gusev, P. Carlone, F. Tucci, I. Akhatov. *Spring-in experimental evaluation of L-shaped pultruded profiles*. IOP Conference Series: Materials Science and Engineering. 2020. doi:10.1088/1757-899X/747/1/012013.

Conferences

1. **A. Vedernikov**, L. Gemi, E. Madenci, Y. O. Özkılıç, Ş. Yazman, S. Gusev, J. Bondareva, S. Evlashin, I. Akhatov, A. Safonov. *Effects of high pulling speeds on mechanical properties and morphology of pultruded flat laminates*. ICCS 25. 25th International Conference on Composite Structures. 19 - 22 July 2022. University of Porto, Porto, Portugal.
2. A. Safonov, **A. Vedernikov**, P. Carlone, F. Tucci, I. Akhatov. *Time dependent spring-in of pultruded L-shaped profile*. MECHCOMP 7. 7th International Conference on Mechanics of Composites. 1 - 3 September 2021. University of Porto, Porto, Portugal.
3. **A. Vedernikov**, A. Safonov, F. Tucci, P. Carlone, I. Akhatov. *Analysis of spring-in deformation in L-shaped profiles pultruded at different pulling speeds: mathematical simulation and experimental results*. ESAFORM 2021. 24th International Conference on Material Forming. 14 - 16 April 2021. Liege, Belgium.
4. **A. Vedernikov**, F. Tucci, P. Carlone, I. Akhatov, A. Safonov. *Modelling spring-in distortions of L-shaped structural profiles pultruded at different pulling speeds*. ICOMP 2021. 2nd International Conference on Theoretical, Analytical and Computational Methods for Composite Materials and Composite Structures. 5 - 7 March 2021. University of Porto, Porto, Portugal.
5. **A. Vedernikov**, A. Safonov, I. Akhatov. *Modelling and experimental validation of thermoset resin curing during pultrusion*. 32nd International Conference of Young Scientists and Students on Topical Problems of Mechanical Engineering. 2 - 4 December 2020. Mechanical Engineering Research Institute of the Russian Academy of Sciences, Moscow, Russia.
6. **A. Vedernikov**, F. Tucci, P. Carlone, A. Safonov, I. Akhatov. *Effect of pulling speed on structural performance of L-shaped pultruded profiles*. ICCS 23. 23rd International Conference on Composite Structures. 1 - 4 September 2020. University of Porto, Porto, Portugal.

7. **A. Vedernikov**, F. Tucci, A. Safonov, P. Carlone, S. Gusev, I. Akhatov. *Investigation on the shape distortions of pultruded profiles at different pulling speed*. ESAFORM 2020. 23rd International Conference on Material Forming. 4 - 8 May 2020. Brandenburg University of Technology, Cottbus, Germany.
8. **A. Vedernikov**, A. Safonov, S. Gusev, P. Carlone, F. Tucci, I. Akhatov. *Spring-in experimental evaluation of L-shaped pultruded profiles*. 31st International Conference of Young Scientists and Students on Topical Problems of Mechanical Engineering. 4 - 6 December 2019. Mechanical Engineering Research Institute of the Russian Academy of Sciences, Moscow, Russia.
9. **A. Vedernikov**, A. Safonov, S. Gusev, I. Akhatov. *Numerical modeling of the viscoelastic behavior of pultruded profiles after manufacturing*. 12th Russian Conference on Fundamental Problems of Theoretical and Applied Mechanics. 19 - 24 August 2019. Ufa, Russia.

Acknowledgments

First of all, I would like to express my sincere gratitude to my supervisor Professor Alexander Safonov for his guidance, patience and numerous advice in the course of my Ph.D. project. Professor Safonov assumed the responsibility for becoming my supervisor and believed in me when I had no ideas of “pultrusion” and scientific research work. Considering the progress we have made in these years, I think he was right, and our collaboration was very fruitful. Today, I’m only in the beginning of my scientific career and it is Alexander who put the first bricks in the foundation of my scientific profile. Thank you very much.

I would like to express my sincere gratitude to Professor Iskander Akhatov for the provided opportunity to join the team of the Center for Materials Technologies of Skolkovo Institute of Science and Technology, and for sharing his invaluable experience.

I would also like to thank Ph.D. committee members — Chairman, Professor Clement Fortin, Professor Costanzo Bellini, Professor Ugur Koklu, Doctor Wahid Ferdous, Professor Ivan Sergeichev, Professor Igor Shishkovsky — for their time and useful recommendations on improving my Ph.D. thesis.

I would also like to thank Doctor Fausto Tucci and Professor Pierpaolo Carlone from University of Salerno for the collaboration and significant contribution in our projects performed in the course of this Ph.D. I was happy to spend several months with Fausto during his research visit to Moscow both in formal and informal environments. I hope we will see each other sooner or later in Italy, enjoy Italian cuisine, listen to all the best songs and play harmonica.

I would also like to express gratitude to my colleagues in the Laboratory of Composite Materials and Structures and especially to Senior engineer Sergey Gusev for his constant assistance and support in the experimental part of this Ph.D. project, and absorbing conversations on composite materials and pultrusion in particular.

I would also like to thank my colleagues from the Center for Materials Technologies, I had an honour to work with during my Ph.D. project.

And, last but not the least, I would like to thank my co-authors and colleagues

from all over the world for the opportunity of working together and for their contribution to our collaborative research projects: Professor Guijun Xian from Harbin Institute of Technology; Professor Lokman Gemi, Professor Emrah Madenci, and Professor Yasin Onuralp Özkılıç from Necmettin Erbakan Üniversitesi, and Professor Şakir Yazman from Selçuk Üniversitesi; Doctor Omar Alajarmeh from the University of Southern Queensland.

Contents

1	Introduction	15
1.1	Motivation	15
1.2	Pultrusion process	18
1.3	State of the art	20
1.3.1	Studies investigating the effects of pulling speed	21
1.3.2	Studies investigating the effects of additives	28
1.3.3	Studies investigating shape distortions	30
1.4	Novelty and scientific contribution	32
1.5	Structure of the thesis	33
2	Constitutive material behavior	35
2.1	2D heat transfer model	36
2.2	2D mechanical model	39
2.2.1	Calculation of instantaneous mechanical properties of the resin	39
2.2.2	Calculation of composite effective mechanical properties of unidirectional laminate	40
2.2.3	Calculation of composite effective mechanical properties of quasi-isotropic composite laminate	42
2.2.4	Calculation of thermal strain	43
2.2.5	Calculation of chemical strain	44
2.3	Stress-strain analysis	45
3	Results	47
3.1	Pultruded materials and structures: A review	48
3.2	Design criteria for pultruded structural elements	48
3.3	Effects of pulling speed on structural performance of L-shaped pultruded profiles	49
3.4	Effects of high pulling speeds on mechanical properties and morphology of pultruded GFRP composite flat laminates	53
3.5	Modelling and experimental validation of thermoset resin curing during pultrusion	59
3.6	Modeling spring-in of L-shaped structural profiles pultruded at different pulling speeds	61
3.7	Effects of additives on the cure kinetics of vinyl ester pultrusion resins	65
3.8	Shape memory behavior of unidirectional pultruded laminate	70
4	Pultruded materials and structures: A review	74

5	Design criteria for pultruded structural elements	112
6	Effects of pulling speed on structural performance of L-shaped pultruded profiles	131
7	Effects of high pulling speeds on mechanical properties and morphology of pultruded GFRP composite flat laminates	141
8	Modelling and experimental validation of thermoset resin curing during pultrusion	159
9	Modeling spring-in of L-shaped structural profiles pultruded at different pulling speeds	167
10	Effects of additives on the cure kinetics of vinyl ester pultrusion resins	196
11	Shape memory behavior of unidirectional pultruded laminate	214
12	Conclusion and outlook	225
	12.1 Summary	225
	12.2 Practical implementation	228
	12.3 Outlook	229
	Bibliography	232

Chapter 1

Introduction

In this Chapter the motivation for this Ph.D. thesis is presented. The pultrusion manufacturing process is explained along with its central technological challenges. Subsequently, a comprehensive literature review of publications dealing with these challenges is presented. The main limitations and research gaps of the previous studies are analyzed. Concluding this Chapter, a brief structure of the Ph.D. thesis is presented, highlighting the main content of each Chapter of the thesis.

1.1 Motivation

In recent decades, fiber-reinforced polymer (FRP) composites have been increasingly used in various engineering applications. Wide application of FRP composites is explained by numerous advantages of composites over their traditional counterparts (steel, timber, and concrete), such as high strength-to-weight ratio, improved durability and corrosion resistance, ease of transportation, assembly and maintenance. Several manufacturing techniques for production of FRP composites currently exist, such as injection molding, compression molding, hand lay-up, spray-up, vacuum bagging, filament winding, resin transfer molding, autoclave processing, and pultrusion. The latter is claimed to be the most efficient process for manufacturing of structural profiles having constant cross-section. Pultrusion is a compound word consisting of two terms "pull" and "extrusion" that gave birth to the name of the manufacturing process. Depending on the polymer matrix used, there are two types

of pultrusion — thermoset and thermoplastic. This Ph.D. thesis is devoted to the study of thermoset pultrusion. Therefore, hereinafter, the term "pultrusion" will refer to a thermoset pultrusion process.

From the production volume standpoint, the construction market is the sector with the largest demand for pultruded profiles. Consequently, it can be considered as one of the biggest markets to implement and provide opportunities for pultrusion in the future. Bridges and bridge decks made of composite materials surpass their conventional counterparts in almost every aspect: weight, ease of transportation and installation, corrosion resistance, etc. All these benefits make it possible to reduce or even eliminate the need in traffic/railway shutdowns and to decrease shipping and erection costs. Moreover, composite bridges are more durable in the context of extreme temperatures or de-icing treatments resistance. This enables dramatic reductions in the bridge maintenance and inspection costs.

The main function of a bridge deck is to carry vertical loads and to spread them to the superstructure in the transverse direction. The increasing maintenance costs of traditional bridge decks is an aggravating global issue. Multiple studies are dedicated to the examination of the deteriorating condition of bridges and other related infrastructure. For instance, steel elements (concrete reinforcement, structural members) are very likely to corrode, and concrete is susceptible to such degradation mechanisms as sulfate attack, freeze–thaw cycling, and other detrimental processes causing cracking. Thus, the bridge construction today is in dire need of a breakthrough to deal with these shortcomings of conventional materials. In this respect, FRP bridge decks are rapidly emerging as a possible solution, both in new construction and in rehabilitation projects. FRP bridge decks are mainly made of E-glass fibers and thermosetting resins such as polyester (owing to their low cost) and vinyl ester (material of choice for moist environments). This solution has proved its efficiency, owing to the advantages of low weight, high strength, and improved durability. Moreover, among the benefits of FRP decks is high corrosion resistance and, therefore, longer service life with lower life-cycle costs. Composite bridge decks allow rapid and easy installation and can be used to replace deteriorating existing structures. Due to the low weight of FRP structures used for bridge rehabilitation, such

infrastructures can carry increased live loads because of reduced dead loads. The application of traditional materials for bridge construction usually involves increased energy consumption and higher carbon emissions, as compared to their composite counterparts. Considering this and other reasons, such as fewer traffic disruptions during construction, lower maintenance and repair costs, smaller footprint, less air and noise pollution, FRP decks demonstrate the potential to deliver sustainable bridges with low environmental impact.

However, several manufacturing issues are to be solved to further promote the use of pultruded structural profiles in bridge construction. Among them, the need to ensure quality and safety of pultruded profiles. Another key issue is a necessity to increase the profitability of pultrusion process while maintaining the mechanical performance of manufactured composite structural profiles. Increasing the profitability of pultrusion process is an important engineering challenge that can be solved by increasing the pulling speed of pultrusion. However, the increase in pulling speed can lead to incomplete polymerization of the composite, and, therefore, to the process-induced defects and impaired mechanical properties of manufactured profiles. Process-induced defects in composites can lead to rejection of produced profiles due to their inability to meet geometrical requirements listed in Table B.1 of the standard EN 13706-2:2003 "Reinforced plastic composites – Specifications for pultruded profiles – Part 2: Methods of test and general requirements" (1). In addition, these defects may significantly impair mechanical properties of pultruded composite structural profiles, the minimum allowable values of which are listed in Table 1 of the standard EN 13706-2:2003 "Reinforced plastic composites – Specifications for pultruded profiles – Part 3: Specific requirements" (2), and may require costly and time-consuming shimming operations during the assembly of the final structures.

Thus, the pultrusion manufacturer needs to find a compromise between the pulling speed increase and mechanical performance of pultruded profiles. Typically, in industrial production, due to the complexity of the pultrusion process, such search is disregarded, or the balance is determined by a costly trial-and-error approach, implying shutdown of the pultrusion line and waste of raw materials.

To tackle this challenge, a series of experimental and numerical studies of pul-

truded flat laminates and L-shaped structural profiles were performed at the Laboratory of Composite Materials and Structures of the Center for Materials Technologies (Skolkovo Institute of Science and Technology, Moscow, Russia). Such profiles are widely applied in bridge construction as external reinforcement and beam elements, respectively. First, the analysis of the published scientific literature and standards on design of pultruded structures was carried out. The existing limitations and research gaps were identified, and, based on these findings, the plan of the Ph.D. research was outlined. In the first phase, experimental studies were conducted. A series of pultrusion trials made it possible to determine the relationship between pulling speed and mechanical properties, morphology, time-dependent spring-in, and warpage distortions of pultruded structural profiles. Further on, the numerical model was developed and validated based on experimental results obtained previously. This model predicts the value of spring-in distortion in pultruded L-shaped composite structural profiles fabricated at different pulling speeds. Moreover, with the use of this numerical model, the efficiency of spring-in reduction methods (such as the use of a post-die cooling tool, and reducing the chemical shrinkage of the matrix) was numerically analyzed. Subsequently, the influence of flame-retardant additives, such as aluminum hydroxide $\text{Al}(\text{OH})_3$, and of internal release agents, such as zinc stearate $\text{Zn}(\text{C}_{18}\text{H}_{35}\text{O}_2)_2$, on cure kinetics of vinyl ester pultrusion resins was studied based on the mathematical model of pultrusion process, and the pulling speed necessary for production of high-quality composite structural profiles was determined. Next, the thermomechanical and thermophysical properties of the cured epoxy resin exhibiting shape memory performance properties, that are to be used for further numerical simulations and optimization of the pultrusion process, were also determined in the course of the experimental studies.

1.2 Pultrusion process

The scheme of the conventional thermosetting pultrusion line is presented in Fig. 1.1 (3). The conventional pultrusion process starts with pulling the reinforcement material, initially placed on fiber creel racks, through an open impregnation bath

filled with a liquid polymer resin. Various types of reinforcement materials, such as unidirectional rovings, continuous filament mats, stitched and woven fabrics, can be used in pultrusion process (4). Impregnated reinforcement pack is then pulled through collimating plates, where the excess resin is squeezed out, and guided to the die block electrically heated by heating platens. The temperature regime is typically controlled with the use of thermocouples inserted into the body of the heated die. The polymerization of resin and, therefore, solidification of the composite take place inside the die block. Then, with the help of puller units, cured composite is pulled along the pulling line to the cutting saw, where the composite profile is cut into sections of desired length at predetermined time intervals. Pultrusion is a continuous manufacturing process and when it becomes stationary, it needs very little attention from the engineers, since the pullers and cutting saw act in an almost fully automated mode.

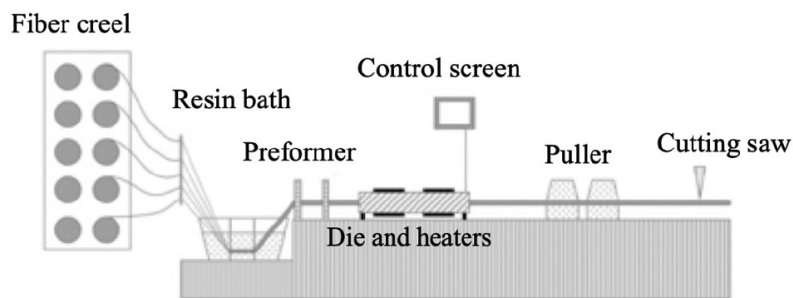


Figure 1.1: Conventional thermosetting pultrusion line (3).

Different types of polymer resins (epoxy, vinyl ester, polyester) and reinforcing materials (glass, carbon, aramid, basalt) can be used in pultrusion of composite structural profiles. The reinforcement ensures the strength and stiffness of the composite material, while the resin bonds fibers together and ensures the uniform distribution of internal forces between them. Unidirectional fibers provide the longitudinal strength, while mat and fabric reinforcements enhance the composite's strength in the transverse direction. The result is a pultruded composite profile with virtually unlimited length, and constant cross-section, such as round, square, rectangular, hollow circular, I-, L-, C-, U-shape profiles (see Fig. 1.2).

Technological parameters, such as the choice of raw materials and their proportions, fiber impregnation and resin infiltration techniques, temperature conditions,

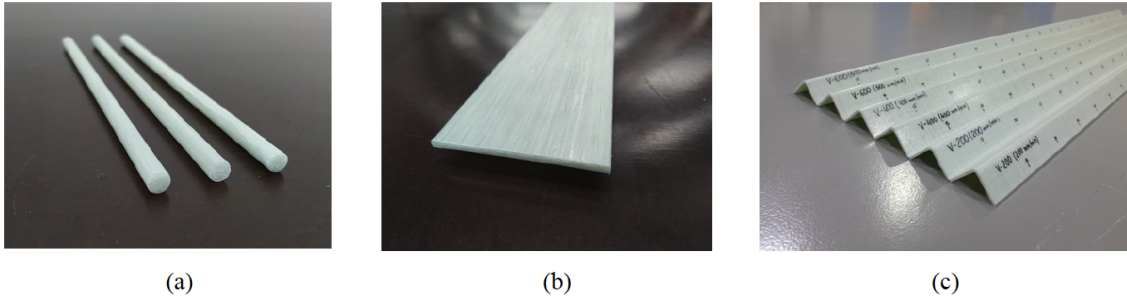


Figure 1.2: Profiles pultruded at the Laboratory of Composite Materials and Structures of the Center for Materials Technologies (Skolkovo Institute of Science and Technology, Moscow, Russia): (a) Rods; (b) Flat laminates; (c) L-shaped profiles.

pulling force, and pulling speed, influence the profitability of pultrusion process. On the one hand, to increase the profitability of the pultrusion process, the manufacturer strives to increase the production rate by increasing the pulling speed. However, on the other hand, the increase in pulling speed leads to formation of shape distortions and internal defects impairing the mechanical performance of pultruded profiles. Thus, it is necessary to find a certain balance between the increase in pulling speed and mechanical performance of pultruded profiles. Moreover, it is necessary to study the possibility of increasing the pulling speed while preserving the mechanical performance of pultruded profiles.

1.3 State of the art

Numerous studies on the influence of technological parameters on the structural properties of pultruded profiles have been initiated in the early 1980s'. The results of these studies allowed scientists to better understand the pultrusion process, its controls and optimization. These studies can be divided into three categories:

1. Experimental studies, when, by varying the raw materials and technological parameters, researchers establish the effect of these parameters on the structural properties of composite profiles, which can be measured, calculated, compared, and analyzed. The structural properties to be studied include mechanical characteristics, morphology, and process-induced shape distortions;
2. An analytical solutions establishing a mathematical relationship between the

properties of the raw materials, the chosen technological parameters, and the final structural properties of pultruded profiles;

3. Numerical models simulating the pultrusion process, using personal computers and finite-element softwares.

Following is a comprehensive review of the studies on the influence of pulling speed, additives and shape distortions, as these three subtopics form the core of this Ph.D. thesis, including the analysis of limitations and research gaps of the mentioned studies.

1.3.1 Studies investigating the effects of pulling speed

In 1984, to better understand the pultrusion process and the influence of pulling force, Price and Cupschalk (5) conducted experimental studies of carbon fiber/epoxy flat laminates of 20×2 mm manufactured at pulling speeds of 12.5, 25, and 50 mm/min. They concluded that with the same raw materials and at the same temperatures, the highest quality profiles are obtained at pulling speeds corresponding to the highest pulling force.

Ten years later, based on Patankar's method, Gorthala et al. (6) made a step forward and used numerical modelling tools to develop the numerical model of heat transfer and resin cure, which was then successfully validated by seven pultrusion experiments with glass fiber/epoxy and graphite/epoxy composites. The authors varied process parameters such as temperature conditions, fiber volume fractions, and pulling speeds (200 and 400 mm/min, i.e. higher than those used by Price and Cupschalk in (5)). A good agreement between the results of the proposed model and the experiments was obtained for all considered cases.

Simultaneously, Lackey and Vaughan (7) conducted a series of thirty-two pultrusion experiments to determine the effect of technological parameters such as fiber volume fraction, temperature regime, and pulling speed (203, 254, 305, 356, 406 mm/min) on the pulling force observed during the pultrusion of graphite/epoxy composites.

Subsequently, Ma et al. (8) were the first to study the possibility of furfuryl alcohol prepolymer preparation and its use in the pultrusion process. They also investigated the relationship between the pultrusion process parameters and properties of obtained composites. The glass fiber/furfuryl alcohol composites were produced at pulling speeds varying from 400 to 1500 mm/min, previously not studied. It was found that flexural strength and flexural modulus of pultruded composites may be improved either by increasing the die block temperature or by reducing the pulling speed. In addition, it has been shown that mechanical properties can also be improved by the post-cure treatment. However, the optimum post-cure time should be considered, as its exceedance at certain temperatures may result in degradation of matrix and, consequently, in impaired mechanical performance of pultruded composite. In the accompanying article (9) Ma et al. established the relationship between the dynamic mechanical properties of pultruded glass fiber/furfuryl alcohol composites and selected pulling speeds (namely, 500, 1000, and 1500 mm/min). The lower values of damping ($\tan \delta$) were obtained at lower pulling speeds. The reduced energy dissipation at lower pulling speeds makes it possible to produce profiles with higher rigidity. The authors related it to the time during which the the curing composite stays inside the die, and consequently to the value of cure degree. Although it has been noted that in the case of the high-speed pultrusion the post-cure treatment can help enhance the properties of the pultruded composite.

A year later, in 1996, Valliappan et al. (10) continued the Gorthala's work (6) and, using numerical modelling tools to describe pultrusion process, proposed the numerical model to predict the distribution of temperature and degree of polymerization in the composite at the die and post-die regions. For model validation, they performed a series of pultrusion experiments with graphite/epoxy \varnothing 9.5 mm rods at different pulling speeds (203, 305, and 406 mm/min), fiber volume fractions, and temperature conditions. The results of simulations and experiments correlated well with each other. It was also shown that an increase in the pulling speed leads to an increase in the corresponding centerline temperature of the composite, registered at the die exit. It was also shown that the degree of polymerization at the die exit for the composite manufactured at low pulling speed, is higher than that for profiles

manufactured at high pulling speeds. However, at the post-die region, polymerization is significantly higher for profiles manufactured at the high pulling speeds as compared to those manufactured at the lower pulling speeds.

Kim et al. (11) performed a series of experiments with pultrusion of \varnothing 6 mm rods and 6×12 mm rectangular profiles based on epoxy and vinyl ester resins, respectively. The experiments were conducted at pulling speeds ranging from 160 to 360 mm/min and from 200 to 470 mm/min. The results of experiments were then used to validate the model describing the distribution of temperature and degree of polymerization in the composite during pultrusion. The thermochemical submodel proposed in that study was based on the same energy equation as described in Valliappan et al. (10). However, in addition to the proposed thermochemical submodel, the study also proposed the submodel of the pulling force. A satisfactory agreement between the results of the proposed model and the experimental data has been reported.

Experimental validation of the developed numerical model was performed by Roux et al. (12). In their study a glass fiber/epoxy 63.5×63.5 mm I-beam profile was pultruded at a pulling speed of 200 mm/min.

In 2000, Methven et al. (13) were the first (among the studies discussed earlier in this Chapter (5; 6; 7; 8; 9; 10; 11; 12)) to study the microwave-assisted pultrusion at pulling speeds ranging from 25 to 2000 mm/min. The subject of their research was a glass fiber/epoxy \varnothing 6 mm rod.

However, contrary to all studies mentioned above, no effects of pulling speed (varied from 100 to 300 mm/min) on the mechanical properties, void fraction, and water absorption of pultruded glass/vinyl ester profiles were observed by Garland in his master thesis (14). He supposed, that the future investigations conducted at higher pulling speed would reveal this dependence.

Two years later, Freed in his master thesis (15) reported a minor effect of the pulling speeds variations (100, 200, and 300 mm/min) on the void fraction in glass fiber/vinyl ester $76.2 \times 76.2 \times 10$ mm L-shaped profiles. This probably can be explained by reasons discussed in Garland's thesis (14), i.e., by relatively low pulling speeds, insufficient to reveal the influence of pulling speed on formation of internal defects.

In 2001, the feasibility of pultrusion of small cross-section composite profiles based on glass fiber/urea-formaldehyde composition at the pulling speeds of 200, 400, and 600 mm/min was demonstrated by Chen et al. (16). The study extended the experimental findings reported by Ma et al. (8) on the influence of pulling speed on flexural properties, and confirmed that the increase in pulling speed impairs mechanical properties of pultruded composites, namely, the storage modulus.

Simultaneously, Sarrionandia et al. (17) developed a mathematical model to predict the influence of various process conditions, such as pulling speed, die temperature, laminate thickness, and fiber volume fraction, on performance of a manufacturing process. Authors used the same heat transfer model that was used by Kim et al. (11) and by Valliappan et al. (10), the only difference being the use of the phenomenological autocatalytic model to describe polymerization kinetics. Pultrusion experiments with glass fiber/acrylic-urethane composites were performed at pulling speeds ranging from 100 to 800 mm/min, demonstrating good agreement with the numerical predictions.

Yun and Lee (18) were the first to use the numerical simulation apparatus not only to describe distribution of polymerization degree and temperature during pultrusion ((6; 10; 12; 17)), but to predict the occurrence of internal defects. In 2008 they developed and experimentally validated a model to predict the influence of process variables on the occurrence of bubbles in glass fiber/phenolic 20×10 mm rectangular cross-section composite profiles. The profiles were pultruded at pulling speeds of 95, 190, 285, and 380 mm/min. It was shown that higher pulling speeds resulted in a larger bubble size and lower number of nucleated bubbles. In a follow-up study (19), the authors developed a numerical model to predict the pulling force occurring during pultrusion of phenolic foam profiles. The same pulling speeds were utilized. The authors reported a relationship between the pulling speed and the pulling force.

To find the optimal technological parameters and pulling speed, Chen and Chen (20) performed pultrusion of small cross-section pultruded profiles of glass fiber/furfuryl alcohol. Among the four analyzed values of pulling speed (200, 400, 600, and 800 mm/min), only the three lowest ones were found optimal from the mechanical

properties point of view, thus confirming the results of previous studies, that increase in pulling speed may result in impaired mechanical performance of pultruded composites.

In 2015, Borges et al. (21) conducted the experimental study of pultrusion of glass fiber/polyester \varnothing 13 mm rods at the pulling speed of 460 mm/min to better understand the correlation between the resin bath temperature and tensile strength, elastic modulus, and, previously not analyzed, hardness.

Chiang and Chen (22) in their study produced glass-fiber-reinforced small section profiles based on vinyl ester/nano-mica matrix at pulling speeds of 400, 500, 600, 700, and 800 mm/min and performed their mechanical characterization. Supporting the results of previous studies, it was shown that the increase in pulling speed results in reduced flexural strength, modulus, and hardness. Besides, their study was the first one to demonstrate the reduction of notched Izod impact strength with increase in pulling speed.

While previous studies were dealing with straight pultruded profiles, Tena et al. (23) became the first to investigate the influence of ultraviolet (UV) intensity and pulling speed on the performance of the UV-cured, out-of-die bent pultrusion process. Glass/polyester 10×2 mm rectangular cross-section profiles were produced at pulling speeds of 105, 157, and 210 mm/min, and the optimum pulling speed was found to be 157 mm/min.

Fairuz et al. (24) analyzed the effects of a micro-sized calcium carbonate filler on the mechanical characteristics (tensile, flexural, and compressive) of kenaf fiber/vinyl ester pultruded rods of \varnothing 10 mm, produced at the pulling speed of 4000 mm/min. It should be noted that this is the first study of pultruded composites produced at such a high pulling speed. The results demonstrated that an increase in filler loading provokes an increase in mechanical characteristics. In the follow up study (25) the authors investigated the influence of pulling speed (varied from 100 to 500 mm/min) on mechanical properties of kenaf fiber/vinyl ester composites and determined the optimum pulling speed in terms of tensile, flexural, and compressive characteristics. It was found that specimens made at pulling speed of 300 and 100 mm/min demonstrated the maximum tensile strength and tensile modulus, respectively; the

maximum compressive strength was obtained at pulling speed of 300 mm/min; the maximum flexural strength and flexural modulus were registered for specimens made at 400 and 200 mm/min.

In an attempt to optimize the pulling speed and temperature conditions, and to better understand the phenomenon of surface crack formation, Safonov et al. (26) performed an experimental and numerical study with a pultruded glass fiber/epoxy \varnothing 80 mm rod, manufactured at a pulling speed of 50 mm/min. Although, the pulling speed analyzed in the study is relatively low, this is the first one to study large, industrial-sized rods. Following Yun and Lee (18), this work uses numerical simulation and experimental data to analyze formation of defects in pultruded profiles.

In Tucci et al. (27) a numerical model simulating the impregnation of fibers during injection pultrusion was developed to analyze rectangular glass fiber/epoxy 60×5 mm flat laminates produced at pulling speeds of 300 and 500 mm/min. It was found that number of voids in pultruded composites decreases with increase in pulling speed. In the follow-up study (28) the authors also used numerical simulation and experimental data to study the relationship between pulling force and polymerization of the resin in the injection pultrusion process. The glass fiber/epoxy \varnothing 6 mm pultruded rods were produced at the pulling speeds of 100, 140, 180, and 220 mm/min. The study demonstrated that increase in pulling speed leads to the reduction in composite's cure degree at the die exit and, according to results of microscopic analysis, impairs the quality of manufactured composites.

Thus, the trends in pulling speed / composite quality studies observed by pultrusion researchers can be summarized as follows:

- Experimental studies of pultrusion at various pulling speeds in the range of 12.5 to 4000 mm/min, conducted with profiles of various cross sections: L-shape and I-shape beams, rods, flat laminates, etc.;
- Experimental studies on the influence of pulling speed on mechanical properties, morphology, and formation of internal defects in pultruded composites;
- Development of numerical models of heat transfer, resin curing, pulling force

and pultrusion process, and their successful validation by numerous pultrusion experiments at different pulling speeds; development and experimental validation of models describing occurrence of process-induced defects in relation to selected technological parameters of pultrusion process;

- Experimental demonstration that reduced pulling speeds improve mechanical properties of pultruded composites; in addition, it has been shown that improvement in the mechanical properties can also be achieved by the post-cure treatment;
- Experimental demonstration that the maximum number and quality of profiles are obtained at pulling speeds corresponding to the highest pulling force;
- Demonstration that increase in the pulling speed leads to an increase in the corresponding centerline temperature of the composite, registered at the die exit;
- Demonstration, that degree of polymerization, measured at the die exit for the composites manufactured at low pulling speeds, is higher than that of profiles manufactured at high pulling speeds. However, the polymerization of composites, happening at the post-die region, is significantly higher for profiles manufactured at the high pulling speeds, as compared to those manufactured at lower pulling speeds;
- Experimental demonstration of feasibility of microwave-assisted pultrusion at different pulling speeds, and of the UV-cured out-of-die bent pultrusion process.

One part of this work is a synthesis of experimental study and numerical simulations, where experimental data are used to validate the developed numerical models. Another part investigates the effects of pulling speed on mechanical properties, morphology, and formation of internal defects in pultruded elements. Only a few works are devoted to the study of non-conventional types of pultrusion such as microwave-assisted pultrusion and UV-cured out-of-die bent pultrusion. However, none of the

mentioned studies offer a comprehensive analysis of relationships between pulling speed and structural parameters of pultruded profiles, such as mechanical properties, internal defects, and shape distortions.

Majority of these studies analyze the pultrusion of small cross-section elements and rods produced at regular pulling speeds. The influence of pulling speed on mechanical properties and morphology of large cross-section profiles suitable for structural applications (L-shape (15) and I-shape beams (12), \varnothing 80 mm rods (26), and flat laminates (27)) was analyzed at pulling speeds not exceeding 600 mm/min. A small fraction of experimental studies in high speed pultrusion discussed production of small cross-section profiles such as \varnothing 6 mm (13), \varnothing 10 mm rods (24), and other elements (8; 9; 20; 22). No studies of high speed pultrusion of large cross-section structural profiles have been conducted before. Moreover, no relationships have been established between high pulling speeds and structural performance of large cross-section composite profiles.

1.3.2 Studies investigating the effects of additives

In 1988 Han and Chin (29) developed a numerical model describing the behavior of unsaturated polyester resin during pultrusion. The kinetics of polymerization was modelled using a mechanistic model based on the free radical polymerization method. The authors simulated polymerization of resin systems with one, two, and three initiators, and then compared the efficiency of the two latter resin systems. It was shown that a more uniform distribution of temperature and cure degree in a composite can be achieved with the use of mixed initiators rather than a single one. However, the synergistic effect of initiators onto the polymerization process has not been explained.

The polymerization process of unsaturated polyester resin during pultrusion was described in the study by Ng and Manas-Zloczower (30), with the use of a mechanistic kinetic model. Based on results of the differential scanning calorimetry (DSC), the authors developed the model of the pultrusion process and described the effect of kaolinite and fiberglass on resin polymerization. It was shown that increase in the content of the fillers leads to a decrease both in the rate and peak of exothermic

polymerization reaction.

The effect of concentration of carboxyl-terminated copolymer of butadiene and acrylonitrile liquid rubber on the polymerization kinetics of epoxy resin was studied by Calabrese and Valenza (31). The experimental data obtained from DSC analysis were fitted by the kinetic model and a good correlation was obtained. The authors detected an increase in the reaction rate of the modified resin polymerization caused by the catalytic effect of the additive.

Liang et al. (32) experimentally and numerically confirmed the possibility of the pultrusion process with pure epoxy resin, and its modifications, either by allyl epoxidized soybean oil or by methyl epoxidized soybean oil. These resins were analyzed by DSC and their kinetic constants were determined. It was shown that the addition of allyl epoxidized soybean oil to pure epoxy resin contributes to the increase in the pultrusion performance.

Badrinarayanan et al. (33) studied the effects of boron trifluoride diethyl etherate initiator concentration, varying from 1 wt % to 3 wt %, on polymerization and mechanical properties of a soybean oil/styrene-divinylbenzene resin used in pultrusion. Based on the DSC experiments the authors obtained constants of the kinetic model. It was also found that the maximum values of mechanical properties of resin are achieved at 2 wt % concentration of boron trifluoride diethyl etherate.

Wang et al. (34) experimentally demonstrated the possibility to limit formation of internal cracks in carbon fiber/epoxy resin circular rods by using certain fillers such as ultrafine graphite powder, ground calcium carbonate, ultrafine powder, and ultrafine barium sulfate. They also studied the effect of accelerator concentrations on the reaction rate of polymerization and concluded that reduced concentrations lead to lower polymerization rate and, as a result, to more uniform curing, improving the appearance and impeding propagation of cracks.

Saenz-Dominguez et al. (35) studied the influence of the deep curing and surface curing photoinitiators on the polymerization of vinyl ester resin, which, in turn, affects the mechanical properties of composites produced with the use the out-of-die ultraviolet (UV) cured pultrusion method. The authors have shown that the use of optimal concentrations of said photoinitiators, which is a function of the thickness of

produced composite, makes it possible to significantly increase the interlaminar shear and flexural strength, as well as to reduce the number of voids in the manufactured composites.

There are several issues limiting the application of pultruded structural composites based on vinyl ester resins in the construction sector, with the major ones being the low fire retardancy and high smoke emission. The challenge is to improve composites' fire behavior and to reduce smoke emission when subjected to fire by using flame-retardant additives, such as aluminum hydroxide $\text{Al}(\text{OH})_3$. Another challenge is to reduce the pulling force during pultrusion by reducing the friction between the composite and the die. This can be achieved through the use of internal release agent, such as zinc stearate $\text{Zn}(\text{C}_{18}\text{H}_{35}\text{O}_2)_2$. It should be noted that the use of such agents may impair the physical properties and visual appearance of pultruded structural composites. Besides, the use of flame retardants and internal release agents should not compromise the performance of pultrusion process as well as mechanical characteristics of the manufactured composites. There are earlier studies exploring pultrusion of epoxy and polyester resins modified by different types of additives. However, the influence of flame retardants and internal release agents on the cure kinetics of vinyl ester resins, as well as the choice of the pulling speed, and the profitability of pultrusion process have not been investigated so far. In addition, scholars have failed to investigate the cure kinetic of pultrusion resins comprehensively, since only a small number of known kinetic laws have been used, such as the first-order reaction (F1) (36), the second-order reaction (F2) (37; 38), the n th-order reaction (Fn) (26; 39; 40; 41; 42; 43), the n th-order autocatalytic reaction (Cn) (33), the expanded Prout–Tompkins equation (Bna) (16; 44; 45), and the Kamal–Sourour autocatalytic model (46).

1.3.3 Studies investigating shape distortions

In Wang et al. (47), the numerical model predicting residual stresses and spring-in distortions has been developed and validated through the pultrusion experiment. The contribution of the chemical shrinkage of the polymer matrix to the development of spring-in distortions in pultruded composite was shown to significantly exceed

that of the thermal shrinkage. However, no quantification of these contributions was performed. Moreover, the experimental validation of the developed numerical model was carried out only for one pulling speed of 350 mm/min.

Significant contributions to the state of the art in numerical simulations allowing predictions of process-induced shape distortions and stress analysis were made by Remko Akkerman, Jesper Hattel, and Ismet Baran. Stresses and distortions occurring during the pultrusion of wind turbine blades were modelled by Baran et al. (48). In the subsequent study (49), Baran et al. proposed the pultrusion process model allowing prediction of the temperature and cure degree distribution, as well as the process-induced residual stresses and distortions occurring during pultrusion of thin and thick flat beams. This model utilized the 3D approach to solve the thermochemical problem, and the 2D approach to solve the mechanical problem, based on the Cure Hardening Instantaneous Linear Elastic (CHILE) model. However, no experimental validation of the developed model was performed in the course of the study. One year later, the authors proposed the numerical model (50) that also used the 3D thermochemical and 2D mechanical models to predict spring-in distortions in pultruded L-shaped profiles made of unidirectional rovings and continuous filament mats. Based on the numerical simulation results, the conclusion has been made that an increase in the pulling speed causes an increase in spring-in. However, the validation of the model was carried out only for pulling speed of 600 mm/min. Further on, the relationship between the thickness of pultruded L-shaped profiles and the spring-in value was analyzed in (51). In the follow-up paper, Baran et al. (52) presented a model of a pultrusion process to predict the process-induced warpage in a rectangular hollow profile. The predicted values of warpage show good agreement with those obtained by measuring the pultruded profiles.

One of the main limitations of these studies is the lack of experimental validation of numerical simulation results at more than one pulling speed. Moreover, the authors did not pay much attention to analyzing the reasons of spring-in increase with increasing pulling speed, nor did they study the contributions of thermal and chemical shrinkage to the development of spring-in during the pultrusion process. Besides, the studies gave little attention to the methods of spring-in reduction.

1.4 Novelty and scientific contribution

This Ph.D. project contributes to the pultrusion state-of-the-art and makes another step toward tackling the challenges listed in Section 1.1, by filling the research gaps mentioned in Section 1.3. More specifically, the novelty and scientific contribution of this Ph.D. thesis can be represented as a bulleted list as follows:

- This project is the first attempt to analyze mechanical properties, spring-in, matrix cracking and delaminations as functions of the pulling speed, using a holistic approach. A relationship between these properties and the pulling speed used has been established;
- This work is the first one to demonstrate that high speed pultrusion of large cross-section composite structural profiles is not only feasible, but it also makes it possible to increase production rate by tens of percent at only a slight sacrifice in mechanical performance of pultruded composite structural profiles, as compared to their counterparts produced at regular pulling speeds;
- This study became the first one to develop a numerical model of pultrusion process in the ABAQUS software suite with the use of user subroutine mechanism, making it possible to model the process of spring-in formation in pultruded composite structural profiles produced at different pulling speeds. The model was successfully validated in the course of two experiments conducted at the interval of 6 months, studying pultruded profiles produced at three different pulling speeds. Besides, this work is the first one to study the contributions of chemical and thermal shrinkage leading to spring-in distortions occurred in the pultrusion process. Also, a relationship between these contributions and selected pulling speed was established. Based on contributions of chemical and thermal shrinkage, methods of increasing the process output while preserving the given spring-in value through the use of the post-die cooling tool, or through the use of additives reducing chemical shrinkage of polymer matrix were proposed and analyzed;
- This work is the first one to study time-dependent behavior of process-induced

shape distortions, such as spring-in and warpage pultruded L-shaped composite structural profiles. Besides, it is the first one to study experimentally the influence of pulling speed on the shape distortions increment in time;

- This study is also the first one to study the influence of additives — aluminum hydroxide ($\text{Al}(\text{OH})_3$) flame retardant, and zinc stearate ($\text{Zn}(\text{C}_{18}\text{H}_{35}\text{O}_2)_2$) internal release agent reducing the pulling force — on polymerization kinetics of vinyl-ester pultrusion resins and, in turn, on the choice of pulling speeds;
- Besides, this study is the first one to demonstrate the possibility of producing pultruded composite laminates exhibiting shape memory properties, showing a considerable promise for future structural applications.

1.5 Structure of the thesis

This Ph.D. thesis includes 12 Chapters contributing to the research of the effects of technological regimes on the structural performance of pultruded profiles. The content of the Chapters is briefly described below.

Chapter 1: Introduction.

This Chapter describes the motivation for the research performed in the course of this Ph.D. project. Several technological challenges posed by pultrusion process are outlined. Previous scientific studies investigating the mentioned challenges are discussed and main limitations are highlighted. A brief structure of the Ph.D. thesis is presented.

Chapter 2: Constitutive material behavior.

This Chapter formulates the mathematical model of the pultrusion process, which is a combination of heat transfer and mechanical models. Main governing equations are presented.

Chapter 3: Results.

This Chapter serves as a brief discussion of main results presented in the articles published in the course of this Ph.D. project.

Chapters 4-11.

The articles that have been published in the course of this Ph.D. project are presented in these Chapters.

Chapter 12: Conclusion and outlook.

This Chapter concludes the research performed in the course of this Ph.D. project. Main findings are outlined, and future research possibilities for the scholars and practitioners working in pultrusion are highlighted.

Chapter 2

Constitutive material behavior

In this Chapter, a thermomechanical initial boundary value problem (IBVP) predicting the response of a body to applied temperature loads is discussed. The solution of such problem makes it possible to predict stresses and shape distortions occurring during pultrusion manufacturing. However, to accomplish these goals, two problems should be solved in resin polymerization modelling, namely, the heat transfer problem (Section 2.1) and the mechanical problem (Section 2.2). As the properties of resin and, therefore, of composite material depend on the temperature, in order to solve this IBVP, the distribution of temperature and polymerization degree should be modelled with the Equations (2.1) – (2.12) of 2D heat transfer model presented in Section 2.1. Then, based on results obtained and using the equations presented in 2.2, it is possible to determine cure- and temperature-dependent Young's modulus (Equations (2.13) and (2.14)), bulk modulus (Equations (2.15) and (2.16)), and Poisson's ratio (Equation (2.17)) of the resin. These mechanical properties of the resin are to be used further to calculate mechanical properties of a composite, based on the Self-Consistent Field Micromechanics (SCFM) approach (53; 54). Finally, obtained mechanical properties of a composite should be used to determine the stress-strain state in the composite (Section 2.3).

Earlier, it was shown that axial conduction can be neglected when solving the heat transfer problem (55). Also, no significant differences were found in the distributions of stresses and displacements in the transverse direction, obtained in 2D and 3D simulations of mechanical behavior (56). Thus, to accelerate computations,

a two-dimensional model was used to solve the thermochemical and mechanical problems. However, these assumptions may result in overestimated values of thermal peak. Besides, the 2D approach makes it impossible to account for stresses, occurring along the longitudinal axis of the profile and causing additional shape distortions in the pulling direction. However, as will be shown in Chapter 9, these assumptions are reasonable and will not result in large discrepancy between predicted and experimental spring-in data.

2.1 2D heat transfer model

The steady-state pultrusion process with a pulling speed of u is considered. By disregarding the heat conduction along the length of the composite profile, the heat transfer equation in a Lagrangian (material) frame of reference can be expressed as follows (55):

$$C_{p_comp}(T)\rho_{comp}\frac{\partial T}{\partial t} = k_{comp}\frac{\partial^2 T}{\partial x^2} + k_{comp}\frac{\partial^2 T}{\partial y^2} + q \quad (2.1)$$

where x and y are the coordinates of the cross-section of the composite profile, T is instantaneous temperature, $C_{p_comp}(T)$ is the temperature-dependent heat capacity of a composite material, ρ_{comp} is the composite density, k_{comp} is the thermal conductivity of the composite in the cross-sectional plane, and q is the heat released due to the exothermic reaction in a polymer matrix.

The temperature-dependent heat capacity of a composite material $C_{p_comp}(T)$ is obtained as (55):

$$C_{p_comp}(T) = C_{p_f}w_f + C_{p_r}(T)(1 - w_f) \quad (2.2)$$

where C_{p_f} is the heat capacity of fibers, $C_{p_r}(T)$ is the temperature-dependent heat capacity of resin, and w_f is the fiber mass fraction calculated as (55):

$$w_f = \frac{V_f}{V_f + \frac{\rho_r}{\rho_f}(1 - V_f)} \quad (2.3)$$

$$\frac{1}{\rho_{comp}} = \frac{w_f}{\rho_f} + \frac{(1 - w_f)}{\rho_r} \quad (2.4)$$

where V_f is the fiber volume fraction, ρ_r is the density of resin, ρ_f is the density of fibers, ρ_{comp} is the density of a composite.

As the heat Equation 2.1 is expressed in the Lagrangian (material) frame of reference, the pulling speed (u), absent in Equation 2.2, affects the boundary condition Equations 2.5 and 2.6, corresponding to the position of the composite profile cross-section inside or outside the die, respectively:

$$k_{comp} \frac{\partial T}{\partial n} \Big|_{\Gamma} = -h_{die}(T - T_{die}(z)) \text{ at } z = ut < L_{die} \quad (2.5)$$

$$k_{comp} \frac{\partial T}{\partial n} \Big|_{\Gamma} = -h_{air}(T - T_{amb}(z)) \text{ at } z = ut \geq L_{die} \quad (2.6)$$

where Γ is the surface of the profile, h_{die} is the coefficient of convective heat transfer between the die block and the profile, h_{air} is the coefficient of convective heat transfer between the air and the profile after the die block exit, T_{die} is the temperature of the die block, varying in the pulling direction z , and T_{amb} is the ambient temperature. The stage inside the die block was modelled with account for convective heat exchange instead of the thermal contact, in accordance with the state-of-the-art approach to modelling of pultrusion heat transfer problem, described by Batch (55). For this purpose, a sufficiently high value of the coefficient of convective heat transfer between the die block and the profile (h_{die}), constituting $5000 \text{ W}/(\text{m}^2 \cdot \text{K})$, was assumed.

Thermal conductivity of unidirectional composite in longitudinal ($k_{comp_ud_long}$) and transverse ($k_{comp_ud_trans}$) direction are obtained as (41):

$$\frac{1}{k_{comp_ud_long}} = \frac{w_f}{k_{f_long}} + \frac{1 - w_f}{k_r} \quad (2.7)$$

$$\frac{1}{k_{comp_ud_trans}} = \frac{w_f}{k_{f_trans}} + \frac{1 - w_f}{k_r} \quad (2.8)$$

where k_{f_long} and k_{f_trans} are thermal conductivities of fibers in longitudinal

and transverse direction, k_r is the thermal conductivity of the resin.

Assuming the temperature of the composite at the die block entrance, T_{in} to be uniform over the entire cross-section, it can be expressed as follows:

$$T \Big|_{t=0} = T_{in} \quad (2.9)$$

The internal heat released due to the exothermic reaction of the resin polymerization (q) of the Equation 2.1 can be expressed as:

$$q = (1 - V_f)\rho_r H_{tot} \frac{d\alpha}{dt} \quad (2.10)$$

where V_f is the volume fraction of reinforcement in a composite, ρ_r is the resin density, H_{tot} is total heat released during curing, and $\frac{d\alpha}{dt}$ is the resin curing rate.

To describe the rate of resin polymerization, the equation of the n th-order autocatalytic reaction is used (57):

$$\frac{d\alpha}{dt} = A_0 e^{-\frac{E_a}{R(T + 273.15)}} (1 - \alpha)^n (1 + K_{cat}\alpha) \quad (2.11)$$

where A_0 is the pre-exponential coefficient, E_a is the activation energy, R is the universal gas constant, T is the instantaneous temperature of the resin in degrees Celsius, n is the order of reaction, and K_{cat} is the activation constant.

It is assumed that preheating the material before the entrance into the die block will not result in its polymerization; hence, the degree of polymerization at the die block entrance is taken to be zero:

$$\alpha \Big|_{t=0} = 0 \quad (2.12)$$

2.2 2D mechanical model

2.2.1 Calculation of instantaneous mechanical properties of the resin

Based on the results obtained in Section 2.1, it is possible to determine cure- and temperature-dependent Young's modulus (Equations 2.13 and 2.14), bulk modulus (Equations 2.15 and 2.16), and Poisson's ratio (Equation 2.17) of the resin. It is assumed that after the gelation point ($\alpha_{gel}=0.6$) the resin starts gaining Young's modulus (E_r) and becomes able to sustain stresses. To account for changes in the Young's modulus of the resin during the polymerization process and to describe the mechanical behavior of the resin, the Cure Hardening Instantaneous Linear Elastic (CHILE) model is used in its modified form (58):

$$E_r = \begin{cases} E_r^0 & \text{if } T^* \leq T_{c1} \\ E_r^0 + \frac{T^* - T_{c1}}{T_{c2} - T_{c1}}(E_r^1 - E_r^0) & \text{if } T_{c1} < T^* < T_{c2} \\ E_r^1 + \frac{T^* - T_{c2}}{T_{c3} - T_{c2}}(E_r^2 - E_r^1) & \text{if } T_{c2} < T^* < T_{c3} \\ E_r^2 + \frac{T^* - T_{c3}}{T_{c4} - T_{c3}}(E_r^3 - E_r^2) & \text{if } T_{c3} < T^* < T_{c4} \\ E_r^3 + \frac{T^* - T_{c4}}{T_{c5} - T_{c4}}(E_r^4 - E_r^3) & \text{if } T_{c4} < T^* < T_{c5} \\ E_r^4 + \frac{T^* - T_{c5}}{T_{c6} - T_{c5}}(E_r^\infty - E_r^4) & \text{if } T_{c5} < T^* < T_{c6} \\ E_r^\infty & \text{if } T_{c6} \leq T^* \end{cases} \quad (2.13)$$

where $T^* = T_g(\alpha) - T$ is the difference between the instantaneous glass transition temperature ($T_g(\alpha)$) and the instantaneous temperature (T) of the resin in degrees Celsius; T_{c1} , T_{c2} , T_{c3} , T_{c4} , T_{c5} , and T_{c6} are the critical temperatures in degrees Celsius, and E_r^0 , E_r^1 , E_r^2 , E_r^3 , E_r^4 , and E_r^∞ are the corresponding elastic moduli. $T_g(\alpha)$ is the glass transition temperature depending on the degree of cure, expressed as follows (59; 60):

$$T_g(\alpha) = T_{g0} + (T_{g\infty} - T_{g0}) \frac{\lambda\alpha}{1 - (1 - \lambda)\alpha} \quad (2.14)$$

where T_{g0} is the glass transition temperature of the uncured resin ($\alpha=0$) and $T_{g\infty}$ is the glass transition temperature of the fully cured resin ($\alpha=1$), λ is the material parameter.

To account for changes in Poisson's ratio during resin polymerization, it should be noted that the bulk modulus of resin has the same order of magnitude in both rubber-like and glassy states (61). According to Svanberg (62), the bulk modulus of the matrix decreases by the factor of 2.5 during the transition from the glassy (K_r^∞) to the rubber-like state (K_r^0). By determining the bulk modulus of the matrix in glassy and rubber-like states based on the linear elastic theory (Equation 2.15) (61), the instantaneous bulk modulus of the matrix (K_r) and the corresponding Poisson's ratio (ν_r) can be determined using Equations 2.16 and 2.17, accordingly:

$$K_r^\infty = \frac{E_r^\infty}{3(1 - 2\nu_r^\infty)} \quad (2.15)$$

$$K_r(E_r) = K_r^0 + (K_r^\infty - K_r^0) \frac{E_r - E_r^0}{E_r^\infty - E_r^0} \quad (2.16)$$

$$\nu_r(E_r) = \frac{3K_r - E_r}{6K_r} \quad (2.17)$$

2.2.2 Calculation of composite effective mechanical properties of unidirectional laminate

The relationships for the calculation of the unidirectional composite effective mechanical properties are defined in accordance with Self-Consistent Field Micromechanics (SCFM) approach, based on the instantaneous mechanical properties of fiber (E_{1f} is Young's modulus of fiber reinforcement in longitudinal direction, ν_{12f} is Poisson's ratio of fiber reinforcement in longitudinal direction, G_{12f} is shear modulus of fiber reinforcement in longitudinal direction, ν_{23f} is Poisson's ratio of fiber reinforcement in transverse direction, k_f is isotropic plane strain bulk modulus of fiber, V_f is fiber volume fraction) and the resin (E_r is instantaneous resin modulus, ν_r is instantaneous Poisson's ratio of resin, G_r instantaneous is shear modulus of resin,

k_r is instantaneous isotropic plane strain bulk modulus of resin) (63; 64). Young's modulus of unidirectional composite in longitudinal direction is calculated as:

$$E_1 = E_{1f}V_f + E_r(1 - V_f) + \frac{4(\nu_r - \nu_{12f}^2)k_f k_r G_r (1 - V_f)V_f}{(k_f + G_r)k_r + (k_f - k_r)G_r V_f} \quad (2.18)$$

where the isotropic plane strain bulk modulus of fiber (k_f) and resin (k_r) are calculated from:

$$k_f = \frac{E_{1f}}{2(1 - \nu_{12f} - 2\nu_{12f}^2)} \quad (2.19)$$

$$k_r = \frac{E_r}{2(1 - \nu_r - 2\nu_r^2)} \quad (2.20)$$

the shear moduli of the unidirectional composite are expressed as:

$$G_{12} = G_{13} = G_r \frac{(G_{12f} + G_r) + (G_{12f} - G_r)V_f}{(G_{12f} + G_r) - (G_{12f} - G_r)V_f} \quad (2.21)$$

$$G_{23} = \frac{G_r[k_r(G_r + G_{23f}) + 2G_{23f}G_r + k_r(G_{23f} - G_r)V_f]}{k_r(G_r + G_{23f}) + 2G_{23f}G_r - (k_r + 2G_r)(G_{23f} - G_r)V_f} \quad (2.22)$$

$$G_{23f} = \frac{E_{3f}}{2(1 + \nu_{23f})} \quad (2.23)$$

subsequently, the Young's moduli of unidirectional composite in transverse direction are given as:

$$E_2 = E_3 = \frac{1}{(4k_T)^{-1} + (4G_{23})^{-1} + (\nu_{12}^2/E_1)} \quad (2.24)$$

where k_T is the effective plane strain bulk modulus obtained from:

$$k_T = \frac{(k_f + G_r)k_r + (k_f - k_r)G_r V_f}{(k_f + G_r) - (k_f - k_r)V_f} \quad (2.25)$$

finally, the Poisson's ratios of unidirectional composite are calculated from:

$$\nu_{12} = \nu_{13} = \nu_{12f}V_f + \nu_r(1 - V_f) + \frac{(\nu_r - \nu_{12f})(k_r - k_f)G_r(1 - V_f)V_f}{(k_f + G_r)k_r + (k_f - k_r)G_rV_f} \quad (2.26)$$

$$\nu_{23} = \frac{2E_1k_T - E_1E_2 - 4\nu_{12}^2k_TE_2}{2E_1k_T} \quad (2.27)$$

2.2.3 Calculation of composite effective mechanical properties of quasi-isotropic composite laminate

The relationships used to calculate the effective mechanical properties of the quasi-isotropic composite laminate are presented as in (64; 65; 66). Where E_1 , E_2 are Young's moduli of composite in longitudinal and transverse direction, G_{12} , G_{23} are the in-plane and out-of-plane shear moduli, ν_{12} , ν_{23} are the in-plane and out-of-plane Poisson's ratios. First of all, mentioned properties are calculated as effective mechanical properties of unidirectional laminate, using the Self-Consistent Field Micromechanics (SCFM) approach with the same volume fraction of reinforcement as in the case of the quasi-isotropic laminate (67). These properties are then used to calculate effective mechanical properties of quasi-isotropic laminate. First, the in-plane Young's moduli of quasi-isotropic composite are obtained as:

$$E_x = E_y = 2(1 + \nu_{xy})G_{xy} \quad (2.28)$$

then, the in-plane Poisson's ratio of quasi-isotropic composite:

$$\nu_{xy} = \frac{-\frac{1}{2}G_{12} + \frac{1}{8} \frac{E_1(E_1 + E_2 + 6\nu_{12}E_2)}{E_1 - \nu_{12}^2} E_2}{\frac{1}{2}G_{12} + \frac{1}{8} \frac{E_1(3E_1 + 3E_2 + 2\nu_{12}E_2)}{E_1 - \nu_{12}^2} E_2} \quad (2.29)$$

the in-plane shear modulus of quasi-isotropic composite is derived from:

$$G_{xy} = \frac{1}{2}G_{12} + \frac{1}{8} \frac{E_1(E_1 + E_2 - 2\nu_{12}E_2)}{E_1 - \nu_{12}^2} E_2 \quad (2.30)$$

while the out-of-plane Young's modulus of quasi-isotropic composite is obtained from:

$$E_z = \frac{E_1 + (1 + 2\nu_{12})E_2}{(1 - \nu_{23}^2)\frac{E_1}{E_2} + (1 + 2\nu_{12} + 2\nu_{12}\nu_{23}) - \nu_{12}^2\frac{E_2}{E_1}} \quad (2.31)$$

and, subsequently, the out-of-plane Poisson's ratio of quasi-isotropic composite is calculated:

$$\nu_{xz} = \nu_{yz} = \frac{E_x}{E_1} \frac{(\nu_{12} + \nu_{23} + \nu_{12}\nu_{23}) + \nu_{12}^2\frac{E_1}{E_2}}{1 + (1 + 2\nu_{12})\frac{E_2}{E_1}} \quad (2.32)$$

and the out-of-plane shear modulus of quasi-isotropic composite can be found as:

$$G_{xz} = 2\left(\frac{G_{12}G_{23}}{G_{12} + G_{23}}\right) \quad (2.33)$$

2.2.4 Calculation of thermal strain

The in-plane coefficient of thermal expansion of the unidirectional composite can be calculated as follows (63):

$$\alpha_1 = \frac{\alpha_{1f}E_{1f}V_f + \alpha_r E_r(1 - V_f)}{E_{1f}V_f + E_r(1 - V_f)} \quad (2.34)$$

where α_r is the coefficient of thermal expansion of the resin, α_{1f} , α_{2f} are the coefficients of thermal expansion of fiber reinforcement in longitudinal and transverse direction.

The out-of-plane coefficients of thermal expansion of the unidirectional composite are obtained as (63):

$$\alpha_2 = \alpha_3 = (\alpha_{2f} + \nu_{12f}\alpha_{1f})V_f + \alpha_r(1 + \nu_r)(1 - V_f) - (\nu_{12f}V_f + \nu_r(1 - V_f))\alpha_1 \quad (2.35)$$

at the same time the in-plane coefficients of thermal expansion of the quasi-isotropic composite are (67):

$$\alpha_x = \alpha_y = \frac{(E_1 + \nu_{12}E_2)\alpha_1 + (1 + \nu_{12})E_2\alpha_2}{E_1 + (1 + 2\nu_{12})E_2} \quad (2.36)$$

and the out-of-plane coefficient of thermal expansion of the quasi-isotropic composite is obtained (67):

$$\alpha_z = \frac{(\nu_{12}E_2 - \nu_{23}E_1)\alpha_1 + ((1 + \nu_{23})E_1 + (1 + \nu_{12}E_2)\alpha_2)}{E_1 + (1 + 2\nu_{12})E_2} \quad (2.37)$$

subsequently, the incremental effective thermal strain of the composite is derived from:

$$\Delta\varepsilon_i^{th} = \alpha_i\Delta T \quad (2.38)$$

2.2.5 Calculation of chemical strain

The incremental specific volume shrinkage of the resin is calculated as (63):

$$\Delta V_r = \Delta\alpha V_{sh} \quad (2.39)$$

where $\Delta\alpha$ is the change in the degree of cure, V_{sh} is the total volumetric resin shrinkage.

Subsequently, the isotropic incremental resin shrinkage strain is obtained as (63):

$$\Delta\varepsilon_r = \Delta V_r/3 \quad (2.40)$$

then, the effective in-plane incremental chemical shrinkage strain of the unidirectional composite is derived as (63):

$$\Delta\varepsilon_1^{ch} = \frac{\Delta\varepsilon_r E_r (1 - V_f)}{E_{1f} V_f + E_r (1 - V_f)} \quad (2.41)$$

and the effective out-of-plane incremental chemical shrinkage strain of the unidirectional composite as (63):

$$\Delta\varepsilon_2^{ch} = \Delta\varepsilon_3^{ch} = \Delta\varepsilon(1 + \nu_r)(1 - V_f) - (\nu_{12f} V_f + \nu_r(1 - V_f))\Delta\varepsilon_1^{ch} \quad (2.42)$$

at the same time, the effective in-plane incremental chemical shrinkage strain of

the quasi-isotropic composite is calculated as (67):

$$\Delta\varepsilon_x^{ch} = \Delta\varepsilon_y^{ch} = \frac{(E_1 + \nu_{12}E_2)\Delta\varepsilon_1^{ch} + (1 + \nu_{12})E_2\Delta\varepsilon_2^{ch}}{E_1 + (1 + 2\nu_{12})E_2} \quad (2.43)$$

and the effective out-of-plane incremental chemical shrinkage strain of quasi-isotropic composite is obtained as (67):

$$\Delta\varepsilon_z^{ch} = \frac{(\nu_{12}E_2 - \nu_{23}E_1)\Delta\varepsilon_1^{ch} + ((1 + \nu_{23})E_1 + (1 + \nu_{12})E_2)\Delta\varepsilon_2^{ch}}{E_1 + (1 + 2\nu_{12})E_2} \quad (2.44)$$

2.3 Stress-strain analysis

The effective mechanical properties of the composite, obtained in Section 2.2, are then used to find the Jacobian matrix (\mathbf{J}) (49). Subsequently, in the case of orthotropic material, the incremental stress tensor ($\Delta\sigma_{ij}$) is calculated based on the Jacobian matrix (\mathbf{J}) and the incremental mechanical strain tensor ($\Delta\varepsilon_{ij}^{mech}$) (63), (68).

First, the total incremental strain is derived as:

$$\Delta\varepsilon_{ij}^{tot} = \Delta\varepsilon_{ij}^{mech} + \Delta\varepsilon_{ij}^{th} + \Delta\varepsilon_{ij}^{ch} \quad (2.45)$$

and the incremental process-induced strain as:

$$\Delta\varepsilon_{ij}^{pr} = \Delta\varepsilon_{ij}^{th} + \Delta\varepsilon_{ij}^{ch} \quad (2.46)$$

then, the incremental mechanical strain is calculated as:

$$\Delta\varepsilon_{ij}^{mech} = \Delta\varepsilon_{ij}^{tot} - \Delta\varepsilon_{ij}^{pr} \quad (2.47)$$

subsequently, the incremental stress tensor is obtained as:

$$\Delta\sigma_{ij} = \mathbf{J}\Delta\varepsilon_{ij}^{mech} \quad (2.48)$$

finally, at the end of each increment the update of the stress and strains tensors

is taking place as following:

$$\varepsilon_{ij}^{n+1} = \varepsilon_{ij}^n + \Delta\varepsilon_{ij}^n \quad (2.49)$$

$$\sigma_{ij}^{n+1} = \sigma_{ij}^n + \Delta\sigma_{ij}^n \quad (2.50)$$

Chapter 3

Results

In this Chapter the synopsis of main results obtained in the course of this Ph.D. project are presented, while complete results can be found in Chapters 4–11. The literature review of thermoset pultruded materials and structures is presented in Chapter 4, with the aim to analyze the applications and mechanical properties of pultruded FRPs, and to outline future research possibilities. It is then followed by Chapter 5, where a review of the criteria and guidelines adopted for the design of pultruded structural elements is presented. The relationship between the pulling speed and structural performance of L-shaped pultruded profiles is discussed in Chapter 6, while the effects of high pulling speed on mechanical properties and morphology of pultruded flat laminates are analyzed in Chapter 7. The temperature-dependent specific heat and the thermal conductivity of the resin are determined in Chapter 8. The obtained results are then used in Chapter 9, where the numerical model predicting the spring-in distortions occurring in L-shaped profiles pultruded at different pulling speeds is developed and successfully validated against the experimental results obtained previously in Chapter 6. The mathematical model of pultrusion process is then employed in Chapter 10 to establish the relationship between the composition of vinyl ester pultrusion resin (modified with the flame retardants, such as aluminum hydroxide $\text{Al}(\text{OH})_3$, and internal release agents, such as zinc stearate $\text{Zn}(\text{C}_{18}\text{H}_{35}\text{O}_2)_2$) and its curing behavior, and the choice of the necessary pulling speed. Finally, the thermomechanical and thermophysical properties of the cured epoxy resin, affecting its shape memory behavior, were determined in Chapter 11.

These properties will be used for further numerical simulations and optimization of the pultrusion process.

3.1 Pultruded materials and structures: A review

The analysis of main applications of pultruded structural profiles, such as bridges and bridge decks, cooling towers, building elements, and complete building systems, marine structures, transportation and energy systems, is presented in Chapter 4. The scientific publications dealing with the mechanical behavior of pultruded elements are discussed, and the future research possibilities are highlighted, giving the researchers and practitioners the directions for further investigation of specific features of pultruded FRP composites.

The studies discussed in Chapter 4 show that pultruded FRPs, owing to their particular advantages over traditional materials, provide a wide range of possibilities to designers. The huge variety of products and their characteristics demonstrate the high versatility of pultrusion process. The enhanced mechanical performance of pultruded elements promotes their use as a competitive alternative to conventional construction materials of civil buildings and structures.

3.2 Design criteria for pultruded structural elements

Chapter 5 is dedicated to the review of the criteria and guidelines adopted for the design of pultruded structural elements. Design codes make it possible to build civil engineering structures with a high level of safety and confidence. Currently, the construction market is experiencing rapid growth in FRP applications. In some countries, the development of relevant standards and guidelines has begun as early as in 1980s'. The development starts from the review of differences in mechanical and physical properties of composites and conventional materials. The performance uncertainty of FRPs can be significantly reduced by the introduction of common-based testing procedures together with material identification schemes. Today, a

single set of guidelines can be developed, as there is sufficient theoretical and practical experience accumulated, owing to the FRP-based projects realized all over the world. The development of standards and codes is an ongoing process, which is even expected to accelerate in the forthcoming years.

Peculiarities of the pultrusion process and the nature of composites impose certain limitations on the quality of the final product, namely, process-induced shape distortions and residual stresses. Therefore, part of the elements produced will not be able to pass quality control, while another part will require extra shimming operations during the assembly process, which may impair mechanical performance of pultruded structures. Hence, a more optimized design should account for these geometrical deviations. Although, experimental and numerical studies addressing the mentioned problems are currently underway, there is a lack of studies relating technological parameters and composite architecture with the resultant process-induced shape distortions.

3.3 Effects of pulling speed on structural performance of L-shaped pultruded profiles

In Chapter 6, an experimental research is conducted to reveal the influence of pulling speed on the structural characteristics of pultruded glass fiber/epoxy-vinyl-based L-shaped profiles of $75 \times 75 \times 6$ mm. The profiles were manufactured at three pulling speeds: 200 (V-200), 400 (V-400), and 600 (V-600) mm/min. The values of spring-in in produced profiles were measured at regular intervals of two to three days during the period of 90 days, starting on the day of manufacture, at cross-sections located at 150 mm intervals. An optical microscope was used to analyze the cross-sections of profiles, in order to assess the number, size, and location of cracks and delaminations. A series of mechanical tests of pultruded profiles was conducted to evaluate the strength and Young's modulus under compression, tension, flexure, in-plane shear, and interlaminar shear loading.

During the pultrusion experiments, at each pulling speed after reaching a steady state, 5 m long sections of the profile were pultruded with a thermocouple embedded

in the material (between the unidirectional rovings and fabric layer) to measure the temperature evolutions, cure rate, and cure degree of the material, relative to the thermocouple position (see Fig. 3.1).

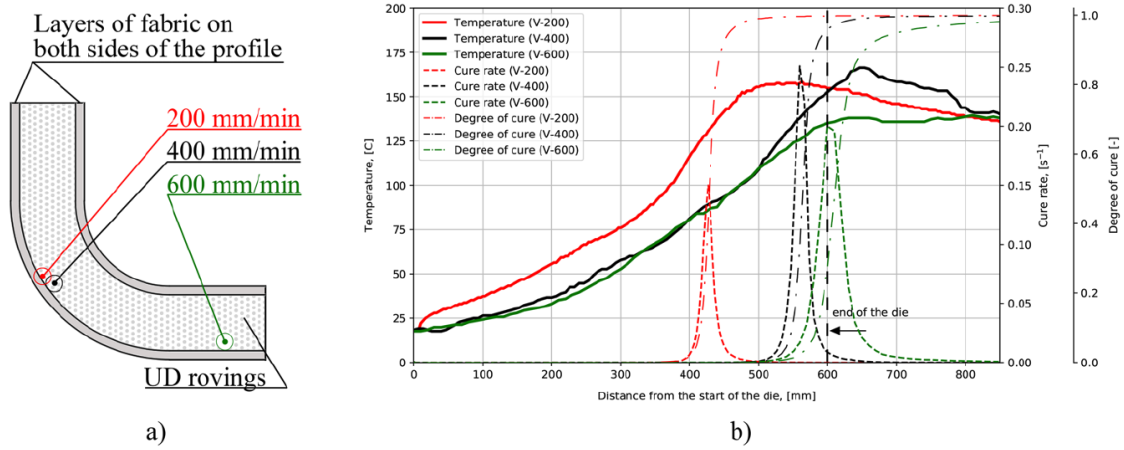


Figure 3.1: Internal structure (i.e., placement of the thermocouples, UD rovings, and fabric layers) of the pultruded profile and the evolution of the temperature of the composite, as measured by the thermocouples: (a) Thermocouple placement; (b) Evolution of the temperature (solid line), degree of curing (dashed-dotted line), and cure rate (dashed line). The line color corresponds to the pulling speed: red (V-200), black (V-400), or green (V-600).

At the lower pulling speeds (V-200 and V-400), the polymerization peak was located within the die block, while at the highest pulling speed (V-600) the peak position shifted to the post-die region. Further, while the temperature distributions and cure degree evolutions were similar for the V-200 and V-400 profiles, they differed significantly from those of the V-600 sample. These factors explain the principal distinctions between the considered profiles. The structural performance (i.e., the spring-in distortions, matrix cracking, and mechanical characteristics) of the V-200 and V-400 profiles was also similar, differing from that of the V-600 profile.

As can be seen from Fig. 3.2, the initial value of spring-in also depended on the pulling speed: the higher the speed, the larger the spring-in angle. Further, higher speeds (V-400 and V-600) resulted in more significant variations in the spring-in at all cross-sections taken along the profile, and the absolute increase in spring-in was greater for the higher pulling speeds (V-400 and V-600) than for the lowest one (V-200). Therefore, a manufacturer should account not only for the value of the initial spring-in but also for its absolute growth over time. The profiles produced at higher speeds may meet geometrical tolerance requirements immediately after

manufacture, but fail to do so after storage.

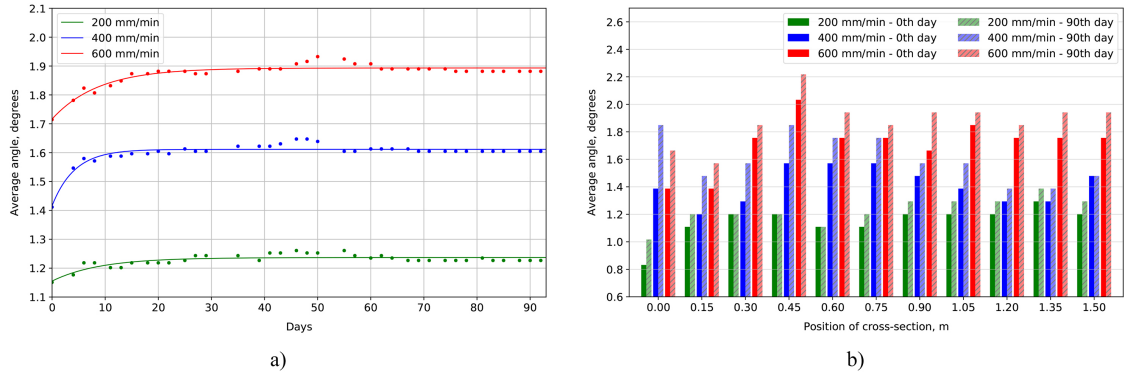


Figure 3.2: Spring-in evolutions for the different pulling speeds of 200, 400, and 600 mm/min: (a) The average value of the spring-in over 90 days; (b) Initial and final values of the spring-in at the cross-sections along the 1.5 m long profile sections.

The V-200 and V-400 specimens exhibited similar matrix cracking behaviors, having similar numbers, locations, and sizes of matrix cracks (see Fig. 3.3). Increasing the pulling speed (i.e., V-600) resulted in the formation of considerably larger delaminations perpendicular to the matrix cracks, due to the polymerization peak being shifted beyond the die block exit. According to the research conducted by Awaja et al. (69), who discussed the thermal treatment of already cured composites, the formation and development of cracks can be dictated by the presence of air bubbles initially trapped in the composite. The expansion of these bubbles caused by heating provokes the formation of cracks and their propagation. During the pultrusion process, the evaporation of styrene gas could be observed in the die block and post-die regions. The phenomenon was more pronounced at higher pulling speeds and could contribute to the occurrence of delaminations in the V-600 profiles.

During the mechanical testing, results of which are presented in Table 3.1, similar values of strength and Young's modulus in tension and compression were obtained for all specimens. However, the V-600 specimens demonstrated a distinctly lower level of flexural stress at breaking, as compared to the V-200 and V-400 specimens (29% and 33% lower, respectively). Additionally, when tested perpendicular to the fiber orientation, the interlaminar shear stress of the V-600 specimens was considerably lower than that of the V-200 and V-400 specimens (by 35% and 33%, respectively). Moreover, the highest pulling speed (V-600) resulted in the broader spread of the

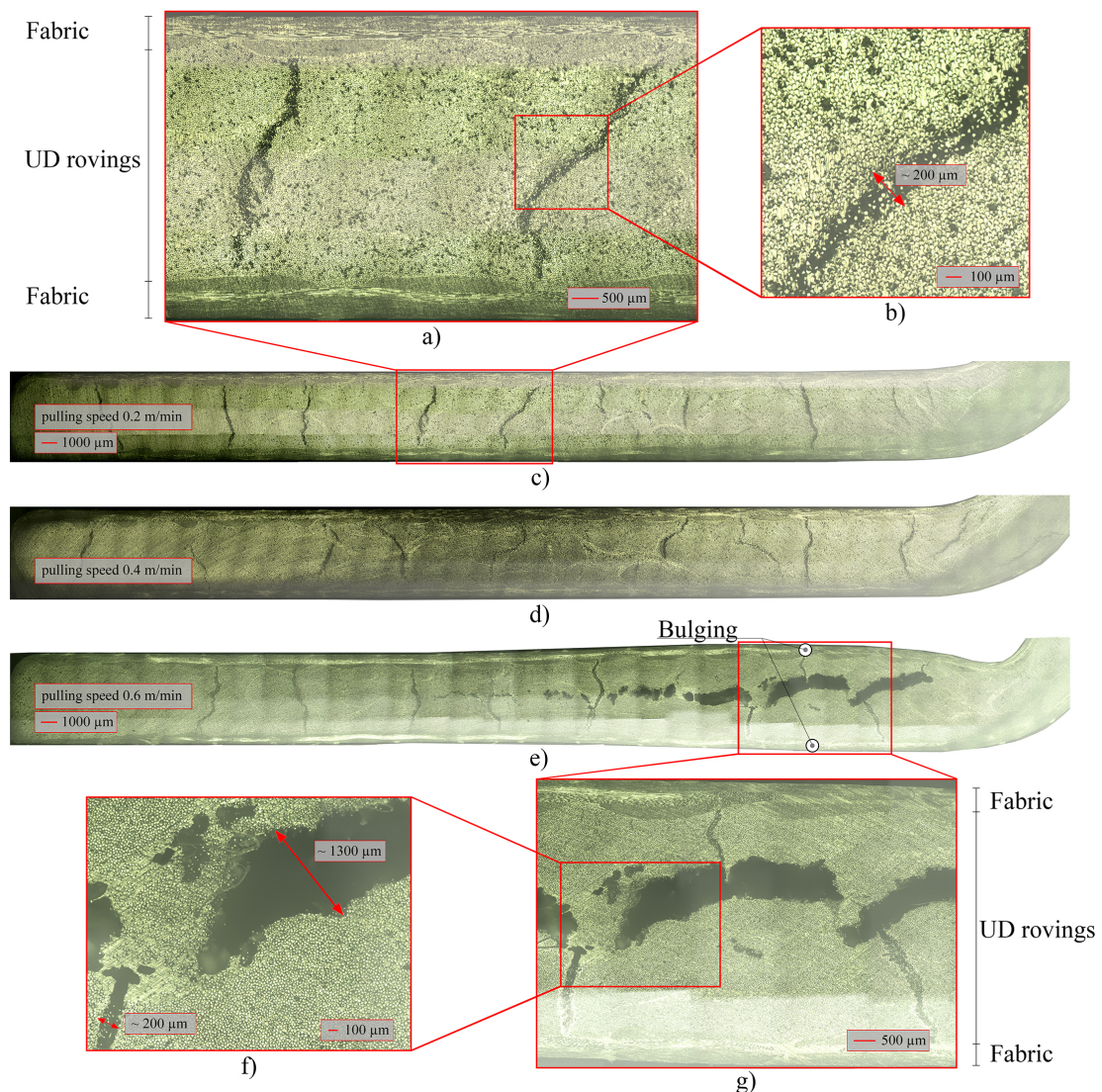


Figure 3.3: Microphotographs of the cross-sections of the V-200, V-400, and V-600 profiles that were cut transverse to the pultrusion direction: (a) Position of the matrix cracks (V-200). Scale bar = 500 μm ; (b) Size of matrix cracks (V-200). Scale bar = 100 μm ; (c) Distribution of the matrix cracks on half of the profile V-200. Scale bar=1000 μm ; (d) Distribution of the matrix cracks on half of the profile V-400. Scale bar=1000 μm ; (e) Distribution of the matrix crack and delaminations on half of the profile V-600, showing the bulging areas. Scale bar = 1000 μm ; (f) Size of the matrix crack and delaminations on the V-600 profile. Scale bar = 100 μm ; (g) Position of the matrix crack and delaminations on the V-600 profile. Scale bar = 500 μm .

strength and shear modulus values because the standard deviation was significantly higher than for the V-200 and V-400 profiles. This could be attributed to the large number of internal defects observed in the V-600 specimens. The shift of the polymerization peak to the post-die region resulted in the major part of the curing reaction taking place in a constraint-free conditions (in regards to the profile). If

distortions arise outside the die block when the polymerization is incomplete (as in V-600), significantly more internal defects and shape distortions will manifest themselves, for example, as thicker cracks and delaminations in the roving area. The opposite could be observed at the lower pulling speeds, wherein the thermal peaks were located within the die block boundary; the hard contact constraints imposed by the metal surfaces of the die block prevented excessive profile distortions.

Table 3.1: Results of the mechanical tests in compression, tension, flexure, and in-plane and interlaminar shear.

Specimen	Compression		Tension		Flexure		In-plane shear		Interlaminar shear	
	Strength [MPa]	Elastic Modulus [GPa]	Strength [MPa]	Elastic Modulus [GPa]	Strength [MPa]	Modulus of elasticity in bending [GPa]	Strength [MPa]	Shear Modulus [GPa]	Strength in 0° direction [MPa]	Strength in 90° direction [MPa]
V-200	502 ± 38.3	42.8 ± 2.7	396 ± 18.2	44.6 ± 3.5	658 ± 65.6	34.6 ± 1.7	40.7 ± 1.9	2.62 ± 0.13	22.7 ± 1.7	6.7 ± 0.76
V-400	445 ± 35.5	41.8 ± 2.8	412 ± 27.2	45.9 ± 4.2	697 ± 68.1	34.7 ± 2.9	43.1 ± 1.6	2.66 ± 0.42	24.1 ± 1.2	7.4 ± 1.25
V-600	427 ± 59.9	43.5 ± 3.1	408 ± 48.5	42.9 ± 4.1	464 ± 124	33.7 ± 2.2	45.0 ± 2.7	2.87 ± 0.15	22.9 ± 3.6	4.33 ± 1.93

Results of this paper show that the shift of the polymerization peak toward the post-die region significantly reduces structural properties of pultruded profiles. Thus, researchers and engineers aiming to increase the profitability of the pultrusion process must pay attention to the thermal peak position and ensure its position right before the die exit.

3.4 Effects of high pulling speeds on mechanical properties and morphology of pultruded GFRP composite flat laminates

In Chapter 7, an experimental study was performed to establish the relationship between high pulling speeds and the mechanical properties and morphology of pultruded glass fiber/epoxy-vinyl flat laminates of 150×3.5 mm. The profiles were produced at four pulling speeds: 200 (V-200), 600 (V-600), 1000 (V-1000), and 1400 mm/min (V-1400). The cross-section cuts of manufactured composites were studied

by optical and scanning electron microscopy (SEM). Series of mechanical experiments to determine the flexural and interlaminar shear properties of the composite specimens with 0° and 90° fiber orientations were performed.

At high pulling speeds of 1000 mm/min (Fig. 3.6) and 1400 mm/min (Fig. 3.7) glass fiber rovings pass through the impregnation bath much faster than at pulling speeds of 200 mm/min (Fig. 3.4) and 600 mm/min (Fig. 3.5). Consequently, the resin has less time to penetrate the rovings. This results in poor impregnation of rovings and formation of air inclusions and dry spots, which, in turn, causes formation of internal defects significantly impairing structural performance of pultruded composites (70). Moreover, at high pulling speeds the polymerization peak shifts to the post-die region as there is less time for the composite to polymerize within the die block boundaries. Thus, a considerable part of polymerization process occurs in unconstrained conditions. This results in formation of severe internal defects (longitudinal voids and matrix cracks) caused by the chemical and thermal shrinkage of the unconstrained composite. The increase in the dimensions, severity, and propagation of internal defects can also be attributed to the expansion of air bubbles initially trapped in a composite (69). The evaporation of styrene gas, i.e., unreacted styrene monomer, observed at the die block exit region during high speed pultrusion process, may cause severe longitudinal voids and branched matrix cracks in the V-1400 profiles. Conversely, at regular pulling speeds (200 and 600 mm/min), resin has more time to properly impregnate fiber reinforcement, and air inclusions are significantly less frequent than at high pulling speeds. This reduces the number of internal defects formed during pultrusion process. Besides, the rigid contact constraints of the die block where the polymerization peak occurs prevent excess profile distortions and formation of severe internal defects.

3.4. Effects of high pulling speeds on mechanical properties and morphology of pultruded GFRP composite flat laminates

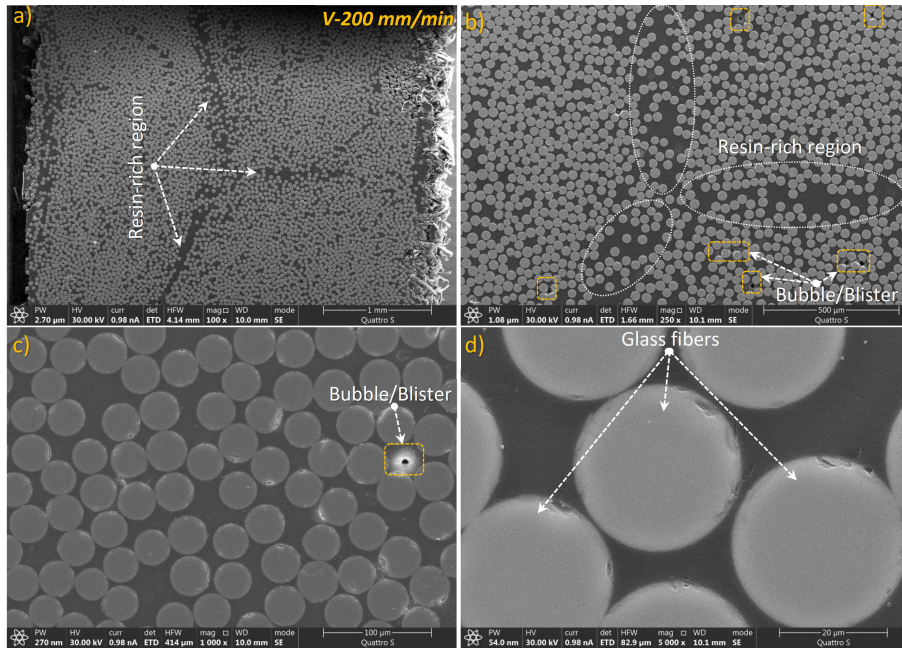


Figure 3.4: SEM images of the V-200 laminate cross-section cut perpendicular to the pulling direction: (a) The entire cross-section of the composite and resin-rich regions at 100x magnification; (b) Resin-rich regions and bubbles and blisters at 250x magnification; (c) Glass fibers and bubble/blister at 1000x magnification; (d) Glass fibers at 5000x magnification.

3.4. Effects of high pulling speeds on mechanical properties and morphology of pultruded GFRP composite flat laminates

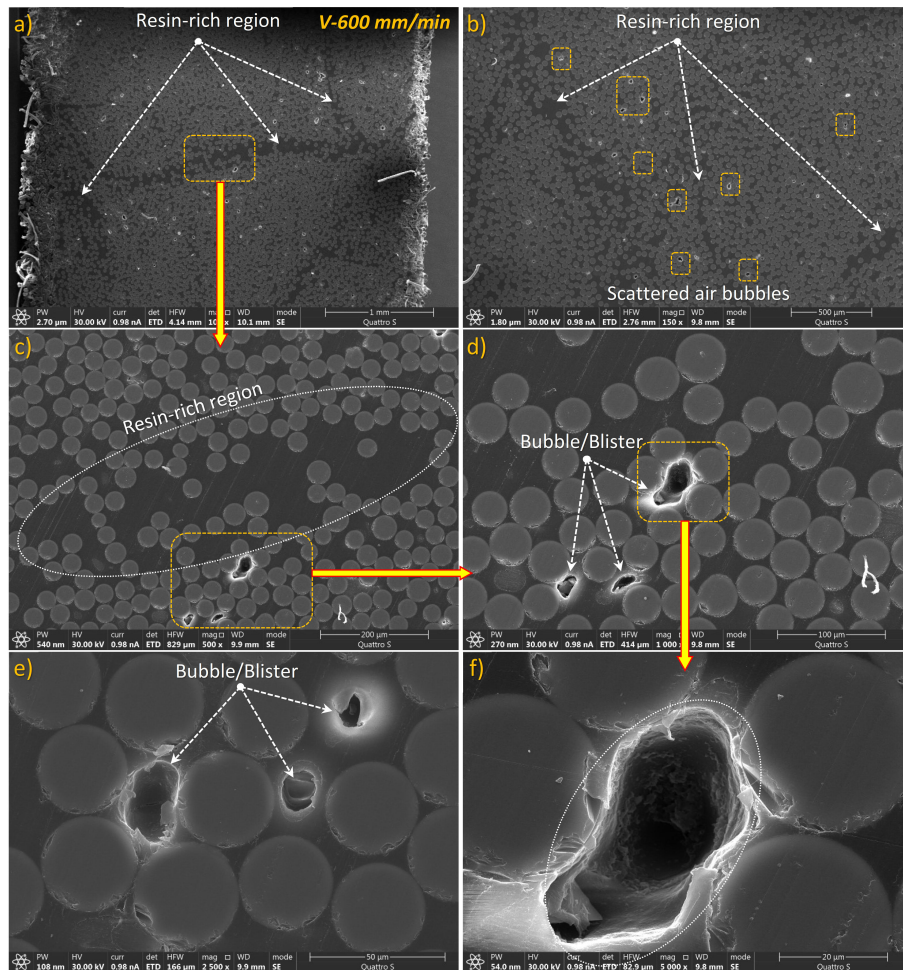


Figure 3.5: SEM images of the V-600 laminate cross-section cut perpendicular to the pulling direction: (a) The entire cross-section of the composite and resin-rich regions at 100x magnification; (b) Resin-rich regions and scattered air bubbles at 150x magnification; (c) Resin-rich region and bubbles/blisters at 500x magnification; (d) Bubbles/blisters at 1000x magnification; (e) Glass fibers and bubbles/blisters at 2500x magnification; (f) Bubble/blister at 5000x magnification.

3.4. Effects of high pulling speeds on mechanical properties and morphology of pultruded GFRP composite flat laminates

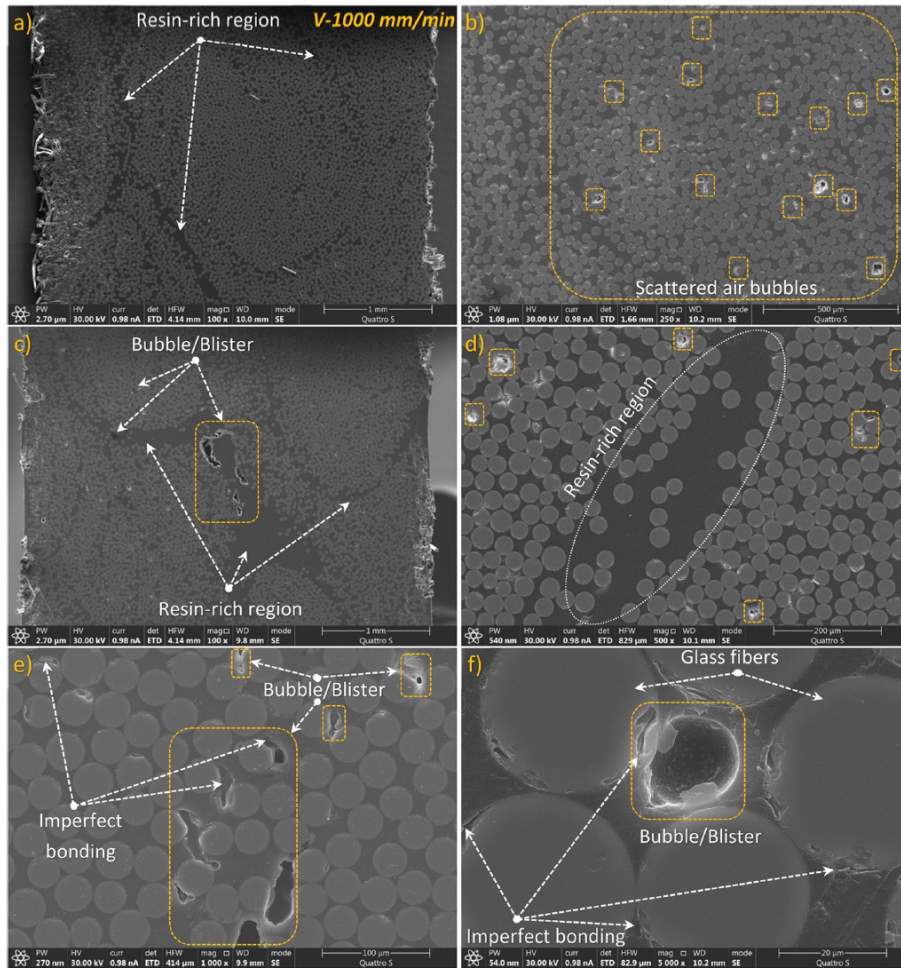


Figure 3.6: SEM images of the V-1000 laminate cross-section cut perpendicular to the pulling direction: (a) The entire cross-section of the composite and resin-rich regions at 100x magnification; (b) Scattered air bubbles at 250x magnification; (c) The entire cross-section of the composite, resin-rich regions, and bubbles/blisters at 100x magnification; (d) Resin-rich region and bubbles/blisters at 500x magnification; (e) Glass fibers, imperfect bonding, and bubbles/blisters at 1000x magnification; (f) Glass fibers and bubbles/blisters at 5000x magnification.

3.4. Effects of high pulling speeds on mechanical properties and morphology of pultruded GFRP composite flat laminates

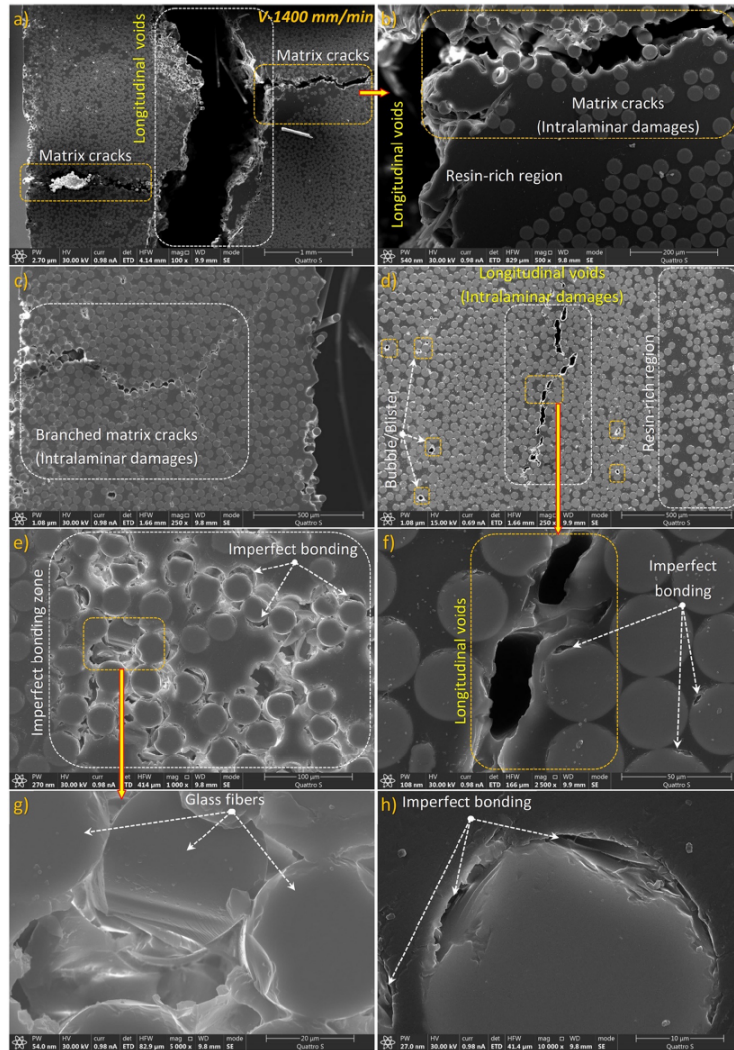


Figure 3.7: SEM images of cross-section of the V-1400 flat laminate cut perpendicular to the pulling direction: (a) The entire cross-section of the composite. Matrix cracks and longitudinal voids at 100x magnification; (b) Matrix cracks, longitudinal voids, and resin-rich region at 500x magnification; (c) Branched matrix crack at 250x magnification; (d) Scattered bubbles/blister, longitudinal voids, and resin-rich region at 250x magnification; (e) Imperfect bonding zone at 1000x magnification; (f) Longitudinal voids and imperfect bonding at 2500x magnification; (g) Glass fibers at 5000x magnification; (h) Imperfect bonding at 10000x magnification.

The results of the mechanical tests (Table 3.2) show that the increased number and severity of process-induced defects caused by the increased pulling speed impair the mechanical performance of the composite laminates. The effect of such defects, particularly in the matrix component of the composite, was more evident in the flexural testing of the specimen in the 90° fiber orientation. The considerably larger standard deviation of certain mechanical properties of the V-1400 specimens, compared with those of the V-200/V-600/V-1000 specimens, clearly demonstrates the influence of internal defects on the structural performance of composite laminates.

Table 3.2: Results of the mechanical tests in flexure and interlaminar shear.

Specimen	Flexure												Interlaminar shear					
	0° fiber orientation						90° fiber orientation						0° fiber orientation			90° fiber orientation		
	Strength [MPa]			Tangent modulus of Elasticity [GPa]			Strength [MPa]			Tangent modulus of Elasticity [GPa]			Interlaminar fracture toughness at maximum load [MPa]			Short beam strength [MPa]		
	Mean	σ	CV [%]	Mean	σ	CV [%]	Mean	σ	CV [%]	Mean	σ	CV [%]	Mean	σ	CV [%]	Mean	σ	CV [%]
V-200	1473	54	3.7	51.78	1.46	2.81	23.49	1.94	8.25	14.57	1.08	7.41	37.10	2.04	5.49	3.12	0.29	9.34
V-600	1307	141	10.8	50.29	2.87	5.71	22.56	1.68	7.45	12.12	0.62	5.11	35.50	2.44	6.88	2.60	0.51	19.63
V-1000	1260	193	15.3	49.52	4.06	8.20	21.71	2.23	10.28	11.97	0.37	3.09	32.10	3.73	11.60	2.56	0.55	21.35
V-1400	1170	463	39.6	48.23	5.83	12.08	2.24	1.03	46.07	0.34	0.30	85.80	30.20	4.00	13.23	2.00	0.54	27.19

This work pioneers the use of high pulling speeds (1000 mm/min) to produce pultruded composite profiles of large cross-section, suitable for structural applications. High pulling speeds make it possible to increase pultrusion output by at minimum 1.7 times without compromising the mechanical performance of produced profiles as compared to their regular speed produced counterparts.

3.5 Modelling and experimental validation of thermoset resin curing during pultrusion

Cure modelling of the Atlac 430 vinyl ester resin and experimental validation of the model were performed in Chapter 8. Temperature-dependent specific heat of the resin was determined by differential scanning calorimetry (DSC) and the relationship between the temperature and thermal conductivity of the resin was established. These parameters were then used for numerical simulation of the pultrusion heat

transfer problem in ABAQUS software. The temperature and cure degree evolutions obtained from the pultrusion experiments at different pulling speeds of 200, 400, and 600 mm/min, and those obtained from the numerical model were shown to be correlated.

The results of the temperature-dependent specific heat as well as thermal conductivity of the resin experimental evaluation are presented in Table 3.3. According to equation 3.1, the first-order polynomial was then used for the approximation of temperature dependent resin specific heat experimental results:

$$C_p = 5.1T + 1080 \quad (3.1)$$

where T represents the instantaneous temperature of the resin; C_p is instantaneous specific heat of the resin.

The correlation between resin thermal conductivity and temperature is found to be weak. Therefore, resin thermal conductivity is considered to be independent from the temperature and adopted as the average value of experimental results equal to 0.177 W/(m·K).

Table 3.3: Temperature dependence of resin specific heat and thermal conductivity.

Temperature [°C]	Measured value of specific heat			Measured value of thermal conductivity		
	C_{p1}	C_{p2}	$C_{average}$	λ_1	λ_2	$\lambda_{average}$
	[J/(kg·K)]	[J/(kg·K)]	[J/(kg·K)]	[W/(m·K)]	[W/(m·K)]	[W/(m·K)]
20	1181	1199	1190	0.1730	0.1761	0.1746
30	1227	1241	1234	0.1741	0.1718	0.1730
40	1277	1290	1284	0.1773	0.1704	0.1739
50	1333	1339	1336	0.1800	0.1769	0.1785
60	1386	1384	1385	0.1802	0.1787	0.1795
70	1430	1421	1425	0.1773	0.1784	0.1779
80	1476	1461	1468	0.1793	0.1765	0.1779
90	1538	1518	1528	0.1796	0.1785	0.1791
100	1628	1610	1619	0.1823	0.1817	0.1820

Figure 3.8 represents the evolution of composite's temperature and cure degree as functions of coordinate measured in the pulling direction of pultrusion starting from the die entrance. Since the most significant part of the polymerization process happens within the die, only 600 mm length is considered. The solid line represents the results of mathematical modelling, while the dashed line is related to the

experimentally obtained values. Good correlation between numerical and experimental results for all the pulling speeds is observed. The thermochemical model of pultrusion presented above is considered to be experimentally validated.

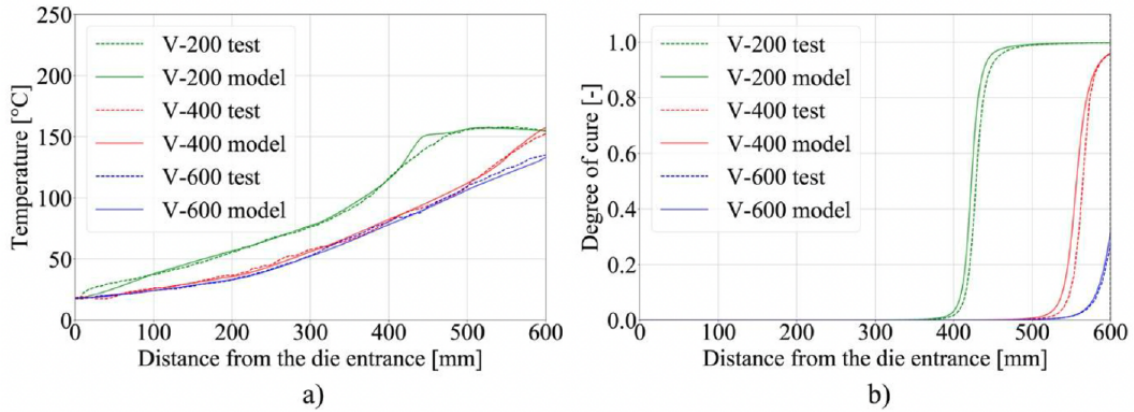


Figure 3.8: Comparison of modelling and experimental results. (a) Evolution of composite's temperature; (b) Evolution of composite's cure degree.

The values of temperature-dependent specific heat as well as thermal conductivity of the resin were then used for the numerical modelling of spring-in occurrence performed in Chapter 9.

3.6 Modeling spring-in of L-shaped structural profiles pultruded at different pulling speeds

Numerical model that is able to predict spring-in in $75 \times 75 \times 6$ mm L-shaped profiles pultruded at different pulling speeds was developed in Chapter 9. This model was developed in the ABAQUS finite-element package utilizing user subroutines such as UMAT, FILM, USDFLD, HETVAL, and UEXPAN. The 2D approach was used to solve both heat transfer and mechanical problems. The Young's modulus of resin was described via the modified Cure Hardening Instantaneous Linear Elastic (CHILE) model. The results of the numerical model were compared against the data collected from two experiments. One of the experiments is described in Chapter 6 and in (71), where glass fiber/epoxy-vinyl resin $75 \times 75 \times 6$ mm L-shaped profiles were produced at pulling speeds of 200, 400, and 600 mm/min. The obtained experimental results correlate well with the spring-in values calculated by means of the

developed numerical model. Based on this model, the possibility of achieving the same level of spring-in at increased pulling speeds from 200 to 900 mm/min, either by using a post-die cooling tool or by reducing the chemical shrinkage of the resin, is demonstrated.

Figure 3.9 shows the simulation results obtained with the model described in Chapter 2. It demonstrates the final spring-in values obtained at different pulling speeds, together with the experimental values of spring-in for pulling speeds of 200, 400, and 600 mm/min. The predicted values fall between corresponding experimental data points. A slight decrease in spring-in values from 1.15° to 1.12° can be observed with the reduction in pulling speed from 200 to 100 mm/min. Starting from 200 mm/min, the increase in pulling speed results in a considerable increase in spring-in values. Thus, the increase in pulling speed from 200 to 1000 mm/min results in an over 3 times increase in spring-in (from 1.15° to 3.60°). Figure 3.9a also shows the fraction of uncured matrix material ($\alpha < 85\%$) within the cross-section of the profile after the die exit. It can be seen that the increase in the fraction of uncured material at the die exit corresponds to an increase in the final values of spring-in. Thus, at the pulling speed of 200 mm/min, the exothermic peak is located inside the die block, and the composite exits the die block fully cured (see Fig. 3.9a), giving the final spring-in value of 1.15° . The increase in pulling speed forces the exothermic peak further along the pultrusion line, beyond the die block exit. Thus, at pulling speeds of 600 mm/min and 1000 mm/min, the fraction of uncured resin within the cross-section of the profile constitutes 31% and 81%, resulting in final spring-in values of 1.69° and 3.60° (see Fig. 3.9a), respectively.

Spring-in formation in the post-die region takes place in three stages (Fig. 3.9b). Starting from the pulling speed of 400 mm/min, the largest contribution to the increase in final spring-in comes from the Stage I (solid line) which corresponds to spring-in changes from the moment the profile exits the die block and to the moment of exothermic peak occurrence (marked by the bold cross). The second contribution comes from the Stage II (dotted and dashed line) which corresponds to spring-in changes from the moment of the exothermic peak and to the vitrification point (marked by the bold point). The lowest contribution to spring-in development

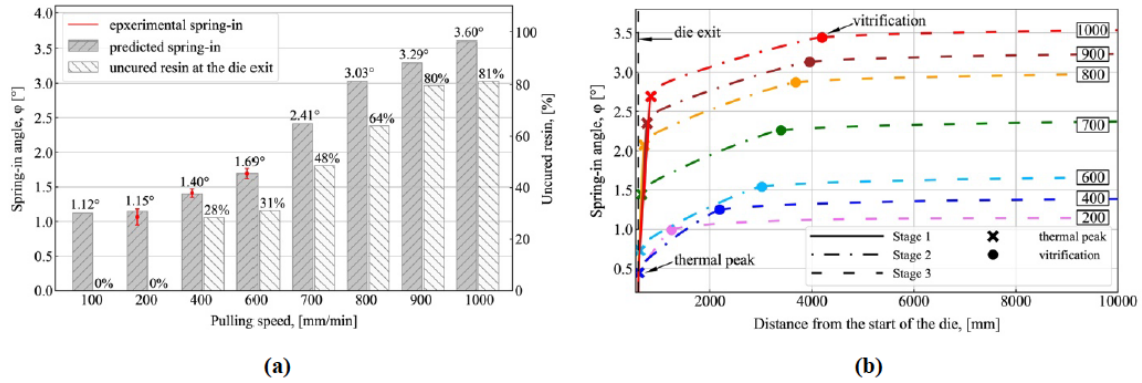


Figure 3.9: Numerical simulation results: (a) Final values of spring-in vs. fraction of uncured resin ($\alpha < 85\%$) at the die exit for different pulling speeds; (b) Spring-in evolution during fabrication for different pulling speeds. The solid lines in (b) correspond to Stage I (spring-in evolutions from the moment the profile exits the die block to the exothermic peak occurrence); the dot-dash line corresponds to Stage II (from the exothermic peak occurrence to the vitrification point); the dashed line corresponds to Stage III (after vitrification and to the full cooldown of the profile); the bold cross marks the occurrence of the exothermic peak; the bold point marks the vitrification point; the values shown in rectangles correspond to pulling speed (mm/min).

comes from the Stage III (dashed line) which corresponds to spring-in changes after vitrification and to the full cooldown of the profile. The increase in pulling speed raises the contribution from the Stage I and reduces the role of the Stage II, while the contribution from the Stage III remains unchanged. Therefore, the final value of spring-in depends on the position of the exothermic peak and vitrification point on the pultrusion line, relative to the end of the constrained region of the die, which, in turn, is determined by the selected pulling speed. The closer the exothermic peak position to the constrained region of the die, the lower the obtained spring-in values. Alternatively, higher spring-in values can be observed with the increase in the distance of the peak from the die exit because the composite can no longer sustain stresses from chemical shrinkage in the unconstrained environment of the post-die region. It was shown that higher pulling speeds result in a higher fraction of uncured material in a composite exiting the constrained environment of the die block. This leads to an increase in the total chemical shrinkage of the material under unconstrained conditions and, hence, results in increased values of spring-in.

Hence, to increase the process output, the capability is needed to reduce the contributions from chemical and thermal shrinkages to trade the slight increase in spring-in for a significant increase in pulling speed. The spring-in can be reduced by installing a post-die cooling tool or by using additives that reduce chemical

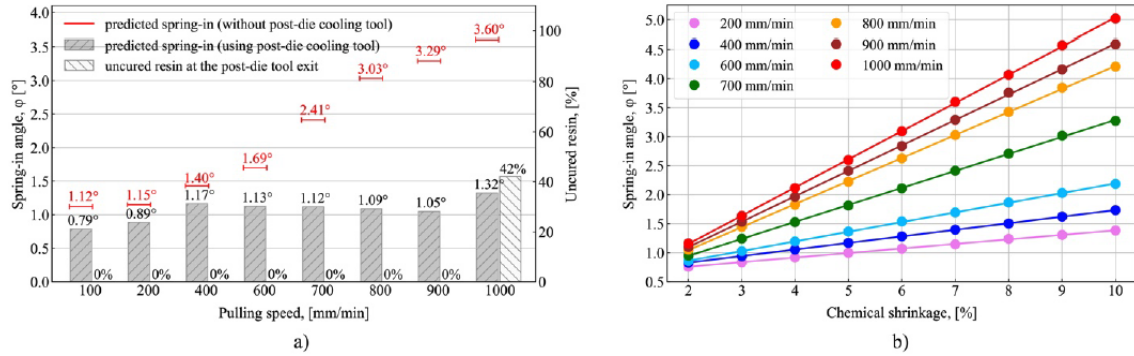


Figure 3.10: Simulation results for methods of spring-in reduction: (a) With the use of a post-die cooling tool. Gray columns mark the spring-in values obtained with the use of the post-die cooling tool; red lines indicate values obtained without the post-die cooling tool. The corresponding fraction of uncured resin ($\alpha < 85\%$) is shown at the bottom of the graph; (b) Spring-in vs. chemical shrinkage of the resin at different pulling speeds (for shrinkage values within the range of 2 to 10%).

shrinkage of the resin (carbon nanofibers (72), silica nanoparticles (73), aluminum oxide nanoparticles (74), and low-profile additives (75)). Fig. 3.10 shows the results of simulations conducted to estimate the efficiency of methods reducing the spring-in in composite parts, such as the use of a post-die cooling tool (Fig. 3.10a), and the reduced chemical shrinkage of the matrix (Fig. 3.10b). Fig. 3.10a shows results of spring-in simulation in L-shaped profiles pultruded at different pulling speeds with the use of a rigid post-die cooling tool with a length constituting $1/3$ of that of the die block ($L_{die}/3$), which was installed in a pultrusion manufacturing line immediately after the exit of the heated die block.

The use of a post-die cooling tool makes it possible to significantly increase the process output by increasing the pulling speed without increasing the final spring-in value. Thus, using the post-die cooling tool at the pulling speed of 900 mm/min makes it possible to obtain the same level of spring-in as at 200 mm/min without the cooling tool. Thus, the pulling speed can be increased by a factor of 4.5, while maintaining the same level of spring-in, i.e., 1.05° and 1.15° , respectively (see Fig. 3.10a). The efficiency of this method can be explained by the smaller fraction of uncured material exiting the constrained environment. This, in turn, results in a reduction in the total chemical shrinkage of a profile under unconstrained conditions. Thus, at 900 mm/min, the final value of spring-in obtained with the use of the post-die cooling tool is 1.05° , which is 3.1 times less than that obtained without the use

of a cooling tool, where the final spring-in constitutes 3.29°.

Reduction of the total chemical shrinkage is also a very effective method of reducing the spring-in, which plays an important role in the case of resins featuring high chemical shrinkage because the difference between the final values of spring-in at different pulling speeds becomes more evident at higher values of chemical shrinkage. Thus, for resins with chemical shrinkage of 10%, the final values of spring-in obtained at pulling speeds of 200 mm/min and 1000 mm/min differ by a factor of 3.6, i.e. 1.39° and 5.02°, respectively. For resins with 2% chemical shrinkage, the corresponding values differ only by a factor of 1.5, i.e., 0.76° and 1.16°, respectively. In addition, at a pulling speed of 1000 mm/min, the use of additives to reduce the chemical shrinkage of resin from 7 to 2% makes it possible to obtain the level of spring-in equal to that of a resin with a chemical shrinkage of 7% without additives, at a pulling speed of 200 mm/min. That is, the pulling speed can be increased by as much as five times, maintaining constant spring-in values of 1.16° and 1.15°, respectively (see Fig. 3.10b).

This study is the first one to isolate and evaluate the contributions of thermal and chemical shrinkage into spring-in evolution in pultruded profiles. The study provides insight into the factors significantly affecting the spring-in, and it analyzes the methods of spring-in reduction that can be used by scholars to minimize the spring-in in the pultrusion process.

3.7 Effects of additives on the cure kinetics of vinyl ester pultrusion resins

Chapter 10 shows the influence of aluminum hydroxide $\text{Al}(\text{OH})_3$ flame retardant additive, and zinc stearate $\text{Zn}(\text{C}_{18}\text{H}_{35}\text{O}_2)_2$ internal release agent on the cure kinetics of vinyl ester pultrusion resin (Atlac 430) and, as a consequence, on the choice of pultrusion pulling speed. Four different resin compositions were studied: neat resin composition, composition with $\text{Al}(\text{OH})_3$, composition comprising $\text{Zn}(\text{C}_{18}\text{H}_{35}\text{O}_2)_2$, and composition containing both $\text{Al}(\text{OH})_3$ and $\text{Zn}(\text{C}_{18}\text{H}_{35}\text{O}_2)_2$. These compositions were designated as M-I, M-II, M-III and M-IV hereafter. To analyze each compo-

sition, differential scanning calorimetry (DSC) at the heating rates of 5, 7.5, and 10 K/min was performed. The obtained results were then fitted by 16 different kinetic models, performances of which has been compared. Subsequently, a numerical simulation of a flat laminate pultrusion was performed using different heating temperatures and pulling speeds. The results made it possible to correlate the presence of the additives and the curing behaviors of resin compositions. Moreover, the maximum pulling speeds of pultrusion process for all compositions were found based on the curing time of the resin subjected to isothermal heating at 115, 120, 125, and 130 °C.

Results show that the presence of processing additives significantly affects the curing behavior of resin compositions (Fig. 3.11). For instance, the addition of $\text{Al}(\text{OH})_3$ (M-II) reduced the amount of released heat by 29%, whereas the addition of $\text{Zn}(\text{C}_{18}\text{H}_{35}\text{O}_2)_2$ (M-III) increased the amount of heat by 35%. However, the addition of both $\text{Al}(\text{OH})_3$ and $\text{Zn}(\text{C}_{18}\text{H}_{35}\text{O}_2)_2$ (M-IV) had almost no effect on the amount of heat released.

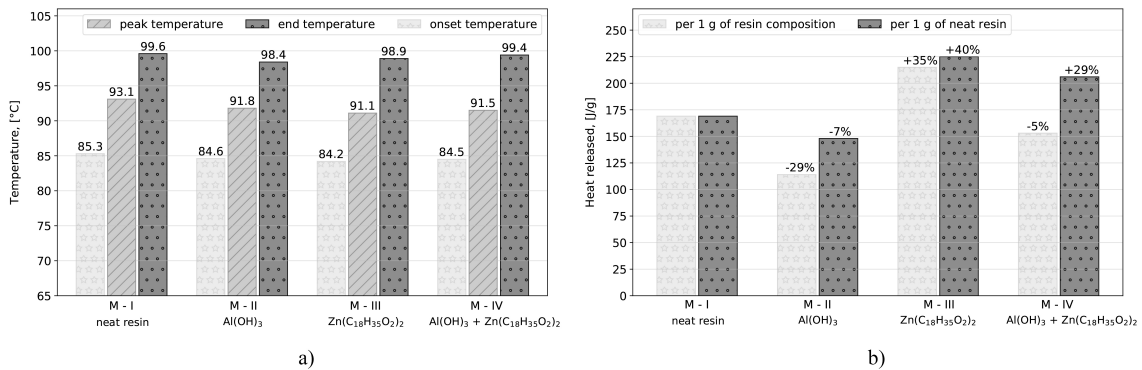


Figure 3.11: Effects of processing additives on the polymerization behaviors of M-I, M-II, M-III, and M-IV:(a) Onset, peak, and end temperatures at a heating rate of 5 K/min and (b) Average amount of heat released.

Moreover, as compared to the M-I composition, the polymerization peak values for the M-II composition, obtained at 5, 7.5, and 10 K/min, were lower by 10, 36, and 33%, respectively (Fig. 3.12). Simultaneously, the addition of $\text{Zn}(\text{C}_{18}\text{H}_{35}\text{O}_2)_2$ (M-III) resulted in a shift (by 9 s at 10 K/min, 15 s at 7.5 K/min, and 24 s at 5 K/min) and earlier occurrence of the polymerization peak. The difference between the exothermic peak values of M-III and M-I compositions constituted 30% at 5 K/min, 16% at 7.5 K/min, and 3% at 10 K/min.

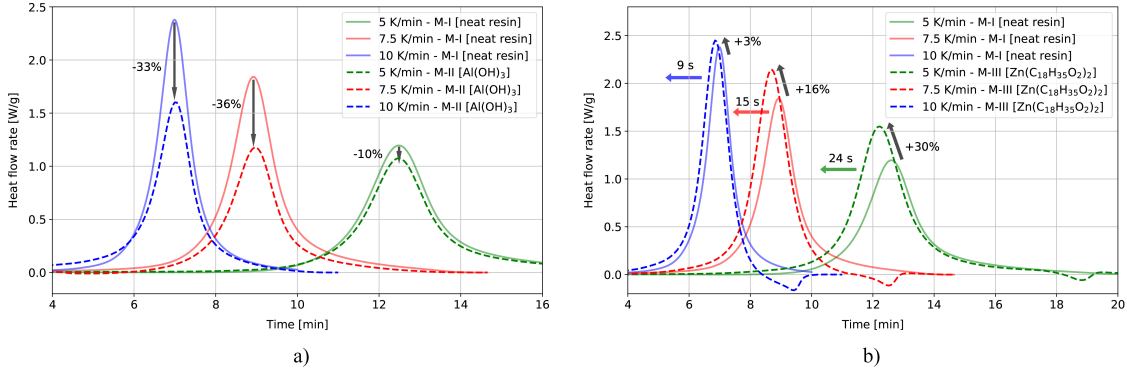


Figure 3.12: Effect of processing additives on the polymerization behaviors of resin compositions: (a) MI vs M-II and (b) M-I vs. M-III.

In the attempt to describe the experimental data of DSC, the performance of 16 phenomenological kinetic models was tested, among which the model based on the n th-order autocatalytic reaction (76) (see Equation (3.2)) demonstrated the best results, with a 4.5% mean squared error (MSE) between the experimental and predicted data. The obtained kinetic constants were then used to simulate the pultrusion of flat laminate.

$$\frac{d\alpha}{dt} = Ae^{-\frac{E_a}{RT}}(1-\alpha)^n(1+K_{cat}\alpha) \quad (3.2)$$

where $\frac{d\alpha}{dt}$ is the cure rate of vinyl ester, T is the absolute temperature, R is the universal gas constant, A is a pre-exponential coefficient, E_a is the activation energy, n is the order of reaction, and K_{cat} is the activation constant.

Numerical simulations were carried out for the pulling speeds of 600 and 1000 mm/min (Fig. 3.13). Two isothermal curing processes were considered: at 115 °C (Fig. 3.13a and 3.13c) and 125 °C (Fig. 3.13b and 3.13d). As can be seen, the curing of M-II is the slowest process, whereas curing of M-III is the fastest. The difference between the final cure degrees of these compositions under isothermal conditions at 115 °C was 5.4% at 600 mm/min (Fig. 3.13a) and 15.4% at 1000 mm/min (Fig. 3.13c). The resin composition with a cure degree exceeding 0.95 is considered to be completely polymerized. Thus, at 600 mm/min (Fig. 3.13a), three specimens of acceptable quality were obtained (with the cure degree of 0.959, 0.985, and 0.975 for M-I, M-III, and M-IV, respectively); however, at 1000 mm/min (Fig.

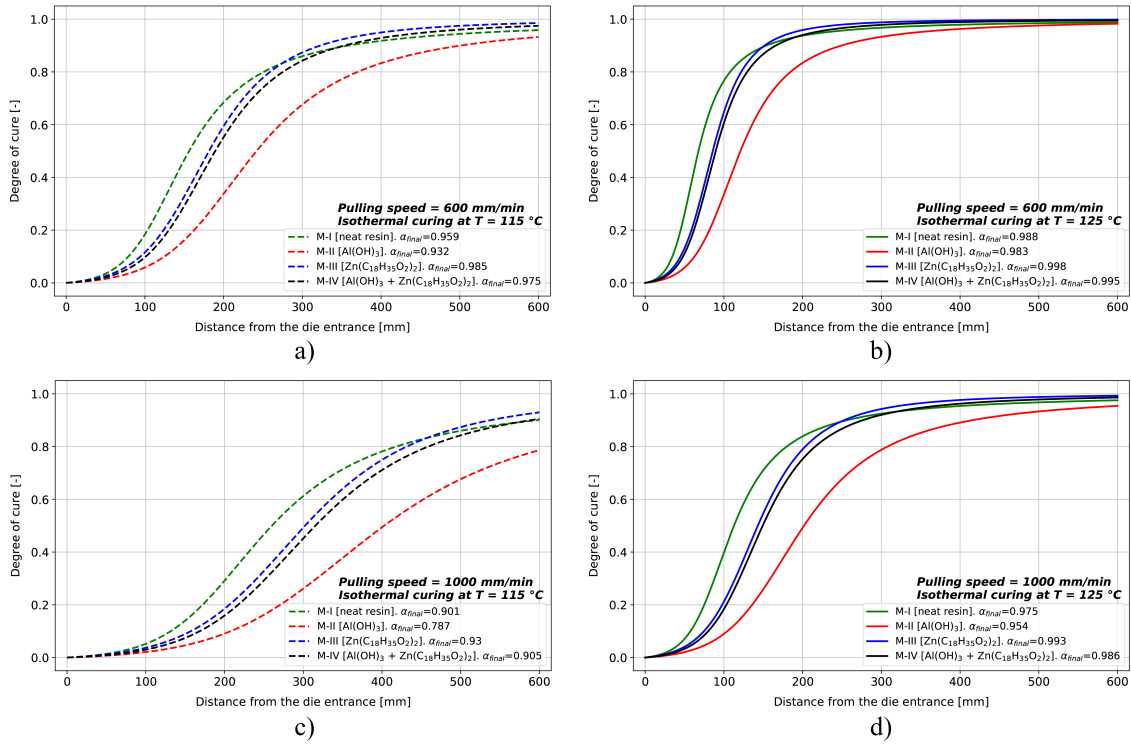


Figure 3.13: Curing of M-I, M-II, M-III, and M-IV simulated with the model based on the nth-order autocatalytic reaction: (a) Isothermal curing at 115 °C and the pulling speed of 600 mm/min; (b) Isothermal curing at 125 °C and the pulling speed of 600 mm/min; (c) Isothermal curing at 115 °C and the pulling speed of 1000 mm/min; and (d) Isothermal curing at 125 °C and the pulling speed of 1000 mm/min. Dashed lines represent isothermal curing at 115 °C, and solid lines indicate isothermal curing at 125 °C.

3.13c), it was impossible to obtain a fully cured composite at the die exit for all compositions. Therefore, the failure to describe the effects of processing additives on the cure behavior of the resin and the improper choice of kinetic equation may result in substantial differences between the predicted and real degrees of cure at the end of polymerization.

Numerical simulation of the pultrusion of a flat laminate profile at different heating temperatures of 115, 120, 125, and 130 °C (Fig. 3.14) showed that different resin compositions require different curing times and therefore different pulling speeds. With an increase in heating temperature, the polymerization graphs of all compositions shifted to the left; therefore, less time was required for the resin to reach the cured state. The maximum pulling speed was determined as the ratio of the die block length (600 mm) to the polymerization time for each resin composition. The maximum pulling speed was considerably affected by the temperature conditions.

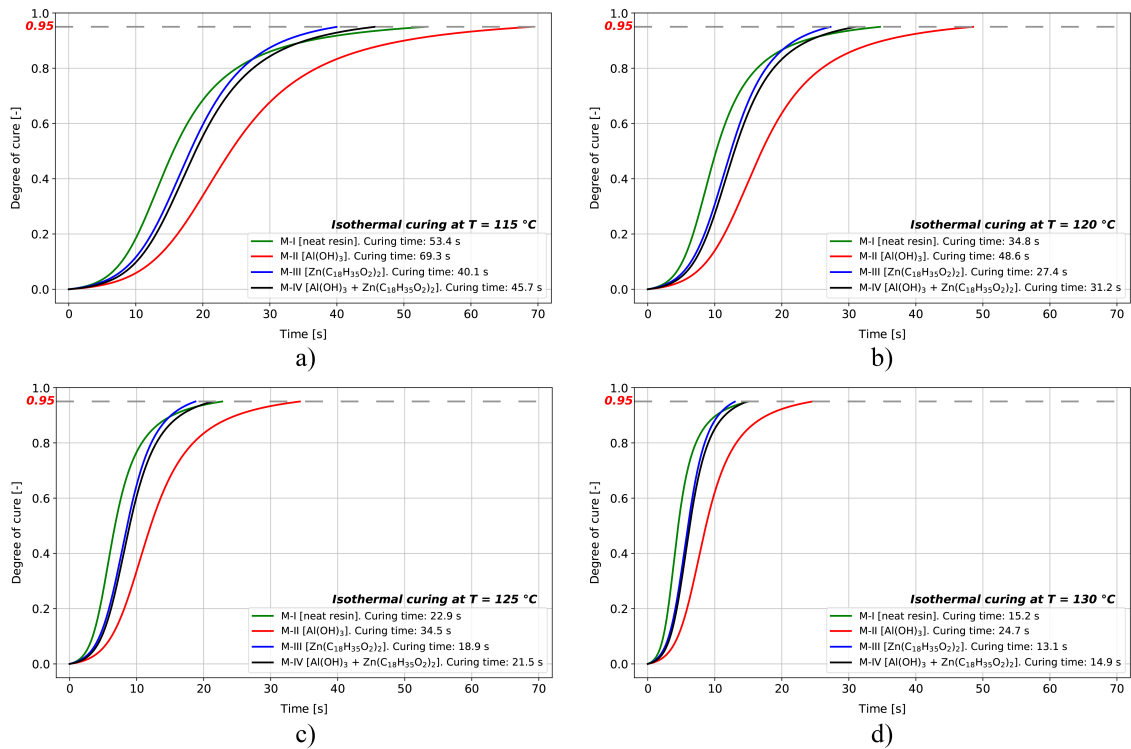


Figure 3.14: Polymerization of M-I, M-II, M-III, and M-IV to the degree of cure of 0.95, simulated by the model based on the nth-order autocatalytic reaction: Isothermal curing at (a) 115, (b) 120, (c) 125, and (d) 130 °C.

For example, the maximum pulling speeds at 115 °C and 130 °C differed by the factors of 3.5, 2.8, 3.1, and 3.1 for M-I, M-II, M-III, and M-IV compositions, respectively, and the maximum difference between the predicted values of pulling speed for these compositions at each heating temperature exceeded 1.7 times. For instance, at 115 °C, the maximum pulling speed for M-II composition was 519 mm/min, whereas the maximum pulling speed for M-III was 899 mm/min, which is 1.73 times that for M-II.

This study shows that ignoring the effects of certain processing additives may result in a significant difference between the predicted and experimental degrees of cure obtained at the die exit. Simulation results showed that for a resin with a final degree of cure exceeding 95% at the die exit, the maximum difference between the predicted values of pulling speed for the specified set of compositions may exceed 1.7 times. It was demonstrated that the effect of processing additives and the selection of an appropriate kinetic model should be taken into account when choosing pulling speed and predicting the outcomes of pultrusion.

3.8 Shape memory behavior of unidirectional pultruded laminate

The analysis of unidirectional glass fiber/epoxy resin 150×3.5 mm pultruded flat laminates exhibiting shape memory behavior is performed in Chapter 11. In an attempt to analyze shape memory performance, a series of tests has been conducted by bending flat specimens of cured resin and pultruded composite to the shape programming angle. Furthermore, the relationship between the shape fixing angle and the shape programming angle of the composite specimens was studied, as well as the influence of shape memory cycling on the shape memory performance of composite specimens during 10 shape memory cycles. The study also determined the shape fixity and shape recovery ratios for cured resin specimens. Series of mechanical tests to determine the tensile, compression, flexural, and interlaminar shear properties of the cured resin and composite specimens with 0° and 90° fiber orientations were performed. The resin cure kinetics, thermomechanical and thermophysical properties of the cured resin were determined experimentally. This data is of a great importance for the next studies aiming to simulate and optimize the manufacturing of pultruded shape memory polymer composites.

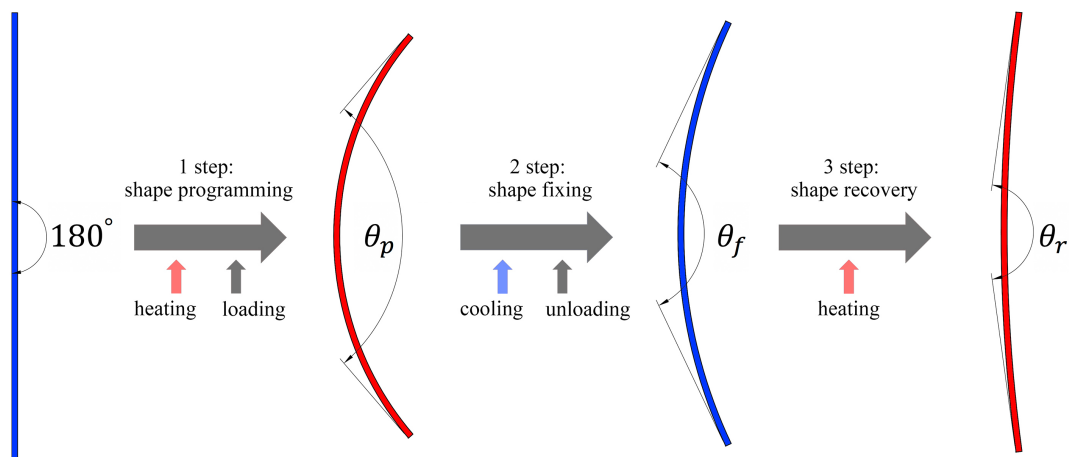


Figure 3.15: Flowchart of shape memory testing of cured resin and pultruded composite specimens.

The shape fixity (R_f) and shape recovery (R_r) ratios for the pultruded composite

specimens with 0° fiber orientation, determined according to Equations (3.3) and (3.4), constituted 13.3% and 91.9%, respectively. For specimens with 90° fiber orientation, the shape fixity and shape recovery ratios (77; 78) were 78.4% and 92.6%, respectively. The shape fixity and shape recovery ratios of the cured resin specimens constituted 99.7% and 98.2%, respectively. It was also found that the shape programming angle has no effect on the shape fixity and shape recovery ratios. The shape fixity and shape recovery ratios remained virtually unchanged during the 10 cycles of shape memory cycling.

$$R_f = \frac{\theta_0 - \theta_f}{\theta_0 - \theta_p} \cdot 100\% \quad (3.3)$$

$$R_r = \frac{\theta_r - \theta_f}{\theta_0 - \theta_f} \cdot 100\% \quad (3.4)$$

where θ_f is the shape fixing angle, θ_r is the shape recovery angle, θ_p is the shape programming angle, and $\theta_0=180^\circ$ is the initial angle value.

The inclusion of glass fiber affects the shape fixity and shape recovery ratios, as compared to the neat resin. One can see a reduction in shape fixity ratio in pultruded composite specimens with 0° and 90° fiber orientation as compared to the neat resin (79), as the use of glass fibers, featuring high elastic modulus, results in the considerable increase in bending stiffness of the composite specimens. This, in turn, leads to a significant spring back displacement observed at the unloading step of the shape programming process (80; 81). Bending stiffness of unidirectional pultruded laminate in 0° orientation is considerably higher, compared to that in 90° orientation, resulting in lower shape properties in the case of 0° fiber orientation, than in 90° fiber orientation.

Considering the results of mechanical tests, pultruded shape memory polymer composites (SMPC) show significant promise for structural applications based on the shape memory phenomenon. The ability of pultrusion to produce composite profiles of virtually unlimited length, with excellent mechanical and shape memory performance, makes it possible to expand the existing applications of SMPC's in civil engineering (beams (82), rods (82), plates (82), structural shock absorbers for

vibration control (83), damping elements in the earthquake engineering structures (84), self-healing structural components (85), elements of active building facades with self-regulating sun protectors (86), kinetic building envelopes (84) and actuating systems (85)). To illustrate, the application of shape memory concept in construction of bridges (87) and transmission towers (88) makes it possible to implement high-performance snap-fit joints (87; 88; 89) able to lock under heating, thus obviating the need for bolted joints. Pultrusion may also expand the applications of SMPs in aerospace engineering, for example in morphing aircrafts (90), deployable structures (91), hinges (92), antennas (93), solar panels (94) and solar sails (95).

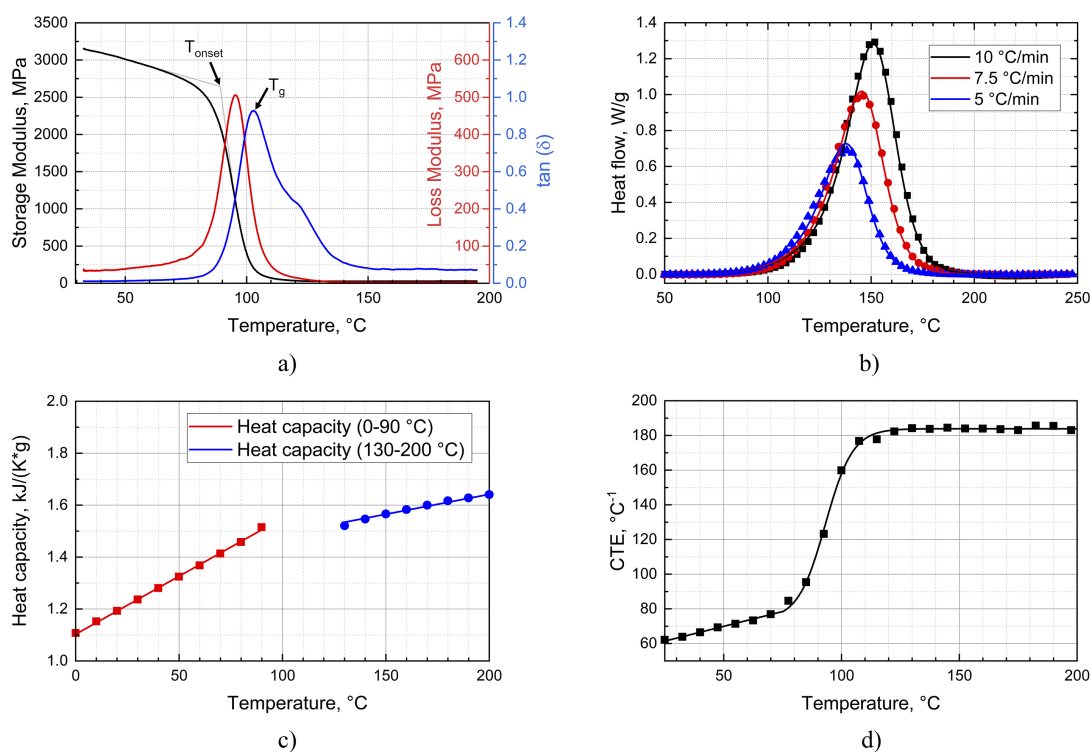


Figure 3.16: Results of thermomechanical, thermophysical, and cure kinetics analysis: (a) DMA measurements for cured resin. Changes in storage modulus, loss modulus, and $\tan(\delta)$ obtained at heating rate of 5 °C/min; (b) Polymerization enthalpy of uncured resin, and numerical simulation by expanded Prout–Tompkins equation. Markers (squares, circles, upward triangles) represent experimental data, solid lines – approximations; (c) Temperature dependence of heat capacity of cured resin. Markers (circles, squares) represent experimental data, solid lines – approximation; and (d) Changes in coefficient of thermal expansion (CTE) with temperature. Markers represent experimental data, solid line – approximation.

The thermomechanical and thermophysical properties of cured resin, such as temperature dependence of the storage modulus, glass transition temperature, heat capacity, coefficient of thermal expansion, density, and thermal conductivity were

determined (see Fig. 3.16). All the obtained data can be found in Chapter 11. These data may be used for further numerical simulations and optimization of the pultrusion process. To model the cure kinetics, the constants for the expanded Prout–Tompkins model were obtained.

This work is the first study on the shape memory effect in pultruded composites. However, further studies are necessary to better understand the shape memory effect in pultruded composites and to allow for the numerical simulation and optimization necessary to promote the application of pultruded shape memory polymer composites in various structures.

Chapter 4

Pultruded materials and structures: A review

Vedernikov Alexander, Safonov Alexander, Tucci Fausto, Carlone Pierpaolo, Akhatov Iskander. Pultruded materials and structures: A review. *Journal of Composite Materials* 2020. DOI: 10.1177/0021998320922894.

Contribution: I contributed to the development of the original draft, final writing, and editing. I would like to thank all the authors for their valuable contributions to the development of this paper.

Pultruded materials and structures: A review

Alexander Vedernikov¹ , Alexander Safonov¹ ,
Fausto Tucci² , Pierpaolo Carlone² and Iskander Akhatov¹

Abstract

Currently, the application of pultruded profiles is increasing owing to their advantages, such as light weight, high strength, improved durability, corrosion resistance, ease of transportation, speed of assembly, and nonmagnetic/nonconductive characteristics. This review analyzes the main application fields of elements produced by pultrusion manufacturing processes: bridges and bridge decks, cooling towers, building elements and complete building systems, marine construction, transportation, and energy systems. Analysis of the scientific literature in relation to the mechanical behavior of pultruded elements is presented as well. Finally, this review outlines the future study possibilities, giving the researchers and practitioners the directions for deeper investigation of specific features and exploration of new ones concerning the mentioned aspects of pultruded fiber-reinforced polymer composites.

Keywords

Pultrusion, mechanical properties, composite materials, fiber-reinforced materials

Introduction

Pultrusion is a method that allows the manufacture of composite materials. Not only open-section geometries but also single- or multi-celled close-shaped profiles can be manufactured by pultrusion processes, exhibiting a maximum production speeds of 5 m/min.¹ Pultrusion is accomplished by pulling reinforced material (glass, carbon, or aramid) through a guide while precisely distributing fibers accordingly to the cross-section of the intended profile. At the first step, the fibers are impregnated with a resin material in a bath. In the next step, the obtained mixture is pulled through the heated die, allowing the curing process to be accomplished and the final shaping of the profile to be conducted. The manufactured profile is then pulled forward to a floating suspended saw, which cuts the profiles into parts of the desired lengths.

Of all the literature published thus far, it is worth highlighting the principal books^{2–5} and prominent review papers,^{6–8} which provide a comprehensive introduction to the pultrusion process, its theoretical and practical peculiarities, historical checkpoints, the key patents filed, as well as the parameters influencing the design of pultruded profiles, structural design, and process models.

At present, conventional materials (such as concrete, steel, aluminum, timber) are rapidly losing prevalence and giving way to highly efficient composite materials across many markets. As with all the other composites produced by various available techniques, pultruded profiles have also proved their ability to satisfy the cost, mechanical, physical, and environmentally resistant requirements while still demonstrating outstanding performance. Furthermore, expanding interest toward composite materials in general and pultruded materials in particular has led to the appearance and rapid development of large, medium, and even small production lines on the market.

Nevertheless, it is well known that the construction market is a challenging sector to enter. In spite of the advantages listed above, there exist factors restraining the widespread use of fiber-reinforced polymer (FRP)

¹Center for Design, Manufacturing and Materials, Skolkovo Institute of Science and Technology, Russia

²Department of Industrial Engineering, University of Salerno, Italy

Corresponding author:

Alexander Safonov, Center for Design, Manufacturing and Materials, Skolkovo Institute of Science and Technology, Moscow, Russia.
Email: a.safonov@skoltech.ru

profiles, because design guidelines and codes are rarely written in consideration of the behavior of composites. Hence, the contemporary composite market faces a need for well-prepared specialists, which can be reached by training, in conjunction with the improvement of existing design-normative documentation.

In recent decades, the usage of profiles produced by the pultrusion process has attracted increasing attention from different industries. In raising the awareness of pultruded FRP composite materials in buildings and infrastructure facilities, the purpose of this paper is to review applications as well as mechanical properties of pultruded FRPs.

Pultrusion applications

Currently, composite elements produced by pultrusion processes are in widespread use across the world. In particular, the production of pultruded composites is increasing every year, covering different market sectors. Figure 1 demonstrates the scope of pultrusion elements' application, including bridges and bridge decks construction, cooling towers, building system and elements, marine structures, communication, and energy systems.

Bridge construction

From the production volume standpoint, the construction market is the largest sector demanding pultruded profiles. Consequently, it can be considered as one of the biggest markets to implement and provide opportunities for pultrusion in the future. Bridges made of composite materials exceed their conventional counterparts for various reasons: light-weight characteristics,^{15,16} ease of transportation, speed of installation, noncorrosive properties, etc. All these advantages make it possible to reduce or sometimes even eliminate necessity for traffic/railway shutdowns as well as decreasing shipping and erection costs. Moreover, composite bridges are more durable in the context of extreme temperatures or treated by de-icing salts. This enables dramatic reductions in the bridges' maintenance costs and inspection regularity.

Examples of FRP applications in bridge construction are listed in Table 1, with a particular emphasis on bridges' locations, structural design/construction process features, and production companies; a cost comparison between bridges made of FRP and bridges constructed by conventional methods is presented in Table 2.¹⁷

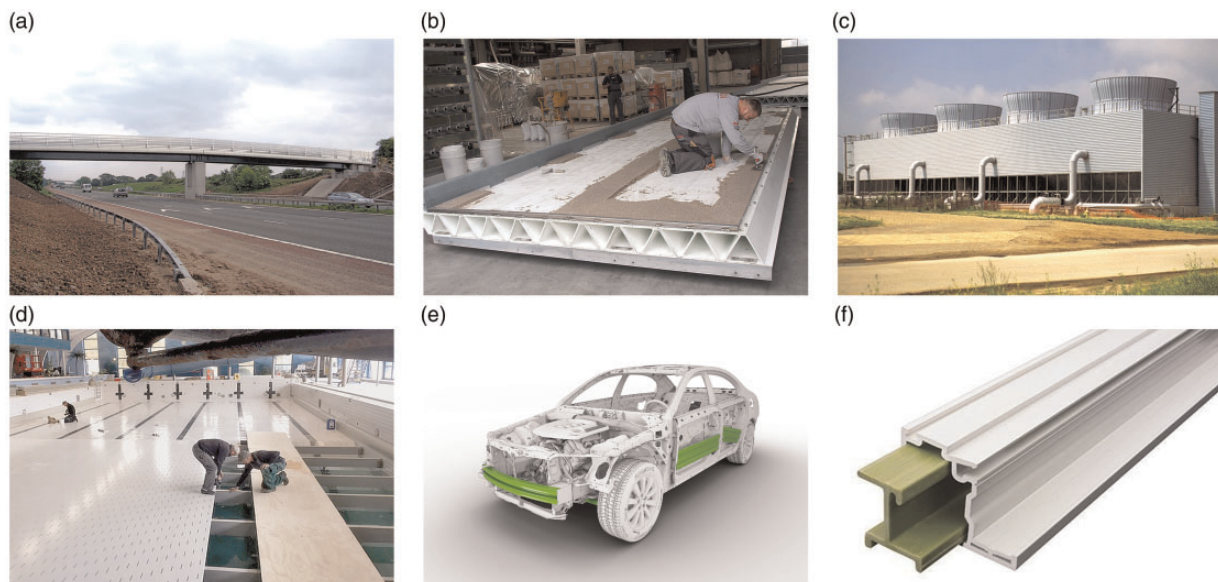


Figure 1. Application of pultruded elements: (a) bridge construction: GRP bridge across UK M6 motorway, Lancashire, UK. Fiberline production;⁹ (b) bridge deck construction: bridge deck of vehicular bascule “Grasshopper” bridge at Karrebæksmunde on the west coast of Zealand, Denmark. Fiberline production;¹⁰ (c) cooling tower construction: custom cooling towers. Marley Cooling Towers, SPX production. Image used with permission of SPX Cooling Technologies, Inc. for educational and informational purposes only. Copyright ©2019 SPX Cooling Technologies, Inc. All rights reserved;¹¹ (d) water-related construction: flexible and durable pool bottom for Danish waterpark, Denmark. Fiberline production;¹² (e) usage of thermoplastic composite with extremely high fiber content combined with PA6 for the cars' bumper. CQFD composites production;¹³ (f) windows' elements production: replacement of the traditional aluminum insert with pultruded polyurethane inserts comprising 80% glass fiber and 20% Baydur 3500 polyurethane. Deceuninck production.¹⁴

Table 1. Major pedestrian bridges constructed of pultruded structural parts.

Location	Year	Structural design	Production company of pultrusion parts	Application pros	References
Aberfeldy footbridge, Aberfeldy, Scotland	1992	Three-span cable-stay structure, with spans of 25, 63, and 25 m	Fibreforce composites	The first cable-stay, wholly made of plastic (GFRP bridge decks and pylons) footbridge. Exploiting light-weight advantage of pultruded materials, it was assembled with no help of heavy machinery. Sixteen years later, its durability was estimated and classified as highly satisfactory.	18
Kolding pedestrian and cyclist bridge, Denmark	1997	40-m-long and 3.2-m wide cable-stayed structure	Fiberline	The first composite bridge in Scandinavia crossing a railway. Only conventional power tools were applied during the bridge's erection. Train traffic shutdown was avoided owing to the rapid assembly process within a few hours on three nights.	19
Vehicular bridge, Klipphausen, Germany	2005	Span of 6.3 m and width of 6.0 m	Fiberline	The first traffic bridge made of GFRP in Germany in particular and continental European in general. The composite nature allowed overcoming maintenance and durability issues that damaged steel and concrete bridges constructed previously at this location. The unique technical solution allows removing the bridge in case of flooding. The bridge structure comprises 26 pultruded GFRP (E-glass fibers and isophthalic polyester resin) elements that were adhesively bonded to each other.	20
Pontresina pedestrian bridge, Switzerland	1997	Two 12.5 m spans of truss form	Fiberline	Light-weight and easy handling advantages of FRP profiles were exploited during the assembly process in the mountainous area. The particular technical solution allows disassembly of the bridge to avoid flooding that occurs every spring in this area.	21,22
Chertanovo pedestrian bridge, Chertanovo, Russia	2005	41 m length and 3 m width	ApATeCH in partnership with Fiberline	Corrosion is wide-spread across Russia, owing to its harsh winters and severe climate. This has pushed the Russian company ApATeCH in partnership with Fiberline Composites to construct the first Russian GFRP pultruded bridge. The installation process took just less than 1 h, enabling the avoidance of railway traffic disruption.	23
GRP vehicle bridge across UK M6 motorway, Lancashire	2006	52 m long	Fiberline	The first GFRP traffic bridge within the motorway network. The use of pultruded elements not only reduced the weight by almost 35%, but also decreased the future maintenance costs. The bridge has enhanced strength compared to steel or concrete analogs, apart from being durable against the harsh water and salt environment.	9
Vehicular bridge, Kujalleq, Greenland	2016	Span of 11.9 m	Fiberline	Greenland's first bridge made of GFRP pultruded elements. GFRP is an ideal solution allowing reduced costs and time savings. Fiberline's composite bridge performance was stable, unlike the Arctic temperature that constantly imposed tough conditions on the newly constructed structure.	24

Table 2. Cost comparison between bridges made of FRP and steel material.¹⁷

Indicative costs assuming 15 m footbridge 2 m wide (120 years design life)			FRP footbridge £, K	Steel bridge £, K
A	Acquisition cost (£, K)	Design and certification	12	9
		Product fee	100	70
		Transportation	3	5
		Install/commission	3	6
B	Operation cost (£, K)	Inspections (GI and PI)	108	180
		Inspections (SI)	24	80
		Coatings	30	240
		Joints	20	20
		Surfacing	25	25
		Major maintenance	Nil	20
		Traffic management	54	86
		Project management	20	30
C	Disposal (£, K)	Decommissioning	25	25
		Disposal	10	5
D	Salvage (£, K)	Material recycling	Nil	–5
		Total cost ownership	434	796

Bridge decks

The principal function of a bridge deck is to carry vertical loads and spread them to the superstructure in the transverse direction. The increasing maintenance costs of traditional bridge decks is an escalating global issue. Previously, many researches were devoted to the examination of the deteriorating conditions of bridges and other related infrastructure.²⁵ For instance, steel elements (concrete reinforcement, structural members) will very likely to be corroded one day,²⁶ and concrete is susceptible to such degradation mechanisms as sulfate attack, freeze–thaw cycles, and other detrimental processes causing cracking. Therefore, a breakthrough allowing to overcome these disadvantages of conventional materials in bridge construction is needed. In this respect, FRP bridge decks are rapidly emerging as a possible solution^{6,27–32} in both new construction and rehabilitation projects. FRP bridge decks are mainly made of E-glass fibers and thermosetting resins such as polyester (owing to their low cost) and vinylester (preferable material used in moist environments⁶). This solution has proved its efficiency owing to the advantages of light weight,^{18,25,33–46} high strength,^{6,18,25,34,36,40,41,45–51} and improved durability.^{34,36,45,46,48,49,52–55} Moreover, the benefits of FRP decks include corrosion resistance^{18,25,35,36,47,52} and, therefore, longer service life³³ while still demonstrating lower life-cycle costs.^{45,46,48} The application of composite bridge decks allows rapid and easy installation or replacement of deteriorated existing structures.^{6,18,25,33–35,45,46,52,56} Owing to the low weight of FRP structures applied while working on

rehabilitated bridges, such infrastructures can carry increased live loads because of the decreased dead loads.^{6,33,48} The application of traditional materials for bridge construction generally has consequences in terms of increased energy consumption and carbon emissions compared with their composite counterparts. Not only for this reason but also because of fewer traffic disruptions, lower maintenance, and repair needs,²⁵ FRP decks demonstrate smaller footprints, less air, and noise pollution and have the potential to deliver sustainable bridges with less negative environmental impact.

Cooling tower components

The next market that typically applies FRP profiles is that of cooling tower construction.⁵ Conventional cooling tower materials undergo continual deterioration during their service life. In relation to traditional materials, composite profiles show such advantages as low weight,⁵⁷ high strength,⁵⁷ dimensional stability,⁵⁷ customizability,⁵⁷ excellent electrical, corrosion, and environmental resistance.^{57–59} FRP is a material well suited to the evaporative cooling tower environment, as it can be easily characterized as a truly versatile structural material with good predictability for service in all of the severe exposures offered by the cooling tower industry: immersion/basin, splash/fill, and 100% humidity/plenum.⁵⁷

Building elements and complete building systems

In recent decades, FRP composites have been widely used for constructing entire civil engineering structures

and their elements (profiles,^{60–62} columns,^{63–69} floor,^{70–75} concrete structure reinforcement,⁷⁶ and wall systems,⁷⁷ modular panels,⁷⁸ different types of staging, stairways and walkways,⁷⁹ and applications related to fencing, railings, and personal safety barriers⁸⁰). At the moment, all these elements made of composite materials are competitive solutions over their classical counterparts. FRP composites can be used as non-load-bearing and load-bearing building elements in the refurbishment of structures as well as the construction of new ones.⁸¹ Significant strength-to-weight ratio,^{82–84} rapid assembly, excellent corrosion resistance at relatively low maintenance costs,^{84–94} increased durability,⁹² fatigue resistance,^{82–84} nonmagnetic/nonconductive characteristics,⁹⁵ and an extensive range of thermal properties depending on the type of matrix and fibers used are just some of their various advantages.^{96–100} The non-sparking nature of FRP elements (i.e. risk of sparks generation during the use of such structures is greatly reduced) allows their utilization in an extensive range of industrial applications subject to limitations on sparking.³

More than 30 years have passed since the first appearance of FRP elements in the window market. Currently, an increasing number of engineers, technicians, and architects are employing this material for both the refurbishment and installation of new windows. This has occurred because the nature of the pultruded composites permits the incorporation of the best features of traditional window elements made of aluminum, vinyl, or wood, which have been in use for a long time. The ability to withstand the infiltration of water and air along with soundproofing are the main criteria for this type of structural element, and FRP materials satisfy these requirements. Window lineals made of fiber-reinforced composites demonstrate excellent insulating properties,¹⁰¹ improved protection from condensation, and low U-values. These significant advantages enable decreased heat losses due to conduction processes and the presence of thermal bridging in windows. Low coefficients of thermal expansion result in excellent dimensional stability of windows in extreme climatic zones. Therefore, all the geometrical deformations (warping, expansion/contraction, shrinking) are minimized. With respect to temperature, FRP composites are able to withstand heating to 90 °C and cooling to –40 °C.

Pultruded elements are attracting considerable attention due to the possibility of being used for rehabilitation or retrofitting of existing concrete structures¹⁰² or steel beams.¹⁰³ The pultruded plates are often used to repair or to strengthen the structural beams, columns, or slabs^{103–105} or to provide enhanced seismic resistance to the structural building elements.¹⁰⁶ The FRPs are adhesively fixed on the concrete surfaces, oriented in

such a way to provide enhanced resistance to the external loads.¹⁰⁶ The blast resistance of concrete slabs can be significantly improved by the application of pultruded reinforcement.¹⁰⁵ In case of beams with web openings, the installation of pultruded supports improves the structural behavior and extends the service life.¹⁰⁴ The defected steel beams retrofitted with pultruded plates demonstrate remarkably better fatigue behavior in terms of crack propagation and number of loading cycles, compared to those repaired by conventional methods.¹⁰³

Marine construction

Owing to their advantages, during recent decades, advanced composite materials have started to penetrate the marine construction industry, and now they have spread across the market. FRPs are used as a substitution for conventional materials with the primary aim to overcome the corrosion issues due to the harsh marine conditions (harbors, ocean and floating constructions, energy systems, container wharfs, tidal power structure, handrails, and gratings¹⁰⁷). Composites' lightweight and high strength characteristics,^{108–110} improved durability,^{111,112} insensitivity to the degradation processes occurring within marine environments,^{113,114} lower expenses for shipping, installation, and maintenance processes,¹⁰⁹ resistance to corrosion,^{108,109,115} and prolonged lifespan render them a cost-effective and environmentally friendly solution. Moreover, the nonsparking nature of FRP composites avoids sparks generation, which should be prevented in certain offshore applications due to the flammability of the related products.³

One of the possible applications of the pultrusion technique in this field is the production of marine piles. Indeed, traditional piles have a shorter life cycle in comparison to composite piles, mainly because of the lower corrosion resistance and greater susceptibility to the degradation mechanisms initiated by the harsh marine environment.¹⁰⁹ The five most common types of composite piles on the market are FRP (hollow^{109,116}/concrete core¹⁰⁹) piles, steel pipe plastic core piles, reinforced plastic matrix piles, and fiberglass pultruded piles.¹⁰⁹

The application of pultruded FRP shapes for waterfront sheet piling started in the 1990s, and it is currently rapidly increasing in the construction of waterfront retaining structures (newly installed and renovated).¹¹⁷ FRP based on glass reinforcement is the most common type (mostly owing to their competitive cost¹¹⁸) of composites applied within sheet piling construction. Apart from the mentioned applications, composite materials are widely employed, particularly in shipbuilding¹¹⁹ as well as the naval industry.¹²⁰

Transportation

One of the main challenges of the transportation industry in the current century is the fossil-fuel shortage. Limiting energy consumption by modifying the existing elements of vehicles, either replacing old features with newer or more advanced ones, is one of the ways to satisfy energy-saving regulations. Therefore, FRP composites appear to be logical solution to these issues, owing to their corrosion resistance, dielectric properties, high strength,¹²¹ and low weight.^{122–124} Considering the growth of light vehicle sales, the increasing use of FRP composites in the transportation industry has led to the adoption of the pultrusion manufacturing method.¹²⁵ Applying pultruded materials instead of steel, it is possible to decrease the overall weight of the components by up to 40%. Many authors have contributed and advanced the research related to the energy absorption capabilities of composite materials.^{126–135} It was found that pultruded profiles with improved impact energy absorption characteristics can be successfully used in vehicle designs to ensure the safety of passengers in accidents. Automobile bumpers,¹³⁶ bus components,¹³⁷ truck/trailer elements,¹³⁸ bus luggage racks, and subway contact rail support brackets¹³⁹ are just some examples of current pultruded component applications within the transportation industry. Owing to the vast range of various available shapes and cross-section elements, pultrusion has attracted much attention from transportation manufacturers.¹⁴⁰

Along with terrestrial transportation, pultruded elements are applied within the aeronautic sector as well. There is a constant battle between aerospace giants, with the primary aim to minimize the weight of aerospace craft as well as decreasing acquisition and operating expenses. Composite materials, offering better performance at a lower price in comparison to the traditionally applied aluminum, fulfill all the main requirements to aerospace craft. Currently, it is difficult to imagine any aerospace vehicle built without any parts manufactured by the pultrusion process.^{141–147} Every year, composites become more and more involved in the aerospace industry,¹⁴⁰ thereby increasing the efficiency, performance, and competitiveness of aerospace vehicles. The aerospace industry is now applying such pultruded elements as shapes and profiles.¹⁴⁵ The increasing use of FRP composites in the aviation industry has led to the adoption of pultrusion manufacturing in order to exploit all the advantages of this technology.^{148,149} To date, the application of polymer-based parts in civil airplanes has mostly been restricted to the production of secondary structures (doors, slats). However, the situation has now changed. Currently, components demonstrating high stiffness in one direction (such as spar caps, panel stiffeners, and

longerons) are only some examples of unidirectional pultruded profiles applied in the aircraft industry.¹⁴⁹ FRP components are widespread not only in the construction of civil aircraft but also in the military industry, where composites account for approximately 30% of the overall airplane's weight.

With the accelerated worldwide development and expansion of railway systems, the utilization of pultruded profiles has increased as well.¹⁵⁰ In addition to the major applications, many smaller uses of FRP in service on the railway network also exist. Currently, pultrusion is considered to be the most suitable manufacturing method for light rail vehicle track applications.¹⁵¹ Minor load-bearing structures such as staircases, window-level walkways on the outside of signal boxes, access walkways on station roofs, foot-bridge treads, and decking are constructed by pultrusion profiles. FRP materials have also been used for the replacement of handrails on underline bridges and to provide anti-trespass covers for tunnel ventilation shafts. They have also been applied for the provision of brackets to support lighting systems on bridges.¹⁵² Moreover, crash barriers made of pultruded composites are widely applied along highways and autobahns. Such structures (which are often subjected to vehicular impacts) made of composite material are highly energy-absorbent,^{153,154} which prevents the entry of the vehicle into on-going traffic lanes or undergoing a catapult-like return in the original direction of travel and ensures the safety of the traffic.¹⁵⁵ All these advantages demonstrate that pultruded polymers are an economical alternative to traditional roadside structures.

Energy systems

Wind power is a type of renewable energy source that can be used for the long term and is an excellent solution to the energy crisis. The beginning of the 21st century has marked a boom of wind energy production, and the role of renewable energy is even expected to increase in the coming years. Wind turbines are already able to generate electricity at costs competitive to traditional methods. Pultrusion is potentially a way to produce long constant-chord blades and wind turbine blade roots.^{156–159} For instance, the cost of wind-generated energy fell dramatically from \$0.25/kWh in the last 40 years, and now, it costs almost the same as fossil fuels. FRP-based wind-turbine blades provide high stiffness at reduced weight and are ideally suited for increasing the length of the structure. Moreover, increased durability and resistance to fatigue is one of the main requirements. Composite blades exhibit increased stiffness and resistance against aerodynamic and vibration loads. In addition to the mentioned cases, spar-cap applications (seeking improved compressive

and tensile properties) can be achieved owing to the high alignment obtained in pultrusion.

Pultruded FRPs are incorporated within the energy field as constitutive elements of distribution facility networks such as in utility poles, which are structures used to support any types of telephone, utility, and power cables. Traditionally, utility poles have been produced with the use of concrete, metal, or timber materials. However, such materials are susceptible to frequent replacement due to degradation mechanisms (corrosion in the case of steel, woodpeckers', and insects' attacks in case of timber). Costly replacement and frequent maintenance have become reasons for the introduction of composites. The first FRP poles appeared in Hawaii in the middle of the last century.¹⁶⁰ Currently, the industry is experiencing rapid growth in the application of composite poles and transmission towers.¹⁶¹ Particular advantages of FRP poles are the longer life-span of the composite profile, fast shipment, ease of assembly, improved strength-to-weight properties, durability, and stability under UV rays.¹⁶⁰ Composite poles overcome such issues as decomposition, breakage, and environmental problems.¹⁶⁰ Having nonconductive properties,¹⁶⁰ transmission towers made of pultruded profiles no longer require the application of costly insulators. Therefore, there is no need for frequent cleaning and replacement of these insulators, which was a reason for the increased cost in the past.

Fiber-optic technologies have spread across many industries and have many applications (underground cables, submarine cables, and aerial cables) as a result of the rapid growth in recent years.¹⁶² One of the main elements within optic cables that provides stiffness and strength is known as the central strength member. Recently, FRPs have received much attention as cable cores for overhead power transmission lines to replace standard steel cores wrapped by aluminum wires, owing to its high strength, low weight,¹⁶³ nonmagnetic, non-corrosive,¹⁶³ and nonconductive properties.¹⁶³ Contrary to their traditional counterparts, FRP-based optic cables have several unique characteristics. They possess higher transmission rates over long distances in addition to higher capacity compared with coaxial cables.¹⁶³

Future applications

Forecast made by European Pultrusion Technology Association (EPTA) predicts the growth of pultruded elements and structures market to more than \$100 billion in 2022.¹⁶⁴ Authors envision the rise in pultrusion applications both within the existing markets and within new ones that are out of the scope of current research. In order to draw the attention of scientists

and practitioners, this section will briefly discuss some of the possible future trends in pultrusion applications.

In 2011, Thomas Technik & Innovation patented a new concept of pultrusion process that makes it possible to manufacture non-linear profiles, thanks to the use of the curved moving die. Indeed, this process can be used to manufacture components for aerospace, automotive and transportation industries, construction, architecture, and unique infrastructure applications.^{3,4,165,166}

Pultrusion is a perfect candidate when it comes to manufacturing of structural parts for space stations and power generation platforms.¹⁶⁷ The possibility to ship the pultrusion machine directly to the orbital space has been demonstrated already.³ Nowadays, colonization of Mars and the Moon seems fairly possible. In fact, Magna Parva, Space Engineering and Technology company claims that pultrusion can be utilized to manufacture the kind of parts needed for settlement on the other planets.¹⁶⁸

Shortage of heavy and medium oil seems inevitable in the future. However, the application of novel methods has made it possible to discover vast reserves of oil under the ocean floor. The only possible way to pump this oil out is to use deep-water piping. Contrary to the traditional materials and techniques, pultruded pipes made with the help of a mobile production platform can help with the transportation of black gold, giving a temporary answer to the issue of oil shortage.³

Pultruded thermoplastic profiles offer significant advantages over the thermoset ones. They are rather cheap and fast to produce, environmentally friendly, and can be joined by welding. This relatively new technology is full of challenges to be solved by researchers.¹⁶⁹

Many specialists agree that pultruded components should be applied for the realization of dense 5G networks that are about to be deployed very soon. The thing is that the loss of 5G signal can be minimized due to enhanced radio frequency transparency characteristics of pultruded structures.¹⁷⁰

Fi:resist is a new material that has been introduced in the EPTA press release issued in 2018. Fi:resist-based pultruded elements can retain structural properties even at elevated temperatures. Fi:resist is non-flammable, does not emit fumes, and is an excellent thermal insulation material. It will definitely find broad application in the construction, ship, and rail markets.¹⁶⁴

Microwave-assisted pultrusion presented by Rudolf Emmerich of the Fraunhofer Institute of Chemical Technology provides the possibility of quick, either uniform or selective heating of resin. So far, it has not found industrial application, since some technological issues related to the die design are yet to be solved.

To implement this concept, existing pultrusion dies can be modified.¹⁶⁴

Fraunhofer Institute for Production Technology in Aachen conducts research in the area of micro-pultrusion.¹⁷¹ With the current level of technology, the profiles as small as 280 micrometers in diameter can be pultruded.¹⁷² It is possible to pultrude both thermoset and thermoplastic components.^{172,173} An extensive outlook regarding the possible future of thermoplastic micro-pultrusion can be found in the recent paper of Callens and Bergsma.¹⁷² Generally speaking, knowledge of micro-pultrusion is very limited, and the only applications discussed in the literature so far are the following: medical^{174–176} and aircraft industry.¹⁷²

Development of fast curing alternatives for composites manufacturing processes still goes on. Some issues related to the pultrusion technology can be solved with the help of ultraviolet (UV) curing.¹⁷⁷ Here, the curing takes place outside the die, while the latter is just a device for shaping the profile and eliminating the excess resin. This strategy makes it possible to produce non-linear profiles. Utilization of a robot arm has been reported in Britnell et al.¹⁷⁸ and Tena et al.,¹⁷⁹ where a CAD model was applied to achieve even higher degree of process automation.

Another promising research direction is the application of smart polymers. Being under the influence of different stimuli, these polymers are able to react to it, thus, changing either chemical or physical characteristics.¹⁸⁰ There are several principal types available: temperature-sensitive, pH-sensitive, photosensitive polymers, biological molecules, etc. These materials are of great interest not only for medical industry¹⁸⁰ but also in civil engineering. In fact, they are also able to respond to vibration and sonic waves; thus, one can foresee their use in seismic applications.¹⁸¹ Ability to recover predefined shape while being under external influence is the key characteristic of shape memory polymers which are a particular subgroup of smart polymers.^{182,183} Current and potential areas of their application are the following: medicine and biomedical devices,¹⁸⁴ aerospace,¹⁸⁵ textiles,¹⁸⁴ civil engineering,^{184,186} microfluidics,¹⁸⁰ lithography,¹⁸⁰ electronic engineering,¹⁸⁴ self-healing systems,¹⁸⁷ and household products.¹⁸⁰ Although at the moment smart polymers have nothing in common with pultrusion, in authors' opinion, introducing of mentioned smart properties can be another possible area for the practitioners of pultrusion to work on.

Pultrusion seems to be the most promising direction of composites manufacturing to be considered as a part of the last years trend—Industry 4.0. This breakthrough can be made due to the highly automated

nature of pultrusion and opportunity to integrate robot arms, cyber-physical systems, internet of things, and cognitive computing together with artificial intelligence within the single production process. Indeed, it is easier to recount applications where pultrusion cannot be applied than trying to recall all possible pultrusion applications, as every year some new applications emerge. The awareness, recognition, and worldwide acceptance of the FRPs in general and pultrusion in particular are growing.³

Mechanical properties of pultruded materials

The mechanical and physical properties of pultruded parts are strictly related to the mechanical characteristics of their components, their volume fractions, the reinforcement architecture, and the pultrusion process operation parameters.⁴ In general, the fibrous architecture of pultruded FRPs is composed by a combination of several different reinforcement structures designed to respond to any case-specific necessities. Typically, the core is reinforced by unidirectional rovings, which provide the longitudinal resistance and stiffness of the profile.³ Unidirectional or multiaxial fabrics, made of well-ordered woven tows, are employed to enhance the transversal or off-axis properties in a specific direction.³ Continuous filament mats, which are randomly oriented long fiber tissues, are commonly used on the external faces of the profile to enhance surface properties and UV resistance.³ For simple convex cross-sections, external braids provide enhanced transversal properties and ductility.¹⁸⁸ In the case of major aesthetic requirements, a thin veil of a mat is used at the external surfaces.³

This part of the paper discusses the main features with regard to the mechanical properties of pultruded elements.

Static mechanical properties

The properties of the involved components determine the mechanical characteristics of the pultruded parts. Several models have been proposed to define the constitutive relation of FRPs as a function of the component properties and volume fractions.^{189,190} Bogetti and Gillespie¹⁹¹ developed an analytical model to compute the mechanical properties of transversely isotropic fiber-reinforced laminas. They analytically expressed the relation between the final composite mechanical properties and the volume fractions as well as the properties of each component. One of the main points of this model was the prediction of the resin evolution during the cure reaction, in terms of elastic modulus,

thermal expansion, and chemical shrinkage. Although it was not specifically developed for pultruded components, this approach fits well for pultrusion modeling. Indeed, it has been used to simulate the effects of pultrusion process parameters on the final mechanical properties and the process-induced stresses and strains on the pultruded parts.^{192,193} The stiffness and strength of pultruded laminates in design can be estimated using Carpet Plots.¹⁹⁴

Apart from the matrix and reinforcement, FRPs in general and pultruded parts in particular contain small amounts of other phases, such as fillers, additives, and embedded air, also known as voids.¹⁹⁵ The latter are process-related defects. Indeed, voids are stress concentrators, which cause crack initiation.¹⁹⁶ Several traditional property homogenization techniques are available in the scientific literature (Eshelby model,¹⁹⁷ Mori–Tanaka model,¹⁹⁸ and self-consistent model¹⁹⁹). These models have been improved to predict the FRP composite mechanical properties accounting for the presence of voids and fillers.¹⁹⁵

Components of pultruded elements. Generally, pultruded elements are composed of fibrous discontinuous phase, known as reinforcement, embedded in a polymeric continuous phase, known as the matrix.²⁰⁰ In some cases, fillers can be used to improve the matrix properties, reduce the costs, or enhance the interaction between the matrix and reinforcement.²⁰¹ Many authors have reported or tested the mechanical properties of the components in order to analyze the mechanical behavior of pultruded parts. The material properties of the most commonly used matrices and reinforcement are reported in Table 3. It is worth noting that the resin system properties change remarkably, depending on the way it was cured and on the matrix system composition. The main mechanical characteristics of some commonly used pultruded profiles are reported in Table 4.

Tensile behavior. The actual material properties depend on the reinforcement architecture and its orientation.^{3,255} Examples are available in scientific literature characterizing the tensile behavior of pultruded FRPs with respect to off-axis loads.^{217,256} Composite elements show much higher performance in the case of external loads parallel to the fiber direction. The elastic modulus as well as the ultimate stress value considerably decrease for small tilt angles, whereas for tilt angles higher than 45°, the modulus variations are negligible.²¹⁷ Some authors adapted and calibrated the Hankinson’s formulas²⁵⁷ to predict the tensile strength σ_θ and modulus E_θ of pultruded parts (equations (1)

and (2)) for any tilt angle θ as a function of the longitudinal (σ_0 and E_0) and transversal (σ_{90} and E_{90}) properties²⁵⁶

$$\sigma_\theta = \frac{\sigma_0 \sigma_{90}}{\sigma_0 (\sin \theta)^{1.248} + \sigma_{90} (\cos \theta)^{1.248}} \quad (1)$$

$$E_\theta = \frac{E_0 E_{90}}{E_0 (\sin \theta)^{1.386} + E_{90} (\cos \theta)^{1.386}} \quad (2)$$

In recent decades, many scientists combined the pultrusion process with the fiber braiding technique to produce enhanced FRPs.⁸³ The profiles produced by this combined approach match the tensile properties of the common pultruded parts with improved ductility, owing to the braided fibers. Their properties approach those of steel, while avoiding corrosive problems as well as being light-weight, nonconductive, and non-magnetic.⁸³ The braid angle, which can reach values up to 55°, remarkably influences the properties of braided pultruded elements. Higher braid angles improve the transverse properties; nevertheless, the longitudinal tensile characteristics of components made with lower braid angles exhibit higher axial tensile modulus. This behavior is mainly due to the fiber of the braided cover, which provides a major contribution in resisting the axial loads when the braid angle is lower.¹⁸⁸

Considering a typical pultruded element, with a roving/mat reinforcement structure and loaded with longitudinal tensile force, that fails due to the formation of transversal cracks in one of the mat reinforced layers, which are characterized by lower stiffness. The transversal crack provokes the relative sliding of the layers and, therefore, the delamination. On the contrary, in the case of a transversal load, the roving reinforced layers are the weakest ones. The failure occurs due to vertical cracks arising between adjacent rovings.²⁵⁸

To achieve efficient performance of pultruded structural elements, understanding of mechanical properties is needed. There are a lot of papers studying the work of both real structures and specimens. This paragraph gives a short overview of literature regarding the work of such structures under tension. Various aspects of pultruded bolted and joints connections under tension have been discussed in several papers. Mottram in his article compares the analytical predictions of tension strength of multi-row bolted connections (based on Hart–Smith semi-empirical model) with experimental data available in the literature by that time.²⁵⁹ The effects of the elevated service temperatures/humidity are studied in Turvey and Sana²⁶⁰ and Turvey and Wang;^{261,262} analysis of numerous variables and factors influencing the performance of structures can be found

Table 3. Mechanical properties of pultrusion components.

Typical matrix properties									
Material	Tensile strength (MPa)	Tensile modulus (GPa)	Flexural strength (MPa)	Flexural modulus (GPa)	Shear strength (MPa)	Shear modulus (GPa)	Density (kg/m ³)	Poisson's ratio (ν)	References
Epoxy	55–130	2.5–4.1	70–140	3.0	46–70	0.98–1.24	1100–1300	0.2–0.37	90,202–209
Polyester	20–100	1.8–4.1	70–132	3.9–4.0	56–70	1.38–1.6	1000–1450	0.1–0.38	55,90,210–213
Vinylester	70–87	3.0–5.1	149–156	3.2–3.5	–	1.43–1.6	1100–1300	0.3–0.4	90,213–219
Acrylic	56–88	2.2–3.1	117–215	2.9–3.7	–	–	–	–	3,220
Phenolic	35–60	1.2–4.1	48	–	43	–	1200–1400	–	221–225
Polypropylene	34–37.2	0.7	34	1.2–1.5	–	–	900	–	220,226
ABS	28–45	1.5–2.4	63–76	2.1–2.2	62.1	1.06	1020–1050	–	220,226–228
Nylon	55–90	1.3–3.5	108–117	2.8	–	–	1100–1160	–	220,225,226
Typical reinforcement fiber properties									
Basalt	2500–4800	85–110	–	21.7	7–17	2600–2800	0.2–0.26	209,229–233	
Carbon	3650–7000	207–600	1400	90	3–7	1700–1800	0.25–0.3	203,212,232,234–237	
E-glass	2500–4800	70–81.2	830	26–28.8	7–20	2540–2570	0.2–0.3	55,90,202,204,210,212–218,231,232,238	
S-glass	4200–4800	83–93	–	35–39	–	2485–2540	0.21–0.23	3,232,239,240	
Kenaf	–	4.5	–	–	–	1400	0.15	211	
Kevlar (Aramid)	2900–3400	70–152	280	2.9	12	1390–1467	0.35	3,228,232,236	
Flax	500–900	50	–	–	–	1400–1500	–	241	
Boron	4137	400	–	167	140	2630	0.2	242	

Table 4. Mechanical properties of the typical pultruded elements.

Material	Fiber volume fraction (%)	Density (kg/m ³)	Tensile strength (MPa)	Tensile modulus (GPa)	Compressive strength (MPa)	Shear strength (MPa)	Shear modulus (GPa)	Reference
E-glass roving/polyester	46–80%	1600–2000	307–1320	21–59	290–1240	27	3.5	3,68,243,244
E-glass mat+roving/polyester	48–61%	1750–1900	235–400	18–36	220–485	25–52	2.6–5.0	243,245–249
E-glass roving/vinylester	62%	1770	240	18–42	240	22	4.0	215,250
E-glass mat+roving/vinylester				24			3.7	247
E-glass roving/epoxy	52–53%		414–790	32–40			3.0–4.5	40,251,252
E-glass mat+roving/epoxy	56%	2000		42			7.0	253
E-glass roving/polyurethane	58%		310–850	37–47				251
Carbon roving/epoxy	65%	1500–1600	1430–2200	130–180	985–1450	72	3.6–4.2	73,234,254
Carbon roving/vinylester		1600	2000	140–145	1400			254
Kevlar roving/styrene acrylonitrile	61%	1180	170	9.4	120			228
Kevlar roving/styrene acrylonitrile	61%	1130	170	9.3	90			228
Kevlar roving/polyethylene	61%	1235	165	9.2	40			228

in the following works;^{263–268} and stress–strain analysis and failure modes in the following works.^{269–273} Aside from the structural elements described above, there are several works on rods and bars available as well. Searching for the most reliable material architecture, You et al.²⁷⁴ investigate both non-hybrid and hybrid rods (glass and carbon-based) under tensile loading.

The analytical investigation of pultruded rod behavior under tension, taking into account the presence of stress concentration at the gripped region can be found in the study by Portnov and Bakis.²⁷⁵

Compressive behavior. In contrast to the tensile case, the compressive strength of the pultruded elements is

much lower. Mechanical compressive testing of pultruded structural coupons presents several challenging aspects related to fiber alignment, coupon geometry, load introduction, stress concentration, buckling stability, and specimen end crushing. In particular, FRP profiles exhibit high longitudinal strength but low transverse strength.²⁷⁶ Indeed, instead of failure due to compression, they are more prone to geometric instability, local end crushing, or local end brooming.

The compressive behavior of pultruded FRP depends on the fiber volume fraction, properties of the raw materials involved, and the bond between matrix and reinforcement.^{236,277} The compressive strength reaches higher values as the fiber volume fraction increases. Nevertheless, in the cases of excessive fiber volume fractions, the compressive strength slightly decreases.²³⁶ Indeed, with few fibers, FRPs exhibit a brittle behavior, failing due to the propagation of multiple transverse cracks, whereas with excessive fibers, the failure mainly occurs owing to the longitudinal debonding at the interface between the fibers and matrix.²³⁶ Compressive tests on coupons reinforced with different materials demonstrate that glass and carbon fiber show similar behavior: high strength and brittle failure. On the contrary, Kevlar-reinforced polymers exhibit low modulus and strength while having high ductility. The post-treatment of the compressive tests outcomes has allowed researchers to evaluate indirectly the fibers' compressive properties by means of the reverse rule of mixture.²³⁶

As in the tensile case, the compressive mechanical behavior of pultruded profiles depends on the fiber architecture as well as on the tilt angle between the load direction and the unidirectional roving orientation.^{217,278} Experimental tests (performed on the coupons reinforced with glass rovings and continuous filament mats) have proved that the transverse compressive modulus is approximately 30% lower compared to the longitudinal one.²¹⁷ In the absence of mat and fabric layers (which are usually used in addition to the unidirectional rovings), pultruded structures exhibit lower transversal strength and stiffness.⁵ The ultimate stress is influenced by the tilt angle as well. The experimental outcomes demonstrate its decrease of approximately 45% between the coupons compressed longitudinally and transversally.²¹⁷ The pultruded profile under compressive loads typically fails owing to delamination related to buckling phenomena.²⁷⁹ The evolution of compression load and lateral displacement at the mid-length presents different behaviors, depending on the slenderness of the sample.^{279–282} A higher slenderness implies lower buckling failure strength. Slender pultruded FRPs under compression present two different behaviors that lead to failure: the lateral displacement at the mid-length and the internal

delamination. The former prevails in the compression tests of high slender ratio coupons; on the contrary, the latter is more evident in the case of short or thick coupons.²⁷⁹

Knowledge of peculiarities related to the compression behavior of pultruded elements allows engineers to design structures in a better, more efficient way. In recent years, there has been an increasing interest among scientists in regards to the mentioned loading scenario. Plenty of papers considering the compressive behavior of full-size structural profiles have been published. The most prominent and essential publications are briefly discussed in this paragraph. A comparison between the compressive behavior of full-scale profiles and coupons has been made by Barbero et al.²⁷⁶ In addition to the experimental part, the analytical equation to predict compressive characteristics of full-size structures was obtained and then verified with the data from the experiment. A significant number of articles are devoted to the characterization of behavior of compressed columns. Particular interest is paid to such topics as: analysis of failure criteria,²⁸³ built-up columns,^{65,284–290} hybrid columns,^{291,292} various aspects of buckling (global and local) and postbuckling behavior of structures,^{293–297} peculiarities in the influence of elevated temperatures,^{298–300} strength of web-flange junctions,³⁰¹ the influence of concentricity,^{302,303} and eccentricity.^{68,304} Aside from columns, some other types of structures were investigated as well. Riebel and Keller³⁰⁵ performed experimental research of pultruded hybrid GFRP/steel joints used in concrete structures. Their paper studies the influence of moist and alkaline environment on the durability of such compressed structural elements.³⁰⁵ Bai and Keller³⁰⁶ experimentally demonstrated the possibility to improve the endurance of FRP structural elements under combined thermal and compressive loading with the help of a liquid-cooling system. In their other paper, a reliable theoretical model to predict the shear failure of pultruded profiles subjected to the axial compression was proposed, followed by the comparison with data available in the literature so far.³⁰⁷

Shear behavior. Owing to the structural morphology of pultruded FRPs, different types of shear behaviors occur depending on the direction of the external shear load with respect to the reinforcement architecture. The commonly investigated behaviors are the in-plane and interlaminar shear. In the scientific literature, different procedures of shear modulus measurement have been reported. The most commonly used techniques are the cylinder torsion test,²⁷⁶ the V-notch test (also known as the *Iosipescu* technique),^{217,308–310} the off-axis test,^{217,311,312} and three- and four-point bending test.^{310,313} Besides, Minghini et al.³¹⁴ in their

experimental paper have proposed the novel four-point bending setup to determine shear modulus and compared it to traditionally applied three- and four-point bending. An experimental comparison of the *Iosipescu* technique, off-axis compression tests, and off-axis tensile tests to measure in-plane shear demonstrated that the off-axis compression tests and the V-notch tests results are compliant, whereas the shear response of the off-axis tensile test results is lower. This behavior is probably due to the stress state in tensile tests, which opens microcracks and microvoids existing inside the FRP. Therefore, the shear behavior cannot be measured by the off-axis tensile test. Nevertheless, it is noteworthy that the shear moduli computed analyzing the initial linear response from both off-axis tests results are very close to each other.²¹⁷

Typically, interlaminar shear stress is defined as a source of failure that causes relative sliding between the different layers of a laminated FRP and thus its delamination. In three-point bending tests, interlaminar shear and flexural rigidities of the tested part withstand the load at the same time.³¹³ The important advantage of this procedure is that it is applicable to full-size elements, and, therefore, not only to small coupons that can exhibit particular behavior due to local inhomogeneity.³¹⁵ Because the shear deformation is not negligible in pultruded FRPs, the Timoshenko beam theory approximates the actual behavior better than the Euler beam theory.^{315,316} The Timoshenko beam theory for an I-beam in a three-point bending test can be expressed as follows³¹⁵

$$\frac{4Av}{PL} = \frac{1}{12E_f} \left(\frac{L}{r}\right)^2 + \frac{1}{G_{LT}K_y} \quad (3)$$

where A is the transversal section area, v is the deflection at the midspan, P is the applied load, L is the span length, E_f is the flexural elastic modulus, k_y is the shear area coefficient, and r is the gyration radius, which is defined as $\sqrt{I_y A}$, where I_y is the moment of inertia of the section. Equation (3) expresses the linear relation between the independent variable $(L/r)^2$ and the dependent variable $(4Av)/(PL)$. Repeating the experiment with different span length on profiles with the same cross-section and plotting the regression line, the shear modulus can be obtained from the intercept, as expressed in equation (4)³¹⁵

$$G_{LT} = \frac{1}{K_y \times \text{intercept}} = \frac{PL}{4K_y Av} \quad (4)$$

Clear comprehension of shear performance of the real-scale pultruded structures is the key to successful design. In the last decades, much effort had been devoted to better understand the phenomena related

to the shear stress–strain behavior of real-scale structural elements as opposed to cut-out coupons. Serious attention has been paid to stress–strain analysis, failure modes, and determination of shear moduli of such structures and elements as beams;^{64,314,315,317,318} beams and structures reinforced/retrofitted with pultruded elements by means of internal or external reinforcement;^{319–325} box beams;³²⁶ bridge decks;^{31,258,327,328} columns;^{286,307} connectors;³²⁹ hybrid structures;^{330,331} sheet piles;¹¹⁸ and studs.³³² Besides, the influence of environmental conditions (such as water or elevated temperatures) on the shear characteristics of structures and joints was studied as well.^{38,333,334} It is worth noting that particular attention has also been paid to web-flange junctions.^{38,335} A number of papers published so far investigate the behavior of bolted and adhesively bonded connections.^{330,336–339} Several researchers also studied the influence of shear deformations and stress on the buckling behavior of pultruded structures.^{310,340–344}

Table 5 presents primary studies (experimental, analytical, and finite element modeling (FEM)) investigating the influence of the fiber/matrix type and cross-sectional characteristics on the shear behavior of pultruded elements due to different load cases as well as aiming to determine their shear moduli.

Flexural behavior. A high percentage of pultrusion products is used as beams, their components, or as a reinforcement for concrete beams. Therefore, their resistance to bending has been widely analyzed to date. Three- or four-point bending tests are the most commonly used procedures to evaluate flexural properties.^{310,315} Furthermore, highly reliable novel four-point bending setup has been suggested by Minghini et al.³¹⁴ to determine bending rigidity.

Nevertheless, as it was specified in the previous section, in this type of test, shear and bending phenomena occur at the same time. Generally, in the case of a high anisotropy ratio or high span length, the shear effects are negligible.³¹⁵ On the contrary, in case the above-mentioned conditions are not fulfilled, accounting for the Timoshenko beam model, expressed in equation (3), the flexural modulus E_f can be obtained considering the slope of the regression line, as described in equation (5)³¹⁵

$$E_f = \frac{1}{12 \times \text{slope}} \quad (5)$$

In the failure-related phenomena, a combination of different behaviors occurs within the same part. Indeed, the top layer is compressed, while the bottom layer is subjected to a tensile load. In the case of coupons with the unidirectional rovings arranged longitudinally, the

Table 5. Different approaches and their features toward investigation of pultrusion elements during shear loading and shear failure.

Approaches	References
Fiber type	
Basalt	345
Carbon	345
Glass	64,154,195,216,217,258,308,309,315,316,327,335,341,342,345–352
Glass-carbon	349
Resin type	
Isophthalic polyester	315,327,342,351,352
Isophthalic vinylester	345
Polyester	64,308,316,347,348,350
Vinylester	195,216,217,308,309,316,346
Investigation type	
Analytical	64,195,216,258,310,314,315,327,341,346–349,351–353
Experimental	64,154,195,216,217,258,308–310,314–316,327,335,341,342,345–352
FEM	154,217,258,315,341,345,350
Tested element type	
Bar	320,321,334
Bridge deck	31,258,327,328
Channel section profile	318
Circular hollow section profile	349
Column	286
Connector	329
Hollow rectangular section profiles	326,333,349
Hybrid structures	330,331,345
I section profile	38,64,310,314,315,318,333,340–343,348
Plate	323,337,351
Sheet piles	118
Sheet strip stirrup	319,320
Specimen	195,216,217,258,308–310,335,346,347,350,352
Stiffener	322
Wide-flange section profile	335,349
Loading/test type	
Bending	64,154,258,309,310,314–316,327,341,342,348
Biaxial stress condition	350
Iosipescu test	217,308,310,335,346,352
Off-axis tension and compression	217
Shear test	195,258,335,350,351
Torsion	64,216,310,345–349
Shear modulus	
In-plane	64,154,195,216,258,308,309,314,315,327,341,342,346–1348,350,352–354
Out-of-plane	216,310,347,350,353
St. Venant	64,310,348,354
Warping torsional rigidity	64,310
Full-scale structural elements investigations	
Beam	64,314,315,317,318
Bolted and adhesively bonded connections	330,336–339
Box beams	326
Bridge decks	31,258,327,328
Buckling instability	310,340–344

(continued)

Table 5. Continued

Approaches	References
Columns	286,307
Connectors	329
External or internal reinforcement of structures	319–325
Hybrid structures	330,331
Influence of external conditions	38,333,334
Sheet piles	118
Studs	332
Web-flange junction strength	38,335

test bends the fibers. This type of load in an inhomogeneous material, as pultruded FRPs, provokes internal sliding between material layers as a result of the resin brittle failure, finally leading to the generation of delamination. In case of transversely cut coupons, the three-point bending test causes the arising of intralaminar transversal cracks at the application load location.^{258,355}

Since bending of beams is, probably, the most common loading scenario observed in the structural elements, plenty of academic papers are available at the moment. Therefore, only the most remarkable works are listed here. General stress–strain analysis of the pultruded beams,^{64,142,314,315,326,346,353,356–363} straightening and restoration of existing beams,^{246,364–366} buckling instability,^{247,310,342,367–379} thermal loading,^{380,381} and web-flange junction strength³⁷⁹ are just primary examples of what composite scholars are working on in regard to the flexural behavior of full-scale pultruded structures. Other types of structural elements were also widely studied: application of composite bars and strips for reinforcement,^{382–389} space frame structures,^{390–394} hybrid beams,^{79,395–398} sandwich structures and bridge deck systems.^{71,258,327,399–406}

Table 6 reviews the principal studies (experimental, analytical, and FEM), investigating the influence of the fiber and matrix type as well as the cross-sectional characteristics on the flexural behavior of pultruded elements due to three/four-point bending.

Fatigue

One of the advantages of composite materials is that they are less prone to fatigue. However, there are scientific reports discussing this phenomenon.^{425,426} There are two main goals that engineers should keep in mind dealing with fatigue: fatigue strength (with an adequate level of probability) is to be ensured for n cycles of fatigue loading; repairing the damage caused by n cycles of a fatigue load should not be needed.⁴²⁷ The

matrix and fiber materials, fiber content by volume, fiber direction, porosity, environmental conditions,⁴²⁸ applied load and its amplitude, stress ratio R ,^{429–434} and load frequency¹³⁷ are the factors that influence the fatigue life and the mechanical characteristics of pultruded composite materials. However, investigations have shown that strain in the matrix is the key factor influencing the fatigue behavior.⁴³⁵ All these factors require additional considerations compared to traditional materials,^{436,437} which impose the necessity to use different design methods to predict the fatigue life of composites.⁴³⁸

With respect to repetitive loads, up to 10 million cycles within the overall life of a structure are to be considered.⁴³⁹ Not only structural elements made of FRPs, but also connections^{440–443} between them as well as large-scale experiments⁴⁴⁴ have been studied to date by different researchers. Further development of theoretical models able to estimate the fatigue life of composites is needed in order to provide engineers with better design tools together with more efficient nondestructive test methods. All the models proposed previously can be categorized into three classes according to different methods applied:^{445,446}

1. Fatigue life models offering a fatigue failure criterion based on S–N curves without accounting for actual degradation mechanisms. S–N curves serve as the primary tool for the analysis of fatigue behavior in composite structures. They can be obtained for certain loading conditions and then can be used to model the constant-amplitude fatigue behavior of the studied materials;
2. Models for which residual stiffness and strength are the key factors of damage;
3. Models considering actual damage mechanisms (matrix cracks, fiber fractures).¹³⁷

The stress ratio is used to characterize the fatigue-loading type, and it can be calculated as the proportion between minimum and maximum applied cyclic stress

Table 6. Different approaches and their features toward investigation of pultrusion elements during flexural loading and flexural failure.

Approaches	References
Fiber type	
Carbon	355,407
Glass	64,118,142,204,243,246,258,315,326,346,356,357,361,362,400,402–404,407–424
Kevlar	407
Resin type	
Epoxy	204,355,421
Isophthalic polyester	246,400,409,419,420
Orthophthalic polyester	419
Polyester	64,118,243,358,403,410,413,415,416,422
Polyurethane	407,411,412
Vinylester	142,326,346,356–358,362,404,408,413,414,418,419
Investigation type	
Analytical	64,118,142,204,258,314,315,326,346,353,356,362,404,405,409,415,418,423,424
Experimental	64,118,204,243,246,258,310,314,315,326,346,355–358,361,362,400,402–404,406,407–424
FEM	142,258,315,356,358,361,400,403,405,406,409,424
Tested element type	
Bonded I section profile	246
Bridge deck	258,400,402–406
Hollow rectangular and box section profiles	326,356,357,361,362,410,413,424
I section profile	64,142,246,310,314,315,353,356–358,409,410,422
Rope	355
Sandwich panel	418
Sheet pile panel	118
Specimen	204,243,310,407,411,412,414,416,419
Strip	421
Wide-flange section profile	346,413,415,417,420,423
Loading/test type	
Four-point bending	64,118,142,243,246,258,310,314,356,357,361,362,403,410,413,423
Three-point bending	64,118,142,204,310,314,315,326,346,356–358,402,404,408–410,413,415–424
Full-scale structural elements investigations	
Bars and strips for the reinforcement	382–389
Buckling instability	247,310,342,367–379
Hybrid beams	79,395–398
Sandwich structures and bridge deck systems	71,258,327,399–406
Space frame structures	390–394
Straightening and restoration of the existing beams	246,364–366
Stress–strain analysis of beams	64,142,314,315,326,346,353,356–363
Thermal loading	380,381
Web-flange junction strength	379

$R = \sigma_{\min}/\sigma_{\max}$.⁴⁴⁷ $0 < R < 1$ is tension–tension (T–T) fatigue; $1 < R < +\infty$ is compression–compression (C–C) fatigue; $-\infty < R < 0$ indicates mixed tension–compression (T–C) fatigue loading that can be either tension- or compression-prevalent. In the case of $R \approx 1$, a creep effect can be considered.

Minner’s linear rule is one of the most commonly used damage models, owing to its simplicity

and efficiency in case of constant-amplitude loading.⁴⁴⁸ Nevertheless, a more complete model, accounting for spectrum loading, yields much more accurate results in many real cases, in which the acting repetitive force does not have constant amplitude.⁴⁴⁹ According to this model, the total life N_m of an FRP under the effect of m different cyclic loads depends on the residual life “consumption” of each of the cyclic

loads, according to the relation reported in equation (6)⁴⁴⁹

$$\frac{1}{\ln N_m} \sum_{i=1}^m \frac{n_i}{N_i} N_i = 1 \quad (6)$$

In contrast to transport, aerospace, and marine sectors, the application of pultruded structures in civil engineering is relatively immature. This is the primary reason explaining the lack of information and data on the fatigue performance of such structures in the construction sector, as the main source of knowledge related to the fatigue performance is, typically, an experimental study.⁴⁵⁰ However, outcomes of fatigue experiments can usually be characterized as very volatile even at the very similar conditions. Earlier that was not a problem since large safety factors were employed. These days, on the other hand, engineers, starving for a better, advanced results, seek for accurate characterization of fatigue behavior. Statistical characterization of fatigue life is indeed a burning topic among scientists.⁴⁵¹

Even more effort should be made to investigate natural fiber composites (NFC) since available knowledge about their fatigue behavior is very limited. For an advanced structural design of NFC, damage mechanisms, changes in mechanical properties, and critical failure development must be studied as well.⁴⁵²

Authors envision that the increase in computational power and spreading of molecular dynamics modeling methods will allow researchers to better understand mechanical characteristics of pultruded composites in general and fatigue in particular both at the atomic and nano scales. This will allow better understanding of strain distribution across the fiber-matrix interface during the loading. This research would also explain the dependency of macro parameters on the microscale ones.

Last but not the least, most of the experiments concerning fatigue performance were conducted on the coupons under quite simple loading conditions. However, elements of real structures are subjected to much more complex loading scenarios. Therefore, it would be of great interest to conduct laboratory tests on real structural elements, with loading scenarios more less close to the real-life ones.⁴⁵³

Table 7 shows a summary of primary studies (experimental, analytical, and FEM) investigating the influence of fiber/matrix type, cross-sectional characteristics, and stress ratio on the fatigue behavior of pultruded elements owing to different loads while still considering influence of cycle number.

Creep

A structure being constantly loaded can experience time-dependent deformation.⁴⁵⁴ This phenomenon is

called creep. The history of FRP-pultruded elements' application is relatively short, which narrows the knowledge about their behavior at creep. An understanding of creep's influence on the structure is used to determine not only the expected cost of maintenance but even more critically, the anticipated life of the structural element. It is noteworthy that the nature of the polymer matrix is susceptible to the viscous phenomena, and, thus, time-dependent effects are especially significant in the life cycle of composite structures.^{455,456}

Every type of material has its own creep behavior. However, typically, regardless of the material, this process includes three steps: primary, secondary, and tertiary creep. Deformation, initially quickly increasing with time and slowing thereafter, characterizes the primary stage as an instant result of continuously applied loading. This phase can be characterized by the presence of relatively low values of stresses and strains, at less than 0.2%. It has an almost negligible rate of creep. After the removal of the external load, the strain could be almost eliminated with time. During the secondary stage, the strain of the material is nearly even. As a result of internal stress reorganization within the material, there is a moderate but limited damage increase. It is interlinked with the existence of a time interval, where a low constant creep rate over a characteristic time is presented. This creep stage is usually observed over decades. At some reasonable degree, the strain developed at this stage can be recovered. The essential aspect is that, at this stage, the profile's strength can be very similar to the initial strength in the case where the deformation is not extreme. In case the environment does not affect the structure harshly, this phase can still be considered as appropriate for practical applications. In contrast to these two already mentioned phases, during the third stage, the strain increases rapidly until the collapse of the structure. It even can happen that primary creep will be followed immediately by tertiary creep in the case of high loads. The value of the applied load defines the duration of each stage.⁴⁵⁷

Numerous studies have been done so far, aiming to develop analytical models and equations for the prediction of composites' creep behavior. Chief among these theories are: the Findley's power law model for describing the long-term behavior of FRP elements subjected to constant stresses;⁴⁵⁸ the rule of mixtures approach for combining the effects of the time-dependent behavior of the matrix and the fibers, the Scharepy single integral procedure, the Boltzmann superposition principle, and the Prony series that is analogous to springs and dashpots (Kelvin and Maxwell arrangements).^{218,459} Specifically, a pultruded elements model accounting for the viscoelastic nature of the resin as well as elastic behavior of fiber reinforcement and its architecture was presented in Cardoso and Harries.⁴⁶⁰

Table 7. Different approaches and their features toward investigation of pultrusion elements during fatigue loading and fatigue failure.

Approaches	References
Fiber type	
Carbon	25,149,355
Glass	25,29,56,137,418,426,434,437–440,442–444,447,495–513
Resin type	
Epoxy	355,496,509
Isophthalic polyester	426,434,439,440,442,447,506,510–512
Phenolic	495
Polyester	137,443,499,501,507,508,513
Polyurethane	505
Vinylester	25,418,497,498,500,502,504
Loading type	
Compression	447,509,510
Flexural	25,29,355,418,438,496–499,501,503,508,512
Reversed (combination of tensile and compressive)	447,509
Tension	437,440,442,443,447,500,502,503,505,506,509–511
Stress ratio “R”	
$-\infty < R < 0$ (mixed tension–compression)	447,509
$0 < R < 1$ (tension–tension)	25,29,137,426,434,437–440,442,443,447,495–497,499,500,502,503,505–510,512,513
$1 < R < +\infty$ (compression–compression)	447,498,509,510
Tested element type	
Adhesively bonded double cantilever beam joint	426,434
Adhesively bonded double lap joint	442,443,447,503,506,507,509–511
Adhesively bonded pultruded GFRP joint	512
Adhesively bonded stepped-lap joint	442,507
Box section profile	438,497,499,501
Bridge deck	25,56,503,504,508
Circular hollow section profile	444
Flat rectangular section profile	439
Frame	444
Hybrid girder	29
Plate strip	440
Rope	355
Sandwich panel	418
Specimen	495,498,500,502,505
Trapezoidal section profile	137
U section profile	437,499,501
Wide Flange section profile	438,497
Investigation type	
Analytical	137,426,434,438,442,447,496,502,505–507,509,511,512
Experimental	25,29,56,137,355,418,426,434,437,439,440,442–444,447,495–512
FEM	137
S–N curves are plotted	137,355,437,439,440,443,447,495,496,498,499,505,506,511
Number of cycles	
$0 < \dots < 10^5$	56
$10^5 < \dots$	25,29,137,355,418,426,438–440,442–444,447,495–501,503–513

Among all the listed models, Findley's power law is currently the most widely accepted.⁴⁶¹ Moreover, according to the ASCE structural plastics design manual, this model is to be used for the analysis and design of FRP composite sections in the case of creep.⁴⁵⁹ Considering sustained stress (σ), causing creep, as well as instantaneous modulus (E_0) and time-dependent modulus (E_t), the equation for the total strain can be derived⁴⁵⁷

$$\varepsilon(t) = \frac{\sigma}{E_0} + \left(\frac{\sigma}{E_t}\right) \cdot t^n = \sigma \left(\frac{1}{E_0} + \frac{t^n}{E_t}\right) = \frac{\sigma}{E(t)} \quad (7)$$

where n is a specific parameter of the material. Rearranging equation (7), the apparent time-dependent modulus ($E(t)$) can be estimated as the value depending on E_0 and E_t ⁴⁵⁷

$$E(t) = E_0 / (1 + (E_0/E_t) \cdot t^n) \quad (8)$$

As was noted earlier in this section, pultruded elements are anisotropic and nonhomogeneous. Therefore, the viscoelastic stiffness $E(t)$ assumes different values depending on the architecture of fiber and the direction of load.⁴⁶² The shear modulus will also vary accordingly. Considering the instantaneous modulus (G_0), the time-dependent modulus (G_t), and the shear exponent (n_g), the creep in shear direction can be considered by equation (9)⁴⁶³

$$G(t) = G_0 / (1 + (G_0/G_t) \cdot t^{n_g}) \quad (9)$$

The study of Cardoso and Harries⁴⁶⁰ is the first successful attempt to account for creep in the direction longitudinal and transversal to the pultrusion axis. The model proposed in the study takes into account both elastic and viscoelastic nature of reinforcement and matrix. A comparison of theoretical assumptions and experimental data, presented in the second chapter of the study, shows good agreement with the model.

As was already mentioned before, the role of pultruded elements as the structural parts is relatively new for the construction sector. Thus, composite community is experiencing the lack of knowledge in terms of long-term performance of pultruded elements. For better design, further research of full-scale structures is needed.^{363,457} Besides, there is also a gap in the creep characterization of hybrid FRP structures. For instance, very small number of papers are available regarding the GFRP-concrete hybrid structures.⁴⁶⁴⁻⁴⁶⁷

Relation between degree of polymerization and the corresponding creep response of matrix-dominated (shear and transverse) properties is still not clear enough.⁴⁶⁰ Until now, almost no attention has been paid to shear creep investigation.^{462,463}

Moreover, very little published research is available on the influence of stresses acting orthogonally to the longitudinal direction of profiles.⁴⁶⁰ There is still a great deal of work to be done in these areas.

Table 8 presents primary studies (experimental, analytical, and FEM) investigating the influence of the fiber and matrix type as well as cross-sectional characteristics on the creep behavior of pultruded elements due to different load cases and its duration. Moreover, different models are reviewed as well.

Future trends

The analysis of mechanical characteristics of pultruded profiles makes it clear that further research is needed to better understand the properties of material. All the topics mentioned below will require substantial research efforts since only a limited number of relevant publications are currently available. This final subchapter discusses the highlights and promising directions for further investigations.

The use of different types of additives in the manufacturing process makes it possible to improve mechanical characteristics of the final product and, therefore, to promote widespread practical application of structural profiles. At the moment, research regarding the influence of the micro- and nanoparticles on the characteristics of pultruded end products is very limited. Kuruvilla and Renukappa⁴⁶⁸ have studied the effect of nano- and microparticles on die penetration, water diffusion, and leakage current in pultruded GFRP composites. The influence of nano-sized alumina, silica, and micron-sized alumina trihydrate fillers on mechanical properties of pultruded GFRP epoxy composites was studied by Manjunath et al.⁴²¹

Human safety is a priority in any design process. Fire propagation and emission of toxic gases are very dangerous. Flame-retardant (FR) treatment of reinforcement with chemicals and filling of matrix with micro- and nanofillers are intended to deal with this issue. However, Bar et al.⁴⁶⁹ have discovered that mechanical properties of composite materials are greatly affected by different FR treatments. Therefore, an adequate compromise has to be found between preservation of mechanical properties of structural elements and minimization of fire hazards. And, last but not the least, is the use of various types of hardening agents enhancing the strength properties of epoxy resins and improving the overall performance of structures.⁴⁷⁰

There is no doubt that process parameters directly influence the formation of process-induced shape distortions.^{92,471,472} The mismatch in coefficients of linear thermal expansion of reinforcement and matrix leads to the formation of residual stresses.^{473,474} They provoke various imperfections in the final structure, such as

Table 8. Different approaches and their features toward investigation of pultrusion elements during creep loading and creep failure.

Approaches	References
Fiber type	
Carbon	455
Glass	218,454,457,461–463,466,467,514–521
Resin type	
Epoxy	519
Isophthalic polyester	457,461,466,514,515,517,520,521
Polyester	454,462,467,518
Polyurethane	519
Vinylester	218,463,516
Loading type	
Compression	218,454,515,516,518
Flexural	457,461,463,466,467,514,517,519–521
Shear force	462
Tension	455,462
Transversal loading	460
Test duration	
... < 100 h	218,517–520
100 h < ... < 1000 h	457,520
1000 h < ... < 10,000 h	454,461,466,463,467,514–516,521
10,000 h < ...	455,462
Tested element type	
Bridge deck	521
Beam assembly	517
Full-size portal frame	463
Hollow box section profile	454,520
I section profile	466,467,514
Laminate	455,522
Plate	457
Sheet panel pile	461
Specimen	218,462,514–516,518,519
Wide-flange section profile	454
Investigation type	
Analytical	218,454,457,461–463,466,515–518,521,523
Experimental	218,454,455,457,461–463,466,467,514–522
FEM	466,467
Model discussed	
Boltzmann superposition principle	459,515
Bruger–Kelvin model	523
Findley power law model	454,457,459,461–463,466,467,515–518,521,523
Maxwell chain model	467
Prony–Dirichlet series	523
Scharepy single integral procedure	218,459,518
Time–stress superposition principle	523
Time–temperature superposition principle	518

spring-in,⁴⁷⁵ warpage,⁴⁷⁵ transverse matrix cracks in the unidirectional layer, delamination at the interface between unidirectional roving and continuous filament mat layers, etc.¹⁵⁹ Insufficient impregnation of fibers

with the polymer matrix results in porosities, voids, and fiber misalignment.^{158,476,477}

Non-destructive testing (NDT) is a technique allowing to investigate the quality of the final product

without compromising its integrity, saving both time and money. Regardless of the papers mentioned previously, there is still a lack of knowledge on the application of NDT for examination of pultruded structures. In the very recent work by Geng et al.,⁴⁷⁸ the application of different NDT techniques for the assessment of delaminations in composite materials is reviewed and compared together with their pros and cons. Baran et al.¹⁵⁸ pioneered the use of X-ray computed tomography for the examination of defects in pultruded L-shaped profiles. Essiga and Kreutzbruck⁴⁷⁹ confirmed the possibility of using air-coupled ultrasonic transducers to examine the quality of thermoplastic-pultruded CFRP tapes. Xu⁴⁸⁰ successfully applied an optical interferometer to detect delaminations at the web/flange junction in I-section composite beams.

Different stress-states in various zones of pultruded structures can necessitate the use of dissimilar fiber types. The so-called “hybridized reinforcement” technique can be a solution to this problem. For instance, in order to increase the resistance of structural pultruded GFRP elements to most unfavorable loading scenarios, namely, buckling or increased deformations, glass fiber reinforcement can be partially substituted with that of carbon fibers. Further on, in order to improve mechanical properties of composites, namely shear, interlaminar shear, and off-axis strength, novel techniques employing the off-axis reinforcement are of special interest.¹⁶⁹ Today, the hybrid reinforcement technique is a reality. However, it is applied in a very cautious manner due to the lack of knowledge on structural behavior of hybrid-reinforced elements⁴⁸¹ and requires further research.

Unfortunately, most of the constitutive models developed so far are not good enough to give an accurate result when dealing with a composite structure loaded in slightly varied conditions. Indeed, assumptions valid for the metal structures can not be just taken and used to model the complex behavior of a composite.^{482,483} However, a vast number of composite models treat a composite as a homogeneous anisotropic material, which, in fact, is not true. And, therefore, fail to provide accurate prediction of properties and mechanisms governing the response. Preferably, composites should be considered as heterogeneous structures. In order to account for the primary mechanisms responsible for mechanical performance, these mechanisms should be modeled simultaneously. The ability to model them at the lower levels is also of great importance. As was already mentioned before, supercomputers and molecular dynamics can make it possible.⁴⁵³

Last decade has seen the rise in popularity of natural fibers reinforcement and bio-based materials among the world’s largest composite manufacturing

companies.^{484,485} Among the most significant advantages of natural fibers are their moderate specific strength, light weight, less damage to processing equipment, lower price and energy consumption, environmental friendliness, good mechanical,⁴⁸⁴ and thermal properties. On the other hand, there are certain disadvantages as well: low allowed manufacturing temperatures, tendency to form clumps, and hydrophilic nature.⁴⁸⁶ Currently, pultruded structures with natural fiber reinforcement are rather uncommon, compared with the glass fiber-reinforced structures occupying a huge part of the market. In order to push the production of green composites forward, their weak points should be improved.^{487,488} This can be done via the application of novel surface treatments and coatings, introduction of additives, and improvement of hydrophobic characteristics.^{489–491}

Thermoplastic-pultruded profiles have definite advantages over thermoset ones and even over metallic counterparts. It is worth mentioning that the nature of thermoplasts makes it possible to join them both with similar and dissimilar polymers.⁴⁹² However, the topic of welding in regard to thermoplastic pultrusion still requires further investigation.

Different constituent materials of a composite provide different properties of the final product. One of the characteristics which is still poorly investigated on the structural level (as opposed to the laminate one) is the strain rate sensitivity. Generally, the properties of specific profiles included in the datasheets of companies correspond to the very low strain rates, so-called quasi-static. Review paper by Zhang et al.²⁵⁵ provides synopsis of available studies of strain-rate sensitivity and corresponding material properties of pultruded structures, together with the recommendations on future research directions.²⁵⁵ According to the authors, the following aspects require further investigation: the boundary between nonlinear behavior at high strain rates and linear elastic behavior at quasi-static rates; compressive and tensile experiments at intermediate strain rates for different fiber orientations; the influence of strain rate on shear modulus of pultruded GFRP; value of Poisson’s ratio of pultruded GFRP at different strain rates; development of an improved constitutive material model (in respect to the existing ones: elastic/viscoplastic, elastic/viscoelastic, and micromechanical models) for accurate representation of material response at higher strain rates for different fiber orientations.

The core challenge of every engineering task is to optimize the outputs of the process as much as possible. Numerical optimization tools have gained significant popularity in recent years due to the necessity of realizing the full potential of composite materials.⁴⁹³ Optimization can be done in regard to many variables,

starting from process parameters to the geometrical topology of the final product.⁴⁹⁴ Though multi-objective optimization is commonly in the composite sector, pultrusion process, however, still experiences a lack of studies concerning this topic.

Finally, aside from the experimental and theoretical work, the existing mathematical models are to be refined in order to improve fiber wet-out, determine optimal temperatures of heating platens for the proper polymerization process, minimize process induced shape distortions, solve problems related to cracking and delamination, and optimize outcomes of the process, while reducing energy consumption.⁴

Conclusions

The paper provides a synopsis of the main applications of pultruded elements, describing their peculiar mechanical behavior. The studies reported in this paper demonstrate that pultruded FRPs provide a wide range of possibilities to designers owing to their particular advantages over traditional materials. The huge variety of products and the differences between their characteristics demonstrate the high versatility of the pultrusion technique. Pultruded elements combine the typical customizability of advanced reinforced FRPs, achieved through the choice of raw materials and fibrous structure, with the low cost and the high specific properties, related to the highly effective manufacturing process. Moreover, the low energy consumption, low quantity of scrap, and the possibility to easily use biomaterials, both as fiber and matrix, make this process particularly interesting from the perspective of sustainability. The enhanced mechanical behavior of pultruded elements promoted their usage as a competitive alternative to the conventional materials of civil buildings and structures.

For the sake of brevity, several critical aspects were not covered in this work. It is worth dedicating separate review papers to each topic not treated in the present work, as further deep analysis remains to be done. These include structural design of pultruded elements; the connections, adhesive or bolted, which are dramatically important in the load transmission and distribution; environmental ageing under aggressive conditions, which are very common in typical applications; the impact of technological or in-service defects on the mechanical performance; and the use of biocompatible materials.

Acknowledgements

The authors would like to express their gratitude to the Skoltech Center for Design, Manufacturing and Materials for support provided within the frames of Collaboration Programs.

Declaration of Conflicting Interests

The author(s) declared no potential conflicts of interest with respect to the research, authorship, and/or publication of this article.

Funding

The author(s) received no financial support for the research, authorship, and/or publication of this article.

ORCID iDs

Alexander Vedernikov  <https://orcid.org/0000-0003-2127-0934>

Alexander Safonov  <https://orcid.org/0000-0002-5031-9058>

Fausto Tucci  <https://orcid.org/0000-0002-3664-2051>

References

1. Shaw-Stewart D and Sumerak JE. *Pultrusion for engineers*. Sawston, UK: Woodhead Publishing, 2000.
2. Meyer RW. *Handbook of Pultrusion Technology*. Berlin, Germany: Springer, 1985, pp. 51–93.
3. Starr TF. *Pultrusion for engineers*. Sawston, UK: Woodhead Publishing, 2000.
4. Baran I. *Pultrusion: state-of-the-art process models*. Shropshire: Smithers Rapra, 2015.
5. Bank LC. *Composites for construction: structural design with FRP materials*. Epub ahead of print 2007. DOI: 10.1002/9780470121429.
6. Bakis CE, Bank LC, Brown VL, et al. Fibre reinforced polymer composites for construction – state-of-the-art review. *J Compos Constr* 2002; 6: 73–87.
7. Fairuz AM, Sapuan SM, Zainudin ES, et al. Polymer composite manufacturing using a pultrusion process: a review. *Am J Appl Sci* 2014; 11: 1798–1810.
8. Safonov AA, Carlone P and Akhatov I. Mathematical simulation of pultrusion processes: a review. *Compos Struct* 2018; 184: 153–177.
9. GRP bridge across UK M6 motorway, <https://fiberline.com/grp-bridge-across-uk-m6-motorway> (2009, accessed 28 August 2019).
10. A grasshopper with fibre glass, <https://fiberline.com/grasshopper-fibre-glass> (2009, accessed 28 August 2019).
11. Marley 400 – 800MD – Unilite, <https://spxcooling.com/products/detail/counterflow-field-erected-cooling-tower> (2005, accessed 28 August 2019).
12. Flexible and durable pool bottom for Danish waterpark, <https://fiberline.com/other-structures/flexible-and-durable-pool-bottom-danish-waterpark> (2009, accessed 28 August 2019).
13. Engineered for the automotive industry, <http://cqfd-composites.com/ultimate-mechanics> (2007, accessed 28 August 2019).
14. Performance 700 Times Better Than Aluminum, www.deceuninckna.com/windows-and-doors/innery/feature-and-benefits (2014, accessed 28 August 2019).
15. Zhang D, Zhao Q, Huang Y, et al. Flexural properties of a lightweight hybrid FRP-aluminum modular space truss bridge system. *Compos Struct* 2014; 108: 600–615.

16. Turvey GJ. CFRP stiffened GFRP continuous beams – a simple closed-form analysis and its experimental verification for serviceability limit deformations. *Compos Struct* 2016; 153: 952–960.
17. CIRIA C779. In: Mottram JT and Hendersen J (eds) *Fibre-reinforced polymer bridges – guidance for designers*. London, UK: CIRIA, 2018, pp. 6.
18. Hollaway LC. A review of the present and future utilisation of FRP composites in the civil infrastructure with reference to their important in-service properties. *Constr Build Mater* 2010; 24: 2419–2445.
19. Braestrup MW. Footbridge constructed from glass-fibre-reinforced profiles, Denmark. *Struct Eng Int J Int Assoc Bridg Struct Eng* 1999; 9: 256–258.
20. Road. bridge built entirely with pultruded profiles. *Adv Compos Bull* 2005; 19: 6–7.
21. Keller T, Bai Y and Vallée T. Long-term performance of a glass fiber-reinforced polymer truss bridge. *J Compos Constr* 2007; 11: 99–108.
22. Keller T, De Castro J and Schollmayer M. Adhesively bonded and translucent glass fiber reinforced polymer sandwich girders. *J Compos Constr* 2004; 8: 461–470.
23. Moscow gets GRP bridge to beat corrosion, <https://fiberline.com/moscow-gets-grp-bridge-beat-corrosion> (2009, accessed 29 August 2019).
24. Greenland's first bridge of GFRP composite, <https://fiberline.com/groenlands-foerste-kompositbro> (2009, accessed 28 August 2019).
25. Kumar P, Chandrashekhara K and Nanni A. Structural performance of a FRP bridge deck. *Constr Build Mater* 2004; 18: 35–47.
26. Muttashar M, Manalo A, Karunasena W, et al. Flexural behaviour of multi-celled GFRP composite beams with concrete infill: experiment and theoretical analysis. *Compos Struct* 2017; 159: 21–33.
27. Park KT. Analytical verification of a composite level of bolted GFRP bridge deck-to-girder connection system. *Compos Struct* 2009; 89: 484–488.
28. Tinkov DV and Safonov AA. Design optimization of truss bridge structures of composite materials. *J Mach Manuf Reliab* 2017; 46: 46–52.
29. Keller T and Gürtler H. Composite action and adhesive bond between fiber-reinforced polymer bridge decks and main girders. *J Compos Constr* 2005; 9: 360–368.
30. King L, Toutanji H and Vuddandam R. Load and resistance factor design of fiber reinforced polymer composite bridge deck. *Compos Part B Eng* 2012; 43: 673–680.
31. Xin H, Mosallam A, Liu Y, et al. Experimental and numerical investigation on in-plane compression and shear performance of a pultruded GFRP composite bridge deck. *Compos Struct* 2017; 180: 914–932.
32. Karbhari VM, Chin JW, Hunston D, et al. Durability gap analysis for fiber-reinforced polymer composites in civil infrastructure. *J Compos Constr* 2003; 7: 238–247.
33. Reising RMW, Shahrooz BM, Hunt VJ, et al. Close look at construction issues and performance of four fiber-reinforced polymer composite bridge decks. *J Compos Constr* 2004; 8: 33–42.
34. Sutherland LS, Sá MF, Correia JR, et al. Impact response of pedestrian bridge multicellular pultruded GFRP deck panels. *Compos Struct* 2017; 171: 473–485.
35. Sebastian WM, Ross J, Keller T, et al. Load response due to local and global indeterminacies of FRP-deck bridges. *Compos Part B Eng* 2012; 43: 1727–1738.
36. Halabe UB, Vasudevan A, Klinkhachorn P, et al. Detection of subsurface defects in fiber reinforced polymer composite bridge decks using digital infrared thermography. *Nondestruct Test Eval* 2007; 22: 155–175.
37. Aluri S, Jinka C and GangaRao HVS. Dynamic response of three fiber reinforced polymer composite bridges. *J Bridg Eng*, Epub ahead of print November 2005. DOI: 10.1061/(ASCE)1084-0702(2005)10:6(722).
38. Xin H, Mosallam A, Liu Y, et al. Hygrothermal aging effects on shear behavior of pultruded FRP composite web-flange junctions in bridge application. *Compos Part B Eng* 2017; 110: 213–228.
39. Park K-T, Hwang Y-K, Lee Y-H, et al. Performance verification of a new pultruded GFRP bridge deck-to-girder connection system. *Compos Struct* 2007; 81: 114–124.
40. Mara V, Al-Emrani M and Haghani R. A novel connection for fibre reinforced polymer bridge decks: conceptual design and experimental investigation. *Compos Struct* 2014; 117: 83–97.
41. Yanes-Armas S, de Castro J and Keller T. Energy dissipation and recovery in web-flange junctions of pultruded GFRP decks. *Compos Struct* 2016; 148: 168–180.
42. Zi G, Kim BM, Hwang YK, et al. The static behavior of a modular foam-filled GFRP bridge deck with a strong web-flange joint. *Compos Struct* 2016; 85: 155–163.
43. Zi G, Kim BM, Hwang YK, et al. An experimental study on static behavior of a GFRP bridge deck filled with a polyurethane foam. *Compos Struct* 2008; 82: 257–268.
44. Yanes-Armas S, de Castro J and Keller T. Rotational stiffness of web-flange junctions of pultruded GFRP decks. *Eng Struct* 2017; 140: 373–389.
45. Davalos JF, Chen A and Qiao P. *FRP deck and steel girder bridge systems: analysis and design*. Abingdon, UK: Routledge, 2013.
46. Davalos JF, Chen A and Zou B. Stiffness and strength evaluations of a shear connection system for FRP bridge decks to steel girders. *J Compos Constr* 2011; 15: 441–450.
47. Davey SW, Van Erp GM and Marsh R. Fibre composite bridge decks – an alternative approach. *Compos – Part A Appl Sci Manuf* 2001; 32: 1339–1343.
48. Kim HY, Hwang YK, Park KT, et al. Fiber reinforced plastic deck profile for I-girder bridges. *Compos Struct* 2005; 67: 411–416.
49. Park K-T, Kim S-H, Lee Y-H, et al. Pilot test on a developed GFRP bridge deck. *Compos Struct* 2005; 70: 48–59.
50. Zou X, Feng P and Wang J. Perforated FRP ribs for shear connecting of FRP-concrete hybrid beams/decks. *Compos Struct* 2016; 152: 267–276.
51. Zou B, Chen A, Davalos JF, et al. Evaluation of effective flange width by shear lag model for orthotropic FRP bridge decks. *Compos Struct* 2011; 93: 474–482.
52. Sebastian W, Gegeshidze G and Luke S. Positive and negative moment behaviours of hybrid members

- comprising cellular GFRP bridge decking epoxy-bonded to reinforced concrete beams. *Compos Part B Eng* 2013; 45: 486–496.
53. Keller T and Schollmayer M. Through-thickness performance of adhesive joints between FRP bridge decks and steel girders. *Compos Struct* 2009; 87: 232–241.
 54. Schollmayer M and Keller T. Modeling of through-thickness stress state in adhesive joints connecting pultruded FRP bridge decks and steel girders. *Compos Struct* 2009; 90: 67–75.
 55. Kim H-Y, Park K-T, Jeong J, et al. A pultruded GFRP deck panel for temporary structures. *Compos Struct* 2009; 91: 20–30.
 56. Moon DY, Zi G, Lee DH, et al. Fatigue behavior of the foam-filled GFRP bridge deck. *Compos Part B Eng* 2009; 40: 141–148.
 57. Mortensen KP and Petterson RW. Fiberglass reinforced polyester in cooling towers – structural application. In: *Cooling Technology Institute Annual Conference* (eds. Rees B, Nelissen P, Cerra H, et al.). Corpus Christi, Texas, 3-7 February 2013, Red Hook, pp. 286–294. New York: Curran Associates.
 58. Lamberti M, Maurel-Pantel A, Ascione F, et al. Influence of web/flange reinforcement on the GFRP bonded beams mechanical response: a comparison with experimental results and a numerical prediction. *Compos Struct*, Epub ahead of print March 2016. DOI: 10.1016/j.compstruct.2016.03.043.
 59. Feo L, Mosallam AS and Penna R. Mechanical behavior of web-flange junctions of thin-walled pultruded I-profiles: an experimental and numerical evaluation. *Compos Part B Eng* 2013; 48: 18–39.
 60. Safonov A, Bondarchuk D, Saratov A, et al. Optimal process design for large-scale pultrusion structures. In: *ICCM international conferences on composite materials*. International Committee on Composite Materials, www.scopus.com/inward/record.uri?eid=2-s2.0-85053113602&partnerID=40&md5=b6cbbef7c9e313-c123e471d2a3554f8 (2017, accessed 1 February 2020).
 61. Safonov AA and Konstantinov AY. Mathematical simulation of residual deformation of complex composite profiles during pultrusion. In: *International SAMPE technical conference*. Society for the Advancement of Material and Process Engineering, www.scopus.com/inward/record.uri?eid=2-s2.0-84987662493&partnerID=40&md5=64ff6a1cc68e7b3254cd2b9eef030f32 (2015, accessed 1 February 2020).
 62. Evernden MC and Mottram JT. Characterization of unistrut connection method with pultruded fiber-reinforced polymer channels. *J Mater Civ Eng* 2006; 18: 700–709.
 63. Qiao P, Davalos JF and Barbero EJ. Design optimization of fiber reinforced plastic composite shapes. *J Compos Mater* 1998; 32: 177–196.
 64. Roberts TM and Al-Ubaidi H. Flexural and torsional properties of pultruded fiber reinforced plastic I-profiles. *J Compos Constr* 2002; 6: 28–34.
 65. Boscato G, Casalegno C and Russo S. Performance of built-up columns made by pultruded FRP material. *Compos Struct* 2015; 121: 46–63.
 66. Barbero EJ. Local buckling of FRP beams and columns. *J Mater Civ Eng* 1993; 5: 339–355.
 67. Kim YJ and Qian KZ. Effect of geometric discontinuities on failure of pultruded GFRP columns in axial compression. *Compos Struct* 2016; 136: 171–181.
 68. Xie L, Bai Y, Qi Y, et al. Pultruded GFRP square hollow columns with bolted sleeve joints under eccentric compression. *Compos Part B Eng* 2019; 162: 274–282.
 69. Youssef J and Hadi MNS. Axial load-bending moment diagrams of GFRP reinforced columns and GFRP encased square columns. *Constr Build Mater* 2017; 135: 550–564.
 70. Correia JR, Branco FA, Ferreira JG, et al. Fire protection systems for building floors made of pultruded GFRP profiles, part 1: experimental investigations. *Compos Part B Eng* 2010; 41: 617–629.
 71. Satasivam S and Bai Y. Mechanical performance of modular FRP-steel composite beams for building construction. *Mater Struct* 2016; 49: 4113–4129.
 72. Bai Y, Keller T, Correia JR, et al. Fire protection systems for building floors made of pultruded GFRP profiles, part 2: modeling of thermomechanical responses. *Compos Part B Eng* 2010; 41: 630–636.
 73. Gao Y, Chen J, Zhang Z, et al. An advanced FRP floor panel system in buildings. *Compos Struct* 2013; 96: 683–690.
 74. Gao Y, Chen J and Fox D. Shear effects on bending behaviour of CFRP floor panels. *Compos Struct* 2014; 107: 11–18.
 75. Satasivam S, Bai Y and Zhao X-L. Adhesively bonded modular GFRP web-flange sandwich for building floor construction. *Compos Struct* 2014; 111: 381–392.
 76. Creazza G and Russo S. Crack width evaluation in FRP reinforced concrete members. *Mater Struct Constr* 2001; 34: 119–125.
 77. Ferdous W, Almutairi AD, Huang Y, et al. Short-term flexural behaviour of concrete filled pultruded GFRP cellular and tubular sections with pin-eye connections for modular retaining wall construction. *Compos Struct* 2018; 206: 1–10.
 78. Green A. Glass-fiber-reinforced composites in building construction. *Transpl Res Rec* 1987; 1118: 73–76.
 79. Deskovic N, Triantafillou TC and Meier U. Innovative design of FRP combined with concrete: short-term behavior. *J Struct Eng (United States)* 1995; 121: 1069–1078.
 80. Turvey G. Experimental investigation of the load–deformation behaviour of pultruded GFRP modular and custom safety barriers. *Compos Struct* 2015; 133: 659–666.
 81. Satasivam S, Bai Y, Yang Y, et al. Mechanical performance of two-way modular FRP sandwich slabs. *Compos Struct* 2018; 184: 904–916.
 82. Ferreira AJM, Camanho PP, Marques AT, et al. Modelling of concrete beams reinforced with FRP rebars. *Compos Struct* 2001; 53: 107–116.
 83. Kocaoz S, Samaranayake VA and Nanni A. Tensile characterization of glass FRP bars. *Compos Part B Eng* 2005; 36: 127–134.
 84. Correia JR. Fibre-reinforced polymer (FRP) composites. In: Gonçalves MC and Margarido F (eds) *Materials for construction and civil engineering*. Cham: Springer International Publishing, pp.501–556.

85. Chen Y, Davalos JF, Ray I, et al. Accelerated aging tests for evaluations of durability performance of FRP reinforcing bars for concrete structures. *Compos Struct* 2007; 78: 101–111.
86. Davalos JF, Chen Y and Ray I. Long-term durability prediction models for GFRP bars in concrete environment. *J Compos Mater*, Epub ahead of print 10 November 2011. DOI: 10.1177/0021998311427777.
87. Alsayed SH, Al-Salloum YA and Almusallam TH. Performance of glass fiber reinforced plastic bars as a reinforcing material for concrete structures. *Compos Part B Eng* 2000; 31: 555–567.
88. Caratelli A, Meda A, Rinaldi Z, et al. Optimization of GFRP reinforcement in precast segments for metro tunnel lining. *Compos Struct*, Epub ahead of print September 2017. DOI: 10.1016/j.compstruct.2017.08.083.
89. Yang W-R, He X-J and Dai L. Damage behaviour of concrete beams reinforced with GFRP bars. *Compos Struct*, Epub ahead of print November 2016. DOI: 10.1016/j.compstruct.2016.11.041.
90. Benmokrane B, Chaallal O and Masmoudi R. Glass fibre reinforced plastic (GFRP) rebars for concrete structures. *Constr Build Mater* 1995; 9: 353–364.
91. Meisami MH, Mostofinejad D and Nakamura H. Punching shear strengthening of two-way flat slabs using CFRP rods. *Compos Struct* 2013; 99: 112–122.
92. Gooranorimi O, Suaris W, Dauer E, et al. Microstructural investigation of glass fiber reinforced polymer bars. *Compos Part B Eng*, Epub ahead of print November 2016. DOI: 10.1016/j.compositesb.2016.11.029.
93. Sayyar M, Soroushian P, Sadiq MM, et al. Low-cost glass fiber composites with enhanced alkali resistance tailored towards concrete reinforcement. *Constr Build Mater* 2013; 44: 458–463.
94. Won JP, Yoon YN, Hong BT, et al. Durability characteristics of nano-GFRP composite reinforcing bars for concrete structures in moist and alkaline environments. *Compos Struct* 2012; 94: 1236–1242.
95. Mahroug MEM, Ashour AF and Lam D. Experimental response and code modelling of continuous concrete slabs reinforced with BFRP bars. *Compos Struct* 2014; 107: 664–674.
96. Quadrino A, Penna R, Feo L, et al. Mechanical characterization of pultruded elements: fiber orientation influence vs web-flange junction local problem. Experimental and numerical tests. *Compos Part B Eng* 2018; 142: 68–84.
97. Nunes F, Silvestre N and Correia JR. Progressive damage analysis of web crippling of GFRP pultruded I-sections. *J Compos Constr*, Epub ahead of print June 2017. DOI: 10.1061/(ASCE)CC.1943-5614.0000762.
98. Okeil AM, Bingol Y and Ferdous MR. Novel technique for inhibiting buckling of thin-walled steel structures using pultruded glass FRP sections. *J Compos Constr* 2009; 13: 547–557.
99. Wu C and Bai Y. Web crippling behaviour of pultruded glass fibre reinforced polymer sections. *Compos Struct* 2014; 108: 789–800.
100. Lee J and Kim S-E. Flexural-torsional buckling of thin-walled I-section composites. *Comput Struct* 1995; 5: 321–342.
101. Dispenza C, Pisano AA and Fuschi P. Numerical simulations of the mechanical characteristics of glass fibre reinforced C-profiles. *Compos Sci Technol* 2006; 66: 2980–2989.
102. Van Den Einde L, Zhao L and Seible F. Use of FRP composites in civil structural applications. *Constr Build Mater* 2003; 17: 389–403.
103. Jiao H, Mashiri F and Zhao X-L. A comparative study on fatigue behaviour of steel beams retrofitted with welding, pultruded CFRP plates and wet layup CFRP sheets. *Thin-Walled Struct* 2012; 59: 144–152.
104. Altaee MJ, Cunningham LS and Gillie M. Experimental investigation of CFRP-strengthened steel beams with web openings. *J Constr Steel Res* 2017; 138: 750–760.
105. Wu C, Oehlers DJ, Rebentrost M, et al. Blast testing of ultra-high performance fibre and FRP-retrofitted concrete slabs. *Eng Struct* 2009; 31: 2060–2069.
106. Goksu C, Uzunhasanoglu A, Seyhan EC, et al. Seismic retrofit of sub-standard RC columns with embedded aramid FRP reinforcement. In: *Second conference on smart monitoring, assessment and rehabilitation of civil struct (SMAR 2013)*, Istanbul, Turkey, 9–11 September 2013.
107. Ascione F, Lamberti M, Razaqpur AG, et al. Strength and stiffness of adhesively bonded GFRP beam-column moment resisting connections. *Compos Struct* 2017; 160: 1248–1257.
108. Sakr M, El Nagggar MH and Nehdi M. Interface characteristics and laboratory constructability tests of novel fiber-reinforced polymer/concrete piles. *J Compos Constr* 2005; 9: 274–283.
109. Zyka K and Mohajerani A. Composite piles: a review. *Constr Build Mater* 2016; 107: 394–410.
110. Ahn N, Lee J, Lee K, et al. An experimental study on flexural behavior for a FRP composite girder. *Constr Build Mater* 2014; 50: 13–21.
111. Boscato G, Mottram JT and Russo S. Dynamic response of a sheet pile of fiber reinforced polymer for water front barriers. *J Compos Constr* 2011; 15: 974.
112. Sousa JM, Correia JR, Gonilha J, et al. Durability of adhesively bonded joints between pultruded GFRP adherends under hygrothermal and natural ageing. *Compos Part B Eng* 2019; 158: 475–488.
113. Mosallam AS, Abdelhamid MK and Conway JH. Performance of pultruded FRP connections under static and dynamic loads. *J Reinf Plast Compos*, Epub ahead of print 1 May 1994. DOI: 10.1177/073168449401300501.
114. Shao Y and Shanmugam J. Moment capacities and deflection limits of PFRP sheet piles. *J Compos Constr* 2006; 10: 520–528.
115. Rubino F, Nisticò A, Tucci F, et al. Marine application of fiber reinforced composites: a review. *J Mar Sci Eng* 2020; 8: 26.
116. Guades E, Aravinthan T, Islam M, et al. A review on the driving performance of FRP composite piles. *Compos Struct* 2012; 94: 1932–1942.

117. Shao Y and Kouadio S. Durability of fiberglass composite sheet piles in water. *J Compos Constr* 2002; 6: 280–287.
118. Giroux C and Shao Y. Flexural and shear rigidity of composite sheet piles. *J Compos Constr* 2003; 7: 348–355.
119. Boyd SW, Dulieu-Barton JM and Rumsey L. Stress analysis of finger joints in pultruded GRP materials. *Int J Adhes Adhes* 2006; 26: 498–510.
120. Tonatto MLP, Forte MMC, Tita V, et al. Progressive damage modeling of spiral and ring composite structures for offloading hoses. *Mater Des* 2016; 108: 374–382.
121. Abd Allah MH, Abdin EM, Selmy AI, et al. Short communication effect of mean stress on fatigue behaviour of GFRP pultruded rod composites. *Compos Part A Appl Sci Manuf* 1997; 28: 87–91.
122. Hörold S. Phosphorus flame retardants in thermoset resins. *Polym Degrad Stab* 1999; 64: 427–431.
123. Yang Y, Ahmed K, Zhang R, et al. A study on the energy absorption capacity of braided rod composites. *Compos Struct* 2018; 206: 933–940.
124. Saito H, Chirwa EC, Inai R, et al. Energy absorption of braiding pultrusion process composite rods. *Compos Struct* 2002; 55: 407–417.
125. Charoenphan S, Bank LC and Plesha ME. Progressive tearing failure in pultruded composite material tubes. *Compos Struct* 2004; 63: 45–52.
126. Hull D. A unified approach to progressive crushing of fibre-reinforced composite tubes. *Compos Sci Technol* 1991; 40: 377–421.
127. Palanivelu S, Van Paepegem W, Degrieck J, et al. Experimental study on the axial crushing behaviour of pultruded composite tubes. *Polym Test* 2010; 29: 224–234.
128. Esnaola A, Tena I, Saenz-Dominguez I, et al. Effect of the manufacturing process on the energy absorption capability of GFRP crush structures. *Compos Struct* 2018; 187: 316–324.
129. Thornton PH. Energy absorption in composite structures. *J Compos Mater* 1979; 13: 247–262.
130. Carruthers JJ, Kettle AP and Robinson AM. Energy absorption capability and crashworthiness of composite material structures: a review. *Appl Mech Rev* 1998; 51: 635.
131. Mamalis AG, Manolakos DE, Ioannidis MB, et al. On the response of thin-walled CFRP composite tubular components subjected to static and dynamic axial compressive loading: experimental. *Compos Struct* 2005; 69: 407–420.
132. Ochelski S and Gotowicki P. Experimental assessment of energy absorption capability of carbon-epoxy and glass-epoxy composites. *Compos Struct* 2009; 87: 215–224.
133. Saenz-Dominguez I, Tena I, Esnaola A, et al. Design and characterisation of cellular composite structures for automotive crash-boxes manufactured by out of die ultraviolet cured pultrusion. *Compos Part B Eng* 2019; 160: 217–224.
134. Tarlochan F, Ramesh S and Harpreet S. Advanced composite sandwich structure design for energy absorption applications: blast protection and crashworthiness. *Compos Part B Eng* 2012; 43: 2198–2208.
135. Van Paepegem W, Palanivelu S, Degrieck J, et al. Blast performance of a sacrificial cladding with composite tubes for protection of civil engineering structures. *Compos Part B Eng* 2014; 65: 131–146.
136. Belingardi G, Beyene AT, Koricho EG, et al. *Lightweight solutions for vehicle frontal bumper: crash design and manufacturing issues*. Swaston, UK: Woodhead Publishing, 2017.
137. Colombo C and Vergani L. Experimental and numerical analysis of a bus component in composite material. *Compos Struct* 2010; 92: 1706–1715.
138. Verhaeghe J. Composite trailer: from prototype to industrialisation. In: *International SAMPE symposium and exhibition (proceedings)* (Repecka L and Saremi FF eds), 2001, pp.1612–1620.
139. Fedulov BN, Safonov AA, Sergeichev IV, et al. Strength analysis and process simulation of subway contact rail support bracket of composite materials. *Appl Compos Mater* 2016; 23: 999–1013.
140. Park S-J. *Carbon fibers*. Berlin, Germany: Springer, 2018.
141. Taylor JG. *Composites*. In: Pilato I (ed) *Phenolic resins: a century of progress*. Berlin, Germany: Springer, 2010, pp.263–306.
142. Davalos JF and Qiao P. A computational approach for analysis and optimal design of FRP beams. *Comput Struct* 1999; 70: 169–183.
143. Mosallam AS, Feo L, Elsadek A, et al. Structural evaluation of axial and rotational flexibility and strength of web-flange junctions of open-web pultruded composites. *Compos Part B Eng* 2014; 66: 311–327.
144. Singamsethi SK, LaFave JM and Hjelmstad KD. Fabrication and testing of cuff connections for GFRP box sections. *J Compos Constr*, Epub ahead of print December 2005. DOI: 10.1061/(ASCE)1090-0268(2005)9:6(536).
145. Hardesty EE. Advanced composites, the on-going transition from handmade prototypes to machine-fabricated components. In: *Proceedings of the 28th SPI RP/CI meeting*, Washington, DC, 6–9 February 1973.
146. Sorina TG, Safonov AA and Khairuddinov AK. Peculiarities of using carbon glass-reinforced plastic in pultrusion composite profiles for bridge engineering. *J Mach Manuf Reliab* 2010; 39: 47–51.
147. Dubinskii SV and Safonov AA. Composite-friendly approach to certification of advanced materials and fabrication methods used in aviation industry. *J Mach Manuf Reliab* 2017; 46: 501–506.
148. Lau STW, Said MR and Yaakob MY. On the effect of geometrical designs and failure modes in composite axial crushing: a literature review. *Compos Struct* 2012; 94: 803–812.
149. Green AK and Shikhmanter L. Coupon development for fatigue testing of bonded assemblies of pultruded rods. *Compos Part A Appl Sci Manuf* 1999; 30: 611–613.

150. Safonov AA and Suvorova YV. Optimization of the pultrusion process for a rod with a large diameter. *J Mach Manuf Reliab* 2009; 38: 572–578.
151. Richardson MOW and Robinson AM. Design and mechanical aspects of composite materials for light rail vehicle tracks. *Composites* 1994; 25: 438–442.
152. Bell B. Fibre-reinforced polymer in railway civil engineering. *Proc Inst Civ Eng Eng Comput Mech* 2009; 162: 119–126.
153. Kakogiannis D, Yuen SCK, Palanivelu S, et al. Response of pultruded composite tubes subjected to dynamic and impulsive axial loading. *Compos Part B Eng* 2013; 55: 537–547.
154. Li Z, Khennane A, Hazell PJ, et al. Impact behaviour of pultruded GFRP composites under low-velocity impact loading. *Compos Struct*, Epub ahead of print February 2017. DOI: 10.1016/j.compstruct.2017.02.073.
155. Bank LC and Gentry TR. Development of a pultruded composite material highway guardrail. *Compos Part A Appl Sci Manuf* 2001; 32: 1329–1338.
156. Paulsen US, Madsen HA, Kragh KA, et al. The 5 MW deepwind floating offshore vertical wind turbine concept design – status and perspective. In: *European wind energy association conference and exhibition (EWEA 2014)*, Barcelona, Spain, 10–13 March 2014.
157. Paulsen US, Madsen HA, Hattel JH, et al. Design optimization of a 5 MW floating offshore vertical-axis wind turbine. *Energy Proc* 2013; 35: 22–32.
158. Baran I, Straumit I, Shishkina O, et al. X-ray computed tomography characterization of manufacturing induced defects in a glass/polyester pultruded profile. *Compos Struct* 2018; 195: 74–82.
159. Yuksel O, Baran I, Ersoy N, et al. Investigation of transverse residual stresses in a thick pultruded composite using digital image correlation with hole drilling. *Compos Struct* 2019; 223: 110954.
160. Sarmiento M and Lacoursiere B. A state of the art overview: composite utility poles for distribution and transmission applications. In: *2006 IEEE PES transmission and distribution conference and exposition: Latin America, TDC'06*. Epub ahead of print 2006. DOI: 10.1109/TDCLA.2006.311616.
161. Yeh H-Y and Yang SC. Building of a composite transmission tower. *J Reinf Plast Compos* 1997; 16: 414–424.
162. Kukureka SN and Wei CY. Damage development in pultruded composites for optical telecommunications cables under tensile and flexural fatigue. *Compos Sci Technol* 2003; 63: 1795–1804.
163. Kiekens P. A preliminary study about the production by the pultrusion technique of a fiber reinforced plastic (FRP) tension member for use in dielectric composite optical fibre communication cable. *Bull Soc Chim Belges* 1985; 94: 165–170.
164. The European Pultrusion Technology Association: EPTA, <https://pultruders.org> (2016, accessed 26 April 2020).
165. Curved pultrusion? No longer an oxymoron, www.compositesworld.com/articles/curved-pultrusion-no-longer-an-oxymoron (2003, accessed 12 November 2019).
166. Tonatto MLP, Tita V and Amico SC. Composite spirals and rings under flexural loading: experimental and numerical analysis. *J Compos Mater*, Epub ahead of print 28 January 2020. DOI: 10.1177/0021998320902504.
167. Wilson ML, MacConochie IO and Johnson GS. *Potential for on-orbit manufacture of large space structures using the pultrusion process*, www.scopus.com/inward/record.uri?eid=2-s2.0-0023591568&partnerID=40&md5=164d51a4aa36a289353c5f6b603-e19c6 (1987, accessed 25 January 2020).
168. British Company Has Plans to Manufacture Big Structures in Space, www.21stcentech.com/british-company-plans-manufacture-big-structures-space/ (2012, accessed 12 November 2019).
169. Correia JR. *Pultrusion of advanced fibre-reinforced polymer (FRP) composites*. Amsterdam, Netherlands: Elsevier.
170. EPTA highlights attractive prospects for pultruded composites in infrastructure, <http://www.jeccomposites.com/knowledge/international-composites-news/epta-highlights-attractive-prospects-pultruded-composites> (2002, accessed 26 April 2020).
171. Brecher C, Emonts M, Brack A, et al. Micro-pultrusion and micro-pultrusion – technology and applications. *JEC Compos Mag* 2012; 49: 71–73.
172. Callens SJP and Bergsma OK. Two-matrix composites: carbon fiber micropultrusions embedded in flexible epoxy matrices. *Compos Part A Appl Sci Manuf* 2018; 114: 1–12.
173. Brack A, Janssen H and Brecher C. Manufacturing of miniaturized thermoplastic frp components using a novel reaction injection pultrusion process. In: *International SAMPE technical conference society for the advancement of material and process engineering* (ed Blohowiak K), pp.944–957. California: SAMPE.
174. Brecher C, Schmitz S and Krüger S. Guide wire for intervention using magnetic-resonance tomography. *Kunststoffe Int* 2007; 97: 63–65.
175. Krueger S, Schmitz S, Weiss S, et al. An MR guidewire based on micropultruded fiber-reinforced material. *Magn Reson Med* 2008; 60: 1190–1196.
176. Krämer NA, Krüger S, Schmitz S, et al. Preclinical evaluation of a novel fiber compound MR guidewire in vivo. *Invest Radiol* 2009; 44: 390–397.
177. Tena I, Esnaola A, Sarrionandia M, et al. Out of die ultraviolet cured pultrusion for automotive crash structures. *Compos Part B Eng* 2015; 79: 209–216.
178. Britnell DJ, Tucker N, Smith GF, et al. Bent pultrusion – a method for the manufacture of pultrudate with controlled variation in curvature. *J Mater Process Technol* 2003; 138: 311–315.
179. Tena I, Sarrionandia M, Torre J, et al. The effect of process parameters on ultraviolet cured out of die bent pultrusion process. *Compos Part B Eng* 2016; 89: 9–17.
180. Aguilar MR and San Román J. *Introduction to smart polymers and their applications*. Amsterdam, Netherlands: Elsevier, ■■.

181. Li X, Shang J and Wang Z. Intelligent materials: a review of applications in 4D printing. *Assem Autom* 2017; 37: 170–185.
182. Sun L, Huang WM, Ding Z, et al. Stimulus-responsive shape memory materials: a review. *Mater Des* 2012; 33: 577–640.
183. Xin X, Liu L, Liu Y, et al. Mechanical models, structures, and applications of shape-memory polymers and their composites. *Acta Mech Solid Sin* 2019; 32: 535–565.
184. Meng H and Li G. A review of stimuli-responsive shape memory polymer composites. *Polymer (Guildf)* 2013; 54: 2199–2221.
185. Liu Y, Du H, Liu L, et al. Shape memory polymers and their composites in aerospace applications: a review. *Smart Mater Struct*, Epub ahead of print 1 February 2014. DOI: 10.1088/0964-1726/23/2/023001.
186. Xie F, Huang L, Leng J, et al. Thermoset shape memory polymers and their composites. *J Intell Mater Syst Struct* 2016; 27: 2433–2455.
187. Pilate F, Toncheva A, Dubois P, et al. Shape-memory polymers for multiple applications in the materials world. *Eur Polym J* 2016; 80: 268–294.
188. Ahmadi MS, Johari MS, Sadighi M, et al. An experimental study on mechanical properties of GFRP braid-pultruded composite rods. *Express Polym Lett* 2009; 3: 560–568.
189. Hashin Z and Rosen BW. The elastic moduli of fiber-reinforced materials. *J Appl Mech* 1964; 31: 223–232.
190. Jones RM. *Mechanics of composite materials*. New York: Taylor and Francis, Inc., 1999.
191. Bogetti TA and Gillespie JWJ. Process-induced stress and deformation in thick-section thermoset composite laminates. *J Compos Mater* 1992; 26: 626–660.
192. Baran I, Akkerman R and Hattel JH. Modelling the pultrusion process of an industrial L-shaped composite profile. *Compos Struct* 2014; 118: 37–48.
193. Baran I, Tutum CC, Nielsen MW, et al. Process induced residual stresses and distortions in pultrusion. *Compos Part B Eng* 2013; 51: 148–161.
194. Davalos JF, Qiao P and Shan L. *Advanced fiber-reinforced polymer (FRP) structural composites for use in civil engineering*. Amsterdam, Netherlands: Elsevier, 2011.
195. Park JY and Zureick A-H. Effect of filler and void content on mechanical properties of pultruded composite materials under shear loading. *Polym Compos* 2005; 26: 181–192.
196. Mehdikhani M, Steensels E, Standaert A, et al. Multi-scale digital image correlation for detection and quantification of matrix cracks in carbon fiber composite laminates in the absence and presence of voids controlled by the cure cycle. *Compos Part B Eng* 2018; 154: 138–147.
197. Eshelby JD. The Determination of the Elastic Field of an Ellipsoidal Inclusion, and Related Problems. *Math Proc Cambridge Philos Soc* 1957; A241: 376–396.
198. Mori T and Tanaka K. Average stress in matrix and average elastic energy of materials with misfitting inclusions. *Acta Metall* 1973; 21: 571–574.
199. Budiansky B. On the elastic moduli of some heterogeneous materials. *J Mech Phys Solid* 1965; 13: 223–227.
200. Safonov AA and Shcheglov BA. Mathematical modeling of polymerization in the manufacturing of polymeric composite materials. *J Mach Manuf Reliab* 2011; 40: 549–553.
201. Ye BS, Svenson AL and Bank LC. Mass and volume fraction properties of pultruded glass fibre-reinforced composites. *Composites* 1995; 26: 725–731.
202. Carlone P, Palazzo GS and Pasquino R. Pultrusion manufacturing process development by computational modelling and methods. *Math Comput Model* 2006; 44: 701–709.
203. Creighton CJ and Clyne TW. The compressive strength of highly-aligned carbon-fibre/epoxy composites produced by pultrusion. *Compos Sci Technol* 2000; 60: 525–533.
204. Xin H, Liu Y, Mosallam A, et al. Hygrothermal aging effects on flexural behavior of pultruded glass fiber reinforced polymer laminates in bridge applications. *Constr Build Mater* 2016; 127: 237–247.
205. Baptista R, Mendão A, Guedes M, et al. An experimental study on mechanical properties of epoxy-matrix composites containing graphite filler. In: Iacoviello F, Reis L, Fonte M, et al. (eds), *Procedia structural integrity*. Amsterdam, Netherlands: Elsevier, 130pp.74–81.
206. Technical data: Epoxy resin L 20, www.swiss-composite.ch/pdf/t-Epoxydharz-L20-e.pdf (1997, accessed 30 August 2019)..
207. Datasheet: Araldite LY 8615/Aradur 8615 high temperature epoxy system, www.mouldlife.net/ekmps/shops/mouldlife/resources/Other/araldite-ly-8615-aradur-8615-eur-e-1-.pdf (2007, accessed 30 August 2019).
208. Datasheet: Araldite LY 8615/Aradur 8615/Hardener XB 5173 high temperature epoxy system, https://samaro.fr/pdf/FT/Araldite_FT_LY_8615_Aradur_8615_Hardener_XB5173_EN.pdf (2008, accessed 30 August 2019).
209. Mengal AN, Karuppanan S and Wahab AA. Structural analysis of basalt fiber reinforced plastic wind turbine blade. *MATEC Web Conf*. Epub ahead of print July 2014. DOI: 10.1051/mateconf/20141304019.
210. Zhang L, Liu W, Wang L, et al. Mechanical behavior and damage monitoring of pultruded wood-cored GFRP sandwich components. *Compos Struct* 2019; 215: 502–520.
211. Abu Seman SAH, Ahmad R and Md Akil H. Mesoscale modelling and failure analysis of kenaf fiber reinforced composites under high strain rate compression loading. *Compos Part B Eng* 2019; 163: 403–412.
212. Garrido M, Madeira JFA, Proença M, et al. Multi-objective optimization of pultruded composite sandwich panels for building floor rehabilitation. *Constr Build Mater* 2019; 198: 465–478.
213. Ji H-S, Byun J-K, Lee C-S, et al. Structural performance of composite sandwich bridge decks with hybrid GFRP-steel core. *Compos Struct* 2011; 93: 430–442.
214. Boscato G and Russo S. Free vibrations of pultruded FRP elements: mechanical characterization, analysis, and applications. *J Compos Constr*, Epub ahead of

- print December 2009. DOI: 10.1061/(ASCE)1090-0268(2009)13:6(565).
215. Wallace CA, Saha GC, Afzal MT, et al. Experimental and computational modeling of effective flexural/tensile properties of microwave pyrolysis biochar reinforced GFRP biocomposites. *Compos Part B Eng* 2019; 175: 107180.
 216. Davalos JF, Qiao P, Wang J, et al. Shear moduli of structural composites from torsion tests. *J Compos Mater* 2002; 36: 1151–1173.
 217. Haj-Ali R and Kilic H. Nonlinear behavior of pultruded FRP composites. *Compos Part B Eng* 2002; 33: 173–191.
 218. Haj-Ali RM and Muliana AH. A micromechanical constitutive framework for the nonlinear viscoelastic behavior of pultruded composite materials. *Int J Solid Struct* 40: 1037–1057.
 219. Technical data sheet vinylester 702-A, www.composites.dk/wp-content/uploads/2015/12/TDS_ICOM_Vinylester-702-A_EN2016UU.pdf (1998, accessed 30 August 2019).
 220. Plastic Properties Table, www.curbellplastics.com/Research-Solutions/Plastic-Properties (2000, accessed 30 August 2019).
 221. Pilato L. *Resin chemistry*. Berlin Heidelberg: Springer.
 222. Tascioglu C, Goodell B, Lopez-Anido R, et al. Monitoring fungal degradation of E-glass/phenolic fiber reinforced polymer (FRP) composites used in wood reinforcement. *Int Biodeterior Biodegrad* 2003; 51: 157–165.
 223. Dong Y, He J and Yang R. Phenolic resin/polyhedral oligomeric silsesquioxane (POSS) composites: mechanical ablative, thermal, and flame retardant properties. *Polym Adv Technol* 2019; 30: 2075–2085.
 224. Resins P. *Phenolic resins: chemistry, applications, standardization, safety and ecology*. Berlin, Germany: Springer, 2000.
 225. Dixit D, Pal R, Kapoor G, et al. *Lightweight composite materials processing*. Amsterdam, Netherlands: Elsevier, 2011.
 226. Technical Design Guide for FRP Composite Products and Parts, www.moldedfiberglass.com/sites/default/files/docs/MFG_Technical_Design_Guide_FRP_Composites_2018.pdf (1997, accessed 30 August 2019).
 227. Abdellah M, Fathi H, Abdelhaleem A, et al. Mechanical properties and wear behavior of a novel composite of acrylonitrile–butadiene–styrene strengthened by short basalt fiber. *J Compos Sci* 2018; 2: 34.
 228. Yeung KKH and Rao KP. Mechanical properties of Kevlar-49 fibre reinforced thermoplastic composites. *Polym Polym Compos* 2012; 20: 411–424.
 229. Abdelkerim DSE, Wang X, Ibrahim HA, et al. Static and fatigue behavior of pultruded FRP multi-bolted joints with basalt FRP and hybrid steel-FRP bolts. *Compos Struct* 2019; 220: 324–337.
 230. Lu Z, Xian G and Li H. Effects of exposure to elevated temperatures and subsequent immersion in water or alkaline solution on the mechanical properties of pultruded BFRP plates. *Compos Part B Eng* 2015; 77: 421–430.
 231. Lopresto V, Leone C and De Iorio I. Mechanical characterisation of basalt fibre reinforced plastic. *Compos Part B Eng* 2011; 42: 717–723.
 232. Basalt fibers, www.lbie.com/PDF/n3011.pdf (2000, accessed 30 August 2019).
 233. Valentino P, Furgiuele F and Gebbeken N. Mechanical characterization of basalt fibre reinforced plastic with different fabric reinforcements – tensile tests and FE-calculations with representative volume elements (RVEs). *Convegno Naz IGF XXII* 2013; 1: 231–244.
 234. Wu P, Xu L, Luo J, et al. Tension-tension fatigue performances of a pultruded carbon fiber reinforced epoxy plate at elevated temperatures. *Compos Struct* 2019; 215: 421–431.
 235. Carlone P, Baran I, Hattel JH, et al. Computational approaches for modeling the multiphysics in pultrusion process. *Adv Mech Eng*, Epub ahead of print January 2015. DOI: 10.1155/2013/301875.
 236. Piggott MR and Harris B. Compression strength of carbon, glass and Kevlar-49 fibre reinforced polyester resins. *J Mater Sci* 1980; 15: 2523–2538.
 237. High-strength and high-modulus carbon fiber TORAYCA T1100G, www.torayca.com/en/download/pdf/torayca_t1100g.pdf (2000, accessed 30 August 2019).
 238. Cordeiro GC, Vieira JD and C6 CM. Tensile properties and color and mass variations of GFRP composites under alkaline and ultraviolet exposures. *Matéria (Rio Janeiro)* 2016; 21: 1–10.
 239. Material Property Data. S-glass fiber, www.matweb.com/search/DataSheet.aspx?MatGUID=6eb41a1324834878a1524129d915ca09 (accessed 30 August 2019).
 240. S-Glass Fibre, www.azom.com/properties.aspx?ArticleID=769 (1999, accessed 30 August 2019).
 241. Charlet K, Jernot J, Gomina M, et al. Mechanical properties of flax fibers and of the derived unidirectional composites. *J Compos Mater* 2010; 44: 2887–2896.
 242. Yeung KKH and Rao KP. Comparison of mechanical properties of boron and Kevlar-49 reinforced thermosetting composites and their economic implications. In: *8th Asian-Australasian conference on composite materials 2012, ACCM 2012 – composites: enabling tomorrow's industry today* (ed. M Jaafar), Kuala Lumpur, Malaysia, 2012, pp.666–671. New York: Curran Associates.
 243. Benfratello S, Fiore V, Palizzolo L, et al. Evaluation of continuous filament mat influence on the bending behaviour of GFRP pultruded material via electronic speckle pattern interferometry. *Arch Civ Mech Eng* 2017; 17: 169–177.
 244. Zhang D, Lv Y, Zhao Q, et al. Development of lightweight emergency bridge using GFRP–metal composite plate-truss girder. *Eng Struct* 2019; 196: 109291.
 245. Aniskevich K, Aniskevich A, Arnautov A, et al. Mechanical properties of pultruded glass fiber-reinforced plastic after moistening. *Compos Struct* 2012; 94: 2914–2919.
 246. Ascione F, Mancusi G, Spadea S, et al. On the flexural behaviour of GFRP beams obtained by bonding simple

- panels: an experimental investigation. *Compos Struct* 2015; 131: 55–65.
247. Ascione F, Feo L, Lamberti M, et al. A closed-form equation for the local buckling moment of pultruded FRP I-beams in major-axis bending. *Compos Part B Eng* 2016; 97: 292–299.
248. Ascione F, Feo L, Lamberti M, et al. Experimental and numerical evaluation of the axial stiffness of the web-to-flange adhesive connections in composite I-beams. *Compos Struct* 2017; 176: 702–714.
249. Kim H-Y and Lee S-Y. Static and fatigue load performance of a pultruded GFRP deck panel reinforced with steel wires. *Compos Struct* 2019; 207: 166–175.
250. Castellaro S and Russo S. Dynamic characterization of an all-FRP pultruded construction. *Compos Struct* 2019; 218: 1–14.
251. Mourad A-HI, Idrisi AH, Wrage MC, et al. Long-term durability of thermoset composites in seawater environment. *Compos Part B Eng* 2019; 168: 243–253.
252. O’Leary K, Pakrashi V and Kelliher D. Optimization of composite material tower for offshore wind turbine structures. *Renew Energy* 2019; 140: 928–942.
253. Du A, Liu Y, Xin H, et al. Progressive damage analysis of PFRP double-lap bolted joints using explicit finite element method. *Compos Struct* 2016; 152: 860–869.
254. Technical Datasheet ZOLTEKTM PX35 Pultruded Profiles, https://zoltek.com/wp-content/uploads/2017/09/TDS_PX35_Pultruded_Profiles.pdf (2017, accessed 2 September 2019).
255. Zhang S, Caprani CC and Heidarpour A. Strain rate studies of pultruded glass fibre reinforced polymer material properties: a literature review. *Constr Build Mater* 2018; 171: 984–1004.
256. Zhang S, Caprani C and Heidarpour A. Influence of fibre orientation on pultruded GFRP material properties. *Compos Struct* 2018; 204: 368–377.
257. Hankinson RL. Investigation of crushing strength of spruce at varying angles of grain. *Air Serv Inf Circ* 1921; 3: 130.
258. Xin H, Mosallam A, Liu Y, et al. Analytical and experimental evaluation of flexural behavior of FRP pultruded composite profiles for bridge deck structural design. *Constr Build Mater* 2017; 150: 123–149.
259. Mottram JT. Prediction of net-tension strength for multirow bolted connections of pultruded material using the Hart-Smith semiempirical modeling approach. *J Compos Constr* 2010; 14: 105–114.
260. Turvey GJ and Sana A. Pultruded GFRP double-lap single-bolt tension joints – temperature effects on mean and characteristic failure stresses and knock-down factors. *Compos Struct*, Epub ahead of print June 2016. DOI: 10.1016/j.compstruct.2016.06.016.
261. Turvey GJ and Wang P. Failure of pultruded GRP single-bolt tension joints under hot-wet conditions. *Compos Struct* 2007; 77: 514–520.
262. Turvey GJ and Wang P. Thermal preconditioning study for bolted tension joints in pultruded GRP plate. *Compos Struct* 2007; 77: 509–513.
263. Lee Y-G, Choi E and Yoon S-J. Effect of geometric parameters on the mechanical behavior of PFRP single bolted connection. *Compos Part B Eng* 2015; 75: 1–10.
264. Turvey GJ and Wang P. Failure of pultruded GRP bolted joints: a Taguchi analysis. *Proc Inst Civ Eng Eng Comput Mech* 2009; 162: 155–166.
265. de Castro J and Keller T. Ductile double-lap joints from brittle GFRP laminates and ductile adhesives, part I: experimental investigation. *Compos Part B Eng* 2008; 39: 271–281.
266. Vallée T and Keller T. Adhesively bonded lap joints from pultruded GFRP profiles. Part III: effects of chamfers. *Compos Part B Eng* 2006; 37: 328–336.
267. Turvey GJ and Wang P. Effect of hole clearance on bolt loads in pultruded GRP tension joints. In: *ICCM international conferences on composite materials*. International Committee on Composite Materials, www.scopus.com/inward/record.uri?eid=2-s2.0-85076868120&partnerID=40&md5=b3878eac7ce65ada4249b73eeff285b5 (2007, accessed 15 January 2020).
268. Turvey GJ. Single-bolt tension joint tests on pultruded GRP plate – effects of tension direction relative to pultrusion direction. *Compos Struct* 1998; 42: 341–351.
269. Keller T and Vallée T. Adhesively bonded lap joints from pultruded GFRP profiles. Part I: stress-strain analysis and failure modes. *Compos Part B Eng* 2005; 36: 331–340.
270. Keller T and Vallée T. Adhesively bonded lap joints from pultruded GFRP profiles. Part II: joint strength prediction. *Compos Part B Eng* 2005; 36: 341–350.
271. Cowin AR. Test and analysis of bonded joint configurations for pultruded E-glass in a thermosetting resin matrix. In: *International SAMPE symposium and exhibition (proceedings)* (eds Green J and Rodgers S). Covina, CA: The Society, pp.3882–3891..
272. Kilic H and Haj-Ali R. Progressive damage and non-linear analysis of pultruded composite structures. *Compos Part B Eng* 2003; 34: 235–250.
273. Prabhakaran R, Razzaq Z and Devara S. Load and resistance factor design (LRFD) approach for bolted joints in pultruded composites. *Compos Part B Eng* 1996; 27: 351–360.
274. You Y-J, Park Y-H, Kim H-Y, et al. Hybrid effect on tensile properties of FRP rods with various material compositions. *Compos Struct* 2007; 80: 117–122.
275. Portnov G and Bakis CE. Analysis of stress concentration during tension of round pultruded composite rods. *Compos Struct* 2008; 83: 100–109.
276. Barbero EJ, Makkapati S and Tomblin JS. Experimental determination of the compressive strength of pultruded structural shapes. *Compos Sci Technol* 1999; 59: 2047–2054.
277. Hancox NL. The compression strength of unidirectional carbon fibre reinforced plastic. *J Mater Sci* 1975; 10: 234–242.
278. Zhang L, Liu W, Wang L, et al. On-axis and off-axis compressive behavior of pultruded GFRP composites at elevated temperatures. *Compos Struct* 2020; 236: 111891.

279. Bai Y, Vallée T and Keller T. Delamination of pultruded glass fiber-reinforced polymer composites subjected to axial compression. *Compos Struct* 2009; 91: 66–73.
280. Puente I, Insausti A and Azkune M. Buckling of GFRP columns: an empirical approach to design. *J Compos Constr* 2006; 10: 529–537.
281. Wu C, Zhang LT, Bai Y, et al. Web crippling behavior of pultruded GFRP channel sections under transverse bearing load. *Compos Struct* 2019; 209: 129–142.
282. Ding L, Liu X, Wang X, et al. Mechanical properties of pultruded basalt fiber-reinforced polymer tube under axial tension and compression. *Constr Build Mater* 2018; 176: 629–637.
283. Gangarao HV and Blandford MM. Critical buckling strength prediction of pultruded glass fiber reinforced polymeric composite columns. *J Compos Mater* 2014; 48: 3685–3702.
284. Boscato G, Casalegno C, Russo S, et al. Buckling of built-up columns of pultruded fiber-reinforced polymer C-sections. *J Compos Constr*, Epub ahead of print August 2014. DOI: 10.1061/(ASCE)CC.1943-5614.0000453.
285. Minghini F, Tullini N, Ascione F, et al. Numerical failure analysis of built-up columns composed of closely spaced pultruded FRP channels. *Compos Struct* 2019; 207: 478–487.
286. Russo S. Shear and local effects in All-FRP bolted built-up columns. *Adv Struct Eng* 2015; 18: 1227–1240.
287. Russo S. Bucklings interactions in columns made by built-up thin, open, pultruded FRP shapes. *J Reinf Plast Compos* 2015; 34: 972–988.
288. Russo S. Investigation on buckling of all-FRP bolted built-up columns. *IES J Part A Civ Struct Eng* 2014; 7: 174–194.
289. Boscato G and Russo S. Dissipative capacity on FRP spatial pultruded structure. *Compos Struct* 2014; 113: 339–353.
290. Boscato G, Casalegno C, Russo S, et al. Buckling of GFRP pultruded built-up columns. In: *Advanced composites in construction 2013, ACIC 2013 – conference proceedings* (eds Whysall C and Taylor SE), Belfast, UK, pp.178–189..
291. Qi Y, Xie L, Bai Y, et al. Axial compression behaviours of pultruded GFRP–wood composite columns. *Sensors (Switzerland)* 2019; 19: 755.
292. Boscato G. Structural performance of a new column's prototype made by FRP pultruded material and light concrete. *Adv Mater Res* 2014; 900: 468–472.
293. Laudiero F, Minghini F and Tullini N. Buckling and postbuckling finite-element analysis of pultruded FRP profiles under pure compression. *J Compos Constr*, Epub ahead of print February 2014. DOI: 10.1061/(ASCE)CC.1943-5614.0000384.
294. Vanevenhoven LM, Shield CK and Bank LC. LRFDFactors for pultruded wide-flange columns. *J Struct Eng* 2010; 136: 554–564.
295. Barbero EJ, Dede EK and Jones S. Experimental verification of buckling-mode interaction in intermediate-length composite columns. *Int J Solid Struct* 2000; 37: 3919–3934.
296. Hashem ZA and Yuan RL. Experimental and analytical investigations on short GFRP composite compression members. *Compos Part B Eng* 2000; 31: 611–618.
297. Russo S. A review on buckling collapses of simple and complex columns made from pultruded frp material. *Compos Mech Comput Appl* 2017; 8: 1–34.
298. Bai Y, Hugi E, Ludwig C, et al. Fire performance of water-cooled GFRP columns. I: fire endurance investigation. *J Compos Constr* 2011; 15: 404–412.
299. Kim YJ and Qian KZ. Compressive behavior of non-slender hollow GFRP structural shapes in thermomechanical loading. *Compos Struct* 2017; 160: 813–823.
300. Wong PMH and Wang YC. An experimental study of pultruded glass fibre reinforced plastics channel columns at elevated temperatures. *Compos Struct* 2007; 81: 84–95.
301. Turvey GJ and Zhang Y. A computational and experimental analysis of the buckling, postbuckling and initial failure of pultruded GRP columns. *Comput Struct* 2006; 84: 1527–1537.
302. Cardoso DCT, Harries KA and de Batista EM. Compressive strength equation for GFRP square tube columns. *Compos Part B Eng* 2014; 59: 1–11.
303. Mottram JT, Brown ND and Anderson D. Physical testing for concentrically loaded columns of pultruded glass fibre reinforced plastic profile. *Struct Build* 2003; 156: 205–219.
304. Nunes F, Correia M, Correia JR, et al. Experimental and numerical study on the structural behavior of eccentrically loaded GFRP columns. *Thin-Walled Struct* 2013; 72: 175–187.
305. Riebel F and Keller T. Long-term compression performance of a pultruded gfrp element exposed to concrete pore water solution. *J Compos Constr* 2007; 11: 437–447.
306. Bai Y and Keller T. Pultruded GFRP tubes with liquid-cooling system under combined temperature and compressive loading. *Compos Struct* 2009; 90: 115–121.
307. Bai Y and Keller T. Shear failure of pultruded fiber-reinforced polymer composites under axial compression. *J Compos Constr* 2009; 13: 234–242.
308. Bank LC. Shear properties of pultruded glass FRP materials. *J Mater Civ Eng*, Epub ahead of print May 1990. DOI: 10.1061/(ASCE)0899-1561(1990)2:2(118).
309. Zureick A and Scott D. Short-term behavior and design of fiber-reinforced polymeric slender members under axial compression. *J Compos Constr* 1997; 1: 140–149.
310. Roberts TM and Masri HMKJAH. Section properties and buckling behavior of pultruded FRP profiles. *J Reinf Plast Compos* 2003; 22: 1305–1317.
311. Marín JC, Cañas J, París F, et al. Determination of G12 by means of the off-axis tension test, part I: review of gripping systems and correction factors. *Compos Part A Appl Sci Manuf* 2002; 33: 87–100.
312. Marín JC, Cañas J, París F, et al. Determination of G12 by means of the off-axis tension test, part II: a self-consistent approach to the application of correction factors. *Compos Part A Appl Sci Manuf* 2002; 33: 101–111.

313. Wagner HD, Fischer S, Roman I, et al. The effect of fibre content on the simultaneous determination of Young's and shear moduli of unidirectional composites. *Composites* 1981; 12: 257–259.
314. Minghini F, Tullini N and Laudiero F. Identification of the short-term full-section moduli of pultruded FRP profiles using bending tests. *J Compos Constr* 2014; 18: 04013030.
315. Neto ABSS and La Rovere HL. Flexural stiffness characterization of fiber reinforced plastic (FRP) pultruded beams. *Compos Struct* 2007; 81: 274–282.
316. Bank LC. Flexural and shear moduli of full-section fiber reinforced plastic (FRP) pultruded beams. *J Test Eval* 1989; 17: 40–45.
317. Feo L and Mancusi G. The influence of the shear deformations on the local stress state of pultruded composite profiles. *Mech Res Commun* 2013; 47: 44–49.
318. Kabir MZ and Sherbourne AN. Shear strain effects on flexure and torsion of thin-walled pultruded composite beams. *Can J Civ Eng* 1999; 26: 852–868.
319. Tahir M, Wang Z, Ali KM, et al. Shear behavior of concrete beams reinforced with CFRP sheet strip stirrups using wet-layup technique. *Structures* 2019; 22: 43–52.
320. Yuan Y and Wang Z. Shear behavior of large-scale concrete beams reinforced with CFRP bars and handmade strip stirrups. *Compos Struct* 2019; 227: 111253.
321. Al-Mahmoud F, Castel A, Minh TQ, et al. Reinforced concrete beams strengthened with NSM CFRP rods in shear. *Adv Struct Eng* 2015; 18: 1563–1574.
322. Ulger T and Okeil AM. Strengthening by stiffening: fiber-reinforced plastic configuration effects on behavior of shear-deficient steel beams. *J Compos Constr*, Epub ahead of print August 2017. DOI: 10.1061/(ASCE)CC.1943-5614.0000788.
323. Perrella M, Berardi VP and Cricri G. A novel methodology for shear cohesive law identification of bonded reinforcements. *Compos Part B Eng* 2018; 144: 126–133.
324. Brunton J, Bank LC and Oliva M. Punching shear failure in double-layer pultruded FRP grid reinforced concrete bridge decks. *Adv Struct Eng* 2012; 15: 601–614.
325. Mohamed Ali MS, Oehlers DJ and Seracino R. Vertical shear interaction model between external FRP transverse plates and internal steel stirrups. *Eng Struct* 2006; 28: 381–389.
326. Estep DD, GangaRao HVS, Dittenber DB, et al. Response of pultruded glass composite box beams under bending and shear. *Compos Part B Eng* 2016; 88: 150–161.
327. Yanes-Armas S, de Castro J and Keller T. System transverse in-plane shear stiffness of pultruded GFRP bridge decks. *Eng Struct* 2016; 107: 34–46.
328. Keller T and Gürtler H. In-plane compression and shear performance of FRP bridge decks acting as top chord of bridge girders. *Compos Struct* 2006; 72: 151–162.
329. Xiong Z, Liu Y, Zuo Y, et al. Experimental evaluation of shear behavior of pultruded GFRP perforated connectors embedded in concrete. *Compos Struct*, Epub ahead of print 15 August 2019. DOI: 10.1016/j.compstruct.2019.110938.
330. Satasivam S, Feng P, Bai Y, et al. Composite actions within steel-FRP composite beam systems with novel blind bolt shear connections. *Eng Struct* 2017; 138: 63–73.
331. Neaogoe CA and Gil L. Analytical procedure for the design of PFRP-RC hybrid beams including shear interaction effects. *Compos Struct* 2015; 132: 122–135.
332. Etim O, Gand AK, Saidani M, et al. Shear characterisation of pultruded superstructural FRP-concrete push-outs. *Structures* 2020; 23: 254–266.
333. Alachek I, Reboul N and Jurkiewicz B. Experimental and finite element analysis of push-out shear test for adhesive joints between pultruded GFRP and concrete. *Int J Adhes Adhes* 2020; 98: 102552.
334. Sawpan MA. Shear properties and durability of GFRP reinforcement bar aged in seawater. *Polym Test* 2019; 75: 312–320.
335. Turvey GJ and Zhang Y. Shear failure strength of web-flange junctions in pultruded GRP WF profiles. *Constr Build Mater* 2006; 20: 81–89.
336. Alderucci T, Rossi M, Chiappini G, et al. Effect of different aging conditions on the shear performance of joints made between GFRP and glass with a UV absorbance coating. *Int J Adhes Adhes* 2019; 94: 76–83.
337. Oehlers DJ, Liu IST and Seracino R. Shear deformation debonding of adhesively bonded plates. *Proc Inst Civ Eng Struct Build* 2005; 158: 77–84.
338. Genedy M, Chennareddy R, Soliman EM, et al. Improving shear strength of bolted joints in pultruded glass fiber reinforced polymer composites using carbon nanotubes. *J Reinf Plast Compos* 2017; 36: 958–971.
339. Chataigner S, Caron J-F, Benzarti K, et al. Use of a single lap shear test to characterize composite-to-concrete or composite-to-steel bonded interfaces. *Constr Build Mater* 2011; 25: 468–478.
340. Roberts TM. Influence of shear deformation on buckling of pultruded fiber reinforced plastic profiles. *J Compos Constr* 2002; 6: 241–248.
341. Brooks RJ and Thrvey GJ. Lateral buckling of pultruded GRP I-section cantilevers. *Compos Struct* 1995; 32: 203–215.
342. Correia JR, Branco FA, Silva NMF, et al. First-order, buckling and post-buckling behaviour of GFRP pultruded beams, part 1: experimental study. *Comput Struct* 2011; 89: 2052–2064.
343. Park JY and Lee JW. Determination of the shear buckling load of a large polymer composite I-section using strain and displacement sensors. *Sensors (Switzerland)* 2012; 12: 16024–16036.
344. Ascione F and Mancusi G. The influence of the web-flange junction stiffness on the mechanical behaviour of thin-walled pultruded beams. *Compos Part B Eng* 2013; 55: 599–606.
345. Zhang D, Zhao Q, Li F, et al. Experimental and numerical study of the torsional response of a modular hybrid FRP-aluminum triangular deck-truss beam. *Eng Struct* 2017; 133: 172–185.
346. Sonti SS and Barbero EJ. Material characterization of pultruded laminates and shapes. *J Reinf Plast Compos* 1996; 15: 701–717.

347. Turvey GJ. Torsion tests on pultruded grp sheet. *Compos Sci Technol* 1998; 58: 1343–1351.
348. Roberts T and Al-Ubaidi H. Influence of shear deformation on restrained torsional warping of pultruded FRP bars of open cross-section. *Thin-Walled Struct* 2001; 39: 395–414.
349. Qureshi MAM and Ganga Rao H. Torsional response of closed FRP composite sections. *Compos Part B Eng* 2014; 61: 254–266.
350. El-Hajjar R and Haj-Ali R. In-plane shear testing of thick-section pultruded FRP composites using a modified Arcan fixture. *Compos Part B Eng* 2004; 35: 421–428.
351. Correia JR, Gomes MM, Pires JM, et al. Mechanical behaviour of pultruded glass fibre reinforced polymer composites at elevated temperature: experiments and model assessment. *Compos Struct* 2013; 98: 303–313.
352. Rosa IC, Morgado T, Correia JR, et al. Shear behavior of GFRP composite materials at elevated temperature. *J Compos Constr* 2018; 22: 04018010.
353. Barbero EJ. Pultruded structural shapes – from the constituents to the structural behavior. *SAMPE J*, <http://citeseerx.ist.psu.edu/viewdoc/summary?doi=10.1.1.151.6975> (1991, accessed 25 February 2019).
354. Mottram JT. Shear modulus of standard pultruded fiber reinforced plastic material. *J Compos Constr* 2004; 8: 141–147.
355. Kwon D-J, Kim J-H, Park S-M, et al. Damage sensing, mechanical and interfacial properties of resins suitable for new CFRP rope for elevator applications. *Compos Part B Eng* 2019; 157: 259–265.
356. Davalos JF, Salim HA, Qiao P, et al. Analysis and design of pultruded FRP shapes under bending. *Compos Part B Eng* 1996; 27: 295–305.
357. Barbero EJ, Fu S-H and Raftoyiannis I. Ultimate bending strength of composite beams. *J Mater Civ Eng* 1991; 3: 292–306.
358. Borowicz DT and Bank LC. Behavior of pultruded fiber-reinforced polymer beams subjected to concentrated loads in the plane of the web. *J Compos Constr* 2011; 15: 229–238.
359. Mottram JT. Evaluation of design analysis for pultruded fibre-reinforced polymeric box beams. *Struct Eng Lond* 1991; 69: 211–220.
360. Palmer DW, Bank LC and Gentry TR. Progressive tearing failure of pultruded composite box beams: experiment and simulation. *Compos Sci Technol* 1998; 58: 1353–1359.
361. Lee J, Hollaway L, Thorne A, et al. The structural characteristic of a polymer composite cellular box beam in bending. *Constr Build Mater* 1995; 9: 333–340.
362. Muttashar M, Manalo A, Karunasena W, et al. Influence of infill concrete strength on the flexural behaviour of pultruded GFRP square beams. *Compos Struct*, Epub ahead of print 10 June 2016. DOI: 10.1016/j.compstruct.2016.02.071.
363. Cavaleri L, Di Paola M, Ferrotto MF, et al. Structural performances of pultruded GFRP emergency structures, part 1: experimental characterization of materials and substructure. *Compos Struct* 2019; 214: 325–334.
364. Alam P, Ansell MP and Smedley D. Mechanical repair of timber beams fractured in flexure using bonded-in reinforcements. *Compos Part B Eng* 2009; 40: 95–106.
365. Rescalvo FJ, Rodríguez M, Bravo R, et al. Acoustic emission and numerical analysis of pine beams retrofitted with FRP and poplar wood. *Materials (Basel)* 2020; 13: 435.
366. Shekarchi M, Oskouei AV and Raftery GM. Flexural behavior of timber beams strengthened with pultruded glass fiber reinforced polymer profiles. *Compos Struct* 2020; 241: 112062.
367. Pandey MD, Kabir MZ and Sherbourne AN. Flexural-torsional stability of thin-walled composite I-section beams. *Compos Eng* 1995; 5: 321–342.
368. Mancusi G and Feo L. Non-linear pre-buckling behavior of shear deformable thin-walled composite beams with open cross-section. *Compos Part B Eng* 2013; 47: 379–390.
369. Bank LC, Gentry TR and Nadipelli M. Local buckling of pultruded FRP beams – analysis and design. *J Reinf Plast Compos*, Epub ahead of print 1 March 1996. DOI: 10.1177/073168449601500304.
370. Minghini F, Tullini N and Laudiero F. Buckling analysis of FRP pultruded frames using locking-free finite elements. *Thin-Walled Struct* 2008; 46: 223–241.
371. Barbero EJ and Raftoyiannis IG. Lateral and distortional buckling of pultruded I-beams. *Compos Struct* 1994; 27: 261–268.
372. Razaq Z, Prabhakaran R and Sirjani MM. Load and resistance factor design (LRFD) approach for reinforced-plastic channel beam buckling. *Compos Part B Eng* 1996; 27: 361–369.
373. Insausti A, Puente I and Azkune M. Interaction between local and lateral buckling on pultruded I-beams. *J Compos Constr* 2009; 13: 315–324.
374. Qiao P, Zou G and Davalos JF. Flexural-torsional buckling of fiber-reinforced plastic composite cantilever I-beams. *Compos Struct* 2003; 60: 241–250.
375. Davalos JF, Qiao P and Salim HA. Flexural-torsional buckling of pultruded fiber reinforced plastic composite I-beams: experimental and analytical evaluations. *Compos Struct* 1997; 38: 241–250.
376. Shan L and Qiao P. Flexural-torsional buckling of fiber-reinforced plastic composite open channel beams. *Compos Struct* 2005; 68: 211–224.
377. Laudiero F, Minghini F and Tullini N. Postbuckling failure analysis of pultruded FRP beams under uniform bending. *Compos Part B Eng* 2013; 54: 431–438.
378. Ascione F, Lamberti M and Razaqpur G. Modifications of standard GFRP sections shape and proportions for improved stiffness and lateral-torsional stability. *Compos Struct* 2015; 132: 265–289.
379. Bank LC and Yin J. Failure of web-flange junction in postbuckled pultruded I-beams. *J Compos Constr* 1999; 3: 177–184.
380. Khan F and Kim YJ. Time-dependent and residual behavior of pultruded GFRP beams subjected to sustained intensities and cold temperature. *Cold Reg Sci Technol* 2012; 74–75: 43–51.

381. Wijayawardane ISK, Mutsuyoshi H, Nguyen H, et al. Flexural behaviour of glass fibre-reinforced polymer and ultra-high-strength fibre-reinforced concrete composite beams subjected to elevated temperature. *Adv Struct Eng* 2017; 20: 1357–1374.
382. Harris HG, Somboonsong W and Ko FK. New ductile hybrid FRP reinforcing bar for concrete structures. *J Compos Constr* 1998; 2: 28–37.
383. Bradberry TE. Concrete bridge decks reinforced with fiber-reinforced polymer bars. *Transp Res Rec* 2001; 1814: 94–104.
384. Kadioglu F and Pidaparti RM. Composite rebars shape effect in reinforced structures. *Compos Struct* 2005; 67: 19–26.
385. Colombi P and Poggi C. An experimental, analytical and numerical study of the static behavior of steel beams reinforced by pultruded CFRP strips. *Compos Part B Eng* 2006; 37: 64–73.
386. Tavares CML, Ribeiro MCS, Ferreira AJM, et al. Creep behaviour of FRP-reinforced polymer concrete. *Compos Struct* 2002; 57: 47–51.
387. Eshwar N, Ibell TJ and Nanni A. Effectiveness of CFRP strengthening on curved soffit RC beams. *Adv Struct Eng* 2005; 8: 55–68.
388. Ribeiro AS, de Jesus AMP, Lima AM, et al. Study of strengthening solutions for glued-laminated wood beams of maritime pine wood. *Constr Build Mater* 2009; 23: 2738–2745.
389. Balsamo A, Nardone F, Iovinella I, et al. Flexural strengthening of concrete beams with EB-FRP, SRP and SRCM: experimental investigation. *Compos Part B Eng* 2013; 46: 91–101.
390. Yang X, Bai Y and Ding F. Structural performance of a large-scale space frame assembled using pultruded GFRP composites. *Compos Struct* 2015; 133: 986–996.
391. Minghini F, Tullini N and Laudiero F. Vibration analysis with second-order effects of pultruded FRP frames using locking-free elements. *Thin-Walled Struct* 2009; 47: 136–150.
392. Minghini F, Tullini N and Laudiero F. Elastic buckling analysis of pultruded FRP portal frames having semi-rigid connections. *Eng Struct* 2009; 31: 292–299.
393. Minghini F, Tullini N and Laudiero F. Vibration analysis of pultruded FRP frames with semi-rigid connections. *Eng Struct* 2010; 32: 3344–3354.
394. Cavaleri L, Di Paola M, Ferrotto MF, et al. Structural performances of pultruded GFRP emergency structures, part 2: full-scale experimental testing. *Compos Struct* 2019; 214: 304–315.
395. Correia JR, Branco FA and Ferreira JG. Flexural behaviour of multi-span GFRP-concrete hybrid beams. *Eng Struct* 2009; 31: 1369–1381.
396. Ribeiro MCS, Tavares CML, Ferreira AJM, et al. Static flexural performance of GFRP-polymer concrete hybrid beams. *Key Eng Mater* 2002; 230–232: 148–151.
397. Correia JR, Branco FA and Ferreira JG. Flexural behaviour of GFRP-concrete hybrid beams with interconnection slip. *Compos Struct* 2007; 77: 66–78.
398. Speranzini E and Agnetti S. Flexural performance of hybrid beams made of glass and pultruded GFRP. *Constr Build Mater* 2015; 94: 249–262.
399. Satasivam S and Bai Y. Mechanical performance of bolted modular GFRP composite sandwich structures using standard and blind bolts. *Compos Struct* 2014; 117: 59–70.
400. Keller T and Schollmayer M. Plate bending behavior of a pultruded GFRP bridge deck system. *Compos Struct* 2004; 64: 285–295.
401. Salim HA, Davalos JF, Qiao P, et al. Analysis and design of fiber reinforced plastic composite deck-and-stringer bridges. *Compos Struct* 1997; 38: 295–307.
402. Keller T, Schaumann E and Vallée T. Flexural behavior of a hybrid FRP and lightweight concrete sandwich bridge deck. *Compos Part A Appl Sci Manuf* 2007; 38: 879–889.
403. Lee J, Kim Y, Jung J, et al. Experimental characterization of a pultruded GFRP bridge deck for light-weight vehicles. *Compos Struct* 2007; 80: 141–151.
404. Zhu J and Lopez MM. Performance of a lightweight GFRP composite bridge deck in positive and negative bending regions. *Compos Struct* 2014; 113: 108–117.
405. Kim Y and Lee J. An analytical model for the flexural response of a fiber reinforced plastic deck using higher-order shear deformable plate theory. *Compos Struct* 2008; 85: 275–283.
406. Wu Z, Mirmiran A, Zhu Z, et al. Flexural behavior of prestressed FRP tubular bridge deck. *Compos Part B Eng* 2009; 40: 125–133.
407. Chen C-H and Ma C-CM. Pultruded fibre-reinforced polyurethane composites. III. Static mechanical, thermal, and dynamic mechanical properties. *Compos Sci Technol* 1994; 52: 427–432.
408. Paciornik S, Martinho F, de Mauricio MH, et al. Analysis of the mechanical behavior and characterization of pultruded glass fiber–resin matrix composites. *Compos Sci Technol* 2003; 63: 295–304.
409. Correia JR, Branco F, Gonilha J, et al. Glass fibre reinforced polymer pultruded flexural members: assessment of existing design methods. *Struct Eng Int J Int Assoc Bridg Struct Eng* 2010; 20: 362–369.
410. Sims GD, Johnson AF and Hill RD. Mechanical and structural properties of a GRP pultruded section. *Compos Struct* 1987; 8: 173–187.
411. Chen C-H and Ma C-CM. Pultruded fibre reinforced polyurethane composites II. Effect of processing parameters on mechanical and thermal properties. *Compos Sci Technol* 1992; 45: 345–352.
412. Chen C-H and Ma C-CM. Pultruded fibre-reinforced PMMA/PU IPN composites: processability and mechanical properties. *Compos Part A Appl Sci Manuf* 1997; 28: 65–72.
413. Nagaraj V and GangaRao HVS. Static behavior of pultruded GFRP beams. *J Compos Constr* 1997; 1: 120–129.
414. Liao K, Schultheisz CR and Hunston DL. Effects of environmental aging on the properties of pultruded GFRP. *Compos Part B Eng* 1999; 30: 485–493.

415. Turvey G. Flexure of pultruded GRP beams with semi-rigid end connections. *Compos Struct* 1999; 47: 571–580.
416. Correia JR, Cabral-Fonseca S, Branco FA, et al. Durability of pultruded glass-fiber-reinforced polyester profiles for structural applications. *Mech Compos Mater* 2006; 42: 325–338.
417. Turvey GJ and Zhang Y. Characterisation of the rotational stiffness and strength of web-flange junctions of pultruded GRP WF-sections via web bending tests. *Compos Part A Appl Sci Manuf* 2006; 37: 152–164.
418. Dawood M, Taylor E, Ballew W, et al. Static and fatigue bending behavior of pultruded GFRP sandwich panels with through-thickness fiber insertions. *Compos Part B Eng* 2010; 41: 363–374.
419. Carra G and Carvelli V. Long-term bending performance and service life prediction of pultruded glass fibre reinforced polymer composites. *Compos Struct* 2015; 127: 308–315.
420. Turvey GJ and Cerutti X. Flexural behaviour of pultruded glass fibre reinforced polymer composite beams with bolted splice joints. *Compos Struct* 2015; 119: 543–550.
421. Manjunath M, Renukappa N and Suresha B. Influence of micro and nanofillers on mechanical properties of pultruded unidirectional glass fiber reinforced epoxy composite systems. *J Compos Mater* 2016; 50: 1109–1121.
422. Oskouei AV, Bazli M, Ashrafi H, et al. Flexural and web crippling properties of GFRP pultruded profiles subjected to wetting and drying cycles in different sea water conditions. *Polym Test* 2018; 69: 417–430.
423. Turvey GJ and Zhang Y-S. Flexural moduli and end connection stiffnesses of symmetrically loaded GFRP beams for limit state serviceability design analysis. *Compos Struct* 2018; 202: 1164–1175.
424. Madenci E, Özkılıç YO and Gemi L. Experimental and theoretical investigation on flexure performance of pultruded GFRP composite beams with damage analyses. *Compos Struct*, Epub ahead of print 6 March 2020. DOI: 10.1016/j.compstruct.2020.112162.
425. Vassilopoulos AP. Introduction to the fatigue life prediction of composite materials and structures: past, present and future prospects. In: Vassilopoulos AP (ed) *Fatigue life prediction of composites and composite structures*. Amsterdam, Netherlands: Elsevier, pp.1–44.
426. Shahverdi M, Vassilopoulos AP and Keller T. A total fatigue life model for the prediction of the R-ratio effects on fatigue crack growth of adhesively-bonded pultruded GFRP DCB joints. *Compos Part A Appl Sci Manuf* 2012; 43: 1783–1790.
427. Clarke JL. *Structural design of polymer composites: EUROCOMP design code and handbook*. E & FN Spon, www.crcpress.com/Structural-Design-of-Polymer-Composites-Eurocomp-Design-Code-and-Background/Clarke/p/book/9780419194507 (1996, accessed 17 May 2019).
428. Tanimoto T and Amijima S. Progressive nature of fatigue damage of glass fiber reinforced plastics. *J Compos Mater* 1975; 9: 380–390.
429. Ellyin F and El-Kadi H. A fatigue failure criterion for fiber reinforced composite laminae. *Compos Struct* 1990; 15: 61–74.
430. Beheshty MH and Harris B. A constant-life model of fatigue behaviour for carbon-fibre composites: the effect of impact damage. *Compos Sci Technol* 1998; 58: 9–18.
431. Kawai M and Koizumi M. Nonlinear constant fatigue life diagrams for carbon/epoxy laminates at room temperature. *Compos Part A Appl Sci Manuf* 2007; 38: 2342–2353.
432. Vassilopoulos AP, Manshadi BD and Keller T. Piecewise non-linear constant life diagram formulation for FRP composite materials. *Int J Fatigue* 2010; 32: 1731–1738.
433. Vassilopoulos AP, Manshadi BD and Keller T. Influence of the constant life diagram formulation on the fatigue life prediction of composite materials. *Int J Fatigue* 2010; 32: 659–669.
434. Shahverdi M, Vassilopoulos AP and Keller T. Experimental investigation of R-ratio effects on fatigue crack growth of adhesively-bonded pultruded GFRP DCB joints under CA loading. *Compos Part A Appl Sci Manuf* 2012; 43: 1689–1697.
435. Curtis PT. The fatigue behaviour of fibrous composite materials. *J Strain Anal Eng Des* 1989; 24: 235–244.
436. Hahn HT. Fatigue behavior and life prediction of composite laminates. In: *Composite materials: testing and design (fifth conference)* (ed A Tsai), 1979, pp.383–417. West Conshohocken, PA: ASTM International.
437. Vieira PR, Carvalho EML, Vieira JD, et al. Experimental fatigue behavior of pultruded glass fibre reinforced polymer composite materials. *Compos Part B Eng* 2018; 146: 69–75.
438. Dittenber DB and Rao HVG. Fatigue equation considerations for the American Society of Civil Engineers pre-standard for load and resistance factor design of pultruded fiber-reinforced polymer structures. *J Compos Mater* 2013; 47: 1943–1949.
439. Keller T and Tirelli T. Fatigue behavior of adhesively connected pultruded GFRP profiles. *Compos Struct* 2004; 65: 55–64.
440. Keller T, Tirelli T and Zhou A. Tensile fatigue performance of pultruded glass fiber reinforced polymer profiles. *Compos Struct* 2005; 68: 235–245.
441. Bai Y and Keller T. Modal parameter identification for a GFRP pedestrian bridge. *Compos Struct* 2008; 82: 90–100.
442. Zhang Y, Vassilopoulos AP and Keller T. Stiffness degradation and fatigue life prediction of adhesively-bonded joints for fiber-reinforced polymer composites. *Int J Fatigue* 2008; 30: 1813–1820.
443. Wu C, Feng P and Bai Y. Comparative study on static and fatigue performances of pultruded GFRP joints using ordinary and blind bolts. *J Compos Constr* 2015; 19: 04014065.
444. Yang X, Bai Y, Luo FJ, et al. Dynamic and fatigue performances of a large-scale space frame assembled using pultruded GFRP composites. *Compos Struct* 2016; 138: 227–236.

445. Degrieck J and Van Paepegem W. Fatigue damage modeling of fibre-reinforced composite materials: review. *Appl Mech Rev* 2001; 54: 279.
446. Harris B. *A historical review of the fatigue behaviour of fibre-reinforced plastics*, Epub ahead of print 1 October 2003. DOI: 10.1016/B978-1-85573-608-5.50006-1.
447. Sarfaraz R, Vassilopoulos AP and Keller T. Experimental investigation and modeling of mean load effect on fatigue behavior of adhesively-bonded pultruded GFRP joints. *Int J Fatigue* 2012; 44: 245–252.
448. Ascione L, Caron J-F, Godonou P, et al. *Prospect for new guidance in the design of FRP. Support to the implementation, harmonization and further development of the Eurocodes*. Epub ahead of print January 2016. DOI: 10.2788/22306.
449. Kassapoglou C. Fatigue of composite materials under spectrum loading. *Compos Part A Appl Sci Manuf* 2010; 41: 663–669.
450. Noël M. Probabilistic fatigue life modelling of FRP composites for construction. *Constr Build Mater* 2019; 206: 279–286.
451. Fathy A, Shaker A, Hamid MA, et al. The effects of nano-silica/nano-alumina on fatigue behavior of glass fiber-reinforced epoxy composites. *J Compos Mater* 2017; 51: 1667–1679.
452. Mahboob Z and Bougherara H. Fatigue of flax-epoxy and other plant fibre composites: critical review and analysis. *Compos Part A Appl Sci Manuf* 2018; 109: 440–462.
453. Alam P, Mamalis D, Robert C, et al. The fatigue of carbon fibre reinforced plastics – a review. *Compos Part B Eng* 2019; 166: 555–579.
454. Choi Y and Yuan RL. Time-dependent deformation of pultruded fiber reinforced polymer composite columns. *J Compos Constr* 2003; 7: 356–362.
455. Ascione F, Berardi VP, Feo L, et al. An experimental study on the long-term behavior of CFRP pultruded laminates suitable to concrete structures rehabilitation. *Compos Part B Eng* 2008; 39: 1147–1150.
456. Choi K-K, Meshgin P and Taha MMR. Shear creep of epoxy at the concrete–FRP interfaces. *Compos Part B Eng* 2007; 38: 772–780.
457. Harries KA, Guo Q and Cardoso D. Creep and creep buckling of pultruded glass-reinforced polymer members. *Compos Struct* 2017; 181: 315–324.
458. Findley WN. 26-Year creep and recovery of poly(vinyl chloride) and polyethylene. *Polym Eng Sci* 1987; 27: 582–585.
459. Scott DW, Lai JS and Zureick AH. Creep behavior of fiber-reinforced polymeric composites: a review of the technical literature. *J Reinf Plast Compos*, Epub ahead of print 1 June 1995. DOI: 10.1177/073168449501400603.
460. Cardoso DCT and Harries KA. A viscoelastic model for time-dependent behavior of pultruded GFRP. *Constr Build Mater* 2019; 208: 63–74.
461. Shao Y and Shanmugam J. Deflection creep of pultruded composite sheet piling. *J Compos Constr* 2004; 8: 471–479.
462. Bottoni M, Mazzotti C and Savoia M. Creep tests on GFRP pultruded specimens subjected to traction or shear. *Compos Struct* 2014; 108: 514–523.
463. Bank LC and Mosallam AS. Creep and failure of a full-size fiber-reinforced plastic pultruded frame. *Compos Eng* 1992; 2: 213–215, 217–227.
464. Gonilha JA, Correia JR and Branco FA. Creep response of GFRP-concrete hybrid structures: application to a footbridge prototype. *Compos Part B Eng* 2013; 53: 193–206.
465. Mendes PJD, Barros JAO, Sena-Cruz JM, et al. Development of a pedestrian bridge with GFRP profiles and fiber reinforced self-compacting concrete deck. *Compos Struct* 2011; 93: 2969–2982.
466. Gonilha JA, Barros J, Correia JR, et al. Static, dynamic and creep behaviour of a full-scale GFRP-SFRSCC hybrid footbridge. *Compos Struct* 2014; 118: 496–509.
467. Alachek I, Reboul N and Jurkiewicz B. Experimental and finite element analysis of the long-term behaviour of GFRP-concrete hybrid beams fabricated using adhesive bonding. *Compos Struct* 2019; 207: 148–165.
468. Kuruvilla SP and Renukappa NM. Effects of nano- and micro-filler on water diffusion and leakage current of GRP composites. In: *Lecture notes in mechanical engineering*. Berlin, Germany: Springer, 2019, pp.53–61.
469. Bar M, Alagirusamy R and Das A. Flame retardant polymer composites. *Fiber Polym* 2015; 16: 705–717.
470. Rafique I, Kausar A and Muhammad B. Epoxy resin composite reinforced with carbon fiber and inorganic filler: overview on preparation and properties. *Polym Plast Technol Eng* 2016; 55: 1653–1672.
471. Hassan MH, Othman AR and Kamaruddin S. A review on the manufacturing defects of complex-shaped laminate in aircraft composite structures. *Int J Adv Manuf Technol* 2017; 91: 4081–4094.
472. Safonov A, Gusev M, Saratov A, et al. Modeling of cracking during pultrusion of large-size profiles. *Compos Struct* 2019; 235: 111801.
473. Tucci F, Rubino F and Carlone P. Strain and temperature measurement in pultrusion processes by fiber Bragg grating sensors. In: *AIP conference proceedings* (eds G Buffa, L Fratini, Ingarao G, et al.). College Park, pp. 020036. MD: American Institute of Physics..
474. Tucci F, Rubino F, Esperto V, et al. Integrated modeling of injection pultrusion. In: *AIP conference proceedings* (eds P Arrazola, ES de Argandona and O de Bmmagl). College Park, pp. 060006. MD: American Institute of Physics..
475. Vedernikov AN, Safonov AA, Gusev SA, et al. Spring-in experimental evaluation of L-shaped pultruded profiles. *IOP Conf Ser Mater Sci Eng* 2020; 747: 012013.
476. Safonov AA. Mathematical description of the technological process of injection pultrusion. *J Mach Manuf Reliab* 2011; 40: 68–73.
477. Tucci F, Bezerra R, Rubino F, et al. Multiphase flow simulation in injection pultrusion with variable properties. *Mater Manuf Process*, Epub ahead of print 9 January 2020. DOI: 10.1080/10426914.2020.1711928.

478. Geng D, Liu Y, Shao Z, et al. Delamination formation, evaluation and suppression during drilling of composite laminates: a review. *Compos Struct* 2019; 216: 168–186.
479. Essiga W and Kreutzbruck M. Development of an inline monitoring system for quality assurance of thermoplastic CFRP tape using air-coupled ultrasound. In: *AIP conference proceedings* (ed OCF Manero). pp. 110002. College Park, MD: American Institute of Physics.
480. Xu Y. Delamination detection at web/flange junction of I-section composite beam with fiber optical interferometer sensor. *Compos Part B Eng* 2014; 58: 140–146.
481. Nunes F, Correia JR and Silvestre N. Structural behaviour of hybrid FRP pultruded columns, part 1: experimental study. *Compos Struct* 2016; 139: 291–303.
482. Fallahi H, Taheri-Behrooz F and Asadi A. Nonlinear mechanical response of polymer matrix composites: a review. *Polym Rev*, Epub ahead of print 11 September 2019. DOI: 10.1080/15583724.2019.1656236.
483. Ascione F. Influence of initial geometric imperfections in the lateral buckling problem of thin walled pultruded GFRP I-profiles. *Compos Struct* 2014; 112: 85–99.
484. Ahmad F, Choi HS and Park MK. A review: natural fiber composites selection in view of mechanical light and weight, and economic properties. *Macromol Mater Eng* 2015; 300: 10–24.
485. Sarasini F and Fiore V. A systematic literature review on less common natural fibres and their biocomposites. *J Clean Prod* 2018; 195: 240–267.
486. Kiruthika AV. A review on physico-mechanical properties of bast fibre reinforced polymer composites. *J Build Eng* 2017; 9: 91–99.
487. Gholampour A and Ozbakkaloglu T. A review of natural fiber composites: properties, modification and processing techniques, characterization, applications. *J Mater Sci* 2020; 55: 829–892.
488. Jariwala H and Jain P. A review on mechanical behavior of natural fiber reinforced polymer composites and its applications. *J Reinf Plast Compos* 2019; 38: 441–453.
489. Sadasivuni KK, Saha P, Adhikari J, et al. Recent advances in mechanical properties of biopolymer composites: a review. *Polym Compos*, Epub ahead of print 7 August 2019. DOI: 10.1002/pc.25356.
490. Sanjay MR, Madhu P, Jawaid M, et al. Characterization and properties of natural fiber polymer composites: a comprehensive review. *J Clean Prod* 2018; 172: 566–581.
491. Nasonov Y, Safonov A, Gusev S, et al. Mathematical simulation the kinetics of polymerization of vinyl ester resin using in pultrusion. *IOP Conf Ser Mater Sci Eng* 2020; 747: 12010.
492. Kumar R, Singh R, Ahuja IPS, et al. Weldability of thermoplastic materials for friction stir welding – a state of art review and future applications. *Compos Part B Eng* 2018; 137: 1–15.
493. Struzziero G, Teuwen JJE and Skordos AA. Numerical optimisation of thermoset composites manufacturing processes: a review. *Compos Part A Appl Sci Manuf*, Epub ahead of print June 2019. DOI: 10.1016/j.compositesa.2019.105499.
494. Safonov AA. 3D topology optimization of continuous fiber-reinforced structures via natural evolution method. *Compos Struct* 2019; 215: 289–297.
495. Branco CM, Ferreira JM, Fael P, et al. A comparative study of the fatigue behaviour of GRP hand lay-up and pultruded phenolic composites. *Int J Fatigue* 1996; 18: 255–263.
496. Salvia M. Flexural fatigue behaviour of UDGFRP experimental approach. *Int J Fatigue* 1997; 19: 253–262.
497. Nagaraj V and Gangarao HVS. Fatigue behavior and connection efficiency of pultruded GFRP beams. *J Compos Constr* 1998; 2: 57–65.
498. Liao K. Long-term environmental fatigue of pultruded glass-fiber-reinforced composites under flexural loading. *Int J Fatigue* 1999; 21: 485–495.
499. Chotard T, Pasquier J and Benzeggagh M. Impact response and residual performance of GRP pultruded shapes under static and fatigue loading. *Compos Sci Technol* 2000; 60: 895–912.
500. McBagonluri F, Garcia K, Hayes M, et al. Characterization of fatigue and combined environment on durability performance of glass/vinyl ester composite for infrastructure applications. *Int J Fatigue* 2000; 22: 53–64.
501. Chotard T, Pasquier J and Benzeggagh M. Residual performance of scarf patch-repaired pultruded shapes initially impact damaged. *Compos Struct* 2001; 53: 317–331.
502. Post N, Bausano J, Case S, et al. Modeling the remaining strength of structural composite materials subjected to fatigue. *Int J Fatigue* 2006; 28: 1100–1108.
503. Keller T and Zhou A. Fatigue behavior of adhesively bonded joints composed of pultruded GFRP adherends for civil infrastructure applications. *Compos Part A Appl Sci Manuf* 2006; 37: 1119–1130.
504. Jeong J, Lee Y-H, Park K-T, et al. Field and laboratory performance of a rectangular shaped glass fiber reinforced polymer deck. *Compos Struct* 2007; 81: 622–628.
505. Qiao P and Yang M. Fatigue life prediction of pultruded E-glass/polyurethane composites. *J Compos Mater* 2006; 40: 815–837.
506. Zhang Y, Vassilopoulos AP and Keller T. Environmental effects on fatigue behavior of adhesively-bonded pultruded structural joints. *Compos Sci Technol* 2009; 69: 1022–1028.
507. Zhang Y, Vassilopoulos AP and Keller T. Fracture of adhesively-bonded pultruded GFRP joints under constant amplitude fatigue loading. *Int J Fatigue* 2010; 32: 979–987.
508. Kim H-Y, Lee Y-H and Lee S-Y. Ultimate strength of a GFRP deck panel for temporary structures. *Compos Struct* 2011; 93: 528–537.
509. Sarfaraz R, Vassilopoulos AP and Keller T. Experimental investigation of the fatigue behavior of adhesively-bonded pultruded GFRP joints under different load ratios. *Int J Fatigue* 2011; 33: 1451–1460.
510. Sarfaraz R, Vassilopoulos AP and Keller T. Block loading fatigue of adhesively bonded pultruded GFRP joints. *Int J Fatigue* 2013; 49: 40–49.

511. Sarfaraz R, Vassilopoulos AP and Keller T. Variable amplitude fatigue of adhesively-bonded pultruded GFRP joints. *Int J Fatigue* 2013; 55: 22–32.
512. Shahverdi M, Vassilopoulos AP and Keller T. Mixed-mode fatigue failure criteria for adhesively-bonded pultruded GFRP joints. *Compos Part A Appl Sci Manuf* 2013; 54: 46–55.
513. Mendes PJD, Barros JAO, Sena-Cruz J, et al. Influence of fatigue and aggressive exposure on GFRP girder to SFRSCC deck all-adhesive connection. *Compos Struct* 2014; 110: 152–162.
514. Sá MF, Gomes AM, Correia JR, et al. Creep behavior of pultruded GFRP elements, part 1: literature review and experimental study. *Compos Struct* 2011; 93: 2450–2459.
515. McClure G and Mohammadi Y. Compression creep of pultruded e-glass-reinforced-plastic angles. *J Mater Civ Eng*, Epub ahead of print November 1995. DOI: 10.1061/(ASCE)0899-1561(1995)7:4(269).
516. Scott DW and Zureick A-H. Compression creep of a pultruded e-glass/vinylester composite. *Compos Sci Technol*, Epub ahead of print January 1998. DOI: 10.1016/S0266-3538(98)00009-8.
517. Mottram JT. Short- and long-term structural properties of pultruded beam assemblies fabricated using adhesive bonding. *Compos Struct* 1993; 25: 387–395.
518. Dutta PK and Hui D. Creep rupture of a GFRP composite at elevated temperatures. *Comput Struct* 2000; 76: 153–161.
519. Abdel-Magid B, Lopez-Anido R, Smith G, et al. Flexure creep properties of E-glass reinforced polymers. *Compos Struct* 2003; 62: 247–253.
520. Engindeniz M and Zureick A-H. Deflection response of glass fiber-reinforced pultruded components in hot weather climates. *J Compos Constr* 2008; 12: 355–363.
521. Sá MF, Gomes AM, Correia JR, et al. Flexural creep response of pultruded GFRP deck panels: proposal for obtaining full-section viscoelastic moduli and creep coefficients. *Compos Part B Eng* 2016; 98: 213–224.
522. Ascione F and Mancusi G. An experimental analysis on the time-dependent behaviour of a CFRP retrofitting under sustained loads. In: *Proceedings of the 6th international conference on fracture mechanics of concrete and concrete structures* (ed Carpinteri A, Gambarova P, Ferro G, et al.), pp.1085–1090..
523. Sá MF, Gomes AM, Correia JR, et al. Creep behavior of pultruded GFRP elements – part 2: analytical study. *Compos Struct* 2011; 93: 2409–2418.

Chapter 5

Design criteria for pultruded structural elements

Tucci Fausto*, **Vedernikov Alexander***. Design criteria for pultruded structural elements. *Reference Module in Materials Science and Materials Engineering 2021*. DOI: 10.1016/B978-0-12-819724-0.00086-0.

* – equal contribution

Contribution: I contributed to the development of the original draft, final writing, and editing. I would like to thank Doctor Fausto Tucci for his valuable contribution to the development of this paper. I would also like to thank Professor Robertt Valente for the invitation to contribute to the development of the *Encyclopedia of Materials: Composites*.

Design Criteria for Pultruded Structural Elements

Fausto Tucci¹, University of Salerno, Fisciano, Italy

Alexander Vedernikov¹, Skolkovo Institute of Science and Technology, Moscow, Russia

© 2021 Elsevier Inc. All rights reserved.

Introduction

In the last decades, structures made of traditional materials have faced the problems of increased restoration and maintenance costs due to their relatively short service-life. This issues promoted the introduction of composites, which are less prone to corrosion (Martins *et al.*, 2017), (Smith *et al.*, 1998), (Back and Will, 2008), lighter (Nguyen *et al.*, 2015), (Bai and Yang, 2013), and easier to build (Mottram and Zheng, 1996), to the construction sector.

FRPs have been widely employed as structural element, whereas high strength to weight ratio is pursued (Bank, 2007). These materials consist of two main constituents: dispersed fibrous reinforcement (providing mechanical resistance) and low-density matrix (ensuring the corrosion resistance) embedding the fibers. The matrix is usually constituted by a polymeric resin mixed with other components aimed to improve the resin flow and reaction during processing, to provide the composite with the required physical properties (Devendra and Rangaswamy, 2013).

Among all the FRPs, the composites manufactured by pultrusion process cover a particular role due to the marked anisotropy and the high content of fibrous reinforcement achievable (Starr, 2000). The pultrusion is a continuous automated process for the production of FRP profiles with constant cross-section. The pultruded composites are widely applied as structural elements in many different fields: civil, marine, automotive, aeronautic, energy and bridge construction (Vedernikov *et al.*, 2020a,b,c). Pultruded profiles have been employed in the construction of buildings and civil structures as beams (Ascione and Mancusi, 2013), columns (Xie *et al.*, 2019), reinforcing rebars (Benmokran *et al.*, 1995), for the rehabilitation or retrofitting of existing concrete structures (Altaee *et al.*, 2017).

Generally, the pultruded profiles present a marked anisotropy, depending on the fibrous architecture. In the most of the cases, the pultruded profiles are reinforced with longitudinal unidirectional fiber rovings. Fabric or mat reinforced layers are often used to provide the pultruded surface with higher resistance to tangential transverse loads (Bank, 2007). Due to this kind of reinforcement architecture, pultruded composites exhibit their best mechanical performances in the longitudinal direction (Haj-Ali and Kilic, 2002).

The structural performance of the pultruded elements is strictly related to the process parameters employed during the production stage. Once defined the cross-section shape and the profile length, the main operative parameters tunable in pultrusion processes are the pulling velocity, the heating platens temperature and, in case of injection pultrusion, the resin pressure at the injection slots (Baran, 2015). The heating temperature and the pulling speed define the curing cycle provided to the polymeric system to achieve the polymerization reaction. Incomplete reaction at the die outlet provokes shape distortions, delamination and internal defects (Vedernikov *et al.*, 2020a,b,c). On the other hand, excessive thermal energy also results in low-quality profiles due to possible local or global degradation of the matrix. The contact between advancing material and the pultrusion die generates forces resisting to the pulling action, which produce internal stresses in the pultruded products (Safonov *et al.*, 2018).

The pultruded FRP structures should also be designed by taking into account circumstances that can influence their durability and design life: the chemical-physical environment where the structure is applied (including UV (Carra and Carvelli, 2014; Stazi *et al.*, 2015), temperature influences (Ghadimi *et al.*, 2017), (Russo *et al.*, 2016), (Turvey and Sana, 2016), humidity, water (Xin *et al.*, 2017), (Cabral-Fonseca *et al.*, 2012), (Gómez *et al.*, 2012), (Kafodya *et al.*, 2015) and chemical agents (Gómez *et al.*, 2012)); time-dependent influences such as creep and wear; fatigue; accidental loads including: (fire, lightning strike, impact (Guades and Aravinthan, 2013; Guades *et al.*, 2013), explosion); the transportation and installation phases; as well as inspection and maintenance. A further important factor, remarkably affecting the mechanical performances of pultruded structures, is related to the connections. Indeed, pultruded FRPs present particular issues at the bolted joints, which should be taken into account in the design step (Feroldi and Russo, 2017), (Feroldi and Russo, 2016), (Russo, 2019).

Design Criteria for Pultruded Structural Elements

“Allowable Stress Design” (ASD), “Load and Resistance Factor Design” (LRFD) and “Limit State” are the three main ideologies currently employed in structural design of elements produced by pultrusion process.

According to ASD philosophy described by Eq. (1), under nominal service load no element within the structure should reach its ultimate stress:

$$\sigma_{reqd} \leq \frac{\sigma_{ult}}{SF}, \quad (1)$$

¹The two authors contributed equally to the development of this work.

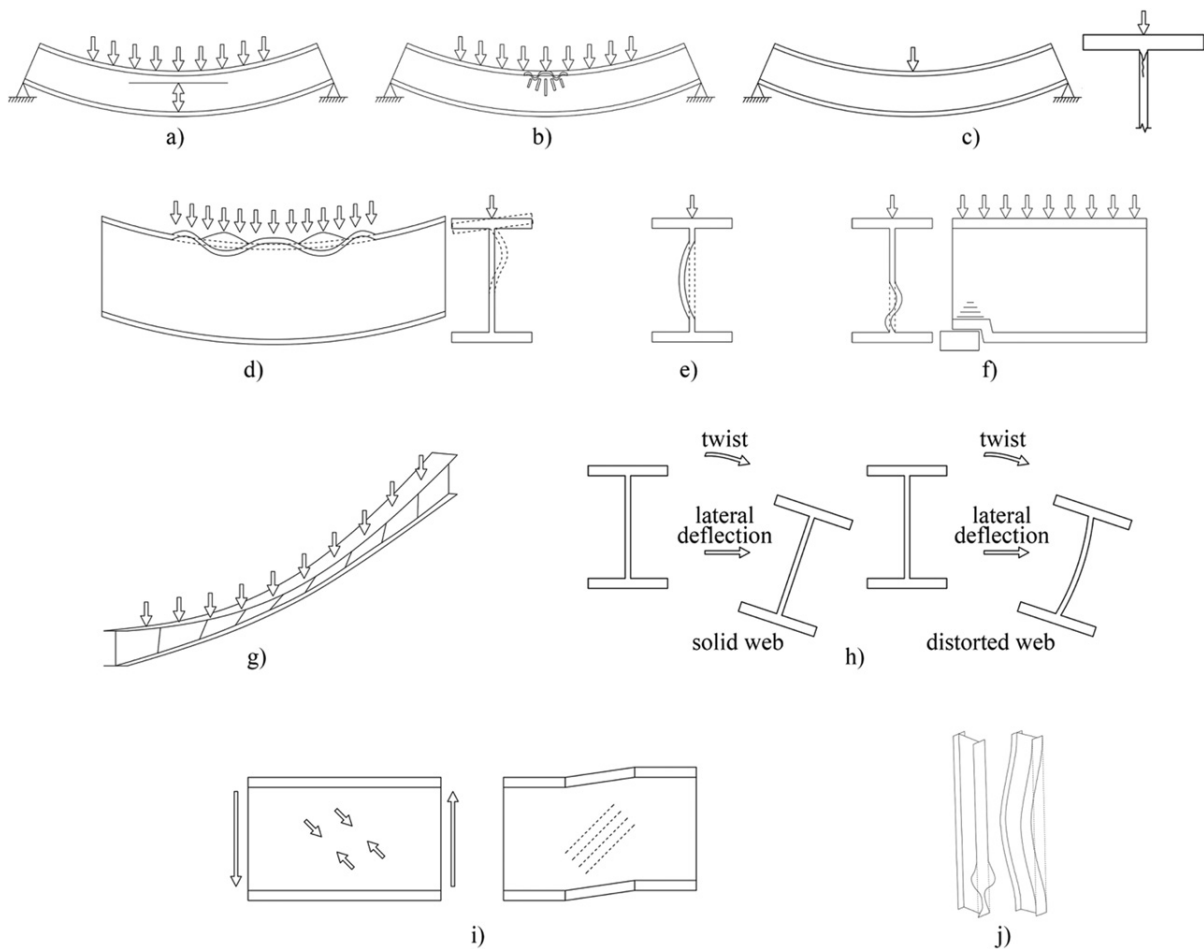


Fig. 1 Failure modes of composite elements. (a) Failing of SLS requirements due to excessive deflection during flexural loading; (b) beam failure due to flexural loading; (c) beam failure due to shear loading; (d) compression flange local buckling due to flexural loading: front view and side view of the profile; (e) web local buckling due flexural loading. Side view of the profile; (f) web transverse crushing failure: side view and front view of the profile; (g) lateral torsional buckling failure; (h) buckling failure: lateral torsional buckling mode (side view of the profile) and lateral-distortional buckling mode (side view of the profile) respectively; (i) web local buckling due shear loading. Front view of the profile; (j) beam failure due to buckling: local buckling mode and global (Euler) buckling mode respectively.

where σ_{reqd} represents the required stress (or design stress in every member), σ_{ult} is the ultimate strength of the material and SF represents safety factor. While being over-conservative in some cases, this approach provides underestimated results in others as loads are considered at service values only. As the Serviceability Limits are not considered in ASD, loading of a structure can result in a failure to meet service requirements, even if the element is still safe from the bearing capacity point of view. This structural design philosophy is widely accepted in manuals of pultrusion companies in the United States (Bank, 2007).

LRFD philosophy, on the other hand, is represented by Eq. (2). The main idea of this approach is that applied loads are increased according to their combinations and types, while resistance of the structural members is decreased due to material properties variability, type of resistance required etc. A number of coefficients are utilized for the mentioned scaling procedure. Moreover, the serviceability limit state is considered here:

$$R_{reqd} \leq \phi R_n, \quad (2)$$

where R_{reqd} is the required resistance of a structural member, R_n represents the nominal resistance of structure or material and ϕ is the resistance factors.

Finally, the Limit State design philosophy is based on the assumption that a structure is considered failed whereas it is not capable anymore to perform the function for which it has been designed. A deeper analysis of this philosophy is provided in the following section.

Number of factors employed in each philosophy creates a critical difference between them. One factor for resistance and several factors for loads are used within LRFD, while ASD utilizes only a safety factor. LRFD, being more advanced and rational, is applied more often than ASD.

Having appeared first in Norway in 1963, the Performance-Based Design (PBD) philosophy is spreading across the whole world in the last decades (Inokuma, 2002). At the core of PBD philosophy are the structural objectives that have to be fulfilled. These goals are initially set by engineers and client together. The final design must comply with the predetermined targets. This philosophy has not found its place in structural design of pultruded FRPs. Careful research and understanding of possible applications of this philosophy can be another target for the pultrusion society to go.

This article reviews analytical, experimental, and numerical investigations that have been done so far regarding the structural behavior of pultruded profiles. Certain analytical formulas available in the literature for the design of FRP members at both ultimate and serviceability limit state are presented as well.

Limit States

The design process of FRP structures is similar to that of steel, with the only regards of the orthotropic and linear elastic response of composites to be considered (Correia *et al.*, 2010). The serviceability limit states (SLS) and the ultimate limit states (ULS) check should be performed for the elements and connections. The limit state can be defined as the case when the structure ceases to fulfill its intended purpose in some way.

To examine the condition in which none of the limit states is violated, the partial factors method should be applied, keeping in mind all the values of actions and resistances acting on the structure. The corresponding requirement must be ensured (Grimaldi, 2007):

$$E_d < R_d = \varphi L_d, \quad (3)$$

where E_d represents the design value of the action, R_d is the related capacity (resistance or deformation) within a considered limit state, φ is a corrective safety factor accounting for uncertainties of service conditions and L_d is the actual property limit of the designed element. By employing appropriate partial factors for the corresponding limit state, the design value can be calculated.

Serviceability Limit State

In case the structural behavior falls below the prescribed service requirements, the SLS is violated (American Society for Civil Engineers, 2010). The SLS to be considered are the following:

- (1) deformations or deflections leading to an inappropriate appearance of the structure as well as its ineffective use (including disruption of machines or service processes) either to damage of finishes or nonload bearing elements;
- (2) vibrations generating discomfort to staff, damage of the building or its indoor elements, or confining limitation on its effective use;
- (3) cracking or delamination of the FRP composites, which is likely to promote the worsening of the appearance, durability, or waterproof properties;
- (4) local damage of FRP composite (due to impact or local bearing failure) experiencing extreme stress, which likely causes loss of durability. Linear elastic theory should be the basis for the SLS calculations (Clarke, 1996).

Fig. 1 depicts the main failure modes of pultruded I-beams.

There is no difference whether a material or structural level is considered, the bending behavior of FRP elements demonstrates certain distinctions compared to the conventional material design. Structural elements made of FRP possess relatively low elastic modulus in contrast to steel (Ascione *et al.*, 2015a,b), and therefore bending stiffness as well. As a result, in the case of FRP profiles, the design process has its peculiarities and is driven either by SLS, restricting deflections (Satasivam and Bai, 2014; Minghini *et al.*, 2016) (**Fig. 1(a)**), or by a buckling phenomenon (considering thin-walled sections) opposing to the ULS (Barros da *et al.*, 2007). This is the reason why pultruded profiles are frequently applied in the cases of lighter and shorter spans.

Barbero *et al.* proved that in bending pultruded beams possess linear-elastic behavior even for large deflections. It can be explained by huge elongations allowed by fibers (4%) and matrix (4.5%). This value is certainly higher than those for conventional materials such as concrete (cracking) and steel (plasticity) (Barbero *et al.*, 1991).

Considering the shear contribution to the overall deformation, in other words relying on analytical beam models based upon Timoshenko theory, flexural deflections of pultruded profiles can be calculated and, therefore, the corresponding SLS criteria can be verified. Indeed, the shear contribution can be essential and should be included in the overall consideration. Long-term deformations of composites have their own peculiarities as a result of different viscoelastic behavior and polymeric properties of the matrix (Correia *et al.*, 2010).

Ultimate Limit State

ULS is the case when a structure reaches its critical point, and further growth of the load will lead to a collapse or another form of failure. It may place both inhabitants and performance of the structural components in danger. The ULS cases to be considered are the following: violation of the construction's equilibrium or even any part of this structure accounted as a rigid body; collapse due

to exceeding deformation, break, or stability loss of the structure in general or any of its parts in particular (Clarke, 1996). Historically, in the related documents, design codes, and guidelines, more attention was paid to ULS than to SLS owing to its importance, ensuring the buildings' safety from the first glance (American Society for Civil Engineers, 2010).

Pultruded FRP members can fail owing to several reasons that must be considered during ULS design. This means that the design resistance should be not less than the action or resistance force acting on the structure. The following states are to be verified: (1) flexural strength; (2) shear strength (3) web local buckling due to flexure; (4) web local buckling due to shear; (5) web local buckling due to flexure and shear; (6) compression flange local buckling; (7) lateral-torsional buckling; (8) web transverse crushing; (9) axial strength.

Flexural strength

The design value of the internal bending moment (M_{Sd}) in any cross-section of the beam shall satisfy (Clarke, 1996):

$$M_{Sd} \leq M_{Rd}, \quad (4)$$

where M_{Rd} is the design moment resistance of the cross-section corresponding to the flexural failure of FRP member. Its value can be computed as follows (Correia *et al.*, 2010):

$$M_{Rd} = \sigma_{x,u} \cdot W_x, \quad (5)$$

where $\sigma_{x,u}$ is the longitudinal failure stress (either compressive or tensile) of the pultruded profile and W_x is the cross-sectional elastic modulus about the strong axis.

Typical failure occurring because of bending moment is shown in the Fig. 1(b).

Shear strength

In contrast to the tensile strength, composite-based profiles possess a relatively low value of shear strength. This fact should be considered during the design stage, because shear deformation is significant and the effects can be crucial (Barros da *et al.*, 2007). Nonuniformity in load application or cross-section can cause large shear stresses and eventually lead to sudden shear failure (Davalos *et al.*, 2002).

The design value of the shear force (V_{Sd}) in any section of the beam should be less than the critical value (Clarke, 1996):

$$V_{Sd} \leq V_{Rd} \quad (6)$$

In the case of thin-walled open sections the critical shear force (V_{Rd}) of a FRP beam under bending can be calculated as follows (Correia *et al.*, 2010):

$$V_{Rd} = \frac{\tau_u \cdot I_x \cdot t}{S_x} \approx \tau_u \cdot A_v, \quad (7)$$

where τ_u represents the in-plane shear strength of the beam, S_x is the first moment of area about the strong axis, t represents the laminate (web/flanges) thickness and A_v is shear area (for most common element it is equal to the web(s) of the element) (Correia *et al.*, 2010).

To proceed with the design of the elements, corresponding mechanical properties are needed. Conducting an experiment in which only pure shear is applied toward pultruded FRP materials is a challenging task. Currently adopted standard test methods have technical weaknesses. For instance, an accurately manufactured coupon of pultruded material is needed, as well as expensive and precise experimental tooling.

Typical failure occurring due to the action of shear forces is shown in the Fig. 1(c).

Buckling

As it was mentioned before, pultruded elements exhibit orthotropic behavior. A composite's strength and elastic constants are much higher in the longitudinal direction compared to the transverse directions (Pecce and Cosenza, 2000). As a consequence, designers should consider pultruded structures as the elements being linear, elastic, homogeneous, and transversely isotropic with the isotropy plane perpendicular to the fiber direction (Ascione *et al.*, 2011). The bearing capacity of the pultruded elements generally defined by the critical buckling load. This is due to the fact that FRP composites being loaded, first of all, violate the deformability and stability requirements and not the strength requirements (Ascione and Mancusi, 2013).

As far as steel has different mechanical properties compared to composites, its design guides regarding buckling calculations cannot be applied toward pultruded elements. Moreover, orthotropic behavior creates some peculiarities pushing forward local buckling issues of section components, flanges, and web (Pecce and Cosenza, 2000).

Slender elements are generally subjected first to global (Euler) buckling failure rather any other types. This is in stark contrast to the behavior of short columns, where local buckling is more likely to occur before global buckling. As a consequence, local buckling leads to large deformations resulting in global buckling or material degradation (crippling phenomenon).

The majority of the theoretical models developed so far have focused on the prediction of FRP structural elements' behavior simply transferring formulations of isotropic models to the anisotropic ones. The results of contemporary analytical and FEM methods correlate well with data obtained during the experiments of both long and short columns (Barbero and Tomblin, 1994).

All members shall be checked for local buckling of their flange(s) and web(s) that are subjected to compressive stresses and shear stresses due to flexure of the member. These cases are described in detail in the following subarticles with respect to the most

Table 1 Different approaches and their features toward investigation of pultrusion elements during buckling loading and buckling failure

Approaches		References
Type of buckling	Global (Euler)	(Barbero and Tomblin, 1994), (Puente <i>et al.</i> , 2006), (Harries <i>et al.</i> , 2017), (Gan <i>et al.</i> , 1999a,b), (Hashem and Yuan, 2001), (Di Tommaso and Russo, 2003)
	Local	(Barbero, 1993), (Ascione <i>et al.</i> , 2016), (Puente <i>et al.</i> , 2006), (Mottram <i>et al.</i> , 2003a,b), (Nunes <i>et al.</i> , 2013), (Bank <i>et al.</i> , 2008)
	Flexural	(Minghini <i>et al.</i> , 2008), (Roberts, 2002), (Roberts and Masri, 2003)
	Torsional	(Minghini <i>et al.</i> , 2008), (Roberts, 2002), (Roberts and Masri, 2003)
	Flexural-torsional	(Minghini <i>et al.</i> , 2008), (Pandey <i>et al.</i> , 1995), (Davalos <i>et al.</i> , 1997), (Qiao <i>et al.</i> , 2003), (De Lorenzis and La Tegola, 2005), (Shan and Qiao, 2005)
	Lateral-torsional	(Minghini <i>et al.</i> , 2008), (Pandey <i>et al.</i> , 1995), (Mottram, 1992b), (Razzaq <i>et al.</i> , 1996), (Sapkás and Kollár, 2002), (Nguyen <i>et al.</i> , 2014)
	Lateral	(Brooks and Thrvey, 1995), (Barbero and DeVivo, 1999), (Bai <i>et al.</i> , 2013), (Mancusi <i>et al.</i> , 2014), (Barbero and Raftoyiannis, 1994), (Turvey, 1996b)
	Distortional	(Silvestre and Camotim, 2003), (Barbero and Raftoyiannis, 1994)
	Lateral-distortional	(Davalos <i>et al.</i> , 1997), (Davalos and Qiao, 1997)
	Flexural-distortional	(Silvestre and Camotim, 2003)
Tested element type	Angle section profile	(Cardoso <i>et al.</i> , 2014a,b), (Ragheb, 2017)
	C section profile	(Silvestre and Camotim, 2003), (Wong and Wang, 2007), (Minghini <i>et al.</i> , 2008), (Cardoso <i>et al.</i> , 2014a,b), (Ragheb, 2017), (Shan and Qiao, 2005), (Razzaq <i>et al.</i> , 1996), (Nguyen <i>et al.</i> , 2014), (Kabir and Sherbourne, 1998), (Minghini <i>et al.</i> , 2009)
	Circular hollow section profile	(Puente <i>et al.</i> , 2006)
	Deck panel	(Gan <i>et al.</i> , 1999a,b)
	Frame	(Minghini <i>et al.</i> , 2008), (Minghini <i>et al.</i> , 2009)
	Girder	(Bai <i>et al.</i> , 2013)
	Hat section profile	(Silvestre and Camotim, 2003)
	Hollow box section profile	(Barbero, 1993), (Barbero <i>et al.</i> , 1991), (Estep <i>et al.</i> , 2016), (Barbero and Raftoyiannis, 1993), (Hashem and Yuan, 2001), (Cardoso <i>et al.</i> , 2014a,b), (Hashem and Yuan, 2000), (Qiao <i>et al.</i> , 2001)
	Hollow rectangular section profile	(Cardoso <i>et al.</i> , 2014)
	I section profile	(Barbero, 1993), (Ascione <i>et al.</i> , 2016), (Brooks and Thrvey, 1995), (Pecce and Cosenza, 2000), (Ascione <i>et al.</i> , 2011), (Barbero and Tomblin, 1993), (Gan <i>et al.</i> , 1999a,b), (Di Tommaso and Russo, 2003), (Minghini <i>et al.</i> , 2008), (Nunes <i>et al.</i> , 2013), (Laudiero, Minghini and Tullini, 2014), (Mancusi <i>et al.</i> , 2014), (Bank <i>et al.</i> , 2008), (Cardoso <i>et al.</i> , 2014a,b), (Cardoso <i>et al.</i> , 2015), (Fernandes <i>et al.</i> , 2015a,b), (Fernandes <i>et al.</i> , 2015a,b), (Ragheb, 2017), (Roberts, 2002), (Roberts and Masri, 2003), (Pandey <i>et al.</i> , 1995), (Qiao <i>et al.</i> , 2003), (De Lorenzis and La Tegola, 2005), (Mottram, 1992b), (Mottram, 1992a), (Sapkás and Kollár, 2002), (Nguyen <i>et al.</i> , 2014), (Barbero and Raftoyiannis, 1994), (Turvey, 1996a), (Minghini <i>et al.</i> , 2009), (Mancusi and Feo, 2013), (Ascione <i>et al.</i> , 2015a,b)
	Laminate	(Bai and Keller, 2011)
	Plate	(Saha <i>et al.</i> , 2004)
	Rectangular section profile	(Turvey, 1996b)
	Universal section profile	(Hashem and Yuan, 2001), (Hashem and Yuan, 2000)
	Wide Flange section profile	(Barbero <i>et al.</i> , 1991), (Barbero and Tomblin, 1994), (Barbero and Raftoyiannis, 1993), (Barbero and DeVivo, 1999), (Barbero <i>et al.</i> , 2000), (Barbero, 2000), (Lane and Mottram, 2002), (Di Tommaso and Russo, 2003), (Mottram <i>et al.</i> , 2003a,b), (Laudiero <i>et al.</i> , 2014), (Tomblin and Barbero, 1994), (Bank <i>et al.</i> , 1995), (Bank <i>et al.</i> , 1996), (Qiao <i>et al.</i> , 2001), (Mottram, 2004), (Davalos <i>et al.</i> , 1997), (Davalos and Qiao, 1997), (Qiao <i>et al.</i> , 2003), (Barbero and Raftoyiannis, 1994), (Turvey and Zhang, 2006)
	Z section profile	(Ragheb, 2017)

applied cross-sections. Nevertheless, the reader can refer to the ASCE standard for all the other cross-sections (American Society for Civil Engineers, 2010). Critical buckling stress should be adopted as the minimum of compression flange local buckling and web local buckling. **Table 1** reviews primary studies (experimental, analytical, and FEM) investigating the influence of the cross-sectional characteristics and load cases on the buckling behavior of pultruded elements at its different modes.

Web local buckling due to flexure

In the case of singly and doubly symmetric I-shaped members as well as singly symmetric channels bent about their strong axis critical buckling stress (σ_{cr}^{local}) due to compression web local buckling can be found as (American Society for Civil Engineers, 2010):

$$\sigma_{cr}^{local} = \frac{11.1\pi^2 t_w^2}{12h^2} (1.25\sqrt{E_{L,w}E_{T,w}} + E_{T,w}\nu_{LT} + 2G_{LT}), \quad (8)$$

where t_w represents the web thickness, h is the full height of the member, $E_{L,w}$ and $E_{T,w}$ are the characteristic elastic modulus of the web(s) respectively in longitudinal and transversal direction, ν_{LT} represents the characteristic longitudinal Poisson's ratio and G_{LT} is the characteristic in-plane shear modulus.

Web local buckling due to shear

At cross-sections of the highest shear force, which occurs typically at supports and concentrated force points, the web may buckle in shear. For webs of I-members, back-to-back channels, single channels and square/rectangular box members bent about their strong axis, the critical shear buckling stress (τ_{cr}^{local}) can be evaluated as (American Society for Civil Engineers, 2010):

$$\tau_{cr}^{local} = \frac{t_w^2 k_{LT1} \sqrt{E_{L,w} (E_{T,w})^3}}{3h^2}, \quad (9)$$

in the case of $2G_{LT} + E_{T,w}\nu_{LT} \leq \sqrt{E_{L,w}E_{T,w}}$. Otherwise, it should be found from the following formula:

$$\tau_{cr}^{local} = \frac{k_{LT2} E_{T,w} t_w^2}{3h^2} \sqrt{\nu_{LT} + \frac{2G_{LT}}{E_{T,w}}}, \quad (10)$$

where t_w represents the web thickness, $k_{LT1,2}$ is the shear buckling coefficients, $E_{L,w}$ and $E_{T,w}$ are the characteristic moduli of the web respectively in longitudinal and in transversal direction, h represents the full height of the member, G_{LT} is the characteristic in-plane shear modulus; ν_{LT} represents the characteristic longitudinal Poisson's ratio and A_s : shear area.

Web local buckling due to flexure and shear

In the case of high shear forces and high bending moments acting on the beam simultaneously, its web is subjected to combined in-plane shear stress (τ) and in-plane axial compressive (flexural) stress (σ) at the same time. Therefore, the critical web buckling stress is likely to be reduced. The following check should be performed (Bank, 2007):

$$\left(\frac{\sigma}{\sigma_{cr}^{local}}\right)^2 + \left(\frac{\tau}{\tau_{cr}^{local}}\right)^2 \leq 1, \quad (11)$$

or in terms of internal actions as (Bank, 2007):

$$\left(\frac{M_x}{M_{cr}^{local}}\right)^2 + \left(\frac{V_y}{V_{cr}^{local}}\right)^2 \leq 1. \quad (12)$$

Compression flange local buckling

In regular profiles, low values of the in-plane moduli and slenderness of the plate elements are the main reasons for the increased possibility to experience local buckling due to transverse loads. A load exceeding elastic buckling can lead to the failure characterized by detachment of the flange from the web of the profile. This is then followed by in-plane buckling of the web. For the most common single and doubly symmetric I-shaped members bent about their strong axis, as well as for T cross-section and back-to-back angles bent about their strong axis, the critical buckling stress (σ_{cr}^{local}) due to compression flange local buckling can be found as (American Society for Civil Engineers, 2010):

$$\sigma_{cr}^{local} = \frac{4t_f^2}{b_f^2} \left(\frac{7}{12} \sqrt{\frac{E_{L,f}E_{T,f}}{1+4.1\xi}} + G_{LT} \right), \quad (13)$$

where $E_{L,f}$ and $E_{T,f}$ are the characteristic moduli of the flange respectively in longitudinal and transversal directions, G_{LT} represents the characteristic in-plane shear modulus, b_f is the full width of the flange, t_f represents the thickness of the flange and ξ is the coefficient of restraint.

Lateral-torsional buckling

A loaded element should be braced against lateral displacement and rotation of the cross-section. In case this is not done, this could lead to the lateral-torsional buckling (Nguyen et al., 2015). Generally, this type of instability is more likely to occur in open-section (typically, I-shaped) elements subjected to transverse loads. At the moment of lateral-torsional buckling failure, the structure can be described by two phenomena: flanges displaced laterally (in relation to the transverse load direction), and twisted web that forces the whole beam to get out of its vertical plane (Bank, 2007).

In case of an I cross-section bent about its strong axis, the critical normal stress (σ_{cr}) due to lateral-torsional buckling shall be determined as follows (Correia et al., 2010):

$$\sigma_{cr} = \frac{C_b}{W_x} \sqrt{\frac{\pi^2 E_{L,f} I_y G_{LT} J}{(k_f L_b)^2} + \frac{\pi^4 E_L^2 I_y C_w}{(k_f L_b)^2 (k_w L_b)^2}}, \quad (14)$$

Table 2 Different approaches and their features toward investigation of pultrusion elements during axial loading and axial failure.

Approaches		References
Fiber type	Basalt	(Lu <i>et al.</i> , 2015)
	Carbon	(Creighton and Clyne, 2000), (Kwon <i>et al.</i> , 2019), (Chen and Ma, 1994)
	Glass	(Bai and Keller, 2009), (Cunningham <i>et al.</i> , 2015), (Zafari and Mottram, 2016), (Aydin, 2016), (Kim and Qian, 2017), (Liberatore <i>et al.</i> , 2018)
Resin type	Kevlar	(Chen and Ma, 1994)
	Epoxy	(Creighton and Clyne, 2000), (Lu, Xian and Li, 2015), (Kwon <i>et al.</i> , 2019)
	Isophthalic polyester	(Correia <i>et al.</i> , 2013), (Wang and Zureick, 1994), (Riebel and Keller, 2007), (Cunningham <i>et al.</i> , 2015), (Zafari and Mottram, 2016), (Kim and Qian, 2017)
	Phenolic	(Cordeiro <i>et al.</i> , 2016)
	Polyester	(Barbero <i>et al.</i> , 1999), (Turvey and Zhang, 2018), (Sigley <i>et al.</i> , 1991), (Sigley <i>et al.</i> , 1992), (Aydin, 2016), (Liberatore <i>et al.</i> , 2018)
	Polyurethane	(Chen and Ma, 1994)
	Vinylester	(Haj-Ali and Kilic, 2002), (Cordeiro <i>et al.</i> , 2016), (Barbero <i>et al.</i> , 1999), (Sonti and Barbero, 1996), (Mottram, 2011)
Investigation type	Analytical	(Barbero <i>et al.</i> , 1999), (Sonti and Barbero, 1996), (Correia <i>et al.</i> , 2013), (Sigley <i>et al.</i> , 1992)
	Experimental	(Turvey and Zhang, 2018), (Mottram, 2011), (Sigley <i>et al.</i> , 1991), (Sigley <i>et al.</i> , 1992), (Wang and Zureick, 1994), (Gosling and Saribiyik, 2003), (Masran <i>et al.</i> , 2013)
Tested element type	Numerical	(Creighton and Clyne, 2000), (Haj-Ali and Kilic, 2002), (Gosling and Saribiyik, 2003), (Girão Coelho <i>et al.</i> , 2015)
	Circular hollow section	(Bai and Keller, 2009)
	I section profile	(Correia <i>et al.</i> , 2013)
	Hollow box section profile	(Barbero <i>et al.</i> , 1999), (Aydin, 2016), (Kim and Qian, 2017), (Liberatore <i>et al.</i> , 2018), (Masran <i>et al.</i> , 2013)
	Plate	(Saha <i>et al.</i> , 2004), (Girão Coelho <i>et al.</i> , 2015)
	Rope	(Kwon <i>et al.</i> , 2019)
	Specimen	(Creighton and Clyne, 2000), (Haj-Ali and Kilic, 2002), (Barbero <i>et al.</i> , 1999), (Correia <i>et al.</i> , 2013), (Chen and Ma, 1994), (Mottram, 2011)
	Wide Flange section profile	(Barbero <i>et al.</i> , 1999)
Loading/test type	Compression	(Creighton and Clyne, 2000), (Haj-Ali and Kilic, 2002), (Barbero <i>et al.</i> , 1999), (Correia <i>et al.</i> , 2013), (Turvey and Zhang, 2018), (Saha <i>et al.</i> , 2004)
	Tension	(Haj-Ali and Kilic, 2002), (Lu <i>et al.</i> , 2015), (Cordeiro <i>et al.</i> , 2016), (Sonti and Barbero, 1996), (Correia <i>et al.</i> , 2013), (Kwon <i>et al.</i> , 2019)

where C_b represents the coefficient accounting for moment variation along the beam length, C_w is the warping constant, W_x is the section modulus of the strong axis, $E_{L,f}$ and G_{LT} are respectively the characteristic longitudinal modulus of the flange and the characteristic in-plane shear modulus. I_y represents the moment of inertia about the weak axis of bending, J is the torsional constant, k_f and k_w are the effective length coefficients respectively for flexural buckling of the weak axis and for torsional buckling of the section and L_b represents unbraced length of the beam.

Web transverse crushing

Points where concentrated loads or reactions meet a pultruded structural element are the weakest places of the beam in terms of web resistance to transverse forces. This occurs because webs of composite beams are especially subjected to local failure at these points, as the beam's web possess relatively low compressive strength and stiffness in the transverse direction.

Considering a design against web transverse crushing, transverse compressive strength ($\sigma_{T,c}$) of the web should be equal to critical crushing stress ($(\sigma_y)_{cr}^{crush}$) (Bank, 2007):

$$(\sigma_y)_{cr}^{crush} = \sigma_{T,c} \quad (15)$$

and the critical crushing force (F_{cr}^{crush}) is (Bank, 2007):

$$F_{cr}^{crush} = (\sigma_y)_{cr}^{crush} A_{eff}. \quad (16)$$

The effective area (A_{eff}) can be evaluated taking into account that the transverse concentrate loads and the consequent reactions at the supports produce a compressive load at the web. Therefore A_{eff} can be estimated as a function of the effective bearing length (L_{eff}), the web thickness (t_w), the flange thickness (t_f) and, if it is present, the thickness of a bearing element (t_{bp}), as described either in Eq. (17) for the case when flanges stand on the both sides of the web (Bank, 2007):

$$A_{eff} = (t_w + 2t_f + 2t_{bp})L_{eff}, \quad (17)$$

Table 3 Design guidance and standards of pultruded structural profiles

Approaches		References
Country	UK	(CIRIA C779, 2018), (Clarke, 1996), (The Highways Agency, 2005), (Arya <i>et al.</i> , 2004), (TR57 Strengthening Concrete Structures with Fiber Composite Materials: Acceptance, Inspection and Monitoring, 2003), (BS EN 13706–1:2002. 'Reinforced plastic composites - Specification for pultruded profiles - Part 1: Designation,' British Standards Institution, 2002), (BS EN 13706–2:2002. 'Reinforced plastic composites - Specification for pultruded profiles - Part 2: Methods of test and general requirements,' British Standards Institution, 2002), (BS EN 13706–3:2002. 'Reinforced plastics composites. Specifications for pultruded profiles. - Part 3: Specific requirements,' British Standards Institution, 2002), (TR57 Strengthening Concrete Structures With Fibre Composite Materials: Acceptance, Inspection And Monitoring, The Concrete Society, UK., 2003)
	Denmark	(Fiberline Design Manual, 2003)
	Finland	(Clarke, 1996)
	France	(Clarke, 1996)
	Sweden	(Clarke, 1996)
	Netherlands	(CUR 96. Fiber Reinforced Polymers in Civil Load Bearing Structures, 2003)
	Italy	(Grimaldi, 2007), (Boscato <i>et al.</i> , 2017)
	USA	(American Society for Civil Engineers, 2010), (BS EN 13706–1:2002. 'Reinforced plastic composites - Specification for pultruded profiles - Part 1: Designation,' British Standards Institution, 2002), (AC 125 Acceptance Criteria for Concrete and Reinforced and Unreinforced Masonry Strengthening Using Fiber-Reinforced Polymer (FRP) Composite Systems, 2001), (AC 125 ACCEPTANCE CRITERIA FOR CONCRETE AND REINFORCED AND UNREINFORCED MASONRY STRENGTHENING USING EXTERNALLY BONDED FIBER-REINFORCED POLYMER (FRP) COMPOSITE SYSTEMS, 2010), (AC 187 (2001)), (ACI 440.2R-02, 2002), (Fouad <i>et al.</i> , 2003), (Code of standard practice for fabrication and installation of pultruded FRP structures,' ANSI standard, American Composites Manufacturers Association, 1st Edition, Arlington, VA. 2012., 2012), (Structural design of FRP components,' CTI Bulletin ESG-152 (13), Cooling Technology Institute, 2013), (Fibreglass pultruded structural products for use in cooling towers,' CTI Code Tower - Standard Specification, CTI Bulletin STD-137, Cooling Technology Institute, 2013, no date), (Standard definitions of terms relating to reinforced plastic pultruded products, D3918–96 (2003), ASTM, 2003), (Standard test method for shear properties of composite materials by the –notched beam method, D5379–05, ASTM, 2005), (ASTM International, 2013), (Standard test method for compressive residual strength properties of damaged polymer polymer matrix composite plates,' D7290–06, ASTM, 2006), (Standard test method for indentation hardness of rigid plastics by means of a barcol impressor,' D2583, ASTM, 2007), (Standard test method for deflection temperature of plastics under flexural load,' D648–07, ASTM, 2007), (Standard test method for tension-tension fatigue of oriented fiber, resin matrix composites, ASTM D3479/D3479M - 96(2007), ASTM, 2007), (Standard test method for in-plane shear properties of composite laminates, D4255/D4255M - 01(2007), ASTM, 2007), (Standard test method for open-hole tensile strength of polymer matrix composite laminates,' D5766–07, ASTM, 2007), (ASTM, 2007), (Standard test method for compressive properties of rigid plastics,' D695–08, ASTM, 2008), (Standard test method for tensile properties of plastics,' D638–08, ASTM, 2008), (Standard test method for density and specific gravity (relative density) of plastics by displacement,' D792–08, ASTM, 2008), (Standard test method for ignition loss of cured reinforced resins,' D2584–08, ASTM, 2008), (Standard test method for tensile properties of polymer matrix materials,' D3039/D3039M - 08, ASTM, 2008), (Standard test methods for compressive properties of unidirectional or crossply fiber-resin composites, D3410/D3410M-03(2008), ASTM, 2008), (Standard test method for transition temperature and enthalpies of fusion and crystallization of polymers by differential scanning calorimetry,' D3418–08, ASTM, 2008), (Standard specification for dimensional tolerance of thermosetting glass-reinforced plastic pultruded shape,' D3917–8, ASTM, 2008), (Standard practice for classifying visual defects in thermosetting plastic pultruded shapes,' D4385–08, ASTM, 2008), (Standard guide for testing polymer matrix composite materials,' D4762–08, ASTM, 2008), (Standard test method for bearing strength,' D953–09, ASTM, 2009), (Standard test method for tensile, compressive, and flexural creep and creep rupture of plastics,' D2990–09, ASTM, 2009), (Standard test method for determining the compressive properties of polymer matrix composite laminates using a combined loading compression (CLC) test fixture,' D6641/D6641M-09, ASTM, 2009), (Standard test method for void content of reinforced plastics,' D2734–09, ASTM, 2009), (Standard practice for classifying reinforced plastic pultruded

Table 3 Continued

Approaches	References
Germany	shapes according to composition,' D3647–09, ASTM, 2009), (Standard practice for testing pultruded composites,' D7745–11, ASTM, 2011), (Bedford Reinforced Plastics Design Guide, 2012), (Creative Pultrusions, 2017), (Strongwell design manual, 2010) (DIN EN 13121. <i>Structural Polymer Components for Building and Construction</i> , 2010), (BÜV-Tragende Kunststoff Bauteile im Bauwesen TKB – Richtlinie für Entwurf, Bemessung und Konstruktion, 2019)
Japan	(Japan Society of Civil Engineers (JSCE), 2001), (JSCE Recommendation for Upgrading of Concrete Structures with use of Continuous Fiber Sheets, Concrete Engineering Series 41, Japan Society of Civil Engineers, 2001)
Canada	(CSA Specification for Fiber-Reinforced Polymers, CSA-S807–10, Canadian Standards Association (CSA) International, 2010), (ISIS Design Manual No. 4 – FRP Rehabilitation of Reinforced Concrete Structures, ISIS Canada., 2001), (ISIS Durability Monograph – Durability of Fiber Reinforced Polymers in Civil Infrastructure, ISIS Canada., no date)
Switzerland	(FIB Externally Bonded FRP Reinforcement for RC Structures, <i>International Federation for Structural Concrete</i> , 2001)
Belgium	(CEN Reinforced Plastic Composites: Specifications for Pultruded Profiles, Parts 1–3, EN 13706, 2002)
Brazil	(Petroleum and natural gas industries - pultruded shapes - Part 1: materials, test methods and dimensional tolerances,' Associacao Brasileira de Normas Tecnicas – ABNT, NBR 15708–1: 2011, Rio de Janeiro, Brazil, 2011), (Petroleum and natural gas industries - pultruded shapes - Part 5: structural shapes,' Associacao Brasileira de Normas Tecnicas – ABNT, NBR 15708–5: 2011, Rio de Janeiro, Brazil, 2011)
Year of publication	<p data-bbox="309 916 1417 972">Before 2000 (Clarke, 1996), (BS EN 13706–1:2002. 'Reinforced plastic composites - Specification for pultruded profiles - Part 1: Designation,' British Standards Institution., 2002)</p> <p data-bbox="309 972 1417 1912">2000–2009 (Grimaldi, 2007), (The Highways Agency, 2005), (TR 55 Design Guidance for Strengthening Concrete Structures Using Fiber Composite Materials, 2004), (TR57 Strengthening Concrete Structures with Fiber Composite Materials: Acceptance, Inspection and Monitoring, 2003), (BS EN 13706–1:2002. 'Reinforced plastic composites - Specification for pultruded profiles - Part 1: Designation,' British Standards Institution., 2002), (BS EN 13706–2:2002. 'Reinforced plastic composites - Specification for pultruded profiles - Part 2: Methods of test and general requirements,' British Standards Institution, 2002), (TR57 Strengthening Concrete Structures WithFibre Composite Materials: Acceptance, Inspection And Monitoring, The Concrete Society, UK., 2003), (Fiberline Design Manual, 2003), (CUR 96. Fiber Reinforced Polymers in Civil Load Bearing Structures, 2003), (AC 125 Acceptance Criteria for Concrete and Reinforced and Unreinforced Masonry Strengthening Using Fiber-Reinforced Polymer (FFP) Composite Systems, 2001), (AC 187 (2001)), (ACI 440.2R-02, 2002), (Fouad <i>et al.</i>, 2003), (Standard definitions of terms relating to reinforced plastic pultruded products, D3918–96(2003), ASTM, 2003), (Standard test method for shear properties of composite materials by the –notched beam method, D5379–05, ASTM, 2005), (Standard test method for compressive residual strength properties of damaged polymer polymer matrix composite plates,' D7290–06, ASTM, 2006), (Standard test method for indentation hardness of rigid plastics by means of a barcol impressor,' D2583, ASTM, 2007), (Standard test method for in-plane shear properties of composite laminates, D4255/D4255M - 01(2007), ASTM, 2007), (Standard test method for open-hole tensile strength of polymer matrix composite laminates,' D5766–07, ASTM, 2007), (ASTM, 2007), (Standard test method for compressive properties of rigid plastics,' D695–08, ASTM, 2008), (Standard test method for tensile properties of plastics,' D638–08, ASTM, 2008), (Standard test method for density and specific gravity (relative density) of plastics by displacement,' D792–08, ASTM, 2008), (Standard test method for ignition loss of cured reinforced resins,' D2584–08, ASTM, 2008), (Standard test method for tensile properties of polymer matrix materials,' D3039/D3039M - 08, ASTM, 2008), (Standard test methods for compressive properties of unidirectional or crossply fiber-resin composites, D3410/D3410M-03(2008), ASTM, 2008), (Standard test method for transition temperature and enthalpies of fusion and crystallization of polymers by differential scanning calorimetry,' D3418–08, ASTM, 2008), (Standard specification for dimensional tolerance of thermosetting glass-reinforced plastic pultruded shape,' D3917–8, ASTM, 2008), (Standard practice for classifying visual defects in thermosetting plastic pultruded shapes,' D4385–08, ASTM, 2008), (Standard guide for testing polymer matrix composite materials,' D4762–08, ASTM, 2008), (Standard test method for bearing strength,' D953–09, ASTM, 2009), (Standard test method for tensile, compressive, and flexural creep and creep rupture of plastics,' D2990–09, ASTM, 2009),</p>

(Continued)

Table 3 Continued

Approaches	References
2010–2015	<p>(Standard test method for determining the compressive properties of polymer matrix composite laminates using a combined loading compression (CLC) test fixture,' D6641/D6641M-09, ASTM, 2009), (Standard test method for void content of reinforced plastics,' D2734–09, ASTM, 2009), (Standard practice for classifying reinforced plastic pultruded shapes according to composition,' D3647–09, ASTM, 2009), (Japan Society of Civil Engineers (JSCE), 2001), (JSCE Recommendation for Upgrading of Concrete Structures with use of Continuous Fiber Sheets, Concrete Engineering Series 41, Japan Society of Civil Engineers, 2001), (ISIS Design Manual No. 4 – FRP Rehabilitation of Reinforced Concrete Structures, ISIS Canada., 2001), (<i>FIB Externally Bonded FRP Reinforcement for RC Structures, International Federation for Structural Concrete</i>, 2001), (CEN Reinforced Plastic Composites: Specifications for Pultruded Profiles, Parts 1–3, EN 13706, 2002), (MBrace Composite Strengthening System: Engineering Design Guidelines, Master Builders, OH., 2006), (Bank <i>et al.</i>, 2003)</p> <p>(American Society for Civil Engineers, 2010), (AC 125 ACCEPTANCE CRITERIA FOR CONCRETE AND REINFORCED AND UNREINFORCED MASONRY STRENGTHENING USING EXTERNALLY BONDED FIBER-REINFORCED POLYMER (FRP) COMPOSITE SYSTEMS, 2010), (Code of standard practice for fabrication and installation of pultruded FRP structures,' ANSI standard, American Composites Manufacturers Association, 1st Edition, Arlington, VA. 2012., 2012), (Structural design of FRP components,' CTI Bulletin ESG-152 (13), Cooling Technology Institute, 2013), (Fibreglass pultruded structural products for use in cooling towers,' CTI Code Tower - Standard Specification, CTI Bulletin STD-137, Cooling Technology Institute, 2013, 2017), (ASTM International, 2013), (Standard test method for tension-tension fatigue of oriented fiber, resin matrix composites, ASTM D3479/D3479M - 96(2007), ASTM, 2007), (Standard practice for testing pultruded composites,' D7745–11, ASTM, 2011), (Bedford Reinforced Plastics Design Guide, 2012), (Strongwell design manual, 2010), (<i>DIN EN 13121. Structural Polymer Components for Building and Construction</i>, 2010), (BÜV-Tragende Kunststoff Bauteile im Bauwesen TKB – Richtlinie für Entwurf, Bemessung und Konstruktion, 2019), (CSA Specification for Fiber-Reinforced Polymers, CSA-S807–10, Canadian Standards Association (CSA) International, 2010), (Petroleum and natural gas industries - pultruded shapes - Part 1: materials, test methods and dimensional tolerances,' Associacao Brasileira de Normas Tecnicas – ABNT, NBR 15708–1: 2011, Rio de Janeiro, Brazil, 2011), (Petroleum and natural gas industries - pultruded shapes - Part 5: structural shapes,' Associacao Brasileira de Normas Tecnicas – ABNT, NBR 15708–5: 2011, Rio de Janeiro, Brazil, 2011),</p>
2016–present	<p>(CIRIA c779, 2018), (Creative Pultrusions, 2017)</p> <p>(Clarke, 1996), (Grimaldi, 2007), (American Society for Civil Engineers, 2010), (BS EN 13706–1:2002. 'Reinforced plastic composites - Specification for pultruded profiles - Part 1: Designation,' British Standards Institution., 2002), (BS EN 13706–2:2002. 'Reinforced plastic composites - Specification for pultruded profiles - Part 2: Methods of test and general requirements,' British Standards Institution., 2002), (TR57 Strengthening Concrete Structures With Fibre Composite Materials: Acceptance, Inspection And Monitoring, The Concrete Society, UK., 2003), (CUR 96. Fiber Reinforced Polymers in Civil Load Bearing Structures, 2003), (Code of standard practice for fabrication and installation of pultruded FRP structures,' ANSI standard, American Composites Manufacturers Association, 1st Edition, Arlington, VA. 2012., 2012), (Standard definitions of terms relating to reinforced plastic pultruded products, D3918–96(2003), ASTM, 2003), (Standard specification for dimensional tolerance of thermosetting glass-reinforced plastic pultruded shape,' D3917–8, ASTM, 2008), (Standard practice for classifying visual defects in thermosetting plastic pultruded shapes,' D4385–08, ASTM, 2008), (Standard practice for testing pultruded composites,' D7745–11, ASTM, 2011), (<i>DIN EN 13121. Structural Polymer Components for Building and Construction</i>, 2010), (BÜV-Tragende Kunststoff Bauteile im Bauwesen TKB – Richtlinie für Entwurf, Bemessung und Konstruktion, 2019), (CEN Reinforced Plastic Composites: Specifications for Pultruded Profiles, Parts 1–3, EN 13706, 2002), (CSA Specification for Fiber-Reinforced Polymers, CSA-S807–10, Canadian Standards Association (CSA) International, 2010), (ISIS Durability Monograph – Durability of Fiber Reinforced Polymers in Civil Infrastructure, ISIS Canada, no date), (Bank <i>et al.</i>, 2003)</p>
Area	Structural design and structural profiles in civil infrastructure
Bridges and highway structures	(CIRIA C779, 2018), (The Highways Agency, 2005), (Fouad, <i>et al.</i> , 2003)
Design of structures in seismic zones	(Boscato <i>et al.</i> , 2017)

Table 3 Continued

Approaches	References
Strengthening systems and rehabilitation of concrete structures	(Arya <i>et al.</i> , 2004), (TR57 Strengthening Concrete Structures with Fiber Composite Materials: Acceptance, Inspection and Monitoring, 2003), (AC 125 Acceptance Criteria for Concrete and Reinforced and Unreinforced Masonry Strengthening Using Fiber-Reinforced Polymer (FRP) Composite Systems, 2001), (AC 125 ACCEPTANCE CRITERIA FOR CONCRETE AND REINFORCED AND UNREINFORCED MASONRY STRENGTHENING USING EXTERNALLY BONDED FIBER-REINFORCED POLYMER (FRP) COMPOSITE SYSTEMS, 2010), (AC 187 (2001)), (ACI 440.2R-02, 2002), (Japan Society of Civil Engineers (JSCE), 2001), (JSCE Recommendation for Upgrading of Concrete Structures with use of Continuous Fiber Sheets, Concrete Engineering Series 41, Japan Society of Civil Engineers, 2001), (ISIS Design Manual No. 4 – FRP Rehabilitation of Reinforced Concrete Structures, ISIS Canada., 2001), (FIB Externally Bonded FRP Reinforcement for RC Structures, International Federation for Structural Concrete, 2001)
Petroleum and natural gas industries – pultruded shapes	(Petroleum and natural gas industries - pultruded shapes - Part 1: materials, test methods and dimensional tolerances,' Associacao Brasileira de Normas Tecnicas – ABNT, NBR 15708-1: 2011, Rio de Janeiro, Brazil, 2011), (Petroleum and natural gas industries - pultruded shapes - Part 5: structural shapes,' Associacao Brasileira de Normas Tecnicas – ABNT, NBR 15708-5: 2011, Rio de Janeiro, Brazil, 2011)
Cooling towers	(Structural design of FRP components,' CTI Bulletin ESG-152 (13), Cooling Technology Institute, 2013), (Fibreglass pultruded structural products for use in cooling towers,' CTI Code Tower - Standard Specification, CTI Bulletin STD-137, Cooling Technology Institute, 2013, 2017)
Test methods	(Standard test method for shear properties of composite materials by the –notched beam method, D5379–05, ASTM, 2005), (ASTM International, 2013), (Standard test method for compressive residual strength properties of damaged polymer matrix composite plates,' D7290–06, ASTM, 2006), (Standard test method for indentation hardness of rigid plastics by means of a barcol impressor,' D2583, ASTM, 2007), (Standard test method for deflection temperature of plastics under flexural load,' D648–07, ASTM, 2007), (Standard test method for tension-tension fatigue of oriented fiber, resin matrix composites, ASTM D3479/D3479M - 96(2007),ASTM, 2007), (Standard test method for in-plane shear properties of composite laminates,' D4255/D4255M - 01(2007), ASTM, 2007), (Standard test method for open-hole tensile strength of polymer matrix composite laminates,' D5766–07, ASTM, 2007), (ASTM, 2007), (Standard test method for compressive properties of rigid plastics,' D695–08, ASTM, 2008), (Standard test method for tensile properties of plastics,' D638–08, ASTM, 2008), (Standard test method for density and specific gravity (relative density) of plastics by displacement,' D792–08, ASTM, 2008), (Standard test method for ignition loss of cured reinforced resins,' D2584–08, ASTM, 2008), (Standard test method for tensile properties of polymer matrix materials,' D3039/D3039M - 08, ASTM, 2008), (Standard test methods for compressive properties of unidirectional or crossply fiber-resin composites,' D3410/D3410M-03(2008), ASTM, 2008), (Standard test method for transition temperature and enthalpies of fusion and crystallization of polymers by differential scanning calorimetry,' D3418–08, ASTM, 2008), (Standard guide for testing polymer matrix composite materials,' D4762–08, ASTM, 2008), (Standard test method for bearing strength,' D953–09, ASTM, 2009), (Standard test method for tensile, compressive, and flexural creep and creep rupture of plastics,' D2990–09, ASTM, 2009), (Standard test method for determining the compressive properties of polymer matrix composite laminates using a combined loading compression (CLC) test fixture,' D6641/D6641M-09, ASTM, 2009), (Standard test method for void content of reinforced plastics,' D2734–09, ASTM, 2009), (Standard practice for classifying reinforced plastic pultruded shapes according to composition,' D3647–09, ASTM, 2009)
Manufacturers' design manuals	(Fiberline Design Manual, 2003), (Bedford Reinforced Plastics Design Guide, 2012), (Creative Pultrusions, 2017), (Strongwell design manual, 2010)

or just on the one side in relation to the web (Bank, 2007):

$$A_{eff} = (t_w + t_f + t_{bp})L_{eff}. \quad (18)$$

The effective bearing length (L_{eff}) is accounted in the longitudinal direction of the pultruded element. It should be calculated considering either the width of the support or the length of the area where load is concentrated (Bank, 2007).

It is worth to notice that the mechanism accounts only for a crushing failure and not for local buckling of the web, which can happen due to the presence of concentrated load. More detailed procedure of the calculation accounting for both phenomena can be found in (Bank, 2007).

Though much effort was made to study transverse crushing of the web in metal structures, there are still a lot of missing points that need to be addressed when dealing with pultruded composites (Fernandes *et al.*, 2015a,b).

Axial loading: Tension and compression

The remarkable advantage of pultruded FRP elements is their high axial tensile strength as a result of the unidirectional position of the fibers within the profile. Tension members are those structural elements that are subjected to direct axial stress without significant flexure. During the service-life of the structure, stress concentrations due to discontinuities and reductions in the cross-sectional area can arise. This must be considered at the design stage of tension members providing sufficient resistance. As glass fiber composites have a relatively low Young's modulus, the axial strain can be significant. In the case of an axial tensile load imposed on the pultruded structural element, design value of axial tensile load ($N_{t,Sd}$) should be not more than the design value of the axial tensile resistance ($N_{t,Rd}$) (Grimaldi, 2007):

$$N_{t,Sd} \leq N_{t,Rd}. \quad (19)$$

In the case of the axial compressive load imposed on the pultruded structural element, the design value ($N_{c,Sd}$) should be not more than the design value of the axial tensile resistance ($N_{c,Rd}$) (Grimaldi, 2007):

$$N_{c,Sd} \leq N_{c,Rd}, \quad (20)$$

where $N_{c,Rd}$ can be obtained from (Grimaldi, 2007):

$$N_{c,Rd} = \min\{N_{c,Rd1}, N_{c,Rd2}\}. \quad (21)$$

$N_{c,Rd1}$ is the value of the compressive force acting on the cross-section of the pultruded element. It can be estimated as follows (Grimaldi, 2007):

$$N_{c,Rd1} = A \cdot \sigma_{c,d}, \quad (22)$$

where $\sigma_{c,d}$ is the design compressive strength of the material, A represents the area of the cross-section of the profile and $N_{c,Rd2}$ is the design compression value of the forces initiating the instability of the element. It can be estimated by testing or numerical/analytical modeling.

Table 2 shows primary studies (experimental, analytical, and numerical) investigating the influence of the fiber/matrix type and cross-sectional characteristics on the tensile/compressive behavior of pultruded elements due to different load cases.

Design Guidance and Standards

Design codes make it possible to realize civil engineering structures with a high level of safety and confidence. Currently, the construction market is experiencing accelerated growth of FRP composite applications. The process of standard and guideline development has already been initiated in some countries. The 1980s marked the starting point of this process. This procedure has been launched by considering their differences in mechanical and physical properties compared to conventional materials. The performance uncertainty of FRP materials can be significantly limited by the appearance of common-based testing procedures together with material identification schemes. A single set of guidelines can be developed, as sufficient theoretical and practical experience has been already gained, owing to the FRP-based projects realized all over the world. The development of standards and codes is an ongoing process and is expected to even accelerate in the coming years.

Sudden unexpected loading events such as car accidents, explosions, or even terroristic attacks can lead to the so-called progressive failure. Such possible situations when failure of one structure within the whole building is followed by a domino-effect collapse of other structures is not accounted for in the current design codes. However, this is not a problem exclusive to composite structures; it also exists for concrete and steel ones (Stylianidis and Nethercot, 2017). This topic still remains poorly investigated. Therefore, various relevant indicators, coefficients, and equations must be included in the developing composite design codes to deal with such type of structural occasions. Specific subarticles within the guidelines are to be established in order to minimize or even avoid enormous damages resulting from progressive failure (Abdelwahed, 2019), (Jiang and Li, 2018).

Table 3 presents primary design guidance and standards of the pultruded structural profiles, listing the countries where they were developed, years of publication, and areas of applications.

Conclusions and Future Trends

Residual stresses within the structure can be easily evaluated with the help of fiber optic sensor technology, especially with the cost of sensors drastically decreased in the last decades. Although this technique has already been implemented for inspection and monitoring of FRP bars, it would be of great interest in the coming future to install actuators allowing a distant control of the composite elements (Correia, 2013).

Peculiarities of pultrusion process and the nature of composites impose certain limitations on the quality of the final product, namely, process induced shape distortions and residual stresses. Therefore, part of the elements produced do not pass quality control, while another part requires extra shimming operations during the assembly process. These additional manipulations result in decreased mechanical performance of pultruded structures (Abouhamzeh *et al.*, 2015). For a better optimized design,

appropriate consideration of these geometrical deviations is required (Kappel, 2018). Experimental as well as numerical studies regarding the mentioned problems are currently underway. Authors of this review paper intend to address some of these problems in their future studies. However, there are still a lot of missing points at the moment (Ding *et al.*, 2019). Studies relating process parameters and composite architecture with the resultant process induced shape distortions are still necessary.

In the case of local buckling of pultruded I-profiles, contemporary analytical methods represent their web and flanges as orthotropic plates separated from each other. Local buckling capacity of the profile is greatly affected by the fact that in the web-flange junction these plates affect each other by restraining rotational displacement to some extent. Development of more precise closed-form equations for the proper consideration of the mentioned effect is needed since all the existing methods are strictly restricted by certain approximations (Nunes, Silvestre and Correia, 2017), (Ragheb, 2017). It is of great interest to examine the case when this happens. Besides, the loss of stability can be viewed from a completely different perspective. Novel structural and mechanical systems can be designed where the buckling effect is considered as a positive source of energy for motion-related applications, and not as the detrimental effect (Hu and Burgueño, 2015).

Current technological level allows engineers to collect and analyze data related to the structural performance of the element at any specific point in the lifecycle (Skels *et al.*, 2018), (Tuloup *et al.*, 2019), (Amabilia *et al.*, 2017). This technique is called Structural Health Monitoring (SHM). It became a reality due to a wide range of available integrated devices such as resistance strain gauges, fiber optic sensors, piezoelectric sensors, eddy current sensors and micro-electromechanical systems sensors (Christof *et al.*, 2015), (Ramakrishnan *et al.*, 2016). This novel technique makes it possible to identify, locate, evaluate, and predict possible failures (Gomes *et al.*, 2018). Carbon-based composites obviate the need in extra sensors due to the nature of this material. Carbon composites form a conductive carbon material network (Roh *et al.*, 2016) that possesses the piezoresistivity effect. This will require further research in order to advance the state of the art in SHM further on (Giurgiutiu, 2015).

Initially, cross-sections of pultruded structural profiles were designed based on the corresponding sections of their metal counterparts. However, pultruded profiles exhibit completely different behavior, which makes the development and optimization of material-adapted shapes the matter of great importance. Consequently, the profile connection technologies should be developed as well. In the attempt of creating affordable, lightweight profiles with good thermal insulating properties, composite manufacturers are developing profiles with the core consisting of low-density and low-price materials (Correia, 2013).

Random variations of parameters within the processes (structural, chemical, or kinetic) related to material science due to random effects can be described by statistic term of stochasticity. Hull *et al.* highlighted six large categories of fluctuations: equilibrium (thermodynamic), structural/compositional, kinetic, frustration/degeneracy, imprecision in measurements, and uncertainties in modeling and simulation. Practically, speaking of materials in general and of composites in particular, these variations play a remarkable role. Material performance can be easily improved if manufacturers are able to understand, analyze, and handle this stochasticity (Hull *et al.*, 2018).

The main purpose of scientists involved in engineering tasks is to pursue the optimal working conditions to achieve optimal final products. In the recent years, the numerical optimization tools have been successfully employed to detect optimal working conditions in many different fiber reinforced polymers manufacturing processes (Struzziero *et al.*, 2019). In the case of pultrusion, the numerical optimization can be applied to the process parameters (Carlone *et al.*, 2007) as well as to the geometrical topology of the final product (Safonov, 2019). Multi-objective optimization of pultrusion still needs further investigations to fulfill the industrial requirements, therefore, it is a promising topic for future research.

References

- Abdelwahed, B., 2019. A review on building progressive collapse, survey and discussion. *Case Studies in Construction Materials* 11. <http://doi.org/10.1016/j.cscm.2019.e00264>.
- Abouhamzeh, M., *et al.*, 2015. Closed form expression for residual stresses and warpage during cure of composite laminates. *Composite Structures* 133, 902–910. <http://doi.org/10.1016/j.compstruct.2015.07.098>.
- AC 125 Acceptance Criteria for Concrete and Reinforced and Unreinforced Masonry Strengthening Using Externally Bonded Fiber-Reinforced Polymer (FRP) Composite Systems 2010.
- AC 125 Acceptance Criteria for Concrete and Reinforced and Unreinforced Masonry Strengthening Using Fiber-Reinforced Polymer (FFP) Composite Systems 2001.
- AC 187, 2001, Acceptance Criteria for Inspection and Verification of Concrete and Reinforced and Unreinforced Masonry Strengthening Using Fiber-Reinforced Polymer (FFP) Composite Systems.
- ACI 440.2R-02, 2002. Guide for the design and construction of externally bonded FRP systems for strengthening concrete structures reported by ACI committee 440 Construction.
- Altaee, M.J., Cunningham, L.S., Gillie, M., 2017. Experimental investigation of CFRP-strengthened steel beams with web openings. *Journal of Constructional Steel Research* 138, 750–760. <http://doi.org/10.1016/j.jcsr.2017.08.023>.
- Amabilia, D.-A.M., *et al.*, 2017. A review of structural health monitoring techniques as applied to composite structures. *SDHM Structural Durability and Health Monitoring* 11 (2), 91–147. <https://doi.org/10.3970/sdhm.2017.011.091>.
- American Society for Civil Engineers, 2010. Pre-Standard for Load and Resistance Factor Design (LRFD) of Pultruded Fiber Reinforced Polymer (FRP) Structures (Final) American Composites Manufacturers Association (ACMA).
- Arya, C., Clarke, J.L., Kay, E.A., O'Regan, P.D., 2004. TR 55 Design Guidance for Strengthening Concrete Structures Using Fibre Composite Materials— A Review. *Proceedings of the International Conference on Structural Engineering, Mechanics and Computation 2–4 April 2001, Cape Town, South Africa*.
- Ascione, F., *et al.*, 2016. A closed-form equation for the local buckling moment of pultruded FRP I-beams in major-axis bending. *Composites Part B Engineering* 97. <http://doi.org/10.1016/j.compositesb.2016.04.069>.
- Ascione, F., Mancusi, G., 2013. The influence of the web-flange junction stiffness on the mechanical behaviour of thin-walled pultruded beams. *Composites Part B Engineering* 55, 599–606. <https://doi.org/10.1016/j.compositesb.2013.07.021>.

- Ascione, F., Lamberti, M., Razaqpur, G., 2015a. Modifications of standard GFRP sections shape and proportions for improved stiffness and lateral-torsional stability. *Composite Structures* 132, 265–289. <https://doi.org/10.1016/j.compstruct.2015.05.005>.
- Ascione, L., *et al.*, 2015b. Pre-buckling imperfection sensitivity of pultruded FRP profiles. *Composites Part B Engineering* 72, 206–212. <https://doi.org/10.1016/j.compositesb.2014.12.014>.
- Ascione, L., Giordano, A., Spadea, S., 2011. Lateral buckling of pultruded FRP beams. *Composites Part B: Engineering* 42 (4), 819–824. <https://doi.org/10.1016/j.compositesb.2011.01.015>.
- ASTM, 2007. Standard test method for measuring the damage resistance of a fiber-reinforced polymer matrix composite to a drop-weight impact event, D7136/D7136M – 07, ASTM.
- ASTM International, 2013. ASTM Standard D2344/D2344M-13, Standard Test Method for Short-Beam Strength of Polymer Matrix Composite Materials and Their Laminates.
- Aydin, F., 2016. Effects of various temperatures on the mechanical strength of GFRP box profiles. *Construction and Building Materials* 127, 843–849. <https://doi.org/10.1016/j.conbuildmat.2016.09.130>.
- Back, S.Y., Will, K.M., 2008. Shear-flexible thin-walled element for composite I-beams. *Engineering Structures* 30 (5), 1447–1458. <https://doi.org/10.1016/j.engstruct.2007.08.002>.
- Bai, Y., Keller, T., 2009. Pultruded GFRP tubes with liquid-cooling system under combined temperature and compressive loading. *Composite Structures* 90 (2), 115–121. <https://doi.org/10.1016/j.compstruct.2009.02.009>.
- Bai, Y., Keller, T., 2011. Delamination and kink-band failure of pultruded GFRP laminates under elevated temperatures and compression. *Composite Structures* 93 (2), 843–849. <https://doi.org/10.1016/j.compstruct.2010.07.010>.
- Bai, Y., Yang, X., 2013. Novel joint for assembly of all-composite space truss structures: Conceptual design and preliminary study. *Journal of Composites for Construction* 17 (1), [https://doi.org/10.1061/\(ASCE\)CC.1943-5614.0000304](https://doi.org/10.1061/(ASCE)CC.1943-5614.0000304).
- Bai, Y., Keller, T., Wu, C., 2013. Pre-buckling and post-buckling failure at web-flange junction of pultruded GFRP beams. *Materials and Structures* 46 (7), <https://doi.org/10.1617/s11527-012-9960-9>.
- Bank, L.C., *et al.*, 2003. A model specification for FRP composites for civil engineering structures. *Construction and Building Materials* 17 (6–7), 405–437. [https://doi.org/10.1016/S0950-0618\(03\)00041-2](https://doi.org/10.1016/S0950-0618(03)00041-2).
- Bank, L.C., Yin, J., Nadipelli, M., 1995. Local buckling of pultruded beams – Nonlinearity, anisotropy and inhomogeneity. *Construction and Building Materials* 9 (6), 325–331. [https://doi.org/10.1016/0950-0618\(95\)00051-8](https://doi.org/10.1016/0950-0618(95)00051-8).
- Bank, L.C., Gentry, T.R., Nadipelli, M., 1996. Local buckling of pultruded FRP beams – Analysis and design. *Journal of Reinforced Plastics and Composites* 15 (3),
- Bank, L.C., Nadipelli, M., Gentry, T.R., 2008. Local buckling and failure of pultruded fiber-reinforced plastic beams. *Journal of Engineering Materials and Technology* 116 (2), 233–237. <https://doi.org/10.1115/1.2904278>.
- Bank, L.C., 2007. *Composites for Construction: Structural Design with FRP Materials*, *Composites for Construction: Structural Design with FRP Materials*. doi: 10.1002/9780470121429.
- Baran, I., 2015. Pultrusion: State-of-the-Art Process Models. *Smithers Rapra*.
- Barbero, E., Tomblin, J., 1993. Euler buckling of thin-walled composite columns. *Thin-Walled Structures* 17 (4), 237–258. [https://doi.org/10.1016/0263-8231\(93\)90005-U](https://doi.org/10.1016/0263-8231(93)90005-U).
- Barbero, E., Tomblin, J., 1994. A phenomenological design equation for FRP columns with interaction between local and global buckling. *Thin-Walled Structures* 18 (2), 117–131. [https://doi.org/10.1016/0263-8231\(94\)90013-2](https://doi.org/10.1016/0263-8231(94)90013-2). (Elsevier).
- Barbero, E.J., 1993. Local buckling of FRP beams and columns. *Journal of Materials in Civil Engineering* 5 (3), [https://doi.org/10.1061/\(ASCE\)0899-1561\(1993\)5:3\(339\)](https://doi.org/10.1061/(ASCE)0899-1561(1993)5:3(339)).
- Barbero, E.J., 2000. Prediction of buckling-mode interaction in composite columns. *Mechanics of Composite Materials and Structures* 7 (3), 269–284. <https://doi.org/10.1080/10759410050031130>.
- Barbero, E.J., Raftoyiannis, I.G., 1993. Euler buckling of pultruded composite columns. *Composite Structures* 24 (2), 139–147. [https://doi.org/10.1016/0263-8223\(93\)90035-0](https://doi.org/10.1016/0263-8223(93)90035-0).
- Barbero, E.J., Raftoyiannis, I.G., 1994. Lateral and distortional buckling of pultruded I-beams. *Composite Structures* 27 (3), 261–268. [https://doi.org/10.1016/0263-8223\(94\)90087-6](https://doi.org/10.1016/0263-8223(94)90087-6).
- Barbero, E.J., DeVivo, L., 1999. Beam-column design equations for wide-flange pultruded structural shapes. *Journal of Composites for Construction* 3 (4), [https://doi.org/10.1061/\(ASCE\)1090-0268\(1999\)3:4\(185\)](https://doi.org/10.1061/(ASCE)1090-0268(1999)3:4(185)).
- Barbero, E.J., Fu, S.-H., Raftoyiannis, I., 1991. Ultimate bending strength of composite beams. *Journal of Materials in Civil Engineering* 3 (4), 292–306. [https://doi.org/10.1061/\(ASCE\)0899-1561\(1991\)3:4\(292\)](https://doi.org/10.1061/(ASCE)0899-1561(1991)3:4(292)).
- Barbero, E.J., Makkapati, S., Tomblin, J.S., 1999. Experimental determination of the compressive strength of pultruded structural shapes. *Composites Science and Technology* 59 (13), 2047–2054. [https://doi.org/10.1016/S0266-3538\(99\)00063-9](https://doi.org/10.1016/S0266-3538(99)00063-9).
- Barbero, E.J., Dede, E.K., Jones, S., 2000. Experimental verification of buckling-mode interaction in intermediate-length composite columns. *International Journal of Solids and Structures* 37 (29).
- Barros da S., Santos Neto, A., Lebre La Rovere, H., 2007. Flexural stiffness characterization of fiber reinforced plastic (FRP) pultruded beams. *Composite Structures* 81 (2), 274–282. <https://doi.org/10.1016/j.compstruct.2006.08.016>.
- Bedford Reinforced Plastics Design Guide, 2012.
- Benmokrane, B., Chaallah, O., Masmoudi, R., 1995. Glass fibre reinforced plastic (GFRP) rebars for concrete structures. *Construction and Building Materials* 9 (6), [https://doi.org/10.1016/0950-0618\(95\)00048-8](https://doi.org/10.1016/0950-0618(95)00048-8).
- Brooks, R.J., Thrvey, G.J., 1995. Lateral buckling of pultruded GRP I-section cantilevers. *Composite Structures* 32 (1–4), 203–215. [https://doi.org/10.1016/0263-8223\(95\)00018-6](https://doi.org/10.1016/0263-8223(95)00018-6).
- Boscato, G., Casalegno, C., Russo, S., 2017. Design of FRP Structures in Seismic Zone. Available at: <https://www.topglass.it/en/design-of-frp-structures-in-seismic-zone/>, (c.d. 19/04/2021).
- BS EN 13706-1:2002. 'Reinforced plastic composites - Specification for pultruded profiles - Part 1: Designation,' British Standards Institution. (29 November 2002).
- BS EN 13706-2:2002. 'Reinforced plastic composites - Specification for pultruded profiles - Part 2: Methods of test and general requirements,' British Standards Institution. (11/11/2002).
- BS EN 13706-3:2002. 'Reinforced plastics composites. Specifications for pultruded profiles. - Part 3: Specific requirements,' British Standards Institution. (11/11/2002).
- BÜV-Tragende Kunststoff Bauteile im Bauwesen [TKB] – Richtlinie für Entwurf, Bemessung und Konstruktion, 2019.
- Cabral-Fonseca, S., *et al.*, 2012. Artificial accelerated ageing of GFRP pultruded profiles made of polyester and vinyl ester resins: Characterisation of physical-chemical and mechanical damage. *Strain* 48 (2), 162–173. <https://doi.org/10.1111/j.1475-1305.2011.00810.x>.
- Cardoso, D.C.T., Harries, K.A., Batista, E.D.M., 2014a. Closed-form equations for compressive local buckling of pultruded thin-walled sections. *Thin-Walled Structures* 79, 16–22. <https://doi.org/10.1016/j.tws.2014.01.013>.
- Cardoso, D.C.T., Harries, K.A., Batista, E.D.M., 2014b. Compressive strength equation for GFRP square tube columns. *Composites Part B: Engineering* 59, 1–11. <https://doi.org/10.1016/j.compositesb.2013.10.057>.
- Cardoso, D.C.T., Harries, K.A., Batista, E.D.M., 2015. Compressive local buckling of pultruded GFRP I-sections: Development and numerical/experimental evaluation of an explicit equation. *Journal of Composites for Construction* 19 (2), [https://doi.org/10.1061/\(ASCE\)CC.1943-5614.0000501](https://doi.org/10.1061/(ASCE)CC.1943-5614.0000501).
- Carlone, P., Palazzo, G.S., Pasquino, R., 2007. Pultrusion manufacturing process development: Cure optimization by hybrid computational methods. *Computers and Mathematics with Applications* 53 (9), 1464–1471. <https://doi.org/10.1016/j.camwa.2006.02.031>.

- Carra, G., Carvelli, V., 2014. Ageing of pultruded glass fibre reinforced polymer composites exposed to combined environmental agents. *Composite Structures* 108 (1), <https://doi.org/10.1016/j.compstruct.2013.10.042>.
- CEN Reinforced Plastic Composites: Specifications for Pultruded Profiles, Parts 1–3, EN 13706, 2002.
- Chen, C.-H., Ma, C.-C.M., 1994. Pultruded fibre-reinforced polyurethane composites. III. Static mechanical, thermal, and dynamic mechanical properties. *Composites Science and Technology* 52 (3), 427–432. [https://doi.org/10.1016/0266-3538\(94\)90177-5](https://doi.org/10.1016/0266-3538(94)90177-5).
- Christof, H., *et al.*, 2015. Integration methods of sensors in FRP components. In: Edtmaier C., R.G. (Ed.), *Materials Science Forum*. Trans Tech Publications Ltd. (825–826, pp. 586–593. doi:10.4028/www.scientific.net/MSF.825-826.586)
- CIRIA C779, 2018. In: Mottram, J.T., Hendersen, J., Eds., *Fibre-reinforced polymer bridges – guidance for designers*. p. 6, CIRIA: London, UK.
- Clarke, J.L., 1996. (John L. and European Structural Polymeric Composites Group. (1996) *Structural design of polymer composites : EUROCOMP design code and handbook*. E & FN Spon.
- Code of standard practice for fabrication and installation of pultruded FRP structures,' ANSI standard, American Composites Manufacturers Association, 1st Edition, Arlington, VA. 2012.
- Cordeiro, G.C., Vieira, J.D., C6, C.M., 2016. Tensile properties and color and mass variations of GFPR composites under alkaline and ultraviolet exposures. *Matéria* 21 (1), 1–10. <https://doi.org/10.1590/S1517-707620160001.0001>.
- Correia, J.R., *et al.*, 2010. Glass fibre reinforced polymer pultruded flexural members: Assessment of existing design methods. *Structural Engineering International: Journal of the International Association for Bridge and Structural Engineering* 20 (4), 362–369.
- Correia, J.R., 2013. Pultrusion of advanced fibre-reinforced polymer (FRP) composites. In: Bai, J. (Ed.), *Advanced Fibre-Reinforced Polymer ((FRP)) Composites for Structural Applications*. Woodhead Publishing, pp. 207–251. . <https://doi.org/10.1533/9780857098641.2.207>.
- Correia, J.R., *et al.*, 2013. Mechanical behaviour of pultruded glass fibre reinforced polymer composites at elevated temperature: Experiments and model assessment. *Composite Structures* 98, 303–313. <https://doi.org/10.1016/j.compstruct.2012.10.051>.
- Creative Pultrusions, 2017. The Pultrux[®] Pultrusion Design Manual. Available at: [https://i.hubspotusercontent10.net/hubfs/457166/DMV5R12%20\(002\).pdf](https://i.hubspotusercontent10.net/hubfs/457166/DMV5R12%20(002).pdf) (c.d. 19/04/2021).
- Creighton, C.J., Clyne, T.W., 2000. The compressive strength of highly-aligned carbon-fibre/epoxy composites produced by pultrusion. *Composites Science and Technology* 60 (4), [https://doi.org/10.1016/S0266-3538\(99\)00153-0](https://doi.org/10.1016/S0266-3538(99)00153-0).
- CSA Specification for Fibre-Reinforced Polymers, CSA-S807-10, Canadian Standards Association (CSA) International, 2010.
- Cunningham, D., Harries, K.A., Bell, A.J., 2015. Open-hole tension capacity of pultruded GFRP having staggered hole arrangement. *Engineering Structures* 95, 8–15. <https://doi.org/10.1016/j.engstruct.2015.03.042>.
- CUR 96. Fibre Reinforced Polymers in Civil Load Bearing Structures, 2003.
- Davalos, J.F., *et al.*, 2002. Shear moduli of structural composites from torsion tests. *Journal of Composite Materials* 36 (10), 1151–1173. <https://doi.org/10.1177/0021998302036010486>.
- Davalos, J.F., Qiao, P., 1997. Analytical and experimental study of lateral and distortional buckling of FRP wide-flange beams. *Journal of Composites for Construction* 1 (4), 362–369.
- Davalos, J.F., Qiao, P., Salim, H.A., 1997. Flexural-torsional buckling of pultruded fiber reinforced plastic composite I-beams: Experimental and analytical evaluations. *Composite Structures* 38 (1–4), 241–250. [https://doi.org/10.1016/S0263-8223\(97\)00059-7](https://doi.org/10.1016/S0263-8223(97)00059-7).
- De Lorenzis, L., La Tegola, A., 2005. Effect of the actual distribution of applied stresses on global buckling of isotropic and transversely isotropic thin-walled members: Theoretical analysis. *Composite Structures* 68 (3), 339–348. <https://doi.org/10.1016/j.compstruct.2004.03.027>.
- Devendra, K., Rangaswamy, T., 2013. Strength characterization of E-glass fiber reinforced epoxy composites with filler materials. *Journal of Minerals and Materials Characterization and Engineering* 01 (06), 353–357. <https://doi.org/10.4236/jmmce.2013.16054>.
- Di Tommaso, A., Russo, S., 2003. Shape influence in buckling of GFRP pultruded columns. *Mechanics of Composite Materials* 39 (4), <https://doi.org/10.1023/A:1025694427941>.
- DIN EN 13121. Structural Polymer Components for Building and Construction, 2010.
- Ding, A., *et al.*, 2019. A new analytical solution for cure-induced spring-in of L-shaped composite parts. *Composites Science and Technology* 171, 1–12. <https://doi.org/10.1016/j.compscitech.2018.12.004>.
- Estep, D.D., *et al.*, 2016. Response of pultruded glass composite box beams under bending and shear. *Composites Part B Engineering* 88, 150–161. <https://doi.org/10.1016/j.compositesb.2015.11.008>.
- Fernandes, L.A., *et al.*, 2015a. Web-crippling of GFRP pultruded profiles. Part 1: Experimental study. *Composite Structures* 120, 565–577. <https://doi.org/10.1016/j.compstruct.2014.09.027>.
- Fernandes, L.A., *et al.*, 2015b. Web-crippling of GFRP pultruded profiles. Part 2: Numerical analysis and design. *Composite Structures* 120, 578–590. <https://doi.org/10.1016/j.compstruct.2014.09.026>.
- Feroldi, F., Russo, S., 2016. Structural behavior of All-FRP beam-column plate-bolted joints. *Journal of Composites for Construction* 20 (4), [https://doi.org/10.1061/\(ASCE\)CC.1943-5614.0000667](https://doi.org/10.1061/(ASCE)CC.1943-5614.0000667).
- Feroldi, F., Russo, S., 2017. Mechanical performance of pultruded FRP plates in beam-to-beam connections. *Journal of Composites for Construction* 21 (4), [https://doi.org/10.1061/\(ASCE\)CC.1943-5614.0000779](https://doi.org/10.1061/(ASCE)CC.1943-5614.0000779) (American Society of Civil Engineers (ASCE)).
- FIB Externally Bonded FRP Reinforcement for RC Structures, International Federation for Structural Concrete, 2001. (Bulletin 40).
- Fiberline Design Manual, 2003. Composites.
- Fibreglass pultruded structural products for use in cooling towers,' CTI Code Tower - Standard Specification, CTI Bulletin STD-137, Cooling Technology Institute, 2013 (01/08/2017).
- Fouad, F.H., Davidson, J., Delatte, N., *et al.*, 2003. Structural supports for highway signs, luminaires, and traffic signals, National cooperative highway research program – Report 494. Transportation Research Board 50. ISBN: 0-309-08753-8. Available at: <https://doi.org/10.17226/13746>.
- Fouad, F.H., Davidson, J., Delatte, N., Calvert, E., 2003. Structural supports for highway signs, luminaires, and traffic signals. National cooperative highway research program – Report 494. Transportation Research Board. 50. ISBN: 0-309-08753-8. Available at: <https://doi.org/10.17226/13746>.
- Gan, L.H., Ye, L., Mai, Y.-W., 1999a. Design and evaluation of various section profiles for pultruded deck panels. *Composite Structures* 47 (1–4), 719–725. [https://doi.org/10.1016/S0263-8223\(00\)00042-8](https://doi.org/10.1016/S0263-8223(00)00042-8).
- Gan, L.-H., Ye, L., Mai, Y.-W., 1999b. Simulations of mechanical performance of pultruded I-beams with various flange-web conjunctions. *Composites Part B Engineering* 30 (4), 423–429. [https://doi.org/10.1016/S1359-8368\(99\)00009-8](https://doi.org/10.1016/S1359-8368(99)00009-8).
- Ghadimi, B., Russo, S., Rosano, M., 2017. Predicted mechanical performance of pultruded FRP material under severe temperature duress. *Composite Structures* 176, 673–683. <http://doi.org/10.1016/j.compstruct.2017.05.061>.
- Girão Coelho, A.M., Toby Mottram, J., Harries, K.A., 2015. Finite element guidelines for simulation of fibre-tension dominated failures in composite materials validated by case studies. *Composite Structures* 126, 299–313. <https://doi.org/10.1016/j.compstruct.2015.02.071>.
- Giurgiutiu, V., 2015. SHM of aerospace composites – Challenges and opportunities. In: *Proceedings of the CAMX 2015 - Composites and Advanced Materials Exposition*. pp. 1426–1442.
- Gomes, G.F., *et al.*, 2018. The use of intelligent computational tools for damage detection and identification with an emphasis on composites – A review. *Composite Structures* 196, 44–54. <http://doi.org/10.1016/j.compstruct.2018.05.002>.
- Gómez Hoyos, C., Vázquez, A., 2012. Flexural properties loss of unidirectional epoxy/fique composites immersed in water and alkaline medium for construction application. *Composites Part B Engineering* 43 (8), 3120–3130. <https://doi.org/10.1016/j.compositesb.2012.04.027>.

- Gosling, P.D., Saribiyik, M., 2003. Nonstandard tensile coupon for fiber-reinforced plastics. *Journal of Materials in Civil Engineering* 15 (2), 108–117. [https://doi.org/10.1061/\(ASCE\)0899-1561\(2003\)15:2\(108\)](https://doi.org/10.1061/(ASCE)0899-1561(2003)15:2(108)).
- Grimaldi, A., 2007. Guide for the Design and Construction of Structures made of FRP Pultruded Elements, Cnr-Dt 205/2007.
- Guades, E., *et al.*, 2013. Experimental investigation on the behaviour of square FRP composite tubes under repeated axial impact. *Composite Structures* 97, 211–221. <http://doi.org/10.1016/j.compstruct.2012.10.033>.
- Guades, E., Aravinthan, T., 2013. Residual properties of square FRP composite tubes subjected to repeated axial impact. *Composite Structures* 95, 354–365. <http://doi.org/10.1016/j.compstruct.2012.08.041>.
- Haj-Ali, R., Kilic, H., 2002. Nonlinear behavior of pultruded FRP composites. *Composites Part B Engineering* 33 (3), [https://doi.org/10.1016/S1359-8368\(02\)00011-2](https://doi.org/10.1016/S1359-8368(02)00011-2).
- Harries, K.A., Guo, Q., Cardoso, D., 2017. Creep and creep buckling of pultruded glass-reinforced polymer members. *Composite Structures* 181, 315–324. <https://doi.org/10.1016/j.compstruct.2017.08.098>.
- Hashem, Z.A., Yuan, R.L., 2000. Experimental and analytical investigations on short GFRP composite compression members. *Composites Part B Engineering* 31 (6–7), 611–618. [https://doi.org/10.1016/S1359-8368\(99\)00042-6](https://doi.org/10.1016/S1359-8368(99)00042-6).
- Hashem, Z.A., Yuan, R.L., 2001. Short vs. long column behavior of pultruded glass-fiber reinforced polymer composites. *Construction and Building Materials* 15 (8), 369–378. [https://doi.org/10.1016/S0950-0618\(01\)00018-6](https://doi.org/10.1016/S0950-0618(01)00018-6).
- Hu, N., Burgueno, R., 2015. Buckling-induced smart applications: Recent advances and trends. *Smart Materials and Structures* 24 (6), <https://doi.org/10.1088/0964-1726/24/6/063001>. (Institute of Physics Publishing).
- Hull, R., *et al.*, 2018. Stochasticity in materials structure, properties, and processing – A review. *Applied Physics Reviews* 5 (1), <https://doi.org/10.1063/1.4998144>. (American Institute of Physics Inc.).
- Inokuma, A., 2002. Basic study of performance-based design in civil engineering. *Journal of Professional Issues in Engineering Education and Practice* 128 (1), 30–35. [https://doi.org/10.1061/\(ASCE\)1052-3928\(2002\)128:1\(30\)](https://doi.org/10.1061/(ASCE)1052-3928(2002)128:1(30)).
- ISIS Design Manual No. 4 – FRP Rehabilitation of Reinforced Concrete Structures, ISIS Canada, 2001.
- ISIS Durability Monograph – Durability of Fibre Reinforced Polymers in Civil Infrastructure, ISIS Canada, (no date).
- Japan Society of Civil Engineers (JSCE), 2001. JSCE Recommendations for Upgrading of Concrete Structures with use of Continuous Fiber Sheets.
- Jiang, J., Li, G.-Q., 2018. Progressive collapse of steel high-rise buildings exposed to fire: Current state of research. *International Journal of High-Rise Buildings* 7 (4), 375–387. <https://doi.org/10.2102/IJHRB.2018.7.4.375>.
- JSCE Recommendation for Upgrading of Concrete Structures with use of Continuous Fiber Sheets, Concrete Engineering Series 41, Japan Society of Civil Engineers, 2001.
- Kabir, M.Z., Sherbourne, A.N., 1998. Optimal fibre orientation in lateral stability of laminated channel section beams. *Composites Part B Engineering* 29 (1), 81–87. [https://doi.org/10.1016/S1359-8368\(97\)00022-X](https://doi.org/10.1016/S1359-8368(97)00022-X).
- Katodya, I., Xian, G., Li, H., 2015. Durability study of pultruded CFRP plates immersed in water and seawater under sustained bending: Water uptake and effects on the mechanical properties. *Composites Part B Engineering* 70, 138–148. <https://doi.org/10.1016/j.compositesb.2014.10.034>.
- Kappel, E., 2018. Compensating process-induced distortions of composite structures: A short communication. *Composite Structures* 192, 67–71. <http://doi.org/10.1016/j.compstruct.2018.02.059>.
- Kim, Y.J., Qian, K.Z., 2017. Compressive behavior of non-slender hollow GFRP structural shapes in thermomechanical loading. *Composite Structures* 160. <https://doi.org/10.1016/j.compstruct.2016.10.085>.
- Kwon, D.-J., *et al.*, 2019. Damage sensing, mechanical and interfacial properties of resins suitable for new CFRP rope for elevator applications. *Composites Part B Engineering* 157, 259–265. <https://doi.org/10.1016/j.compositesb.2018.08.049>.
- Lane, A., Mottram, J.T., 2002. Influence of modal coupling on the buckling of concentrically loaded pultruded fibre-reinforced plastic columns. *Proceedings of the Institution of Mechanical Engineers Part L Journal of Materials: Design and Applications* 216 (2), 133–144. <https://doi.org/10.1243/146442002320139333>.
- Laudiero, F., Minghini, F., Tullini, N., 2014. Buckling and postbuckling finite-element analysis of pultruded FRP profiles under pure compression. *Journal of Composites for Construction* 18 (1), [https://doi.org/10.1061/\(ASCE\)CC.1943-5614.0000384](https://doi.org/10.1061/(ASCE)CC.1943-5614.0000384).
- Liberatore, V., *et al.*, 2018. Microstructural analysis of GFRP failure mechanisms after compressive load and temperature duress. *Composite Structures* 203, 875–885. <http://doi.org/10.1016/J.COMPSTRUCT.2018.07.089>.
- Lu, Z., Xian, G., Li, H., 2015. Effects of exposure to elevated temperatures and subsequent immersion in water or alkaline solution on the mechanical properties of pultruded BFRP plates. *Composites Part B Engineering* 77, 421–430. <https://doi.org/10.1016/j.compositesb.2015.03.066>.
- Mancusi, G., Feo, L., 2013. Non-linear pre-buckling behavior of shear deformable thin-walled composite beams with open cross-section. *Composites Part B Engineering* 47. <https://doi.org/10.1016/j.compositesb.2012.11.003>.
- Mancusi, G., Ascione, F., Lamberti, M., 2014. Pre-buckling behavior of composite beams: A mechanical innovative approach. *Composite Structures* 117 (1), 396–410. <https://doi.org/10.1016/j.compstruct.2014.06.041>. (Elsevier Ltd).
- Martins, D., *et al.*, 2017. Development of a novel beam-to-column connection system for pultruded GFRP tubular profiles. *Composite Structures* 171, 263–276. <https://doi.org/10.1016/j.compstruct.2017.03.049>.
- Masran, S.H., Ismail, A.E., Marian, M.F., 2013. A study of energy absorption performances of pultruded composites under quasi-static compressive loadings. *Applied Mechanics and Materials* 465–466, 662–666. <https://doi.org/10.4028/www.scientific.net/AMM.465-466.662>.
- MBrace Composite Strengthening System: Engineering Design Guidelines, Master Builders, OH, 2006.
- Minghini, F., Tullini, N., Laudiero, F., 2008. Buckling analysis of FRP pultruded frames using locking-free finite elements. *Thin-Walled Structures* 46 (3), 223–241. <https://doi.org/10.1016/j.tws.2007.09.001>.
- Minghini, F., Tullini, N., Laudiero, F., 2009. Elastic buckling analysis of pultruded FRP portal frames having semi-rigid connections. *Engineering Structures* 31 (2), 292–299. <https://doi.org/10.1016/j.engstruct.2008.09.003>.
- Minghini, F., Tullini, N., Ascione, F., 2016. Updating Italian design guide CNR DT-205/2007 in view of recent research findings: Requirements for pultruded FRP profiles. *American Journal of Engineering and Applied Sciences* 9 (3), <https://doi.org/10.3844/ajeassp.2016.702.712>.
- Mottram, J.T., 1992a. Lateral-torsional buckling of a pultruded I-beam. *Composites* 23 (2), 81–92. [https://doi.org/10.1016/0010-4361\(92\)90108-7](https://doi.org/10.1016/0010-4361(92)90108-7).
- Mottram, J.T., 1992b. Lateral-torsional buckling of thin-walled composite I-beams by the finite difference method. *Composites Engineering* 2 (2), 91–104. [https://doi.org/10.1016/0961-9526\(92\)90048-B](https://doi.org/10.1016/0961-9526(92)90048-B).
- Mottram, J.T., 2004. Determination of critical load for flange buckling in concentrically loaded pultruded columns. *Composites Part B Engineering* 35 (1), 35–47. <https://doi.org/10.1016/j.compositesb.2003.08.006>.
- Mottram, J.T., 2011. Structural properties of a pultruded E-Glass fibre-reinforced polymeric I-Beam. *Composite Structures*. 1–28. https://doi.org/10.1007/978-94-011-3662-4_1.
- Mottram, J.T., Zheng, Y., 1996. State-of-the-art review on the design of beam-to-column connections for pultruded frames. *Composite Structures* 35 (4), 387–401. [https://doi.org/10.1016/S0263-8223\(96\)00052-9](https://doi.org/10.1016/S0263-8223(96)00052-9).
- Mottram, J.T., Brown, N.D., Anderson, D., 2003a. Physical testing for concentrically loaded columns of pultruded glass fibre reinforced plastic profile. *Proceedings Of The Institution Of Civil Engineers*. 205–219. <https://doi.org/10.1680/stbu.156.2.205.37877>. (May).
- Mottram, J.T., Brown, N.D., Anderson, D., 2003b. Buckling characteristics of pultruded glass fibre reinforced plastic columns under moment gradient. *Thin-Walled Structures* 41 (7), 619–638. [https://doi.org/10.1016/S0263-8231\(03\)00008-9](https://doi.org/10.1016/S0263-8231(03)00008-9).
- Nguyen, H., Mutsuyoshi, H., Zatar, W., 2015. Hybrid FRP-UHPFRC composite girders: Part 1 - experimental and numerical approach. *Composite Structures* 125, 631–652. <http://doi.org/10.1016/j.compstruct.2014.10.038>.

- Nguyen, T.T., Chan, T.M., Mottram, J.T., 2014. Lateral-torsional buckling resistance by testing for pultruded FRP beams under different loading and displacement boundary conditions. *Composites Part B: Engineering* 60, 306–318. <https://doi.org/10.1016/j.compositesb.2013.12.025>.
- Nguyen, T.T., Chan, T.M., Mottram, J.T., 2015. Lateral-Torsional Buckling design for pultruded FRP beams. *Composite Structures* 133, 782–793. <http://doi.org/10.1016/j.compstruct.2015.07.079>.
- Nunes, F., *et al.*, 2013. Experimental and numerical study on the structural behavior of eccentrically loaded GFRP columns. *Thin-Walled Structures* 72, 175–187. <https://doi.org/10.1016/j.tws.2013.07.002>.
- Nunes, F., Silvestre, N., Correia, J.R., 2017. Progressive damage analysis of web crippling of GFRP pultruded I-sections. *Journal of Composites for Construction* 21 (3), [https://doi.org/10.1061/\(ASCE\)CC.1943-5614.0000762](https://doi.org/10.1061/(ASCE)CC.1943-5614.0000762).
- Pandey, M.D., Kabir, M.Z., Sherbourne, A.N., 1995. Flexural-torsional stability of thin-walled composite I-section beams. *Composites Engineering* 5 (3), 321–342. [https://doi.org/10.1016/0961-9526\(94\)00101-E](https://doi.org/10.1016/0961-9526(94)00101-E).
- Pecce, M., Cosenza, E., 2000. Local buckling curves for the design of FRP profiles. *Thin-Walled Structures* 37 (3), [https://doi.org/10.1016/S0263-8231\(00\)00023-9](https://doi.org/10.1016/S0263-8231(00)00023-9).
- Petroleum and natural gas industries - pultruded shapes - Part 1: materials, test methods and dimensional tolerances,' *Associação Brasileira de Normas Técnicas – ABNT, NBR 15708-1: 2011, Rio de Janeiro, Brazil, 2011.*
- Petroleum and natural gas industries - pultruded shapes - Part 5: structural shapes,' *Associação Brasileira de Normas Técnicas – ABNT, NBR 15708-5: 2011, Rio de Janeiro, Brazil, 2011.*
- Puente, I., Insausti, A., Azkune, M., 2006. Buckling of GFRP columns: An empirical approach to design. *Journal of Composites for Construction* 10 (6), 529–537. [https://doi.org/10.1061/\(ASCE\)1090-0268\(2006\)10:6\(529\)](https://doi.org/10.1061/(ASCE)1090-0268(2006)10:6(529)).
- Qiao, P., Davalos, J.F., Wang, J., 2001. Local buckling of composite FRP shapes by discrete plate analysis. *Journal of structural engineering* 127 (3), [https://doi.org/10.1061/\(ASCE\)0733-9445\(2001\)127:3\(245\)](https://doi.org/10.1061/(ASCE)0733-9445(2001)127:3(245)).
- Qiao, P., Zou, G., Davalos, J.F., 2003. Flexural-torsional buckling of fiber-reinforced plastic composite cantilever I-beams. *Composite Structures* 60 (2), [https://doi.org/10.1016/S0263-8223\(02\)00304-5](https://doi.org/10.1016/S0263-8223(02)00304-5).
- Ragheb, W.F., 2017. Development of closed-form equations for estimating the elastic local buckling capacity of pultruded FRP structural shapes. *Journal of Composites for Construction* 21 (4), 1–11. [https://doi.org/10.1061/\(ASCE\)CC.1943-5614.0000798](https://doi.org/10.1061/(ASCE)CC.1943-5614.0000798).
- Ramakrishnan, M., *et al.*, 2016. Overview of fiber optic sensor technologies for strain/temperature sensing applications in composite materials. *Sensors* 16(1), <https://doi.org/10.3390/s16010099>.
- Razzaq, Z., Prabhakaran, R., Sirjani, M.M., 1996. Load and resistance factor design (LRFD) approach for reinforced-plastic channel beam buckling. *Composites Part B: Engineering* 27 (3–4), [https://doi.org/10.1016/1359-8368\(95\)00025-9](https://doi.org/10.1016/1359-8368(95)00025-9).
- Riebel, F., Keller, T., 2007. Long-term compression performance of a pultruded GFRP element exposed to concrete pore water solution. *Journal of Composites for Construction* 11 (4), 437–447. [https://doi.org/10.1061/\(ASCE\)1090-0268\(2007\)11:4\(437\)](https://doi.org/10.1061/(ASCE)1090-0268(2007)11:4(437)).
- Roberts, T.M., 2002. Influence of shear deformation on buckling of pultruded fiber reinforced plastic profiles. *Journal of Composites for Construction* 6 (4), 241–248. [https://doi.org/10.1061/\(ASCE\)1090-0268\(2002\)6:4\(241\)](https://doi.org/10.1061/(ASCE)1090-0268(2002)6:4(241)).
- Roberts, T.M., Masri, H.M.K.J.A.H., 2003. Section properties and buckling behavior of pultruded FRP profiles. *Journal of Reinforced Plastics and Composites* 22 (14), 1305–1317. <https://doi.org/10.1177/0731684403035584>.
- Roh, H.D., Lee, H., Park, Y.-B., 2016. Structural health monitoring of carbon-material-reinforced polymers using electrical resistance measurement. *International Journal of Precision Engineering and Manufacturing - Green Technology* 3 (3), 311–321. <https://doi.org/10.1007/s40684-016-0040-4>.
- Russo, S., *et al.*, 2016. Failure analysis using acoustic and energy emission assessment of fibre reinforced polymer material performance under severe conditions. *Journal of Reinforced Plastics and Composites* 35 (13), 1075–1090. <https://doi.org/10.1177/0731684416638552>.
- Russo, S., 2019. On failure modes and design of multi-bolted FRP plate in structural joints. *Composite Structures* 218, 27–38. <http://doi.org/10.1016/j.compstruct.2019.03.048>.
- Safonov, A.A., 2019. 3D topology optimization of continuous fiber-reinforced structures via natural evolution method. *Composite Structures* 215, 289–297. <http://doi.org/10.1016/j.compstruct.2019.02.063>.
- Safonov, A.A., Carlone, P., Akhatov, I., 2018. Mathematical simulation of pultrusion processes: A review. *Composite Structures* 184. <https://doi.org/10.1016/j.compstruct.2017.09.093>.
- Saha, M., Prabhakaran, R., Waters Jr., W.A., 2004. Compressive behavior of pultruded composite plates with circular holes. *Composite Structures* 65 (1), 29–36. <https://doi.org/10.1016/j.compstruct.2003.10.002>.
- Sapkás, A., Kollár, L.P., 2002. Lateral-torsional buckling of composite beams. *International Journal of Solids and Structures* 39 (11), [https://doi.org/10.1016/S0020-7683\(02\)00236-6](https://doi.org/10.1016/S0020-7683(02)00236-6).
- Satasivam, S., Bai, Y., 2014. Mechanical performance of bolted modular GFRP composite sandwich structures using standard and blind bolts. *Composite Structures* 117 (1), 59–70. <https://doi.org/10.1016/j.compstruct.2014.06.011>.
- Shan, L., Qiao, P., 2005. Flexural-torsional buckling of fiber-reinforced plastic composite open channel beams. *Composite Structures* 68 (2), <https://doi.org/10.1016/j.compstruct.2004.03.015>.
- Sigley, R.H., Wronski, A.S., Parry, T.V., 1991. Tensile failure of pultruded glass-polyester composites under superimposed hydrostatic pressure. *Composites Science and Technology* 41 (4), 395–409. [https://doi.org/10.1016/0266-3538\(91\)90074-Y](https://doi.org/10.1016/0266-3538(91)90074-Y).
- Sigley, R.H., Wronski, A.S., Parry, T.V., 1992. Axial compressive failure of glass-fibre polyester composites under superposed hydrostatic pressure: Influence of fibre bundle size. *Composites Science and Technology* 43 (2), 171–183. [https://doi.org/10.1016/0266-3538\(92\)90007-P](https://doi.org/10.1016/0266-3538(92)90007-P).
- Silvestre, N., Camotim, D., 2003. GBT buckling analysis of pultruded FRP lipped channel members. *Computers and Structures* 81 (18–19), 1889–1904. [https://doi.org/10.1016/S0045-7949\(03\)00209-8](https://doi.org/10.1016/S0045-7949(03)00209-8).
- Skels, P., Janeliukstis, R., Haritonovs, V., 2018. Review on structural health interrogation using fiber bragg grating sensors. *Engineering for Rural Development*. 1346–1353. <https://doi.org/10.22616/ERDev2018.17.N134>.
- Smith, S.J., Parsons, I.D., Hjeltnad, K.D., 1998. An experimental study of the behavior of connections for pultruded GFRP I-beams and rectangular tubes. *Composite Structures* 42 (3), [https://doi.org/10.1016/S0263-8223\(98\)00082-8](https://doi.org/10.1016/S0263-8223(98)00082-8).
- Sonti, S.S., Barbero, E.J., 1996. Material characterization of pultruded laminates and shapes. *Journal of Reinforced Plastics and Composites* 15 (7), 701–717. <https://doi.org/10.1177/073168449601500705>.
- Standard definitions of terms relating to reinforced plastic pultruded products, D3918- 96(2003), ASTM, 2003.
- Standard guide for testing polymer matrix composite materials,' D4762-08, ASTM, 2008.
- Standard practice for classifying reinforced plastic pultruded shapes according to composition,' D3647-09, ASTM, 2009.
- Standard practice for classifying visual defects in thermosetting plastic pultruded shapes,' D4385-08, ASTM, 2008.
- Standard practice for testing pultruded composites,' D7745–11, ASTM, 2011.
- Standard specification for dimensional tolerance of thermosetting glass-reinforced plastic pultruded shape,' D3917–8, ASTM, 2008.
- Standard test method for bearing strength,' D953–09, ASTM, 2009.
- Standard test method for compressive properties of rigid plastics,' D695–08, ASTM, 2008.
- Standard test method for compressive residual strength properties of damaged polymer polymer matrix composite plates,' D7290–06, ASTM, 2006.
- Standard test method for deflection temperature of plastics under flexural load,' D648–07, ASTM, 2007.
- Standard test method for density and specific gravity (relative density) of plastics by displacement,' D792–08, ASTM, 2008.

- Standard test method for determining the compressive properties of polymer matrix composite laminates using a combined loading compression (CLC) test fixture,' D6641/D6641M-09, ASTM, 2009.
- Standard test method for ignition loss of cured reinforced resins,' D2584-08, ASTM, 2008.
- Standard test method for indentation hardness of rigid plastics by means of a barcol impressor,' D2583, ASTM, 2007.
- Standard test method for in-plane shear properties of composite laminates,' D4255/D4255M - 01(2007), ASTM, 2007.
- Standard test method for open-hole tensile strength of polymer matrix composite laminates,' D5766-07, ASTM, 2007.
- Standard test method for shear properties of composite materials by the -notched beam method, D5379-05, ASTM, 2005.
- Standard test method for tensile properties of plastics,' D638-08, ASTM, 2008.
- Standard test method for tensile properties of polymer matrix materials,' D3039/D3039M - 08, ASTM, 2008.
- Standard test method for tensile, compressive, and flexural creep and creep rupture of plastics,' D2990-09, ASTM, 2009.
- Standard test method for tension-tension fatigue of oriented fiber, resin matrix composites, ASTM D3479/D3479M - 96(2007), ASTM, 2007.
- Standard test method for transition temperature and enthalpies of fusion and crystallization of polymers by differential scanning calorimetry,' D3418-08, ASTM, 2008.
- Standard test method for void content of reinforced plastics,' D2734-09, ASTM, 2009.
- Standard test methods for compressive properties of unidirectional or crossply fiber-resin composites,' D3410/D3410M-03(2008), ASTM, 2008.
- Starr, T.F., 2000. Pultrusion for Engineers. England: Abington Hall, Abington Cambridge, <http://doi.org/10.1533/9781855738881.97>.
- Stazi, F., *et al.*, 2015. Environmental ageing on GFRP pultruded joints: Comparison between different adhesives. *Composite Structures* 133, 404–414. <http://doi.org/10.1016/j.compstruct.2015.07.067>.
- Strongwell design manual, 2010. Available at: <https://www.strongwell.com/designmanual>. (c.d. 19/04/2021).
- Structural design of FRP components,' CTI Bulletin ESG-152 (13), Cooling Technology Institute, 2013.
- Struzziero, G., Teuwen, J.J.E., Skordos, A.A., 2019. Numerical optimisation of thermoset composites manufacturing processes: A review. *Composites Part A: Applied Science and Manufacturing* 124. <http://doi.org/10.1016/j.compositesa.2019.105499>.
- Stylianiadis, P., Nethercot, D., 2017. Considerations for robustness in the design of steel and composite frame structures. *Structural Engineering International: Journal of the International Association for Bridge and Structural Engineering* 27 (2), 263–280. <https://doi.org/10.2749/101686617x14881932436212>.
- The Highways Agency, 2005. BD 90/05 Design of FRP Bridges and Highway Structures Design Manual for Roads and Bridges 2005 21. HIGHWAY STRUCTURES: APPROVAL PROCEDURES AND GENERAL DESIGN, 1(May)
- Tomblin, J., Barbero, E., 1994. Local buckling experiments on FRP columns. *Thin-Walled Structures* 18 (2), [https://doi.org/10.1016/0263-8231\(94\)90012-4](https://doi.org/10.1016/0263-8231(94)90012-4).
- TR57 Strengthening Concrete Structures With Fibre Composite Materials: Acceptance, Inspection And Monitoring, The Concrete Society, UK, 2003.
- Tuloup, C., *et al.*, 2019. On the use of in-situ piezoelectric sensors for the manufacturing and structural health monitoring of polymer-matrix composites: A literature review. *Composite Structures* 215, 127–149. <http://doi.org/10.1016/j.compstruct.2019.02.046>.
- Turvey, G.J., 1996a. Effects of load position on the lateral buckling response of pultruded GRP cantilevers – Comparisons between theory and experiment. *Composite Structures* 35 (1), 33–47. [https://doi.org/10.1016/0263-8223\(96\)00022-0](https://doi.org/10.1016/0263-8223(96)00022-0).
- Turvey, G.J., 1996b. Lateral buckling tests on rectangular cross-section pultruded GRP cantilever beams. *Composites Part B Engineering* 27 (1), 35–42. [https://doi.org/10.1016/1359-8368\(95\)00004-6](https://doi.org/10.1016/1359-8368(95)00004-6).
- Turvey, G.J., Zhang, Y., 2006. A computational and experimental analysis of the buckling, postbuckling and initial failure of pultruded GRP columns. *Computers and Structures* 84 (22–23), 1527–1537. <https://doi.org/10.1016/j.compstruc.2006.01.028>.
- Turvey, G.J., Sana, A., 2016. Pultruded GFRP double-lap single-bolt tension joints – Temperature effects on mean and characteristic failure stresses and knock-down factors. *Composite Structures* 153, 624–631. <http://doi.org/10.1016/j.compstruct.2016.06.016>.
- Turvey, G.J., Zhang, Y., 2018. Mechanical properties of pultruded GFRP WF, channel and angle profiles for limit state/permissible stress design. *Composites Part B Engineering* 148, 260–271. <https://doi.org/10.1016/j.compositesb.2018.04.010>.
- Vedernikov, A., Tucci, F., *et al.*, 2020a. Investigation on the shape distortions of pultruded profiles at different pulling speed. *Procedia Manufacturing* 47 (2019), 1–5. <https://doi.org/10.1016/j.promfg.2020.04.107>.
- Vedernikov, A., Safonov, A., *et al.*, 2020b. Pultruded materials and structures: A review. *Journal of Composite Materials* 54 (26), <https://doi.org/10.1177/0021998320922894>.
- Vedernikov, A.N., Safonov, A.A., *et al.*, 2020c. Spring-in experimental evaluation of L-shaped pultruded profiles. *IOP Conference Series: Materials Science and Engineering* 747 (1), <https://doi.org/10.1088/1757-899X/747/1/012013>.
- Wang, Y., Zureick, A.-H., 1994. Characterization of the longitudinal tensile behavior of pultruded I-shape structural members using coupon specimens. *Composite Structures* 29 (4), [https://doi.org/10.1016/0263-8223\(94\)90115-5](https://doi.org/10.1016/0263-8223(94)90115-5).
- Wong, P.M.H., Wang, Y.C., 2007. An experimental study of pultruded glass fibre reinforced plastics channel columns at elevated temperatures. *Composite Structures* 81 (1), 84–95. <https://doi.org/10.1016/j.compstruct.2006.08.001>.
- Xie, L., *et al.*, 2019. Pultruded GFRP square hollow columns with bolted sleeve joints under eccentric compression. *Composites Part B: Engineering* 162.
- Xin, H., *et al.*, 2017. Impact of hygrothermal aging on rotational behavior of web-flange junctions of structural pultruded composite members for bridge applications. *Composites Part B: Engineering* 110. <https://doi.org/10.1016/j.compositesb.2016.09.105>.
- Zafari, B., Mottram, J.T., 2016. On the Mechanical Characterisation of Pultruded Fibre Reinforced Plate Material Subjected to Hygrothermal Aging. (July 2015).

Chapter 6

Effects of pulling speed on structural performance of L-shaped pultruded profiles

Vedernikov Alexander, Tucci Fausto, Carlone Pierpaolo, Gusev Sergey, Konev Stepan, Firsov Denis, Akhatov Iskander, Safonov Alexander. Effects of pulling speed on structural performance of L-shaped pultruded profiles. *Composite Structures* 2021. DOI: 10.1016/j.compstruct.2020.112967.

Contribution: I participated in the pultrusion experiment and was responsible for preparing specimens for optical microscopy and mechanical testing, as well as for performing the optical microscopy experiments. In the 90-day experiment I was responsible for measuring the spring-in in pultruded structural profiles. I also performed the analysis of pultrusion experiments, mechanical tests, optical microscopy, and spring-in measurement results. Besides, I prepared all the figures in this article and contributed to the development of the original draft, final writing, and editing. I would like to thank all the authors for their valuable contributions to the development of this paper.



Effects of pulling speed on structural performance of L-shaped pultruded profiles



Alexander Vedernikov^{a,*}, Fausto Tucci^b, Pierpaolo Carlone^b, Sergey Gusev^a, Stepan Konev^a, Denis Firsov^a, Iskander Akhatov^a, Alexander Safonov^a

^a Skolkovo Institute of Science and Technology, Center for Design, Manufacturing and Materials, Moscow, Russia

^b Department of Industrial Engineering, University of Salerno, Fisciano, Italy

ARTICLE INFO

Keywords:

Pultrusion
Mechanical properties
Matrix cracking
Delamination
Spring-in
Curing

ABSTRACT

Pultrusion is a highly automated process for manufacturing structural composite elements, wherein the production rate depends on the pulling speed. This study analyzed the influence of pulling speed on the structural characteristics of pultruded glass fiber/epoxy-vinyl resin $75 \times 75 \times 6$ mm L-shaped profiles. The profiles were pultruded at three pulling speeds: 200, 400, and 600 mm/min. After fabrication, the spring-in values of the fabricated profiles were measured; the profiles were examined under a microscope to identify and study their cracking; and the mechanical properties of the pultruded composite were determined. The spring-in was measured immediately after fabrication and then at intervals of two to three days over a 90-day period. The spring-in angle was found to increase with increments in the pulling speed. The profiles produced at the lower pulling speeds (200 and 400 mm/min) exhibited no significant differences in matrix cracking or mechanical characteristics. By comparison, at the high pulling speed (600 mm/min), wherein a large part of the profile is polymerized after exiting the die, the formation of delamination perpendicular to the matrix cracks was observed. Furthermore, at this pulling speed, there were increased variations in the strength and Young's modulus values and decreased interlaminar shear strength.

1. Introduction

In recent years, fiber reinforced polymers (FRPs) have garnered considerable interest from the engineering community, resulting in the widespread adoption of composite structures by the construction industry [1,2]. Due to the high strength-to-weight ratio, ease of handling, improved durability, and corrosion resistance FRPs overcome the conventional materials [3,4]. Among the many current composite manufacturing processes, pultrusion is the most efficient, combining high production rates with low material waste [5,6]. In thermoset pultrusion, fiber reinforcement is guided through a polymer matrix and then into a heated die where the polymerization reaction takes place [7]. Pulling units continuously pull the material, resulting in an automated process requiring almost no involvement by the engineer [8]. Although the pultrusion process may seem conceptually simple, its optimization involves careful consideration of the many parameters influencing the quality of the final product: the choice of raw materials and their proportions [9,10], fiber impregnation and resin infiltration techniques [11], pulling force and speed [12,13], resin viscosity [14],

and temperature regime and heating conditions [15,16]. Maximizing the pulling speed while preserving the quality of the profiles produced is necessary to increase efficiency and, thus, the profitability of the pultrusion process [17,18].

The influence of various process parameters and raw materials properties on the successful implementation of the pultrusion process and the final properties of the pultruded profiles have been analyzed in multiple studies over the last 35 years. The experimental research conducted by Price and Cupschalk (1984) on the optimum value of the pulling force as a function of die temperature, pulling speed, and the ratio between the resin and reinforcement contents can be considered as the starting point of such investigations [19]. A mathematical model describing the influence of the initiator type, pulling speed, and reinforcement and resin selection on the evolution of the degree of curing and the temperature of the profile during the pultrusion process was developed by Han et al. [20]. Chen and Wang discussed in [21] the influence of mechanical characteristics such as tensile strength, flexural strength, and flexural modulus, on the pultrusion process parameters, including the die temperature, pulling speed, post-cure

* Corresponding author.

E-mail address: aleksandr.vedernikov@skoltech.ru (A. Vedernikov).

temperature and time, filler type and proportion, and glass fiber percentage. In [22], Chen and Chen studied the relationships between the flexural strength and modulus and the pultrusion process parameters, such as the pulling speed, die temperature, post-cure time and temperature, and filler type and content. Chen and Ma studied the relationships between process parameters and the dynamic mechanical moduli of the final profiles [23]. Moschiar et al. [24] investigated the effects of pulling speed variations on the pulling force values and degree of curing. A model that accounted for the influence of the pulling speed on the pulling force and was, therefore, able to predict the optimized process parameters, was developed and experimentally validated by Kim et al. in [25]. Giordano and Nicolais proposed a model based on lubrication theory that established the relationships between the pulling speed and force, resin viscosity, degree of curing, and die temperature [26]. Subsequently, Raper et al. [27] developed a numerical model to analyze the influence of the process parameters, including the pulling speed, volume of reinforcement, and resin viscosity, on the pressure rise and velocity distribution at the die entrance, thus enabling the use of optimized parameters to improve the quality of pultruded profiles. In a similar study [28], Gadam et al. proposed a mathematical model that accounted for the influence of pultrusion process parameters, including the temperature regime, geometry of the profile, resin viscosity, pulling speed, and amount of reinforcement, on the variations in the pressure at the die entrance. In [29], Li et al. analyzed the influence of the pulling speed and the shape and length of the die block on the degree of curing and the pulling force during the pultrusion process. They also studied the formation of blisters resulting from high pulling speeds. The effect of water immersion and freeze-thaw cycling on the strength of composite elements pultruded at different speeds was studied by Garland et al. [30]. In [31], Freed et al., seeking to improve the durability and strength of pultruded composites, analyzed void formation at different pulling speeds. The nature of blister formation in the pultruded profiles and the influence of the die length, pulling speed, die temperature, and thickness of the cured profiles on the blister formation was experimentally evaluated by Li et al. [32]. In [12], Li et al. experimentally investigated the influences of process parameters, such as temperature conditions, resin conversion, normal force, and pulling speed, on the friction coefficients for conventional and resin injection pultrusion techniques. In the accompanying paper, the authors developed a theoretical model capable of predicting the pulling force based on the listed process parameters [13]. Aiming to achieve an optimum distribution of degree of curing and, therefore, improved mechanical properties, Lam et al. developed a numerical model able to predict the best combination of the heating temperatures of the platens and the pulling speed [18]. In [33], Baran et al. validated two approaches to optimizing the pultrusion process (i.e., the genetic algorithm (GA) and mixed genetic algorithm (MIGA)) and proposed further research on the maximization of the pulling speed through the application of evolutionary algorithms. In the follow-up paper, Baran et al. investigated the influences of the pulling speed on the values of spring-in for an L-shaped structural profile, using the finite element method (FEM) [34]. The effects of the pulling force, die temperature, and presence of additives on the flexural strength of a pultruded jute fiber strip were studied by Gupta et al. in [35]. Variations in the mechanical characteristics of composites reinforced with kenaf fibers as a function of pulling speed were analyzed by Fairuz et al. [36]. In an attempt to prevent cracking in larger pultruded profiles, Safonov et al. developed a numerical model to optimize the pulling speed during the pultrusion process [37]. Recently, the influence of the pulling speed on the time-dependent values of spring-in and warpage was studied by Vedernikov et al. [17,38].

In the aforementioned studies, the structural parameters were analyzed separately from each other. Thus, their interrelations were not accounted for when discussing the influence of the pulling speed on the spring-in, matrix cracking and delamination, and the mechanical

properties of the pultruded profiles fabricated at different pulling speeds.

The objective of the present study was to establish the influence of the pulling speed on the previously mentioned characteristics of the pultruded profiles. For this study, three batches of $75 \times 75 \times 6$ mm L-shaped structural profiles produced at pulling speeds of 200, 400, and 600 mm/min were analyzed. The spring-in angles were measured at regular intervals of two to three days for 90 days, starting on the day of manufacture, at cross-sections located at 150 mm intervals. Cross-sections perpendicular to the pulling direction were studied using an optical microscope to evaluate the number, size, and location of the cracks and delamination. A series of mechanical tests was conducted to evaluate the strength and Young's modulus during compression, tension, flexure, in-plane shear, and interlaminar shear.

2. Materials and methods

2.1. Pultrusion process setup

All the experimental profiles used in this study were manufactured using a Pultrex Px500-6T (Pultrex, UK) pultrusion machine at the Laboratory of Composite Materials and Structures of the Center for Design, Manufacturing and Materials (Skolkovo Institute of Science and Technology, Moscow, Russia). L-shaped profiles measuring $75 \text{ mm} \times 75 \text{ mm} \times 6 \text{ mm}$ were utilized for the experiments (Fig. 1a).

A total of 104 threads of E-glass unidirectional rovings PS 2100 (Owens Corning Composite Materials, USA) with a linear density of 9600 TEX (9600 g/1000 m) and two layers of E-glass fabric LT 0600/S 300/06H 01/125 GUS (Owens Corning Composite Materials, USA) with a surface density of 900 g/m² were used as the reinforcement (Fig. 1c). The matrix was epoxy vinyl-based Atlac 430 (DSM Composite Resins AG, Switzerland) resin with the following additives: Triganox C (Akzo Nobel Polymer Chemicals B.V., The Netherlands), Perkadox 16 (Akzo Nobel Polymer Chemicals B.V., The Netherlands), BYK-A555 (BYK Additives & Instruments, Germany), and Zinc Stearate (Baerlocher GmbH, Germany). The resin mixture composition is shown in Table 1.

The length of the pultrusion die was 600 mm. Four 350-mm-long platens were used to heat the die block: two platens each at the top and bottom of the die block were aligned with the longitudinal axis of the die (Fig. 1b). Two thermocouples were provided within the die block (Fig. 1d) to control the die temperature. The allowable temperature range was set at 135–155 °C. Wired 7-m-long Chromel-Copel thermocouples were embedded in the profile (in the corner zone, between the UD rovings and fabric layer) to monitor the temperature changes in the polymer during pultrusion.

The pultrusion process was performed at three pulling speeds: 200, 400, and 600 mm/min. Upon reaching a stationary state for each pulling speed, 5 m long sections of the profile were pultruded with a thermocouple embedded in the material (between the UD rovings and fabric layer). After the thermocouple wire was cut off, an additional 2.5-m-long section of the profile was pultruded, which yielded a 1.5-m-long section that was used for the investigation of the time-dependent spring-in and a 1-m-long section that was used for evaluating the mechanical properties (Fig. 1e). At the end of the pultrusion line, the profiles were cut into sections of the desired length with a cutting saw and stored according to their batch. The profiles fabricated at pulling speeds of 200, 400, and 600 mm/min were labeled V-200, V-400, and V-600, respectively (Fig. 1f).

2.2. Spring-in measurement

The spring-in was measured on the day of manufacture, three hours after fabrication, which was when the profiles had cooled to room temperature. A set of thin metallic strips (0.1 to 1 mm thick) and a calibrated analog tool (ensuring the correctness of the 90° angle

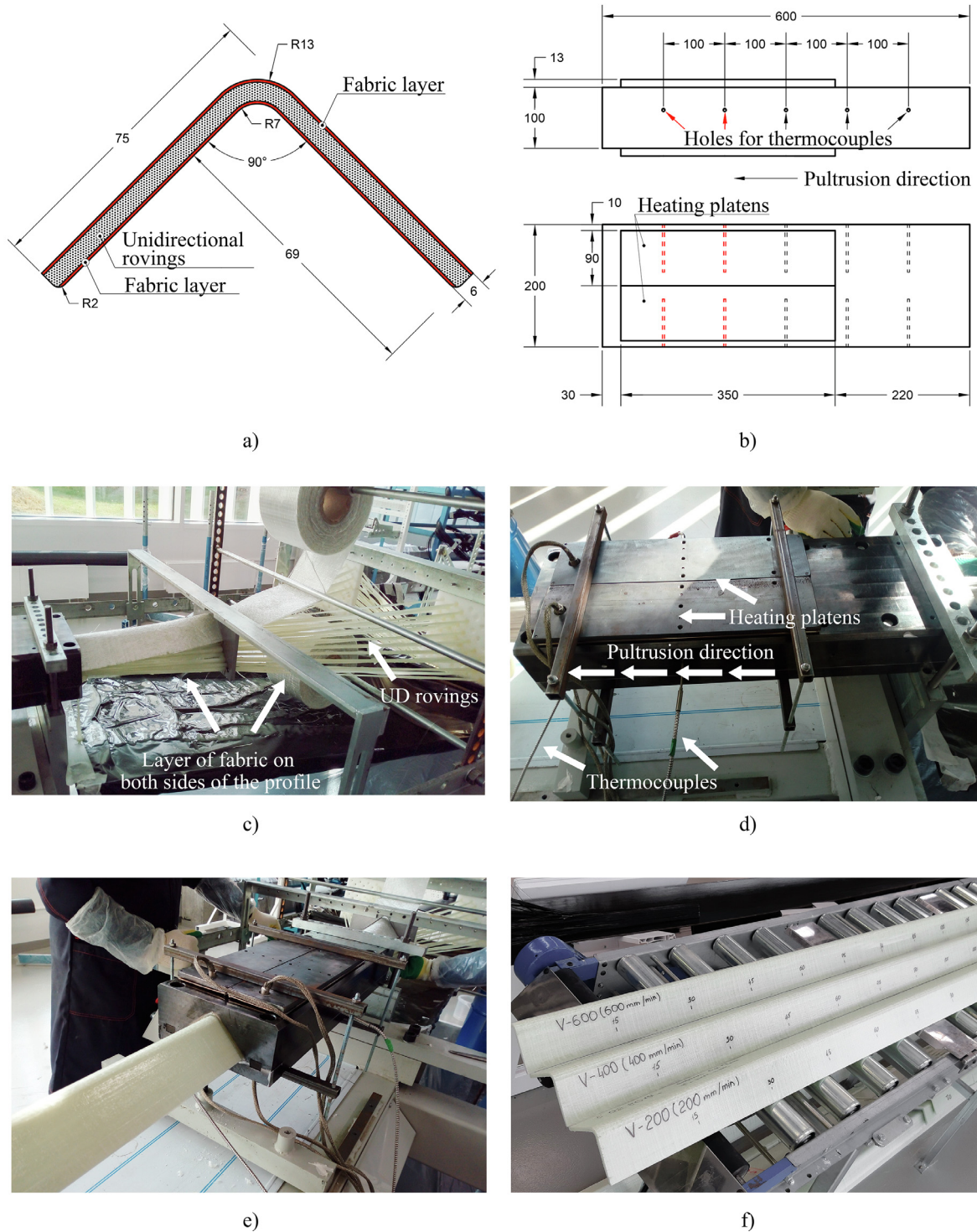


Fig. 1. Experimental setup: a) Cross-section of a 75 × 75 × 6 mm L-shaped pultruded profile and the position of the unidirectional rovings and fabric layers; b) Die block dimensions and the position of the heating platens: top and side views; red indicates the positions of the thermocouples; c) Placement of the fabric and UD reinforcement before entering the die; d) Die block during the pultrusion; e) Cured composite leaving the die; f) Profiles fabricated at the studied pulling speeds of 200, 400, and 600 mm/min.

measurements) were used to measure the spring-in shape distortion (Fig. 2). Any deviations of the angles of the L-shaped profiles from 90° were measured at intervals of 150 mm along the profile through the placement of thin metallic strips of sufficient thickness (t_s) [39]. Based on the web size of the profile ($L_w = 62 \text{ mm}$), the thickness measurement obtained in mm was then converted to the actual value of spring-in (φ) in degrees as follows:

$$\varphi = \frac{180^\circ}{\pi} \tan^{-1}(t_s/L_w) \tag{1}$$

The applied technique ensured accuracy of $\pm 0.09^\circ$. The mean spring-in angle was calculated by averaging the spring-in values measured at the 11 cross-sections of each profile. The measurements were repeated every two to three days to record the spring-in evolution over

Table 1
Components of the resin mixture.

Component	Unit	Amount
Resin Atlac 430 (DSM Composite Resins AG, Switzerland)	kg	25.07
BYK-A555 (BYK Additives & Instruments, Germany)	kg	0.09
Triganox C (Akzo Nobel Polymer Chemicals B.V., The Netherlands)	kg	0.38
Perkadox 16 (Akzo Nobel Polymer Chemicals B.V., The Netherlands)	kg	0.13
Zinc Stearate (Baerlocher GmbH, Germany)	kg	1.00

time. The evaluated pultruded profiles were stored in the laboratory under normal atmospheric conditions, and the spring-in data were collected during the 90-day experiment.

2.3. Microscopy investigation

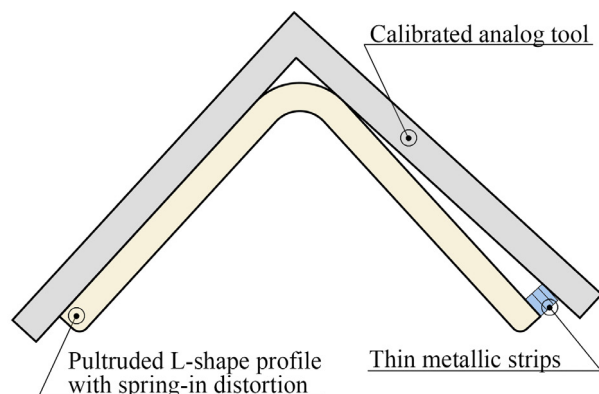
All procedures related to the microscopy investigation were performed at the Additive Manufacturing Laboratory of the Center for Design, Manufacturing and Materials (Skolkovo Institute of Science and Technology, Moscow, Russia). The size, location, and number of cracks were analyzed using an optical microscope. Three 20 mm long specimens were cut from the pultruded profiles – one from each group, i.e., V-200, V-400, and V-600. The cutting was performed using a Struers Accutom 100 machine (Struers, USA). The cut surfaces were further smoothed via polishing with a Metprep 3/PH-3 polisher (Allied High Tech Products Inc., USA), after which the samples were dried. The microstructures were analyzed using a Zeiss Axio Scope.A1 optical microscope (ZEISS Microscopy, Germany). Due to the symmetry of the profiles, only the half of each specimen was considered.

2.4. Mechanical testing

All mechanical tests were performed at the Mechanical testing Laboratory of the Center for Design, Manufacturing and Materials (Skolkovo Institute of Science and Technology, Moscow, Russia). Coupons were cut from the pultruded L-shaped profiles using a CNC milling machine. All experiments were performed under normal atmospheric conditions (temperature of 20 °C and relative humidity of 42%). An Instron 5969 testing machine (Instron, USA) was utilized to determine the mechanical properties of the profiles. Tests on the compression, tension, flexure, in-plane shear, and interlaminar shear were performed in accordance with ASTM D6641-16 [40], ISO 527-5 [41], ASTM D790-15e2 [42], ASTM D7078/7078M-12 [43], and ASTM D2344-16 [44], respectively.



a)



b)

Fig. 2. Spring-in measurement technique: a) Laboratory measurement; b) Schematic representation of the measurement process.

3. Results

3.1. Degree of curing and temperature distributions in the profiles during pultrusion

Fig. 3 shows the temperature evolution, cure rate, and degree of curing of the material relative to the thermocouple position. Three curves corresponding to the pulling speeds of 200, 400, and 600 mm/min show the evolutions of these parameters in the die block and within 250 mm after exiting the die.

A kinetic model of the n -th order reaction with autocatalysis was applied to predict the distribution of the degree of curing [45]:

$$\frac{d\alpha}{dt} = Ae^{-\frac{E_a}{RT}}(1-\alpha)^n(1+K_{cat}\alpha) \quad (2)$$

where $\alpha(t) = H(t)/H_{tot}$ is the degree of curing of the resin; $H(t)$ is the current amount of exothermal heat; H_{tot} is the total exothermal heat; t is time; $d\alpha/dt$ represents the cure rate; T is the absolute temperature; R is the universal gas constant; A is a preexponential factor; E_a represents the activation energy; n is the order of the reaction; K_{cat} represents the activation constant. The parameters of the model (2) for the current resin mixture were determined per Nasonov et al. [46], and the obtained values are presented in Table 2. The numerical solution of Eq. (2) using the Euler method with a one-second time step was applied to calculate the degree of curing and cure rate.

Table 3 shows the results of the degree of curing simulation for the three pulling speeds. The table includes the distances from the die entrance to the cure rate peak zone and to the zone where the degree of curing exceeded 95%, which represents a high degree of material polymerization. The table also provides the values of the degree of curing at the die exit.

For the V-200 sample, the curing process was completed entirely within the die block. For Sample V-400, the peak of the polymerization process occurred within the die block, while the end of the curing process occurred near the die exit. The peak of the reaction in the V-600 profile was observed at the die exit, and the end of the reaction was shifted in the direction of the pultrusion to far beyond the die exit; higher pulling speeds pushed the peak of the reaction further along the pultrusion line. For Sample V-200, after the temperature of the polymer exceeded the temperature of the heating platens, the die block started to act as a cooling medium for the composite. When the polymerization was complete, the resin ceased producing heat, and the temperature began decreasing. The metal of the die block had a considerably higher thermal conductivity than that of air. Thus, in contrast with the V-200 sample, the V-400 profile leaving the die block still experienced the heat generated by the exothermic reaction

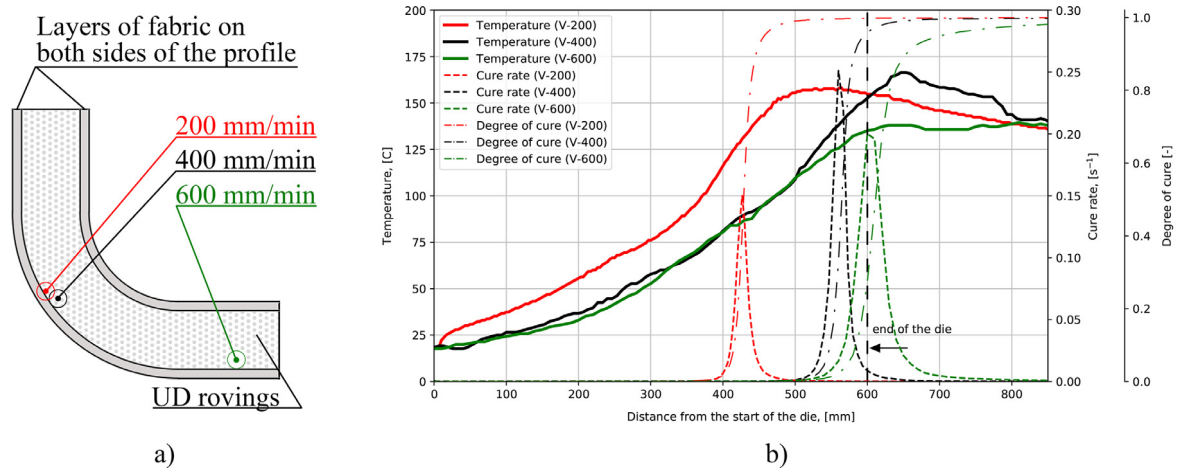


Fig. 3. Internal structure (i.e., placement of the thermocouples, UD rovings, and fabric layers) of the pultruded profile and the evolution of the temperature of the composite, as measured by the thermocouples: a) Thermocouple placement; b) Evolution of the temperature (solid line), degree of curing (dashed-dotted line), and cure rate (dashed line). The line color corresponds to the pulling speed: red (V-200), black (V-400), or green (V-600). (For interpretation of the references to color in this figure legend, the reader is referred to the web version of this article.)

Table 2
Resin kinetic parameters.

$A [s^{-1}]$	$E_a [\frac{kJ}{mol \cdot K}]$	$n [-]$	$K_{cat} [-]$
$10^{9.34}$	93.3	1.91	$10^{2.73}$

Table 3
Milestones of the thermochemical evolution process at different pulling speeds.

Sample	Coordinate from the die entrance [mm]		Degree of curing at the die exit [-]
	Cure rate peak	Degree of curing over 95%	
V-200	427	460	0.997
V-400	560	600	0.959
V-600	600	710	0.273

and did not cool in the air as quickly as within the die block. It thus experienced a higher peak temperature (166 °C compared to 158 °C for the V-200 sample). The V-600 composite had a significantly lower degree of curing at the die exit: 0.273 versus the values of 0.997 for V-200 and 0.959 for V-400. Thus, the bulk of the curing reaction occurred in a constraint-free environment. Because the active polymerization took place in the air, the heat generated by the exothermic reaction was unable to dissipate as quickly as in the cases of the V-200 and V-400 profiles. Therefore, compared to V-200 and V-400, the temperature profile of the V-600 sample in the post-die region was slightly more linear. Additionally, the absence of external thermal influences after the die exit resulted in a significant increase in the duration of the curing process, compared to the profiles produced at the lower pulling speeds.

3.2. Evolution of the spring-in

Fig. 4 shows the evolutions of the spring-in angles of the 1.5-m-long sections of the profiles (for V-200, V-400, and V-600) over time, starting from the day of manufacture. The initial value of the spring-in is the angle measured on the day of manufacture three hours after fabrication and after the profiles had cooled to room temperature. The points in Fig. 4a correspond to the average spring-in values obtained from 11 cross-sections of the profile measured at two- to three-day

intervals during the 90-day experiment. The histogram in Fig. 4b shows the values of the spring-in angle for each profile cross-section, as measured on the day of fabrication and the last day of the experiment. Fig. 4a provides the graph of Eq. (3). Curves on the graph are the fitted exponential decay curves obtained by interpolating the averaged spring-in measurement data:

$$\varphi = \varphi_0 + \Delta\varphi(1 - e^{-\frac{t}{B}}), \quad (3)$$

where t is the time from the day of manufacture (day); φ_0 represents the initial value of the spring-in angle (degree); $\Delta\varphi$ defines the change in the spring-in angle at the end of the 90-day experiment (degree); $1/B$ is the decay constant that determines how many days are required to reach 63% of the overall spring-in variation. The least-squares method was used to determine the values of the constants, based on the spring-in measurements. The values of the constants for the V-200, V-400, and V-600 profiles are listed in Table 4.

The first 10–15 days after fabrication were characterized by sharp growth in the spring-in values. During the first ten days after fabrication, the spring-in of the V-200, V-400, and V-600 profiles increased by 67%, 91%, and 68%, respectively, relative to the overall growth over 90 days. During the second ten days, the spring-in angle increased an additional 22%, 8%, and 22% for the V-200, V-400, and V-600 profiles, respectively. The growth of the spring-in value to $0.99\Delta\varphi$ plateaued at the 41st, 20th, and 40th days for V-200, V-400, and V-600, respectively.

The initial spring-in angle values for the V-200, V-400, and V-600 profiles were 1.16°, 1.41°, and 1.72°, respectively, which corresponds to absolute differences of 0.25° (V-200 versus V-400) and 0.31° (V-400 versus V-600), while the relative differences were the same for both cases at 22%. Additionally, the values of the spring-in angle measured at the end of the 90-day experiment were 1.24°, 1.61°, and 1.89° for the V-200, V-400, and V-600 profiles, respectively, corresponding to absolute differences of 0.37° (V-200 versus V-400) and 0.28° (V-400 versus V-600), or 30% and 17%, respectively. The analysis of the initial and final spring-in values showed that the absolute increases in the spring-in angle values were 0.08° for V-200, 0.2° for V-400, and 0.17° for V-600. Fig. 4b shows that the V-400 and V-600 profiles exhibited similar behavior in terms of their variations in spring-in at each cross-section, while there were fewer variations in the spring-in of the V-200 profile. Thus, the increase in both the initial and final spring-in values due to increased pulling speed could be considered as having been experimentally verified.

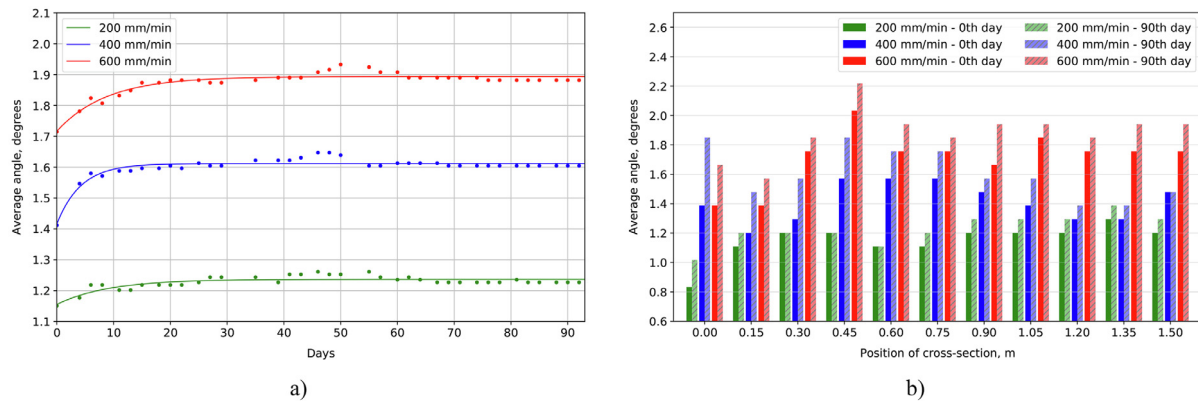


Fig. 4. Spring-in evolutions for the different pulling speeds: 200, 400, and 600 mm/min: a) The average value of the spring-in over 90 days; b) Initial and final values of the spring-in at the cross-sections along the 1.5 m long profile sections.

Table 4

Constants of the spring-in growth law equation.

Sample	$\varphi_0 [^\circ]$	$\Delta\varphi [^\circ]$	B [d]
V-200	1.16	0.081	8.98
V-400	1.42	0.196	4.22
V-600	1.72	0.177	8.76

3.3. Microscopy results

Fig. 5 shows the microphotographs of the cross-sections of the V-200 (Fig. 5c), V-400 (Fig. 5d), and V-600 (Fig. 5e) profiles. The cross-sections were cut perpendicular to the direction of pultrusion. Photographs of the entire cross-sections were obtained via compositing of the microphotographs using the internal Thixomet PRO software of the Zeiss Axio Scope.A1 optical microscope (ZEISS Microscopy, Germany). The structure, position, size, and number of cracks were studied. Two types of defects were analyzed: the matrix cracks that extended from one layer of fabric to another and were, therefore, located entirely in the unidirectional rovings layer, and the delaminations that were located perpendicular to the matrix cracks in the middle of the unidirectional rovings layer.

The matrix cracks were almost invisible without a microscope, while the delaminations in the V-600 profiles were quite noticeable. The V-200 and V-400 profiles demonstrated similar behavior in terms of their numbers and sizes of cracks. The V-200 profile had ten matrix cracks that were almost uniformly distributed over the half of the cross-section that was analyzed (Fig. 5c), while the V-400 profile had 11 cracks (Fig. 5d). The average width of the matrix cracks was approximately 200 μm (Fig. 5b). The length of the cracks was approximately 3.9 mm for the V-200 and 4.6 mm for the V-400 profiles. The average area of the matrix cracks constituted 0.66 mm^2 of the V-200 and 0.7 mm^2 of the V-400 profiles. These cracks were entirely located within the region of the unidirectional rovings, without transition to the fabric reinforcement layer. While the cracking behaviors of the V-200 and V-400 profiles were similar, the results obtained from the V-600 profile differed significantly due to the presence of additional defects. Fig. 5e shows that matrix cracks extended through the entire internal layer thickness of the unidirectional material, in the same manner as in the V-200 and V-400 profiles, while delaminations (absent in V-200 and V-400) were located along the centerline of the V-600 profile cross-section, i.e., perpendicular to the matrix cracks. There were fewer matrix cracks in the V-600 profile than in the V-200 and V-400 profiles, with five independent cracks extending through the entire thickness of the unidirectional layer and three cracks of significantly smaller length that were connected to the

delaminations. The thickness of the delaminations was approximately 1 mm and reached 1.3 mm at some points (Fig. 5f), which is one order of magnitude higher than the thickness of the matrix cracks (0.2 mm). Three independent delaminations had lengths of 4.7 mm, 6.3 mm, and 6 mm. The delaminations did not propagate in a longitudinal direction over the entire length of the profile and resulted in bulges that were observable on the outer side of the profile, approximately 20 cm long and located approximately 50 cm from each other.

The occurrence of matrix cracks was related to the residual stresses developed during manufacturing [47] and did not vary with the pulling speed, as evidenced by their presence in all specimens (i.e., V-200, V-400, and V-600). However, delaminations were detected only in the V-600 profile. Therefore, the formation of delaminations was directly influenced by the shift in the polymerization peak from the die block region towards the post-die section of the pultrusion line [48].

3.4. Mechanical testing results

All results correspond to the samples cut along the pultrusion direction. For the interlaminar shear tests, additional samples were cut across the longitudinal axis of the unidirectional rovings. Samples from the V-600 profile were cut from regions without bulges. The results of the mechanical testing of the compression, tension, flexure, in-plane shear, and interlaminar shear are summarized in Table 5.

The results showed that the pulling speed only minorly impacted the compressive, tension, and in-plane shear behaviors of the tested specimens in terms of the strength and elastic modulus in tension and compression. There was almost no difference between the flexural test results for the V-200 and V-400 specimens. In contrast, the V-600 specimens had distinctly lower values of flexural stress upon breaking, as compared to the V-200 and V-400 specimens (by 29% and 33%, respectively). Regarding the interlaminar shear stress, all profile specimens tested at the 0° fiber orientation exhibited similar strength upon breaking. For the tests at the 90° fiber orientation, the results for the V-200 and V-400 specimens were similar. However, the V-600 specimens exhibited considerably lower values of the stress at breaking, as compared with the V-200 and V-400 specimens (by 35% and 41%, respectively). Notably, pultrusion at the high pulling speed (600 mm/min), which caused the polymerization peak to shift to beyond the die block, resulted in greater variability.

4. Discussion

At the lower pulling speeds (V-200 and V-400), the polymerization peak was located within the die block, while at the highest pulling speed (V-600), the peak position shifted to the post-die region. Further, while the temperature distributions and evolution of the degree

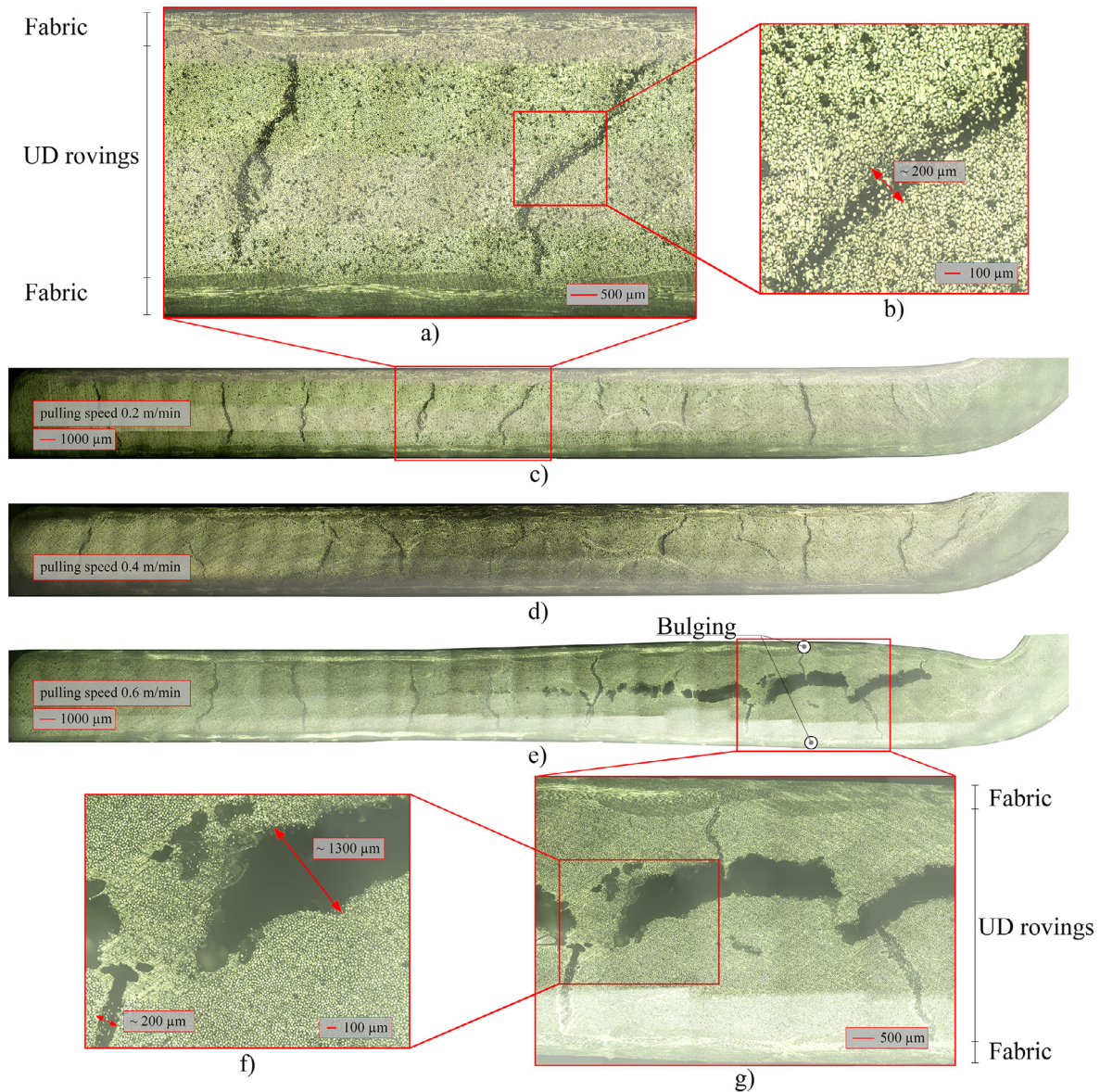


Fig. 5. Microphotographs of the cross-sections of the V-200, V-400, and V-600 profiles that were cut transverse to the pultrusion direction: a) Position of the matrix cracks (V-200). Scale bar = 500 μm; b) Size of matrix cracks (V-200). Scale bar = 100 μm; c) Distribution of the matrix cracks on half of the profile V-200. Scale bar = 1000 μm; d) Distribution of the matrix cracks on half of the profile V-400. Scale bar = 1000 μm; e) Distribution of the matrix crack and delaminations on half of the profile V-600, showing the bulging areas. Scale bar = 1000 μm; f) Size of the matrix crack and delaminations on the V-600 profile. Scale bar = 100 μm; g) Position of the matrix crack and delaminations on the V-600 profile. Scale bar = 500 μm.

Table 5

Results of the mechanical tests in compression, tension, flexure, and in-plane and interlaminar shear.

Specimen	Compression		Tension		Flexure		In-plane shear		Interlaminar shear	
	Strength [MPa]	Elastic Modulus [GPa]	Strength [MPa]	Elastic Modulus [GPa]	Strength [MPa]	Modulus of elasticity in bending [GPa]	Strength [MPa]	Shear Modulus [GPa]	Strength in 0° direction [MPa]	Strength in 90° direction [MPa]
V-200	502 ± 38.3	42.8 ± 2.7	396 ± 18.2	44.6 ± 3.5	658 ± 65.6	34.6 ± 1.7	40.7 ± 1.9	2.62 ± 0.13	22.7 ± 1.7	6.7 ± 0.76
V-400	445 ± 35.5	41.8 ± 2.8	412 ± 27.2	45.9 ± 4.2	697 ± 68.1	34.7 ± 2.9	43.1 ± 1.6	2.66 ± 0.42	24.1 ± 1.2	7.4 ± 1.25
V-600	427 ± 59.9	43.5 ± 3.1	408 ± 48.5	42.9 ± 4.1	464 ± 124	33.7 ± 2.2	45.0 ± 2.7	2.87 ± 0.15	22.9 ± 3.6	4.33 ± 1.93

of curing were similar for the V-200 and V-400 profiles, they differed significantly from those of the V-600 sample. These factors resulted in the principal distinctions between the considered profiles. The structural performance (i.e., the spring-in distortions, occurrence of matrix

cracking, and mechanical characteristics) of the V-200 and V-400 profiles was also similar, differing from that of the V-600 profile.

The initial value of spring-in also depended on the pulling speed: the higher the speed, the larger the spring-in angle. Further, higher

speeds (V-400 and V-600) resulted in more significant variations in the spring-in at all cross-sections taken along the profile, and the absolute increase in spring-in was greater for the higher pulling speeds (V-400 and V-600) than for the lowest one (V-200). Therefore, a manufacturer should account not only for the value of the initial spring-in but also for its absolute growth over time. The profiles produced at higher speeds could meet geometrical tolerance requirements immediately after being manufactured, but failed to do so after storage.

The V-200 and V-400 specimens exhibited similar matrix cracking behaviors, having similar numbers, locations, and sizes of matrix cracks. Increasing the pulling speed (i.e., V-600) resulted in the formation of considerably larger delaminations perpendicular to the matrix cracks, due to the polymerization peak being shifted beyond the die block exit. According to research conducted by Awaja et al. [49], who discussed the thermal treatment of already cured composites, the formation and development of cracks can be dictated by the presence of air bubbles initially trapped in the composite. The expansion of these bubbles caused by heating provokes the formation of cracks and their propagation. During the pultrusion process, the evaporation of styrene gas could be observed in the die block and post-die regions. The phenomenon was more pronounced at higher pulling speeds and could contribute to the occurrence of delaminations in the V-600 profiles; as such, it warrants further investigation.

During the mechanical testing, all specimens had similar strength and Young's modulus values in tension and compression. However, the V-600 specimens demonstrated a distinctly lower level of flexural stress at breaking, as compared to the V-200 and V-400 specimens (29% and 33% lower, respectively). Additionally, when tested perpendicular to the fiber orientation, the interlaminar shear stress of the V-600 specimens was considerably lower than those of the V-200 and V-400 specimens (by 35% and 33%, respectively). Additionally, the highest pulling speed (V-600) resulted in the broader spread of the strength and shear modulus results because the standard deviation was significantly higher than for the V-200 and V-400 profiles. This could be attributed to the large number of internal defects observed in the V-600 specimens. The shift of the polymerization peak to the post-die region resulted in the majority of the curing reaction occurring in a constraint-free condition (in regards to the profile). Should distortions arise outside of the die block when the polymerization is incomplete (as in V-600), significantly more internal defects and shape distortions will manifest themselves, for example, as thicker cracks and delaminations in the roving area. The opposite could be observed for the lower pulling speeds, wherein the thermal peaks were located within the die block boundary; the hard contact constraints imposed by the metal surfaces of the die block prevented excessive profile distortions.

5. Conclusions

An experimental study of pultruded glass fiber/epoxy-vinyl resin L-shaped profiles was performed to understand the relationships between the pulling speed and structural performance more clearly. Profiles were pultruded using a Pultrex Px500-6T machine at three different pulling speeds: 200, 400, and 600 mm/min. Based on the differential scanning calorimetry results and data from thermocouples embedded within the profiles, the evolution of the thermochemical parameters (i.e., temperature, degree of curing, and cure rate) of the advancing material during the pultrusion process were determined. Furthermore, the evolution of the spring-in angle was analyzed through a 90-day experiment. The cracks and their structures after manufacturing were examined using an optical microscope. The relationship between the tensile, compressive, flexural, in-plane shear, and interlaminar shear properties of the pultruded profiles and the pulling speed were determined using a testing machine according to the corresponding ASTM standards.

The results showed that the differences in the pulling speed influenced the shape distortions and the microstructural and mechanical properties of the composite. Higher pulling speeds resulted in increased spring-in angles. For example, the spring-in values of the profiles pultruded at 200 and 600 mm/min differed by nearly 50%. Moreover, increased pulling speeds resulted in more considerable changes in the spring-in angle over 90 days. Besides, increasing the pulling speed to 600 mm/min resulted in the occurrence of pronounced delaminations not observable in the profiles produced at the 200 and 400 mm/min pulling speeds. The delamination thickness was one order of magnitude larger (~1.3 mm) as compared to the thickness of the matrix cracks observed at the lower speeds (~0.2 mm). The higher pulling speeds also resulted in more significant variations in the breaking stress under compression and tension, substantially lower values of the breaking stress under flexure, considerable variations in the interlaminar shear stress values when tested at a 0° fiber orientation, and appreciably lower breaking interlaminar shear stress when tested at a 90° fiber orientation.

CRediT authorship contribution statement

Alexander Vedernikov: Investigation, Software, Data curation, Visualization, Writing - original draft, Writing - review & editing. **Fausto Tucci:** Investigation, Software, Data curation, Writing - review & editing. **Pierpaolo Carlone:** Writing - review & editing. **Sergey Gusev:** Investigation, Resources. **Stepan Konev:** Investigation. **Denis Firsov:** Investigation. **Iskander Akhatov:** Project administration, Funding acquisition. **Alexander Safonov:** Software, Data curation, Supervision, Conceptualization, Writing - original draft, Writing - review & editing.

Declaration of Competing Interest

The authors declare that they have no known competing financial interests or personal relationships that could have appeared to influence the work reported in this paper.

Acknowledgements

The authors would like to express their gratitude to the Skoltech Center for Design, Manufacturing and Materials for the support provided within the framework of the Collaboration Programs. This research did not receive any specific grant from funding agencies in the public, commercial, or not-for-profit sectors.

References

- [1] Bakis CE, Bank LC, Brown VL, Cosenza E, Davalos JF, Lesko JJ, et al. Fiber-reinforced polymer composites for construction - State-of-the-art review. *J Compos Constr* 2002;6. [https://doi.org/10.1061/\(ASCE\)1090-0268\(2002\)6:2\(73\)](https://doi.org/10.1061/(ASCE)1090-0268(2002)6:2(73)).
- [2] Bank LC. Composites for construction: structural design with FRP materials; 2007. doi:10.1002/9780470121429.
- [3] Li C, Yin X, Wang Y, Zhang L, Zhang Z, Liu Y, et al. Mechanical property evolution and service life prediction of pultruded carbon/glass hybrid rod exposed in harsh oil-well condition. *Compos Struct* 2020;246. <https://doi.org/10.1016/j.compstruct.2020.112418>.
- [4] Liu T, Feng P, Lu X, Yang J-Q, Wu Y. Flexural behavior of novel hybrid multicell GFRP-concrete beam. *Compos Struct* 2020;250. <https://doi.org/10.1016/j.compstruct.2020.112606>.
- [5] Madenci E, Özkılıç YO, Gemi L. Experimental and theoretical investigation on flexure performance of pultruded GFRP composite beams with damage analyses. *Compos Struct* 2020;242. <https://doi.org/10.1016/j.compstruct.2020.112162>.
- [7] Fairuz AM, Sapuan SM, Zainudin ES, Jaafar CNA. Polymer composite manufacturing using a pultrusion process: a review. *Am J Appl Sci* 2014;11:1798–810. <https://doi.org/10.3844/ajassp.2014.1798.1810>.
- [8] Safonov AA, Carlone P, Akhatov I. Mathematical simulation of pultrusion processes: a review. *Compos Struct* 2018;184. <https://doi.org/10.1016/j.compstruct.2017.09.093>.

- [9] Paciornik S, Martinho F, de Mauricio MH, d'Almeida JR. Analysis of the mechanical behavior and characterization of pultruded glass fiber-resin matrix composites. *Compos Sci Technol* 2003;63:295–304. [https://doi.org/10.1016/S0266-3538\(02\)00249-X](https://doi.org/10.1016/S0266-3538(02)00249-X).
- [10] Fairuz AM, Sapuan SM, Zainudin ES, Jaafar CNA. Effect of filler loading on mechanical properties of pultruded kenaf fibre reinforced vinyl ester composites. *J Mech Eng Sci* 2016;10:1931–42. <https://doi.org/10.15282/jmes.10.1.2016.16.0184>.
- [11] Simacek P, Advani SG. Simulating tape resin infiltration during thermoset pultrusion process. *Compos Part A Appl Sci Manuf* 2015;72:115–26. <https://doi.org/10.1016/j.compositesa.2015.01.020>.
- [12] Li S, Xu L, Ding Z, Lee LJ, Engelen H. Experimental and theoretical analysis of pulling force in pultrusion and resin injection pultrusion (RIP) - Part I: Experimental. *J Compos Mater* 2003;37:163–89. <https://doi.org/10.1106/002199803037003676>.
- [13] Li S, Xu L, Ding Z, Lee LJ, Engelen H. Experimental and theoretical analysis of pulling force in pultrusion and resin injection pultrusion (RIP) - Part II: Modeling and simulation. *J Compos Mater* 2003;37:195–216. <https://doi.org/10.1177/002199803037003675>.
- [14] Shakya N, Roux JA, Jeswani AL. Effect of resin viscosity in fiber reinforcement compaction in resin injection pultrusion process. *Appl Compos Mater* 2013;20:1173–93. <https://doi.org/10.1007/s10443-013-9320-0>.
- [15] Silva FJG, Ferreira F, Costa C, Ribeiro MCS, Meira Castro AC. Comparative study about heating systems for pultrusion process. *Compos Part B Eng* 2012;43. <https://doi.org/10.1016/j.compositesb.2012.01.057>.
- [16] Silva FJG, Ferreira F, Ribeiro MCS, Castro ACM, Castro MRA, Dinis ML, et al. Optimising the energy consumption on pultrusion process. *Compos Part B Eng* 2014;57. <https://doi.org/10.1016/j.compositesb.2013.09.035>.
- [17] Vedernikov A, Tucci F, Safonov A, Carlone P, Gusev S, Akhatov I. Investigation on the shape distortions of pultruded profiles at different pulling speed. *Procedia Manuf* 2020;47:1–5. <https://doi.org/10.1016/j.promfg.2020.04.107>.
- [18] Lam YC, Li J, Joshi SC. Simultaneous optimization of die-heating and pull-speed in pultrusion of thermosetting composites. *Polym Compos* 2003;24:199–209.
- [19] Price HL, Cupschalk SG. Pulling force and its variation in composite materials pultrusion. In: Dae HC, editor. *Adv. Chem. Ser.*, ACS, Washington, DC, USA; 1984. p. 301–22.
- [20] Han CD, Lee DS, Chin HB. Development of a mathematical model for the pultrusion process. *Polym Eng Sci* 1986;26:393–404. <https://doi.org/10.1002/pen.760260604>.
- [21] Chen CH, Wang WS. The development of glass fiber reinforced polystyrene for pultrusion. II: Effect of processing parameters for optimizing the process. *Polym Compos* 1998;19:423–30. <https://doi.org/10.1002/pc.10116>.
- [22] Chen C-H, Chen I-K. The unidirectional glass fiber reinforced furfuryl alcohol for pultrusion. II. Correlation of processing parameters for optimizing the process. *J Appl Polym Sci* 2011;119:1788–96. <https://doi.org/10.1002/app.32879>.
- [23] Chen C-H, Ma CM. Pultruded fiber reinforced blocked polyurethane (PU) composites. II. Processing variables and dynamic mechanical properties. *J Appl Polym Sci* 1992;46:949–57. <https://doi.org/10.1002/app.1992.070460602>.
- [24] Moschiar SM, Reboredo MM, Larrondo H, Vazquez A. Pultrusion of epoxy matrix composites: pulling force model and thermal stress analysis. *Polym Compos* 1996;17:850–8. <https://doi.org/10.1002/pc.10678>.
- [25] Kim D-H, Han P-G, Jin G-H, Lee WI. A model for thermosetting composite pultrusion process. *J Compos Mater* 1997;31:2105–22. <https://doi.org/10.1177/002199839703102005>.
- [26] Giordano M, Nicolais L. Resin flow in a pultrusion process. *Polym Compos* 1997;18:681–6. <https://doi.org/10.1002/pc.10320>.
- [27] Raper KS, Roux JA, McCarty TA, Vaughan JG. Investigation of the pressure behavior in a pultrusion die for graphite/epoxy composites. *Compos Part A Appl Sci Manuf* 1999;30:1123–32. [https://doi.org/10.1016/S1359-835X\(98\)00196-1](https://doi.org/10.1016/S1359-835X(98)00196-1).
- [28] Gadam SUK, Roux JA, McCarty TA, Vaughan JG. The impact of pultrusion processing parameters on resin pressure rise inside a tapered cylindrical die for glass-fibre/epoxy composites. *Compos Sci Technol* 2000;60:945–58. [https://doi.org/10.1016/S0266-3538\(99\)00181-5](https://doi.org/10.1016/S0266-3538(99)00181-5).
- [29] Li S, Ding Z, Lee LJ, Engelen H. Effect of die length on pulling force and composite quality in pultrusion. *Compos* 2000;2000:1–11.
- [30] Garland CA, Gupta RK, Gangarao HVS, Zondlo JW. Effect of manufacturing process conditions on the durability of pultruded vinyl ester/glass composites 2000:136.
- [31] Freed AD. Modeling the pultrusion process to obtain low void fraction composites; 2002.
- [32] Li S, Ding Z, Xu L, Lee LJ, Engelen H. Influence of heat transfer and curing on the quality of pultruded composites. I: Experimental. *Polym Compos* 2002;23:947–56. <https://doi.org/10.1002/pc.10492>.
- [33] Baran I, Tutum CC, Hattel JH. Optimization of the thermosetting pultrusion process by using hybrid and mixed integer genetic algorithms. *Appl Compos Mater* 2013;20:449–63. <https://doi.org/10.1007/s10443-012-9278-3>.
- [34] Baran I, Akkerman R, Hattel JH. Modelling the pultrusion process of an industrial L-shaped composite profile. *Compos Struct* 2014;118:37–48. <https://doi.org/10.1016/j.compstruct.2014.07.018>.
- [35] Gupta A, Singh H, Walia RS. Effect of process parameters on pultruded jute fiber polymer composite flexural strength 2017;19–18.
- [36] Fairuz AM, Sapuan SM, Zainudin ES, Jaafar CNA. The effect of pulling speed on mechanical properties of pultruded kenaf fiber reinforced vinyl ester composites. *J Vinyl Addit Technol* 2018;24:E13–20. <https://doi.org/10.1002/vnl.21552>.
- [37] Safonov A, Gusev M, Saratov A, Konstantinov A, Sergeichev I, Konev S, et al. Modeling of cracking during pultrusion of large-size profiles. *Compos Struct* 2019;111801. <https://doi.org/10.1016/j.compstruct.2019.111801>.
- [38] Vedernikov AN, Safonov AA, Gusev SA, Carlone P, Tucci F, Akhatov IS. Spring-in experimental evaluation of L-shaped pultruded profiles. *IOP Conf Ser Mater Sci Eng* 2020;747. <https://doi.org/10.1088/1757-899X/747/1/012013>.
- [39] Al-Dhaheri M, Khan KA, Umer R, van Liemp F, Cantwell WJ. Process-induced deformation in U-shaped honeycomb aerospace composite structures. *Compos Struct* 2020;248. <https://doi.org/10.1016/j.compstruct.2020.112503>.
- [40] ASTM Standard. ASTM D6641/D6641M-16e1, Standard Test Method for Compressive Properties of Polymer Matrix Composite Materials Using a Combined Loading Compression (CLC) Test Fixture, ASTM International, West Conshohocken, PA; 2016.
- [41] Plastics – Determination of tensile properties – Part 5: Test conditions for unidirectional fibre-reinforced plastic composites. EN ISO 527-5:2009. n.d.
- [42] ASTM D790-03, Standard Test Methods for Flexural Properties of Unreinforced and Reinforced Plastics and Electrical Insulating Materials, ASTM International, West Conshohocken, PA; 2003.
- [43] ASTM D7078/D7078M - 12, Standard Test Method for Shear Properties of Composite Materials by V-Notched Rail Shear Method, ASTM International, West Conshohocken, PA; 2019.
- [44] ASTM D2344/D2344M-16, Standard Test Method for Short-Beam Strength of Polymer Matrix Composite Materials and Their Laminates, ASTM International, West Conshohocken, PA; 2016.
- [45] Worzakowska M. Kinetics of the curing reaction of unsaturated polyester resins catalyzed with new initiators and a promoter. *J Appl Polym Sci* 2006;102:1870–6. <https://doi.org/10.1002/app.24155>.
- [46] Nasonov Y, Safonov A, Gusev S, Akhatov I. Mathematical simulation the kinetics of polymerization of vinyl ester resin using in pultrusion. *IOP Conf Ser Mater Sci Eng* 2020;747:12010. <https://doi.org/10.1088/1757-899X/747/1/012010>.
- [47] Mohseni M, Zobeiry N, Fernlund G. Process-induced matrix defects: Post-gelation. *Compos Part A Appl Sci Manuf* 2020;137. <https://doi.org/10.1016/j.compositesa.2020.106007>.
- [48] Sumerak JE. Pultrusion Process Troubleshooting. *Handb. Troubl. Plast. Process. A Pract. Guid.* 2012. <https://doi.org/10.1002/9781118511183.ch20>.
- [49] Awaja F, Arhatari B, Wiesauer K, Leiss E, Stifter D. An investigation of the accelerated thermal degradation of different epoxy resin composites using X-ray microcomputed tomography and optical coherence tomography. *Polym Degrad Stab* 2009;94:1814–24. <https://doi.org/10.1016/j.polymdegradstab.2009.06.005>.

Chapter 7

Effects of high pulling speeds on mechanical properties and morphology of pultruded GFRP composite flat laminates

Vedernikov Alexander, Gemi Lokman, Madenci Emrah, Özkılıç Yasin Onuralp, Yazman Şakir, Gusev Sergey, Sulimov Artem, Bondareva Julia, Evlashin Stanislav, Konev Stepan, Akhatov Iskander, and Safonov Alexander. Effects of high pulling speeds on mechanical properties and morphology of pultruded GFRP composite flat laminates. *Composite Structures* 2022. DOI: [10.1016/j.compstruct.2022.116216](https://doi.org/10.1016/j.compstruct.2022.116216).

Contribution: I participated in the pultrusion experiment and was responsible for preparing specimens for mechanical testing, optical and scanning electron microscopy, and for Fourier-transform infrared (FTIR) and Raman spectroscopy. I was also responsible for performing optical and scanning electron microscopy experiments. I also performed the analysis of pultrusion experiments, mechanical tests, optical and scanning electron microscopy. I prepared most of the figures for this article and contributed to development of the original draft, final writing, and editing. I would like to thank all the authors for their valuable contributions to the development of this paper.



Effects of high pulling speeds on mechanical properties and morphology of pultruded GFRP composite flat laminates

Alexander Vedernikov^{a,*}, Lokman Gemi^b, Emrah Madenci^c, Yasin Onuralp Özkılıç^c, Şakir Yazman^d, Sergey Gusev^a, Artem Sulimov^a, Julia Bondareva^a, Stanislav Evlashin^a, Stepan Konev^a, Iskander Akhatov^a, Alexander Safonov^a

^a Skolkovo Institute of Science and Technology, Center for Materials Technologies, Moscow, Russia

^b Necmettin Erbakan University, Meram Vocational School, Konya, Turkey

^c Necmettin Erbakan University, Department of Civil Engineering, Konya, Turkey

^d Selçuk University, Ilgın Vocational School, Konya, Turkey

ARTICLE INFO

Keywords:

Pultrusion
Pulling speed
Mechanical properties
Matrix cracking
SEM analysis
Voids
Bubbles
GFRP composite

ABSTRACT

The economic efficiency of pultrusion can be significantly improved by operating the process at higher pulling speeds. This experimental study analyzed the relationships between the pulling speed, morphology, and mechanical properties of pultruded glass fiber/vinyl ester resin structural composites. Four batches of 150 mm × 3.5 mm flat laminates were produced at pulling speeds of 200, 600, 1000, and 1400 mm/min. Optical and scanning electron microscopy (SEM) were used to study the morphology of the produced flat laminates. The flexural and interlaminar shear properties were determined for both 0° and 90° fiber orientations. The observed difference in the mechanical characteristics of flat laminates can be explained by the presence of bubbles, longitudinal voids, and matrix cracks and by an increase in their density and dimensions with an increase in pulling speed. This study is the first one to demonstrate the possibility of high speed pultrusion of large cross-section profiles suitable for structural application. Authors were able to achieve the pulling speed of 1000 mm/min, increasing the output by as much as 1.7 times as compared to the regular speed pultrusion, without compromising significantly the mechanical performance of produced profiles. The results of this study would be of assistance for a better understanding of high-speed pultrusion.

1. Introduction

In the last decade, fiber-reinforced polymer (FRP) composites have been widely used in civil construction [1], transportation [2], and aerospace industries [3,4]. These materials offer multiple benefits such as a high strength-to-weight ratio [5], increased durability [6], fatigue resistance [7], excellent corrosion resistance [8], and ease of transportation, assembly, and maintenance [9]. There are various composite manufacturing processes, with pultrusion being one of the most efficient [10]. In the case of thermoset pultrusion, fiber reinforcement in the form of unidirectional fibers or fabric is pulled through an impregnating bath filled with a liquid polymer resin. Subsequently, the impregnated reinforcement pack is pulled through collimating plates to squeeze out the

excess resin and is fed into a heated forming die. The polymerized composite exits the forming die and is pulled by the pulling unit to a cutting saw, where the produced profile is cut to the desired length [10]. To optimize the production rate of the pultrusion process, an engineer should consider a multitude of factors that influence the structural performance of pultruded profiles, such as the choice of source materials [11], additives [12], pulling force [13], pulling speed [14–16], and heating conditions [17]. Application of polymer matrices with higher viscosity require longer time for the fibers' impregnation. Thus, lower pulling speeds are to be utilized for such matrices. Also, increase in the diameter of fibre reinforcement (i.e., linear density of the fibers) demands longer impregnation time [18], and, thus, choice of lower pulling speeds. On the other hand, the output of the pultrusion process can be

* Corresponding author.

E-mail addresses: aleksandr.vedernikov@skoltech.ru (A. Vedernikov), lgemi@erbakan.edu.tr (L. Gemi), emadenci@erbakan.edu.tr (E. Madenci), yozkilic@erbakan.edu.tr (Y. Onuralp Özkılıç), syazman@selcuk.edu.tr (Ş. Yazman), s.gusev@skoltech.ru (S. Gusev), a.sulimov@skoltech.ru (A. Sulimov), j.bondareva@skoltech.ru (J. Bondareva), s.evlashin@skoltech.ru (S. Evlashin), s.konev@skoltech.ru (S. Konev), i.akhatov@skoltech.ru (I. Akhatov), a.safonov@skoltech.ru (A. Safonov).

<https://doi.org/10.1016/j.compstruct.2022.116216>

Received 26 April 2022; Received in revised form 10 August 2022; Accepted 27 August 2022

Available online 11 September 2022

0263-8223/© 2022 Elsevier Ltd. All rights reserved.

significantly increased by running the process at higher pulling speeds; however, this should not compromise the structural performance of the profiles produced at such speeds.

Numerous experimental studies published over the last four decades have been dedicated to the analysis of pultrusion process performance, utilizing different types of resins, reinforcements, and pulling speeds. In 1984, Price and Cupschalk [19] studied the origin and magnitude of a pulling force arising during the pultrusion of carbon fiber/epoxy profiles at pulling speeds of 12.5, 25, and 50 mm/min. They demonstrated that a pulling speed corresponding to the highest pulling force ensured the highest quality of pultruded composite. Based on Patankar's method, Gorthala et al. [20] developed a numerical heat transfer model and successfully validated it through a series of experiments with fiberglass/epoxy and graphite/epoxy composites pultruded at 200 and 400 mm/min. Simultaneously, Lackey and Vaughan [21] conducted an experimental study of graphite/epoxy composites manufactured at 360 mm/min to understand the factors affecting the pulling force, such as the fiber volume fraction, pulling speed, and temperature regime. Subsequently, Ma et al. [22] investigated the dynamic mechanical properties of glass fiber/furfuryl alcohol and carbon fiber/furfuryl alcohol composites pultruded at pulling speeds of 500, 1000, and 1500 mm/min. They demonstrated that lower pulling speeds resulted in lower values of $\tan\delta$, although this can be increased by post-cure treatment. In a follow-up study [23], Ma et al. analyzed the mechanical properties of glass fiber/furfuryl alcohol composites pultruded at pulling speeds ranging from 400 to 1500 mm/min. The flexural strength and modulus increased with a decrease in the pulling speed. They also observed an improvement in the mechanical properties after the post-cure treatment. In 1996, Valliappan et al. [24] developed a model capable of predicting the temperature and degree of cure distributions at both the die and post-die stages of pultrusion. The results of the experiments with graphite/epoxy composites pultruded at speeds of 203, 305, and 406 mm/min correlated well with those predicted by the model. Kim et al. [25] developed another model and validated it through a series of pultrusion experiments using circular and rectangular profiles. They used glass-fiber rovings as a reinforcement and two resin formulations: epoxy (pulling speed ranging from 160 to 360 mm/min) and vinyl ester (pulling speed varying from 200 to 470 mm/min). Subsequently, a 3D model and its experimental validation were presented by Roux et al. [26], where they manufactured a glass fiber/epoxy I-beam profile at a pulling speed of 200 mm/min. Methven et al. [27] studied the microwave-assisted pultrusion of a 6-mm glass/epoxy cylindrical profile produced at pulling speeds in the range of 250–2000 mm/min. The tensile and interlaminar shear strengths were determined, and their increases after post-curing were recorded. Garland et al. [28] demonstrated that the mechanical properties of glass/vinyl ester profiles were not affected by pulling speed variations in the range of 100–300 mm/min. In an experimental study of glass/urea-formaldehyde pultruded composites, Chen et al. [29] observed an increase in the storage modulus caused by reduced pulling speeds of 200, 400, and 600 mm/min. Simultaneously, Sarrionandia et al. [30] developed a mathematical model to predict the influence of various process conditions, such as pulling speed, die temperature, laminate thickness, and fiber volume fraction, on the performance of a manufacturing process. Pultrusion experiments with glass/acrylic-urethane composites were performed at pulling speeds ranging from 100 to 800 mm/min, yielding good agreement with the numerical predictions. Freed [31] manufactured glass/vinyl ester profiles at pulling speeds of 100, 200, and 300 mm/min, and discovered a minor impact on the final value of the void fraction. Li et al. [32] pultruded vinyl ester-based composites reinforced with rovings and a continuous random mat at pulling speeds in the range of 300–1900 mm/min. In an attempt to produce blister-free composites, they determined the critical pulling speed. They also found that blister-free profiles manufactured at high pulling speeds exhibited poor mechanical characteristics. Yun and Lee [33] developed and experimentally validated a model to predict the influence of process variables on the occurrence of bubbles in glass/

phenolic composites. The profiles were pultruded at pulling speeds of 95, 190, 285, and 380 mm/min. It was shown that higher pulling speeds resulted in a larger bubble size and lower number of nucleated bubbles. In a follow-up study [34] where the same pulling speeds were used in the theoretical analysis, Yun and Lee developed a numerical model to predict the pulling force for pultruded phenolic foam composites. The authors also reported a relationship between the pulling speed and pulling force. To optimize the manufacturing process, Chen and Chen [35] performed pultrusion experiments with glass fiber/furfuryl alcohol composites. Among the four analyzed values of pulling speed (200, 400, 600, and 800 mm/min), only the lowest three were optimal. In 2015, Borges et al. [36] manufactured glass fiber/polyester rods at a pulling speed of 460 mm/min to better understand the correlation between the resin bath temperature and mechanical characteristics, namely, tensile strength, elastic modulus, and hardness. Chiang and Chen [37] produced glass-fiber-reinforced vinyl ester/nano-mica matrix composites at pulling speeds of 400, 500, 600, 700, and 800 mm/min and performed mechanical characterization of pultruded composites. The increase in pulling speed resulted in reduced flexural strength, notched Izod impact strength, flexural modulus, and hardness. Tena et al. [38] studied the influence of ultraviolet (UV) intensity and pulling speed on the performance of the UV-cured out of die bent pultrusion process. Glass/polyester composites were produced at pulling speeds of 105, 157, and 210 mm/min, and the optimum pulling speed was found to be 157 mm/min. Fairuz et al. [11] analyzed the effects of a micro-sized calcium carbonate filler on the mechanical characteristics (tensile, flexural, and compressive) of kenaf/vinyl ester pultruded rods with 10-mm diameter, produced at a pulling speed of 4000 mm/min. The results demonstrated that an increase in filler loading provokes an increase in mechanical characteristics. In a follow-up article [39], the authors studied the influence of pulling speed (which varied from 100 to 500 mm/min) on the mechanical properties of kenaf/vinyl ester composites and determined the optimum pulling speed for tensile, flexural, and compressive characteristics. In an attempt to optimize the pulling speed and temperature conditions and to understand the phenomenon of surface crack formation, Safonov et al. [40] performed an experimental and numerical study with a pultruded glass/epoxy rod 80 mm in diameter, manufactured at a pulling speed of 50 mm/min. Tucci et al. [41] developed a numerical model and performed pultrusion experiments with rectangular glass/epoxy profiles manufactured at pulling speeds of 300 and 500 mm/min. The number of voids in the pultruded composites was found to be affected by the pulling speed and injection pressure. Recently, Vedernikov et al. [14] analyzed the influence of pulling speed on spring-in, mechanical characteristics, and the appearance of cracks/delaminations in glass/vinyl ester L-shaped profiles manufactured at pulling speeds of 200, 400, and 600 mm/min. The authors found that the lower structural performance of the profiles produced at higher pulling speeds was caused by the polymerization peak shifting to the post-die region. In a follow-up studies [42–44], they developed a numerical model to predict spring-in distortions in L-shaped profiles pultruded at different pulling speeds. The possibility of spring-in reduction either by applying a post-die cooling tool or decreasing the chemical shrinkage of the resin was also demonstrated. Tucci et al. [45] performed an experimental and numerical study of injection pultrusion process of glass/epoxy rods at 100, 140, 180, and 220 mm/min pulling speeds aimed to analyze the value of pulling force. The authors observed an increase in the value of pulling force as well as the occurrence of voids and resin reach areas at higher pulling speeds.

Majority of those studies analyzed the pultrusion of small cross-section elements [19–21,25,28–30,33,34,38] and rods [24,36,39,45] produced at regular pulling speeds. The influence of pulling speed on mechanical properties and morphology of large cross-sections profiles suitable for structural applications (such as L-shape [14,31,42] and I-shape [26] beams, \varnothing 80 mm rods [40], and flat laminates [41]) was analyzed at regular pulling speeds not exceeding 600 mm/min. A small fraction of experimental studies dealing with high speed pultrusion

discussed production of small cross-section profiles such as \varnothing 6 mm [27] and \varnothing 10 mm [11] rods, and other elements [22,23,35,37]. Articles analyzing pulling speed arising during the pultrusion of glass fiber composites are summarized in Table 1. No studies of high speed pultrusion of large cross-section structural profiles have been conducted

Table 1
Articles analyzing pulling speed arising during the pultrusion of glass fiber composites.

Article	Reinforcement / matrix material	Pulling speed [mm/min]	Cross-section of manufactured composites	Fiber volume fraction [%]
Vedernikov et al. [14]	glass/vinyl ester	200, 400, 600	75 × 75 × 6 mm L-shaped profile	–
Gorthala et al. [20]	graphit/epoxy, glass/epoxy	200, 400	9-mm diameter rod	graphite – 64, glass – 50
Ma et al. [22]	glass/furfuryl alcohol, carbon/furfuryl alcohol	500, 1000, and 1500	12.7 × 3.29 mm rectangular profile	glass – 52 ÷ 62, carbon – 45 ÷ 56
Ma et al. [23]	glass/furfuryl alcohol	400 ÷ 1500	12.7 × 3.29 mm rectangular profile	–
Kim et al. [25]	glass/epoxy, glass/vinyl ester	epoxy – 160 ÷ 360, vinyl ester – 200 ÷ 470	6-mm diameter rod, 12 × 6 mm rectangular profile	rod – 50, rectangular – 55
Roux et al. [26]	glass/epoxy	200	63.5 × 63.5 mm I-shaped profile	34
Methven et al. [27]	glass/epoxy	250 ÷ 2000	6-mm diameter rod	60
Garland et al. [28]	glass/vinyl ester	100 ÷ 300	–	31 and 45
Lue et al. [29]	glass/urea–formaldehyde	200, 400, 600	12.7 × 3.19 mm, 12.7 × 2.08 mm rectangular profile	67.5, 70.4, 74.5
Sarrionandia et al. [30]	glass/acrylic-urethane	100 ÷ 800	90 × 3 mm rectangular profile	54
Freed [31]	glass/vinyl ester	100, 200, 300	76.2 × 76.2 × 9.53 mm L-shaped profile	47
Yun and Lee [33,34]	glass/phenolic	95, 190, 285, 380	20 × 10 mm rectangular profile	–
Chen and Chen [35]	glass/furfuryl alcohol	200, 400, 600, 800	12.7 × 3.19 mm, 12.7 × 2.08 mm rectangular profile	–
Borges et al. [36]	glass/polyester	460	13-mm diameter rod	–
Chiang and Chen [37]	glass/vinyl ester/nano-mica matrix	400, 500, 600, 700, 800	12.7 × 3.19 mm rectangular profile	67.5 ÷ 78
Safonov et al. [40]	glass/epoxy	50	80-mm diameter rod	65
Tucci et al. [41]	glass/epoxy	300, 500	60 × 5 mm rectangular profile	70
Tucci et al. [45]	glass/epoxy	100, 140, 180, 220	6-mm diameter rod	53

before. Moreover, no relationships have been established between high pulling speeds and structural performance of large cross-section composite profiles.

This experimental study of pultruded glass/vinyl ester structural composites aimed to establish the correlation between regular/high pulling speed and the morphology and mechanical properties of the pultruded composites. For this study, four batches of flat laminates (150 mm × 3.5 mm) were produced at pulling speeds of 200, 600, 1000, and 1400 mm/min using a Pultrex Px500–6 T pultrusion machine (Pultrex, UK). We used optical and scanning electron microscopy (SEM) to analyze the influence of regular and high pulling speeds on the morphology of the produced flat laminates, and Raman and Fourier-transform infrared (FTIR) spectroscopy to analyze the chemical homogeneity of the composite materials and study the influence of pulling speed on the material properties. The flexural and interlaminar shear properties were determined for both 0° and 90° fiber orientations. A relationship between the mechanical characteristics and values of the pulling speed chosen for this study was established. This study is the first one to demonstrate the possibility of high speed pultrusion of large cross-section profiles suitable for structural applications.

2. Materials and methods

2.1. Pultrusion experiments

All the flat laminates examined in this study were manufactured using a Pultrex Px500-6T (Pultrex, UK) pultrusion machine at the Laboratory of Composite Materials and Structures of the Center for Materials Technologies (Skolkovo Institute of Science and Technology, Moscow, Russia). The profiles had a rectangular cross-section with dimensions of 150 mm × 3.5 mm. Overall, 88 threads of unidirectional E-glass rovings PS 2100 (Owens Corning Composite Materials, USA) with a linear density of 9600 TEX (9600 g/1000 m) were used as reinforcements. The composition of the resin mixture is given in Table 2.

The die block had a length of 600 mm. The die block was heated with six 350-mm long heating platens installed at the bottom and top of the die. Two heating zones were used: one closer to the entrance and the other closer to the die exit. The allowed temperature ranges at these zones were set as 120 ± 5 °C and 135 ± 5 °C, respectively. To control these conditions, two thermocouples were embedded into the body of the die block. Pulling speeds of 200, 600, 1000, and 1400 mm/min were chosen to manufacture the flat laminates (Fig. 1). After the pultrusion process reached steady-state, 3-m long sections of the composite were manufactured at each pulling speed for further mechanical testing, optical and scanning microscopy analyses, FTIR, and Raman spectroscopy analyses. The laminates produced were marked according to the pulling speed used during pultrusion as follows: V–200 (200 mm/min), V–600 (600 mm/min), V–1000 (1000 mm/min), and V–1400 (1400 mm/min). Volume fraction of reinforcement in produced flat laminates constituted 63 %.

2.2. Optical and SEM analysis

The specimens were prepared and optical microscopy analysis was carried out at the Additive Manufacturing Laboratory of the Center for

Table 2
Components of the resin mixture.

Component	Amount [kg]
Atac 430 resin (DSM Composite Resins AG, Switzerland)	25.07
BYK-A555 (BYK Additives & Instruments, Germany)	0.075
BYK-W-996 (BYK Additives & Instruments, Germany)	0.25
Trigonox C (Akzo Nobel Polymer Chemicals B.V., The Netherlands)	0.38
Perkadox 16 (Akzo Nobel Polymer Chemicals B.V., The Netherlands)	0.13
Zinc Stearate (Baerlocher GmbH, Germany)	1.00

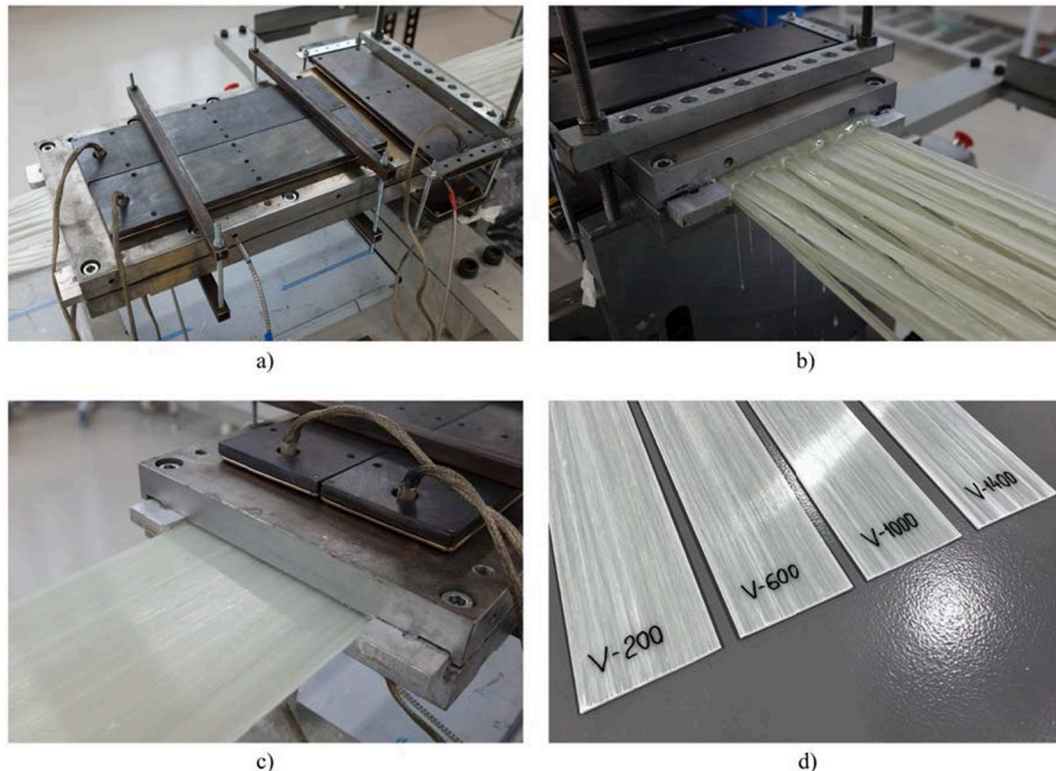


Fig. 1. Pultrusion manufacturing: (a) Die block during the pultrusion; (b) Impregnated fibers entering the die block; (c) Cured flat laminate exiting the die; (d) Flat laminates produced at pulling speeds of 200, 600, 1000, and 1400 mm/min.

Materials Technologies (Skolkovo Institute of Science and Technology, Moscow, Russia). The SEM analysis was performed at the Advanced Imaging Core Facility (Skolkovo Institute of Science and Technology, Moscow, Russia). A Zeiss Axio Scope.A1 (ZEISS Microscopy, Germany) optical microscope and Quattro S (Thermo Fisher Scientific, USA) scanning electron microscope were used for the analysis. The specimens (20-mm long) were cut from the laminates perpendicular to the reinforcement direction using a Struers Accutom 100 machine (Struers, USA). Two specimens, one for optical analysis and one for SEM analysis, were prepared for each pulling speed (V-200, V-600, V-1000, and V-1400), yielding eight specimens in total. The specimens were polished using a Metprep 3/PH-3 polisher (Allied High Tech Products, Inc., USA). The polished specimens were then cleaned with pressurized dry air, washed with pure water, and finally dried. To avoid charging the specimens during SEM analysis, a thin film of gold with a thickness of 10 nm was deposited on the specimens using a magnetron sputtering unit [46]. Because the profile section was symmetric, only half of the specimen was analyzed.

2.3. Raman spectroscopy

Raman scattering spectra were obtained using an inVia Qontor confocal Raman dispersive spectrometer (Renishaw plc, UK) at room temperature and an excitation wavelength of 532 nm from a frequency-doubled yttrium aluminum garnet (YAG) laser focused on the sample through a 50x objective lens to obtain a spot of 100–4000 cm^{-1} . The experiments were initiated at the minimum laser power density. The power density was then increased and the spectra from the same sample area were re-recorded. Bleaching mode was used for 120 s to amplify the signals and quench the possible fluorescence of the sample. All spectra were measured using a bulk composite material.

2.4. FTIR spectroscopy

To obtain FTIR spectra of pultruded composites we used a Nicolet iS50 FTIR spectrometer (Thermo Fisher Scientific, USA) and Attenuated Total Reflection (ATR) technique. Samples of produced pultruded profiles were ground into a fine powder by scratching material of their surfaces. This makes it possible to fit fine powder into the cell suitable for the ATR cell attachment and can reduce scattering losses and absorption band distortions caused by the presence of defects such as bubbles, longitudinal voids, and matrix cracks, present in pultruded profiles. Long-period scanning was used to ensure sufficient signal-to-noise ratio for the co-added spectrum to resolve the necessary peaks. Each spectrum was recorded in the range 400–4000 cm^{-1} .

2.5. Mechanical testing

All the mechanical tests were performed at the Mechanical Testing Laboratory of the Center for Materials Technologies (Skolkovo Institute of Science and Technology, Moscow, Russia). A Shtalmark M1-912 M/2 CNC milling machine (Rusintermash ltd., Russia) was used to cut the mechanical test specimens from the manufactured flat laminates. An Instron 5969 testing machine under control of Bluehill 3 (Instron, USA) software with a three-point bending WTF-EL-173 test fixture (Wyoming test fixtures, USA) were used to perform flexural and interlaminar shear testing in both 0° and 90° fiber orientations. Flexural testing was performed in accordance with ASTM D790-17 [47], and interlaminar shear testing in accordance with ASTM D2234-16 [48].

Specimen deflections were taken by the machine displacement measurement system. An initial run on a thick metallic specimen with assumed zero compliance had been undertaken which gave information about total machine and fixture compliance, which was then used in software-based compliance correction of individual specimens' deflections. This procedure is allowed by Appendix X1 of ASTM D790-17 [47]. Mechanical testing setup parameters are presented in Table 3.

Table 3
Mechanical testing setup parameters.

Test	Specimen thickness* [mm]	Specimen width* [mm]	Upper/support rollers' diameter [mm]	Support span (times average thicknesses)	Speed of test* [mm/min]
Flexure 0° fiber orientation	3.6	13	10/10	×32	6.8
Flexure 90° fiber orientation	3.6	13	10/10	×32	1.6
Interlaminar shear 0° and 90° fiber orientation	3.6	13	6/3	×4	1

* average values.

2.6. Analytical flexure solution

In this study, a static analysis of a first-order shear deformation beam model was conducted. The derivation of analytical equations to calculate displacements and stresses in pultruded composite flat laminates under flexural loading is presented in Appendix.

3. Results and discussion

3.1. Microscopy analysis results

Fig. 2 shows the cross-sectional microphotographs of the V-200 (Fig. 2a), V-600 (Fig. 2b), V-1000 (Fig. 2c), and V-1400 (Fig. 2d) specimens. Pultruded flat laminates were cut perpendicular to the pulling direction. Owing to the symmetry of the profile, only half of the

profile cross-section was considered. To combine the microphotographs into a photograph of the entire specimen, we used the Thixomet PRO software of a Zeiss Axio Scope.A1 optical microscope. Based on the optical microscopy results, at the given scale, the V-200, V-600, and V-1000 specimens demonstrated no difference in terms of longitudinal voids. However, two severe longitudinal voids were observed in the V-1400 specimen (Fig. 2e, d).

Currently, particular emphasis is placed on damage analysis to better understand the influence of process parameters on the morphology of composite materials during manufacturing and mechanical testing [49–53]. Damage analysis and the detection of longitudinal voids, imperfect bonding, bubbles, blisters, and matrix cracks occurring during the process are important for the proper selection of process parameters and process optimization [54–57]. Here, we present the results of damage analysis based on SEM images of cross-sections of pultruded composite laminates fabricated at pulling speeds of V-200 (see Fig. 3), V-600 (see Fig. 4), V-1000 (see Fig. 5), and V-1400 (see Fig. 6).

Minor bubbles, blisters, and voids can be observed in the V 200 specimen (see Fig. 3). These discontinuities are trapped between the fibers, and their dimensions are smaller than the diameter of the fibers. The distribution of fibers is close to homogenous, and the resin-rich regions are smaller than those of the V-600, V-1000, and V-1400 specimens. No imperfect bonding or matrix cracks can be observed in the specimen.

In the V-600 specimen (see Fig. 4), we can observe an increased number of bubbles, blisters, and voids. The defects are distributed homogeneously over the cross-section of the specimen (see Fig. 4a, b). The size of the defects is larger than the diameter of the fibers, and the resin-rich regions are more prominent than in the V-200 specimen.

In the V-1000 specimen (see Fig. 5), the number and dimensions of these defects are further increased compared with those in the V-200 and V-600 specimens. Resin-rich regions are concentrated at certain locations, and the defects in some of these regions merge and grow in the

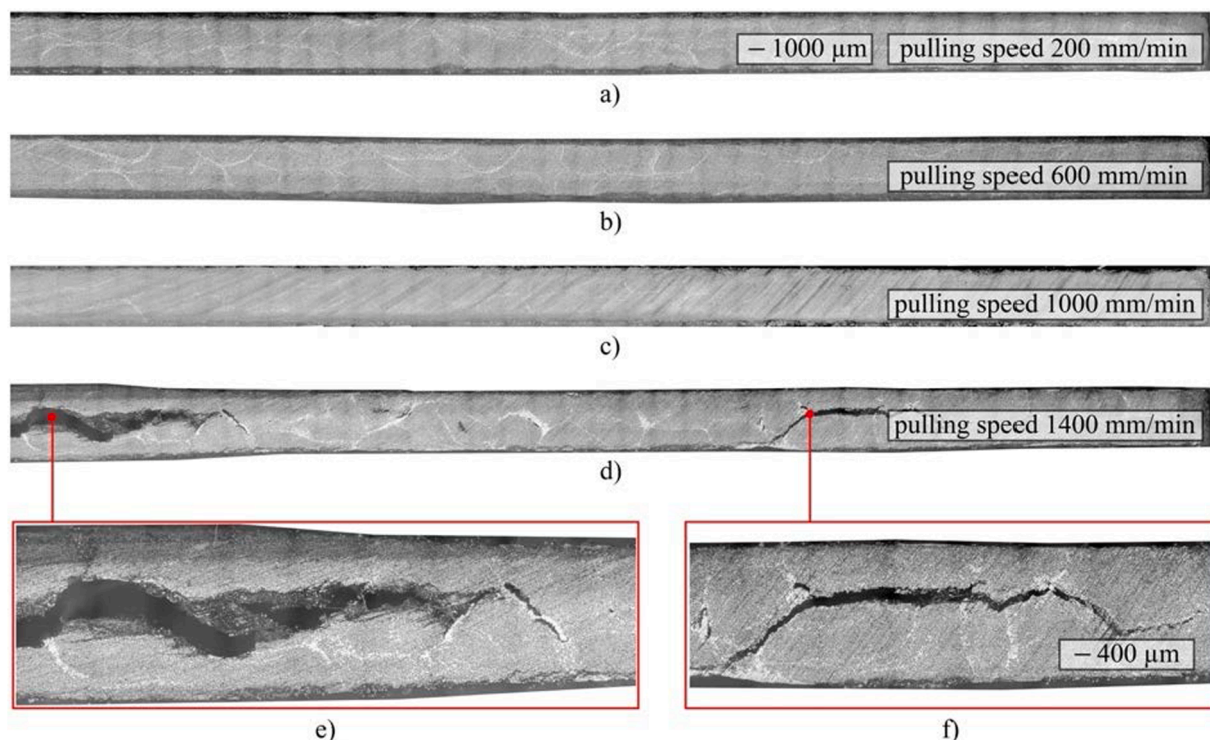


Fig. 2. Cross-section microphotographs of the V-200, V-600, V-1000, and V-1400 specimens cut perpendicular to the pulling direction: (a) Microphotograph of V-200 specimen. Scale bar = 1000 µm; (b) Microphotograph of V-600 specimen. Scale bar = 1000 µm; (c) Microphotograph of V-1000 specimen. Scale bar = 1000 µm; (d) Positions of the longitudinal voids in V-1400 specimen. Scale bar = 1000 µm; (e) Positions of the longitudinal voids in V-1400 specimen. Scale bar = 400 µm; (f) Positions of the longitudinal voids in V-1400 specimen. Scale bar = 400 µm.

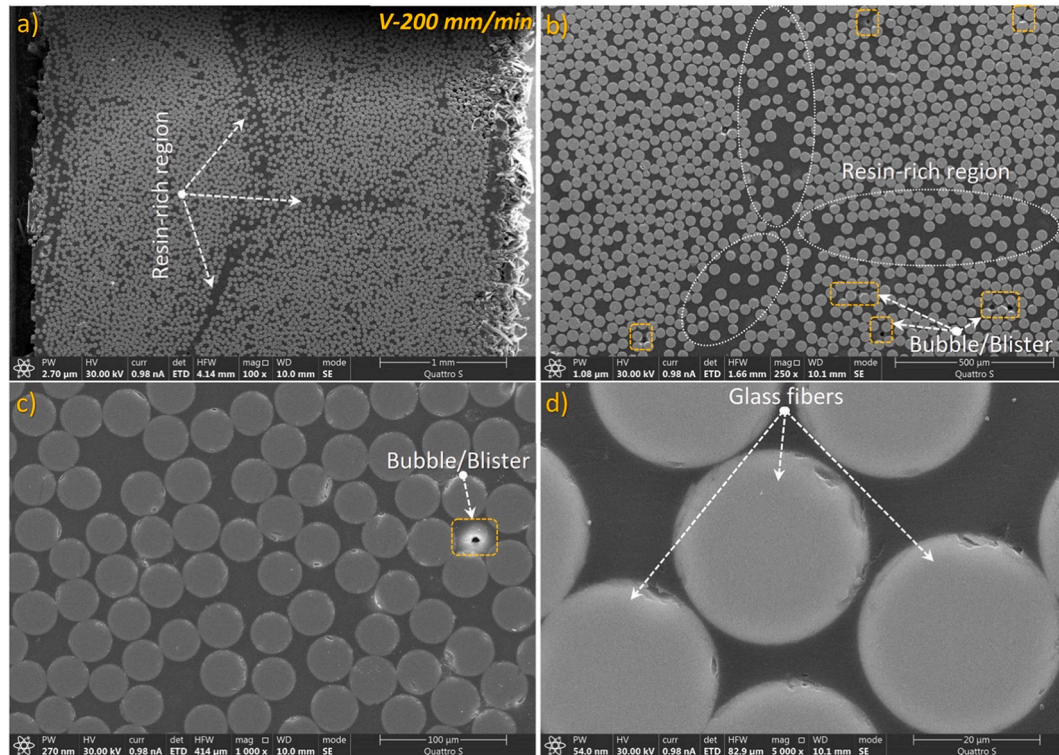


Fig. 3. SEM images of the V-200 laminate cross-section cut perpendicular to the pulling direction: (a) The entire cross-section of the composite and resin-rich regions at 100x magnification; (b) Resin-rich regions and bubbles and blisters at 250x magnification; (c) Glass fibers and bubble/blister at 1000x magnification; (d) Glass fibers at 5000x magnification.

pulling (i.e., fiber) direction. Compared with the V-200 and V-600 specimens, discontinuities in the V-1000 specimen occur at the fiber–matrix interface, resulting in imperfect bonding (see Fig. 5e).

In the V-1400 specimen (see Fig. 6) pultruded at the maximum pulling speed of a 1400 mm/min all common defects, such as longitudinal voids, imperfect bonding, bubbles, blisters, and matrix cracks, can be observed [33]. However, in contrast to the specimens manufactured at other pulling speeds, we can observe the formation of imperfect bonding areas (see Fig. 6e). In some cases, the fiber–matrix interface cannot form at all, and in other cases, despite the initial formation, the interface is destroyed owing to the effect of continuing polymerization (see Fig. 6g, h). Large bubbles/blisters/voids are distributed over the laminate cross-section, and large defects in the middle of the cross-section combine to form longitudinal voids of different patterns (see Fig. 6d). These longitudinal voids are located in the middle of the uni-directional roving layer and propagate deeper in the direction of pultrusion, damaging the entire structure of the V-1400 composite laminate (see Fig. 6f). We can also observe matrix cracks that merge and propagate from the surface of the composite laminate toward its center, where they connect with the longitudinal voids (see Fig. 6a, c).

At high pulling speeds (1000 and 1400 mm/min) glass fiber rovings are pulled through the impregnation bath much faster than in case of pulling speeds of 200 and 600 mm/min. Consequently, the resin has less time to penetrate the rovings. This results in poor impregnation of rovings and formation of air inclusions and dry spots, which, in turn, causes formation of internal defects significantly impairing structural performance of pultruded composites [58]. Moreover, at high pulling speeds the polymerization peak shifts to the post-die region as there is less time for the composite to polymerize within the die block boundaries. Thus, a considerable part of the polymerization process occurs under unconstrained conditions. This results in the formation of severe internal defects (longitudinal voids and matrix cracks) owing to the chemical and thermal shrinkage of the unconstrained composite. The increase in the dimensions, severity, and propagation of internal defects

can also be attributed to the expansion of air bubbles initially trapped in a composite [59]. The evaporation of styrene gas, i.e., unreacted styrene monomer, observed at the die block exit region during high speed pultrusion process, may cause severe longitudinal voids and branched matrix cracks in the V-1400 profiles. Conversely, at regular pulling speeds (200 and 600 mm/min), resin has more time to properly impregnate fiber reinforcement, and air inclusions are significantly less frequent than in case of high pulling speeds. This reduces the number of internal defects formed during pultrusion process. Besides, the rigid contact constraints of the die block where the polymerization peak occurs prevent excess profile distortions and formation of severe internal defects.

Internal defects formed during high-speed pultrusion significantly affect the mechanical performance of the composite laminates (see Figs. 9 and 10 and Table 4). Thus, the considerably larger standard deviation of certain mechanical parameters of the V-1400 specimens (Table 4), compared with those of the V-200/V-600/V-1000 specimens, clearly demonstrates the influence of internal defects on the structural performance of the composite laminates. It has been observed that the main damage modes [60–65], such as imperfect bonding, matrix cracks, and longitudinal voids, typically occurring in composite structures produced with different geometries during service or after experimental studies, can also occur as a result of inappropriate process parameters (such as a high pulling speed of 1400 mm/min).

3.2. Raman spectroscopy results

The wavenumbers of peaks in Raman spectra are characteristic of the active chemical groups of analyzed substances (Fig. 7). Each substance has its own unique Raman spectrum and position of the peak [66]. The Raman bands corresponding to C–O–C stretch lie in the range of 1000–1280 cm^{-1} , which corresponds to the results obtained by Hassan et al. [67]. The peak at 920 cm^{-1} corresponds to the ester group (O–C(O)–C). The peak around 1400 cm^{-1} corresponds to CH₃ deformation,

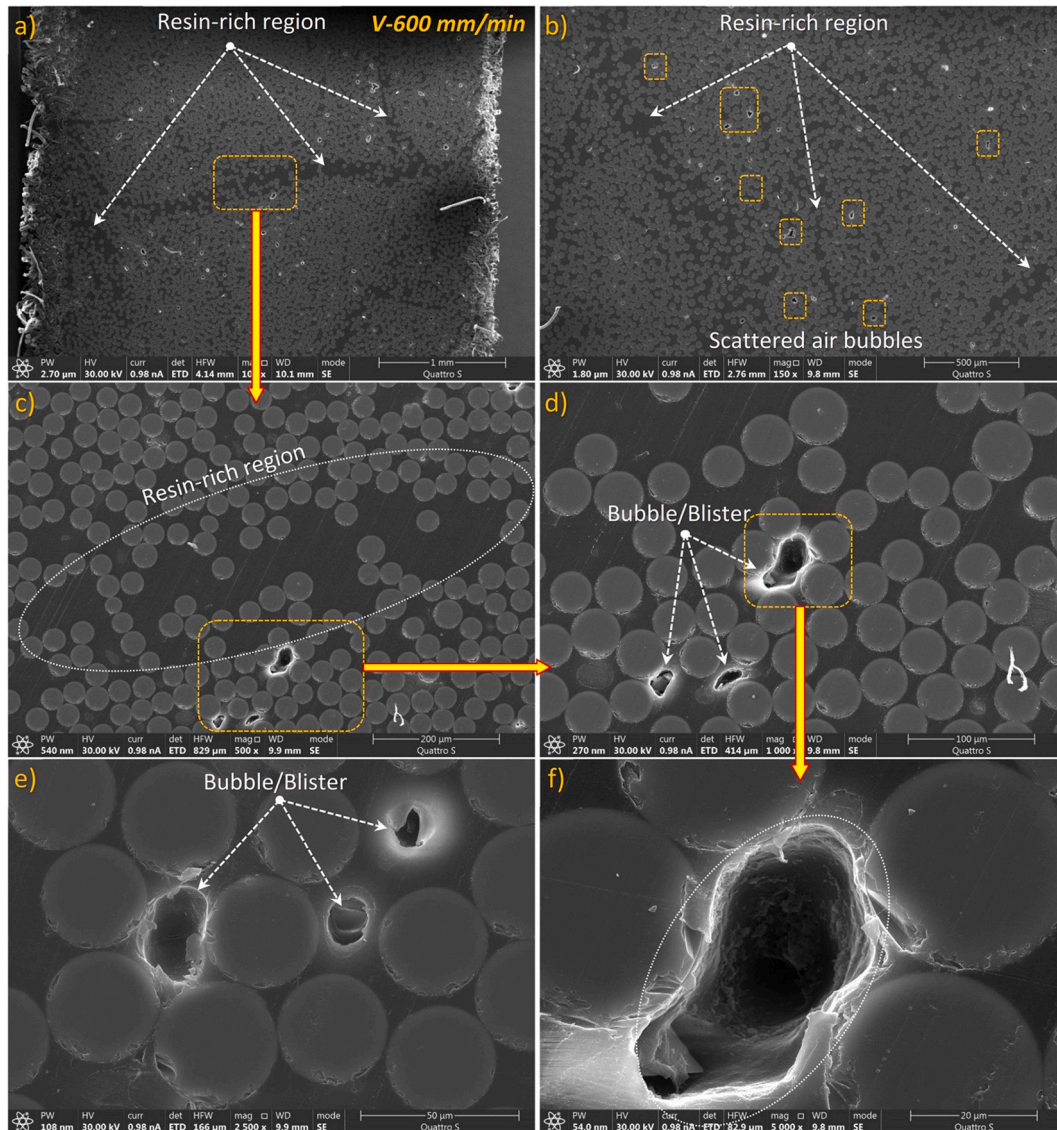


Fig. 4. SEM images of the V-600 laminate cross-section cut perpendicular to the pulling direction: (a) The entire cross-section of the composite and resin-rich regions at 100x magnification; (b) Resin-rich regions and scattered air bubbles at 150x magnification; (c) Resin-rich region and bubbles/blisters at 500x magnification; (d) Bubbles/blisters at 1000x magnification; (e) Glass fibers and bubbles/blisters at 2500x magnification; (f) Bubble/blister at 5000x magnification.

and weak intensity peak at 1780 cm^{-1} corresponds to $\text{C}=\text{O}$ stretching.

Other Raman peaks observed at 840 and 1680 cm^{-1} , corresponding to the resin phenyl ring backbone vibrations, do not change in intensity during the curing reaction [68]. A broad Raman peak at 2500 cm^{-1} corresponding to the hardener used [69,70] was observed in V-200 specimen. At this pulling speed, resin and hardener come into contact and form a strong network. However, an apparent reduction in the intensity of the Raman peak at 2500 cm^{-1} can be observed with an increase in pulling speed. The signals observed in the range $2877\text{--}3100\text{ cm}^{-1}$ in all studied samples can also be detected by FTIR spectroscopy and assigned to symmetric and asymmetric vibrations of the aromatic and methyl (C-H) groups [71].

3.3. FTIR spectroscopy results

As compared to Raman spectroscopy results, chemical composition determined by FTIR spectroscopy shows no differences between analyzed materials (Fig. 8). In fact, the spectra are very similar, indicating a similar chemical composition, which may be due to the preparation of samples by grinding. Absorption bands characteristic of

$\text{C}=\text{O}$ groups can be observed at 825 cm^{-1} . Weak bands at 1590 , 1500 , and 1483 cm^{-1} observed in the spectrum of the cured composite can be assigned to the aromatic ring [72]. The two intense bands observed at 905 cm^{-1} and 1121 cm^{-1} , attributed to C-O stretching vibrations, do not change their position in the spectrum. The band at 3060 cm^{-1} can be assigned to the symmetric stretching of the C-H aromatic groups. The bands at $2960\text{--}2870\text{ cm}^{-1}$ are attributed to alkyl units (C-H and -CH_2) stretching, whereas the band at 1607 cm^{-1} can be assigned to C=C stretching of the aromatic ring. The bands at 1509 , 1236 , and 1036 cm^{-1} can be assigned to C-C stretching of the aromatic ring, -C-C-O-C stretching, and C-O-C stretching of ethers, respectively [73–75].

In this study, the bisphenol A based vinyl ester resin (Atlas 430) dissolved in styrene has been used as a matrix. Such composition provides resistance to many aggressive chemical environments and, due to its heat resistance, makes the resin suitable for use in environments with periodic temperature increases. The curing of resin systems involves several chemical reactions that occur either simultaneously or at different stages of the curing process, depending on the reactivity of the components and processing temperatures. To catalyze the process, we used the system of co-initiators — Triganox C for crosslinking with

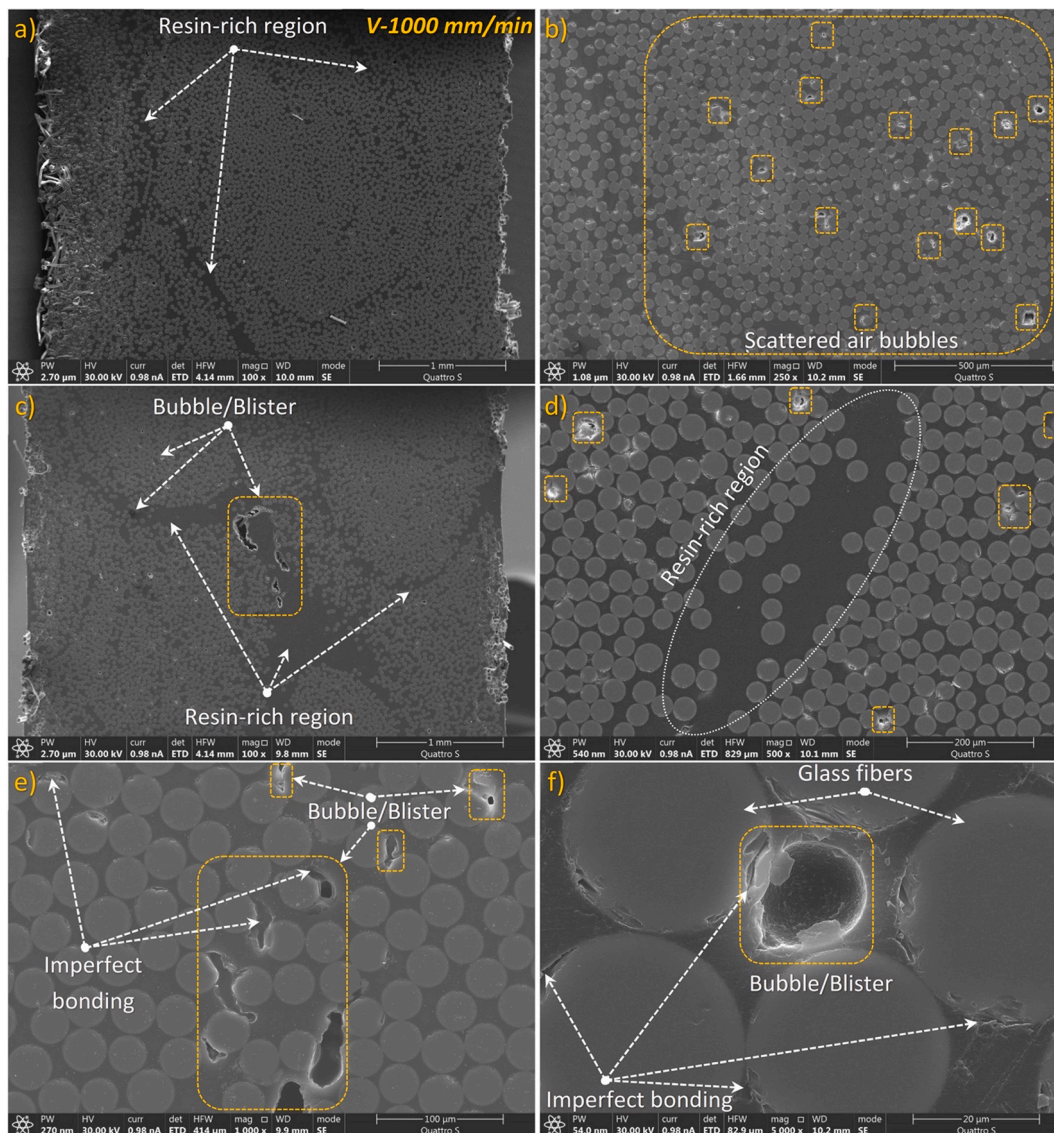


Fig. 5. SEM images of the V-1000 laminate cross-section cut perpendicular to the pulling direction: (a) The entire cross-section of the composite and resin-rich regions at 100x magnification; (b) Scattered air bubbles at 250x magnification; (c) The entire cross-section of the composite, resin-rich regions, and bubbles/blisters at 100x magnification; (d) Resin-rich region and bubbles/blisters at 500x magnification; (e) Glass fibers, imperfect bonding, and bubbles/blisters at 1000x magnification; (f) Glass fibers and bubbles/blisters at 5000x magnification.

styrene monomer, and Percadox 16 for vinyl ester polymerization and further interaction with a silanol groups on the surface of glass fibers.

Despite the similarity of the FTIR spectra in terms of the main characteristic bands, a change in the area of the IR bands of some active functional groups was observed in samples produced at different pulling speeds. It indicates differences in reaction rates of the polymer chain growth, observed at different pulling speeds. Thus, for a wide absorption band in the range from 905 cm^{-1} and 1121 cm^{-1} , present in all samples obtained at different pulling speeds (V-200, V-600, V-1000 and V-1400), different peak densities can be observed, and increase in pulling speed results in decrease in peak densities and in the degree of cure observed during pultrusion.

3.4. Mechanical test results

The results of the flexural and interlaminar shear tests are listed in Table 4. The results demonstrate that the mechanical characteristics of pultruded laminates depend heavily on the pulling speed. When the tests were performed in a 0° fiber orientation, an increase in pulling speed

from V to 200 to V-600, V-1000, and V-1400 resulted in a decrease in flexural strength by 12.7 %, 16.9 %, and 25.9 %, respectively, and a reduction in the tangent modulus of elasticity by 2.96 %, 4.56 %, and 7.36 %, respectively. In the case of the 90° fiber orientation, the increase in the pulling speed from V to 200 to V-600 and V-1000 resulted in a decrease in flexural strength by 4.12 % and 8.20 %, along with a reduction in the tangent modulus of elasticity by 20.21 % and 21.72 %, respectively. For the flexural tests in the 90° fiber orientation, the V-1400 specimens demonstrated values of strength and tangent modulus of elasticity that were one order of magnitude lower than those exhibited by the V-200, V-600, and V-1000 specimens. The growth of pulling speed not only gives rise to bonding imperfections, or large voids, but also increases the possibility of fiber breaking during pultrusion. It explains the decrease in flexural strength and tangent modulus of elasticity at 0° fiber orientation at higher pulling speeds, while the effects of matrix imperfection are not significant. In contrast, at 90° fiber orientation, internal defects play a greater role than the fibers, thus, explaining significant decrease in flexural strength and tangent modulus of elasticity for V-1400 profile. The interlaminar

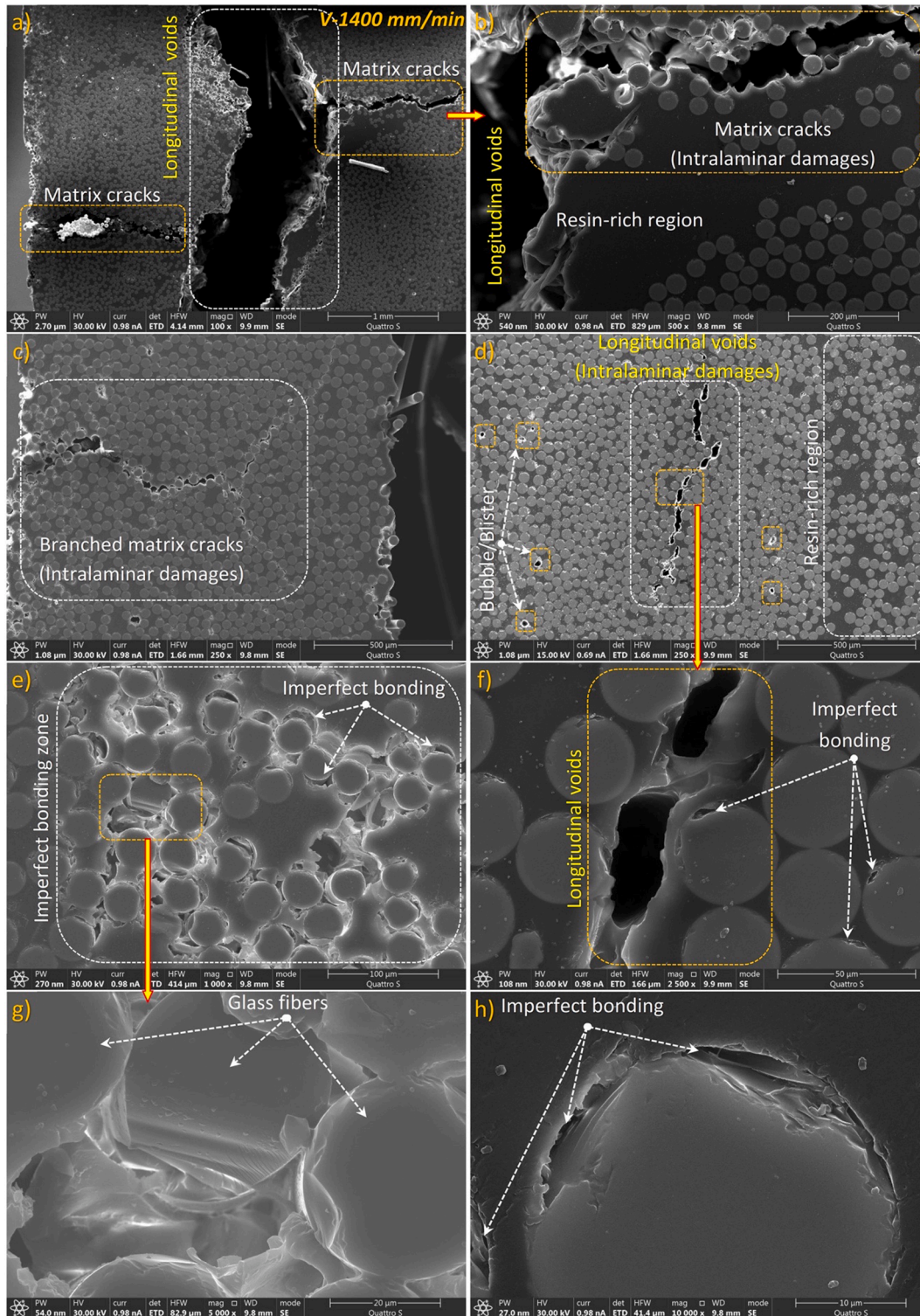


Fig. 6. SEM images of cross-section of the V-1400 flat laminate cut perpendicular to the pulling direction: (a) The entire cross-section of the composite. Matrix cracks and longitudinal voids at 100x magnification; (b) Matrix cracks, longitudinal voids, and resin-rich region at 500x magnification; (c) Branched matrix crack at 250x magnification; (d) Scattered bubbles/blisters, longitudinal voids, and resin-rich region at 250x magnification; (e) Imperfect bonding zone at 1000x magnification; (f) Longitudinal voids and imperfect bonding at 2500x magnification; (g) Glass fibers at 5000x magnification; (h) Imperfect bonding at 10000x magnification.

fracture toughness at the maximum load for the V-600, V-1000, and V-1400 specimens with 0° fiber orientation was found to be lower than that of the V-200 specimens by 4.51 %, 15.6 %, and 22.8 %, respectively. In the interlaminar shear tests of specimens with a 90° fiber orientation, the reduction in the short beam strength for the V-600, V-1000, and V-1400 specimens constituted 20 %, 21.8 %, and 56 %,

respectively, when compared with the V-200 specimens. It should also be noted that an increase in pulling speed resulted in greater variability in the mechanical parameters being studied.

The flexural load–displacement curves are shown in Figs. 9 and 10. The tested specimens of the V-200 profiles exhibited similar behaviors. However, with an increase in pulling speed, we observed a significant

Table 4
Results of the mechanical tests in flexure and interlaminar shear.

Specimen	Flexure						Interlaminar shear											
	0° fiber orientation			90° fiber orientation			0° fiber orientation			90° fiber orientation								
	Strength [MPa]			Tangent modulus of elasticity [GPa]			Strength [MPa]			Interlaminar fracture toughness at maximum load [MPa]								
	Mean	σ	CV* [%]	Mean	σ	CV [%]	Mean	σ	CV [%]	Mean	σ	CV [%]						
V-200	1473	54	3.7	51.78	1.46	2.81	23.49	1.94	8.25	14.57	1.08	7.41	37.10	2.04	5.49	3.12	0.29	9.34
V-600	1307	141	10.8	50.29	2.87	5.71	22.56	1.68	7.45	12.12	0.62	5.11	35.50	2.44	6.88	2.60	0.51	19.63
V-1000	1260	193	15.3	49.52	4.06	8.20	21.71	2.23	10.28	11.97	0.37	3.09	32.10	3.73	11.60	2.56	0.55	21.35
V-1400	1170	463	39.6	48.23	5.83	12.08	2.24	1.03	46.07	0.34	0.30	85.80	30.20	4.00	13.23	2.00	0.54	27.19

* CV: coefficient of variation.

increase in the scatter of mechanical testing results for specimens of the particular batch. Under flexural loading in the 0° fiber orientation, the maximum difference in flexural capacity was 6 %, 18 %, 26 %, and 59 % for the V-200, V-600, V-1000 and V-1400 specimens, respectively. However, some specimens exhibited similar flexural capacities, regardless of the pulling speed. This suggests that the defects formed in the specimens do not propagate continuously over the cross-section of a composite laminate. However, longitudinal voids and matrix cracks can significantly affect the flexural capacity when present in a specimen being tested. Because pultruded profiles represent long structural elements, the defects shown in Fig. 2 and discontinuities in the fiber reinforcement may result in catastrophic consequences. In the future the authors intend to analyse the influence of pulling speed on the mechanical properties of full-scale engineering structures. Similar results were obtained for specimens with 90° fiber orientation.

Table 5 shows the displacements and stresses in composite laminates under flexural loading in 0° and 90° fiber orientations, obtained via solution of the analytical equations described in Appendix. The obtained load values are valid for the elastic region shown in Figs. 9 and 10. The elastic moduli were obtained for the elastic region visible in Figs. 9 and 10. The results of the analytical solution presented here agree well with the experimental results given in Table 4.

In their previous work [76] the authors of this study have performed mechanical testing of glass fiber/epoxy-based 150 mm × 3.5 mm flat laminates produced at 200 mm/min pulling speed. The same number of unidirectional rovings was used to produce these flat laminates. Flexural properties in 0° fiber orientation were close to those obtained in the current study, while flexural properties in 90° fiber orientation as well as interlaminar shear properties were significantly higher. Despite of the same pulling speed and number of unidirectional rovings, difference in the mechanical properties might be attributed to the difference in the utilized resin and additives as well as heating regime. Thus, within the current study the allowed temperature ranges at the first and the second zones were set as 120 ± 5 °C and 135 ± 5 °C, while in [76] 180 ± 5 °C and 200 ± 5 °C were set. In the latter case it ensures faster polymerization and, therefore, less possibilities for the occurrence of the internal defects, that, in turn affect the mechanical properties of the pultruded profiles. The analysis of the combined influence of polymer resin and additives, pulling speed and heating regime on the mechanical performance of the pultruded profiles is planned to be performed in the future works.

FRP composites, that are widely used in transportation and aerospace applications, require specific attention from the fatigue point of view. The occurrence of manufacturing-induced defects might also jeopardize fatigue performance of pultruded profiles. Therefore, the authors plan to investigate the relationship between pulling speed and fatigue characteristics of the pultruded structural profiles in their future works. Also, the authors intend to perform an experimental study revealing the influence of additives on the choice of pulling speed and structural properties of pultruded profiles [12]. Methods of non-destructive testing for inline quality monitoring of the profiles pultruded at high pulling speeds are to be investigated deeper as well. The influence of fiber breakage and internal defects on the mechanical properties of pultruded profiles manufactured at high pulling speeds is to be further studied by means of X-ray computed tomography [77].

4. Conclusions

This study investigated the relationships between the pulling speed, morphology, and mechanical properties of pultruded glass fiber/vinyl ester structural composites. Four batches of 150 mm × 3.5 mm flat laminates were produced at pulling speeds of 200, 600, 1000, and 1400 mm/min. The relationship between the pulling speed and flexural and interlaminar shear properties of pultruded profiles at 0° and 90° fiber orientations was determined in accordance with the relevant ASTM standards. An analysis of the damage in the cross-sections of the

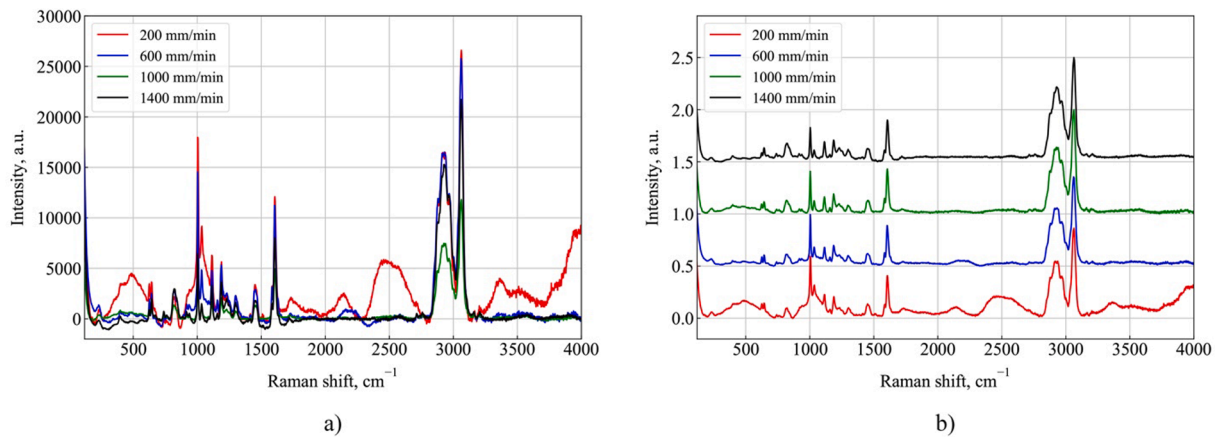


Fig. 7. Raman spectroscopy results: (a) Raman spectra of V-200, V-600, V-1000, and V-1400 specimens irradiated at 532 nm without any separation of the curves; (b) Raman scattering spectra (all the spectra are shifted vertically for the sake of clarity).

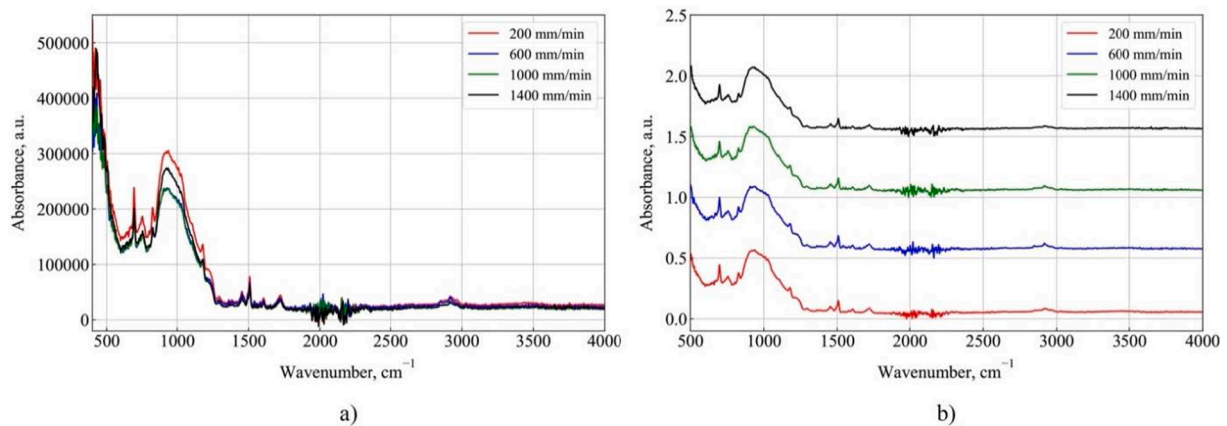


Fig. 8. FTIR spectroscopy results: (a) FTIR spectra of V-200, V-600, V-1000, and V-1400 specimens; (b) FTIR spectra (all the spectra are shifted vertically for the sake of clarity).

composite profiles manufactured at different pulling speeds was performed using optical and scanning electron microscopes. Bubbles, longitudinal voids, matrix cracks, and their structure, density, and dimensions were studied as a function of the pulling speed. Raman and FTIR spectroscopy were used to study the chemical uniformity and variation in the properties of the flat laminates.

The resin curing mechanism consists of styrene monomers copolymerization and chain growth via successive addition of vinyl monomers. Due to the presence of the band corresponding to formation of a strong network between the resin and hardener, the Raman spectra show differences between specimens produced at pulling speeds of 200 mm/min and those produced at 600, 1000 and 1400 mm/min. According to the FTIR spectroscopy results, for a wide absorption band in the range of 905 cm^{-1} to 1121 cm^{-1} , a difference in peak area can be used to determine the degree of curing/crosslinking of the resin.

We show that increasing the pulling speed significantly affected the morphology and mechanical properties of the composites. The size, number, and density of bubbles, blisters, and voids increased with an increase in pulling speed from 200 mm/min to 600 mm/min and further to 1000 mm/min. Unlike other specimens, those manufactured at a pulling speed of 1400 mm/min exhibited all major defects, such as longitudinal voids, imperfect bonding, bubbles, blisters, and matrix cracks. In the case of flat laminates manufactured at 1400 mm/min, the polymerization process could not be completed within the die block boundaries and continued outside the die block. Polymerization outside the die block boundary resulted in macrodefects in the geometry of

various parts of this specimen. An increase in the time required for the polymerization of the composite exiting the forming die resulted in an increased number and severity of internal defects. The results of the mechanical tests showed that the increased number and severity of process-induced defects caused by the increased pulling speed impaired the mechanical performance of the profiles. The effect of such defects, particularly in the matrix component of the composite, was more evident in the flexural testing of the specimen in the 90° fiber orientation.

This work pioneers the use of high pulling speeds (1000 mm/min) to produce pultruded composite profiles of large cross-section, suitable for structural applications. We demonstrated that high speed pultrusion makes it possible to increase pultrusion output by at least 1.7 times without compromising the mechanical performance of produced profiles as compared to their regular speed produced counterparts.

CRediT authorship contribution statement

Alexander Vedernikov: Investigation, Software, Data curation, Visualization, Writing – original draft, Writing – review & editing. **Lokman Gemi:** Software, Data curation, Visualization, Writing – original draft, Writing – review & editing. **Emrah Madenci:** Software, Data curation, Visualization, Writing – original draft, Writing – review & editing. **Yasin Onuralp Özkılıç:** Software, Data curation, Visualization, Writing – original draft, Writing – review & editing. **Şakir Yazman:** Software, Data curation, Visualization, Writing – original draft, Writing

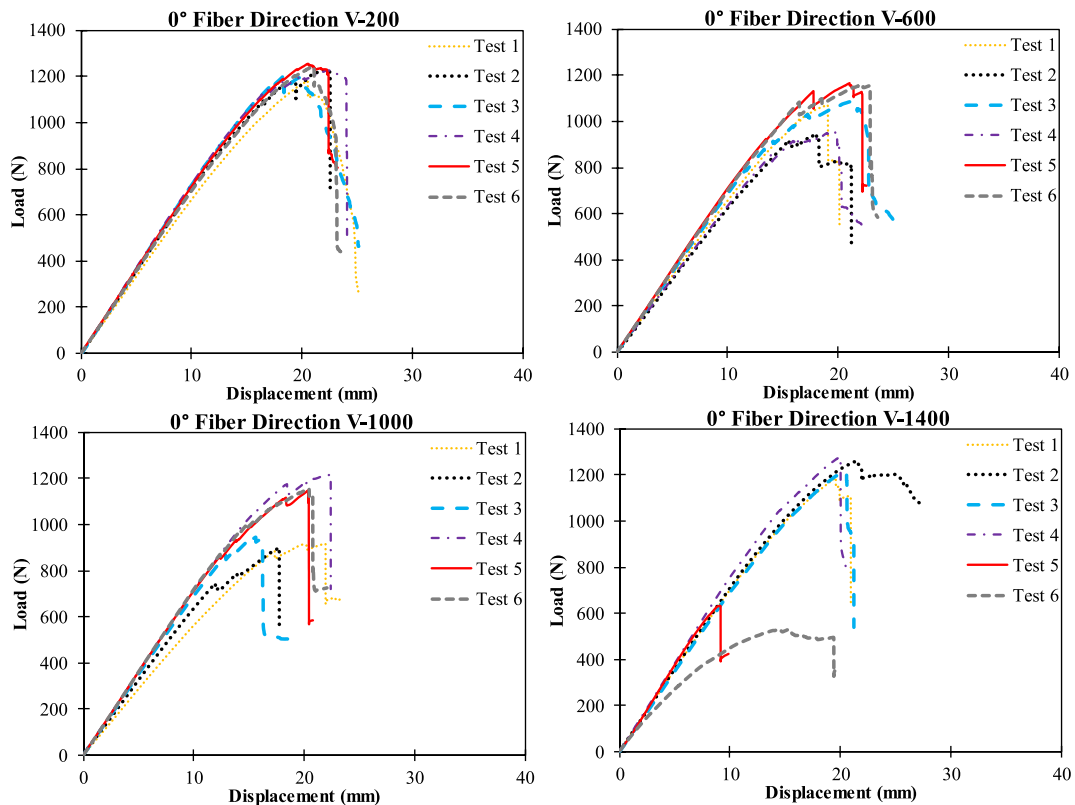


Fig. 9. Flexural load–displacement curves in flexural testing of composite laminates in 0° fiber orientation: (a) V–200 profile; (b) V–600 profile; (c) V–1000 profile; (d) V–1400 profile.

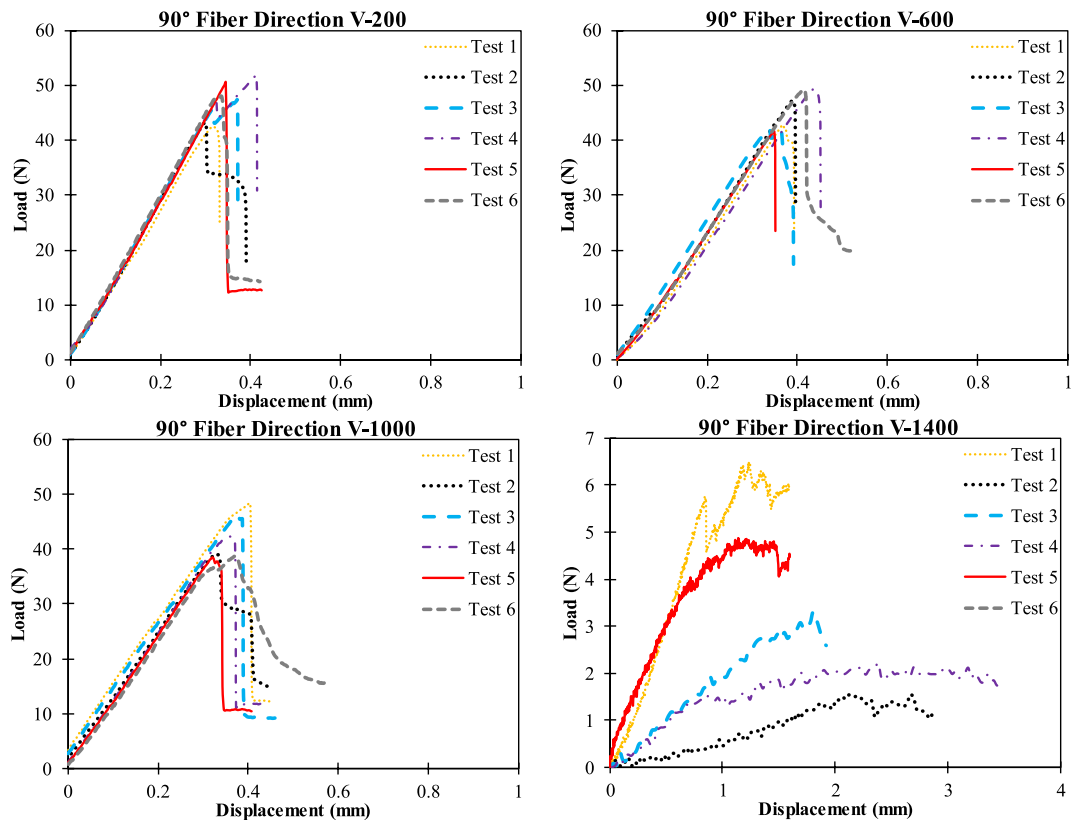


Fig. 10. Flexural load–displacement curves in flexural testing of composite laminates in 90° fiber orientation: (a) V–200 profile; (b) V–600 profile; (c) V–1000 profile; (d) V–1400 profile.

Table 5
Results of the analytical solutions.

Specimen	Load (N)	0°		90°		
		Displacement (mm)	Normal Stress (MPa)	Load (N)	Displacement (mm)	Normal Stress (MPa)
V-200	1191	17.99	1247.81	50.6	0.35	25
V-600	1006.8	15.21	1054.82	49.9	0.25	24
V-1000	956.98	14.56	1002.63	48	0.4	24.5
V-1400	930	19.05	973.56	4	0.8	2.6

– review & editing. **Sergey Gusev**: Investigation, Resources. **Artem Sulimov**: Investigation, Writing – original draft. **Julia Bondareva**: Investigation, Writing – original draft. **Stanislav Evlashin**: Investigation, Writing – original draft. **Stepan Konev**: Investigation, Writing – review & editing. **Iskander Akhatov**: Project administration, Funding acquisition. **Alexander Safonov**: Supervision, Conceptualization, Writing – original draft, Writing – review & editing.

Declaration of Competing Interest

The authors declare that they have no known competing financial interests or personal relationships that could have appeared to influence the work reported in this paper.

Appendix

In this study, a static analysis of a first-order shear deformation beam model was conducted. In the first-order shear deformation beam theory based on the displacement field, the kinematic displacement relations are defined as follows [78]:

$$\begin{aligned}
 u(x, z, t) &= u_0(x, t) + z\phi_x(x, t) \\
 w(x, z, t) &= w_0(x, t)
 \end{aligned}
 \tag{1}$$

where u_0 and w_0 are the axial and transverse displacements in the midplane of the beam, respectively, and t is the time. Rotations about the y axes are denoted by ϕ_x . According to the first-order shear deformation theory, the transverse normals do not remain perpendicular to the midsurface after deformation [79,80]. This theory violates the zero-shear stress conditions on the top and bottom surfaces of the beam and assumes a uniform transverse shear stress distribution through the beam thickness coordinate [81].

The linear strains associated with the displacement field are obtained as follows:

$$\begin{aligned}
 \epsilon_{xx} &= \frac{\partial u_0}{\partial x} + z \frac{\partial \phi_x}{\partial x} \\
 \gamma_{xz} &= \frac{\partial w_0}{\partial x} + \phi_x
 \end{aligned}
 \tag{2}$$

According to the first-order shear deformation theory, the ϵ_{xx} strain is linear through the laminate thickness, while the transverse shear strain, γ_{xz} , is constant through the thickness of the laminate. The strain can be expressed as follows:

$$\begin{Bmatrix} \epsilon_{xx} \\ \gamma_{xz} \end{Bmatrix} = \begin{Bmatrix} \epsilon_{xx}^{(0)} \\ \gamma_{xz}^{(0)} \end{Bmatrix} + z \begin{Bmatrix} \epsilon_{xx}^{(1)} \\ \gamma_{xz}^{(1)} \end{Bmatrix} = \begin{Bmatrix} \frac{\partial u_0}{\partial x} \\ \frac{\partial w_0}{\partial x} + \phi_x \end{Bmatrix} + z \begin{Bmatrix} \frac{\partial \phi_x}{\partial x} \\ 0 \end{Bmatrix}
 \tag{3}$$

To obtain the governing equations for the composite beam, the expression for the dynamic version of the virtual displacements can be written as follows [82]:

$$0 = \int_0^T (\delta U + \delta V - \delta K)
 \tag{4}$$

where the initial and final times are defined as $T = t_2 - t_1$. In addition, the virtual strain energy δU , virtual work δV performed by applied forces, and virtual kinetic energy δK are given by.

$$\delta U = \int_{\Omega_0} \left\{ \int_{-h/2}^{h/2} [\sigma_{xx}(\delta \epsilon_{xx}^{(0)} + z \delta \epsilon_{xx}^{(1)}) + \tau_{xz} \delta \gamma_{xz}^{(0)}] dz \right\} dx
 \tag{5}$$

$$\delta V = - \int_{\Omega_0} [q \delta w_0] dx - \int_{\Gamma_e} [\hat{\sigma}_m (\delta u_n + z \delta \phi_n) + \hat{\tau}_{nz} \delta w_0] dz
 \tag{6}$$

$$\delta K = \int_{\Omega_0} \int_{-h/2}^{h/2} \rho_0 \left[(\dot{u}_0 + z \dot{\phi}_x) (\delta \dot{u}_0 + z \delta \dot{\phi}_x) + \dot{w}_0 \delta \dot{w}_0 \right] dz dx
 \tag{7}$$

By substituting $\delta U, \delta V$, and δK from Eqs. (5–7) into the virtual statement in Eq. (4), and integrating the thickness of the laminate, we obtain the

following equation:

$$0 = \int_0^T \left\{ \int_{\Omega_0} \left[\begin{array}{c} N_{xx} \delta e_{xx}^{(0)} + M_{xx} \delta e_{xx}^{(1)} + Q_x \delta \gamma_{xz}^{(0)} - q \delta w_0 \\ -I_0 (\dot{u}_0 \delta \dot{u}_0 + \dot{w}_0 \delta \dot{w}_0) - I_1 (\dot{\phi}_x \delta \dot{u}_0 + \delta \dot{\phi}_x \dot{u}_0) - I_2 (\dot{\phi}_x \delta \dot{\phi}_x) \\ - \int_{\Gamma_e} (\hat{N}_{nn} \delta u_n + \hat{M}_{nn} \delta \phi_n + \hat{Q}_n \delta w_0) ds \end{array} \right] dx \right\} dt \tag{8}$$

where $I_i (i = 0, 1, 2)$ is the mass moment of inertia given by.

$$I_i = \int_{-h/2}^{h/2} \rho(z) z^i dA \quad (i = 0, 1, 2) \tag{9}$$

Here, N_{xx} , M_{xx} , and Q_x are the stress results in terms of the normal force, bending moment, and shear force, respectively. Hence, the integration of stresses through the laminate thickness requires lamina-wise integration [83]. All the stress resultants are defined as follows:

$$N_{xx} = \int_{-h/2}^{h/2} \sigma_{xx} dz = \sum_{k=1}^N \int_{z_k}^{z_{k+1}} \sigma_{xx} dz \tag{10a}$$

$$M_{xx} = \int_{-h/2}^{h/2} \sigma_{xx} z dA = \sum_{k=1}^N \int_{z_k}^{z_{k+1}} \sigma_{xx} z dA \tag{10b}$$

$$Q_x = k_s \int_{-h/2}^{h/2} \tau_{xz} dA = k_s \sum_{k=1}^N \int_{z_k}^{z_{k+1}} \tau_{xz} dA \tag{10c}$$

Parameter k_s is called the shear correction factor and is taken as 5/6.

The Euler–Lagrange equations are obtained by setting the coefficients of δu_0 , δw_0 , and $\delta \phi_x$ in Ω_0 to zero:

$$\delta u_0 : \frac{\partial N_{xx}}{\partial x} = I_0 \frac{\partial^2 u_0}{\partial t^2} + I_1 \frac{\partial^2 \phi_x}{\partial t^2} \tag{11a}$$

$$\delta w_0 : \frac{\partial Q_x}{\partial x} + q = I_0 \frac{\partial^2 w_0}{\partial t^2} \tag{11b}$$

$$\delta \phi_x : \frac{\partial M_{xx}}{\partial x} - Q_x = I_2 \frac{\partial^2 \phi_x}{\partial t^2} + I_1 \frac{\partial^2 u_0}{\partial t^2} \tag{11c}$$

Because the laminate is composed of several orthotropic layers with their material axes oriented arbitrarily with respect to the laminate coordinates, the constitutive equations for each layer must be transformed to the laminate coordinates. The normal and shear stresses, when transformed to laminate coordinates, can be expressed as follows [84]:

$$\sigma_{xx}^{(k)} = \bar{Q}_{11}^{(k)} \epsilon_{xx} \tag{12a}$$

$$\tau_{xz}^{(k)} = \bar{Q}_{55}^{(k)} \gamma_{xz} \tag{12b}$$

where.

$$\bar{Q}_{11} = Q_{11} \cos^4 \theta + 2(Q_{12} + 2Q_{66}) \sin^2 \theta \cos^2 \theta + Q_{22} \sin^4 \theta \tag{13a}$$

$$\bar{Q}_{55} = Q_{44} \sin^2 \theta + Q_{55} \cos^2 \theta \tag{13b}$$

The coefficient Q_{ij} in terms of the engineering constants of the k^{th} layer can be expressed as follows:

$$\begin{aligned} Q_{11}^{(k)} &= \frac{E_1}{1 - \nu_{12}\nu_{21}}; & Q_{12}^{(k)} &= \frac{\nu_{12}E_2}{1 - \nu_{12}\nu_{21}} = \frac{\nu_{21}E_1}{1 - \nu_{12}\nu_{21}}; \\ Q_{22}^{(k)} &= \frac{E_2}{1 - \nu_{12}\nu_{21}}; & Q_{44}^{(k)} &= G_{23}; & Q_{55}^{(k)} &= G_{13}; \\ & & Q_{66}^{(k)} &= G_{12} \end{aligned} \tag{14}$$

By substituting Eqs. (12a–b) into Eqs. (10a–c), the constitutive equations can be expressed as follows:

$$N_{xx} = A_{11} \frac{\partial u_0}{\partial x} + B_{11} \frac{\partial \phi_x}{\partial x} \tag{15a}$$

$$M_{xx} = B_{11} \frac{\partial u_0}{\partial x} + D_{11} \frac{\partial \phi_x}{\partial x} \tag{15b}$$

$$Q_x = k_s \left[A_{55} \frac{\partial w_0}{\partial x} + \phi_x \right] \tag{15c}$$

where D_{11} denotes the bending stiffness, B_{11} denotes the bending-extensional coupling stiffness, and A_{11} and A_{55} denote the extensional stiffnesses, which are defined as follows:

$$(A_{ij}, B_{ij}, D_{ij}) = \int_{-h/2}^{h/2} \bar{Q}_{ij}(1, z, z^2) dz = \sum_{k=1}^N \int_{z_k}^{z_{k+1}} \bar{Q}_{ij}^{(k)}(1, z, z^2) dz \quad (16)$$

The equations of motion can be expressed in terms of displacements by substituting the force and moment resultants [85].

$$A_{11} \frac{\partial^2 u_0}{\partial x^2} + B_{11} \frac{\partial^2 \phi_x}{\partial x^2} = I_0 \frac{\partial^2 u_0}{\partial t^2} + I_1 \frac{\partial^2 \phi_x}{\partial t^2} \quad (17a)$$

$$B_{11} \frac{\partial^2 u_0}{\partial x^2} + D_{11} \frac{\partial^2 \phi_x}{\partial x^2} - k_s A_{55} \left(\frac{\partial w_0}{\partial x} + \phi_x \right) = I_1 \frac{\partial^2 u_0}{\partial t^2} + I_2 \frac{\partial^2 \phi_x}{\partial t^2} \quad (17b)$$

$$k_s A_{55} \left(\frac{\partial^2 w_0}{\partial x^2} + \frac{\partial \phi_x}{\partial x} \right) + \frac{\partial}{\partial x} \left(N_{xx} \frac{\partial w_0}{\partial x} \right) + q = I_0 \frac{\partial^2 w_0}{\partial t^2} \quad (17c)$$

For bending analysis, Eqs. (17a–c) are reduced to.

$$k_s G_{xz} b h \left(\frac{d^2 w_0}{dx^2} + \frac{d\phi_x}{dx} \right) + \hat{q} = 0 \quad (18a)$$

$$E_{xx} I_{yy} \frac{d^2 \phi_x}{dx^2} - k_s G_{xz} b h \left(\frac{dw_0}{dx} + \phi_x \right) = 0 \quad (18b)$$

$$\hat{q} = bq$$

By integrating Eqs. (18a–b) with respect to x , the following equation is obtained:

$$k_s G_{xz} b h \left(\frac{dw_0}{dx} + \phi_x \right) = - \int_0^x \hat{q}(\xi) d\xi + C_1 \quad (19)$$

Substituting these results into Eqs. (18a–b) and integrating with respect to x leads to [85]:

$$E_{xx} I_{yy} \frac{d\phi_x}{dx} = - \int_0^x \int_0^\eta \hat{q}(\xi) d\xi d\eta + C_1 x + C_2 \quad (20a)$$

$$E_{xx} I_{yy} \phi_x(x) = - \int_0^x \int_0^\zeta \int_0^\eta \hat{q}(\xi) d\xi d\eta d\zeta + C_1 \frac{x^2}{2} + C_2 x + C_3 \quad (20b)$$

Substituting $\phi_x(x)$ from Eq. (20b) into Eq. (19) [85] yields.

$$\frac{dw_0}{dx} = - \frac{1}{E_{xx} I_{yy}} \left[- \int_0^x \int_0^\zeta \int_0^\eta \hat{q}(\xi) d\xi d\eta d\zeta + C_1 \frac{x^2}{2} + C_2 x + C_3 \right] + \frac{1}{k_s G_{xz} b h} \left[- \int_0^x \hat{q}(\xi) d\xi + C_1 \right] \quad (21a)$$

$$w_0(x) = - \frac{1}{E_{xx} I_{yy}} \left[- \int_0^x \int_0^\zeta \int_0^\eta \int_0^\mu \hat{q}(\xi) d\xi d\mu d\eta d\zeta + C_1 \frac{x^3}{6} + C_2 \frac{x^2}{2} + C_3 x + C_4 \right] + \frac{1}{k_s G_{xz} b h} \left[- \int_0^x \int_0^\xi \hat{q}(\zeta) d\zeta d\xi + C_1 x \right] \quad (21b)$$

where the constants of integration C_1 and C_4 can be determined using boundary conditions. Considering a simply supported beam with a center-point load, known as the three-point bending test, the boundary conditions of the problem are given as follows:

$$w_0(0) = 0; \quad \frac{dw_0}{dx}(L/2) = 0 \quad (22)$$

References

- [1] Bakis CE, Bank LC, Brown VL, Cosenza E, Davalos JF, Lesko JJ, et al. Fiber-Reinforced Polymer Composites for Construction—State-of-the-Art Review. *J Compos Constr* 2002;6(2):73–87.
- [2] Ferdous W, Manalo A, AlAjarmeh O, Mohammed AA, Salih C, Yu P, et al. Static behaviour of glass fibre reinforced novel composite sleepers for mainline railway track. *Eng Struct* 2021;229:111627.
- [3] Vedernikov A, Safonov A, Tucci F, Carlone P, Akhatov I. Pultruded materials and structures: A review. *J Compos Mater* 2020;54:4081–117. <https://doi.org/10.1177/0021998320922894>.
- [4] Safonov AA, Carlone P, Akhatov I. Mathematical simulation of pultrusion processes: A review. *Compos Struct* 2018;184:153–77. <https://doi.org/10.1016/j.compstruct.2017.09.093>.
- [5] Zhang D, Mo C, Gao Y, Yuan H, Li F, Zhao Q, et al. Theoretical evaluation of the equivalent torsional rigidity of a unique GFRP-metal box-truss composite girder. *Structures* 2022;36:781–92.
- [6] Liao K, Schultheisz CR, Hunston DL. Effects of environmental aging on the properties of pultruded GFRP. *Compos Part B Eng* 1999;30:485–93. [https://doi.org/10.1016/S1359-8368\(99\)00013-X](https://doi.org/10.1016/S1359-8368(99)00013-X).
- [7] McBagonluri F, Garcia K, Hayes M, Verghese K, Lesko J. Characterization of fatigue and combined environment on durability performance of glass/vinyl ester composite for infrastructure applications. *Int J Fatigue* 2000;22:53–64. [https://doi.org/10.1016/S0142-1123\(99\)00100-0](https://doi.org/10.1016/S0142-1123(99)00100-0).
- [8] Feng P, Wang J, Wang Y, Loughery D, Niu D. Effects of corrosive environments on properties of pultruded GFRP plates. *Compos Part B Eng* 2014;67:427–33. <https://doi.org/10.1016/j.compositesb.2014.08.021>.
- [9] Minchenkov K, Vedernikov A, Safonov A, Akhatov I. Thermoplastic pultrusion: A review. *Polymers (Basel)* 2021;13:1–36. <https://doi.org/10.3390/polym13020180>.
- [10] Starr TF, editor. Pultrusion for engineers. Woodhead Publishing Limited; 2000.
- [11] Fairuz AM, Sapuan SM, Zainudin ES, Jaafar CNA. Effect of filler loading on mechanical properties of pultruded kenaf fibre reinforced vinyl ester composites. *J Mech Eng Sci* 2016;10(1):1931–42.
- [12] Vedernikov A, Nasonov Y, Korotkov R, Gusev S, Akhatov I, Safonov A. Effects of additives on the cure kinetics of vinyl ester pultrusion resins. *J Compos Mater* 2021;55:2921–37. <https://doi.org/10.1177/00219983211001528>.
- [13] Li S, Xu L, Ding Z, Lee LJ, Engelen H. Experimental and theoretical analysis of pulling force in pultrusion and resin injection pultrusion (RIP) - Part I: Experimental. *J Compos Mater* 2003;37:163–89. <https://doi.org/10.1106/002199803028676>.

- [14] Vedernikov A, Tucci F, Carlone P, Gusev S, Konev S, Firsov D, et al. Effects of pulling speed on structural performance of L-shaped pultruded profiles. *Compos Struct* 2021;255:112967.
- [15] Alajarmeh O, Zeng X, Aravinthan T, et al. Compressive behaviour of hollow box pultruded FRP columns with continuous-wound fibres. *Thin-Wall Struct* 2021;168:108300. <https://doi.org/10.1016/j.tws.2021.108300>.
- [16] Vedernikov A, Tucci F, Safonov A, Carlone P, Gusev S, Akhatov I. Investigation on the shape distortions of pultruded profiles at different pulling speed. *Procedia Manuf* 2020;47:1–5. <https://doi.org/10.1016/j.promfg.2020.04.107>.
- [17] Silva FJG, Ferreira F, Costa C, Ribeiro MCS, Meira Castro AC. Comparative study about heating systems for pultrusion process. *Compos B Eng* 2012;43(4):1823–9.
- [18] Ma H, Li Y, Shen Y, Xie L, Wang D. Effect of linear density and yarn structure on the mechanical properties of ramie fiber yarn reinforced composites. *Compos Part A Appl Sci Manuf* 2016;87:98–108. <https://doi.org/10.1016/j.compositesa.2016.04.012>.
- [19] Price HL, Cupschalk SG. Pulling force and its variation in composite materials pultrusion. In: Dae HC, editor. *Adv. Chem. Ser.*, ACS, Washington, DC, USA; 1984, p. 301–22.
- [20] Gorthala R, Roux JA, Vaughan JG, Donti RP. Comparison of processing parameters for pultruded graphite/epoxy and fiberglass/epoxy: A heat transfer and curing model. *J Reinf Plast Compos* 1994;13:288–300. <https://doi.org/10.1177/073168449401300401>.
- [21] Lackey E, Vaughan JG. An Analysis of Factors Affecting Pull Force for the Pultrusion of Graphite/Epoxy Composites. *J Reinf Plast Compos* 1994;13:188–98. <https://doi.org/10.1177/073168449401300301>.
- [22] Ma CC, Yn M, Han J, Chang C, Wu H. Pultruded fibre-reinforced furfuryl alcohol resin composites: 2. Static, dynamic mechanical and thermal properties. *Compos Manuf* 1995;6:53–8. [https://doi.org/10.1016/0956-7143\(95\)93713-T](https://doi.org/10.1016/0956-7143(95)93713-T).
- [23] Ma CCM, Yn MS, Han JL, Chang CJ, Wu HD. Pultruded fibre-reinforced furfuryl alcohol resin composites: 1. Process feasibility study *Compos Manuf* 1995;6:45–52. [https://doi.org/10.1016/0956-7143\(95\)93712-S](https://doi.org/10.1016/0956-7143(95)93712-S).
- [24] Valliappan M, Roux JA, Vaughan JG, Arafat ES. Die and post-die temperature and cure in graphite/epoxy composites. *Compos Part B Eng* 1996;27:1–9. [https://doi.org/10.1016/1359-8368\(95\)00001-1](https://doi.org/10.1016/1359-8368(95)00001-1).
- [25] Kim D-H, Han P-G, Jin G-H, Lee WI. A model for thermosetting composite pultrusion process. *J Compos Mater* 1997;31:2105–22. <https://doi.org/10.1177/002199839703102005>.
- [26] Roux JA, Vaughan JG, Shanku R, Arafat ES, Bruce JL, Johnson VR. Comparison of measurements and modeling for pultrusion of a fiberglass/epoxy I-beam. *J Reinf Plast Compos* 1998;17:1557–78. <https://doi.org/10.1177/073168449801701705>.
- [27] Methven JM, Ghaffariyan SR, Abidin AZ. Manufacture of fiber-reinforced composites by microwave assisted pultrusion. *Polym Compos* 2000;21:586–94. <https://doi.org/10.1002/pc.10214>.
- [28] Garland CA, Gupta RK, Gangarao HVS, Zondlo JW. Effect of Manufacturing Process Conditions on the Durability of Pultruded Vinyl Ester / Glass Composites 2000: 136.
- [29] Chen C-H, Lue J-Y, Yen C-C. In situ pultrusion of urea-formaldehyde matrix composites. I. Processability, kinetic analysis, and dynamic mechanical properties. *J Appl Polym Sci* 2002;83(6):1242–51.
- [30] Sarrionandia M, Mondrago I, Moschiar SM, Reboredo MM, Vazquez A. Heat transfer for pultrusion of a modified acrylic/glass reinforced composite. *Polym Compos* 2002;23:21–7. <https://doi.org/10.1002/pc.10408>.
- [31] Freed AD. Modeling the pultrusion process to obtain low void fraction composites. *West Virginia University*; 2002.
- [32] Li S, Ding Z, Xu L, Lee LJ, Engelen H. Influence of heat transfer and curing on the quality of pultruded composites. I: Experimental. *Polym Compos* 2002;23:947–56. <https://doi.org/10.1002/pc.10492>.
- [33] Yun MS, Lee WI. Analysis of bubble nucleation and growth in the pultrusion process of phenolic foam composites. *Compos Sci Technol* 2008;68(1):202–8.
- [34] Yun MS, Lee WI. Analysis of pulling force during pultrusion process of phenolic foam composites. *Compos Sci Technol* 2008;68:140–6. <https://doi.org/10.1016/j.compscitech.2007.05.032>.
- [35] Chen C-H, Chen I-K. The unidirectional glass fiber reinforced furfuryl alcohol for pultrusion. II. Correlation of processing parameters for optimizing the process. *J Appl Polym Sci* 2011;119:1788–96. <https://doi.org/10.1002/app.32879>.
- [36] Borges SG, Ferreira CA, Andrade JM, Preveldello ALA. The influence of bath temperature on the properties of pultruded glass fiber reinforced rods. *J Reinf Plast Compos* 2015;34(15):1221–30.
- [37] Chiang C-L, Chen C-H. In situ pultrusion of vinyl ester/nano-mica matrix composites: Process feasibility and process parameters. *J Reinf Plast Compos* 2016; 35:1554–65. <https://doi.org/10.1177/0731684416659931>.
- [38] Tena I, Sarrionandia M, Torre J, Aurrekoetxea J. The effect of process parameters on ultraviolet cured out of die bent pultrusion process. *Compos Part B Eng* 2016; 89:9–17. <https://doi.org/10.1016/j.compositesb.2015.11.027>.
- [39] Fairuz AM, Sapuan SM, Zainudin ES, Jaafar CNA. The effect of pulling speed on mechanical properties of pultruded kenaf fiber reinforced vinyl ester composites. *J Vinyl Addit Technol* 2018;24:E13–20. <https://doi.org/10.1002/vnl.21552>.
- [40] Safonov A, Gusev M, Saratov A, Konstantinov A, Sergeichev I, Konev S, et al. Modeling of cracking during pultrusion of large-size profiles. *Compos Struct* 2020; 235:111801.
- [41] Tucci F, Bezerra R, Rubino F, Carlone P. Multiphase flow simulation in injection pultrusion with variable properties. *Mater Manuf Process* 2020;35(2):152–62.
- [42] Vedernikov A, Safonov A, Tucci F, Carlone P, Akhatov I. Modeling Spring-In of L-Shaped Structural Profiles Pultruded at Different Pulling Speeds. *Polymers* 2021;13(16):2748.
- [43] Vedernikov A, Safonov A, Gusev S, Carlone P, Tucci F, Akhatov I. Spring-in experimental evaluation of L-shaped pultruded profiles. *IOP Conf Ser: Mater Sci Eng* 2020;747(1):012013.
- [44] Vedernikov A, Safonov A, Tucci F, Carlone P, Akhatov I. Analysis of spring-in deformation in L-shaped profiles pultruded at different pulling speeds: Mathematical simulation and experimental results. In: Paper presented at ESAFORM 2021. 24th International Conference on Material Forming; 2021. 4743/1–4743/10. <https://doi.org/10.25518/esaform21.4743>.
- [45] Tucci F, Larrea-Wachtendorff D, Ferrari G, Carlone P. Pulling force analysis in injection pultrusion of glass/epoxy composites. *Mater Manuf Process* 2022;1–12. <https://doi.org/10.1080/10426914.2022.2049296>.
- [46] Khmel'nitsky RA, Evlashin SA, Martovitsky VP, Pastchenko PV, Dagesian SA, Alekseev AA, et al. Heteroepitaxy of Ni-Based Alloys on Diamond. *Cryst Growth & Des* 2016;16(3):1420–7.
- [47] ASTM D790-17, Standard Test Methods for Flexural Properties of Unreinforced and Reinforced Plastics and Electrical Insulating Materials, ASTM International, West Conshohocken, PA, 2017, www.astm.org, n.d.
- [48] ASTM D2344 / D2344M-16. Standard Test Method for Short-Beam Strength of Polymer Matrix Composite Materials and Their Laminates. West Conshohocken, PA: ASTM International; 2016.
- [49] Özkılıç YO, Madenci E, Gemi L. Tensile and Compressive Behaviors of the Pultruded FRP Lamina. *Turkish J Eng Environ Sci* 2020;4:169–75. <https://doi.org/10.31127/tuje.631481>.
- [50] Doğan MA, Yazman Ş, Gemi L, Yildiz M, Yapıcı A. A review on drilling of FML stacks with conventional and unconventional processing methods under different conditions. *Compos Struct* 2022;297:115913. <https://doi.org/10.1016/j.compstruct.2022.115913>.
- [51] Gemi L, Madenci E, Özkılıç YO. Experimental, analytical and numerical investigation of pultruded GFRP composite beams infilled with hybrid FRP reinforced concrete. *Eng Struct* 2021;244:112790. <https://doi.org/10.1016/j.engstruct.2021.112790>.
- [52] Madenci E, Özkılıç YO, Gemi L. Theoretical Investigation on Static Analysis of Pultruded GFRP Composite Beams. *Acad Platform - J Eng Sci* 2020;8(3):483–90. <https://doi.org/10.21541/apjes.734770>.
- [53] Gemi DS, Şahin ÖS, Gemi L. Experimental investigation of axial compression behavior after low velocity impact of glass fiber reinforced filament wound pipes with different diameter. *Compos Struct* 2022;280:114929. <https://doi.org/10.1016/j.compstruct.2021.114929>.
- [54] Madenci E, Özkılıç YO, Gemi L. Experimental and theoretical investigation on flexure performance of pultruded GFRP composite beams with damage analyses. *Compos Struct* 2020;242:112162. <https://doi.org/10.1016/j.compstruct.2020.112162>.
- [55] Gemi L, Madenci E, Özkılıç YO, Yazman Ş, Safonov A. Effect of fiber wrapping on bending behavior of reinforced concrete filled pultruded GFRP composite hybrid beams. *Polymers* 2022;14(18):3740. <https://doi.org/10.3390/polym14183740>.
- [56] Özkılıç YO, Aksoylu C, Yazman Ş, Gemi L, Arslan MH. Behavior of CFRP-strengthened RC beams with circular web openings in shear zones: Numerical study. *Structures* 2022;41:1369–89. <https://doi.org/10.1016/j.istruc.2022.05.061>.
- [57] Gemi L, Alsdudi M, Aksoylu C, Yazman Ş, Özkılıç YO, Arslan MH. Optimum amount of CFRP for strengthening shear deficient reinforced concrete beams. *Steel Compos Struct* 2022;43(6):735–57. <https://doi.org/10.12989/scs.2022.43.6.735>.
- [58] Sumerak JE. Pultrusion Process Troubleshooting. *Handb Troubl Plast Process A Pract Guide* 2012. <https://doi.org/10.1002/9781118511183.ch20>.
- [59] Awaja F, Arhatari B, Wiesauer K, Leiss E, Stifter D. An investigation of the accelerated thermal degradation of different epoxy resin composites using X-ray microcomputed tomography and optical coherence tomography. *Polym Degrad Stab* 2009;94:1814–24. <https://doi.org/10.1016/j.polymerdegradstab.2009.06.005>.
- [60] Yazman Ş. The effects of back-up on drilling machinability of filament wound GFRP composite pipes: Mechanical characterization and drilling tests. *J Manuf Process* 2021;68:1535–52. <https://doi.org/10.1016/j.jmapro.2021.06.054>.
- [61] Gemi L, Morkavuk S, Köklü U, Yazman Ş. The effects of stacking sequence on drilling machinability of filament wound hybrid composite pipes: Part-2 damage analysis and surface quality. *Compos Struct* 2020;235:111737. <https://doi.org/10.1016/j.compstruct.2019.111737>.
- [62] Kaybal HB, Ulus H, Eskizeybek V, Avcı A. An experimental study on low velocity impact performance of bolted composite joints-part 2: Influence of long-term seawater aging. *Compos Struct* 2021;272:113571. <https://doi.org/10.1016/j.compstruct.2021.113571>.
- [63] Özbek Ö, Bulut M, Erklığ A, Bozkurt ÖY. Interlaminar shear strength and failure analysis of composite laminates with double and triple hybrid configurations. *Eng Struct* 2022;265:114498. <https://doi.org/10.1016/j.engstruct.2022.114498>.
- [64] Maziz A, Tarfaoui M, Gemi L, Rechak S, Nachtane M. A progressive damage model for pressurized filament-wound hybrid composite pipe under low-velocity impact. *Compos Struct* 2021;276:114520. <https://doi.org/10.1016/j.compstruct.2021.114520>.
- [65] Uslu E, Gavgali M, Erdal MO, Yazman Ş, Gemi L. Determination of mechanical properties of polymer matrix composites reinforced with electrospinning N66, PAN, PVA and PVC nanofibers: A comparative study. *Mater Today Commun* 2021; 26:101939. <https://doi.org/10.1016/j.mtcomm.2020.101939>.
- [66] Wang Q, Brow RK, Li H, Ronchetto EA. Effect of aging on the failure characteristics of E-glass fibers. *J Mater Sci* 2016;51:2404–10. <https://doi.org/10.1007/s10853-015-9549-0>.
- [67] Hassan NM, Migler KB, Hight Walker AR, Kotula AP, Seppala JE. Comparing polarized Raman spectroscopy and birefringence as probes of molecular scale alignment in 3D printed thermoplastics. *MRS Commun* 2021;11:157–67. <https://doi.org/10.1557/s43579-021-00025-z>.

- [68] Lin P-Y, Hsieh C-W, Hsieh S. Rapid and Sensitive SERS Detection of Bisphenol A Using Self-assembled Graphitic Substrates. *Sci Rep* 2017;7:16698. <https://doi.org/10.1038/s41598-017-17030-9>.
- [69] Vaskova H, Křesálek V. Raman spectroscopy of epoxy resin crosslinking. In: 13th WEAS International Conference on Automation Control, Modeling & Simulation (ACMOS'11), Lanzarote, Canary Islands, Spain; 2011.
- [70] Vaskova H, Křesálek V. Quasi real-time monitoring of epoxy resin crosslinking via Raman microscopy. *Int J Math Model Methods Appl Sci* 2011;5:1197–204.
- [71] Lee S-N, Stolarski V, Letton A, Laane J. Studies of bisphenol-A-polycarbonate aging by Raman difference spectroscopy. *J Mol Struct* 2000;521:19–24. [https://doi.org/10.1016/S0022-2860\(99\)00422-6](https://doi.org/10.1016/S0022-2860(99)00422-6).
- [72] Mecozzi M, Pietroletti M, Scarpiniti M, Acquistucci R, Conti ME. Monitoring of marine mucilage formation in Italian seas investigated by infrared spectroscopy and independent component analysis. *Environ Monit Assess* 2012;184:6025–36. <https://doi.org/10.1007/s10661-011-2400-4>.
- [73] Cholake S, Mada M, Raman R, Bai Yu, Zhao Xi, Rizkalla S, et al. Quantitative analysis of curing mechanisms of epoxy resin by mid- and near-fourier transform infra red spectroscopy. *Def Sci J* 2014;64(3):314–21.
- [74] González M, Cabanelas J, Baselga J. Applications of FTIR on Epoxy Resins - Identification, Monitoring the Curing Process. Phase Separation and Water Uptake 2012. <https://doi.org/10.5772/36323>.
- [75] Yazman Ş, Uyaner M, Karabörk F, Akdemir A. Effects of nano reinforcing/matrix interaction on chemical, thermal and mechanical properties of epoxy nanocomposites. *J Compos Mater* 2021;55:4257–72. <https://doi.org/10.1177/00219983211037059>.
- [76] Korotkov R, Vedernikov A, Gusev S, Alajarmeh O, Akhatov I, Safonov A. Shape memory behavior of unidirectional pultruded laminate. *Compos Part A Appl Sci Manuf* 2021;150:106609. <https://doi.org/10.1016/j.compositesa.2021.106609>.
- [77] Baran I, Straumit I, Shishkina O, Lomov SV. X-ray computed tomography characterization of manufacturing induced defects in a glass/polyester pultruded profile. *Compos Struct* 2018;195:74–82. <https://doi.org/10.1016/j.compstruct.2018.04.030>.
- [78] Khdeir AA, Reddy JN. An exact solution for the bending of thin and thick cross-ply laminated beams. *Compos Struct* 1997;37:195–203. [https://doi.org/10.1016/S0263-8223\(97\)80012-8](https://doi.org/10.1016/S0263-8223(97)80012-8).
- [79] Madenci E. A refined functional and mixed formulation to static analyses of fgm beams. *Struct Eng Mech* 2019;69:427–37. <https://doi.org/10.12989/sem.2019.69.4.427>.
- [80] Madenci E, Özkılıç YO, Gemi L. Buckling and free vibration analyses of pultruded GFRP laminated composites: Experimental, numerical and analytical investigations. *Compos Struct* 2020;254:112806.
- [81] Özütok A, Madenci E. Static analysis of laminated composite beams based on higher-order shear deformation theory by using mixed-type finite element method. *Int J Mech Sci* 2017;130:234–43. <https://doi.org/10.1016/j.ijmecsci.2017.06.013>.
- [82] Reddy JN. *Energy Principles and Variational Methods in Applied Mechanics*. Wiley; 2002.
- [83] Madenci E, Özütok A. Variational approximate for high order bending analysis of laminated composite plates. *Struct Eng Mech* 2020;73:97–108.
- [84] Madenci E. Free vibration analysis of carbon nanotube RC nanobeams with variational approaches. *Adv Nano Res* 2021;11:157–71. <https://doi.org/10.12989/anr.2021.11.2.157>.
- [85] Reddy JN. *Mechanics of laminated composite plates and shells: Theory and analysis*. Boca Raton, FL: CRC Press; 2004.

Chapter 8

Modelling and experimental validation of thermoset resin curing during pultrusion

Vedernikov Alexander, Safonov Alexander, Akhatov Iskander. Modelling and experimental validation of thermoset resin curing during pultrusion. *IOP Conference Series: Materials Science and Engineering 2021*. DOI: 10.1088/1757-899X/1129/1/012011.

Contribution: I analyzed the results of experimental measurements of the temperature-dependent specific heat as well as of thermal conductivity of the resin. I improved the 2D thermal model of the pultrusion process initially developed by Professor Alexander Safonov. In particular, I made adjustments to the FILM user subroutine, the procedures used in the .FOR file, as well as implemented a temperature-dependent specific heat of the resin. I prepared all the figures for this article, and contributed to the development of the original draft, final writing, and editing. I would like to thank all the authors for their valuable contributions to the development of this paper.

PAPER • OPEN ACCESS

Modelling and experimental validation of thermoset resin curing during pultrusion

To cite this article: A N Vedernikov *et al* 2021 *IOP Conf. Ser.: Mater. Sci. Eng.* **1129** 012011

View the [article online](#) for updates and enhancements.



240th ECS Meeting ORLANDO, FL

Orange County Convention Center **Oct 10-14, 2021**

Abstract submission deadline extended: April 23rd

SUBMIT NOW

Modelling and experimental validation of thermoset resin curing during pultrusion

A N Vedernikov, A A Safonov and I S Akhatov

Skolkovo Institute of Science and Technology, Center for Design, Manufacturing and Materials, Moscow, Russia

Aleksandr.Vedernikov@skoltech.ru

Abstract. Mathematical modelling of the pultrusion manufacturing process involves many parameters of the resin mixture. In this article thermo-chemical behavior of resin used for pultrusion of glass fiber/epoxy-vinyl L-shaped profiles was characterized. Profiles were manufactured at pulling speeds of 200, 400, and 600 mm·min⁻¹. Dependency of resin specific heat from temperature was determined by differential scanning calorimetry (DSC); the influence of temperature on resin's thermal conductivity was found; parameters of resin cure kinetics were described. Subsequently, the gained parameters were used for numerical simulation of the pultrusion thermo-chemical problem in ABAQUS software. The temperature and cure degree evolutions obtained from the experiments run at different pulling speeds, and those from the numerical model were shown to be correlated.

1. Introduction

Recently fiber reinforced polymers (FRPs) have been widely adopted as structural elements in the civil engineering and construction sector due to their better mechanical properties compared to those of traditional materials (steel, timber, concrete) [1-4]. As the most efficient manufacturing technique of composite materials, pultrusion allows the production of constant cross-section profiles with virtually unlimited length and least engineers' involvement [5,6]. Advantages of pultruded profiles are apparent: high strength-to-weight ratio [7-9] improved corrosion resistance [10-12] and durability [13-15], ease of transportation, installation, and maintenance [16].

The thermoset pultrusion process starts from pulling fiber reinforcement (unidirectional rovings, mats, woven fabric) through the bath, filled with the resin matrix [17,18]. Next, impregnated material is pulled to the preformer for the elimination of excessive resin [19]. Then preformed reinforcement is guided to the heated die for the initiation of resin polymerization process [20]. Cured composite is subsequently directed to the cutting saw by the system of puller units [21]. Nevertheless, the performance of the final pultruded product is very sensitive to processing parameters [22,23] and the choice of raw materials [24-26]. Aiming quality improvement of produced profiles by minimizing residual stresses [27], occurrence of cracks [28] and manufacturing induced shape distortions, mathematical modelling of the pultrusion process is a widely applied tool [29,30]. It allows to avoid time-consuming and expensive trial-error experiments [31,32]. Since the pultrusion manufacturing process incorporates thermo-chemical and mechanical problems, plenty of input parameters of composite raw elements are needed to achieve mathematical modelling reliable results [33,34].



The objective of the current article is to experimentally determine temperature-dependent parameters of resin mixture: specific heat and thermal conductivity. These parameters are subsequently coupled with resin kinetics and utilized to solve the pultrusion thermo-chemical problem in ABAQUS software. The computation procedure results are then compared to those detected during the pultrusion experiment performed at three different pulling speeds (200, 400, and 600 mm·min⁻¹).

2. Materials and methods

2.1. Pultrusion process setup and experimental determination of resin parameters

Resin mixture and pultruded profiles manufactured with Pultrex Px500-6T (Pultrex, UK) pultrusion machine were produced at the Laboratory of Composite Materials and Structures of the Center for Design, Manufacturing and Materials (Skolkovo Institute of Science and Technology, Moscow, Russia).

The matrix used for this study was epoxy vinyl-based Atlac 430 (DSM Composite Resins AG, Switzerland). To improve the quality of the resin mixture the following components were added: Trigonox C (Akzo Nobel Polymer Chemicals B.V., The Netherlands), Perkadox 16 (Akzo Nobel Polymer Chemicals B.V., The Netherlands), BYK-A555 (BYK Additives & Instruments, Germany), and Zinc Stearate (Baerlocher GmbH, Germany). Mentioned additives played the following roles: Trigonox C – initiator for (co)polymerization of ethylene, styrene, acrylonitrile, acrylates, and methacrylates; Perkadox 16 – initiator for suspension polymerization of acrylates and methacrylates; BYK-A555 – deaerator; Zinc Stearate – friction reduction. The amount of each component used in the resin mixture is indicated in table 1.

Table 1. Components of the resin mixture.

Component	Amount [kg]
Resin Atlac 430 (DSM Composite Resins AG, Switzerland)	25.07
BYK-A555 (BYK Additives & Instruments, Germany)	0.09
Trigonox C (Akzo Nobel Polymer Chemicals B.V., The Netherlands)	0.38
Perkadox 16 (Akzo Nobel Polymer Chemicals B.V., The Netherlands)	0.13
Zinc Stearate (Baerlocher GmbH, Germany)	1.00

The length of the die was 600 mm. Four heating platens were used. L-shaped profiles were pultruded at three different pulling speeds: 200, 400, and 600 mm·min⁻¹. Therefore, abbreviations of V-200, V-400, and V-600 are used in this paper. During the pultrusion process temperature evolution of the processing composite was recorded by wired thermocouples. They had a length of 7 m and were introduced within the profile before die entrance.

Independently from pultrusion process, the pure resin mixture was fully cured, and two samples were cut off to evaluate the temperature dependence of resin specific heat. Samples had a shape of cylinders with a radius of 4 mm and a thickness of 2 mm. For the purpose of this study Differential Scanning Calorimeter DSC 204 (NETZSCH-Gerätebau GmbH, Germany) was used. Experiments were carried out at the temperature range from 20°C to 100°C. Two samples were cut off to evaluate the temperature dependence of resin thermal conductivity. Samples had a shape of thin plates 10 × 10 mm and a thickness of 1 mm. For the purpose of this study Laser Flash Apparatus LFA 457 (NETZSCH-Gerätebau GmbH, Germany) was used. Experiments were carried out at the temperature range from 20°C to 100°C.

2.2. Heat-transfer model

The general 3D heat-transfer model describing the pultrusion process is presented in equation (1). Subscript “1” represents the pulling direction of pultrusion, while “2” and “3” are related to the

transversal direction. Index “c” determines the belonging of the property to the entire composite, while “r” and “f” are related to resin and fiber respectively.

$$\rho_c C_{p_c} \left(\frac{\partial T}{\partial t} + v \frac{\partial T}{\partial x_1} \right) = k_{x_1,c} \frac{\partial^2 T}{\partial x_1^2} + k_{x_2,c} \frac{\partial^2 T}{\partial x_2^2} + k_{x_3,c} \frac{\partial^2 T}{\partial x_3^2} + q \quad (1)$$

$$q = (1 - V_f) \rho_r H_{tot} \frac{d\alpha}{dt} \quad (2)$$

Where ρ_c, ρ_r are densities of the composite and resin respectively; C_p represents specific heat; T is temperature; t is time; $k_{x_1,c}, k_{x_2,c}, k_{x_3,c}$ are the thermal conductivities in the corresponding directions; v is pulling speed; q represents internal heat generation due to exothermic reaction of the resin; V_f represents fiber volume fraction; H_{tot} represents total heat released during curing; $\frac{d\alpha}{dt}$ is rate of curing reaction.

Kinetic model of the n^{th} order reaction with autocatalysis was used for the modelling of resin polymerization process [35]:

$$\frac{d\alpha}{dt} = A e^{-\frac{E_a}{RT}} (1 - \alpha)^n (1 + K_{cat} \alpha) \quad (3)$$

Where α represents instantaneous degree of cure; t is time; A represents a preexponential factor; E_a is activation energy; R is universal gas constant; n is the order of the reaction; K_{cat} is activation constant. Parameters of the model are presented in the table 2 in accordance to those described in [22].

Table 2. Resin kinetic parameters.

$A [s^{-1}]$	$E_a [kJ \cdot mol^{-1} \cdot K^{-1}]$	$n [-]$	$K_{cat} [-]$
$10^{9.34}$	93.3	1.91	$10^{2.73}$

2.3. Finite element simulations

Mathematical modelling was performed at the FEM software ABAQUS. The following subroutines were used for the solution of the thermo-chemical problem: FILM (to define die temperatures and heat transfer coefficient as functions of position and time), USDFLD (to define cure degree of the composite as a field variable), HETVAL (to define a heat flux due to internal heat generation in the material during heat transfer analysis). The finite element model consisted of linear quadrilateral element (CPE4RT). The number of elements is over than 1000.

3. Results and discussions

The results of the temperature dependence of resin specific heat evaluation are presented in table 3. According to equation (4), the first-order polynomial was then used for the approximation of temperature dependent resin specific heat experimental results.

$$C_p = 5.1T + 1080 \quad (4)$$

Where T represents the instantaneous temperature of the resin; C_p is instantaneous specific heat of the resin.

The correlation between resin thermal conductivity and temperature is found to be weak. Therefore, further resin thermal conductivity is considered independent from the temperature and adopted as the average value of experimental results equal to $0.177 \text{ W} \cdot \text{m}^{-1} \cdot \text{K}^{-1}$.

Table 3. Temperature dependence of resin specific heat and thermal conductivity.

Temperature [°C]	Measured value of specific heat			Measured value of thermal conductivity		
	C_{p1} [J·kg ⁻¹ ·K ⁻¹]	C_{p2} [J·kg ⁻¹ ·K ⁻¹]	$C_{average}$ [J·kg ⁻¹ ·K ⁻¹]	λ_1 [W·m ⁻¹ ·K ⁻¹]	λ_2 [W·m ⁻¹ ·K ⁻¹]	$\lambda_{average}$ [W·m ⁻¹ ·K ⁻¹]
20	1181	1199	1190	0.1730	0.1761	0.1746
30	1227	1241	1234	0.1741	0.1718	0.1730
40	1277	1290	1284	0.1773	0.1704	0.1739
50	1333	1339	1336	0.1800	0.1769	0.1785
60	1386	1384	1385	0.1802	0.1787	0.1795
70	1430	1421	1425	0.1773	0.1784	0.1779
80	1476	1461	1468	0.1793	0.1765	0.1779
90	1538	1518	1528	0.1796	0.1785	0.1791
100	1628	1610	1619	0.1823	0.1817	0.1820

Figure 1 represents the evolution of composite temperature and cure degree as functions of coordinate measured in the pulling direction of pultrusion starting from the die entrance. Since the most significant part of the polymerization process happens within the die, only 600 mm length is considered. The solid line represents the results of mathematical modelling, while the dashed line is related to the experimentally obtained values. Good correlation between numerical and experimental results for all the pulling speeds is observed. Therefore, the thermo-chemical model of pultrusion presented above is considered to be experimentally verified.

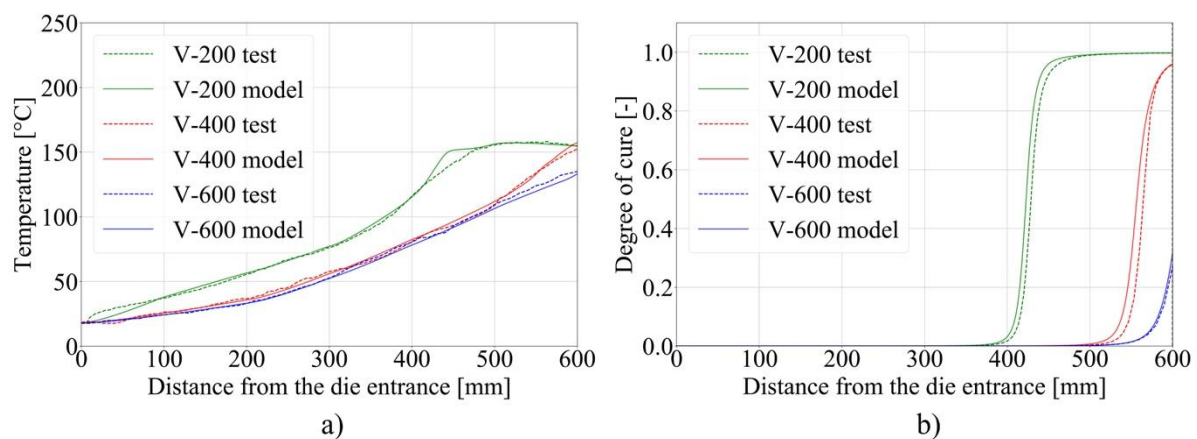


Figure 1. Comparison of modelling and experimental results. (a) Evolution of composite's temperature; (b) Evolution of composite's cure degree.

4. Conclusions

Both an experimental and a numerical study were performed to investigate thermo-chemical problem of pultrusion process in relation to the production of glass fiber/epoxy-vinyl L-shaped profiles. Tests on epoxy-vinyl based matrix were conducted to characterize the dependency of resin specific heat and thermal conductivity on temperature. Specific heat of the resin exhibited a linear temperature dependence, while thermal conductivity demonstrated weak correlation and was adopted as constant.

These results were then jointed to resin kinetic and used for the mathematical modelling of the thermo-chemical problem of pultrusion in ABAQUS software. Simulating the resin curing process, temperature and cure degree evolution profiles of composites were obtained for three pulling speeds: 200, 400, and 600 mm·min⁻¹. Modelling results demonstrated a good agreement with the results detected by thermocouples during the pultrusion experiment.

This paper is the first step of authors to experimentally characterize thermal and mechanical parameters of pultruded composites' constituent parts needed for the further development of the linear viscoelastic mathematical model.

References

- [1] Vedernikov A, Safonov A, Tucci F, Carlone P and Akhatov I 2020 Pultruded materials and structures: A review *J. Compos. Mater.* **54** 4081–117
- [2] Liu T, Feng P, Lu X, Yang J-Q and Wu Y 2020 Flexural behavior of novel hybrid multicell GFRP-concrete beam *Compos. Struct.* **250**
- [3] Shimba Carneiro Vieira P, de Souza F, Taissum Cardoso D C, Domingos Vieira J and de Andrade Silva F 2020 Influence of moderate/high temperatures on the residual flexural behavior of pultruded GFRP *Compos. Part B Eng.* **200**
- [4] Madenci E, Özkılıç Y O and Gemi L 2020 Experimental and theoretical investigation on flexure performance of pultruded GFRP composite beams with damage analyses *Compos. Struct.* **242**
- [5] Vedernikov A N, Safonov A A, Gusev S A, Carlone P, Tucci F and Akhatov I S 2020 Spring-in experimental evaluation of L-shaped pultruded profiles *IOP Conf. Ser. Mater. Sci. Eng.* **747** 012013
- [6] Fairuz A M, Sapuan S M, Zainudin E S and Jaafar C N A 2014 Polymer composite manufacturing using a pultrusion process: A review *Am. J. Appl. Sci.* **11** 1798–810
- [7] Zhu R, Li F, Shao F and Zhang D 2020 Static and dynamic behaviour of a hybrid PFRP-aluminium space truss girder: Experimental and numerical study *Compos. Struct.* **243**
- [8] Sutherland L S, Sá M F, Correia J R, Guedes Soares C, Gomes A and Silvestre N 2017 Impact response of pedestrian bridge multicellular pultruded GFRP deck panels *Compos. Struct.* **171**
- [9] Liu T, Liu X and Feng P 2020 A comprehensive review on mechanical properties of pultruded FRP composites subjected to long-term environmental effects *Compos. Part B Eng.* **191**
- [10] Xiong Z, Liu Y, Zuo Y and Xin H 2019 Experimental evaluation of shear behavior of pultruded GFRP perforated connectors embedded in concrete *Compos. Struct.* **222**
- [11] Madenci E, Onuralp Özkılıç Y and Gemi L 2020 Buckling and free vibration analyses of pultruded GFRP laminated composites: Experimental, numerical and analytical investigations *Compos. Struct.* **254**
- [12] Xin H, Mosallam A, Liu Y, Yang F and Zhang Y 2017 Hygrothermal aging effects on shear behavior of pultruded FRP composite web-flange junctions in bridge application *Compos. Part B Eng.* **110**
- [13] Li C, Yin X, Wang Y, Zhang L, Zhang Z, Liu Y and Xian G 2020 Mechanical property evolution and service life prediction of pultruded carbon/glass hybrid rod exposed in harsh oil-well condition *Compos. Struct.* **246**
- [14] Yang W-R, He X-J and Dai L 2017 Damage behaviour of concrete beams reinforced with GFRP bars *Compos. Struct.* **161**
- [15] Gooranorimi O, Suaris W, Dauer E and Nanni A 2017 Microstructural investigation of glass fiber reinforced polymer bars *Compos. Part B Eng.*
- [16] Liu T, Vieira J D and Harries K A 2020 Predicting flange local buckling capacity of pultruded GFRP I-sections subject to flexure *J. Compos. Constr.* **24**
- [17] Bakis C E, Bank L C, Brown V L, Cosenza E, Davalos J F, Lesko J J, Machida A, Rizkalla S H and Triantafillou T C 2002 Fiber-reinforced polymer composites for construction - State-of-

- the-art review *J. Compos. Constr.* **6**
- [18] Vedernikov A, Tucci F, Safonov A, Carlone P, Gusev S and Akhatov I 2020 Investigation on the shape distortions of pultruded profiles at different pulling speed *Procedia Manuf.* **47** 1–5
- [19] Starr T F 2000 *Pultrusion for engineers*
- [20] Costa Dias R D C, Santos L D S, Ouzia H and Schledjewski R 2018 Improving degree of cure in pultrusion process by optimizing die-temperature *Mater. Today Commun.* **17** 362–70
- [21] Baran I 2015 *Pultrusion: state-of-the-art process models* (Shropshire: Smithers Rapra)
- [22] Vedernikov A, Tucci F, Carlone P, Gusev S, Konev S, Firsov D, Akhatov I and Safonov A 2021 Effects of pulling speed on structural performance of L-shaped pultruded profiles *Compos. Struct.* **255**
- [23] Silva F J G, Ferreira F, Costa C, Ribeiro M C S and Meira Castro A C 2012 Comparative study about heating systems for pultrusion process *Compos. Part B Eng.* **43**
- [24] Sorina T G, Safonov A A and Khairtdinov A K 2010 Peculiarities of using carbon glass-reinforced plastic in pultrusion composite profiles for bridge engineering *J. Mach. Manuf. Reliab.* **39** 47–51
- [25] Paciornik S, Martinho F, de Mauricio M H and d’Almeida J R 2003 Analysis of the mechanical behavior and characterization of pultruded glass fiber–resin matrix composites *Compos. Sci. Technol.* **63** 295–304
- [26] Fairuz A M, Sapuan S M, Zainudin E S and Jaafar C N A 2016 Effect of filler loading on mechanical properties of pultruded kenaf fibre reinforced vinyl ester composites *J. Mech. Eng. Sci.* **10** 1931–42
- [27] Yuksel O, Baran I, Ersoy N and Akkerman R 2019 Investigation of transverse residual stresses in a thick pultruded composite using digital image correlation with hole drilling *Compos. Struct.* **223**
- [28] Safonov A, Gusev M, Saratov A, Konstantinov A, Sergeichev I, Konev S, Gusev S and Akhatov I 2020 Modeling of cracking during pultrusion of large-size profiles *Compos. Struct.* **235**
- [29] Baran I, Tutum C C, Nielsen M W and Hattel J H 2013 Process induced residual stresses and distortions in pultrusion *Compos. Part B Eng.* **51** 148–61
- [30] Safonov A A, Carlone P and Akhatov I 2018 Mathematical simulation of pultrusion processes: A review *Compos. Struct.* **184**
- [31] Ding A, Wang J and Li S 2020 Understanding process-induced spring-in of L-shaped composite parts using analytical solution *Compos. Struct.* **250**
- [32] Al-Dhaheri M, Khan K A, Umer R, van Liempt F and Cantwell W J 2020 Process induced deformations in composite sandwich panels using an in-homogeneous layup design *Compos. Part A Appl. Sci. Manuf.* **137**
- [33] Baran I, Akkerman R and Hattel J H 2014 Material characterization of a polyester resin system for the pultrusion process *Compos. Part B Eng.* **64** 194–201
- [34] de Cassia Costa Dias R, Costa M L, de Sousa Santos L and Schledjewski R 2020 Kinetic parameter estimation and simulation of pultrusion process of an epoxy-glass fiber system *Thermochim. Acta* **690**
- [35] Worzakowska M 2006 Kinetics of the curing reaction of unsaturated polyester resins catalyzed with new initiators and a promoter *J. Appl. Polym. Sci.* **102** 1870–6

Chapter 9

Modeling spring-in of L-shaped structural profiles pultruded at different pulling speeds

Vedernikov Alexander*, Safonov Alexander*, Tucci Fausto, Carlone Pierpaolo, Akhatov Iskander. Modeling spring-in of L-shaped structural profiles pultruded at different pulling speeds. *Polymers 2021*. DOI: 10.3390/polym13162748.

* – equal contribution

Contribution:

I improved the numerical model of the pultrusion process, initially developed by Professor Alexander Safonov, which predicts the spring-in formation. In particular, I made adjustments to the FILM and UMAT user subroutines, as well as to the procedures used in the .FOR file. Moreover, I improved the model to account for the temperature-dependent heat capacity and Poisson's ratio of the resin. I also proposed the modification of the Cure Hardening Instantaneous Linear Elastic (CHILE) model of the resin, based on results of the dynamic mechanical analysis (DMA). I analyzed the results of numerical simulations and evaluated the contributions of thermal and chemical shrinkage in the development of spring-in. I prepared all the figures for this article and contributed to the development of the original draft, final writing, and editing. I would like to thank all the authors for their valuable

contributions to the development of this paper.

Article

Modeling Spring-In of L-Shaped Structural Profiles Pultruded at Different Pulling Speeds [†]

Alexander Vedernikov ^{1,*}, Alexander Safonov ^{1,‡}, Fausto Tucci ², Pierpaolo Carlone ² and Iskander Akhatov ¹

¹ Center for Design, Manufacturing and Materials, Skolkovo Institute of Science and Technology, 30/1 Bolshoi Boulevard, 121205 Moscow, Russia; a.safonov@skoltech.ru (A.S.); i.akhatov@skoltech.ru (I.A.)

² Department of Industrial Engineering, University of Salerno, Via Giovanni Paolo II, 132-84084 Fisciano, Italy; ftucci@unisa.it (F.T.); pcarlone@unisa.it (P.C.)

* Correspondence: aleksandr.vedernikov@skoltech.ru

[†] This paper is an extended version of the conference paper “Analysis of Spring-In Deformation in L-Shaped Profiles Pultruded at Different Pulling Speeds: Mathematical Simulation and Experimental Results”. In Proceedings of the ESAFORM 2021 24th International Conference on Material Forming, Liège, Belgium, 14–16 April 2021, <https://doi.org/10.25518/esaform21.4743>.

[‡] These authors contributed equally to this work.

Citation: Vedernikov, A.; Safonov, A.; Tucci, F.; Carlone, P.; Akhatov, I. Modeling Spring-In of L-Shaped Structural Profiles Pultruded at Different Pulling Speeds [†]. *Polymers* **2021**, *13*, 2748. <https://doi.org/10.3390/polym13162748>

Academic Editor: Francesca Lionetto

Received: 16 July 2021

Accepted: 10 August 2021

Published: 16 August 2021

Publisher's Note: MDPI stays neutral with regard to jurisdictional claims in published maps and institutional affiliations.



Copyright: © 2021 by the authors. Licensee MDPI, Basel, Switzerland. This article is an open access article distributed under the terms and conditions of the Creative Commons Attribution (CC BY) license (<http://creativecommons.org/licenses/by/4.0/>).

Abstract: Cure-induced deformations are inevitable in pultruded composite profiles due to the peculiarities of the pultrusion process and usually require the use of costly shimming operations at the assembly stage for their compensation. Residual stresses formed at the production and assembly stages impair the mechanical performance of pultruded elements. A numerical technique that would allow the prediction and reduction of cure-induced deformations is essential for the optimization of the pultrusion process. This study is aimed at the development of a numerical model that is able to predict spring-in in pultruded L-shaped profiles. The model was developed in the ABAQUS software suite with user subroutines UMAT, FILM, USDFLD, HETVAL, and UEXPAN. The authors used the 2D approach to describe the thermochemical and mechanical behavior via the modified Cure Hardening Instantaneous Linear Elastic (CHILE) model. The developed model was validated in two experiments conducted with a 6-month interval using glass fiber/vinyl ester resin L-shaped profiles manufactured at pulling speeds of 200, 400, and 600 mm/min. Spring-in predictions obtained with the proposed numerical model fall within the experimental data range. The validated model has allowed authors to establish that the increase in spring-in values observed at higher pulling speeds can be attributed to a higher fraction of uncured material in the composite exiting the die block and the subsequent increase in chemical shrinkage that occurs under unconstrained conditions. This study is the first one to isolate and evaluate the contributions of thermal and chemical shrinkage into spring-in evolution in pultruded profiles. Based on this model, the authors demonstrate the possibility of achieving the same level of spring-in at increased pulling speeds from 200 to 900 mm/min, either by using a post-die cooling tool or by reducing the chemical shrinkage of the resin. The study provides insight into the factors significantly affecting the spring-in, and it analyzes the methods of spring-in reduction that can be used by scholars to minimize the spring-in in the pultrusion process.

Keywords: pultrusion; spring-in; finite element analysis (FEA); cure behavior; process modeling

1. Introduction

Pultrusion is the most efficient process for producing composite structural profiles of constant cross-sections [1–3]. Owing to their high strength-to-weight ratio [4,5], superior corrosion resistance [6,7], and improved durability [8,9], pultruded profiles have been successfully used as structural elements in the fields of bridge construction [10–12], civil [13,14], and architectural engineering [15,16]; marine construction [17,18]; aerospace

and aviation engineering [19–21]; transportation [22,23]; and energy systems [24]. However, process-induced deformations, such as spring-in (common in curved elements) and warpage (common in flat elements), may result in a certain loss in the economic efficiency of mass production of composite profiles [25]. Spring-in is the primary contributor [26] to the distortion of a profile, which may require costly and time-consuming shimming operations during assembly [27,28]. Residual stresses developing during the production and assembly stages are detrimental to the final mechanical performance of a structure [29,30]. Thus, the ability to predict, control, and compensate for process-induced deformations is crucial for the effective design and assembly of composite structures [31,32].

The phenomenon of spring-in can be observed in various processes of composite manufacturing, such as autoclave [33–36], resin transfer molding [37–39], vacuum-assisted resin transfer molding [40,41], vacuum bagging [42,43], compression molding [44,45], filament winding [46], microwave curing [47], and pultrusion [48,49]. The main causes of spring-in are the anisotropy of the mechanical properties of a composite [50], [51,52]; chemical [53,54] and thermal [55,56] shrinkage of a material; nonuniform distribution of temperatures [57]; and curing degree [58,59]. The peculiarities of the pultrusion process also contribute to the spring-in because a composite material undergoes all process stages sequentially, i.e., impregnation, heating, polymerization, and cooling. Therefore, the structural properties of the produced profiles depend upon the process conditions used in production [60]. Hence, the creation of numerical models predicting the influence of process conditions on the value of spring-in is a vital problem for the pultrusion process optimization [61–63].

Successful simulation of the pultrusion process requires a model that describes the distribution of temperatures in a composite along with the matrix polymerization process [64–67] and mechanical behavior of a composite during manufacturing [68,69]. To model residual stresses and distortions, Baran et al. [49] applied a 3D approach to solve the thermochemical problem and a 2D approach to explain the mechanical behavior via the Cure Hardening Instantaneous Linear Elastic (CHILE) model. In a follow-up study, they showed that the spring-in value depends on the pulling speed [48]. Wang et al. [70] proposed the numerical model to predict the spring-in and conducted an experiment to compare predictions and experimental results. Predictions were found to be in good agreement with experimental data. It was also found that the contribution of chemical shrinkage into deformations is significantly higher compared to that of thermal expansion. However, those contributions were not quantified.

Despite the lack of studies on spring-in formation in pultruded composites, over the last 30 years, a large number of experimental and numerical studies on the subject have been published in relation to other composite manufacturing processes. Those works studied the influence of cure cycle schedule, thermal shrinkage, and chemical shrinkage on the evolution of cure-induced residual stresses and deformations. Back in 1992, Bogetti and Gillespie [57] proposed a model that is capable of predicting the mechanical characteristics, thermal and chemical strains in resin during polymerization. The study demonstrated the major role of thermal shrinkage and chemical shrinkage in the development of residual stresses and deformations. Jain and Mai [71] have proposed a model based on the modified shell theory, which predicted the evolution of residual stresses and deformations such as spring-in. They have shown that chemical shrinkage, among other factors, has a significant effect on the evolution of residual stresses and shape distortions. Wiersma et al. [53], aiming to build the model capable of accurate prediction of spring-in in L-shaped composites, have considered the thermoelastic model accounting for thermal shrinkage, and the viscoelastic model accounting for irreversible effects occurring during resin polymerization (chemical shrinkage and viscosity evolutions). Subsequently, Radford and Rennick [51] have quantified the contribution of thermoelastic and non-thermoelastic components in spring-in distortion of carbon fiber/epoxy brackets manufactured by the autoclave technique. In 2001, Svanberg and Holmberg [37] studied

the influence of the cure cycle on spring-in evolutions in the resin transfer molding process. They distinguished three major factors accounting for spring-in, i.e., thermal shrinkage, chemical shrinkage, and frozen-in deformations. While studying the cure quenching phenomenon, Ersoy et al. [72] were able to isolate the contribution of thermal shrinkage (happening before and after vitrification) and of chemical shrinkage to spring-in formation. In 2006, Ruiz and Trochu [73] demonstrated the methodology allowing a researcher to optimize polymerization in a liquid composite molding process by way of minimizing the residual stresses resulting from chemical and thermal shrinkage. The methodology makes it possible to improve the process of resin curing while simultaneously minimizing the process time and residual stresses. In the quenching experiment, Wisnom et al. [50] have shown the development of spring-in at different stages of the cure cycle—initial growth, peak, and reduction during subsequent polymerization. It was shown that at the rubbery state, both thermal and chemical shrinkage affect spring-in evolutions, with the contribution of chemical shrinkage constituting as much as 50%. In Wisnom et al. [27], the authors proposed and verified experimentally the analytical solution describing the mechanism of spring-in formation due to thermal and chemical shrinkage, taking place between gelation and vitrification of the resin. Hsiao and Gangireddy [41] in 2008 used the vacuum-assisted resin transfer molding (VARTM) process to prove experimentally that the addition of 1.5 wt % carbon nanofibers to polyester resin allows a spring-in reduction by as much as 73% through a reduction of deformations caused by thermal and chemical shrinkage. The analytical solution and the 3D FEA model proposed confirm the experimental results and predict a complete elimination of spring-in at 10 wt % of carbon nanofibers. Li et al. [47] have shown that it is possible to significantly reduce the cure-induced strains in carbon fiber-reinforced bismaleimide composites by replacing conventional thermal curing process for the microwave one and to achieve spring-in reduction in the L-shaped structure by as much as 1.2°. Subsequently, Kravchenko et al. [74] conducted the experimental and numerical study of deflection in bi-lamina strips caused by thermal and chemical shrinkage, occurring at various stages of the cure cycle. Takagaki et al. [75] in 2017 used Fiber Bragg Grating (FBG) sensors to experimentally measure through-thickness normal and shear strains. The results obtained were used to analyze the curing process and the development of spring-in in the L-shaped carbon-fiber-reinforced polymer (CFRP) part at different stages of the cure process, which are associated with chemical and thermal shrinkage. Nawab et al. [76] showed numerically the evolution of spring-in in a carbon/epoxy woven composite bracket at different stages of the cure cycle and subsequent cooling, and they established that the contribution of thermal shrinkage constituted 81%, while that of chemical shrinkage during curing constituted only 19%. Hu et al. [77] demonstrated an in situ method to monitor gelation and determine the evolution of effective chemical shrinkage during polymerization, using the FBG sensors. The authors have manufactured the C-shape composite specimens and compared the spring-in values predicted with the use of the thermal model (accounting only for the thermal shrinkage) and of Rennick's model [51]. Three methods were used to measure the chemical shrinkage—by bi-material strip, by Thermal Mechanical Analysis, and by FBG sensors—with the latter producing the most reliable results. Exner et al. [78] have shown experimentally that the addition of aluminum oxide nanoparticles in the amount of at least 5 wt % reduces chemical and thermal shrinkage, resulting in a reduction of spring-in in vacuum-infused CFRP L-shaped composites. In 2019, Groh et al. [79] in the experimental study of RTM-fabricated L-shaped CFRP composites based on Fast Curing Epoxy Resin have shown the absence of relation between the spring-in and the cooling rate. Subsequently, Qiao and Yao [80] proposed the 3D numerical model and calculated the contributions of thermal shrinkage, chemical shrinkage, and of tool-part interaction to the spring-in in the L-shaped structure. It was found that the contribution of thermal shrinkage is almost independent of part thickness, and that of the chemical shrinkage reduces with increase in part thickness. It was also found that the spring-in caused by

chemical shrinkage is higher compared to that caused by thermal shrinkage. Shaker et al. [81] through the addition of 5% of silica microparticle fillers were able to reduce the coefficient of thermal expansion of resin and, as a result, to reduce the spring-in in glass/vinyl ester L-shaped composite parts by as much as 65%, from 1.807° to 0.632°. Recently, Struzziero et al. [82] conducted the experimental and numerical study of the residual stress and warpage deformations during cure in laminates produced by VARTM. The authors used the multi-objective optimization and proposed the method of reducing the warpage by as much as 10% and manufacturing time by 33%.

The majority of studies on the subject discussed here are devoted to the composite manufacturing processes other than pultrusion. Hence, the insights from those studies cannot be fully applied when studying the pultrusion process, due to the unique features of pultrusion as the manufacturing process. However, the few existing studies of spring-in in pultruded composites fail to explore the subject comprehensively. For example, these studies do not provide experimental validation of numerical models at various pulling speeds. Moreover, no thorough analysis has been conducted on the reasons for spring-in increase at higher pulling speeds. In addition, the authors failed to separate and evaluate the contributions from thermal and chemical shrinkage to the final value of spring-in during the polymerization and cooling phases. This study is aimed at the analysis of thermal and chemical shrinkage influence on the evolutions of spring-in in L-shaped profiles taking place at different pulling speeds. This study also aims to investigate the ways to minimize the spring-in through the use of a post-die cooling tool or by reducing the chemical shrinkage of the resin. The outcomes of this study can be used by researchers to minimize spring-in deformations occurring during pultrusion.

This paper presents a numerical and experimental study of the influence of pulling speed on the value of spring-in in L-shaped structural pultruded profiles of 75 mm × 75 mm × 6 mm. The pultrusion of vinyl ester-based profiles reinforced with unidirectional glass fiber rovings and fabrics was carried out. Two pultrusion experiments were performed, with a 6-month interval. The spring-in in pultruded profiles was measured on the same day of manufacture after the profiles got cooled to room temperature. A numerical simulation of the pultrusion process at different pulling speeds was performed using a 2D approach to thermochemical and mechanical behavior via the modified CHILE model. The results demonstrate good correlation between numerical predictions and experimental values of spring-in. The study also evaluated the contribution of each mechanism to the formation of spring-in. The results show that the largest contribution to spring-in comes from the chemical shrinkage of the matrix after the exit from the die block and the thermal shrinkage of the composite when cooling to the glass transition temperature. Numerical simulation results were used to analyze the possibility of reducing the spring-in with the help of a post-die cooling tool or by reducing the chemical shrinkage of the resin.

2. Materials and Methods

2.1. Pultrusion Manufacturing

The profiles used for the experiments were manufactured using the Pultrex Px500-6T pultrusion machine (Pultrex, Lawford, UK) at the Laboratory of Composite Materials and Structures of the Center for Design, Manufacturing and Materials (Skolkovo Institute of Science and Technology, Moscow, Russia) (Figure 1a). Two pultrusion experiments with 75 mm × 75 mm × 6 mm L-shaped structural profiles (Figure 1c) have been conducted with a 6-month interval. In total, 104 threads of E-glass unidirectional rovings PS 2100 (Owens Corning Composite Materials, Toledo, OH, USA) with a linear density of 9600 TEX (9600 g/1000 m), and two layers of E-glass fabric LT 0600/S 300/06H 01/125 GUS (Owens Corning Composite Materials, Toledo, OH, USA) with a surface density of 900 g/m² were utilized as reinforcement. The matrix was composed of Atlac 430 vinyl ester resin (DSM Composite Resins AG, Schaffhausen, Switzerland) with the following additives: Triganox C (Akzo Nobel Polymer Chemicals B.V., Amsterdam, The Netherlands),

Perkadox 16 (Akzo Nobel Polymer Chemicals B.V., Amsterdam, The Netherlands), BYK-A555 (BYK Additives & Instruments, Wesel, Germany), and zinc stearate (Baerlocher GmbH, Unterschleißheim, Germany). To fabricate the profiles, the 600 mm-long steel die block was used, with four 350 mm-long heating platens installed by pairs at the top and the bottom of the die block along the pulling axis. In order to control the die block temperature, two thermocouples were installed within the body of the die block. The allowable temperature range was 145 ± 10 °C. In total, six 1.5 m-long profiles were manufactured in two experiments at pulling speeds of 200, 400, and 600 mm/min (see Figure 1b). The spring-in angle was measured 3 h after the pultrusion experiment, after the profiles had cooled to the ambient temperature. To measure the spring-in, a set of thin metallic strips (thicknesses of 0.1–1 mm) and a calibrated L-shaped right-angled tool to ensure the correctness of 90° angle measurements were used [83]. The required number of metallic strips were placed in the gap between the leg of the profile and angle tool, and the total thickness of the strips (t_s) was registered (Figure 1d). The angular value of spring-in (φ) is determined based on the size of the profile legs ($L_w = 62$ mm) and the measured total thickness of metallic strips inserted into the gap (t_s) [60]:

$$\varphi = \frac{180^\circ}{\pi} \arctan(t_s/L_w). \quad (1)$$

The accuracy of this spring-in measurement method constituted $\pm 0.09^\circ$. The average of all values measured at several sections along the length of the profile was taken as the final value of spring-in [84].

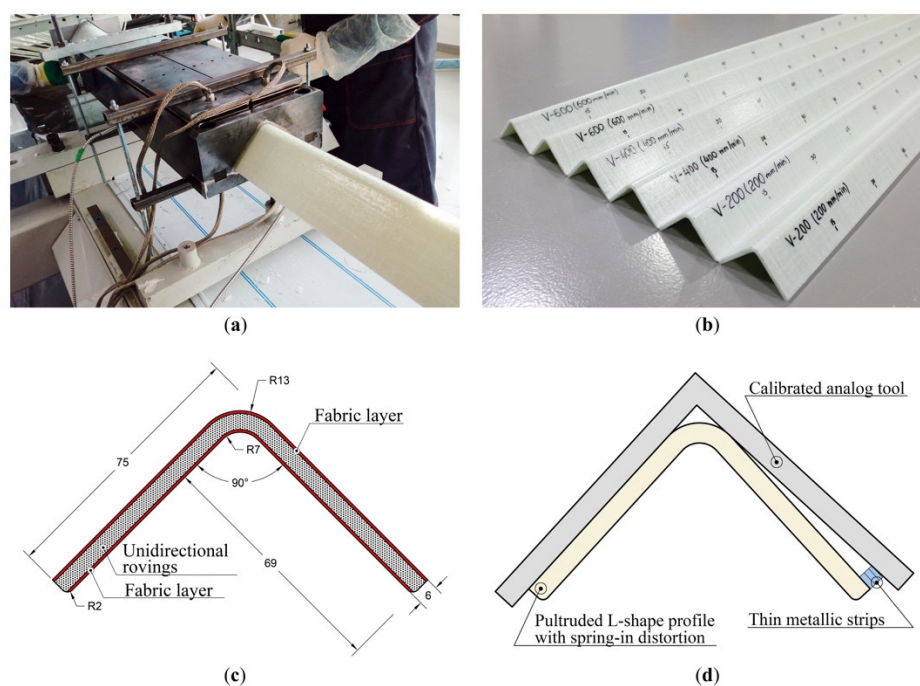


Figure 1. Pultrusion process setup: (a) Pultrusion of an L-shaped profile; (b) L-shaped profiles pultruded at pulling speeds of 200, 400, and 600 mm/min; (c) The cross-section of a 75 mm × 75 mm × 6 mm L-shaped pultruded profile and the position of the unidirectional rovings and fabric layers; (d) Schematic representation of the spring-in measurement process.

2.2. Modeling

In this section, a thermomechanical initial-boundary value problem (IBVP) is discussed. A numerical modeling tool is used to predict the response of a body to applied temperature loads. This can be achieved by solving the given IBVP problem. A more detailed description of this IBVP statement can be found in Zoicher et al. [85] and in Svanberg and Holmberg [56]. Two problems should be solved in resin polymerization modeling,

namely, the heat transfer problem (Section 2.2.1) and the mechanical problem (Section 2.2.2). As the properties of resin and, therefore, of composite material depend on the temperature, in order to solve this IBVP, the distribution of temperature and polymerization degree was modeled with Equations (2)–(8) of the 2D thermochemical model presented in Section 2.2.1. Then, based on results obtained and using the equations presented in Section 2.2.2, it was possible to determine the cure- and temperature-dependent Young's modulus (Equations (9) and (10)), bulk modulus (Equations (11) and (12)), and Poisson's ratio (Equation (13)) of the resin. The given mechanical properties of the resin were used further to calculate mechanical properties of a composite, based on the Self-Consistent Field Micromechanics (SCFM) approach [86,87]. Finally, the obtained mechanical properties of a composite are used to determine the stress–strain state in the composite. A more detailed description of the mechanical problem statement of process-induced residual stresses and distortions can be found in Baran et al. [49]. The novelty of the mechanical problem presented here is in the more accurate CHILE model that uses seven regions to describe changes in Young's modulus of resin, and it accounts for changes in Poisson's ratio of the matrix during phase transitions.

Earlier, it was shown that axial conduction can be neglected when solving the temperature problem [88]. In addition, no significant differences were found in the distributions of stresses and displacements in the transverse direction, which were obtained in 2D and 3D simulations of mechanical behavior [89]. Thus, to accelerate computations, a two-dimensional model was used to solve the thermochemical and mechanical problems in this study. However, these assumptions may result in overestimated values of thermal peak. In addition, the 2D approach makes it impossible to account for stresses, occurring along the longitudinal axis of the profile and causing additional shape distortions in the pulling direction. Nevertheless, further, it will be shown that these assumptions are reasonable and will not result in large discrepancy between predicted and experimental spring-in data.

2.2.1. 2D Thermal Model

A steady-state pultrusion process with a pulling speed of u is considered. By disregarding the heat conduction along the length of the composite profile, the heat transfer equation in a Lagrangian (material) frame of reference can be expressed as follows [88]:

$$C_{p_comp}(T) \rho_{comp} \frac{\partial T}{\partial t} = k_{comp} \frac{\partial^2 T}{\partial x^2} + k_{comp} \frac{\partial^2 T}{\partial y^2} + q, \quad (2)$$

where x and y are the coordinates of a cross-section of the composite profile, T is instantaneous temperature, $C_{p_comp}(T)$ is the temperature-dependent heat capacity of a composite material, ρ_{comp} is the composite density, k_{comp} is the thermal conductivity of the composite in the cross-sectional plane, and q is the heat released due to the exothermic reaction in a polymer matrix. As the heat equation is expressed in the Lagrangian (material) frame of reference, the pulling speed (u), absent in Equation (2), affects the boundary condition equations (Equations (3) and (4)), corresponding to the position of the composite profile cross-section inside or outside the die, respectively:

$$k_{comp} \left. \frac{\partial T}{\partial n} \right|_{\Gamma} = -h_{die}(T - T_{die}(z)) \text{ at } z = ut < L_{die}, \quad (3)$$

$$k_{comp} \left. \frac{\partial T}{\partial n} \right|_{\Gamma} = -h_{air}(T - T_{amb}(z)) \text{ at } z = ut \geq L_{die}, \quad (4)$$

where Γ is the surface of the profile, h_{die} is the coefficient of convective heat transfer between the die block and the profile, h_{air} is the coefficient of convective heat transfer between the air and the profile after exiting the die block, T_{die} is the temperature of the die block, changing along the pulling direction z , and T_{amb} is the ambient temperature.

Assuming the temperature of the composite at the die block entrance, T_{in} , to be uniform over the entire cross-section, it can be expressed as follows:

$$T|_{t=0} = T_{in}, \quad (5)$$

The internal heat released due to the exothermic reaction of the resin (q) during polymerization can be expressed as:

$$q = (1 - V_f)\rho_R H_{tot} \frac{d\alpha}{dt}, \quad (6)$$

where V_f is the volume fraction of reinforcement in a composite, ρ_r is the resin density, H_{tot} is total heat released during curing, and $\frac{d\alpha}{dt}$ is the resin curing rate.

To describe the rate of resin polymerization the equation of the n -th order, an auto-catalytic reaction is used [90]:

$$\frac{d\alpha}{dt} = A_0 e^{-\frac{E_a}{R(T+273.15)}} (1 - \alpha)^n (1 + K_{cat}\alpha), \quad (7)$$

where A_0 is the pre-exponential coefficient, E_a is the activation energy, R is the universal gas constant, T is the instantaneous temperature of the resin in degrees Celsius, n is the order of reaction, and K_{cat} is the activation constant.

It is assumed that preheating the material before the entrance into the die block will not result in its polymerization; hence, the degree of polymerization at the die block entrance is taken to be zero:

$$\alpha|_{t=0} = 0. \quad (8)$$

2.2.2. 2D Mechanical Model

It is assumed that resin starts gaining in Young's modulus (E_r) and becomes able to sustain stresses after the gelation point ($\alpha_{gel}=0.6$). To account for changes in the Young's modulus of the resin (E_r) during the polymerization process and to describe the mechanical behavior of the resin, the CHILE model is used in its modified form [91]:

$$E_r = \begin{cases} E_r^0, & T^* \leq T_{C1} \\ E_r^0 + \frac{T^* - T_{C1}}{T_{C2} - T_{C1}} (E_r^1 - E_r^0), & T_{C1} < T^* < T_{C2} \\ E_r^1 + \frac{T^* - T_{C2}}{T_{C3} - T_{C2}} (E_r^2 - E_r^1), & T_{C2} < T^* < T_{C3} \\ E_r^2 + \frac{T^* - T_{C3}}{T_{C4} - T_{C3}} (E_r^3 - E_r^2), & T_{C3} < T^* < T_{C4} \\ E_r^3 + \frac{T^* - T_{C4}}{T_{C5} - T_{C4}} (E_r^4 - E_r^3), & T_{C4} < T^* < T_{C5} \\ E_r^4 + \frac{T^* - T_{C5}}{T_{C6} - T_{C5}} (E_r^\infty - E_r^4), & T_{C5} < T^* < T_{C6} \\ E_r^\infty, & T_{C6} \leq T^* \end{cases} \quad (9)$$

where $T^* = T_g(\alpha) - T$ is the difference between the instantaneous glass transition temperature (T_g) and the instantaneous temperature (T) of a resin in degrees Celsius; T_{C1} , T_{C2} , T_{C3} , T_{C4} , T_{C5} , and T_{C6} are the critical temperatures in degrees Celsius, and E_r^0 , E_r^1 , E_r^2 , E_r^3 , E_r^4 , and E_r^∞ are the corresponding elastic moduli. $T_g(\alpha)$ is the glass transition temperature depending on the degree of cure, which is expressed as follows [92,93]:

$$T_g(\alpha) = T_{g0} + (T_{g\infty} - T_{g0}) \frac{\lambda\alpha}{1 - (1-\lambda)\alpha} \quad (10)$$

where T_{g0} is the glass transition temperature of the uncured resin ($\alpha = 0$), $T_{g\infty}$ is that of the fully cured resin ($\alpha = 1$), and λ is the material parameter.

To account for the changes in Poisson's ratio during phase transitions, it should be noted that the bulk modulus of resin has the same order of magnitude in both rubber-like and glassy states [94]. According to Svanberg [56], the bulk modulus of the matrix

decreases 2.5 times during the transition from the glassy (K_r^∞) to the rubber-like state (K_r^0). By determining the bulk modulus of the matrix in glassy and rubber-like states based on the linear elastic theory (Equation (11)) [94], the instantaneous bulk modulus of the matrix (K_r) and the corresponding Poisson's ratio (ν_r) can be determined using Equations (12) and (13), accordingly:

$$K_r^\infty = \frac{E_r^\infty}{3(1-2\nu_r^\infty)} \quad (11)$$

$$K_r(E_r) = K_r^0 + (K_r^\infty - K_r^0) \frac{E_r - E_r^0}{E_r^\infty - E_r^0} \quad (12)$$

$$\nu_r(E_r) = \frac{3K_r - E_r}{6K_r} \quad (13)$$

Then, the instantaneous mechanical properties of the resin are used to compute effective mechanical properties of the composite, using the Self-Consistent Field Micromechanics (SCFM) approach [86,87]. Thus, the obtained effective mechanical properties of a composite are subsequently applied to determine the stress–strain state in the composite [49]. The analytical relationships used to predict the effective mechanical properties and stress–strain state in the composite are presented in supplementary materials.

2.2.3. Finite Element Modeling

The IBVP described earlier is solved by means of finite element analysis in ABAQUS FEA software suite (6.14, Dassault Systèmes SE, Vélizy-Villacoublay, France) [95]. Displacements and stresses are computed using the incremental linear elastic approach [49]. The following subroutines are used in the simulations: UMAT, FILM, USDFLD, HETVAL, and UEXPAN. The UMAT subroutine is used to calculate thermal and chemical deformations; to compute the mechanical properties of a composite, using the Self-Consistent Field Micromechanics (SCFM) approach; and to describe constitutive mechanical behavior of a composite. The FILM subroutine is used to assign temperature loads and to describe convective heat transfer between the composite and an environment, both inside and outside the die block. The USDFLD is used to define the cure degree at each point of material as a function of time and temperature; HETVAL is used to specify internal heat generation due to exothermic reaction in a polymer matrix during heat transfer analysis; and UEXPAN is used to add non-mechanical strains (thermal and chemical) to mechanical ones to obtain the total strain tensor. In order to build the model, the 4-node plane strain thermally coupled quadrilateral CPE4RT type elements are used. As the profile section is symmetric, only half of the model, consisting of 1056 elements, is used in simulations. Simulations were performed with different numbers of finite elements in order to calculate the spring-in, using the model described in the “Modeling” section. It was noted that increasing the number of finite elements (starting from 1056 elements), while significantly increasing the simulation time, did not lead to noticeable differences in the final value of spring-in. That is, the refinement of the mesh does not provide significant changes in simulation results.

The numerical model developed for this study uses four different material types (Figure 2c) corresponding to different types of reinforcement used in the pultrusion of L-shaped profiles (Figure 2a,b) as follows: (1) Material_1, transversely isotropic, with the axis of anisotropy oriented along the pulling direction to model the roving; (2) Material_2, transversely isotropic, with the axis of anisotropy oriented along the pulling direction to model the internal layer of fabric; (3) Material_3, with the axis of anisotropy lying within the cross-section plane and oriented parallel to the leg of the L-shaped profile to model the core layer of fabric; and (4) Material_4, transversely isotropic with axis of anisotropy oriented perpendicular to the lay-up plane to model the mat glued to the fabric. Material_1 represents the unidirectional reinforcement used to fabricate L-shaped profiles. Three materials were utilized to model the fabric material used to fabricate L-shaped profiles: Material_2, Material_3, and Material_4. In ABAQUS, Material_2 and Material_3

(representing the unidirectional reinforcement) were assigned the same material properties but with different reinforcement orientation along the direction of pultrusion and in the cross-sectional plane, respectively. Material_4 represents the material with randomly oriented reinforcement in the lay-up plane.

For the AD edge, the symmetrical boundary conditions are set (blue dashed line in Figure 2c). The boundary constraints used to simulate the internal surface of the die block prohibit any motion at the outer perimeter of the profile inside the die block region (the ABCD segment, orange dashed line in Figure 2c). The boundary constraints are deactivated after the die block exit. In addition, any displacements of a composite at the point D are constrained (orange dashed line in Figure 2c).

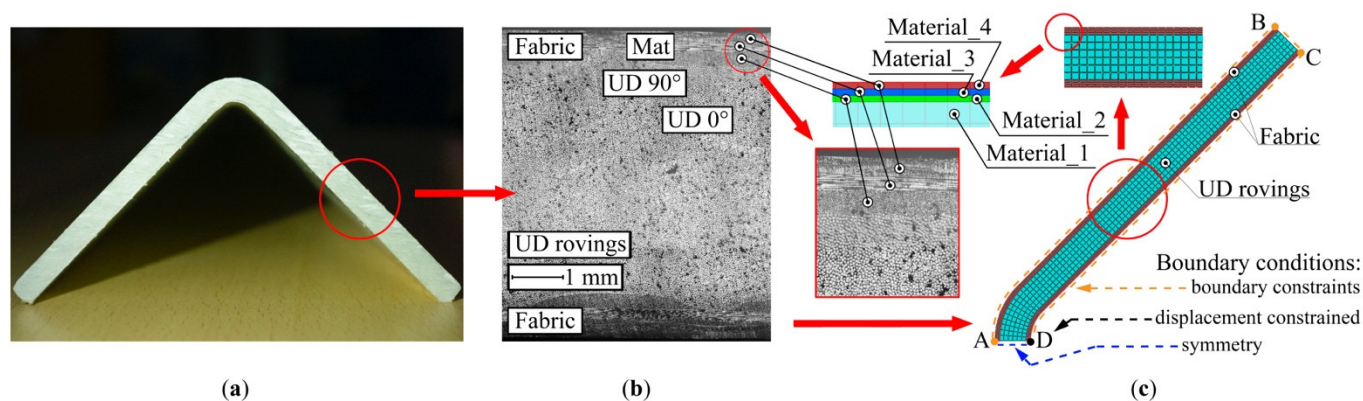


Figure 2. Building the numerical model of a pultruded L-shaped profile: (a) Cross-section of the L-shaped pultruded profile; (b) Microphotograph of the cross-section of the pultruded profile showing the arrangement of UD rovings and fabric layers; (c) Numerical model of the L-shaped pultruded profile built-in ABAQUS software.

Furthermore, the spring-in reduction method that provides for the use of a rigid post-die cooling tool was simulated. The length of the post-die cooling tool constitutes $1/3$ of the length of the die block ($L_{die}/3$). It is assumed that the post-die cooling tool has constant temperature equal to the ambient temperature (T_{amb}) and is installed immediately after the end of the heated die block. The geometry and positions of the heated die block and post-die cooling tool are shown in Figure 3.

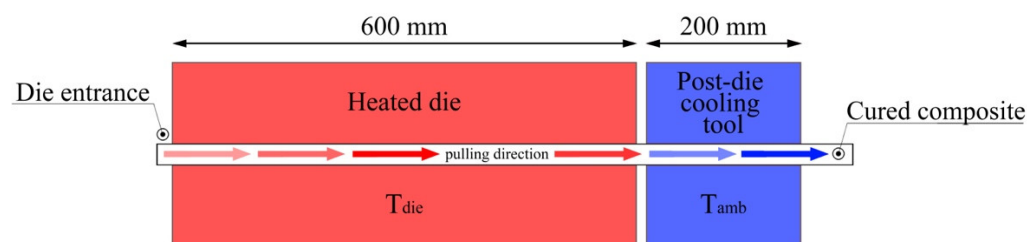


Figure 3. Geometry and position of the heated die and post-die cooling tool.

2.3. Experimental Methods to Determine Model Parameters

To determine the parameters of the model, a series of thermomechanical and thermophysical tests were conducted. Test specimens were cut from plates of cured vinyl ester resin. The plates were polymerized in a laboratory vacuum drying oven XF050 (France Etuves, Chelles, France) under the following procedure: 1.5 h at 120 °C, 30 min at 150 °C, followed by natural cooling for 12 h. An Shtalmark M1-912 M/2 (Rusintermash Ltd., Pushkino, Russia) CNC milling machine was used to cut specimens from polymerized plates. The glass transition temperature and temperature dependence of the storage and loss moduli of cured resin were determined using Dynamic Mechanical Analysis (DMA) following the ISO 6721-1:2011 procedure [96], in the 3-point bending mode, with a Q800

DMA analyzer (TA Instruments Inc., New Castle, DE, USA). Measurements were taken in the temperature range of 30–170 °C, with a heating ramp of 5 °C/min, an oscillation frequency of 1 Hz, and an amplitude of 60 μm . A DSC 204 differential scanning calorimeter (NETZSCH-Gerätebau GmbH, Selb, Germany) was used to measure the heat capacity of the cured resin. Measurements were taken following the procedure specified in ISO 11357-4:2005 [97], within the temperature range of 20–100 °C, with a heating ramp of 10 °C/min. The thermal conductivity of the cured resin was measured according to the ISO 22007-4:2008 procedure [98] in the temperature range of 20–100 °C, using an LFA 457 MicroFlash laser flash apparatus (NETZSCH-Gerätebau GmbH, Selb, Germany). To determine the coefficient of thermal expansion (CTE) of cured resin, a TMA 402F thermomechanical analyzer (NETZSCH-Gerätebau GmbH, Selb, Germany) was used, following the ISO 11359-2:1999 procedure [99], at a temperature of 20 °C. The density of the cured resin was determined by hydrostatic weighing of four samples of 25 mm \times 25 mm \times 2 mm, using HTR-220CE electronic laboratory scales (Shinko Vibra, Tokyo, Japan).

3. Results

3.1. Model Parameters

Figure 4 shows the determined parameters of the model: Young's modulus of resin (Figure 4a) and heat capacity of resin (Figure 4b). The least squares method was used to determine the temperature-dependent specific heat and the constants of the modified CHILE model, based on experimental data. In addition, based on DMA data, the value of $T_{g\infty}$ was found, constituting $T_{g\infty} = 120.4$ °C. The heat capacity demonstrates linear temperature dependence of the form $C_{p,r}(T) = (5.1 \cdot T + 1080)$ J/(kg \cdot °C). Thermal conductivity measurements conducted within the range of 20–100 °C show that the difference in thermal conductivity values does not exceed 2%. That is why thermal conductivity is assumed to be constant and equal to the average experimental value of $k_r = 0.178$ W/(m \cdot °C). The coefficient of thermal expansion measured at the temperature of 20 °C constituted $\alpha_r^\infty = 60 \cdot 10^{-6}$ °C $^{-1}$. The density of resin constitutes $\rho_r = 1140$ kg/m 3 . All measured parameters of the model are given in Table A1.

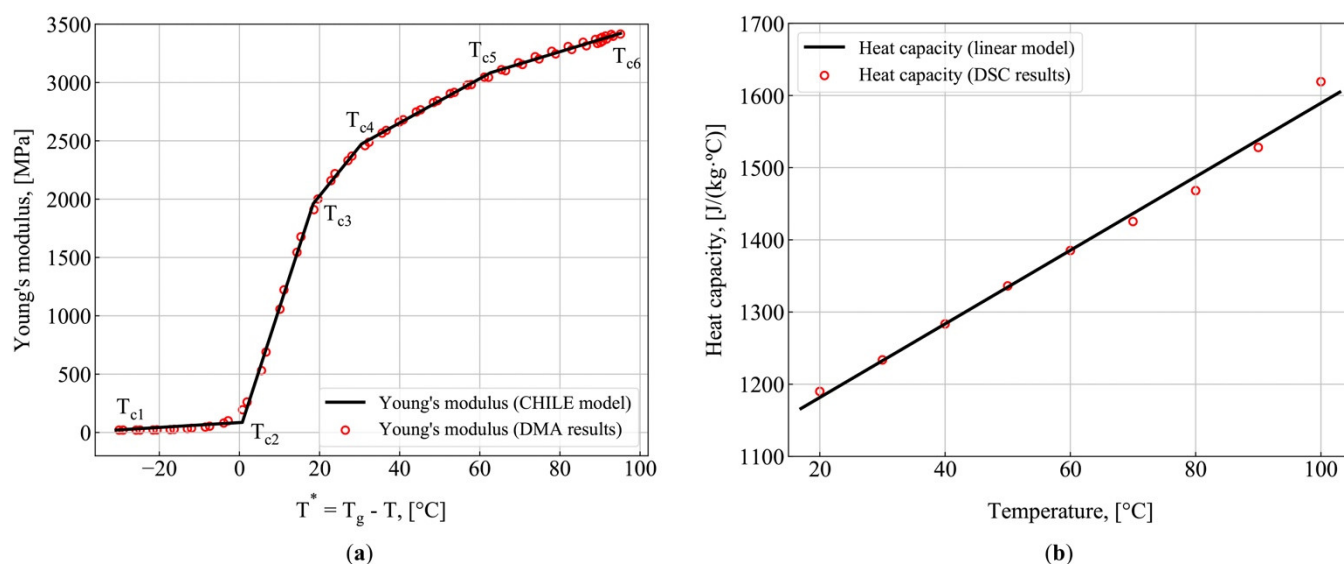


Figure 4. Model parameters measurements: (a) Young's modulus (DMA measurements vs. CHILE model predictions); (b) Heat capacity (DSC measurements vs. predictions obtained with the linear approximation).

3.2. Finite Element Modeling Results

The spring-in values were obtained by simulating the pultrusion of the L-shaped profile at pulling speeds of 200, 400, and 600 mm/min. The results were compared with the values obtained during the two pultrusion experiments. Then, numerical simulations were conducted to analyze the influence of pulling speed increase and of changes in Poisson's ratio during phase transitions (according to Equation (13)) on the value of spring-in. Furthermore, the efficiency of methods of spring-in reduction was analyzed by using a post-die cooling tool or by reducing the chemical shrinkage of the matrix.

Table A1 lists the model parameters used in the computations, together with the information on the source of the data. A key feature of the model discussed here is that it uses experimentally determined values of density, temperature-dependent heat capacity, thermal conductivity, CTE, and mechanical properties of the resin (see Section 2). The values of density, heat capacity, and thermal conductivity of glass-fiber reinforcement were taken from [49], the mechanical properties of glass-fiber reinforcement were taken from [57], the kinetic constants of resin polymerization were taken from [90], and resin properties were taken from [49,56,100]. To determine the properties of the composite layers (Material_1, Material_2, Material_3, Material_4), the following analytical relationships were used: the density and heat capacity were determined as described in [88]; thermal conductivity were determined as described in [101]; the mechanical properties of Material_1, Material_2, and Material_3 were determined as described in [57]; and those of Material_4 were determined as described in [102]. The mentioned relationships and data for each Material_1, Material_2, Material_3, and Material_4 can be found in the supplementary materials.

In addition, at the outer perimeter of the profile, the boundary conditions of thermal contact with the ambient air, based on the given coefficient of convective heat transfer, were imposed. For the profile inside the die block, very high values of the convective heat transfer coefficient ($h_{\text{die}} = 5000 \text{ W}/(\text{m}^2 \cdot ^\circ\text{C})$) were assigned to simulate perfect thermal contact with the die block. To simulate the thermal contact of the profile with the ambient air after the die block exit, the convective heat transfer coefficient of $h_{\text{air}} = 9 \text{ W}/(\text{m}^2 \cdot ^\circ\text{C})$ and the ambient temperature of $T_{\text{amb}} = 18 \text{ }^\circ\text{C}$ were assigned.

Figures 5 and 6 show the spring-in simulation results obtained at various pulling speeds from 100 to 1000 mm/min. Figure 7 shows the distributions of temperature and degree of polymerization obtained at pulling speeds of 200, 600, and 1000 mm/min. Figure 5 shows the simulation results obtained with the model described in the Materials and Methods section. Figure 5a shows the final spring-in values obtained at different pulling speeds, together with the experimental values of spring-in for pulling speeds of 200, 400, and 600 mm/min. At these speeds, the predicted values fall between corresponding experimental data points (see Table 1). For the pulling speed of 200 mm/min, the predicted value constitutes 1.15° and is located between 0.97° (obtained in Experiment 1) and 1.16° (Experiment 2). For the pulling speed of 400 mm/min, the predicted value of 1.40° falls between 1.40° (Experiment 1) and 1.42° (Experiment 2). For the speed of 600 mm/min, the predicted value of 1.69° falls between the corresponding experimental values of 1.67° (Experiment 1) and 1.72° (Experiment 2). A slight decrease in spring-in values from 1.15° to 1.12° can be observed with the reduction in pulling speed from 200 to 100 mm/min. Starting from 200 mm/min, the increase in pulling speed results in a considerable increase in spring-in values. Thus, the increase in pulling speed from 200 to 1000 mm/min results in an over 3 times increase in spring-in (from 1.15° to 3.60°). Figure 5a also shows the fraction of uncured matrix material ($\alpha < 85\%$) within the cross-section of the profile after the die exit. It can be seen that the increase in the fraction of uncured material at the die exit corresponds to an increase in the final values of spring-in. Thus, at the pulling speed of 200 mm/min, the exothermic peak is located inside the die block, and the composite exits the die block fully cured (see Figures 5a and 7e), giving the final spring-in value of 1.15° . The increase in pulling speed forces the exothermic peak further along the pultrusion line, beyond the die block exit. Thus, at pulling speeds of 600 mm/min and 1000 mm/min, the

fraction of uncured resin within the cross-section of the profile constitutes 31% (see Figures 5a and 7f) and 81% (see Figures 5a and 7g), resulting in final spring-in values of 1.69° and 3.60°, respectively.

Figure 5b shows the diagrams of spring-in changes during fabrication for pulling speeds of 200 to 1000 mm/min. The diagram shows three zones corresponding to three stages of spring-in evolution, as follows: Stage I (solid line) corresponds to spring-in changes from the moment the profile exits the die block and to the moment of exothermic peak occurrence (marked by the bold cross); Stage II (dotted and dashed line) corresponds to spring-in changes from the moment of the exothermic peak and to the vitrification point (marked by the bold point); Stage III (dashed line) corresponds to spring-in changes after vitrification and to the full cooldown of the profile. The occurrence of the exothermic peak and vitrification was analyzed within Zone E located at a distance of 2.23 mm from the internal surface of the profile along the AD axis of symmetry (Figure 7h), as simulations show that the maximum temperature of the exothermic peak over the whole section of a composite is observed exactly in this zone at all pulling speeds. Table 1 presents the final values of spring-in, together with the contributions of each stage described above.

Table 1. Spring-in of L-shaped profiles pultruded at different pulling speeds (experimental results and predictions). Contributions of stages to the final spring-in value.

Pulling Speed [mm/min]	Spring-In Angle [°]						Final Value
	Experiment		Model				
	Experiment 1	Experiment 2	Stage I (From the Die Block Exit to the Exothermic Peak)	Stage II (From the Exothermic Peak to the Vitrification Point)	STAGE III (From Vitrification to the Full Cooldown of the Profile)		
100	–	–	0	0.97	0.15		1.12
200	0.97	1.16	0	0.99	0.16		1.15
400	1.40	1.42	0.45	0.80	0.15		1.40
600	1.67	1.72	0.76	0.78	0.15		1.69
700	–	–	1.46	0.80	0.15		2.41
800	–	–	2.10	0.77	0.16		3.03
900	–	–	2.38	0.75	0.16		3.29
1000	–	–	2.72	0.72	0.16		3.60

Starting from the pulling speed of 400 mm/min, the largest contribution to the increase in final spring-in comes from the spring-in occurring at Stage I. This can be attributed to the increase in fraction of uncured material in a composite exiting the die block. It leads to an increase in the corresponding total chemical shrinkage of material in the unconstrained environment. Thus, Stage I (2.72°) contributes 76% to the final spring-in value obtained at 1000 mm/min (3.60°). This can be viewed as the quantitative confirmation of the qualitative results reported by Baran et al. in [48]. It should be noted that at low pulling speeds, the exothermic peak occurs within the die block and the contribution of Stage I to spring-in evolutions in the post-die region is virtually zero (see the corresponding values for pulling speeds of 100 and 200 mm/min in Table 1). At Stage II, a slight decrease in spring-in can be observed with an increase in pulling speed, which is associated with the lower temperature of the exothermic peak. This phenomenon takes place when the exothermic peak occurs outside the die block. With an increase in pulling speed, the composite material stays in the die block for a shorter period of time and takes less heat from the die block. As the same material is considered, the amount of heat generated during the polymerization of the resin is constant and does not depend on the value of chosen pulling speed. Therefore, increasing the pulling speed, the amount of heat transmitted to the composite during pultrusion decreases, and, therefore, the temperature of the exothermic peak also decreases. The Stage III spring-in value virtually does not depend on the pulling speed and constitutes 0.15–0.16°. Thus, for a pulling speed of 1000

mm/min, contributions from Stages II and III to the final spring-in are 20% and 4%, respectively.

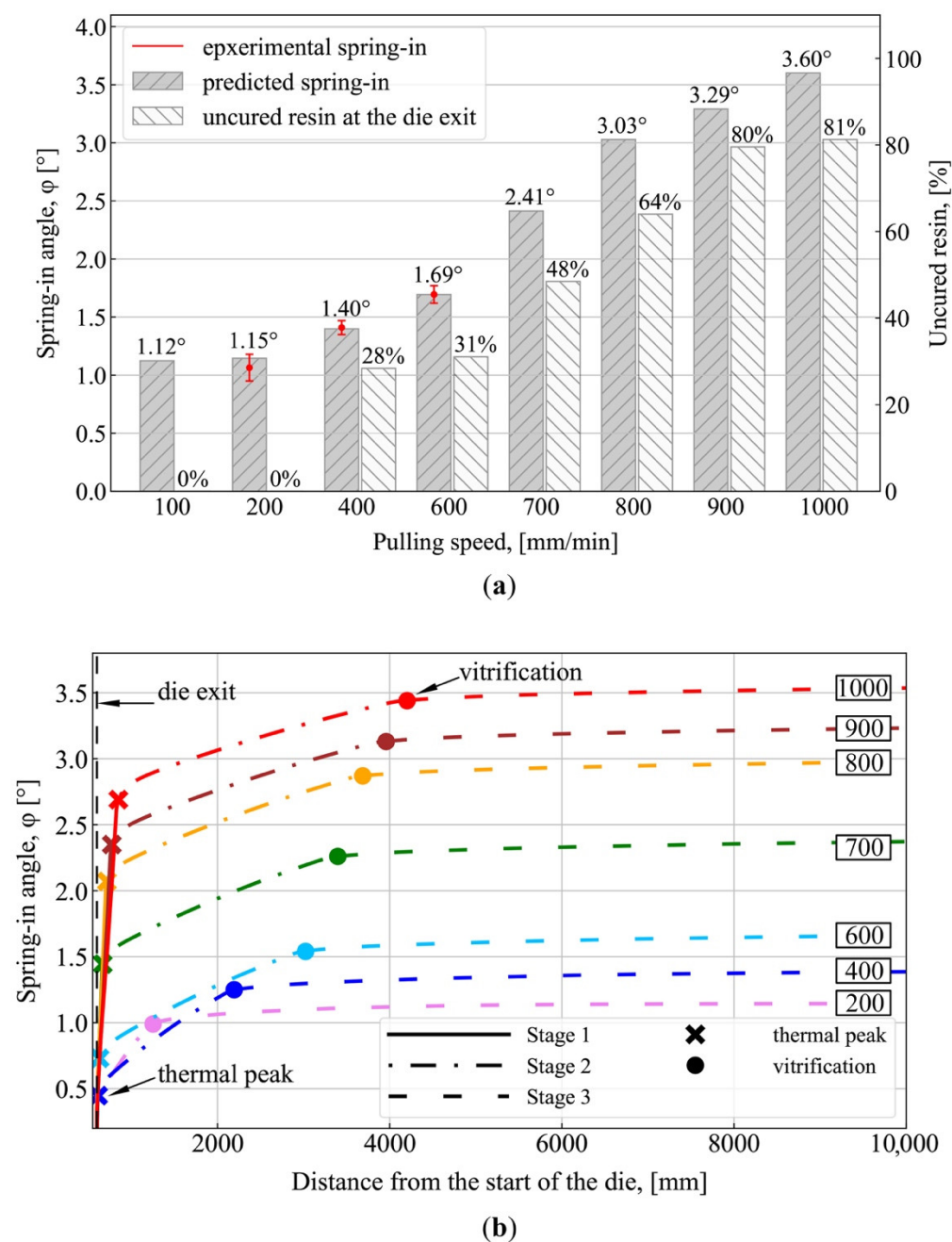


Figure 5. Numerical simulation results: (a) Final values of spring-in vs. fraction of uncured resin ($\alpha < 85\%$) at the die exit for different pulling speeds, obtained with the model described in “Modeling”; (b) Spring-in evolution during fabrication for different pulling speeds, obtained with the model described in “Modeling”. The solid lines in (b) correspond to Stage I (spring-in evolutions from the moment the profile exits the die block to the exothermic peak occurrence); the dot-dash line corresponds to Stage II (from the exothermic peak occurrence to the vitrification point); the dashed line corresponds to Stage III (after vitrification and to the full cooldown of the profile); the bold cross marks the occurrence of the exothermic peak; the bold point marks the vitrification point; the values shown in rectangles correspond to pulling speed (mm/min).

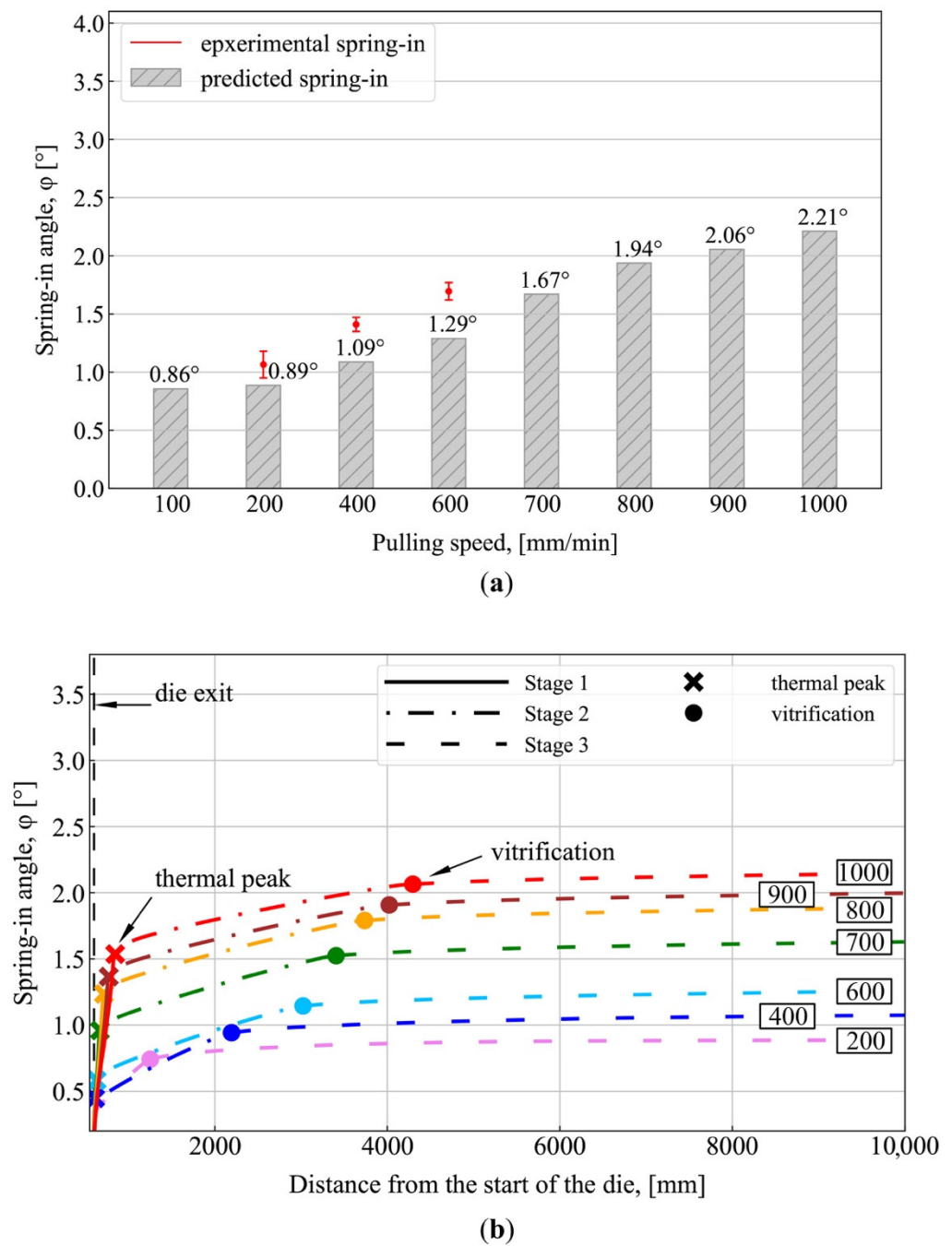


Figure 6. Numerical simulation results: (a) Final values of spring-in at the die exit for different pulling speeds, assuming the constant Poisson’s ratio of matrix; (b) Spring-in evolution during fabrication for different pulling speeds, assuming the constant Poisson’s ratio of matrix. The solid lines in (b) correspond to Stage I (spring-in evolutions from the moment the profile exits the die block and to the exothermic peak occurrence); the dot–dash line corresponds to Stage II (from the exothermic peak occurrence and to the vitrification point); the dashed line corresponds to Stage III (after vitrification and to the full cooldown of the profile); the bold cross marks the occurrence of the exothermic peak; the bold point marks the vitrification point; the values shown in rectangles correspond to pulling speed (mm/min).

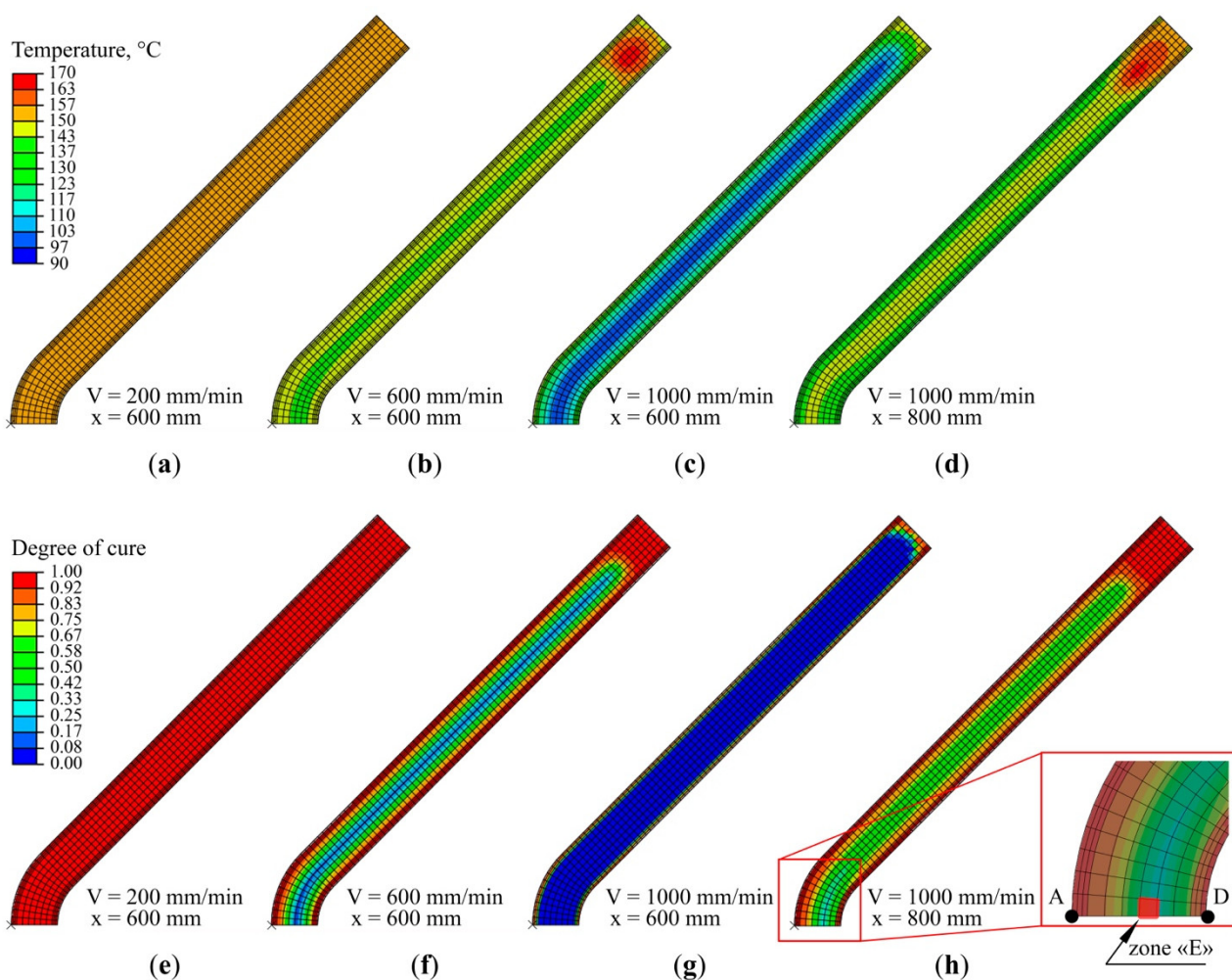


Figure 7. Simulation results: distribution of temperatures (a–d) and degree of polymerization (e–h) in the cross-section of the L-shaped profile: (a) pulling speed—200 mm/min, immediately after the die exit; (b) pulling speed—600 mm/min, immediately after the die exit; (c) 1000 mm/min, immediately after the die exit; (d) 1000 mm/min, at 200 mm after the die exit, or immediately after the post-die cooling tool; (e) 200 mm/min, immediately after the die exit; (f) 600 mm/min, immediately after the die exit; (g) 1000 mm/min, immediately after the die exit; (h) 1000 mm/min, at 200 mm after the die exit or immediately after the post-die cooling tool. Exothermic peak and vitrification were analyzed in Zone E shown to the right in (h).

Figure 6a,b show the results of spring-in simulation for the pultruded L-shaped profile, assuming a constant Poisson's ratio of the matrix, $\nu_r = 0.35$. It can be seen that for a constant Poisson's ratio, the spring-in values are lower than those obtained in simulations that account for changes in Poisson's ratio in accordance with Equation (13). Thus, at the pulling speed of 100 mm/min, the spring-in obtained at a constant Poisson's ratio constitutes 0.86° , while when varying Poisson's ratio, the spring-in constitutes 1.12° , making the difference of 30%. At the pulling speed of 1000 mm/min, the spring-in constitutes 2.21° at a constant Poisson's ratio and 3.60° at a varying Poisson's ratio, making the difference of 63%. For simulations with a constant Poisson's ratio, predicted final values of spring-in are lower than those obtained in the second experiment conducted at pulling speeds of 200, 400, and 600 mm/min by up to 30%, 30%, and 33%, respectively.

Figure 8 shows the results of simulations conducted to estimate the efficiency of methods reducing the spring-in in composite parts, such as the use of a post-die cooling tool (Figure 8a), and the reduced chemical shrinkage of the matrix (Figure 8b). Figure 8a shows results of spring-in simulation in L-shaped profiles pultruded at different pulling speeds with the use of a rigid post-die cooling tool with a length constituting 1/3 of that

of the die block ($L_{\text{die}}/3$), which was installed in a pultrusion manufacturing line immediately after the exit of the heated die block.

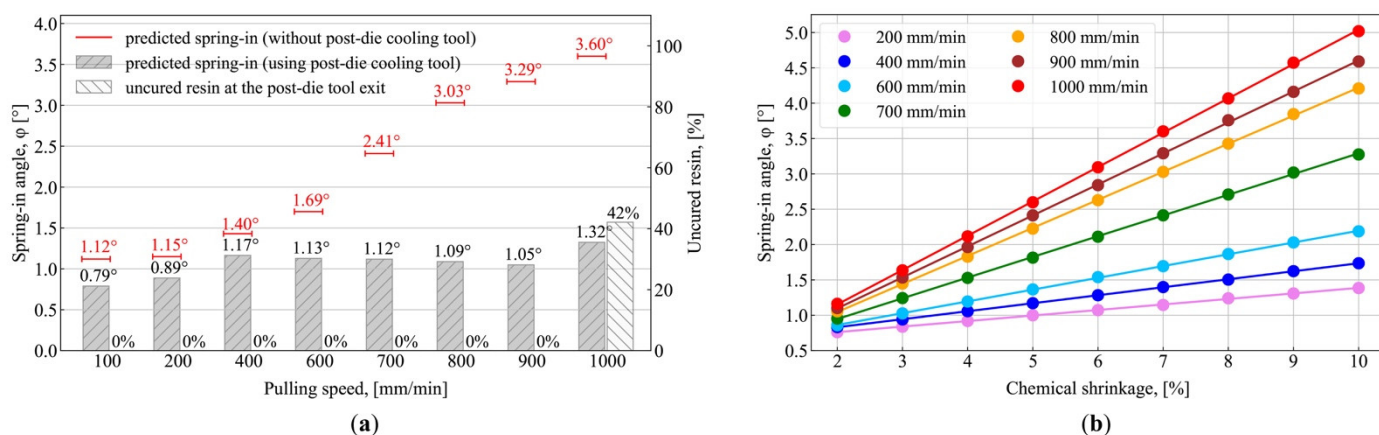


Figure 8. Simulation results for methods of spring-in reduction: (a) With the use of a post-die cooling tool. Gray columns mark the spring-in values obtained with the use of the post-die cooling tool; red lines indicate values obtained without the post-die cooling tool. The corresponding fraction of uncured resin ($\alpha < 85\%$) is shown at the bottom of the graph; (b) Spring-in vs. chemical shrinkage of the resin at different pulling speeds (for shrinkage values within the range of 2 to 10%).

To simulate the post-die cooling tool, boundary constraints within its region are set to prevent all motion at the outer perimeter of the profile (the ABCD segment in Figure 2c). The temperature conditions are set to simulate the cooling down of the profile after the die block exit according to Equation (4). After the exit from the post-die cooling tool, the boundary constraints are deactivated. As a result, a reduction in spring-in for all pulling speeds can be observed, as compared to the absence of the post-die cooling tool. The efficiency of the post-die cooling tool is more evident at higher pulling speeds. Thus, at low pulling speeds where the exothermic peak occurs within the die block, the reduction in spring-in constitutes 0.33° and 0.26° at 100 mm/min and 200 mm/min, respectively. However, at pulling speeds of 400–900 mm/min, where the exothermic peak shifts to the region of a post-die cooling tool, a significant reduction in the final value of spring-in can be observed, which is associated with the absence of uncured material in the profile exiting the post-die cooling tool (Figure 8a). Thus, at a pulling speed of 900 mm/min, the use of the post-die cooling tool results in a final spring-in value of 1.05° , which is 3.1 times lower than the final value of spring-in (3.29°) obtained at the same pulling speed but without the post-die cooling tool. A slight reduction in the final spring-in from 1.17° to 1.05° within the pulling speed range of 400–900 mm/min should also be noted, which can be attributed to the lower temperature of the exothermic peak; this affects the value of thermal shrinkage dependent on the temperature difference. With a further increase in pulling speed to 1000 mm/min, the exothermic peak shifts beyond the post-die cooling tool, resulting in the presence of uncured material at the exit of the post-die cooling tool and in chemical shrinkage taking place under unconstrained conditions. In turn, this results in the increased values of final spring-in compared to those obtained at pulling speeds of 400 to 900 mm/min. At the pulling speed of 1000 mm/min and with the use of the post-die cooling tool, the final value of spring-in is 1.32° , which is 2.7 times lower than the value of 3.60° obtained without the post-die cooling tool; this can be attributed to the lower fraction of uncured matrix material registered at the exit of the constrained environment of the post-die cooling tool, constituting 42% (see Figure 8a) versus 81% registered at the exit of the die block (see Figure 5a). Therefore, the use of the post-die cooling tool can be considered an effective technique to prevent the increase in spring-in at higher pulling speeds by reducing the fraction of uncured material in a composite exiting the constrained environment and, consequently, reducing the total chemical shrinkage occurring in the unconstrained environment.

Figure 8b shows the predictions of spring-in in L-shaped profiles pultruded at different pulling speeds for different values of chemical shrinkage in the range of 2 to 10%. A linear relationship can be observed between the chemical shrinkage of the matrix and the value of spring-in. Chemical shrinkage has a greater influence on the value of spring-in at higher pulling speeds. Thus, the final values of spring-in obtained at 1000 mm/min for 2% and 10% chemical shrinkage differ by a factor of 4.3, as compared to 1.8, which was obtained at a pulling speed of 200 mm/min. Therefore, the reduction of total chemical shrinkage is very important for resins with high chemical shrinkage as the difference between the final values of spring-in at different pulling speeds is particularly noticeable at higher values of chemical shrinkage.

4. Discussion

Spring-in formation in the post-die region takes place in three stages. Starting from the pulling speed of 400 mm/min, the largest contribution to the increase in final spring-in comes from Stage I located before the exothermic peak; this is associated with the exit of uncured resin from the die block and with the subsequent chemical shrinkage taking place in the unconstrained post-die region. The second contribution comes from Stage II, which takes place from the exothermic peak to the vitrification point. The lowest contribution to spring-in development comes from Stage III, which takes place from vitrification and to the complete cooldown of a composite. The increase in pulling speed raises the contribution from Stage I and reduces the role of Stage II, while the contribution from Stage III remains unchanged. Thus, for a pulling speed of 400 mm/min, the contributions to the final spring-in from Stages I, II, and III were 32% (0.45°), 57% (0.8°), and 11% (0.15°), respectively. At 1000 mm/min, the corresponding contributions constitute 76% (2.72°), 20% (0.72°), and 4% (0.16°), respectively.

To increase the efficiency and, thus, the profit from the pultrusion process, it is necessary to maximize pulling speed while preserving the quality of pultruded profiles. Simulations show that lower pulling speeds result in a reduction in spring-in. However, after a certain limit (see Figure 5a), a reduction in pulling speed does not produce a meaningful reduction in spring-in. Thus, the difference between the spring-in values obtained at pulling speeds of 100 and 200 mm/min was only 2.7%. Therefore, a reduction in pulling speed below the value corresponding to the exothermic peak location at the boundary between the die block and the unconstrained post-die region will only result in reduced process output and will not affect spring-in. At lower pulling speeds, the chemical shrinkage providing the largest contribution to spring-in development occurs within the die block. Here, a composite is contained in constrained conditions and, consequently, experiences less deformation compared to the unconstrained environment of the post-die region. Conversely, higher pulling speeds shift the exothermic peak beyond the constrained region of the die block, resulting in higher spring-in values. Thus, final spring-in values obtained at 200 mm/min (with an exothermic peak located inside the die block) and at 1000 mm/min (with an exothermic peak located in the post die region), differ by the factor of 3.1, constituting 1.15° and 3.60°, respectively.

Hence, to increase the process output, the capability is needed to reduce the contributions from chemical and thermal shrinkages to trade the slight increase in spring-in for a significant increase in pulling speed. The spring-in can be reduced by installing a post-die cooling tool or by using additives that reduce chemical shrinkage of the resin (carbon nanofibers [41], silica nanoparticles [103], aluminum oxide nanoparticles [78], and low-profile additives [104]). The use of a post-die cooling tool makes it possible to significantly increase the process output by increasing the pulling speed without increasing the final spring-in value. Thus, using the post-die cooling tool at the pulling speed of 900 mm/min makes it possible to obtain the same level of spring-in as at 200 mm/min without the cooling tool. Thus, the pulling speed can be increased by a factor of 4.5 while maintaining the same level of spring-in, i.e., 1.05° and 1.15°, respectively (see Figure 8a). The efficiency of this method can be explained by the smaller fraction of uncured material exiting the

constrained environment. In turn, this results in a reduction in the total chemical shrinkage of a profile under unconstrained conditions. Thus, at 900 mm/min, the final value of spring-in obtained with the use of the post-die cooling tool is 1.05° , which is 3.1 times less than that obtained without the use of a cooling tool, where the final spring-in constitutes 3.29° .

Reduction of the total chemical shrinkage is also a very effective method of reducing the spring-in, which plays an important role in the case of resins featuring high chemical shrinkage because the difference between the final values of spring-in at different pulling speeds becomes more evident at higher values of chemical shrinkage. Thus, for resins with chemical shrinkage of 10%, the final values of spring-in obtained at pulling speeds of 200 mm/min and 1000 mm/min differ by a factor of 3.6, i.e., 1.39° and 5.02° , respectively. For resins with 2% chemical shrinkage, the corresponding values differ only by a factor of 1.5, i.e., 0.76° and 1.16° , respectively. In addition, at a pulling speed of 1000 mm/min, the use of additives to reduce the chemical shrinkage of resin from 7 to 2% makes it possible to obtain the level of spring-in equal to that of a resin with a chemical shrinkage of 7% without additives, at a pulling speed of 200 mm/min. That is, the pulling speed can be increased by as much as five times, maintaining constant spring-in values of 1.16° and 1.15° , respectively (see Figure 8b). The methods of reducing spring-in via the post-die cooling tool or with shrinkage-reducing additives require further investigation and experimental validation.

This 2D model is limited in that it does not account for changes in heat conduction in the pulling direction. However, it uses boundary conditions to account for the influence of pulling speed. The assumptions used in the model can lead to an overestimated exothermic peak as compared to the experimental values. In addition, the model does not account for stresses along the profile that can lead to additional shape deformations in the longitudinal direction. Nevertheless, these assumptions can be considered allowable in stress-strain analysis, considering large dimensions of produced profile in the pulling direction. In addition, these assumptions produce acceptable predictions of spring-in falling within spring-in values obtained in two pultrusion experiments. In future research, the authors intend to perform 3D analysis for the case of pultruded flat laminate to evaluate the influence of pulling speed and of profile thickness on the formation of cracks and distortions. Thus, a novel steady-state 3D-Eulerian numerical framework is intended to be applied in future works with the aim of accelerating the computational process [31].

The results of this study support findings in Baran et al. [48] that higher pulling speeds lead to increase in spring-in. However, their study is somewhat limited in that it analyzed only four different pulling speeds, and simulation results were experimentally validated only at one pulling speed. Consequently, the authors were unable to conclude that the decrease in spring-in observed with a reduction of pulling speed takes place only to a certain level, and that further reduction of pulling speed would not change the spring-in level. In their simulations, Baran et al. [48,49] assumed the constant and temperature-independent heat capacity of a composite. Considering that, according to our studies, heat capacity significantly affects the final value of spring-in, the assumption of constant and temperature-independent heat capacity of a composite appears unreasonable and will result in considerable disagreement between experimental results and predictions. Our study also demonstrate that chemical shrinkage plays a significant role in spring-in development in pultruded profiles, supporting the results reported by Wang et al. [70]. Moreover, the results obtained by Wang et al. are further extended in our study by calculating the contribution of thermal and chemical shrinkage to the growth of spring-in. The simulations demonstrated that reduced chemical shrinkage results in spring-in reduction, as shown in experiments with additives [41,78]. Moreover, the additives can also reduce the coefficient of thermal expansion of resin and, therefore, the spring-in angle, as shown in [81]. However, no experimental studies on the influence of additives on the development of cure-induced residual stresses and deformations in pultruded profiles have been published before. Therefore, this question will require further investigation. A significant

reduction of cure-induced strains and spring-in can also be achieved through the use of microwave curing, as was demonstrated by Li et al. [47]. The influence of microwave processing on cure-induced strains in pultrusion also requires further investigation, as the application of this process seems to be quite possible [105]. Further experimental investigation of chemical shrinkage in pultrusion is intended to be performed with the use of Fiber Bragg Grating sensors as was done for autoclave technology by Hu et al. [77]. In addition, at high pulling speeds, it is necessary to consider the possible formation of matrix cracks and delamination, reducing the structural performance of pultruded profiles [60]. Therefore, further numerical studies are necessary to analyze the influence of the pultrusion process conditions on the formation of matrix cracks and delamination. It is also necessary to conduct multicriteria optimization of manufacturing conditions to maximize the pulling speed and minimize cure-induced residual stresses, spring-in, and formation of matrix cracks/delaminations, as was already done for other processes [73,106]. The effect of fiber volume fraction variability on the development of residual stresses and, therefore, on spring-in occurrence is to be investigated as well [30]. The authors also intend to simulate the formation of process-induced defects (spring-in, matrix cracks, delaminations) and their influence on the structural performance of other standard [107–109], curved [20], and new types of profiles designed using topology optimization methods [110].

5. Conclusions

To better understand the formation of spring-in in profiles manufactured at different pulling speeds, an experimental study and numerical simulation of 75 mm × 75 mm × 6 mm L-shaped profiles of glass fiber/vinyl ester resin has been conducted. The modified CHILE model accounting for changes in the Young's modulus and Poisson's ratio during phase transitions was used for simulations. The occurrence of spring-in in L-shaped profiles manufactured at pulling speeds of 200, 400, and 600 mm/min was simulated. Then, the simulation results were compared with experimental values obtained in two pultrusion experiments conducted at the interval of 6 months. The predictions show good agreement with the experimental data. The validated model was also used to simulate the influence of pulling speed and of changes in the Poisson's ratio of the matrix during phase transitions on the value of spring-in. Subsequently, the methods of reducing spring-in with the use of a post-die cooling tool and by reducing the chemical shrinkage of the resin were simulated. The following findings can be reported:

- The final value of spring-in depends on the position of the exothermic peak and vitrification point on the pultrusion line, relative to the end of the constrained region of the die, which, in turn, is determined by the selected pulling speed. The closer the exothermic peak position to the constrained region of the die, the lower the obtained spring-in values. Alternatively, higher spring-in values can be observed with the increase in the distance of the peak from the die exit because the composite can no longer sustain stresses from chemical shrinkage in the unconstrained environment of the post-die region. It was shown that higher pulling speeds result in a higher fraction of uncured material in a composite exiting the constrained environment of the die block. This leads to an increase in the total chemical shrinkage of the material under unconstrained conditions and, hence, results in increased values of spring-in;
- Starting from the pulling speed of 400 mm/min, the largest contribution to spring-in comes from the chemical shrinkage of the resin, which takes place before the exothermic peak (Stage I), and from thermal shrinkage taking place before vitrification of the composite (Stage II). However, at the cooling stage (Stage III), thermal shrinkage resulted only in a slight increase in spring-in. The higher pulling speeds increase the contribution from Stage I and reduce the role of Stage II, while the spring-in contribution from Stage III remains unchanged;

- The use of a post-die cooling tool or reduction of resin chemical shrinkage allows a minimum of 4.5 times increase in process output to be obtained while preserving the same level of spring-in.

Supplementary Materials: The following are available online at www.mdpi.com/article/10.3390/polym13162748/s1, Supplementary materials: Calculation of composite properties for heat-transfer problem and composite effective mechanical properties.

Author Contributions: Conceptualization, A.S.; software, A.V. and A.S.; validation, A.V. and A.S.; formal analysis, A.V. and A.S.; investigation, A.V.; data curation, A.V., A.S. and F.T.; writing—original draft preparation, A.V. and A.S.; writing—review and editing, A.V., A.S., F.T. and P.C.; visualization, A.V.; supervision, A.S. and P.C.; project administration, I.A.; funding acquisition, I.A. All authors have read and agreed to the published version of the manuscript.

Funding: This research received no external funding.

Data Availability Statement: The data presented in this study are available on request from the corresponding author.

Acknowledgments: The authors would like to express their gratitude to the Skoltech Center for Design, Manufacturing and Materials for the support provided within the framework of the collaboration programs.

Conflicts of Interest: The authors declare no conflict of interest.

Notations

ρ_r	density of resin, kg/m ³
ρ_f	density of fiber, kg/m ³
ρ_{comp}	density of composite, kg/m ³
k_r	thermal conductivity of resin, W/(m·°C)
k_{f_trans}	thermal conductivity of the fiber in the transverse direction, W/(m·°C)
k_{f_long}	thermal conductivity of the fiber in the longitudinal direction, W/(m·°C)
k_{comp}	thermal conductivity in the cross-sectional plane, W/(m·°C)
T	instantaneous temperature, °C
$C_{p,r}(T)$	temperature-dependent heat capacity of resin, J/(kg·°C)
$C_{p,f}$	heat capacity of the fiber, J/(kg·°C)
$C_{p,comp}(T)$	temperature-dependent heat capacity of a composite, J/(kg·°C)
t	time, sec
q	heat released due to the exothermic reaction in polymer matrix, kJ
x, y	coordinates of a cross-section of the composite profile, mm
z	coordinate of a composite cross-section along the pulling direction of pultrusion, mm
h_{die}	convective heat transfer coefficient between the die block and the profile, W/(m ² ·°C)
h_{air}	convective heat transfer coefficient between the ambient air and the profile after the die block exit, W/(m ² ·°C)
α	resin degree of cure
$d\alpha/dt$	resin curing rate, 1/s
A_0	pre-exponential coefficient, 1/s
E_a	activation energy, kJ/mol
R	universal gas constant, J/(mol·°C)
n	order of reaction
K_{cat}	activation constant
H_{tot}	total heat released, kJ/kg
T_{in}	temperature of material at the die block entrance, °C

T_{die}	temperature at the die block, °C
T_1	temperature at the first zone of the die block, °C
T_2	temperature at the second zone of the die block, °C
T_3	temperature at the third zone of the die block, °C
T_4	temperature at the fourth zone of the die block, °C
T_5	temperature at the fifth zone of the die block, °C
T_6	temperature at the die block exit, °C
T_{amb}	ambient temperature, °C
$T_g(\alpha)$	instantaneous glass transition temperature, °C
T_{g0}	glass transition temperature of uncured resin, °C
$T_{g\infty}$	glass transition temperature of fully cured resin, °C
T^*	difference between the instantaneous glass transition temperature and the instantaneous temperature of the resin, °C
$T_{c1}, T_{c2}, T_{c3}, T_{c4}, T_{c5}, T_{c6}$	critical temperatures, °C
E_r	instantaneous Young's modulus of the resin, MPa
E_r^0	Young's modulus of resin at $T_{c1} = -30.8$ °C, MPa
E_r^1	Young's modulus of resin at $T_{c2} = 0.7$ °C, MPa
E_r^2	Young's modulus of resin at $T_{c3} = 18.4$ °C, MPa
E_r^3	Young's modulus of resin at $T_{c4} = 30.5$ °C, MPa
E_r^4	Young's modulus of resin at $T_{c5} = 62.6$ °C, MPa
E_r^∞	Young's modulus of resin at $T_{c6} = 95.1$ °C, MPa
$K_r(E_r)$	instantaneous bulk modulus of resin, MPa
K_r^∞	bulk modulus of resin at $T = 25.3$ °C, MPa
K_r^0	bulk modulus of resin at $T = T_{g\infty}$, MPa
$\nu_r(E_r)$	instantaneous Poisson's ratio of resin
ν_r^∞	Poisson's ratio of resin at $T = 25.3$ °C
α_r^∞	coefficient of thermal expansion of resin at $T < T_{g\infty}$, 1/°C
α_r^0	coefficient of thermal expansion of resin at $T \geq T_{g\infty}$, 1/°C
E_f	Young's modulus of glass fiber reinforcement, MPa
ν_f	Poisson's ratio of glass fiber reinforcement
α_f	coefficient of thermal expansion of glass fiber reinforcement, 1/°C
u	pulling speed, mm/min
$V_{f,1}$	volume fraction of fabric layer reinforcement
$V_{f,2}$	volume fraction of unidirectional layer reinforcement
ΔV	total volumetric chemical shrinkage, %
α_{gel}	resin cure degree corresponding to the gelation
λ	material constant in Equation (10)
L_{die}	die block length, m
φ	spring-in angle, °
t_s	thickness of the strips, mm
L_w	size of the L-shaped profile legs, mm

Appendix A

Table A1. Model parameters.

Property	Source	Symbol	Value	Unit
Heat transfer problem				
Density of resin	-a	ρ_r	1140	kg/m ³
Density of fiber	[49]	ρ_f	2560	kg/m ³
Thermal conductivity of resin	-e	k_r	0.178	W/(m·°C)

Thermal conductivity of fiber in the transverse direction	[49]	k_{f_trans}	1.04	W/(m·°C)		
Thermal conductivity of fiber in the longitudinal direction	[49]	k_{f_long}	11.4	W/(m·°C)		
Heat capacity of resin depending on the temperature	-b	$C_{p,r}(T)$	$5.1 \times T + 1080$	J/(kg·°C)		
Heat capacity of fiber	[49]	$C_{p,f}$	670	J/(kg·°C)		
Convective heat transfer coefficient between the die block and the profile	-f	h_{die}	5000	W/(m ² ·°C)		
Convective heat transfer coefficient between the ambient air and the profile after the die block exit	-f	h_{air}	9	W/(m ² ·°C)		
Cure kinetics						
Pre-exponential coefficient	[90]	A_0	$10^{9.34}$	1/s		
Activation energy	[90]	E_a	93.3	kJ/mol		
Universal gas constant	[90]	R	8.31	J/(mol·°C)		
Order of reaction	[90]	n	1.91	-		
Activation constant	[90]	K_{cat}	$10^{2.73}$	-		
Total heat released	[90]	H_{tot}	189	kJ/kg		
Temperature conditions						
Temperature at the die block, $T_{die}(z)$:		Pulling speed, mm/min				
			200	400	600	
@ 97–103 mm (1st zone)	-a	T_1	45	31	30	°C
@ 197–203 mm (2nd zone)	-a	T_2	62	42	40	°C
@ 297–303 mm (3rd zone)	-a	T_3	84	66	89	°C
@ 397–403 mm (4th zone)	-a	T_4	127	95	119	°C
@ 497–503 mm (5th zone)	-a	T_5	159	127	141	°C
@ 600 mm (at the die block exit)	-a	T_6	153	148	147	°C
Temperature of material at the die block entrance	-a	T_{in}		18		°C
Ambient temperature	-a	T_{amb}		18		°C
Mechanical properties of resin						
Young's modulus at $T_{c1} = -30.8$ °C	-c	E_r^0	21			MPa
Young's modulus at $T_{c2} = 0.7$ °C	-c	E_r^1	86			MPa
Young's modulus at $T_{c3} = 18.4$ °C	-c	E_r^2	1961			MPa
Young's modulus at $T_{c4} = 30.5$ °C	-c	E_r^3	2473			MPa
Young's modulus at $T_{c5} = 62.6$ °C	-c	E_r^4	3083			MPa
Young's modulus at $T_{c6} = 95.1$ °C	-c	E_r^∞	3421			MPa
Poisson's ratio at $T = 25.3$ °C	[111]	ν_r^∞	0.35			-
Bulk modulus at $T = 25.3$ °C		$\frac{E_r^\infty}{3(1-2\nu_r^\infty)}$	K_r^∞	3801		MPa
Bulk modulus at $T = T_{g\infty}$		$\frac{K_r^\infty}{2.5}$ [56]	K_r^0	1520		MPa
Coefficient of thermal expansion at $T < T_{g\infty}$	-d	α_r^∞		60×10^{-6}		1/°C
Coefficient of thermal expansion at $T \geq T_{g\infty}$	$2.5 \times \alpha_r^\infty$ [56]	α_r^0		150×10^{-6}		1/°C
Mechanical properties of glass fiber reinforcement						
Young's modulus	[57]	E_f	73 080			MPa
Poisson's ratio	[57]	ν_f	0.22			-
Coefficient of thermal expansion	[57]	α_f	5.04×10^{-6}			1/°C
Other properties						
Pulling speed	-a	u	200/400/600			mm/min
The volume fraction of reinforcement						
Fabric layer	-a	$V_{f,1}$	0.5			-
UD layer	-a	$V_{f,2}$	0.59			-
Total volumetric chemical shrinkage	[100]	ΔV	-7			%
Glass transition temperature of the uncured resin	[56]	T_{g0}	-41			°C

Glass transition temperature of the fully cured resin	- ^c	$T_{g\infty}$	120.4	°C
Resin cure degree corresponding to the gelation	- ^f	α_{gel}	0.6	-
Material constant in Equation (10)	[49]	λ	0.4	-
Die block length	- ^a	L_{die}	0.6	m

^a Measured value in pultrusion experiments. ^b Determined from Differential Scanning Calorimetry (DSC) data. ^c Determined from Dynamic Mechanical Analysis (DMA) data. ^d Determined from Thermomechanical Analysis (TMA) data. ^e Determined from Laser Flash Analysis (LFA) data. ^f Assumed value.

References

1. Starr, T.F. *Pultrusion for Engineers*; Woodhead Publishing: Cambridge, UK, 2000.
2. Vedernikov, A.; Safonov, A.; Tucci, F.; Carlone, P.; Akhatov, I. Pultruded Materials and Structures: A Review. *J. Compos. Mater.* **2020**, *54*, 4081–4117. <https://doi.org/10.1177/0021998320922894>.
3. Minchenkov, K.; Vedernikov, A.; Safonov, A.; Akhatov, I. Thermoplastic Pultrusion: A Review. *Polymers* **2021**, *13*, 180. <https://doi.org/10.3390/polym13020180>.
4. Zhu, R.; Li, F.; Zhao, Z.; Zhang, D.; Chen, Y. Compression Behavior of Square Pyramid Substructure of Novel Pultruded FRP-Aluminum Space Truss. *J. Compos. Constr.* **2020**, *24*. [https://doi.org/10.1061/\(ASCE\)CC.1943-5614.0001074](https://doi.org/10.1061/(ASCE)CC.1943-5614.0001074).
5. Shekarchi, M.; Yekrangnia, M.; Biniaz, A.; Raftery, G.M. Effect of Elevated Temperatures on the Compressive Behavior of Timber Filled Steel and Pultruded GFRP Tubes. *Compos. Struct.* **2021**, *271*, 114135. <https://doi.org/10.1016/j.compstruct.2021.114135>.
6. Tucci, F.; Vedernikov, A. Design Criteria for Pultruded Structural Elements. In *Reference Module in Materials Science and Materials Engineering*; Elsevier: Amsterdam, The Netherlands, 2021. <https://doi.org/10.1016/B978-0-12-819724-0.00086-0>.
7. Madenci, E.; Özkılıç, Y.O.; Gemi, L. Buckling and Free Vibration Analyses of Pultruded GFRP Laminated Composites: Experimental, Numerical and Analytical Investigations. *Compos. Struct.* **2020**, *254*, 112806. <https://doi.org/10.1016/j.compstruct.2020.112806>.
8. Gemi, L.; Madenci, E.; Özkılıç, Y.O. Experimental, Analytical and Numerical Investigation of Pultruded GFRP Composite Beams Infilled with Hybrid FRP Reinforced Concrete. *Eng. Struct.* **2021**, *244*, 112790. <https://doi.org/10.1016/j.engstruct.2021.112790>.
9. Li, C.; Yin, X.; Wang, Y.; Zhang, L.; Zhang, Z.; Liu, Y.; Xian, G. Mechanical Property Evolution and Service Life Prediction of Pultruded Carbon/Glass Hybrid Rod Exposed in Harsh Oil-Well Condition. *Compos. Struct.* **2020**, *246*, 112418. <https://doi.org/10.1016/j.compstruct.2020.112418>.
10. Gao, Y.; Zhang, D.; Li, F.; Zhao, Q.; Zhao, Z.; Chen, Y. Bearing Strength and Failure Behaviour of Composite Pre-Tightened Multi-Tooth Joint. *Compos. Struct.* **2021**, *272*, 114208. <https://doi.org/10.1016/j.compstruct.2021.114208>.
11. Tinkov, D.V.; Safonov, A.A. Design Optimization of Truss Bridge Structures of Composite Materials. *J. Mach. Manuf. Reliab.* **2017**, *46*, 46–52. <https://doi.org/10.3103/S1052618817010149>.
12. Sorina, T.G.; Safonov, A.A.; Khairtdinov, A.K. Peculiarities of Using Carbon Glass-Reinforced Plastic in Pultrusion Composite Profiles for Bridge Engineering. *J. Mach. Manuf. Reliab.* **2010**, *39*, 47–51. <https://doi.org/10.3103/S1052618810010073>.
13. Zhu, R.; Li, F.; Chen, Y.; Li, R. A Hybrid Beam-Column Element for Direct Second-Order Nonlinear Analysis of PFRP Frame Structures. *Compos. Struct.* **2021**, *271*, 114171. <https://doi.org/10.1016/j.compstruct.2021.114171>.
14. Sharda, A.; Manalo, A.; Ferdous, W.; Bai, Y.; Nicol, L.; Mohammed, A.; Benmokrane, B. Axial Compression Behaviour of All-Composite Modular Wall System. *Compos. Struct.* **2021**, *268*, 113986. <https://doi.org/10.1016/j.compstruct.2021.113986>.
15. Toubia, E.A.; Alomari, A.; Morgan, A.B.; Klosterman, D. Influence of Heat Damage on the Bolted Double Lap Joint Strength of Pultruded E-Glass/Polyester Composites. *Thin-Walled Struct.* **2021**, *163*, 107764. <https://doi.org/10.1016/j.tws.2021.107764>.
16. Alhawamdeh, M.; Alajarmeh, O.; Aravinthan, T.; Shelley, T.; Schubel, P.; Kemp, M.; Zeng, X. Modelling Hollow Pultruded FRP Profiles under Axial Compression: Local Buckling and Progressive Failure. *Compos. Struct.* **2021**, *262*, 113650. <https://doi.org/10.1016/j.compstruct.2021.113650>.
17. Rubino, F.; Nisticò, A.; Tucci, F.; Carlone, P. Marine Application of Fiber Reinforced Composites: A Review. *J. Mar. Sci. Eng.* **2020**, *8*, 26. <https://doi.org/10.3390/jmse8010026>.
18. Zyka, K.; Mohajerani, A. Composite Piles: A Review. *Constr. Build. Mater.* **2016**, *107*, 394–410. <https://doi.org/10.1016/j.conbuildmat.2016.01.013>.
19. Madenci, E.; Özkılıç, Y.O.; Gemi, L. Experimental and Theoretical Investigation on Flexure Performance of Pultruded GFRP Composite Beams with Damage Analyses. *Compos. Struct.* **2020**, *242*, 112162. <https://doi.org/10.1016/j.compstruct.2020.112162>.
20. Struzziero, G.; Maistros, G.M.; Hartley, J.; Skordos, A.A. Materials Modelling and Process Simulation of the Pultrusion of Curved Parts. *Compos. Part A Appl. Sci. Manuf.* **2021**, *144*, 106328. <https://doi.org/10.1016/j.compositesa.2021.106328>.
21. Dubinskii, S.V.; Safonov, A.A. Composite-Friendly Approach to Certification of Advanced Materials and Fabrication Methods Used in Aviation Industry. *J. Mach. Manuf. Reliab.* **2017**, *46*, 501–506. <https://doi.org/10.3103/S1052618817050041>.
22. Ferdous, W.; Manalo, A.; AlAjarmeh, O.; Mohammed, A.A.; Salih, C.; Yu, P.; Mehrinejad Khotbehsara, M.; Schubel, P. Static Behaviour of Glass Fibre Reinforced Novel Composite Sleepers for Mainline Railway Track. *Eng. Struct.* **2021**, *229*, 111627. <https://doi.org/10.1016/j.engstruct.2020.111627>.
23. Li, C.; Xian, G.; Li, H. Tension-Tension Fatigue Performance of a Large-Diameter Pultruded Carbon/Glass Hybrid Rod. *Int. J. Fatigue* **2019**, *120*, 141–149. <https://doi.org/10.1016/j.ijfatigue.2018.11.007>.

24. Jeppesen, N.; Mikkelsen, L.P.; Dahl, A.B.; Nymark, A.N.; Dahl, V.A. Quantifying Effects of Manufacturing Methods on Fiber Orientation in Unidirectional Composites Using Structure Tensor Analysis. *Compos. Part A Appl. Sci. Manuf.* **2021**, *149*, 106541. <https://doi.org/10.1016/j.compositesa.2021.106541>.
25. Corrado, A.; Polini, W.; Sorrentino, L.; Bellini, C. Geometrical Deviation Analysis of CFRP Thin Laminate Assemblies: Numerical and Experimental Results. *Compos. Sci. Technol.* **2018**, *168*, 1–11. <https://doi.org/10.1016/j.compscitech.2018.09.003>.
26. Hörberg, E.; Nyman, T.; Åkermo, M.; Hallström, S. Thickness Effect on Spring-in of Prepreg Composite L-Profiles – An Experimental Study. *Compos. Struct.* **2019**, *209*, 499–507. <https://doi.org/10.1016/j.compstruct.2018.10.090>.
27. Wisnom, M.R.; Potter, K.D.; Ersoy, N. Shear-Lag Analysis of the Effect of Thickness on Spring-in of Curved Composites. *J. Compos. Mater.* **2007**, *41*, 1311–1324. <https://doi.org/10.1177/0021998306068072>.
28. Hörberg, E.; Åkermo, M.; Hallström, S. Moisture Effect on Shape Distortions of Curved Quasi-Isotropic Prepreg Composite Laminates. *Compos. Part A Appl. Sci. Manuf.* **2021**, *145*, 106361. <https://doi.org/10.1016/j.compositesa.2021.106361>.
29. Abouhamzeh, M.; Sinke, J.; Jansen, K.M.B.; Benedictus, R. Closed Form Expression for Residual Stresses and Warpage during Cure of Composite Laminates. *Compos. Struct.* **2015**, *133*, 902–910. <https://doi.org/10.1016/j.compstruct.2015.07.098>.
30. Yuksel, O.; Sandberg, M.; Hattel, J.H.; Akkerman, R.; Baran, I. Mesoscale Process Modeling of a Thick Pultruded Composite with Variability in Fiber Volume Fraction. *Materials* **2021**, *14*, 3763. <https://doi.org/10.3390/ma14133763>.
31. Sandberg, M.; Yuksel, O.; Baran, I.; Spangenberg, J.; Hattel, J.H. Steady-State Modelling and Analysis of Process-Induced Stress and Deformation in Thermoset Pultrusion Processes. *Compos. Part B Eng.* **2021**, *216*, 108812. <https://doi.org/10.1016/j.compositesb.2021.108812>.
32. Traiforos, N.; Turner, T.; Runeberg, P.; Fernass, D.; Chronopoulos, D.; Glock, F.; Schuhmacher, G.; Hartung, D. A Simulation Framework for Predicting Process-Induced Distortions for Precise Manufacturing of Aerospace Thermoset Composites. *Compos. Struct.* **2021**, 114465. <https://doi.org/10.1016/j.compstruct.2021.114465>.
33. Albert, C.; Fernlund, G. Spring-in and Warpage of Angled Composite Laminates. *Compos. Sci. Technol.* **2002**, *62*, 1895–1912. [https://doi.org/10.1016/S0266-3538\(02\)00105-7](https://doi.org/10.1016/S0266-3538(02)00105-7).
34. Bapanapalli, S.K.; Smith, L.V. A Linear Finite Element Model to Predict Processing-Induced Distortion in FRP Laminates. *Compos. Part A Appl. Sci. Manuf.* **2005**, *36*, 1666–1674. <https://doi.org/10.1016/j.compositesa.2005.03.018>.
35. Fernlund, G.; Rahman, N.; Courdji, R.; Bresslauer, M.; Poursartip, A.; Willden, K.; Nelson, K. Experimental and Numerical Study of the Effect of Cure Cycle, Tool Surface, Geometry, and Lay-up on the Dimensional Fidelity of Autoclave-Processed Composite Parts. *Compos. Part A Appl. Sci. Manuf.* **2002**, *33*, 341–351. [https://doi.org/10.1016/S1359-835X\(01\)00123-3](https://doi.org/10.1016/S1359-835X(01)00123-3).
36. Fernlund, G.; Osooly, A.; Poursartip, A.; Vaziri, R.; Courdji, R.; Nelson, K.; George, P.; Hendrickson, L.; Griffith, J. Finite Element Based Prediction of Process-Induced Deformation of Autoclaved Composite Structures Using 2D Process Analysis and 3D Structural Analysis. *Compos. Struct.* **2003**, *62*, 223–234. [https://doi.org/10.1016/S0263-8223\(03\)00117-X](https://doi.org/10.1016/S0263-8223(03)00117-X).
37. Svanberg, J.M.; Holmberg, J.A. An Experimental Investigation on Mechanisms for Manufacturing Induced Shape Distortions in Homogeneous and Balanced Laminates. *Compos. Part A Appl. Sci. Manuf.* **2001**, *32*, 827–838. [https://doi.org/10.1016/S1359-835X\(00\)00173-1](https://doi.org/10.1016/S1359-835X(00)00173-1).
38. Jain, L.K.; Lutton, B.G.; Mai, Y.-W.; Paton, R. Stresses and Deformations Induced during Manufacturing. Part II: A Study of the Spring-in Phenomenon. *J. Compos. Mater.* **1997**, *31*, 696–719. <https://doi.org/10.1177/002199839703100704>.
39. Svanberg, J.M.; Holmberg, J.A. Prediction of Shape Distortions. Part II. Experimental Validation and Analysis of Boundary Conditions. *Compos. Part A Appl. Sci. Manuf.* **2004**, *35*, 723–734. <https://doi.org/10.1016/j.compositesa.2004.02.006>.
40. Nielsen, M.W. Prediction of Process Induced Shape Distortions and Residual Stresses in Large Fibre Reinforced Composite Laminates: With Application to Wind Turbine Blades. Ph.D. Thesis, Technical University of Denmark, Lyngby, Denmark, 25 June 2013.
41. Hsiao, K.-T.; Gangireddy, S. Investigation on the Spring-in Phenomenon of Carbon Nanofiber-Glass Fiber/Polyester Composites Manufactured with Vacuum Assisted Resin Transfer Molding. *Compos. Part A Appl. Sci. Manuf.* **2008**, *39*, 834–842. <https://doi.org/10.1016/j.compositesa.2008.01.015>.
42. Corrado, A.; Polini, W. Measurement of Flexible Components in Composite Material by a 3-2-1 Locating Scheme. *Compos. Sci. Technol.* **2020**, *189*, 108036. <https://doi.org/10.1016/j.compscitech.2020.108036>.
43. Sorrentino, L.; Bellini, C. Compaction Influence on Spring-in of Thin Composite Parts: Experimental and Numerical Results. *J. Compos. Mater.* **2015**, *49*, 2149–2158. <https://doi.org/10.1177/0021998314542362>.
44. Ding, A.; Wang, J.; Ni, A.; Li, S. A New Analytical Solution for Cure-Induced Spring-in of L-Shaped Composite Parts. *Compos. Sci. Technol.* **2019**, *171*, 1–12. <https://doi.org/10.1016/j.compscitech.2018.12.004>.
45. Hou, M.; Ye, L.; Mai, Y.W. Manufacturing Process and Mechanical Properties of Thermoplastic Composite Components. *J. Mater. Process. Technol.* **1997**, *63*, 334–338. [https://doi.org/10.1016/S0924-0136\(96\)02644-1](https://doi.org/10.1016/S0924-0136(96)02644-1).
46. Ganley, J.M.; Mawi, A.K.; Huybrechts, S. Explaining Spring-In in Filament Wound Carbon Fiber/Epoxy Composites. *J. Compos. Mater.* **2000**, *34*, 1216–1239. <https://doi.org/10.1177/002199830003401404>.
47. Li, N.; Li, Y.; Hao, X.; Gao, J. A Comparative Experiment for the Analysis of Microwave and Thermal Process Induced Strains of Carbon Fiber/Bismaleimide Composite Materials. *Compos. Sci. Technol.* **2015**, *106*, 15–19. <https://doi.org/10.1016/j.compscitech.2014.10.008>.
48. Baran, I.; Akkerman, R.; Hattel, J.H. Modelling the Pultrusion Process of an Industrial L-Shaped Composite Profile. *Compos. Struct.* **2014**, *118*, 37–48. <https://doi.org/10.1016/j.compstruct.2014.07.018>.

49. Baran, I.; Tutum, C.C.; Nielsen, M.W.; Hattel, J.H. Process Induced Residual Stresses and Distortions in Pultrusion. *Compos. Part B Eng.* **2013**, *51*, 148–161. <https://doi.org/10.1016/j.compositesb.2013.03.031>.
50. Wisnom, M.R.; Gigliotti, M.; Ersoy, N.; Campbell, M.; Potter, K.D. Mechanisms Generating Residual Stresses and Distortion during Manufacture of Polymer-Matrix Composite Structures. *Compos. Part A Appl. Sci. Manuf.* **2006**, *37*, 522–529. <https://doi.org/10.1016/j.compositesa.2005.05.019>.
51. Radford, D.W.; Rennick, T.S. Separating Sources of Manufacturing Distortion in Laminated Composites. *J. Reinf. Plast. Compos.* **2000**, *19*, 621–641. <https://doi.org/10.1106/CRMP-ARE5-GVPP-0Y7N>.
52. Kappel, E.; Stefaniak, D.; Hühne, C. Process Distortions in Prepreg Manufacturing—An Experimental Study on CFRP L-Profiles. *Compos. Struct.* **2013**, *106*, 615–625. <https://doi.org/10.1016/j.compstruct.2013.07.020>.
53. Wiersma, H.W.; Peeters, L.J.B.; Akkerman, R. Prediction of Springforward in Continuous-Fibre/Polymer L-Shaped Parts. *Compos. Part A Appl. Sci. Manuf.* **1998**, *29*, 1333–1342. [https://doi.org/10.1016/S1359-835X\(98\)00062-1](https://doi.org/10.1016/S1359-835X(98)00062-1).
54. David, A. Darrow, J.; Smith, L.V. Isolating Components of Processing Induced Warpage in Laminated Composites. *J. Compos. Mater.* **2002**, *36*, 2407–2419. <https://doi.org/10.1177/0021998302036021784>.
55. Ersoy, N.; Garstka, T.; Potter, K.; Wisnom, M.R.; Porter, D.; Stringer, G. Modelling of the Spring-in Phenomenon in Curved Parts Made of a Thermosetting Composite. *Compos. Part A Appl. Sci. Manuf.* **2010**, *41*, 410–418. <https://doi.org/10.1016/j.compositesa.2009.11.008>.
56. Svanberg, J.M.; Holmberg, J.A. Prediction of Shape Distortions Part I. FE-Implementation of a Path Dependent Constitutive Model. *Compos. Part A Appl. Sci. Manuf.* **2004**, *35*, 711–721. <https://doi.org/10.1016/j.compositesa.2004.02.005>.
57. Bogetti, T.A.; Gillespie, J.W., J. Process-Induced Stress and Deformation in Thick-Section Thermoset Composite Laminates. *J. Compos. Mater.* **1992**, *26*, 626–660. <https://doi.org/10.1177/002199839202600502>.
58. Arafath, A.R.A.; Vaziri, R.; Poursartip, A. Closed-Form Solution for Process-Induced Stresses and Deformation of a Composite Part Cured on a Solid Tool: Part II—Curved Geometries. *Compos. Part A Appl. Sci. Manuf.* **2009**, *40*, 1545–1557. <https://doi.org/10.1016/j.compositesa.2009.01.009>.
59. Liu, X.; Wang, X.; Guan, Z.; Jiang, T.; Geng, K.; Li, Z. Study on Cure-Induced Residual Stresses and Spring-in Deformation of L-Shaped Composite Laminates Using a Simplified Constitutive Model Considering Stress Relaxation. *Compos. Struct.* **2021**, *272*, 114203. <https://doi.org/10.1016/j.compstruct.2021.114203>.
60. Vedernikov, A.; Tucci, F.; Carlone, P.; Gusev, S.; Konev, S.; Firsov, D.; Akhatov, I.; Safonov, A. Effects of Pulling Speed on Structural Performance of L-Shaped Pultruded Profiles. *Compos. Struct.* **2021**, *255*, 112967. <https://doi.org/10.1016/j.compstruct.2020.112967>.
61. Safonov, A.A.; Carlone, P.; Akhatov, I. Mathematical Simulation of Pultrusion Processes: A Review. *Compos. Struct.* **2018**, *184*, 153–177. <https://doi.org/10.1016/j.compstruct.2017.09.093>.
62. Struzziero, G.; Teuwen, J.J.E.; Skordos, A.A. Numerical Optimisation of Thermoset Composites Manufacturing Processes: A Review. *Compos. Part A Appl. Sci. Manuf.* **2019**, *124*, 105499. <https://doi.org/10.1016/j.compositesa.2019.105499>.
63. Vedernikov, A.; Nasonov, Y.; Korotkov, R.; Gusev, S.; Akhatov, I.; Safonov, A. Effects of Additives on the Cure Kinetics of Vinyl Ester Pultrusion Resins. *J. Compos. Mater.* **2021**. <https://doi.org/10.1177/00219983211001528>.
64. Safonov, A.; Gusev, M.; Saratov, A.; Konstantinov, A.; Sergeichev, I.; Konev, S.; Gusev, S.; Akhatov, I. Modeling of Cracking during Pultrusion of Large-Size Profiles. *Compos. Struct.* **2020**, *235*, 111801. <https://doi.org/10.1016/j.compstruct.2019.111801>.
65. Sandberg, M.; Yuksel, O.; Baran, I.; Hattel, J.H.; Spangenberg, J. Numerical and Experimental Analysis of Resin-Flow, Heat-Transfer, and Cure in a Resin-Injection Pultrusion Process. *Compos. Part A Appl. Sci. Manuf.* **2020**, *143*, 106231. <https://doi.org/10.1016/j.compositesa.2020.106231>.
66. Barkanov, E.; Akishin, P.; Miazza, N.L.; Galvez, S. ANSYS-Based Algorithms for a Simulation of Pultrusion Processes. *Mech. Adv. Mater. Struct.* **2017**, *24*, 377–384. <https://doi.org/10.1080/15376494.2016.1191096>.
67. Safonov, A.A.; Suvorova, Y.V. Optimization of the Pultrusion Process for a Rod with a Large Diameter. *J. Mach. Manuf. Reliab.* **2009**, *38*, 572–578. <https://doi.org/10.3103/S1052618809060090>.
68. Carlone, P.; Baran, I.; Hattel, J.H.; Palazzo, G.S. Computational Approaches for Modeling the Multiphysics in Pultrusion Process. *Adv. Mech. Eng.* **2013**, *2013*. <https://doi.org/10.1155/2013/301875>.
69. Yuksel, O.; Sandberg, M.; Baran, I.; Ersoy, N.; Hattel, J.H.; Akkerman, R. Material Characterization of a Pultrusion Specific and Highly Reactive Polyurethane Resin System: Elastic Modulus, Rheology, and Reaction Kinetics. *Compos. Part B Eng.* **2020**, *207*, 108543. <https://doi.org/10.1016/j.compositesb.2020.108543>.
70. Wang, J.; Kelly, D.; Hillier, W. Finite Element Analysis of Temperature Induced Stresses and Deformations of Polymer Composite Components. *J. Compos. Mater.* **2000**, *34*, 1456–1471. <https://doi.org/10.1106/76G7-X9QM-C5JF-E4D5>.
71. Jain, L.K.; Mai, Y.-W. Stresses and Deformations Induced during Manufacturing. Part I: Theoretical Analysis of Composite Cylinders and Shells. *J. Compos. Mater.* **1997**, *31*, 672–695. <https://doi.org/10.1177/002199839703100703>.
72. Ersoy, N.; Potter, K.; Wisnom, M.R.; Clegg, M.J. Development of Spring-in Angle during Cure of a Thermosetting Composite. *Compos. Part A Appl. Sci. Manuf.* **2005**, *36*, 1700–1706. <https://doi.org/10.1016/j.compositesa.2005.02.013>.
73. Ruiz, E.; Trochu, F. Multi-Criteria Thermal Optimization in Liquid Composite Molding to Reduce Processing Stresses and Cycle Time. *Compos. Part A Appl. Sci. Manuf.* **2006**, *37*, 913–924. <https://doi.org/10.1016/j.compositesa.2005.06.010>.
74. Kravchenko, O.G.; Kravchenko, S.G.; Pipes, R.B. Chemical and Thermal Shrinkage in Thermosetting Prepreg. *Compos. Part A Appl. Sci. Manuf.* **2016**, *80*, 72–81. <https://doi.org/10.1016/j.compositesa.2015.10.001>.

75. Takagaki, K.; Minakuchi, S.; Takeda, N. Process-Induced Strain and Distortion in Curved Composites. Part I: Development of Fiber-Optic Strain Monitoring Technique and Analytical Methods. *Compos. Part A Appl. Sci. Manuf.* **2017**, *103*, 236–251. <https://doi.org/10.1016/j.compositesa.2017.09.020>.
76. Nawab, Y.; Sonnenfeld, C.; Saouab, A.; Agogu , R.; Beauch ne, P. Characterisation and Modelling of Thermal Expansion Coefficient of Woven Carbon/Epoxy Composite and Its Application to the Determination of Spring-In. *J. Compos. Mater.* **2017**, *51*, 1527–1538. <https://doi.org/10.1177/0021998316661404>.
77. Hu, H.; Li, S.; Wang, J.; Zu, L.; Cao, D.; Zhong, Y. Monitoring the Gelation and Effective Chemical Shrinkage of Composite Curing Process with a Novel FBG Approach. *Compos. Struct.* **2017**, *176*, 187–194. <https://doi.org/10.1016/j.compstruct.2017.04.051>.
78. Exner, W.; Hein, R.; Mahrholz, T.; Wierach, P.; Monner, H.P.; Sinapius, M. Impact of Nanoparticles on the Process-Induced Distortions of Carbon Fiber Reinforced Plastics: An Experimental and Simulative Approach. *J. Appl. Polym. Sci.* **2019**, *136*, 47031. <https://doi.org/10.1002/app.47031>.
79. Groh, F.; Kappel, E.; H hne, C.; Brymerski, W. Investigation of Fast Curing Epoxy Resins Regarding Process Induced Distortions of Fibre Reinforced Composites. *Compos. Struct.* **2019**, *207*, 923–934. <https://doi.org/10.1016/j.compstruct.2018.09.003>.
80. Qiao, W.; Yao, W. Modelling of Process-Induced Deformation for Composite Parts Considering Tool-Part Interaction. *Materials* **2020**, *13*, 4503. <https://doi.org/10.3390/ma13204503>.
81. Shaker, K.; Nawab, Y.; Saouab, A. Experimental and Numerical Investigation of Reduction in Shape Distortion for Angled Composite Parts. *Int. J. Mater. Form.* **2020**, *13*, 897–906. <https://doi.org/10.1007/s12289-019-01510-6>.
82. Struzziero, G.; Nardi, D.; Sinke, J.; Teuwen, J. Cure-Induced Residual Stresses for Warp Reduction in Thermoset Laminates. *J. Compos. Mater.* **2020**, *54*, 3055–3065. <https://doi.org/10.1177/0021998320908631>.
83. Vedernikov, A.N.; Safonov, A.A.; Gusev, S.A.; Carlone, P.; Tucci, F.; Akhatov, I.S. Spring-in Experimental Evaluation of L-Shaped Pultruded Profiles. *IOP Conf. Ser. Mater. Sci. Eng.* **2020**, *747*, 012013. <https://doi.org/10.1088/1757-899X/747/1/012013>.
84. Vedernikov, A.; Tucci, F.; Safonov, A.; Carlone, P.; Gusev, S.; Akhatov, I. Investigation on the Shape Distortions of Pultruded Profiles at Different Pulling Speed. *Procedia Manuf.* **2020**, *47*, 1–5. <https://doi.org/10.1016/j.promfg.2020.04.107>.
85. Zocher, M.A.; Groves, S.E.; Allen, D.H. A Three-Dimensional Finite Element Formulation for Thermoviscoelastic Orthotropic Media. *Int. J. Numer. Methods Eng.* **1997**, *40*, 2267–2288. [https://doi.org/10.1002/\(SICI\)1097-0207\(19970630\)40:12<2267::AID-NME156>3.0.CO;2-P](https://doi.org/10.1002/(SICI)1097-0207(19970630)40:12<2267::AID-NME156>3.0.CO;2-P).
86. White, S.R.; Kim, Y.K. Process-Induced Residual Stress Analysis of AS4/3501-6 Composite Material. *Mech. Compos. Mater. Struct.* **1998**, *5*, 153–186. <https://doi.org/10.1080/10759419808945897>.
87. Hill, R. A Self-Consistent Mechanics of Composite Materials. *J. Mech. Phys. Solids* **1965**, *13*, 213–222. [https://doi.org/10.1016/0022-5096\(65\)90010-4](https://doi.org/10.1016/0022-5096(65)90010-4).
88. Batch, G.L.; Macosko, C.W. Heat Transfer and Cure in Pultrusion: Model and Experimental Verification. *AIChE J.* **1993**, *39*, 1228–1241. <https://doi.org/10.1002/aic.690390713>.
89. Baran, I.; Hattel, J.H.; Akkerman, R.; Tutum, C.C. Mechanical Modelling of Pultrusion Process: 2D and 3D Numerical Approaches. *Appl. Compos. Mater.* **2014**, *22*, 99–118. <https://doi.org/10.1007/s10443-014-9394-3>.
90. Nasonov, Y.; Safonov, A.; Gusev, S.; Akhatov, I. Mathematical Simulation the Kinetics of Polymerization of Vinyl Ester Resin Using in Pultrusion. *IOP Conf. Ser. Mater. Sci. Eng.* **2020**, *747*, 12010. <https://doi.org/10.1088/1757-899X/747/1/012010>.
91. Johnston, A.A. An Integrated Model of the Development of Process-Induced Deformation in Autoclave Processing of Composite Structures. Ph.D. Thesis, The University of British Columbia, Vancouver, Canada, May 1997.
92. Khoun, L.; Centea, T.; Hubert, P. Characterization Methodology of Thermoset Resins for the Processing of Composite Materials—Case Study: CYCOM 890RTM Epoxy Resin. *J. Compos. Mater.* **2010**, *44*, 1397–1415. <https://doi.org/10.1177/0021998309353960>.
93. O’Brien, D.J.; White, S.R. Cure Kinetics, Gelation, and Glass Transition of a Bisphenol F Epoxide. *Polym. Eng. Sci.* **2003**, *43*, 863–874. <https://doi.org/10.1002/pen.10071>.
94. Plepys, A.R.; Farris, R.J. Evolution of Residual Stresses in Three-Dimensionally Constrained Epoxy Resins. *Polymer* **1990**, *31*, 1932–1936. [https://doi.org/10.1016/0032-3861\(90\)90019-U](https://doi.org/10.1016/0032-3861(90)90019-U).
95. Abaqus Analysis User Manual, Version 6.14. 2014. Available online: <https://www.3ds.com/products-services>. (accessed on 1 June 2021).
96. ISO 6721-1:2011. *Plastics—Determination of Dynamic Mechanical Properties—Part 1: General Principles*; International Organization for Standardization: Geneva, Switzerland, 2011.
97. ISO 11357-4:2005. *Plastics—Differential Scanning Calorimetry (DSC)—Part 4: Determination of Specific Heat Capacity*; International Organization for Standardization: Geneva, Switzerland, 2005.
98. ISO 22007-4:2008. *Plastics—Determination of Thermal Conductivity and Thermal Diffusivity—Part 4: Laser Flash Method*; International Organization for Standardization: Geneva, Switzerland, 2008.
99. ISO 11359-2:1999. *Plastics—Thermomechanical Analysis (TMA)—Part 2: Determination of Coefficient of Linear Thermal Expansion and Glass Transition Temperature*; International Organization for Standardization: Geneva, Switzerland, 1999.
100. Baran, I.; *Pultrusion: State-of-the-Art Process. Models*; Shropshire, England, Smithers Rapra: 2015.
101. Chachad, Y.R.; Roux, J.A.; Vaughan, J.G.; Arafat, E. Three-Dimensional Characterization of Pultruded Fiberglass-Epoxy Composite Materials. *J. Reinf. Plast. Compos.* **1995**, *14*, 495–512. <https://doi.org/10.1177/073168449501400506>.

102. Akkerman, R. On the Properties of Quasi-Isotropic Laminates. *Compos. Part B Eng.* **2002**, *33*, 133–140. [https://doi.org/10.1016/S1359-8368\(02\)00002-1](https://doi.org/10.1016/S1359-8368(02)00002-1).
103. Mahrholz, T.; Stängle, J.; Sinapius, M. Quantitation of the Reinforcement Effect of Silica Nanoparticles in Epoxy Resins Used in Liquid Composite Moulding Processes. *Compos. Part A Appl. Sci. Manuf.* **2009**, *40*, 235–243. <https://doi.org/10.1016/j.compositesa.2008.11.008>.
104. Haider, M.; Hubert, P.; Lessard, L. Cure Shrinkage Characterization and Modeling of a Polyester Resin Containing Low Profile Additives. *Compos. Part A Appl. Sci. Manuf.* **2007**, *38*, 994–1009. <https://doi.org/10.1016/j.compositesa.2006.06.020>.
105. Methven, J.M.; Ghaffariyan, S.R.; Abidin, A.Z. Manufacture of Fiber-Reinforced Composites by Microwave Assisted Pultrusion. *Polym. Compos.* **2000**, *21*, 586–594. <https://doi.org/10.1002/pc.10214>.
106. Struzziero, G.; Teuwen, J.J.E. A Fully Coupled Thermo-Mechanical Analysis for the Minimisation of Spring-in and Process Time in Ultra-Thick Components for Wind Turbine Blades. *Compos. Part A Appl. Sci. Manuf.* **2020**, *139*. <https://doi.org/10.1016/j.compositesa.2020.106105>.
107. Liu, T.; Vieira, J.D.; Harries, K.A. Predicting Flange Local Buckling Capacity of Pultruded GFRP I-Sections Subject to Flexure. *J. Compos. Constr.* **2020**, *24*. [https://doi.org/10.1061/\(ASCE\)CC.1943-5614.0001032](https://doi.org/10.1061/(ASCE)CC.1943-5614.0001032).
108. Wu, C.; Zhang, L.-T.; Tam, L.; Yan, L.; He, L. Effect of Bearing Length on Web Crippling Behavior of Pultruded GFRP Channel Section. *Compos. Struct.* **2020**, *253*, 112810. <https://doi.org/10.1016/j.compstruct.2020.112810>.
109. Civera, M.; Boscato, G.; Zanotti Fragonara, L. Treed Gaussian Process for Manufacturing Imperfection Identification of Pultruded GFRP Thin-Walled Profile. *Compos. Struct.* **2020**, *254*, 112882. <https://doi.org/10.1016/j.compstruct.2020.112882>.
110. Safonov, A.A. 3D Topology Optimization of Continuous Fiber-Reinforced Structures via Natural Evolution Method. *Compos. Struct.* **2019**, *215*, 289–297. <https://doi.org/10.1016/j.compstruct.2019.02.063>.
111. Poveda, R.; Gupta, N.; Porfiri, M. Poisson's Ratio of Hollow Particle Filled Composites. *Mater. Lett.* **2010**, *64*, 2360–2362. <https://doi.org/10.1016/j.matlet.2010.07.063>.

Chapter 10

Effects of additives on the cure kinetics of vinyl ester pultrusion resins

Vedernikov Alexander, Nasonov Yaroslav, Korotkov Roman, Gusev Sergey, Akhatov Iskander, Safonov Alexander. Effects of additives on the cure kinetics of vinyl ester pultrusion resins. *Journal of Composite Materials* 2021. DOI: 10.1177/00219983211001528.

Contribution:

I participated in preparation of the resin compositions, as well as in the analysis of the results of differential scanning calorimetry (DSC). I performed simulations of resin cure and pultrusion process. Besides, I prepared all the figures for this article and contributed to development of the original draft, final writing, and editing. I would like to thank all the authors for their valuable contributions to the development of this paper.

Effects of additives on the cure kinetics of vinyl ester pultrusion resins

Journal of Composite Materials
0(0) 1–17
© The Author(s) 2021
Article reuse guidelines:
sagepub.com/journals-permissions
DOI: 10.1177/00219983211001528
journals.sagepub.com/home/jcm



Alexander Vedernikov , Yaroslav Nasonov, Roman Korotkov, Sergey Gusev, Iskander Akhatov and Alexander Safonov 

Abstract

Pultrusion is a highly efficient composite manufacturing process. To accurately describe pultrusion, an appropriate model of resin cure kinetics is required. In this study, we investigated cure kinetics modeling of a vinyl ester pultrusion resin (Atlac 430) in the presence of aluminum hydroxide ($\text{Al}(\text{OH})_3$) and zinc stearate ($\text{Zn}(\text{C}_{18}\text{H}_{35}\text{O}_2)_2$) as processing additives. Herein, four different resin compositions were studied: neat resin composition, composition with $\text{Al}(\text{OH})_3$, composition comprising $\text{Zn}(\text{C}_{18}\text{H}_{35}\text{O}_2)_2$, and composition containing both $\text{Al}(\text{OH})_3$ and $\text{Zn}(\text{C}_{18}\text{H}_{35}\text{O}_2)_2$. To analyze each composition, we performed differential scanning calorimetry at the heating rates of 5, 7.5, and 10 K/min. To characterize the cure kinetics of Atlac 430, 16 kinetic models were tested, and their performances were compared. The model based on the n th-order autocatalytic reaction demonstrated the best results, with a 4.5% mean squared error (MSE) between the experimental and predicted data. This study proposes a method to reduce the MSE resulting from the simultaneous melting of $\text{Zn}(\text{C}_{18}\text{H}_{35}\text{O}_2)_2$. We were able to reduce the MSE by approximately 34%. Numerical simulations conducted at different temperatures and pulling speeds demonstrated a significant influence of resin composition on the pultrusion of a flat laminate profile. Simulation results obtained for the 600 mm long die block at different die temperatures (115, 120, 125, and 130 °C) showed that for a resin with a final degree of cure exceeding 95% at the die exit, the maximum difference between the predicted values of pulling speed for a specified set of compositions may exceed 1.7 times.

Keywords

Pultrusion, vinyl ester resin, additives, cure kinetics, process optimization, numerical simulation

Introduction

Structural elements of fiber-reinforced plastics (FRPs) have found extensive applications in the civil, marine, and road construction fields due to their advantages over conventional materials such as steel, timber, and concrete.^{1–5} Pultrusion is the most efficient technique for the production of fiber-reinforced polymers.^{6–8} Pultruded profiles exhibit a high strength-to-weight ratio, excellent corrosion resistance, and high durability and are easy to handle.^{9,10} In thermoset pultrusion, the reinforcement pack of a unidirectional fiber is pulled through the impregnation bath with a polymer resin.^{11,12} Then, excess resin is removed at the collimating plates, and the preformed reinforcement pack is introduced into the heated die block where polymerization takes place.^{13,14} When the process becomes stationary, it requires very little attention from the engineer as the pulling units and cutting saw operate in an almost fully automated manner.^{15,16} Engineers

widely use mathematical models to optimize composite manufacturing processes, thus avoiding costly trial and error experiments.^{17–20} Numerical simulation of the curing process enables the selection of process parameters and pulling speed such that the thermal peak of the reaction occurs within the die block, ensuring the fabrication of high-quality pultruded profiles.^{21,22} Currently, the following models of polymerization kinetics are applied to simulate pultrusion: first-order reaction (F1),²³ second-order reaction (F2),^{24,25} n th-order reaction (Fn),^{26–31} n th-order autocatalytic

Skolkovo Institute of Science and Technology, Center for Design, Manufacturing and Materials, Moscow, Russia

Corresponding author:

Alexander Vedernikov, Skolkovo Institute of Science and Technology, Center for Design, Manufacturing and Materials, Moscow, Russia.
Email: aleksandr.vedernikov@skoltech.ru

reaction (Cn),³² expanded Prout–Tompkins equation (Bna),^{33–35} Kamal–Sourour autocatalytic model.³⁶ Simulation of vinyl ester polymerization is a very complex task because a large number of reactions take place in the multicomponent resin system during this polymerization. Mechanistic models describing polymerization are relatively complex and require numerous parameters.³⁷ In this study, we employed less complex phenomenological models to simulate the curing process.

In 1973, Kamal and Sourour demonstrated an approach to characterize the polyester resin curing process via isothermal differential scanning calorimetry (DSC) experiments.³⁸ The first studies on the application of cure kinetics in pultrusion were reported in the late 80s. Han and Chin³⁹ proposed a mechanistic kinetic model considering the type and concentration of initiators in an unsaturated polyester resin. Ng and Manas-Zloczower⁴⁰ studied the influence of kaolinite and fiberglass on the kinetic behavior of an unsaturated polyester resin. Subsequently, Trivisano et al.⁴¹ proposed and experimentally verified a kinetic submodel necessary for the development of a mathematical model characterizing the curing of epoxy resin during pultrusion. Valliappan et al.⁴² investigated and verified the multiple-independent-step model describing the polymerization of epoxy resin. Suratno et al.⁴³ proposed a mathematical model of carbon/epoxy composite pultrusion and used it to solve the heat transfer problem. Simultaneously, Roux et al.⁴⁴ reported an experimental and numerical study on unsteady-state three-dimensional (3D) temperature and degree of cure distributions in a fiberglass–epoxy system used for the production of a pultruded I-beam. Atarsia and Boukhili⁴⁵ performed an isothermal and dynamic kinetic analysis to characterize the epoxy and polyester resins. Lin Lui et al.⁴⁶ carried out a numerical simulation to solve the thermochemical problem in pultrusion using a finite element/finite difference/control volume method. To optimize die heating conditions and achieve uniform curing of pultruded profiles, Li et al.⁴⁷ established a relationship between the degree of cure of the composite and temperature conditions in a multi-heater die block. Pantaleão et al.⁴⁸ investigated the influence of anisotropic thermal conductivity on the thermochemical behavior of resins. Simultaneously, Sarrionandia et al.⁴⁹ proposed and experimentally verified a thermochemical model of a modified acrylic resin. Calabrese and Valenza⁵⁰ investigated the influence of different concentrations of a carboxyl-terminated copolymer of butadiene and acrylonitrile liquid rubber on the cure kinetics of epoxy resin. Using DSC, Samaras and Partridge⁵¹ analyzed the effect of styrene loss on the curing of vinyl ester mixtures containing Perkadox 16 and methyl

methacrylate at different concentrations. Liang et al.⁵² conducted an experimental and numerical study on the cure behavior of an epoxy resin system based on soybean oil. Prime et al.²⁴ performed a kinetic analysis of polyurethane resin in a fast reacting system. Bai et al.⁵³ employed thermogravimetric analysis to determine the kinetic parameters of polyester resin using four different techniques: Friedman, Kissinger, Ozawa, and modified Coats–Redfern methods. Badrinarayanan et al.³² studied the effect of a cationic initiator on the polymerization of a soybean oil/styrene–divinylbenzene resin to realize the best composition and determine the coefficients of cure kinetics. Chen et al.⁵⁴ utilized an artificial neural network to discover the relationship between the processing parameters and curing behavior of epoxy resin and optimize the heating conditions and pulling speed. Zhou et al.⁵⁵ carried out a non-isothermal DSC analysis of curing in three different multifunctional epoxy resin systems to evaluate the effects of the composition of the resin system on the cure kinetics. Zheng et al.⁵⁶ conducted a DSC analysis of partially cured Z-pins used in K-Cor sandwich elements to determine the optimal degree of cure of Z-pins for this type of structures. Baran et al.⁵⁷ performed isothermal and dynamic DSC experiments to examine the cure behavior of polyester resin and estimated kinetic parameters for the Bna. In a follow-up study,⁵⁸ they carried out a probabilistic analysis to better understand the relationship between the uncertainties in the kinetic parameters of the epoxy matrix and the quality of pultruded profiles. Tena et al.⁵⁹ studied the effects of ultraviolet (UV) intensity and pulling speed on the UV polymerization of the polyester resin used in bent pultrusions. Saenz-Dominguez et al.⁶⁰ analyzed two resin systems with different concentrations of surface and through-thickness photoinitiators to understand the influence of the resin system composition on the UV cure kinetics. Wang et al.⁶¹ investigated the effects of accelerator concentration on the curing behavior of epoxy resin. Recently, de Cassia Costa Dias et al.⁶² successfully applied empirical and phenomenological kinetic models explaining diffusion effects to characterize the behavior of epoxy resin and determined the kinetic parameters describing polymerization.

Although vinyl ester-based composites offer better mechanical performances as compared to those of polyester resin-based composites, they suffer from some limitations, including low fire retardancy and high smoke emission, owing to their peculiar chemical composition. As the application of pultruded profiles is rapidly increasing in civil engineering and architecture, one of the major problems engineers face is how to improve the fire reaction and reduce smoke emissions of vinyl ester-based composite structures.⁶³ A general

solution to this problem is the use of flame-retardant resins and organic/inorganic flame-retardant additives.⁶⁴ A common flame-retardant additive widely used nowadays is the non-toxic aluminum hydroxide ($\text{Al}(\text{OH})_3$) (or aluminum trihydrate) powder. Howard and Sayers⁶⁵ and Howard et al.⁶⁶ employed $\text{Al}(\text{OH})_3$ with methacrylate resin to improve the fire reaction and reduce smoke emissions of pultruded composites. Stevens et al.⁶⁷ examined the fire reaction of modified acrylic-based pultrusions with $\text{Al}(\text{OH})_3$ as an additive. Although studies have been reported on the use of $\text{Al}(\text{OH})_3$ as a flame-retardant additive in other composite manufacturing processes, the use of $\text{Al}(\text{OH})_3$ as a flame-retardant additive with vinyl ester resins in pultrusion has not been investigated to date. Winkler⁶⁸ compared the fire reaction of $\text{Al}(\text{OH})_3$ and calcium sulfate dihydrate additives used in the fabrication of under-the-hood car components of vinyl ester-based glass FRPs. Kicko-Walczak⁶⁹ reported a review on the performances of $\text{Al}(\text{OH})_3$ and other flame-retardant additives. Le Lay and Gutierrez⁷⁰ investigated the fire reaction of the laminates produced by a hand lay-up process using $\text{Al}(\text{OH})_3$ -doped polyester and vinyl ester resins. Malik et al.⁷¹ experimentally evaluated the influence of $\text{Al}(\text{OH})_3$ and other additives on the smoke density and limiting oxygen index of vinyl ester-based composites. Herzog and Desai⁷² demonstrated the modification of the fire reaction behavior of vinyl ester resins by $\text{Al}(\text{OH})_3$ as an additive. Simultaneously, Weil and Levchik⁷³ reviewed the application of flame-retardant additives (including $\text{Al}(\text{OH})_3$) for improving the flammability behavior of polyester and vinyl ester resins. Kandola and Pornwannachai⁷⁴ evaluated the effect of the ratio of the used flame-retardant additives, such as glass frits, Ultracarb, and $\text{Al}(\text{OH})_3$, on the fire reaction of vinyl ester resins. Mahesh et al.⁷⁵ studied the effects of the simultaneous addition of organomodified nanoclay, magnesium hydroxide, and $\text{Al}(\text{OH})_3$ on both the thermal and fire reaction properties of nanoclay/polyvinyl ester resin. De Freitas Rocha et al.⁷⁶ examined the improvements in the fire reaction performance of glass fiber-reinforced composites based on either polyester or vinyl ester matrices with the addition of $\text{Al}(\text{OH})_3$, decabromodiphenyl ether, and antimony trioxide.

Thermoset resins used in pultrusion exhibit high adhesive properties and therefore tend to stick to the inner surfaces of the die during manufacturing. Zinc stearate ($\text{Zn}(\text{C}_{18}\text{H}_{35}\text{O}_2)_2$) and other stearates are generally used to reduce the pulling force. $\text{Zn}(\text{C}_{18}\text{H}_{35}\text{O}_2)_2$ powder is usually added during the polymer matrix preparation stage.⁶⁴ During polymerization, the additives migrate to the resin-die region and serve as lubricants, thereby reducing friction between the pultruded profile and die surfaces.⁷⁷ However, special care should

be taken when using this type of additives as they can affect the physical properties, visual appearance, and paintability of the manufactured profiles.

Moreover, the influence of $\text{Zn}(\text{C}_{18}\text{H}_{35}\text{O}_2)_2$ on the cure kinetics of vinyl ester resins is poorly understood to date, and to the best of our knowledge, no studies have been reported in this regard. However, Zn compounds may act as catalysts in similar polymerization processes and may influence the curing of vinyl ester resins. Zinc acetate, zinc chloride, and zinc nitrate are commonly used as catalysts in the radical polymerization of vinyl monomers.⁷⁸ Zinc diphenyl is employed as a co-catalyst in the Ziegler–Natta polymerization of styrene.⁷⁹ Metallic Zn is used as a co-catalyst in the radical ring opening of oxiranes, initiating the radical polymerization of styrene.⁸⁰

To date, several studies have been reported on the influence of flame-retardant additives on the cure kinetics of polymer resins. Polymerization kinetics depends on the reactivity of flame-retardant additives: inert additives have a lower effect on the rate of polymerization as compared to that of reactive additives. Shih and Jeng⁸¹ analyzed the polymerization behavior of unsaturated polyester and epoxy resins in the presence of carbon black flame retardants. Pereira and Marques⁸² experimentally investigated the influence of $\text{Al}(\text{OH})_3$ and ammonium polyphosphate on the gelation time and cure rate of unsaturated polyester resin. Zhang et al.⁸³ examined the effect of the concentration of bis-phenoxy(3-hydroxy) phenyl phosphine oxide on the cure kinetics and fire reaction of unsaturated polyester resin. Ittner Mazali and Felisberti⁸⁴ characterized the curing of vinyl ester resin in the absence and presence of a silicon-based flame-retardant additive. Gao et al.⁸⁵ investigated the influence of ammonium pentaborate as a flame-retardant additive on the cure kinetics of phenol–formaldehyde resin. Subsequently, Jinxue et al.⁸⁶ studied the effects of three boron flame retardants on the polymerization behavior of urea–formaldehyde resin. Tan et al.⁸⁷ analyzed the fire reaction and cure kinetics of epoxy resin using a novel fire-retardant hardener obtained by cation exchange between ammonium polyphosphate and diethylenetriamine. Recently, Hamciuc et al.⁸⁸ examined the effect of oligophosphate flame-retardant additives on the polymerization behavior and fire reaction of epoxy resin. Lu et al.⁸⁹ reported that the addition of silsesquioxane as an additive to epoxy resin reduces the reactivity of the resin because of the formation of a less flexible compound when compared with the standard epoxy, oligomeric fragments during polymerization.

Although numerous studies have been reported on the cure kinetics of pultrusion resins and on the influence of flame retardants on polymerization, comprehensive research on the effects of flame retardants

and internal release agents on the cure kinetics of pultrusion resins, specifically vinyl ester resins used in pultrusion, is still lacking. Moreover, with respect to polymerization, only a few kinetic laws have been employed in the aforementioned studies.

The present study is divided into experimental and simulation parts, as shown in Figure 1. DSC experiments and numerical simulations were performed in this study, whereas pultrusion experiments with L-shaped profiles have been described in our previously reported study.²¹ Herein, we conducted experimental and numerical analyses to characterize the effects of $\text{Al}(\text{OH})_3$ and $\text{Zn}(\text{C}_{18}\text{H}_{35}\text{O}_2)_2$ as processing additives on the curing behavior of four different compositions based on Atlac 430 used in pultrusion. Based on the results of DSC performed at the heating rates of 5, 7.5, and 10 K/min, we determined the values of heat released and onset, peak, and end-point temperatures. In this study, 16 kinetic models describing the curing behavior were tested, and their performances were compared. This study also proposes a method to reduce the mean squared error (MSE) caused by the simultaneous melting of $\text{Zn}(\text{C}_{18}\text{H}_{35}\text{O}_2)_2$. A model describing the melting of $\text{Zn}(\text{C}_{18}\text{H}_{35}\text{O}_2)_2$ and its kinetic parameters was proposed. To evaluate the influences of the processing additives, heating conditions, and pulling speed on the curing behavior of the composite during pultrusion, we conducted a numerical simulation of the pultrusion of a flat laminate profile. Results demonstrate that the effect of processing additives and the selection of an appropriate kinetic model should be considered to accurately predict the outcomes of pultrusion.

Materials and methods

Raw materials

All resin compositions used herein were prepared at the Laboratory of Composite Materials and Structures of the Center for Design, Manufacturing and Materials (Skolkovo Institute of Science and Technology, Moscow, Russia). The following materials were used in this study: Atlac 430 (DSM Composite Resins AG, Switzerland); Trigonox C (Akzo Nobel Polymer Chemicals B.V., the Netherlands) as an initiator for the (co)polymerization of ethylene, styrene, acrylonitrile, acrylates, and methacrylates; Perkadox 16 (Akzo Nobel Polymer Chemicals B.V., the Netherlands) as an initiator for the suspension polymerization of acrylates and methacrylates; BYK A555 (BYK Additives & Instruments, Germany) as a deaerator; $\text{Al}(\text{OH})_3$ (Sibelco, Belgium) as a flame retardant; and $\text{Zn}(\text{C}_{18}\text{H}_{35}\text{O}_2)_2$ (Baerlocher GmbH, Germany) as a friction-reducing additive.

Preparation of resin compositions

We used the following procedure to prepare the resin compositions for pultrusion experiments. At first, we prepared the neat resin composition (M-I) by mixing 25.07 kg of Atlac 430, 90 g of BYK A555, 380 g of Trigonox C, and 130 g of Perkadox 16 (Figure 2(a)). To mix these components, we employed a Festool MX 1600/2 EQ DUO Double industrial mixer (Festool GmbH, Germany). M-I was then used for the pultrusion of L-shaped structural profiles (Figure 2(b)–(d)), as reported in our previous study.²¹ Next, M-I was placed in four plastic containers (100 g per container)

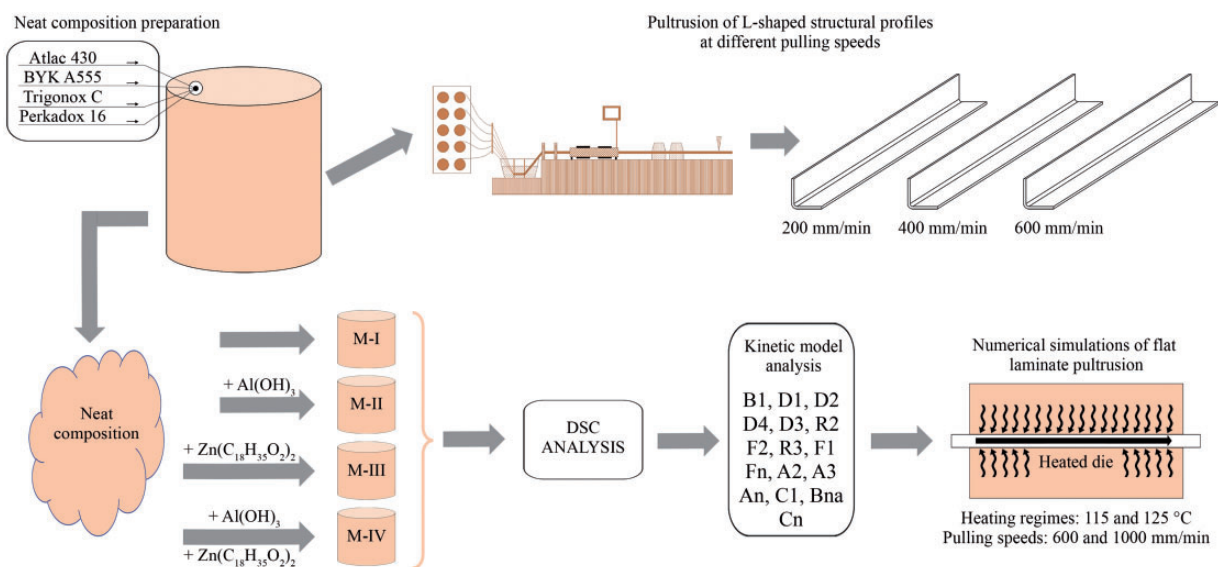


Figure 1. Flowchart of the study.

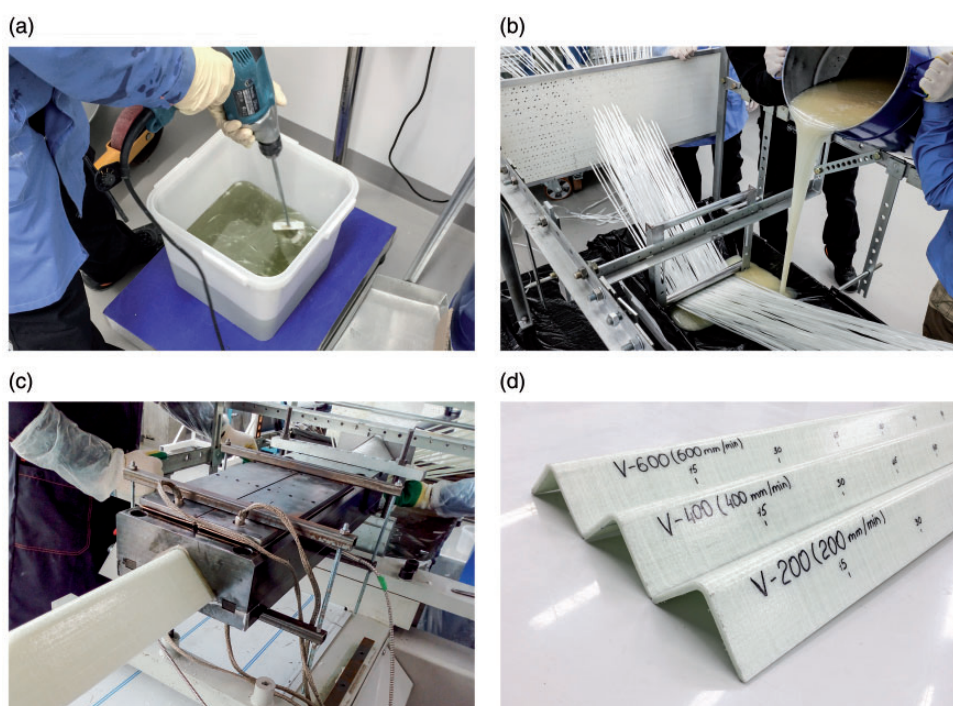


Figure 2. Pultrusion experiment: (a) Preparation of neat composition; (b) addition of the resin mixture to the bath; (c) cured composite leaving the die; and (d) L-shaped profiles pultruded at the different pulling speeds of 200, 400, and 600 mm/min.

Table 1. Properties of aluminum hydroxide and zinc stearate.

Property	Aluminum hydroxide	Zinc stearate
Ash content (%)	65.4	12.8–14.2
Free fatty acid (%)	–	1.5
Moisture (%)	0.3	0.5
Bulk density (g/cm ³)	1270	266
Average size (μm)	7	–
Melting point (°C)	–	121
Decomposition temperature (°C)	210	–
Ignition temperature (°C)	–	435

marked M-I, M-II, M-III, and M-IV. Subsequently, 31 g of Al(OH)₃, 4 g of Zn(C₁₈H₃₅O₂)₂, and both additives (31 g of Al(OH)₃ and 4 g of Zn(C₁₈H₃₅O₂)₂) were added to the M-II, M-III, and M-IV containers, respectively. Contents of all containers were manually mixed, and the containers were closed. To ensure accurate weighing of the additives, we used AND EK-6000i laboratory scales (A&D, USA). The properties of Al(OH)₃ and Zn(C₁₈H₃₅O₂)₂ are listed in Table 1. Table 2 shows the mass ratio of the resin components in all compositions (M-I, M-II, M-III, and M-IV).

DSC measurements and data processing

To synthesize samples for DSC measurements, aluminum sample pans were filled with 5–10 mg of a resin

composition. Herein, three samples were prepared for each resin composition (M-I, M-II, M-III, and M-IV), providing 12 samples in total. We employed Sartorius CPA225D high-precision laboratory scales (Sartorius AG, Germany) to weigh the fabricated samples. Next, a sample pan was installed into the measuring cell of a Netzsch Polyma 204 Differential Scanning Calorimeter (NETZSCH-Gerätebau GmbH, Germany). Measurements were performed in accordance with ISO 11357⁹⁰ at the heating rates of 5, 7.5, and 10 K/min. Tests were carried out at temperatures ranging from 50 to 200 °C.

To analyze the DSC measurement results, we used Netzsch Proteus Thermal Analysis software (NETZSCH-Gerätebau GmbH, Germany). For each scan, we determined the start, peak, and end points of polymerization, the temperatures of these points, width of the polymerization peak, and the amount of heat released. Netzsch Thermal Kinetic v3.1 software (NETZSCH-Gerätebau GmbH, Germany) was employed to estimate the constants of the kinetic equation.

Results and discussion

Effects of processing additives

Table 3 shows the results of the DSC measurements: heat released per 1 g of composition and per 1 g of M-I, peak temperature corresponding to the extremum on

Table 2. Mass ratio of components in the prepared compositions (M-I, M-II, M-III, and M-IV).

Component	M-I (%)	M-II (%)	M-III (%)	M-IV (%)
Atlac 430	97.66	74.55	93.90	72.34
Trigonox C	1.48	1.13	1.42	1.10
Perkadox 16	0.51	0.39	0.49	0.38
BYK A555	0.35	0.27	0.34	0.26
Aluminum hydroxide	–	23.66	–	22.96
Zinc stearate	–	–	3.85	2.96

Table 3. DSC measurement results.

Resin composition	Fraction of M-I within composition	Heating rate (K/min)	Heat released (J/g)	Heat released per gram of M-I (J/g)	Peak temperature (°C)	Onset temperature (°C)	End temperature (°C)
M-I	1.00	5	150	150	93.1	85.3	99.6
		7.5	163	163	97.1	89.2	104
		10	167	167	99.9	92.1	108
M-II	0.76	5	131	170	91.8	84.6	98.4
		7.5	102	132	97.4	88.6	105
		10	109	142	100	91.4	108
M-III	0.96	5	210	219	91.1	84.2	98.9
		7.5	229	239	95.5	87.5	104
		10	207	216	98.8	90.3	108
M-IV	0.74	5	156	211	91.5	84.5	99.4
		7.5	159	215	96.1	88.5	104
		10	143	193	99.4	91.5	108

the DSC curve, and the onset and end temperatures corresponding to the intersection of the baseline extrapolated to the peak region and tangents to the inflection point. The baseline is the virtual line drawn through the reaction or phase transition interval supposing zero heat of the process. Although additives did not change the peak, end, and onset temperatures (Figure 3(a)), they significantly affected the amount of heat released (Figure 3(b)). The temperature at the end of the reaction in all experiments was less than 108°C (Table 3). Therefore, the reaction ends before the decomposition of Al(OH)₃, starting at 230°C, or melting of Zn(C₁₈H₃₅O₂)₂, beginning at 120°C. Thus, the difference between the amounts of heat released for a corresponding composition and M-I can be ascribed to either a chemical reaction between the additive(s) and M-I or to the dissolution of the additive(s) in M-I.

The addition of Al(OH)₃ to M-II caused the reduction of the Atlac 430 mass fraction, thereby reducing the amount of heat released by 29% (Figure 3(b)). Moreover, the addition of 31 g of Al(OH)₃ to 100 g of M-I reduced the average amount of heat released per gram of M-I during polymerization by 7% (Figure 3(b)). Thus, the variation in the amount of heat released

with respect to the addition of Al(OH)₃ is mainly caused by the large amount of Al(OH)₃ introduced into M-I rather than by the chemical reaction between Al(OH)₃ and M-I and may be verified by the removal of moisture from Al(OH)₃ during heating.

Contrary to the case of Al(OH)₃, the addition of Zn(C₁₈H₃₅O₂)₂ (M-III) increased the amount of heat released by approximately 35% (Figure 3(b)). However, the average amount of heat released per gram of M-I during polymerization increased by 40% (Figure 3(b)) when 4 g of Zn(C₁₈H₃₅O₂)₂ was added to 100 g of M-I. Furthermore, with the addition of Zn(C₁₈H₃₅O₂)₂, we observed a shift in the reaction onset temperature, which may be associated with the catalytic participation of Zn²⁺ in vinyl ester polymerization.⁹¹ Due to the significant increase in the thermal effect of the reaction per gram of resin and shifting of the onset temperature caused by the addition of 4% Zn(C₁₈H₃₅O₂)₂, we can speculate that Zn(C₁₈H₃₅O₂)₂ participates in resin polymerization. Zn²⁺ may participate in the decomposition of the initiator and may consequently increase the concentration of active radicals. Moreover, because of its electron-accepting nature, Zn²⁺ may coordinate π -bonds between styrene and

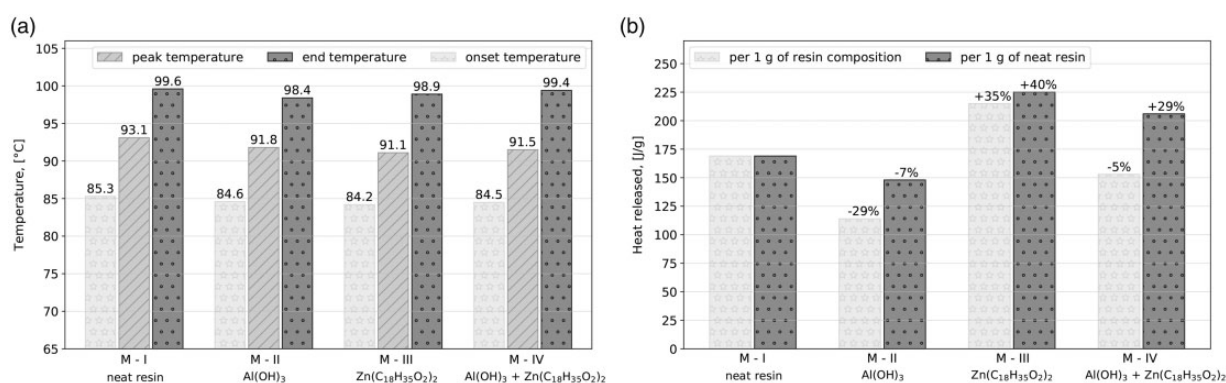


Figure 3. Effects of processing additives on the polymerization behaviors of M-I, M-II, M-III, and M-IV: (a) Onset, peak, and end temperatures at a heating rate of 5 K/min and (b) average amount of heat released.

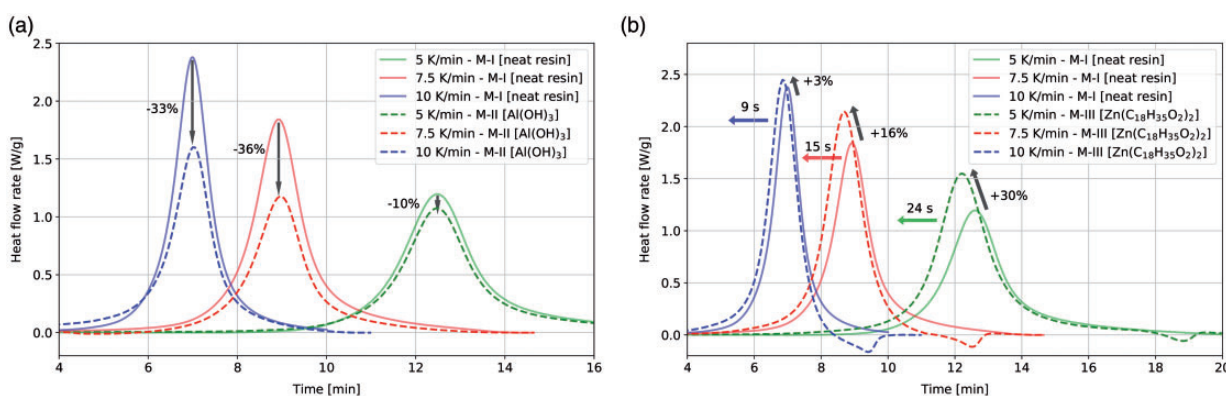


Figure 4. Effect of processing additives on the polymerization behaviors of resin compositions: (a) M-I vs M-II and (b) M-I vs M-III.

vinyl monomers, thus contributing to their polymerization. However, the mechanism of the contribution of Zn^{2+} to the cure kinetics needs further investigation using nuclear magnetic resonance, infrared, UV, and visible light spectroscopies.

The results obtained for M-IV are similar to those obtained for M-I, with a difference of only 5% (Figure 3(b)). However, the average amount of heat released per gram of M-I during polymerization was 29% higher than that in the case of M-I (Figure 3(b)). Nevertheless, due to the presence of $Al(OH)_3$, the additional thermal effect associated with the addition of $Zn(C_{18}H_{35}O_2)_2$ was reduced.

To determine the effects of $Al(OH)_3$ and $Zn(C_{18}H_{35}O_2)_2$ on the polymerization behaviors of the resin compositions, we compared the results obtained for M-I with those acquired for M-II (Figure 4(a)) and M-III (Figure 4(b)). The addition of $Al(OH)_3$ decreased the reaction peak values by 10, 36, and 33% at the heating rates of 5, 7.5, and 10 K/min, respectively. The addition of $Zn(C_{18}H_{35}O_2)_2$ caused

a shift in the peaks values (by 9, 15, and 24 s at 10, 7.5, and 5 K/min, respectively), earlier occurrence of the exothermic peak, and the occurrence of a local minimum at the end of the reaction, caused by the melting of $Zn(C_{18}H_{35}O_2)_2$. The difference between the exothermic peak values of M-III and M-I was 30, 16, and 3% at 5, 7.5, and 10 K/min, respectively. The graphs shown in Figure 4 are plotted with respect to the mass of a particular resin composition (M-I, M-II, M-III, and M-IV).

Resin cure simulation

By applying the linear least-squares method, we tested 16 phenomenological kinetic models and determined their constants to investigate the polymerization behaviors of the resin compositions. Thus, we need to discover the type of function that would statistically provide the best approximation of the experimental data obtained at different heating rates. To calculate the MSE between the experimental and predicted values of the heat flow

rate, we employed the following equation

$$\begin{aligned}
 MSE = & \frac{1}{n_5} \sum_{i=1}^{n_5} (Y_5^{exp} - Y_5^{model})^2 \\
 & + \frac{1}{n_{7.5}} \sum_{j=1}^{n_{7.5}} (Y_{7.5}^{exp} - Y_{7.5}^{model})^2 \\
 & + \frac{1}{n_{10}} \sum_{k=1}^{n_{10}} (Y_{10}^{exp} - Y_{10}^{model})^2 \quad (1)
 \end{aligned}$$

where n_5 , $n_{7.5}$, and n_{10} , Y_5^{exp} , $Y_{7.5}^{exp}$, and Y_{10}^{exp} , and Y_5^{model} , $Y_{7.5}^{model}$, and Y_{10}^{model} represent the number of data points, experimental values of the heat flow rate, and predicted values of the heat flow rate obtained at 5, 7.5, and 10 K/min, respectively.

Table 4 shows a comparison between the performances of various models. Some functions can provide a good description of the experimental data from a statistical point of view. However, the choice of the approximating function should be based on the physical meaning of the process being studied. The NETZSCH Thermokinetics suite offers n-order models (No. 6–10, Table 4) that reduce the curing process to a single F1, F2, and Fn and reactions at two-dimensional (2D) and 3D

interfaces. However, the nth-order models assume a maximum reaction rate at a zero point in time, which does not correlate well with the physics of the vinyl ester curing process. In addition, the NETZSCH Thermokinetics suite provides models typically used to describe processes, such as solid-phase synthesis and pyrolysis, controlled by diffusion (Models 2–5, Table 4)⁹² and nucleation models describing the nucleation of particles (Models 11–13, Table 4) typically used for solid-state chemical reactions.⁹³ These models can also be employed to characterize DSC experimental data; however, the contradiction between the physics of the resin polymerization reaction and the field of application of these models results in a poor correlation between experimental data and numerical simulation results.

Curing of vinyl ester resin is a complex autocatalytic reaction, that is, the reaction products accelerate the reaction itself. Therefore, to describe self-accelerating reactions, an additional term responsible for autocatalysis is introduced into the equations, leading to models 1, 14, 15, and 16 (Table 4). In this way, we can achieve correspondence between the physics of vinyl ester curing and the mathematical model of the process. This can explain the best fit between the experimental

Table 4. Examined kinetic models and their mean squared errors for M-I–M-IV.

Model No.	Kinetic model, abbreviation, reference	Model equation	MSE × 10 ³ [–]			
			M-I	M-II	M-III	M-IV
1	Prout–Tompkins equation, (B1), ⁹⁵	$\frac{dx}{dt} = Ae^{-\frac{E_a}{RT}}(1-\alpha)\alpha$	333	191	333	187
2	One-dimensional diffusion, (D1), ⁹⁶	$\frac{dx}{dt} = Ae^{-\frac{E_a}{RT}}\frac{1}{2\alpha}$	237	111	253	142
3	Two-dimensional diffusion, (D2), ⁹⁷	$\frac{dx}{dt} = Ae^{-\frac{E_a}{RT}}\left(\frac{1}{-\ln(1-\alpha)}\right)$	146	80.4	186	106
4	Ginstling–Brounshtein three-dimensional diffusion, (D4), ⁹⁸	$\frac{dx}{dt} = Ae^{-\frac{E_a}{RT}}\frac{1.5}{(1-\alpha)^{\frac{1}{3}-1}}$	132	71.7	163	94
5	Jander three-dimensional diffusion, (D3), ⁹⁹	$\frac{dx}{dt} = Ae^{-\frac{E_a}{RT}}1.5\frac{(1-\alpha)^{\frac{1}{3}}}{(1-\alpha)^{\frac{1}{3}-1}}$	105	61.9	138	80.8
6	Reaction at a two-dimensional interface, (R2), ¹⁰⁰	$\frac{dx}{dt} = Ae^{-\frac{E_a}{RT}}2(1-\alpha)^{\frac{1}{2}}$	93.5	50.4	111	64.8
7	Second-order reaction, (F2), ¹⁰¹	$\frac{dx}{dt} = Ae^{-\frac{E_a}{RT}}(1-\alpha)^2$	59.2	42	94.6	57.5
8	Reaction at a three-dimensional interface, (R3), ¹⁰²	$\frac{dx}{dt} = Ae^{-\frac{E_a}{RT}}3(1-\alpha)^{\frac{2}{3}}$	79.6	45.1	96.7	57.3
9	First-order reaction, (F1), ¹⁰³	$\frac{dx}{dt} = Ae^{-\frac{E_a}{RT}}(1-\alpha)$	64.6	40.1	83.9	51
10	nth-order reaction, (Fn), ²⁸	$\frac{dx}{dt} = Ae^{-\frac{E_a}{RT}}(1-\alpha)^n$	57.7	39	82.5	50.4
11	Two-dimensional nucleation, (A2), ¹⁰⁴	$\frac{dx}{dt} = Ae^{-\frac{E_a}{RT}}2(1-\alpha)(-\ln(1-\alpha))^{\frac{1}{2}}$	39.8	21.8	36.5	23.3
12	Three-dimensional nucleation, (A3), ¹⁰⁵	$\frac{dx}{dt} = Ae^{-\frac{E_a}{RT}}3(1-\alpha)(-\ln(1-\alpha))^{\frac{2}{3}}$	49.6	23.8	32.2	20
13	n-dimensional nucleation, (An), ¹⁰⁶	$\frac{dx}{dt} = Ae^{-\frac{E_a}{RT}}n(1-\alpha)(-\ln(1-\alpha))^{\frac{n-1}{n}}$	39.2	20.4	29.3	18.7
14	Reaction of first order with autocatalysis, (C1), ¹⁰⁷	$\frac{dx}{dt} = Ae^{-\frac{E_a}{RT}}(1 + K_{cat}\alpha)(1-\alpha)$	27.1	13	18	11.7
15	Expanded Prout–Tompkins equation, (Bna), ¹⁰⁸	$\frac{dx}{dt} = Ae^{-\frac{E_a}{RT}}(1-\alpha)^n\alpha^m$	9.44	15.2	8.48	5.96
16	Reaction of nth-order with autocatalysis, (Cn), ⁹⁴	$\frac{dx}{dt} = Ae^{-\frac{E_a}{RT}}(1 + K_{cat}\alpha)(1-\alpha)^n$	4.66	4.65	6.35	4.46

data and numerical simulation results obtained using the equation of the Cn^{94} (model 16, Table 4), with the smallest MSEs of 4.66×10^{-3} , 4.65×10^{-3} , 6.35×10^{-3} , and 4.46×10^{-3} for M-I, M-II, M-III, and M-IV, respectively. However, this model ignores the melting of $Zn(C_{18}H_{35}O_2)_2$ observed during the DSC measurements of M-III and M-IV. Table 5 shows the kinetic constants of the Cn. These constants were used to compare the experimental DSC data and the results predicted by numerical simulations for M-I, M-II, M-III, and M-IV (Figure 5).

Refinement of the kinetic model considering the melting of $Zn(C_{18}H_{35}O_2)_2$

To reduce the MSE caused by the melting of $Zn(C_{18}H_{35}O_2)_2$ and obtain a more accurate description

of the polymerization process (equation (2)) for M-III and M-IV, we derived two models for separately characterizing the processes of vinyl ester resin polymerization (equation (3)) and $Zn(C_{18}H_{35}O_2)_2$ melting (equation (4)). The following technique was used to isolate the corresponding DSC signals. Initially, we drew a tangent line to the DSC curve for M-IV through the beginning and end points of $Zn(C_{18}H_{35}O_2)_2$ melting (Figure 6(a)). Thus, the polymerization of M-IV (*original data*) was divided into two models to acquire two DSC curves. The first curve (defined by equation (3)) describes the polymerization of vinyl ester resin (*modified data*) and ignores the melting of $Zn(C_{18}H_{35}O_2)_2$. Then, at each point of the first curve within the region of $Zn(C_{18}H_{35}O_2)_2$ melting, we substituted the experimental DSC data with the ordinates of the tangent. Therefore, within this region, the tangent corresponds

Table 5. Kinetic constants for the n th-order autocatalytic reaction of M-I, M-II, M-III, and M-IV.

Resin composition	H_{tot} [J/g]	$\log(A)$ [-]	E_a (kJ/mol)	n (-)	$\log(K_{cat})$ (-)	$MSE \times 10^3$ (-)
M-I	160	12.1	109	1.81	2.13	4.66
M-II	114	9.3	89.7	1.67	2.13	4.65
M-III	215	10.5	97.3	1.41	2.04	6.35
M-IV	153	10.4	97.4	1.44	2.14	4.46

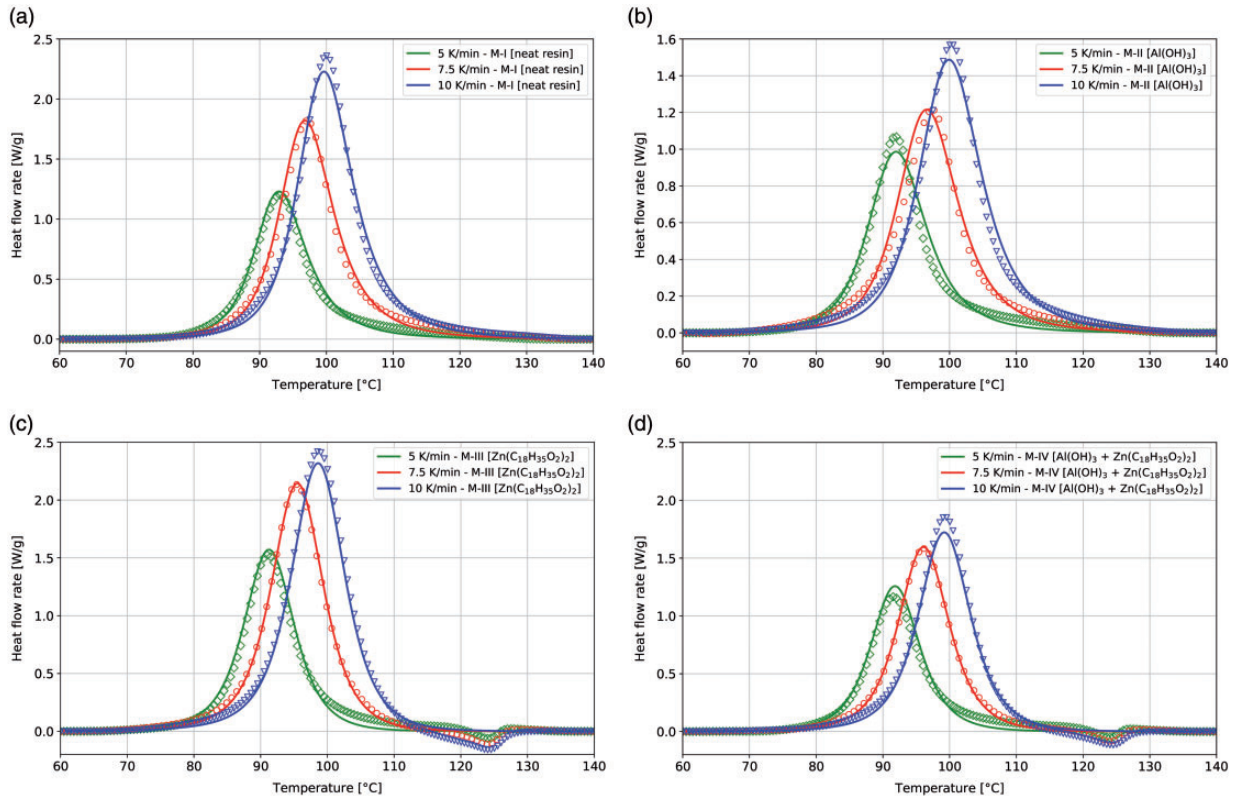


Figure 5. Polymerization enthalpy and numerical simulation by the n th-order autocatalytic reaction: (a) M-I, (b) M-II, (c) M-III, and (d) M-IV. Diamonds, circles, and downward triangles represent experimental data, and solid lines indicate simulation results.

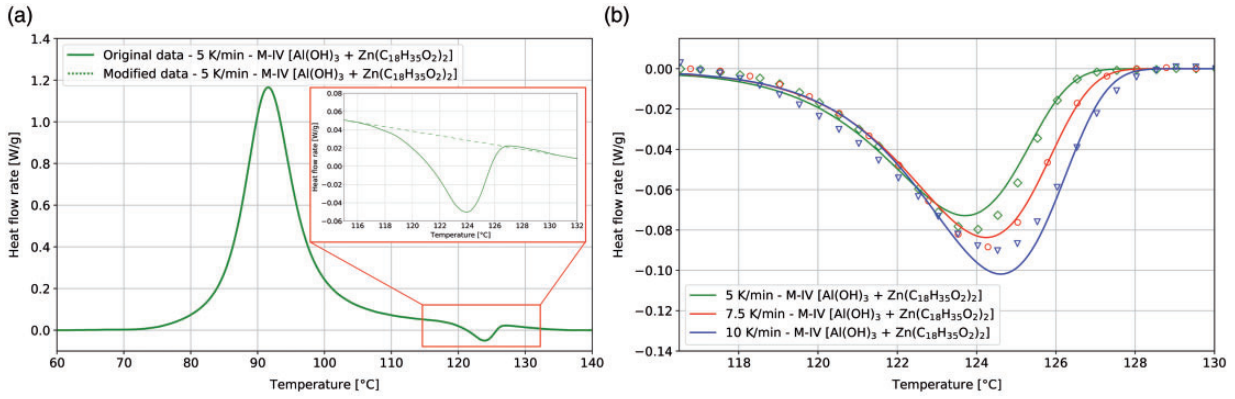


Figure 6. Separation of vinyl ester polymerization and additive melting processes: (a) M-IV polymerization and $\text{Zn}(\text{C}_{18}\text{H}_{35}\text{O}_2)_2$ melting and (b) modeling of $\text{Zn}(\text{C}_{18}\text{H}_{35}\text{O}_2)_2$ melting. Diamonds, circles, and downward triangles represent experimental data, and solid lines denote simulation results.

Table 6. Kinetic constants for the n th-order autocatalytic reaction (Cn)⁹⁴ and for the n -dimensional nucleation model (An)¹⁰⁶

Process	Kinetic model	i	H_{tot_i} (J/g)	\log (Ai) (-)	E_{a_i} (kJ/mol)	n_i (-)	\log (Kcat_i) (-)	MSE $\times 10^3$ (-)
Vinyl ester curing (original data)	Reaction of n th order with autocatalysis (Cn) ⁹⁴	0	153	10.4	97.4	1.44	2.14	4.46
Vinyl ester curing (modified data)	Reaction of n th order with autocatalysis (Cn) ⁹⁴	1	156.27	10.4	97.4	1.53	2.17	2.94
Zinc Stearate melting	n -dimensional nucleation (An) ¹⁰⁶	2	-3.27	132	1010	0.768	-	0.05

to the heat flow rate of the first model. The second DSC curve corresponding to $\text{Zn}(\text{C}_{18}\text{H}_{35}\text{O}_2)_2$ melting is presented by equation (4), where the heat flow rate corresponds to the difference between the downward peak and the tangent line (Figure 6(b)).

$$H(t) = H_1(t) + H_2(t) = \alpha(t)H_{tot-1} + \gamma(t)H_{tot-2} \quad (2)$$

$$\alpha(t) = \frac{H_1(t)}{H_{tot-1}} \quad (3)$$

$$\gamma(t) = \frac{H_2(t)}{H_{tot-2}} \quad (4)$$

where $H(t)$ is an experimental instantaneous value of the heat released during the curing of M-IV; H_{tot} represents the experimental total heat released during the polymerization of M-IV (calculated as the area between the baseline and the graph plotted with original data); $\alpha(t)$ refers to the instantaneous degree of cure of vinyl ester; $H_1(t)$ denotes the experimental instantaneous value of the heat released during the curing of vinyl ester; H_{tot-1} represents the experimental total heat released during the polymerization of vinyl ester (positive sign, calculated as the area between the baseline and the graph plotted with modified data); $\gamma(t)$ denotes the instantaneous melting degree of

$\text{Zn}(\text{C}_{18}\text{H}_{35}\text{O}_2)_2$; $H_2(t)$ is the experimental instantaneous value of the heat absorbed during the melting of $\text{Zn}(\text{C}_{18}\text{H}_{35}\text{O}_2)_2$; and H_{tot-2} indicates the experimental total heat absorbed during the melting of $\text{Zn}(\text{C}_{18}\text{H}_{35}\text{O}_2)_2$ (negative sign, calculated as the area between the baseline and the graph plotted with the $\text{Zn}(\text{C}_{18}\text{H}_{35}\text{O}_2)_2$ melting data).

Table 6 shows the model constants used for characterizing the original and modified polymerization kinetics of vinyl ester curing by the Cn model (equation (5))⁹⁴

$$\frac{d\alpha}{dt} = A_1 e^{-\frac{E_{a-1}}{RT}} (1 - \alpha)^{n_1} (1 + K_{cat-1}\alpha) \quad (5)$$

where $\frac{d\alpha}{dt}$ is the cure rate of vinyl ester, T is the absolute temperature, R is the universal gas constant, A_1 is a pre-exponential factor, E_{a-1} is the activation energy, n_1 is the order of the reaction, and K_{cat-1} is the activation constant.

Table 6 also presents the constants used to describe the melting of $\text{Zn}(\text{C}_{18}\text{H}_{35}\text{O}_2)_2$ by the An model (equation (6))¹⁰⁶

$$\frac{d\gamma}{dt} = A_2 e^{-\frac{E_{a-2}}{RT}} n_2 (1 - \gamma) (-\ln(1 - \gamma))^{\frac{n_2-1}{n_2}} \quad (6)$$

where $\frac{d\gamma}{dt}$ is the melting rate of $\text{Zn}(\text{C}_{18}\text{H}_{35}\text{O}_2)_2$, T is the absolute temperature, A_2 is a pre-exponential factor,

E_{a_2} is the activation energy, and n_2 is the order of the reaction.

By applying the modified data to the Cn model, we reduced the MSE by approximately 34%.

Pultrusion simulations

To better understand the influence of resin kinetics on the pultrusion of a flat laminate specimen, numerical simulations were carried out. As the thickness of the pultruded profile was small (up to 4 mm⁴¹) we ignored the thermal conductivity and speculated a uniform cure distribution over the thickness of the profile during instant heating of the material to the die temperature.⁴¹ As the temperature was supposed to be constant over

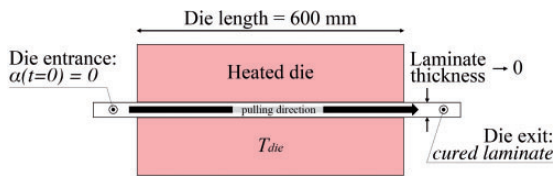


Figure 7. Simulation scheme for the pultrusion of a flat profile.

the entire length of the die block and was equal to T_{die} , the process could be considered isothermic. Zero degree of polymerization at the die entrance was taken as the initial condition. For simulation, we selected a die length of 600 mm, which is typical for production lines.⁶⁴ Figure 7 shows the simulation scheme for the pultrusion of a flat profile together with the initial and boundary conditions for the numerical simulation.

We simulated the polymerization process using the Cn model⁹⁴ (No. 16, Table 4) and the numerical scheme in equation (7) with coefficients acquired from Table 5.

$$\alpha_{i+1} = \alpha_i + A e^{-\frac{E_a}{RT_{die}}} (1 - \alpha_i)^n (1 + K_{cat} \alpha_i) \Delta t \quad (7)$$

where Δt is the time increment equal to 0.1 s. Degree of cure (α_0) = 0 was taken as the initial condition. Numerical simulation was performed using MATLAB software (MathWorks, USA).

For simulation, we selected the pulling speeds of 600 (Figure 8(a)) and 1000 mm/min (Figure 8(b)). Thus, two isothermal curing processes were considered: at 115 (Figure 8(a) and 8(c)) and 125°C (Figure 8(b) and 8(d)). Table 7 shows the final values of the degree of cure

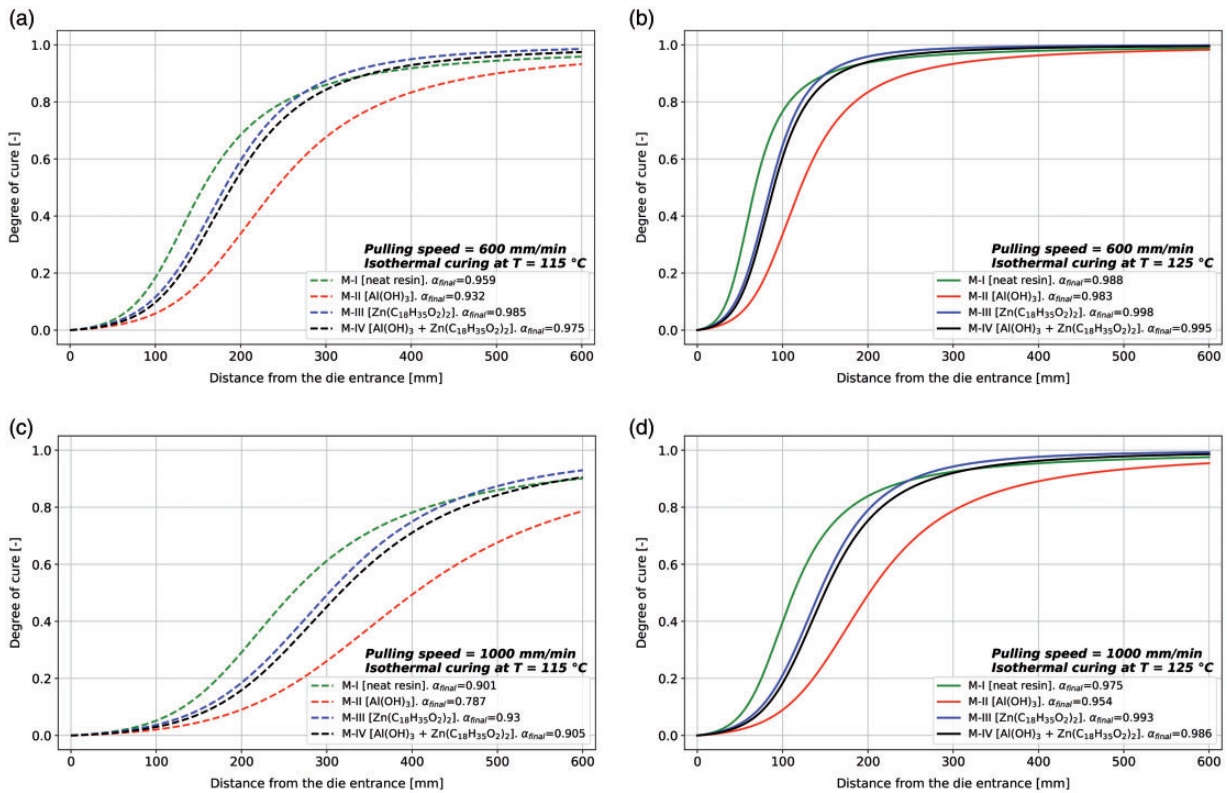


Figure 8. Curing of M-I, M-II, M-III, and M-IV simulated with the model based on the nth-order autocatalytic reaction: (a) Isothermal curing at 115°C and the pulling speed of 600 mm/min; (b) isothermal curing at 125°C and the pulling speed of 600 mm/min; (c) isothermal curing at 115°C and the pulling speed of 1000 mm/min; and (d) isothermal curing at 125°C and the pulling speed of 1000 mm/min. Dashed lines represent isothermal curing at 115°C, and solid lines indicate isothermal curing at 125°C.

(α_{final}) as a function of the pulling speed, temperature, and resin composition. As observed, the curing of M-II is the slowest, whereas that of M-III is the fastest. The difference between the final degrees of cure of these compositions under isothermal conditions at 115°C was 5.4% at 600 mm/min (Figure 8(a)) and 15.4% at 1000 mm/min (Figure 8(c)). The resin composition with a degree of cure above 0.95 is considered to be completely polymerized. Thus, at 600 mm/min (Figure 8(a)), we obtained three specimens of acceptable quality (with the degrees of cure of 0.959, 0.985, and 0.975 for M-I, M III, and M-IV, respectively); however, at 1000 mm/min (Figure 8(c)), it was impossible to acquire a fully cured composite at the die exit for all compositions. Therefore, the failure to describe the effects of processing additives

on the cure behavior of the resin and the improper choice of kinetic equation may result in substantial differences between the predicted and real degrees of cure at the end of polymerization. For isothermal heating at 125°C, the maximum difference between the final degrees of cure for these compositions was 1.5% (at 600 mm/min, Figure 8 (b)) and 3.9% (at 1000 mm/min, Figure 8(d)). The increase in the pulling speed from 600 to 1000 mm/min at a constant heating temperature led to an increase in the difference between the final degrees of cure for the studied compositions: from 5.4 (Figure 8(a)) to 15.4% (Figure 8(c)) at 115°C and from 1.5 (Figure 8(b)) to 3.9% (Figure 8(d)) at 125°C.

For each resin composition, we simulated the curing process at the die temperatures of 115 (Figure 9(a)),

Table 7. Degrees of cure for M-I, M-II, M-III, and M-IV calculated at the die exit.

Pulling speed (mm/min)	Heating temperature (°C)	Degree of cure at the die exit (α_{final}) (-)			
		M-I	M-II	M-III	M-IV
600	115	0.959	0.932	0.985	0.975
	125	0.988	0.983	0.998	0.995
1000	115	0.901	0.787	0.930	0.905
	125	0.975	0.954	0.993	0.986

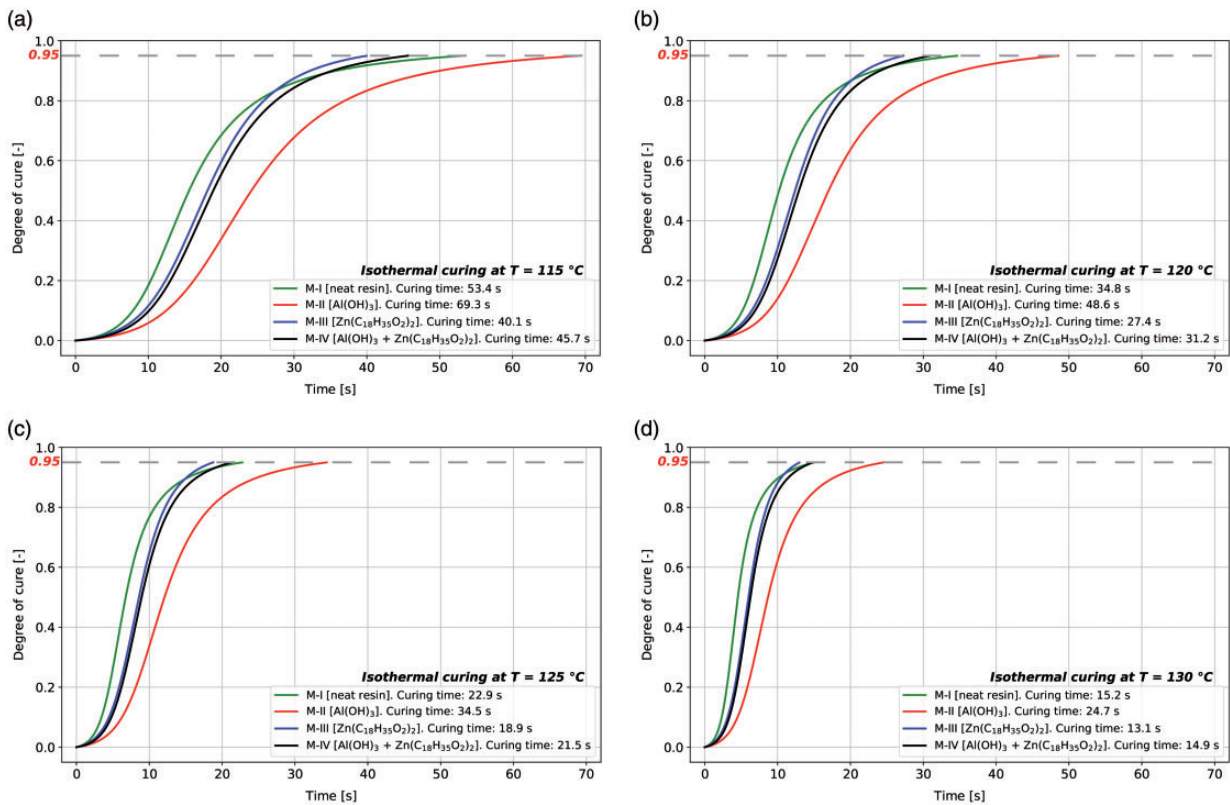


Figure 9. Polymerization of M-I, M-II, M-III, and M-IV to the degree of cure of 0.95, simulated by the model based on the nth-order autocatalytic reaction: Isothermal curing at (a) 115, (b) 120, (c) 125, and (d) 130°C.

Table 8. Maximum pulling speed required for the resin compositions to reach the degree of cure of 0.95.

		Die temperature			
		115°C	120°C	125°C	130°C
Maximum pulling speed (mm/min)	M-I	674	1036	1574	2371
	M-II	519	740	1045	1459
	M-III	899	1315	1907	2751
	M-IV	787	1155	1676	2419

120 (Figure 9(b)), 125 (Figure 9(c)), and 130°C (Figure 9(d)) and calculated the time required for the resin to reach the degree of cure of 0.95. With an increase in heating temperature, the polymerization graphs of all compositions shifted to the left (Figure 9); therefore, less time was required for the resin to reach the cured state. The maximum pulling speed was determined as the ratio of the die block length (600 mm) to the polymerization time for each resin composition (Table 8). The maximum pulling speed was considerably affected by the temperature conditions. For example, the maximum pulling speeds at 115 and 130°C differed by the factors of 3.5, 2.8, 3.1, and 3.1 for M-I, M-II, M-III, and M-IV, respectively, and the maximum difference between the predicted values of pulling speed for these compositions at each heating temperature exceeded 1.7 times. For instance, at 115°C, the maximum pulling speed for M-II was 519 mm/min, whereas the maximum pulling speed for M-III was 899 mm/min, 1.73 times that for M-II. Thus, it is essential to consider the effect of processing additives on the polymerization kinetics of pultrusion resins while predicting the maximum output of pultrusion using mathematical models.

Although in this study, we analyzed the influence of $\text{Zn}(\text{C}_{18}\text{H}_{35}\text{O}_2)_2$ and $\text{Al}(\text{OH})_3$ on the cure kinetics of resin compositions, the number of processing additives used in pultrusion is considerably higher. To optimize the process, all types of additives, such as those protecting against fungal, bacterial, and UV degradation and aesthetic additives, should be investigated. In addition, the effects of additives on other types of pultrusion resins (epoxy and polyester) require further investigation. Further studies are necessary to examine the effects of the components, storage time and temperature, preparation specifics, and refrigeration of resin compositions on the cure kinetics of resins. Moreover, possible chemical interactions between neat resins and additives, affecting the polymerization kinetics, have rarely been explored.

Conclusions

To better understand the relationship between a resin composition (that is, the presence of processing additives) and its curing behavior, we conducted DSC

analysis and numerical simulations of the vinyl ester resin compositions used in pultrusion. Herein, four different compositions based on Atlac 430 were prepared: M-I, M-II, M-III, and M-IV. DSC analysis was performed at the heating rates of 5, 7.5, and 10 K/min. In this study, we tested and compared the performances of 16 kinetic models describing the process of polymerization and proposed a method for characterizing the curing of the resin compositions in the presence of $\text{Zn}(\text{C}_{18}\text{H}_{35}\text{O}_2)_2$. The method demonstrated higher efficiency, and the kinetic law and its constants describing the melting of $\text{Zn}(\text{C}_{18}\text{H}_{35}\text{O}_2)_2$ were obtained. To analyze the influence of the processing parameters and additives on the curing behaviors of resin compositions, we carried out a numerical simulation of the pultrusion of a flat laminate profile at different heating temperatures (115 and 125°C) and pulling speeds (600 and 1000 mm/min) for all four compositions. We also calculated the curing times for all compositions under isothermal conditions at 115, 120, 125, and 130°C and evaluated the maximum pulling speeds.

Results show that the presence of processing additives significantly affects the curing behavior of resin compositions. For instance, the addition of $\text{Al}(\text{OH})_3$ (M-II) reduced the amount of heat released, whereas the addition of $\text{Zn}(\text{C}_{18}\text{H}_{35}\text{O}_2)_2$ (M-III) increased the amount of heat released. However, the addition of both $\text{Al}(\text{OH})_3$ and $\text{Zn}(\text{C}_{18}\text{H}_{35}\text{O}_2)_2$ (M-IV) had almost no effect on the amount of heat released. Moreover, as compared to those for M-I, the polymerization peak values for M-II obtained at 5, 7.5, and 10 K/min were lowered by 10, 36, and 33%, respectively. Simultaneously, the addition of $\text{Zn}(\text{C}_{18}\text{H}_{35}\text{O}_2)_2$ (M-III) resulted in a shift (by 9 s at 10 K/min, 15 s at 7.5 K/min, and 24 s at 5 K/min) and earlier occurrence of the polymerization peak. The difference between the exothermic peak values of M-III and M-I was 30% at 5 K/min, 16% at 7.5 K/min, and 3% at 10 K/min. When the proposed method of cure modeling was applied to M-IV, the MSE was reduced by approximately 34%. Numerical simulation of the pultrusion of a flat laminate profile at different temperatures showed that different resin compositions required different curing times and therefore different production speeds. M-II demonstrated the highest degree of cure at the die exit, whereas M-III

exhibited the lowest degree of cure. This study shows that ignoring the effects of certain processing additives may result in a significant difference between the predicted and experimental degrees of cure obtained at the die exit. The analysis of the pulling speed required for the complete polymerization of the resin compositions indicated that the largest difference occurred between the pulling speeds of M-II and M-III. Furthermore, the maximum difference between the predicted values of pulling speeds for these compositions at each heating temperature exceeded 1.7 times.

Declaration of Conflicting Interests

The author(s) declared no potential conflicts of interest with respect to the research, authorship, and/or publication of this article.

Funding

The author(s) received no financial support for the research, authorship, and/or publication of this article.

ORCID iDs

Alexander Vedernikov  <https://orcid.org/0000-0003-2127-0934>

Alexander Safonov  <https://orcid.org/0000-0002-5031-9058>

References

1. Bakis CE, Bank LC, Brown VL, et al. Fiber-reinforced polymer composites for construction – state-of-the-art review. *J Compos Constr* 2002; 6: 73–87.
2. Bank LC. *Composites for construction: structural design with FRP materials*, 2007. Epub ahead of print. DOI: 10.1002/9780470121429.
3. Lionetto F, Montagna F, Natali D, et al. Correlation between elastic properties and morphology in short fiber composites by X-ray computed micro-tomography. *Compos Part A Appl Sci Manuf* 2021; 140: 106169.
4. Cascardi A, Dell’Anna R, Micelli F, et al. Reversible techniques for FRP-confinement of masonry columns. *Constr Build Mater* 2019; 225: 415–428.
5. Minchenkov K, Vedernikov A, Safonov A, et al. Thermoplastic pultrusion: a review. *Polymers* 2021; 13: 180–136.
6. Vedernikov A, Safonov A, Tucci F, et al. Pultruded materials and structures: a review. *J Compos Mater* 2020; 54: 4081–4117.
7. Xiong Z, Liu Y, Zuo Y, et al. Experimental evaluation of shear behavior of pultruded GFRP perforated connectors embedded in concrete. *Compos Struct* 2019; 222: 110938.
8. Parmar H, Khan T, Tucci F, et al. Advanced robotics and additive manufacturing of composites: towards a new era in industry 4.0. *Mater Manuf Process* 2021; 36: 1–35.
9. Zhu, R., Li, F., Zhao, Z., Zhang, D., & Chen, Y. Compression Behavior of Square Pyramid Substructure of Novel Pultruded FRP-Aluminum Space Truss. *J Compo Constr* 2020; 24(6): 04020062. DOI: 10.1061/(ASCE)CC.1943-5614.0001074.
10. Li, C., Yin, X., Wang, Y., Zhang, L., Zhang, Z., Liu, Y., & Xian, G. Mechanical property evolution and service life prediction of pultruded carbon/glass hybrid rod exposed in harsh oil-well condition. *Compos Struct* 2020; 246: 112418. DOI: 10.1016/j.compstruct.2020.112418.
11. Liu T, Feng P, Wu Y, et al. Developing an innovative curved-pultruded large-scale GFRP arch beam. *Compos Struct* 2021; 256: 113111.
12. Liu T, Liu X and Feng P. A comprehensive review on mechanical properties of pultruded FRP composites subjected to long-term environmental effects. *Compos Part B Eng* 2020; 191: 107958.
13. Irfan MS, Harris D, Paget MA, et al. On-site evaluation of a modified pultrusion process: fibre spreading and resin injection-based impregnation. *J Compos Mater* 2020. Epub ahead of print. DOI: 10.1177/0021998320943268.
14. Irfan MS, Shotton-Gale N, Paget MA, et al. A modified pultrusion process. *J Compos Mater* 2017; 51: 1925–1941.
15. Vedernikov A, Tucci F, Safonov A, et al. Investigation on the shape distortions of pultruded profiles at different pulling speed. *Procedia Manuf* 2020; 47: 1–5.
16. Madenci E, Özkılıç YO and Gemi L. Experimental and theoretical investigation on flexure performance of pultruded GFRP composite beams with damage analyses. *Compos Struct* 2020; 242: 112162.
17. Safonov AA, Carlone P and Akhatov I. Mathematical simulation of pultrusion processes: a review. *Compos Struct* 2018; 184. Epub ahead of print DOI: 10.1016/j.compstruct.2017.09.093.
18. He J, Xian G and Zhang YX. Numerical modelling of bond behaviour between steel and CFRP laminates with a ductile adhesive. *Int J Adhes Adhes* 2021; 104: 102753.
19. Lionetto F, Moscatello A, Totaro G, et al. Experimental and numerical study of vacuum resin infusion of stiffened carbon fiber reinforced panels. *Materials* 2020; 13: 4800–4817.
20. Lionetto F, Pappadà S, Buccoliero G, et al. Finite element modeling of continuous induction welding of thermoplastic matrix composites. *Mater Des* 2017; 120: 212–221.
21. Vedernikov A, Tucci F, Carlone P, et al. Effects of pulling speed on structural performance of L-shaped pultruded profiles. *Compos Struct* 2021; 255: 112967.
22. Vedernikov AN, Safonov AA, Gusev SA, et al. Spring-in experimental evaluation of L-shaped pultruded profiles. *IOP Conf Ser: Mater Sci Eng* 2020; 747: 012013.
23. Joshi SC and Lam YC. Integrated approach for modelling cure and crystallization kinetics of different polymers in 3D pultrusion simulation. *J Mater Process Technol* 2006; 174: 178–182.
24. Prime RB, Michalski C and Neag CM. Kinetic analysis of a fast reacting thermoset system. *Thermochim Acta* 2005; 429: 213–217.
25. Moschiar SM, Reboredo MM, Larrondo H, et al. Pultrusion of epoxy matrix composites: pulling force

- model and thermal stress analysis. *Polym Compos* 1996; 17: 850–858.
26. Barkanov E, Akishin P, Miazza NL, et al. ANSYS-based algorithms for a simulation of pultrusion processes. *Mech Adv Mater Struct* 2017; 24: 377–384.
 27. Carlone P, Palazzo GS and Pasquino R. Pultrusion manufacturing process development: cure optimization by hybrid computational methods. *Comput Math with Appl* 2007; 53: 1464–1471.
 28. Chachad YR, Roux JA, Vaughan JG, et al. Three-dimensional characterization of pultruded fiberglass-epoxy composite materials. *J Reinf Plast Compos* 1995; 14: 495–512.
 29. Gorthala R, Roux JA and Vaughan JG. Resin flow, cure and heat transfer analysis for pultrusion process. *J Compos Mater* 1994; 28: 486–506.
 30. Safonov AA and Suvorova YV. Optimization of the pultrusion process for a rod with a large diameter. *J Mach Manuf Reliab* 2009; 38: 572–578.
 31. Safonov A, Gusev M, Saratov A, et al. Modeling of cracking during pultrusion of large-size profiles. *Compos Struct* 2020; 235: 111801.
 32. Badrinarayanan P, Lu Y, Larock RC, et al. Cure characterization of soybean oil-styrene-divinylbenzene thermosetting copolymers. *J Appl Polym Sci* 2009; 113: 1042–1049.
 33. Lue J, Chen C and Yen C. In situ pultrusion of urea-formaldehyde matrix composites. I. Processability, kinetic analysis, and dynamic mechanical properties. *J Appl Polym Sci* 2002; 83. Epub ahead of print. DOI: 10.1002/app.2291.
 34. Ma CM and Chen CH. The development of a mathematical model for the pultrusion of blocked polyurethane composites. *J Appl Polym Sci* 1993; 50: 759–764.
 35. Sun Y-Y and Chen C-H. Process feasibility and kinetic analysis of glass fiber-reinforced vinyl ester/nano-Al₂O₃ matrix composites for pultrusion. *J Appl Polym Sci* 2012; 125: E429–E434.
 36. Akishin P, Barkanov E, Miazza N, et al. Curing kinetic models of resins for microwave assisted pultrusion. *Key Eng Mater* 201; 721: 92–96.
 37. Yousefi A, Lafleur PG and Gauvin R. Kinetic studies of thermoset cure reactions: a review. *Polym Compos* 1997; 18: 157–168.
 38. Kamal MR and Sourour S. Kinetics and thermal characterization of thermoset cure. *Polym Eng Sci* 1973; 13: 59–64.
 39. Han CD and Chin HB. Development of a mathematical model for the pultrusion of unsaturated polyester resin. *Polym Eng Sci* 1988; 28: 321–332.
 40. Ng H and Manas-Zloczower I. Kinetic studies of a composite thermoset cure reaction—application in pultrusion simulations. *Polym Eng Sci* 1989; 29: 302–307.
 41. Trivisano A, Maffezzoli A, Kenny JM, et al. Mathematical modeling of the pultrusion of epoxy based composites. *Adv Polym Technol* 1990; 10: 251–264.
 42. Valliappan M, Roux JA and Vaughan JG. Temperature and cure in pultruded composites using multi-step reaction model for resin. *J Reinf Plast Compos* 1996; 15: 295–320.
 43. Suratno BR, Ye L and Mai Y-W. Simulation of temperature and curing profiles in pultruded composite rods. *Compos Sci Technol* 1998; 58: 191–197.
 44. Roux JA, Vaughan JG, Shanku R, et al. Comparison of measurements and modeling for pultrusion of a fiberglass/epoxy I-beam. *J Reinf Plast Compos* 1998; 17: 1557–1578.
 45. Atarsia A and Boukhili R. Relationship between isothermal and dynamic cure of thermosets via the isoconversion representation. *Polym Eng Sci* 2000; 40: 607–620.
 46. Lin Liu X, Crouch IG and Lam YC. Simulation of heat transfer and cure in pultrusion with a general-purpose finite element package. *Compos Sci Technol* 2000; 60: 857–864.
 47. Li J, Joshi SC and Lam YC. Curing optimization for pultruded composite sections. *Compos Sci Technol* 2002; 62: 457–467.
 48. Pantaleão AV, DeAndrade CR and Zaparoli EL. The effect of anisotropic thermal conductivity on the pultrusion process simulation. *Int Commun Heat Mass Transf* 2002; 29: 611–621.
 49. Sarrionandia M, Mondragón I, Moschiar SM, et al. Heat transfer for pultrusion of a modified acrylic/glass reinforced composite. *Polym Compos* 2002; 23: 21–27.
 50. Calabrese L and Valenza A. Effect of CTBN rubber inclusions on the curing kinetic of DGEBA-DGEBF epoxy resin. *Eur Polym J* 2003; 39: 1355–1363.
 51. Samaras ZI and Partridge IK. Effects of styrene evaporation on the cure kinetics behaviour of a vinyl ester resin system suitable for composite pultrusion. *Polym Polym Compos* 2003; 11: 623–632.
 52. Liang G, Garg A, Chandrashekhara K, et al. Cure characterization of pultruded soy-based composites. *J Reinf Plast Compos* 2005; 24: 1509–1520.
 53. Bai Y, Vallée T and Keller T. Modeling of thermo-physical properties for FRP composites under elevated and high temperature. *Compos Sci Technol* 2007; 67: 3098–3109.
 54. Chen X, Xie H, Chen H, et al. Optimization for CFRP pultrusion process based on genetic algorithm-neural network. *Int J Mater Form* 2010; 3: 1391–1399.
 55. Zhou Z, Li A, Bai R, et al. Thermal analysis and gelation property of multifunctional epoxy resins used for pultruded composite ropes. *J Therm Anal Calorim* 2014; 115: 1601–1608.
 56. Zheng Y, Xiao J, Duan M, et al. Experimental study of partially-cured Z-pins reinforced foam core composites: K-Cor sandwich structures. *Chin J Aeronaut* 2014; 27: 153–159.
 57. Baran I, Akkerman R and Hattel JH. Material characterization of a polyester resin system for the pultrusion process. *Compos Part B Eng* 2014; 64: 194–201.
 58. Baran I, Tutum CC and Hattel JH. Probabilistic analysis of a thermosetting pultrusion process. *Sci Eng Compos Mater* 2016; 23: 67–76.

59. Tena I, Sarrionandia M, Torre J, et al. The effect of process parameters on ultraviolet cured out of die bent pultrusion process. *Compos Part B Eng* 2016; 89: 9–17.
60. Saenz-Dominguez I, Tena I, Sarrionandia M, et al. Effect of ultraviolet curing kinetics on the mechanical properties of out of die pultruded vinyl ester composites. *Compos Part A Appl Sci Manuf* 2018; 109: 280–289.
61. Wang Y-W, Zhu B, Yuan X-M, et al. Investigation of facile strategy for eliminating internal cracks of pultruded carbon fiber composites. *Mater Res Express* 2019; 6. Epub ahead of print. DOI: 10.1088/2053-1591/ab448e.
62. de Cassia Costa Dias R, Costa ML, de Sousa Santos L, et al. Kinetic parameter estimation and simulation of pultrusion process of an epoxy-glass fiber system. *Thermochim Acta* 2020; 690: 178636.
63. Correia JR, Bai Y and Keller T. A review of the fire behaviour of pultruded GFRP structural profiles for civil engineering applications. *Compos Struct* 2015; 127: 267–287.
64. Starr TF. *Pultrusion for engineers*. 2000. Epub ahead of print 2000. DOI: 10.1533/9781855738881.97.
65. Howard RD and Sayers DR. Development of new methacrylate resins for use in pultrusion. *Sampe Q* 1985; 16: 22–26.
66. Howard RD, Holland SJ and Sayers DR. Methacrylate resins in pultrusion: factors affecting pulling force. In: *Society of the plastics industry, reinforced plastics/composites institute, annual conference—proceedings*. Publ by SPI, Washington, DC, United States, pp. 2B.1–2B.7.
67. Stevens MG, Brandenburg J and Rodriguez B. Modified acrylic resin for low flame spread/low smoke applications with improved processing. In: *CAMX 2019. Composites and advanced materials expo. The Composites and Advanced Materials Expo (CAMX)*. Retrieved 15 November 2020, <https://www.scopus.com/inward/record.uri?eid=2-s2.0-85081104533&partnerID=40&md5=83a62d27732d9ecb4bfe19f28969a557> (2019).
68. Winkler M. Automotive under-the-hood applications in vinyl ester resin SMC/BMC. *SAE Tech Pap*. Epub ahead of print 1990. DOI: 10.4271/900633.
69. Kicko-Walczak E. Study on flame retardant unsaturated polyester resins—an overview of past and new developments. *Polimery/Polym* 1999; 44: 724–729.
70. Le Lay F and Gutierrez J. Improvement of the fire behaviour of composite materials for naval application. *Polym Degrad Stab* 1999; 64: 397–401.
71. Malik M, Choudhary V and Varma IK. Effect of non-halogen flame retardant additives on the properties of vinyl ester resins and their composites. *J Fire Sci* 2002; 20: 329–342.
72. Herzog D and Desai B. Modifying fire-resistant resins for predictable results. *JEC Compos Mag* 2004; 6: 36–38.
73. Weil ED and Levchik SV. Commercial flame retardancy of unsaturated polyester and vinyl resins: review. *J Fire Sci* 2004; 22: 293–303.
74. Kandola BK and Pornwannachai W. Enhancement of passive fire protection ability of inorganic fire retardants in vinyl ester resin using glass frit synergists. *J Fire Sci* 2010; 28: 357–381.
75. Mahesh KV, Murthy HNN, Swamy BEK, et al. Organomodified clay and its influence on thermal and fire behaviors of clay/fire retardant/poly vinyl ester composites. *Key Eng Mater* 2015; 659: 468–473.
76. de Freitas Rocha MA, Landesmann A, da Silva Ribeiro SP, et al. Enhancement of fire retardancy properties of glass fibre-reinforced polyesters composites. *Fire Mater* 2019; 43: 734–746.
77. Dai L, Wang X, Zhang J, et al. Effects of lubricants on the rheological and mechanical properties of wood flour/polypropylene composites. *J Appl Polym Sci* 2019; 136: 47667.
78. Capek I and Barton J. Photoinitiation. IV. The effect of Lewis acid on the vinyl monomer polymerization photo-initiated by aromatic hydrocarbons. *J Polym Sci Polym Chem Ed* 1979; 17: 937–942.
79. Rabagliati FM, Pérez MA, Soto MA, et al. Copolymerization of styrene by diphenylzinc-additive systems I. Copolymerization of styrene/p-tert-butylstyrene by Ph₂Zn–metallocene–MAO systems. *Eur Polym J* 2001; 37: 1001–1006.
80. Asandei AD and Moran IW. TiCp₂Cl-catalyzed living radical polymerization of styrene initiated by oxirane radical ring opening. *J Am Chem Soc* 2004; 126: 15932–15933.
81. Shih Y-F and Jeng R-J. Carbon black-containing interpenetrating polymer networks based on unsaturated polyester/epoxy II. Thermal degradation behavior and kinetic analysis. *Polym Degrad Stab* 2002; 77: 67–76.
82. Pereira CMC and Marques AT. Kinetic studies of flame-retardant unsaturated polyester nanocomposites: the effect of aluminum hydroxide (ATH), ammonium polyphosphate (APP) and nanoclays. In: *ICCM international conferences on composite materials*. International Committee on Composite Materials. Retrieved 15 November 2020, <https://www.scopus.com/inward/record.uri?eid=2-s2.0-85076868080&partnerID=40&md5=9c76ac2e9b26e5c247ef2ede7ecca47c> (2007).
83. Zhang C, Liu S and Huang J. Synthesis and curing kinetics of phosphorus-containing unsaturated polyester with reactive flame retardant. *Shiyou Huagong/Petrochemical Technol* 2009; 38: 515–520.
84. Ittner Mazali CA and Felisberti MI. Vinyl ester resin modified with silicone-based additives: III. Curing kinetics. *Eur Polym J* 2009; 45: 2222–2233.
85. Gao W, Cao J-Z and Li J-Z. Effect of ammonium pentaborate on curing of aqueous phenol formaldehyde resin. *Iran Polym J* 2010; 19: 255–264.
86. Jinxue J, Yonglin Y, Cheng L, et al. Effect of three boron flame retardants on thermal curing behavior of urea formaldehyde resin. *J Therm Anal Calorim* 2011; 105: 223–228.
87. Tan Y, Shao Z-B, Chen X-F, et al. Novel multifunctional organic-inorganic hybrid curing agent with high flame-retardant efficiency for epoxy resin. *ACS Appl Mater Interfaces* 2015; 7: 17919–17928.

88. Hamciuc C, Vlad-Bubulac T, Serbezeanu D, et al. Environmentally friendly fire-resistant epoxy resins based on a new oligophosphonate with high flame retardant efficiency. *RSC Adv* 2016; 6: 22764–22776.
89. Lu T, Chen T and Liang G. Synthesis, thermal properties, and flame retardance of the epoxy-silsesquioxane hybrid resins. *Polym Eng Sci* 2007; 47: 225–234.
90. International Organization for Standardization (ISO) 2016. Plastics – Differential scanning calorimetry (DSC) – Part 1: General principles, ISO 11357-1:2016 (Switzerland: International Organization for Standardization). Retrieved 15 November 2020, <https://www.iso.org/standard/70024.html>
91. Satoh, K., Fujiki, Y., Uchiyama, M., & Kamigaito, M. (2018). Vinyl ether/vinyl ester copolymerization by cationic and radical interconvertible simultaneous polymerization. In *Reversible Deactivation Radical Polymerization: Mechanisms and Synthetic Methodologies* (pp. 323–334). American Chemical Society.
92. Krauklis AE and Dreyer I. A simplistic preliminary assessment of Ginstling-Brounstein model for solid spherical particles in the context of a diffusion-controlled synthesis. *Open Chem* 2018; 16: 64–72.
93. Strømme KO. On the application of the Avrami-Erofeev equation in non-isothermal reaction kinetics. *Thermochim Acta* 1986; 97: 363–368.
94. Zhang K, Hong J, Cao G, et al. The kinetics of thermal dehydration of copper(II) acetate monohydrate in air. *Thermochim Acta* 2005; 437: 145–149.
95. Burnham AK. Application of the Sestak-Berggren equation to organic and inorganic materials of practical interest. *J Therm Anal Calorim* 2000; 60: 895–908.
96. Janowski B and Pieliowski K. A kinetic analysis of the thermo-oxidative degradation of PU/POSS nanohybrid elastomers. *Silicon* 2016; 8: 65–74.
97. Montserrat S and Málek J. A kinetic analysis of the curing reaction of an epoxy resin. *Thermochim Acta* 1993; 228: 47–60.
98. Criado JM, Málek J and Ortega A. Applicability of the master plots in kinetic analysis of non-isothermal data. *Thermochim Acta* 1989; 147: 377–385.
99. Málek J, Criado JM, Šesták J, et al. The boundary conditions for kinetic models. *Thermochim Acta* 1989; 153: 429–432.
100. Arasa M, Ramis X, Salla JM, et al. Kinetic study by FTIR and DSC on the cationic curing of a DGEBA/ γ -valerolactone mixture with ytterbium triflate as an initiator. *Thermochim Acta* 2008; 479: 37–44.
101. Pérez J, Sánchez G, García J, et al. Thermal and kinetic analysis of ortho-palladated complexes with pyridines. *Thermochim Acta* 2000; 362: 59–70.
102. Ramis X, Salla JM, Cadenato A, et al. Simulation of isothermal cure of a powder coating non-isothermal DSC experiments. *J Therm Anal Calorim* 2003; 72: 707–718.
103. Othman MBH, Khan A, Ahmad Z, et al. Kinetic investigation and lifetime prediction of Cs-NIPAM-MBA-based thermo-responsive hydrogels. *Carbohydr Polym* 2016; 136: 1182–1193.
104. Xie Q, Xie Y, Liu W, et al. Thermal decomposition behaviour and kinetics of a mixed solution: n-propyl nitrate and nitric acid solution. *J Therm Anal Calorim* 2020; 140: 1801–1810.
105. Ramis X, Salla JM, Mas C, et al. Kinetic study by FTIR, TMA, and DSC of the curing of a mixture of DGEBA resin and γ -butyrolactone catalyzed by ytterbium triflate. *J Appl Polym Sci* 2004; 92: 381–393.
106. Málek J. A computer program for kinetic analysis of non-isothermal thermoanalytical data. *Thermochim Acta* 1989; 138: 337–346.
107. Worzakowska M. Kinetics of the curing reaction of unsaturated polyester resins catalyzed with new initiators and a promoter. *J Appl Polym Sci* 2006; 102: 1870–1876.
108. Lionetto F, Timo A and Frigione M. Curing kinetics of epoxy-deep eutectic solvent mixtures. *Thermochim Acta* 2015; 612: 70–78.

Chapter 11

Shape memory behavior of unidirectional pultruded laminate

Korotkov Roman*, **Vedernikov Alexander***, Gusev Sergey, AlAjarmeh Omar, Akhatov Iskander, Safonov Alexander. Shape memory behavior of unidirectional pultruded laminate. *Composites Part A: Applied Science and Manufacturing* 2021. DOI: 10.1016/j.compositesa.2021.106609.

* – equal contribution

Contribution:

I participated in the pultrusion experiment and performed the analysis of results of thermomechanical and thermophysical properties measurements. I prepared most of the figures for this article and contributed to development of the original draft, final writing, and editing. I would like to thank all the authors for their valuable contributions to the development of this paper.



Shape memory behavior of unidirectional pultruded laminate

Roman Korotkov^{a,1}, Alexander Vedernikov^{a,1}, Sergey Gusev^a, Omar Alajarmeh^{b,c}, Iskander Akhatov^a, Alexander Safonov^{a,*}

^a Skolkovo Institute of Science and Technology, Center for Design, Manufacturing and Materials, Bolshoy Boulevard 30, bld. 1, Moscow 121205, Russia

^b University of Southern Queensland, Centre for Future Materials, West Street, Toowoomba, Queensland 4350, Australia

^c Tafila Technical University, Department of Civil Engineering, Tafila 66110, Jordan

ARTICLE INFO

Keywords:

Pultrusion
Smart materials
Shape memory polymer composites (SMPC)

ABSTRACT

This study investigates the shape memory behavior of epoxy-based pultruded flat laminates reinforced with unidirectional glass fibers. To evaluate the shape memory performance of the composite material, a series of tests by bending flat specimens to the shape programming angle has been conducted. The shape fixity and shape recovery ratios for the pultruded composite specimens with 90° fiber orientation constituted 78.4% and 92.6%, respectively, and 13.3% and 91.9%, for specimens with 0° fiber orientation. The results obtained in this study show that the shape fixity and recovery ratios of the composite material are only slightly dependent on the shape programming angle and the number of shape memory cycles (up to 10 cycles). The study also determined the shape fixity and shape recovery ratios for cured resin specimens, which constituted 99.7% and 98.2%, respectively. To lay the foundation for further studies on the simulation and optimization of the pultrusion process, the resin cure kinetics, the thermomechanical and thermophysical properties of the cured resin, and the mechanical characteristics of the pultruded shape memory polymer composite were analyzed.

1. Introduction

Shape memory polymers (SMPs) can recover their initial shape under the influence of external stimuli [1,2] such as temperature [3,4], light [5,6], moisture [7,8], pH [9,10], electricity [11], electromagnetic field, etc. [12]. The most common SMPs are thermally induced [13]. SMPs are widely used in aerospace [14], biomedicine [15], automotive industry [16], four-dimensional (4D) printing [17], temperature sensors, and electronic devices [18]. The literature provides many examples of polymer matrices featuring shape memory properties, such as polyurethanes [19], styrene-based polymers [20], polyolefines [21], polyvinylchloride [22], acrylic polymers [23], silicones [24], polylactic acid [25], and epoxy resins [26]. To improve the mechanical properties of materials [27], recovery stresses [28], and to expand the list of possible shape memory stimuli [29], various types of reinforcements can be used, such as carbon, basalt, and glass fibers, etc.

Several methods for producing shape memory polymer composites (SMPCs) and fiber reinforced polymers (FRPs) are described in the literature: press molding [30], resin transfer molding [31], vacuum

infusion [32,33], filament winding [34–37] and three-dimensional (3D) printing [38]. Surprisingly, no studies are available yet on the shape memory effect in pultruded composites, despite the fact that pultrusion is the most efficient manufacturing process for producing polymer composites. In pultrusion process, the continuous reinforcement pack is pulled through the impregnation bath, where it is impregnated with resin. The impregnated pack is then fed into a heated die where the resin is polymerized. After exiting the heated die, the cured composite profile is cut to the required lengths. Being a continuous automated process, pultrusion offers several benefits over traditional manufacturing processes, such as high production speed [39], low waste [40], high strength-to-weight ratio [41], superior corrosion resistance [42], and virtually indefinite length of produced profiles. A high volume fraction of reinforcement [43] ensures excellent mechanical properties for pultruded profiles. As pultruded profiles are easy to ship and install, it is possible to significantly reduce or even to eliminate expenses associated with traffic/railway closures, transportation, and assembly [44]. Due to the mentioned advantages pultruded profiles are widely applied as load-bearing structural members in civil and mechanical engineering [45].

* Corresponding author.

E-mail addresses: r.korotkov@skoltech.ru (R. Korotkov), aleksandr.vedernikov@skoltech.ru (A. Vedernikov), s.gusev@skoltech.ru (S. Gusev), omar.alajarmeh@usq.edu.au (O. Alajarmeh), i.akhatov@skoltech.ru (I. Akhatov), a.safonov@skoltech.ru (A. Safonov).

¹ These authors contributed equally to this work.

<https://doi.org/10.1016/j.compositesa.2021.106609>

Received 18 March 2021; Received in revised form 5 July 2021; Accepted 15 August 2021

Available online 20 August 2021

1359-835X/© 2021 Elsevier Ltd. All rights reserved.

Various types of profiles are utilized: rods, boxes, pipes, 'I', 'T', 'L', 'C', and 'U' sections [46,47]. Moreover, pultrusion also allows manufacturing of curved profiles [48]. Considering the above, it is believed that pultrusion can be successfully used to produce new types of shape memory structural components with unique combinations of geometries and mechanical properties [39], impossible to produce with other processes due to manufacturing limitations.

This study investigated shape memory effects in flat specimens of epoxy-based pultruded composite laminates reinforced with unidirectional glass fibers. Laminates with a cross section of 150×3.5 mm were manufactured using a Pultrex Px500-6T pultrusion machine (Pultrex, UK). To evaluate the shape memory performance of polymer composites, a series of tests were conducted by bending flat specimens with 0° and 90° fiber orientations to the shape programming angle. Furthermore, the relationship between the shape fixing angle and the shape programming angle of the composite specimens was studied, as well as the influence of shape memory cycling on the shape memory performance of composite specimens during 10 shape memory cycles. The shape memory performance of cured epoxy resin was also analyzed. To lay the foundation for further numerical simulations and optimization of the pultrusion process [49,50], the thermomechanical and thermophysical characteristics of uncured epoxy resin and epoxy-based SMPs were tested and analyzed. The mechanical characteristics of the cured resin and pultruded composite specimens were also determined.

2. Materials and methods

2.1. Pultrusion manufacturing

All pultruded profiles used in this study were manufactured using a Pultrex Px500-6T pultrusion machine (Fig. 1b) at the Laboratory of Composite Materials and Structures of the Center for Design, Manufacturing and Materials (Skolkovo Institute of Science and Technology, Moscow, Russia). To produce flat laminate profile with a cross section of 150×3.5 mm (Fig. 1c), 88 threads of unidirectional E-glass rovings PS 2100 (Owens Corning Composite Materials, USA) with a linear density of 9600 TEX (9600 g/1000 m), an epoxy composition based on bisphenol A diglycidyl ether (NPEL-128, Nan Ya Plastics Corporation, Taiwan) with methyltetrahydrophthalic anhydride isomers as the hardener (i-MTHPA, Chimex Ltd., Russia) and 2,4,6-tris(dimethylaminomethyl)phenol (Alkophen, Epital, Russia) as the catalyst were used. To increase its ultimate strain, the resin composition was modified with aliphatic epoxy resin diethylene glycol diglycidyl ether (DEG-1, Chimex Ltd., Russia). Table 1 shows the composition of the shape memory epoxy matrix. The components were weighed with CKE-150-4560 RS floor scales (Scale Enterprise, Russia) and AND EK-6000i laboratory scales (A&D, USA).

A 600-mm-long steel die block with two heating zones—one at the entrance and another closer to the die exit (Fig. 1a) – was used in the pultrusion manufacturing line. The temperature of the heating zones was set as follows: 175–185 °C in the first zone and 195–205 °C in the

Table 1
Components of the resin mixture.

Component	Weight [kg]
Epoxy resin (NPEL-128, Nan Ya Plastics Corporation, Taiwan)	5.60
Hardener (i-MTHPA, Chimex Ltd., Russia)	5.88
Catalyst (Alkophen, Epital, Russia)	0.074
Aliphatic epoxy resin (DEG-1, Chimex Ltd., Russia)	1.40

second zone. The pulling speed was 200 mm/min. After the process reached a steady state, a 5-m-long section of the profile was produced for mechanical testing and shape memory experiments.

2.2. Shape memory tests

The shape memory tests were based on bending the specimens of cured epoxy resin and pultruded composite specimens in a specially designed test fixture. Flat rectangular cured resin specimens of $80 \times 10 \times 4$ mm produced by polymerization of epoxy resin in a silicone mold were used for a comparison with the pultruded composite specimens. The specimens were polymerized in an XF050 laboratory vacuum drying oven (France Etuves, France) for 2 h at 120 °C, followed by post-curing for 10 h at 150 °C. The test fixture (Fig. 2b) represents the structure of two pultruded L-shaped profiles of $75 \times 75 \times 6$ mm made in our previous study [51]. Fig. 2a shows the cross section of the L-shaped profiles.

The test specimens of the pultruded composite were produced by milling the manufactured laminates to a thickness of 1 mm using a Shtalmark M1-912 M/2 CNC milling machine (Rusintermash Ltd., Russia). Then, the 1-mm-thick laminate was cut into rectangular test specimens of 11×150 mm. Overall, 15 specimens with 0° fiber orientation and 15 specimens with 90° fiber orientation were fabricated. Tests were conducted by bending the composite specimens in a circular arc using a constant curvature test fixture made of fluoroplastic (Fig. 2c). Five test fixtures of different depth, w , were manufactured to obtain different shape programming angles (see Fig. 2d). The shape programming angle (θ_p) of a fixture is the angle between tangents passing through the two endpoints of the arc with a length of 150 mm. Table 2 shows the values of the test fixture depth and the corresponding values of the shape programming angle.

Fig. 3 shows a flowchart for the shape memory testing of the cured resin and pultruded composite specimens. Specimens are placed on the female part of the test fixture and held in an oven at a temperature of 150 °C. Whereas the male part of the test fixture is also held in the oven at a temperature of 150 °C. Cured resin (Fig. 4a) and pultruded composite (Fig. 4d) specimens heated to 150 °C are then deformed with the heated male part of the test fixture inside the oven to the shape programming angle (θ_p). Then, a test fixture with a specimen pressed between male and female parts is fastened together and removed from the oven to cool to 40 °C under ambient conditions. An DT-8861 pyrometer (Cem, Shenzhen Everbest Machinery Industry Co., Ltd., China) was used to monitor specimen temperature. After cooling, the test fixtures are opened, and specimens are retrieved to measure the bending angle

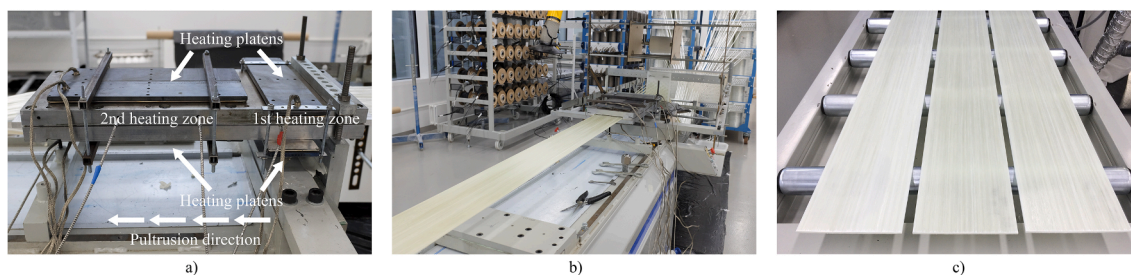


Fig. 1. Pultrusion of the flat laminate profile based on epoxy matrix reinforced with unidirectional glass fiber rovings: (a) Die block during the pultrusion; (b) pultrusion of unidirectional profile; and (c) pultruded flat unidirectional profiles. (For interpretation of the references to colour in this figure legend, the reader is referred to the web version of this article.)

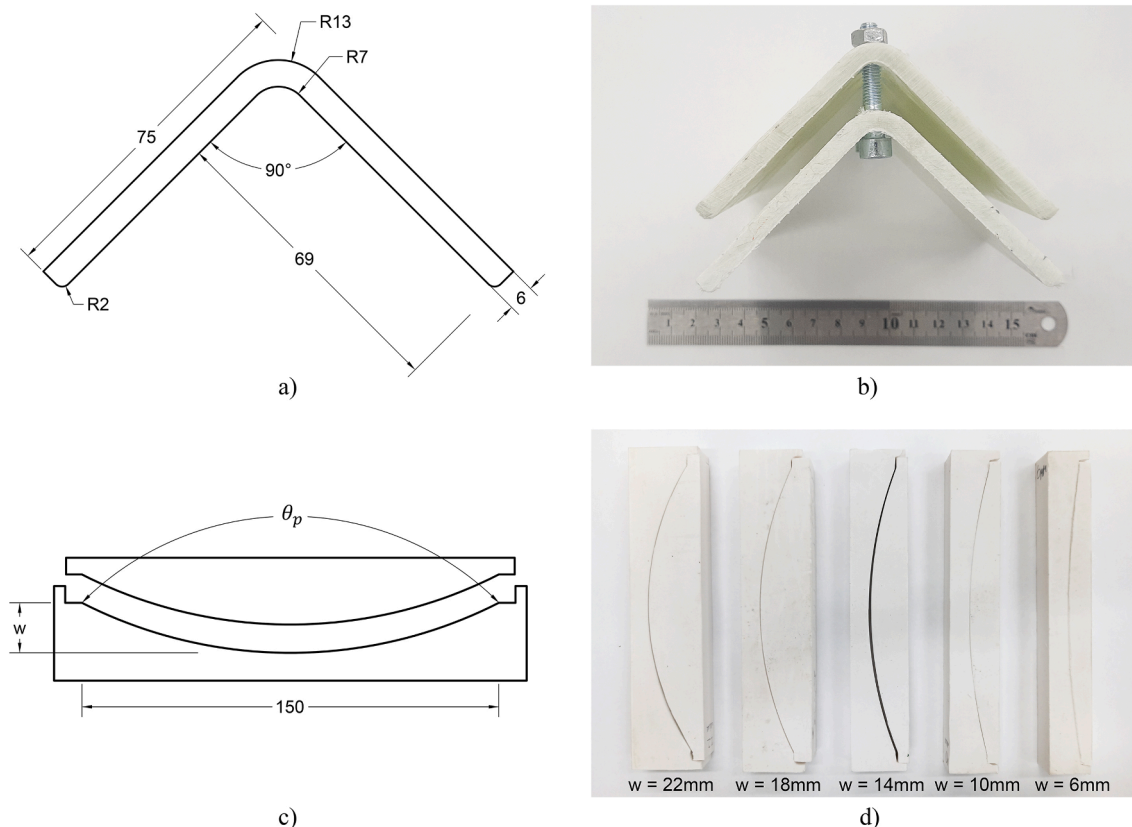


Fig. 2. Test fixtures for shape memory testing of cured resin and composite specimens: (a) Sketch of L-shaped profiles used as component parts of test fixture for shape memory testing of cured resin specimens; (b) test fixture for shape memory testing of cured resin specimens; (c) sketch of test fixture for shape memory testing of pultruded composite specimens; and (d) test fixture for shape memory testing of pultruded composite specimens. (For interpretation of the references to colour in this figure legend, the reader is referred to the web version of this article.)

Table 2
Shape programming angles for shape memory testing of composite specimens in manufactured test fixture.

Fixture depth, w [mm]	6	10	14	18	22
Shape programming angle, θ_p [°]	161.8	150.0	138.7	128.0	118.1

representing the shape fixing angle (θ_f). Angle measurements were made with an ADA AngleMeter 30 A00494 (ADA Instruments, Hong Kong) with an accuracy of $\pm 0.3^\circ$. The cured resin and pultruded

composite specimens after shape fixing are shown in Fig. 4b and e, respectively.

For shape recovery, the cured resin and pultruded composite specimens were held in an oven at 150 °C for 5 min. The specimens bending angle representing the shape recovery angle (θ_r) was measured after cooling to a temperature of 40 °C. Specimens of cured resin and pultruded composite after shape recovery are shown in Fig. 4c and f, respectively.

The shape fixity (R_f) and shape recovery (R_r) ratios were determined using the Eqs. (1) and (2) [52,53] as follows:

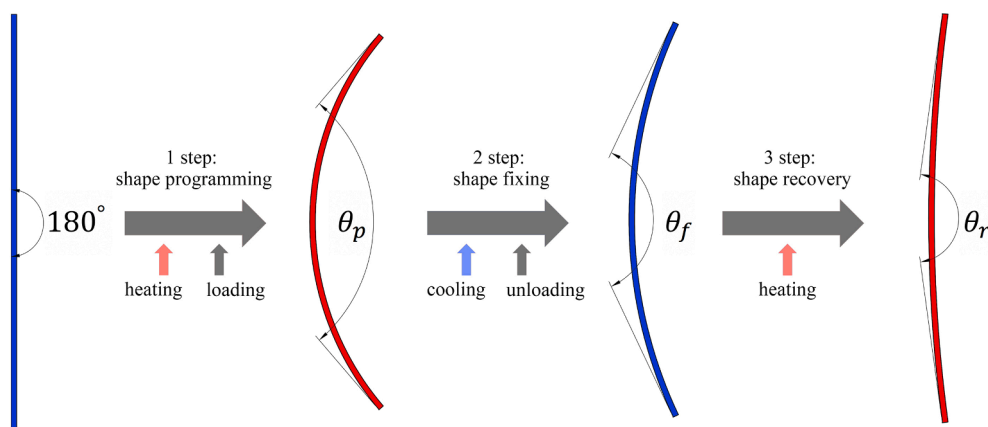


Fig. 3. Flowchart of shape memory testing of cured resin and pultruded composite specimens. (For interpretation of the references to colour in this figure legend, the reader is referred to the web version of this article.)

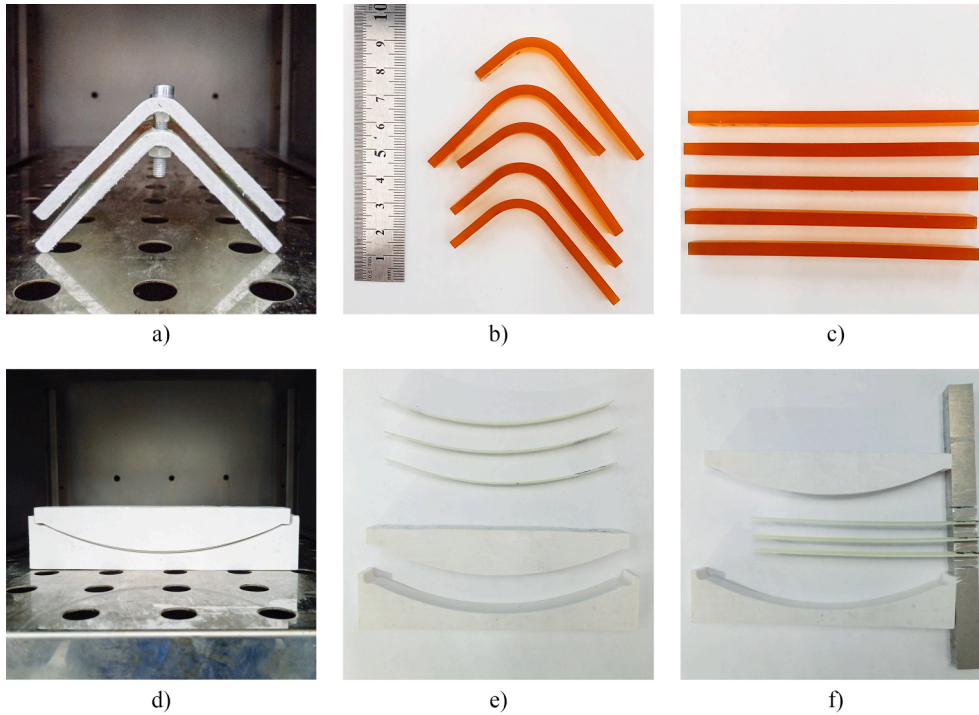


Fig. 4. Shape memory testing of cured resin and pultruded composite specimens: (a) Deformed specimen of cured resin in the test fixture after heating; (b) cured resin specimens after shape fixing; (c) cured resin specimens after shape recovery; (d) deformed specimen of pultruded composite in the test fixture after heating; (e) geometry of pultruded composite specimen after shape fixing as compared to geometry of the test fixture; and (f) pultruded composite specimen after shape recovery. (For interpretation of the references to colour in this figure legend, the reader is referred to the web version of this article.)

$$R_f = \frac{\theta_0 - \theta_f}{\theta_0 - \theta_p} \cdot 100\% \quad (1)$$

$$R_r = \frac{\theta_r - \theta_f}{\theta_0 - \theta_f} \cdot 100\% \quad (2)$$

where θ_f is the shape fixing angle, θ_r is the shape recovery angle, θ_p is the shape programming angle, and $\theta_0 = 180^\circ$ is the initial angle value.

To study the effect of shape memory cycling on the shape memory performance of pultruded composites, 10 heating–cooling cycles using a similar procedure, including the determination of the shape fixity and shape recovery ratios after each cycle, were performed.

2.3. Analysis of thermomechanical and thermophysical properties and cure kinetics

Test specimens for thermomechanical and thermophysical analyses were cut from plates of cured epoxy resin. The plates were produced by curing the resin in the oven using the following procedure: 2 h at 120 °C followed by 10 h at 150 °C. The plates were then cut into test specimens using a CNC milling machine.

The glass transition temperature and temperature dependencies of the storage and loss moduli were determined following the procedure specified in ISO 6721-1:2011 [54], using a Q800 dynamic mechanical analyzer (TA Instruments Inc., USA). Measurements were performed in three-point bending mode within the temperature range of 30–200 °C, at the heating rate of 5 °C/min, and oscillation frequency of 1 Hz and the amplitude of 60 μm .

The cure kinetics and thermal effects of epoxy resin polymerization were analyzed using the procedure specified in ISO 11357-5:1999 [55], using a DSC Q20 differential scanning calorimeter (TA Instruments, USA) in dynamic mode. Measurements were performed in nitrogen atmosphere, within the temperature range of –70 °C to 250 °C at the heating rates of 5, 7.5, and 10 °C/min.

The heat capacity of the cured resin was determined in accordance with the ISO 11357-4:2005 [56] procedure, using a DSC 204 differential scanning calorimeter (NETZSCH-Gerätebau GmbH, Germany). Measurements were performed within the temperature ranges of 0–90 °C

and 130–200 °C, at the heating rate of 10 °C/min.

The coefficient of thermal expansion (CTE) was determined with a TMA 402 thermomechanical analyzer (NETZSCH-Gerätebau GmbH, Germany), following the procedure specified in ISO 11359-2:1999 [57]. Measurements were performed within the temperature range of 0–200 °C at the heating rate of 2 °C/min.

The density of the cured resin was measured by hydrostatic weighing using an HTR-220CE laboratory scale (Shinko Vibra, Japan), with two cured resin samples of 25 × 25 × 2 mm.

For thermal conductivity measurements of the cured resin an LFA 457 MicroFlash laser flash apparatus (NETZSCH-Gerätebau GmbH, Germany) was used, following the procedure defined in ASTM E1461-13 [58]. Measurements were performed in the temperature range of 25–200 °C.

2.4. Mechanical tests

Cured resin specimens for mechanical testing were fabricated using silicone molds. The specimens were polymerized in an oven, using the following curing procedure: 2 h at 120 °C followed by 10 h at 150 °C. Tensile properties were determined using the ISO 527-2:2012 [59] procedure and flexural properties of the specimens were determined following the ASTM D790-17 [60] procedure.

Composite specimens for mechanical testing were cut from pultruded laminate using a CNC milling machine and then postcured for 10 h at 150 °C. Then, the specimens were tested as follows: tensile testing in accordance with the ISO 527-5:2009 procedure [61], compression testing in accordance with ASTM D6641 [62], flexural testing in accordance with ASTM D790-17 [60], and interlaminar shear strength tests in accordance with ASTM D2344 [63].

All mechanical tests were conducted at the Mechanical Testing Laboratory of the Center for Design, Manufacturing and Materials (Skolkovo Institute of Science and Technology, Moscow, Russia). The Instron 8801 electromechanical testing machine (Instron, USA) was used to conduct tensile testing in a 0° fiber orientation. The strains were measured using an Epsilon 3560-BIA-025M-010-ST biaxial extensometer (Epsilon Technology Corp, USA). All other mechanical tests were performed using an Instron 5969 testing machine (Instron, USA). Strain

measurements during tensile tests in 90° fiber orientation and compression tests were conducted using the method of Digital Image Correlation (DIC).

Statistical analysis of mechanical and shape memory test results was conducted in accordance with ISO 2602-1980 procedure [64] for two-sided confidence intervals with a confidence level of 0.95.

3. Results and discussion

3.1. Shape memory testing results

Table 3 shows the shape memory testing results of the cured resin specimens. Shape fixity and shape recovery ratios for cured resin specimens constituted 99.7% and 98.2% respectively, demonstrating the good shape memory performance of the cured epoxy resin [29,65].

Table 4 shows results of shape memory testing of pultruded composite specimens with 0° and 90° fiber orientations. The mean values of shape fixity and shape recovery ratios for pultruded composite specimens with 0° fiber orientation constituted 13.3% and 91.9%, respectively. The tested specimens recovered their shape to the average shape recovery angle of $179.6 \pm 0.2^\circ$. In contrast, the mean values of the shape fixity and shape recovery ratios for pultruded composite specimens with 90° fiber orientation were 78.4% and 92.6%, respectively. The average shape recovery angle for given specimens of pultruded composite constituted $178.0 \pm 0.4^\circ$. It was found that the shape fixity and shape recovery ratios for pultruded composite specimens with 0° and 90° fiber orientation depend little on the shape programming angle. Specimens with 90° fiber orientation demonstrated a 21.4% reduction in shape fixity ratio, whereas those with 0° fiber orientation showed an 86.7% reduction in shape fixity ratio as compared to the cured resin specimens. It is noticeable that the glass fiber inclusion (Table 4) affects the shape fixity and shape recovery ratios, as compared to the neat resin (Table 3). One can see a reduction in shape fixity ratio in pultruded composite specimens with 0° and 90° fiber orientation as compared to neat resin [66], as the use of glass fibers featuring high elastic modulus results in the considerable increase in bending stiffness of the composite specimens. This, in turn, leads to a significant spring-back displacement observed at the unloading step of the shape programming process [67,68]. Bending stiffness of unidirectional pultruded laminate in 0° orientation is considerably higher, compared to that in 90° (see Table 10), resulting in lower shape fixity ratio in case of 0° fiber orientation, than in 90° fiber orientation.

The relationship between the shape fixing (θ_f) and shape programming (θ_p) angles for composite specimens with 0° and 90° fiber orientations (Fig. 5) can be described by the linear law (Eq. (3)):

$$\theta_f = \theta_{int} + k\theta_p \quad (3)$$

where θ_{int} and k are constants of the model. The values of the constants (Eq. (3)) obtained by the least-squares method are given in Table 5. These linear relationships allow researchers to predict the shape fixing angle of a composite during shape programming. Fig. 5 shows the effect of fiber orientation on the difference between the shape programming angle and the shape fixing angle, based on the findings in Table 4. The differences between the shape programming angle and the shape fixing angle in the pultruded composite specimens with 0° and 90° fiber orientations can be attributed to the high values of bending stiffness

Table 3
Shape memory properties of cured epoxy resin specimens.

Shape programming angle, θ_p [°]	Shape fixing angle, θ_f [°]	Shape recovery angle, θ_r [°]	Shape fixity ratio, R_f [%]	Shape recovery ratio, R_r [%]
90	89.5 ± 2.7	178.4 ± 0.9	99.7 ± 3.0	98.2 ± 1.1

resulting in significant spring-back displacements occurring during the unloading step of the shape programming process [67,68]. Due to a higher bending stiffness (Table 10), specimens with 0° fiber orientation display less pronounced shape fixity properties as compared to specimens with 90° fiber orientation. This can explain the lower values of k^0 coefficient compared to k^{90} and, therefore, a gentler slope of the SMPC 0° curve than that of SMPC 90° curve (Fig. 5).

Table 6 shows the results of shape memory cycling for composite specimens with 0° and 90° fiber orientations for a shape programming angle of $\theta_p = 128.0^\circ$. The average shape fixity and shape recovery ratios obtained during shape memory cycling constitute 12.4% and 91.1%, respectively, for fiber orientations of 0°; and 75.5% and 96.3%, respectively, for fiber orientations of 90°. The results show almost no changes in the shape recovery ratio for composite specimens with 0° and 90° fiber orientations within 10 shape memory cycles. The shape fixity ratio for pultruded composite specimens with a 90° fiber orientation remains virtually unchanged. However, for composite specimen with 0° fiber orientation, an increase in the shape fixity ratio from 10% to 14% can be observed.

3.2. Results of thermomechanical, thermophysical, and cure kinetics analysis

3.2.1. Elastic modulus

According to DMA data (Fig. 6a), the glass transition temperature of the cured resin was determined by the peak of $\tan(\delta)$ constituted $T_g = 102.7^\circ\text{C}$. The onset of the critical decrease in storage modulus was observed at the temperature of $T_{onset} = 89.3^\circ\text{C}$. To describe the temperature dependence of the storage modulus, the Cure Hardening Instantaneous Linear Elastic (CHILE) model [69,70] in its modified form (Eq. (4)) was adopted:

$$E_r = \begin{cases} E_0, T^* \leq T_{C1} \\ E_0 + \frac{T^* - T_{C1}}{T_{C2} - T_{C1}}(E_1 - E_0), T_{C1} < T^* < T_{C2} \\ E_1 + \frac{T^* - T_{C2}}{T_{C3} - T_{C2}}(E_2 - E_1), T_{C2} < T^* < T_{C3} \\ E_2 + \frac{T^* - T_{C3}}{T_{C4} - T_{C3}}(E_3 - E_2), T_{C3} < T^* < T_{C4} \\ E_3 + \frac{T^* - T_{C4}}{T_{C5} - T_{C4}}(E_4 - E_3), T_{C4} < T^* < T_{C5} \end{cases} \quad (4)$$

where $T^* = T_g - T$ is the difference between the instantaneous glass transition temperature (T_g) and the instantaneous temperature (T) of the resin in degrees Celsius; T_{C1} , T_{C2} , T_{C3} , T_{C4} , and T_{C5} are the critical temperatures in degrees Celsius; and E_0 , E_1 , E_2 , E_3 , and E_4 are the corresponding elastic moduli. Model constants were determined using the least-squares method based on the obtained experimental data. The obtained values of the model constants are given in Table 7.

3.2.2. Cure kinetics

The expanded Prout–Tompkins equation [71,72] as given by Eq. (5) and Eq. (6) was used to describe the cure kinetics of the resin (Fig. 6b):

$$\alpha(t) = \frac{H(t)}{H_{tot}} \quad (5)$$

$$\frac{d\alpha}{dt} = A e^{-\frac{E_a}{R(T+273.15)}} (1 - \alpha)^n \alpha^m \quad (6)$$

where $\alpha(t)$ is the instantaneous cure degree of epoxy resin, $H(t)$ is the experimental instantaneous value of heat released during the curing of epoxy resin, H_{tot} is the experimental total heat released during polymerization, $\frac{d\alpha}{dt}$ is the cure rate of epoxy resin, A is a preexponential factor, E_a is the activation energy, R is the universal gas constant, T is the

Table 4
Shape memory performance of composite specimens with 0° and 90° fiber orientation for different values of shape programming angle.

Measured parameter	Fiber orientation angle [°]	Test fixture depth, w [mm]				
		6	10	14	18	22
Shape programming angle, θ_p [°]	0/90	161.8	150.0	138.7	128.0	118.1
Shape fixing angle, θ_f [°]	0	177.1 ± 1.7	175.9 ± 1.5	174.5 ± 0.8	174.4 ± 0.7	172.1 ± 1.8
	90	165.6 ± 3.6	156.2 ± 1.2	148.0 ± 2.5	140.0 ± 2.1	130.4 ± 4.7
Shape recovery angle, θ_r [°]	0	179.9 ± 0.2	179.5 ± 0.1	179.6 ± 0.4	179.7 ± 0.2	179.1 ± 0.3
	90	178.4 ± 2.0	177.5 ± 1.3	178.3 ± 0.8	178.0 ± 1.6	177.5 ± 0.8
Shape fixity ratio, R_f [%]	0	16.1 ± 9.6	13.5 ± 5.1	13.2 ± 2.0	10.7 ± 1.3	12.7 ± 3.0
	90	78.3 ± 7.4	79.2 ± 4.1	77.4 ± 6.0	76.9 ± 4.1	80.1 ± 7.6
Shape recovery ratio, R_r [%]	0	96.0 ± 7.0	88.1 ± 7.0	92.5 ± 7.6	94.7 ± 3.2	88.0 ± 5.3
	90	88.6 ± 14.3	89.7 ± 5.0	94.8 ± 2.4	95.1 ± 4.0	95.0 ± 1.8

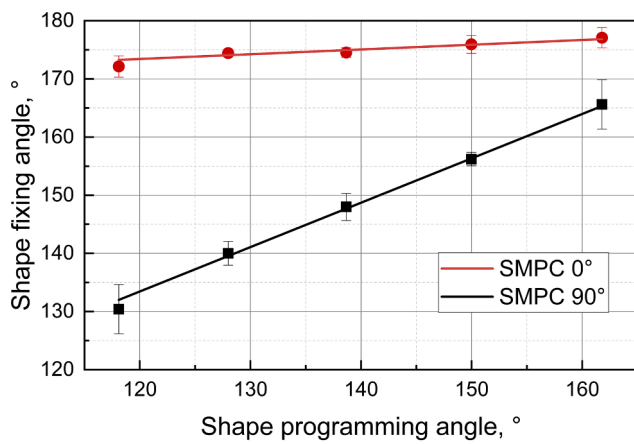


Fig. 5. Relationships between the average shape fixing angle and the shape programming angle for pultruded composite specimens with 0° and 90° fiber orientations. Markers (squares, circles) represent experimental data, and solid lines indicate approximation. (For interpretation of the references to colour in this figure legend, the reader is referred to the web version of this article.)

Table 5
Estimated constants used in the model (Eq. (3)).

θ_{int}^0 [°]	θ_{int}^{90} [°]	k^0 [-]	k^{90} [-]
163.6	41.5	0.082	0.767

instantaneous temperature of the resin in degrees Celsius, n is the order of the reaction, and m is the order of autocatalysis. Constants in Eq. (6) obtained by the least-squares method are given in Table 8.

3.2.3. Heat capacity

The heat capacity of the cured resin (C_p) is measured at two segments (Fig. 6c) and can be described by a piecewise linear function (Eq. (7)). At the first segment (0–90 °C), the resin is in the glassy state, and at the

Table 6
Shape memory cycling of composite specimens with 0° and 90° fiber orientations.

Measured parameter	Fiber orientation angle [°]	Cycle No									
		1	2	3	4	5	6	7	8	9	10
Shape programming angle, θ_p [°]	0/90	128									
Shape fixing angle, θ_f [°]	0	174.8	175.0	174.7	173.6	172.8	173.0	172.9	172.8	173.0	172.7
	90	141.3	142.1	142.8	139.4	139.4	140.2	141.1	140.1	140.5	140.3
Shape recovery angle, θ_r [°]	0	179.8	179.6	179.4	179.2	179.2	179.3	179.4	179.5	179.2	179.6
	90	178.2	179.8	179.4	179.4	177.7	178.1	178.2	178.1	178.2	178.3
Shape fixity ratio, R_f [%]	0	10.0	9.6	10.2	12.3	13.8	13.5	13.7	13.8	13.5	14.0
	90	74.4	72.9	71.5	78.1	78.1	76.5	74.8	76.7	76.0	76.3
Shape recovery ratio, R_r [%]	0	96.2	92.0	88.7	87.5	88.9	90.0	91.5	93.1	88.6	94.5
	90	95.3	99.5	98.4	98.5	94.3	95.2	95.4	95.2	95.4	95.7

second segment (130–200 °C), the resin is in a rubbery state. A phase transition can be observed in the interval of 90–130 °C, therefore, no heat capacity measurements are taken in this interval.

$$C_p = \begin{cases} 1103 + 4.47T, & 0^\circ\text{C} < T < 90^\circ\text{C} \\ 1335 + 1.53T, & 130^\circ\text{C} < T < 200^\circ\text{C} \end{cases} \quad (7)$$

3.2.4. Coefficient of thermal expansion (CTE)

The temperature dependence of the CTE of the cured resin is shown in Fig. 6d. This can be described by Eq. (8) as follows:

$$CTE = \begin{cases} a + bT, & 20^\circ\text{C} < T < 70^\circ\text{C} \\ A_1 + \frac{A_1 - A_2}{1 + e^{-\frac{T-T_0}{dT}}}, & 70^\circ\text{C} < T < 200^\circ\text{C} \end{cases} \quad (8)$$

where $a, b, A_1, A_2, dT,$ and T_0 are the constants of the model, and T is the instantaneous temperature of the cured resin in degrees Celsius. The values of the model constants in Eq. (8) obtained by the least-squares method are given in Table 9.

3.2.5. Thermal conductivity

The thermal conductivity of the cured resin (λ) was determined based on density data (ρ), thermal diffusivity (D), and the heat capacity of the cured resin (C_p), using Eq. (9) [58]:

$$\lambda = DC_p\rho \quad (9)$$

The measured density of the cured resin at the ambient temperature constituted 1.21 g/cm³. It was found that the thermal conductivity of the cured resin remained unchanged with increasing temperature, with an average value of 0.200 ± 0.006 W/(m·K).

3.3. Mechanical testing results

Table 10 shows the mechanical properties of the tested specimens of cured resin and pultruded composite, as compared to previously published data on SMPs and SMPCs produced by other manufacturing processes, available in the literature. The results obtained in this work are shown in bold. It can be seen that pultruded composites demonstrate

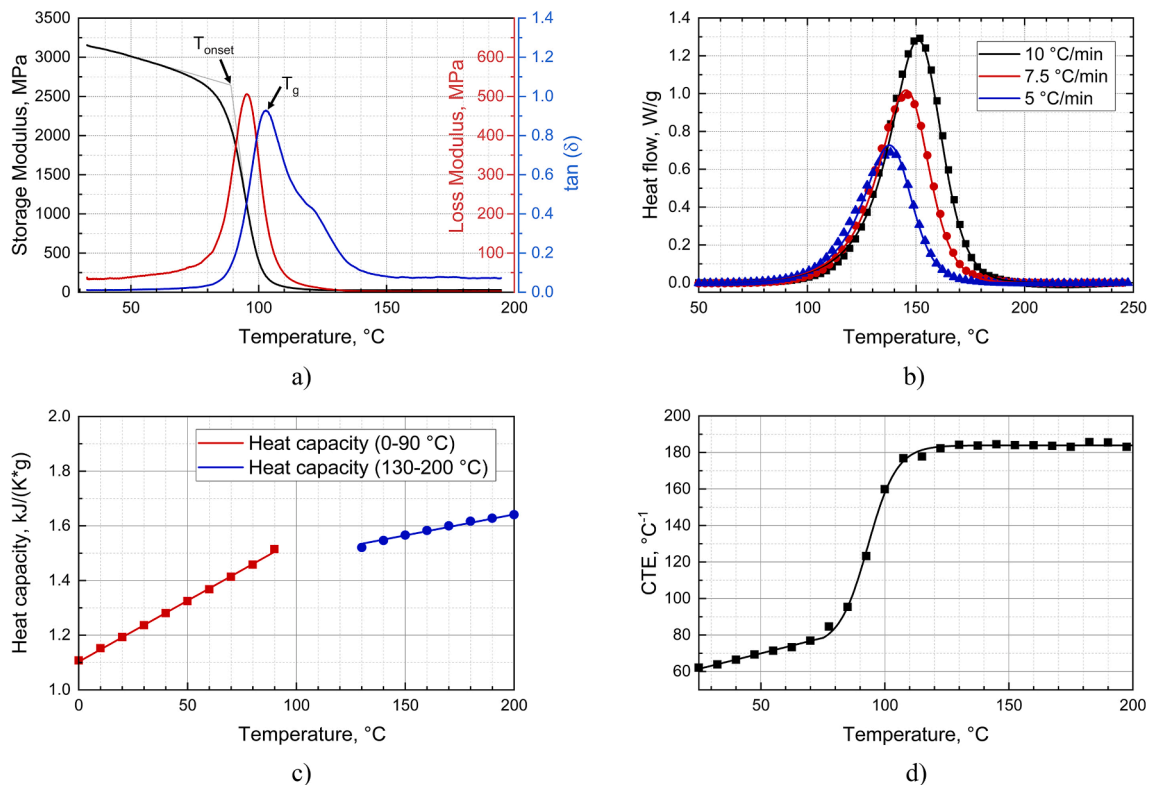


Fig. 6. Results of thermomechanical, thermophysical, and cure kinetics analysis: (a) DMA measurements for cured resin. Changes in storage modulus, loss modulus, and $\tan(\delta)$ obtained at heating rate of 5 °C/min; (b) polymerization enthalpy of uncured resin, and numerical simulation by expanded Prout–Tompkins equation. Markers (squares, circles, upward triangles) represent experimental data, solid lines – approximations; (c) temperature dependence of heat capacity of cured resin. Markers (circles, squares) represent experimental data, solid lines – approximation; and (d) changes in coefficient of thermal expansion (CTE) with temperature. Markers represent experimental data, solid line – approximation. (For interpretation of the references to colour in this figure legend, the reader is referred to the web version of this article.)

Table 7
Estimated constants used in modified CHILE model (Eq. (4)).

T_{c1} [°C]	T_{c2} [°C]	T_{c3} [°C]	T_{c4} [°C]	T_{c5} [°C]	E_0 [MPa]	E_1 [MPa]	E_2 [MPa]	E_3 [MPa]	E_4 [MPa]
-35.9	1.1	15.0	26.0	70.2	29	101	2285	2734	3168

Table 8
Kinetic constants for expanded Prout–Tompkins equation (Eq. (6)).

H_{tot} [J/g]	A [s ⁻¹]	E_a [kJ/mol]	n [-]	m [-]
266	$10^{6.56}$	68	1.05	0.46

Table 9
Constants used in the model of temperature dependence of CTE (Eq. (8)).

a [°C ⁻¹]	b [°C ⁻²]	A_1 [°C ⁻¹]	A_2 [°C ⁻¹]	dT [°C]	T_0 [°C]
$5.294 \cdot 10^{-5}$	$3.405 \cdot 10^{-7}$	$7.370 \cdot 10^{-5}$	$1.839 \cdot 10^{-4}$	5.814	93.138

better performance as compared to composites produced by other processes. This can be explained by a higher volume fraction of reinforcement obtainable in pultruded profiles, suggesting the possibility of their efficient use in structural applications.

The ability of pultrusion to produce composite profiles of virtually unlimited length, with excellent mechanical and shape memory performance, makes it possible to expand the existing applications of SMPs in civil engineering (beam [82], rods [82], plates [82], structural absorbers for vibration control [83], damping elements in the area of

earthquake engineering [84], self-healing structural components [85], elements of active building facades with self-regulating sun protectors [86], kinetic building envelope [84] and actuating systems [85]). To illustrate, the application of shape memory concept in construction of bridges [87,88] and transmission towers [89], makes it possible to implement high-performance snap-fit joints [87–89], able to lock under heating, thus obviating the need for bolted joints. Pultrusion may also expand the applications of SMPs in aerospace engineering, for example in morphing aircrafts [90], deployable structures [91], hinges [92], antennas [93], solar panels [30] and solar sails [94].

To the best of our knowledge, this work is the first study on the shape memory effect in pultruded composites. However, it should be noted that further studies are necessary to better understand the shape memory effect in pultruded composites and to allow for the numerical simulation and optimization necessary to promote the application of pultruded SMPs in various structures. Moreover, authors are planning to perform further theoretical and experimental studies to better understand the influence of fiber orientation on the performance of pultruded SMPs structural elements [95,96].

4. Conclusions

This study investigates the shape memory behavior of epoxy-based

Table 10

Results of mechanical tests of cured resin and pultruded composite specimens, as compared to composites produced by other manufacturing processes. Results obtained in this work are shown in bold.

Material/Manufacturing process	Tension		Compression		Flexure			Interlaminar shear strength [MPa]
	Strength [MPa]	Modulus [GPa]	Strength [MPa]	Modulus [GPa]	Strength [MPa]	Modulus [GPa]	Ultimate strain [%]	
Epoxy	55.4 ± 7.9	2.89 ± 0.21	–	–	134.93 ± 4.28	3.20 ± 0.18	>5	–
GF + epoxy/Pultrusion – 0°	1140 ± 149	56.7 ± 1.4	799 ± 66	57.3 ± 7.2	1470 ± 102	52.6 ± 3.9	2.87 ± 0.06	72.0 ± 0.4
GF + epoxy/Pultrusion – 90°	40.9 ± 6.7	22.1 ± 1.0	147 ± 4	18.2 ± 1.1	96.8 ± 4.8	19.9 ± 0.9	0.518 ± 0.012	12.3 ± 0.6
CF + epoxy/Vacuum bagging [30]	547	52	120	–	–	–	–	–
CF + epoxy/Filament winding 0° [34]	–	–	–	–	833	48.1	–	–
CF fabric + styrene-based/Method is not specified [73]	145	–	–	–	–	–	–	–
CF fabric + epoxy/VARTM – (30°/60°, +45°/–45°, 0°/90°) [74]	–	–	–	–	238/203/242	13.99/8.98/28.88	–	–
Short GF + epoxy/Compression moulding [75]	–	–	–	–	52	–	–	–
CF + polylactic acid/3D printing [38]	–	–	–	–	211	7.41	–	–
CF + epoxy/Filament winding 0 [76]	134	2.175	–	–	–	–	–	–
Bio-based polyester [77]	8.3	–	–	–	–	–	–	–
Epoxy [78]	–	–	127	–	–	–	–	–
Poly(propylene carbonate) + poly(lactic acid) [79]	23	–	–	–	–	–	–	–
Polystyrene [80]	23	1.24	–	–	–	–	–	–
Polyurethane [81]	52	–	–	–	75	1.8	–	–

pultruded flat laminates reinforced with unidirectional glass fiber rovings. During the course of the study, a series of tests has been conducted by bending flat specimens of cured resin and pultruded composite to the shape programming angle. The shape fixity and shape recovery ratios for the pultruded composite specimens with 0° fiber orientation constituted 13.3% and 91.9%, respectively. For specimens with 90° fiber orientation, the shape fixity and shape recovery ratios were 78.4% and 92.6%, respectively. The shape fixity and shape recovery ratios of the cured resin specimens constituted 99.7% and 98.2%, respectively.

It was found that the shape programming angle has no effect on the shape fixity and shape recovery ratios. The shape fixity and shape recovery ratios remained virtually unchanged during the 10 cycles of shape memory cycling. For composite specimens with 0° and 90° fiber orientations, a linear relationship between the shape fixing angle and shape programming angle was established, allowing a researcher to obtain the desired shape after programming.

The thermomechanical and thermophysical properties of the cured resin, such as temperature dependence of the storage modulus, glass transition temperature, heat capacity, coefficient of thermal expansion, density, and thermal conductivity were determined. These data may be used for further numerical simulations and optimization of the pultrusion process. To model the cure kinetics, the constants for the expanded Prout–Tompkins model were obtained.

Series of mechanical tests to determine the tensile, compression, flexural, and interlaminar shear properties of the cured resin and composite specimens with 0° and 90° fiber orientations were performed. Considering these results, pultruded SMPCs show significant promise for structural applications based on shape memory composites.

CRediT authorship contribution statement

Roman Korotkov: Investigation, Software, Data curation, Visualization, Conceptualization, Writing – original draft, Writing – review & editing. **Alexander Vedernikov:** Investigation, Software, Data curation, Visualization, Writing – original draft, Writing – review & editing. **Sergey Gusev:** Investigation, Resources. **Omar Alajarmeh:** Writing – review & editing. **Iskander Akhatov:** Project administration, Funding acquisition. **Alexander Safonov:** Supervision, Conceptualization, Writing – original draft, Writing – review & editing.

Declaration of Competing Interest

The authors declare that they have no known competing financial interests or personal relationships that could have appeared to influence the work reported in this paper.

Acknowledgements

This research did not receive any specific grant from funding agencies in the public, commercial, or not-for-profit sectors. The authors greatly appreciate the suggestions of anonymous reviewers and the help of editor Professor Suresh Advani.

References

- [1] Lendlein A, Kelch S. Shape-memory polymers. *Angew Chemie - Int Ed* 2002;41:2034–57. [https://doi.org/10.1002/1521-3773\(20020617\)41:12<2034::aid-anie2034>3.0.co;2-m](https://doi.org/10.1002/1521-3773(20020617)41:12<2034::aid-anie2034>3.0.co;2-m).
- [2] Liu C, Qin H, Mather PT. Review of progress in shape-memory polymers. *J Mater Chem* 2007;17:1543–58. <https://doi.org/10.1039/b615954k>.
- [3] Xie T. Tunable polymer multi-shape memory effect. *Nature* 2010;464(7286):267–70. <https://doi.org/10.1038/nature08863>.
- [4] Behl M, Lendlein A. Shape-memory polymers. *Mater Today* 2007;10(4):20–8. [https://doi.org/10.1016/S1369-7021\(07\)70047-0](https://doi.org/10.1016/S1369-7021(07)70047-0).
- [5] Lendlein A, Jiang H, Jünger O, Langer R. Light-induced shape-memory polymers. *Nature* 2005;434(7035):879–82. <https://doi.org/10.1038/nature03496>.
- [6] Habault D, Zhang H, Zhao Y. Light-triggered self-healing and shape-memory polymers. *Chem Soc Rev* 2013;42:7244–56. <https://doi.org/10.1039/c3cs35489j>.
- [7] Huang WM, Yang B, An L, Li C, Chan YS. Water-driven programmable polyurethane shape memory polymer: Demonstration and mechanism. *Appl Phys Lett* 2005;86:1–3. <https://doi.org/10.1063/1.1880448>.
- [8] Wang CC, Huang WM, Ding Z, Zhao Y, Purnawali H. Cooling-/water-responsive shape memory hybrids. *Compos Sci Technol* 2012;72(10):1178–82. <https://doi.org/10.1016/j.compscitech.2012.03.027>.
- [9] Han X-J, Dong Z-Q, Fan M-M, Liu Y, Li J-H, Wang Y-F, et al. PH-induced shape-memory polymers. *Macromol Rapid Commun* 2012;33(12):1055–60. <https://doi.org/10.1002/marc.201200153>.
- [10] Li Y, Chen H, Liu D, Wang W, Liu Ye, Zhou S. PH-Responsive Shape Memory Poly(ethylene glycol)-Poly(ε-caprolactone)-based Polyurethane/Cellulose Nanocrystals Nanocomposite. *ACS Appl Mater Interfaces* 2015;7(23):12988–99. <https://doi.org/10.1021/acsami.5b02940>.
- [11] Wang W, Liu D, Liu Y, Leng J, Bhattacharyya D. Electrical actuation properties of reduced graphene oxide paper/epoxy-based shape memory composites. *Compos Sci Technol* 2015;106:20–4. <https://doi.org/10.1016/j.compscitech.2014.10.016>.
- [12] Wei H, Zhang Q, Yao Y, Liu L, Liu Y, Leng J. Direct-write fabrication of 4D active shape-changing structures based on a shape memory polymer and its nanocomposite. *ACS Appl Mater Interfaces* 2017;9(1):876–83. <https://doi.org/10.1021/acsami.6b12824>.

- [13] Stuart MAC, Huck WTS, Genzer J, Müller M, Ober C, Stamm M, et al. Emerging applications of stimuli-responsive polymer materials. *Nat Mater* 2010;9(2):101–13. <https://doi.org/10.1038/nmat2614>.
- [14] Liu Y, Du H, Liu L, Leng J. Shape memory polymers and their composites in aerospace applications: A review. *Smart Mater Struct* 2014;23(2):023001. <https://doi.org/10.1088/0964-1726/23/2/023001>.
- [15] Lendlein A, Biodegradable LR. elastic shape-memory polymers for potential biomedical applications. *Science* (80-) 2002;296:1673–6. <https://doi.org/10.1126/science.1066102>.
- [16] Madbouly SA, Lendlein A. Shape-Memory Polymer Composites. *Adv Polym Sci*, vol. 226, Springer, Berlin, Heidelberg; 2009, p. 41–95. doi: 10.1007/12_2009_28.
- [17] Lee AY, An J, Chua CK. Two-Way 4D Printing: A Review on the Reversibility of 3D-Printed Shape Memory Materials. *Engineering* 2017;3(5):663–74. <https://doi.org/10.1016/J.ENG.2017.05.014>.
- [18] Ohm C, Brehmer M, Zentel R. Liquid Crystalline Elastomers as Actuators and Sensors. *Adv Mater* 2010;22(31):3366–87. <https://doi.org/10.1002/adma.200904059>.
- [19] Kim BK, Lee SY, Xu M. Polyurethanes having shape memory effects. *Polymer (Guildf)* 1996;37(26):5781–93. [https://doi.org/10.1016/S0032-3861\(96\)00442-9](https://doi.org/10.1016/S0032-3861(96)00442-9).
- [20] Du H, Liu L, Zhang F, Leng J, Liu Y. Triple-shape memory effect in a styrene-based shape memory polymer: Characterization, theory and application. *Compos Part B Eng* 2019;173:106905. <https://doi.org/10.1016/j.compositesb.2019.106905>.
- [21] Gao Y, Liu W, Zhu S. Polyolefin Thermoplastics for Multiple Shape and Reversible Shape Memory. *ACS Appl Mater Interfaces* 2017;9(5):4882–9. <https://doi.org/10.1021/acsami.6b14728>.
- [22] Liu W, Zhang R, Huang M, Dong X, Xu W, Ray N, et al. Design and structural study of a triple-shape memory PCL/PVC blend. *Polymer (Guildf)* 2016;104:115–22. <https://doi.org/10.1016/j.polymer.2016.09.079>.
- [23] Yakacki CM, Shandas R, Lanning C, Rech B, Eckstein A, Gall K. Unconstrained recovery characterization of shape-memory polymer networks for cardiovascular applications. *Biomaterials* 2007;28(14):2255–63. <https://doi.org/10.1016/j.biomaterials.2007.01.030>.
- [24] Du H, Song Z, Wang J, Liang Z, Shen Y, You F. Microwave-induced shape-memory effect of silicon carbide/poly(vinyl alcohol) composite. *Sensors Actuators, A Phys* 2015;228:1–8. <https://doi.org/10.1016/j.sna.2015.01.012>.
- [25] Zhang W, Chen L, Zhang Yu. Surprising shape-memory effect of polylactide resulted from toughening by polyamide elastomer. *Polymer (Guildf)* 2009;50(5):1311–5. <https://doi.org/10.1016/j.polymer.2009.01.032>.
- [26] Rousseau IA, Xie T. Shape memory epoxy: Composition, structure, properties and shape memory performances. *J Mater Chem* 2010;20:3431–41. <https://doi.org/10.1039/b923394f>.
- [27] Hung P-Y, Lau K-T, Cheng L-K, Leng J, Hui D. Impact response of hybrid carbon/glass fibre reinforced polymer composites designed for engineering applications. *Compos Part B Eng* 2018;133:86–90. <https://doi.org/10.1016/j.compositesb.2017.09.026>.
- [28] Fejös M, Romhányi G, Karger-Kocsis J. Shape memory characteristics of woven glass fibre fabric reinforced epoxy composite in flexure. *J Reinf Plast Compos* 2012;31(22):1532–7. <https://doi.org/10.1177/0731684412461541>.
- [29] Santhosh Kumar KS, Biju R, Reghunadhan Nair CP. Progress in shape memory epoxy resins. *React Funct Polym* 2013;73(2):421–30. <https://doi.org/10.1016/j.reactfunctpolym.2012.06.009>.
- [30] Herath M, Epaarachchi JA, Islam MM, Al-azzawi W, Leng J, Zhang F. Structural performance and photothermal recovery of carbon fibre reinforced shape memory polymer. *Compos Sci Technol* 2018;167:206–14. <https://doi.org/10.1016/j.compscitech.2018.07.042>.
- [31] Ivens J, Urbanus M, De Smet C. Shape recovery in a thermoset shape memory polymer and its fabric-reinforced composites. *EXPRESS Polym Lett* 2011;5(3):254–61.
- [32] Liu X, Li H, Zeng Q, Zhang Y, Kang H, Duan H, et al. Electro-active shape memory composites enhanced by flexible carbon nanotube/graphene aerogels 2015. doi: 10.1039/c5ta02490k.
- [33] Uslu E, Gavgali M, Erdal MO, Yazman Ş, Gemi L. Determination of mechanical properties of polymer matrix composites reinforced with electrospinning N66, PAN, PVA and PVC nanofibers: A comparative study. *Mater Today Commun* 2021; 26. <https://doi.org/10.1016/j.mtcomm.2020.101939>.
- [34] Li F, Scarpa F, Lan X, Liu L, Liu Y, Leng J. Bending shape recovery of unidirectional carbon fiber reinforced epoxy-based shape memory polymer composites. *Compos Part A Appl Sci Manuf* 2019;116:169–79. <https://doi.org/10.1016/j.compositesa.2018.10.037>.
- [35] Gemi L. Investigation of the effect of stacking sequence on low velocity impact response and damage formation in hybrid composite pipes under internal pressure. A comparative study. *Compos Part B Eng* 2018;153:217–32. <https://doi.org/10.1016/j.compositesb.2018.07.056>.
- [36] Gemi L, Kökçü U, Yazman Ş, Morkavuk S. The effects of stacking sequence on drilling machinability of filament wound hybrid composite pipes: Part-1 mechanical characterization and drilling tests. *Compos Part B Eng* 2020;186:107787. <https://doi.org/10.1016/j.compositesb.2020.107787>.
- [37] Gemi L, Morkavuk S, Kökçü U, Yazman Ş. The effects of stacking sequence on drilling machinability of filament wound hybrid composite pipes: Part-2 damage analysis and surface quality. *Compos Struct* 2020;235:111737. <https://doi.org/10.1016/j.compstruct.2019.111737>.
- [38] Zeng C, Liu L, Bian W, Liu Y, Leng J. 4D printed electro-induced continuous carbon fiber reinforced shape memory polymer composites with excellent bending resistance. *Compos Part B Eng* 2020;194:108034. <https://doi.org/10.1016/j.compositesb.2020.108034>.
- [39] Madenci E, Özkılıç YO, Gemi L. Experimental and theoretical investigation on flexure performance of pultruded GFRP composite beams with damage analyses. *Compos Struct* 2020;242. <https://doi.org/10.1016/j.compstruct.2020.112162>.
- [40] Vedernikov A, Safonov A, Tucci F, Carlone P, Akhatov I. Pultruded materials and structures: A review. *J Compos Mater* 2020;54(26):4081–117. <https://doi.org/10.1177/0021998320922894>.
- [41] Madenci E, Özkılıç Y, Gemi L. Theoretical investigation on static analysis of pultruded GFRP composite beams. *Acad Platf J Eng Sci* 2020;8. <https://doi.org/10.21541/apjes.734770>.
- [42] Özkılıç Y, Madenci E, Gemi L. Tensile and compressive behaviors of the pultruded GFRP lamina. *Turkish J Eng Environ Sci* 2020;4:169–75. <https://doi.org/10.31127/tuje.631481>.
- [43] Li C, Yin X, Liu Y, Guo R, Xian G. Long-term service evaluation of a pultruded carbon/glass hybrid rod exposed to elevated temperature, hydraulic pressure and fatigue load coupling. *Int J Fatigue* 2020;134. <https://doi.org/10.1016/j.ijfatigue.2020.105480>.
- [44] Minchenkov K, Vedernikov A, Safonov A, Akhatov I. Thermoplastic pultrusion: A review. *Polymers (Basel)* 2021;13:1–36. <https://doi.org/10.3390/polym13020180>.
- [45] Madenci E, Onuralp Özkılıç Y, Gemi L. Buckling and free vibration analyses of pultruded GFRP laminated composites: Experimental, numerical and analytical investigations. *Compos Struct* 2020;254. <https://doi.org/10.1016/j.compstruct.2020.112806>.
- [46] Tucci F, Vedernikov A. Design Criteria for Pultruded Structural Elements. *Ref Modul Mater Sci Mater Eng* 2021. <https://doi.org/10.1016/B978-0-12-819724-0.00086-0>.
- [47] Safonov A, Gusev M, Saratov A, Konstantinov A, Sergeichev I, Konev S, et al. Modeling of cracking during pultrusion of large-size profiles. *Compos Struct* 2020; 235. <https://doi.org/10.1016/j.compstruct.2019.111801>.
- [48] Struzziero G, Maistros GM, Hartley J, Skordos AA. Materials modelling and process simulation of the pultrusion of curved parts. *Compos Part A Appl Sci Manuf* 2021; 144:106328. <https://doi.org/10.1016/j.compositesa.2021.106328>.
- [49] Safonov AA, Carlone P, Akhatov I. Mathematical simulation of pultrusion processes: A review. *Compos Struct* 2018;184:153–77. <https://doi.org/10.1016/j.compstruct.2017.09.093>.
- [50] Fascetti A, Feo L, Abbaszadeh H. A critical review of numerical methods for the simulation of pultruded fiber-reinforced structural elements. *Compos Struct* 2021; 273:114284. <https://doi.org/10.1016/j.compstruct.2021.114284>.
- [51] Vedernikov A, Tucci F, Carlone P, Gusev S, Konev S, Firsov D, et al. Effects of pulling speed on structural performance of L-shaped pultruded profiles. *Compos Struct* 2021;255. <https://doi.org/10.1016/j.compstruct.2020.112967>.
- [52] Zhang C-H, Wei H-G, Liu Y-Y, Tan H-F, Guo Z. Enhanced toughness and shape memory behavior of toughened epoxy resin. *High Perform Polym* 2012;24(8):702–9. <https://doi.org/10.1177/0954008312449846>.
- [53] Liu Y, Zhang F, Leng J, Wang L, Cotton C, Sun B, et al. Synergistic effect enhanced shape recovery behavior of metal-4D printed shape memory polymer hybrid composites. *Compos Part B Eng* 2019;179:107536. <https://doi.org/10.1016/j.compositesb.2019.107536>.
- [54] ISO 6721-1:2011 Plastics — Determination of dynamic mechanical properties — Part 1: General principles; n.d.
- [55] ISO 11357-5:1999 Plastics — Differential scanning calorimetry (DSC) — Part 5: Determination of characteristic reaction-curve temperatures and times, enthalpy of reaction and degree of conversion; n.d.
- [56] ISO 11357-4:2005 Plastics — Differential scanning calorimetry (DSC) — Part 4: Determination of specific heat capacity; n.d.
- [57] ISO 11359-2:1999 Plastics — Thermomechanical analysis (TMA) — Part 2: Determination of coefficient of linear thermal expansion and glass transition temperature; n.d.
- [58] ASTM E1461-13. Standard test method for thermal diffusivity by the flash method. West Conshohocken (PA): ASTM International; 2013. www.astm.org.
- [59] ISO 527-2:2012(en) Plastics — Determination of tensile properties — Part 2: Test conditions for moulding and extrusion plastics; n.d.
- [60] ASTM D790-17. Standard Test Methods for Flexural Properties of Unreinforced and Reinforced Plastics and Electrical Insulating Materials. West Conshohocken (PA): ASTM International; 2017. www.astm.org.
- [61] Plastics – Determination of tensile properties – Part 5: Test conditions for unidirectional fibre-reinforced plastic composites. EN ISO 527-5:2009; n.d.
- [62] ASTM Standard. ASTM D6641/D6641M-16e1, Standard test method for compressive properties of polymer matrix composite materials using a combined loading compression (CLC) test fixture. West Conshohocken (PA): ASTM International; 2016.
- [63] ASTM D2344/D2344M-16. Standard test method for short-beam strength of polymer matrix composite materials and their laminates. West Conshohocken (PA): ASTM International; 2016. www.astm.org.
- [64] ISO 2602:1980 Statistical interpretation of test results—Estimation of the mean—Confidence interval; n.d.
- [65] Karger-Kocsis J, Kéki S. Review of progress in shape memory epoxies and their composites. *Polymers (Basel)* 2017;10:34. <https://doi.org/10.3390/polym10010034>.
- [66] Meng Q, Hu J. A review of shape memory polymer composites and blends. *Compos Part A Appl Sci Manuf* 2009;40(11):1661–72. <https://doi.org/10.1016/j.compositesa.2009.08.011>.
- [67] Basit A, Lhostis G, Durand B. Investigation of the shape memory and actuation properties of different asymmetric smart polymer composites. *Adv Compos Mater* 2020. <https://doi.org/10.1080/09243046.2020.1836572>.

- [68] Naito Y, Nishikawa M, Hojo M. Effect of reinforcing layer on shape fixity and time-dependent deployment in shape-memory polymer textile composites. *Compos Part A Appl Sci Manuf* 2015;76:316–25. <https://doi.org/10.1016/j.compositesa.2015.06.011>.
- [69] Johnston A. An integrated model of the development of process-induced deformation in autoclave processing of composite structures; 1997.
- [70] Khoun L, Centea T, Hubert P. Characterization methodology of thermoset resins for the processing of composite materials - Case study: CYCOM 890RTM epoxy resin. *J Compos Mater* 2010;44(11):1397–415. <https://doi.org/10.1177/0021998309353960>.
- [71] Zheng T, Xi H, Wang Z, Zhang X, Wang Y, Qiao Y, et al. The curing kinetics and mechanical properties of epoxy resin composites reinforced by PEEK microparticles. *Polym Test* 2020;91. <https://doi.org/10.1016/j.polymertesting.2020.106781>.
- [72] Vedernikov A, Nasonov Y, Korotkov R, Gusev S, Akhatov I, Safonov A. Effects of additives on the cure kinetics of vinyl ester pultrusion resins. *J Compos Mater* 2021. <https://doi.org/10.1177/00219983211001528>.
- [73] Wei H, Liu L, Zhang Z, Du H, Liu Y, Leng J. Design and analysis of smart release devices based on shape memory polymer composites. *Compos Struct* 2015;133:642–51. <https://doi.org/10.1016/j.compstruct.2015.07.107>.
- [74] Liu Z, Li Q, Bian W, Lan X, Liu Y, Leng J. Preliminary test and analysis of an ultralight lenticular tube based on shape memory polymer composites. *Compos Struct* 2019;223:110936. <https://doi.org/10.1016/j.compstruct.2019.110936>.
- [75] Wei K, Zhu G, Tang Y, Li X, Liu T, Niu L. An investigation on shape memory behaviours of hydro-epoxy/glass fibre composites. *Compos Part B Eng* 2013;51:169–74. <https://doi.org/10.1016/j.compositesb.2013.03.036>.
- [76] Zhao H, Lan X, Liu L, Liu Y, Leng J. Design and analysis of shockless smart releasing device based on shape memory polymer composites. *Compos Struct* 2019;223:110958. <https://doi.org/10.1016/j.compstruct.2019.110958>.
- [77] Tang Z, Sun D, Yang D, Guo B, Zhang L, Jia D. Vapor grown carbon nanofiber reinforced bio-based polyester for electroactive shape memory performance. *Compos Sci Technol* 2013;75:15–21. <https://doi.org/10.1016/j.compscitech.2012.11.019>.
- [78] Li H, Zhong J, Meng J, Xian G. The reinforcement efficiency of carbon nanotubes/shape memory polymer nanocomposites. *Compos Part B Eng* 2013;44(1):508–16. <https://doi.org/10.1016/j.compositesb.2012.03.017>.
- [79] Qi X, Dong P, Liu Z, Liu T, Fu Q. Selective localization of multi-walled carbon nanotubes in bi-component biodegradable polyester blend for rapid electroactive shape memory performance. *Compos Sci Technol* 2016;125:38–46. <https://doi.org/10.1016/j.compscitech.2016.01.023>.
- [80] Li G, John M. A self-healing smart syntactic foam under multiple impacts. *Compos Sci Technol* 2008;68(15-16):3337–43. <https://doi.org/10.1016/j.compscitech.2008.09.009>.
- [81] Rahman AA, Ikeda T, Senba A. Memory effects performance of polyurethane shape memory polymer composites (SMPC) in the variation of fiber volume fractions. *Fibers Polym* 2017;18(5):979–86. <https://doi.org/10.1007/s12221-017-6687-9>.
- [82] Brown R, Singh K, Khan F. Fabrication and vibration characterization of electrically triggered shape memory polymer beams. *Polym Test* 2017;61:74–82. <https://doi.org/10.1016/j.polymertesting.2017.05.015>.
- [83] Lee C-Y, Chen C-C, Yang T-H, Lin C-J. Structural vibration control using a tunable hybrid shape memory material vibration absorber. *J Intell Mater Syst Struct* 2012;23(15):1725–34. <https://doi.org/10.1177/1045389X12451190>.
- [84] Li J, Duan Q, Zhang E, Wang J. Applications of shape memory polymers in kinetic buildings. *Adv Mater Sci Eng* 2018;2018:1–13. <https://doi.org/10.1155/2018/7453698>.
- [85] Abavisani I, Rezaifar O, Kheyroddin A. Multifunctional properties of shape memory materials in civil engineering applications: A state-of-the-art review. *J Build Eng* 2021;44. <https://doi.org/10.1016/j.jobte.2021.102657>.
- [86] Behl M, Kratz K, Noechel U, Sauter T, Lendlein A. Temperature-memory polymer actuators. *Proc Natl Acad Sci U S A* 2013;110(31):12555–9. <https://doi.org/10.1073/pnas.1301895110>.
- [87] Sá MF, Correia JR, Silvestre N, Gomes AM. Transverse bending and in-plane shear behaviours of multicellular pultruded GFRP deck panels with snap-fit connections. *Thin-Walled Struct* 2020;154:106854. <https://doi.org/10.1016/j.tws.2020.106854>.
- [88] Sá MF, Gomes AM, Correia JR, Silvestre N. Flexural behavior of pultruded GFRP deck panels with snap-fit connections. *Int J Struct Stab Dyn* 2018;18. <https://doi.org/10.1142/S0219455418500190>.
- [89] Starr TF. Pultrusion for engineers; 2000. doi: 10.1533/9781855738881.97.
- [90] Love MH, Zink PS, Stroud RL, Bye DR, Rizk S, White D. Demonstration of morphing technology through ground and wind tunnel tests. *Collect. Tech. Pap. – AIAA/ASME/ASCE/AHS/ASC Struct. Struct. Dyn. Mater. Conf., vol. 1, Waikiki (HI): American Institute of Aeronautics and Astronautics Inc.; 2007. p. 337–48. doi: 10.2514/6.2007-1729*.
- [91] Li F, Liu Y, Leng J. Progress of shape memory polymers and their composites in aerospace applications. *Smart Mater Struct* 2019;28. <https://doi.org/10.1088/1361-665X/ab3d5f>.
- [92] Lan X, Liu Y, Lv H, Wang X, Leng J, Du S. Fiber reinforced shape-memory polymer composite and its application in a deployable hinge. *Smart Mater Struct* 2009;18(2):024002. <https://doi.org/10.1088/0964-1726/18/2/024002>.
- [93] Ze Q, Kuang X, Wu S, Wong J, Montgomery SM, Zhang R, et al. Magnetic shape memory polymers with integrated multifunctional shape manipulation. *Adv Mater* 2020;32. <https://doi.org/10.1002/adma.201906657>.
- [94] Santo L, Quadrini F, Accettura A, Villadei W. Shape memory composites for self-deployable structures in aerospace applications. *Procedia Eng* 2014;88:42–7. <https://doi.org/10.1016/j.proeng.2014.11.124>.
- [95] Özütok A, Madenci E. Static analysis of laminated composite beams based on higher-order shear deformation theory by using mixed-type finite element method. *Int J Mech Sci* 2017;130:234–43. <https://doi.org/10.1016/j.ijmecsci.2017.06.013>.
- [96] Madenci E, Özütok A. Variational approximate for high order bending analysis of laminated composite plates. *Struct Eng Mech* 2020;73:97–108.

Chapter 12

Conclusion and outlook

12.1 Summary

This Ph.D. thesis studied the effects of technological regimes on structural performance of pultruded profiles widely applied in the construction sector and various engineering industries in the last decades. In particular, the possibility of increasing the profitability of the pultrusion process while maintaining the structural performance of manufactured composite structural profiles has been analyzed. A complex of the experimental and numerical studies of pultruded flat laminates and L-shaped structural profiles were conducted.

The shape distortions, microstructure and mechanical characteristics of pultruded glass fiber/epoxy-vinyl L-shaped profiles of $75\times 75\times 6$ mm were found to depend significantly on the selected pulling speed. These effects are caused by the shift of the polymerization peak to the post-die region due to the increased pulling speeds. It was found that increase in the pulling speed leads to incomplete polymerization of the composite at the die exit, which, in turn, results in the process-induced defects and impairs mechanical properties of manufactured profiles. Defects occurring in the composites during production can lead to a rejection of pultruded structural profiles due to their inability to meet dimensional and mechanical performance requirements specified in design standards. Pronounced delaminations, large variations, substantially reduced mechanical properties, and increased spring-in angles were observed in the profiles pultruded at higher pulling speeds. Moreover, it was

found advisable that, apart from the initial spring-in values, a manufacturer should account for the absolute growth of spring-in over time as well. The profiles produced at higher pulling speeds may meet dimensional tolerance requirements immediately after production, but fail to do so after storage.

For the first time the possibility of high-speed pultrusion of large cross-section profiles suitable for structural applications is demonstrated by producing glass fiber/epoxy-vinyl flat laminates of 150×3.5 mm. Bubbles, longitudinal voids, matrix cracks, as well as their density and dimensions, being a function of selected pulling speed, cause the differences in mechanical characteristics of pultruded composites. At high pulling speeds the glass fiber rovings are pulled through the impregnation bath much faster than at low pulling speeds. Consequently, the resin has less time to penetrate the rovings. This results in poor impregnation of rovings and the formation of air inclusions and dry spots, which, in turn, causes the formation of internal defects that significantly impair the structural performance of pultruded composites. The output of the pultrusion process can be raised at least by a factor of 1.7 with only slight sacrifice in mechanical properties of pultruded profiles (as compared to their counterparts produced at regular speed) by running the process at high pulling speeds.

Numerical model able to predict spring-in in $75 \times 75 \times 6$ mm L-shaped profiles pultruded at different pulling speeds is developed. The developed model was validated in two experiments conducted within a 6-month interval, using glass fiber/vinyl ester L-shaped profiles enhanced with unidirectional glass fiber rovings and fabrics, and manufactured at pulling speeds of 200, 400, and 600 mm/min. Spring-in predictions obtained with the proposed numerical model fall within the experimental data range. It was demonstrated that the final value of spring-in depends on the position of the exothermic peak and vitrification point on the pultrusion line, relative to the end of the constrained region of the die, which, in turn, is determined by the selected pulling speed. The closer the exothermic peak position to the constrained region of the die, the lower the obtained spring-in values. Alternatively, higher spring-in values can be observed with the increase in the distance of the exothermic peak from the die exit, because the composite can no longer sustain stresses from chemical

shrinkage in the unconstrained environment of the post-die region. It is shown that higher pulling speeds result in a higher fraction of uncured material in a composite exiting the constrained environment of the die block. This leads to an increase in the total chemical shrinkage of the material under unconstrained conditions and, hence, results in increased values of spring-in. It was demonstrated, that the largest contribution to spring-in comes from the chemical shrinkage of the resin, which takes place before the exothermic peak (Stage I), and from thermal shrinkage taking place before vitrification of the composite (Stage II), while thermal shrinkage during cooling (Stage III) results only in a slight increase in spring-in. Higher pulling speeds increase the contribution from Stage I and reduce the role of Stage II, while the spring-in contribution from Stage III remains unchanged. Based on the developed model, it was shown, that by using a post-die cooling tool or by reducing chemical shrinkage of a resin it is possible to obtain at least a 4.5 times increase in process output while preserving the same level of spring-in.

The influence of aluminum hydroxide $\text{Al}(\text{OH})_3$ flame retardant and zinc stearate $\text{Zn}(\text{C}_{18}\text{H}_{35}\text{O}_2)_2$ internal release agent on the cure kinetics of vinyl ester pultrusion resin (Atlac 430) and, consequently, on the choice of pultrusion pulling speed, was investigated. Four different resin compositions and their kinetics were studied experimentally and numerically. The results show that the presence of processing additives significantly affects the curing behavior of resin compositions. It was demonstrated that the predicted and experimental cure degrees of the composite at the die exit can vary considerably if the presence and effects of processing additives are neglected. Simulation results showed that for a resin with a final degree of cure exceeding 95% at the die exit, the maximum difference between the predicted values of pulling speed for a specified set of compositions may exceed 1.7 times. It is of the utmost importance to account for presence of additives and their effects in order to set the appropriate pulling speed and predict the outcomes of pultrusion.

Shape memory behavior of unidirectional glass fiber/epoxy pultruded flat laminates of 150×3.5 mm was studied. Shape fixity and shape recovery ratios for cured resin specimens and pultruded polymer composites were determined. The results show almost no changes in the shape recovery ratio of composite specimens within

10 shape memory cycles. To lay the foundation for further studies on the simulation and optimization of the pultrusion process, the resin cure kinetics, the thermomechanical and thermophysical properties of cured resin, and the mechanical characteristics of the pultruded shape memory polymer composite were analyzed. It is shown that pultruded shape memory polymer composites demonstrate better mechanical performance, as compared to composites produced by other processes. It is concluded that the ability of pultrusion to produce composite profiles of virtually unlimited length, with excellent mechanical and shape memory performance, makes it possible to expand the existing applications of shape memory polymer composites in civil and aerospace engineering. However, further studies are necessary to better understand the shape memory effect in pultruded composites and to allow for the numerical simulation and optimization necessary to promote the application of pultruded shape memory polymer composites in various structures.

12.2 Practical implementation

In this study the influence of pultrusion process conditions on structural performance of pultruded composites was investigated. Various combinations of technological regimes have been investigated, with resulting profiles meeting or failing the requirements of international standards for pultruded composites. In the future, researchers and practitioners aiming to increase the profitability of pultrusion process while preserving the performance of produced profiles may use the pipeline, relationships and findings presented in this Ph.D. thesis to select the optimum technological regimes. It is clear that for each individual pultrusion experiment the optimum technological regimes will depend on the multitude of various factors, such as profile geometry, raw materials, their proportions and contents, fiber impregnation and resin infiltration techniques, pulling force and pulling speed, and temperature and heating conditions. Thus, no study can state the single universal value for each parameter of pultrusion process (such as the optimum heating temperature, the maximum pulling speed, etc.). That is, for each experimental set-up these parameters will be individual. However, this study shows the approach to selection of technological regimes, and

highlights the points deserving attention, in order to increase the profitability of the process and prevent formation of bubbles, voids, and shape distortions impairing the structural performance of pultruded profiles. In other words this work assists in solution of technological challenges of pultrusion process, described in Chapter 1, further promoting the application of structural pultruded profiles both in construction sector, demonstrating the largest demand for pultruded profiles, and in other engineering sectors. Practical implementation of the technological regimes selection pipeline studied here will, in the first place, reduce expenses for costly trial-and-error approach used in selection of pultrusion technological regimes; second, it will improve the dimensional precision of produced profiles; and third, it will allow the use of higher pulling speeds and, in turn, to increase the profitability of pultrusion production while maintaining mechanical performance of manufactured composite profiles, required by international standards.

12.3 Outlook

Despite the research performed in this Ph.D. project, several issues related to the influence of technological regimes on structural performance of pultruded profiles still need to be addressed.

The influence of pulling speed on the compressive, tensile, flexural, interlaminar and in-plane shear properties of pultruded composites was studied in the Chapter 6, while the effects of high pulling speeds on the flexural and interlaminar shear performance of pultruded composites were investigated in the Chapter 7. However, the relationships between pulling speed and other mechanical properties of pultruded composites are yet to be established. In particular, the influence of pulling speed on the brittleness, fatigue, durability, and creep of pultruded profiles requires deeper analysis.

Although the influence of environment on structural behavior of pultruded profiles is actively studied today, the future trends will require investigation of relationships between technological regimes of pultrusion and the ability of produced profiles to resist environmental effects, such as increased humidity, high or low pressure,

thermal exposure, excess or lack of nitrogen, carbon dioxide, harsh environments such as acids, alkalis, sea water, arctic conditions, hygrothermal and freeze-thaw environments, etc.

The assumptions used in the 2D model presented in Chapter 2 and utilized in Chapter 9 can lead to an overestimated exothermic peak as compared to the experimental values. In addition, the proposed model does not account for stresses along the profile, which can result in additional shape deformations in the longitudinal direction. Nevertheless, these assumptions can be acceptable in stress-strain analysis, considering large dimensions of produced profile in the pulling direction. In addition, these assumptions produce acceptable predictions of spring-in, falling within the range of spring-in values obtained in two pultrusion experiments. However, in future research, a 3D numerical analysis should be performed to evaluate the influence of pulling speed and of profile thickness on the occurrence of cure-induced residual stresses and deformations. Moreover, the development of the numerical model describing the time-dependent behavior of shape distortions is needed. It is also necessary to numerically study the formation of matrix cracks and delaminations, arising during the high-speed pultrusion and reducing the structural performance of profiles. Moreover, it is advisable to conduct the multi-objective optimization of process conditions to maximize the pulling speed and minimize cure-induced residual stresses, spring-in, and formation of matrix cracks and delaminations, as was already done for other manufacturing processes (96; 97).

Apart from reducing the chemical shrinkage of the resin and corresponding spring-in reduction, the additives can also reduce the coefficient of thermal expansion of resin and, therefore, the spring-in angle, as shown in (98). However, no experimental studies on the influence of additives on development of cure-induced residual stresses and deformations in pultruded profiles have been performed before. Therefore, this issue will require further investigation.

Although the influence of $\text{Zn}(\text{C}_{18}\text{H}_{35}\text{O}_2)_2$ and $\text{Al}(\text{OH})_3$ on the cure kinetics of resin compositions was analyzed in Chapter 10 of this Ph.D. thesis, the number of processing additives used in pultrusion is considerably higher. To optimize the process, all types of additives, such as pigments, stabilizers, fungal and bioprotectors,

UV protectors, etc. should be investigated. Besides, the influence of additives on other types of pultrusion resins (epoxy and polyester) also requires further investigation. Further studies are necessary to examine the effects of the components, storage time and conditions, refrigeration, and preparation specifics on cure kinetics of resins. Moreover, possible chemical interactions between neat resins and additives, which affect the polymerization kinetics, should also be investigated.

Last but not the least, further research is necessary to better understand the shape memory effects in pultruded composites, as this question was rarely, if ever, addressed in available studies, except those presented in Chapter 11. The research should also account for the numerical simulation and optimization necessary to promote the application of pultruded shape memory polymer composites in various engineering applications.

Bibliography

- [1] EN 13706-2:2003 reinforced plastic composites - specifications for pultruded profiles - part 2: Methods of test and general requirements.
- [2] EN 13706-2:2003 reinforced plastic composites - specifications for pultruded profiles - part 3: Specific requirements.
- [3] A. Safonov, P. Carlone, I. Akhatov, Mathematical simulation of pultrusion processes: A review, *Composite Structures* 184 (2018) 153–177. doi:10.1016/j.compstruct.2017.09.093.
- [4] I. Baran, *Pultrusion: state-of-the-art process models*, Smithers Rapra, Shropshire, 2015.
- [5] H. L. Price, S. G. Cupschalk, Pulling force and its variation in composite materials pultrusion, in: H. C. Dae (Ed.), *Advances in Chemistry Series*, ACS, Washington, DC, USA, 1984, pp. 301–322.
- [6] R. Gorthala, J. A. Roux, J. G. Vaughan, R. P. Donti, Comparison of processing parameters for pultruded graphite/epoxy and fiberglass/epoxy: a heat transfer and curing model, *Journal of Reinforced Plastics and Composites* 13 (4) (1994) 288–300. doi:10.1177/073168449401300401.
- [7] E. Lackey, J. G. Vaughan, An Analysis of Factors Affecting Pull Force for the Pultrusion of Graphite/Epoxy Composites, *Journal of Reinforced Plastics and Composites* 13 (3) (1994) 188–198. doi:10.1177/073168449401300301.
- [8] C. Ma, M. Yn, J. Han, C. Chang, H. Wu, Pultruded fibre-reinforced furfuryl alcohol resin composites: 1. Process feasibility study, *Composites Manufacturing* 6 (1) (1995) 45–52. doi:10.1016/0956-7143(95)93712-S.
- [9] C. Ma, M. Yn, J. Han, C. Chang, H. Wu, Pultruded fibre-reinforced furfuryl alcohol resin composites: 2. Static, dynamic mechanical and thermal properties, *Composites Manufacturing* 6 (1) (1995) 53–58. doi:10.1016/0956-7143(95)93713-T.
- [10] M. Valliappan, J. A. Roux, J. G. Vaughan, E. S. Arafat, Die and post-die temperature and cure in graphite/epoxy composites, *Composites Part B: Engineering* 27 (1) (1996) 1–9. doi:10.1016/1359-8368(95)00001-1.

- [11] D.-H. Kim, P.-G. Han, G.-H. Jin, W. I. Lee, A model for thermosetting composite pultrusion process, *Journal of Composite Materials* 31 (20) (1997) 2105–2122. doi:10.1177/002199839703102005.
- [12] J. A. Roux, J. G. Vaughan, R. Shanku, E. S. Arafat, J. L. Bruce, V. R. Johnson, Comparison of measurements and modeling for pultrusion of a fiberglass/epoxy I-beam, *Journal of Reinforced Plastics and Composites* 17 (17) (1998) 1557–1578. doi:10.1177/073168449801701705.
- [13] J. M. Methven, S. R. Ghaffariyan, A. Z. Abidin, Manufacture of fiber-reinforced composites by microwave assisted pultrusion, *Polymer Composites* 21 (4) (2000) 586–594. doi:10.1002/pc.10214.
- [14] C. A. Garland, R. K. Gupta, H. V. S. Gangarao, J. W. Zondlo, Effect of Manufacturing Process Conditions on the Durability of Pultruded Vinyl Ester/Glass Composites (2000) 136.
- [15] A. D. Freed, Modeling the pultrusion process to obtain low void fraction composites, Ph.D. thesis (2002).
- [16] J. Lue, C. Chen, C. Yen, In situ pultrusion of urea-formaldehyde matrix composites. I. Processability, kinetic analysis, and dynamic mechanical properties, *Journal of Applied Polymer Science* 83 (6) (2002). doi:10.1002/app.2291.
- [17] M. Sarrionandia, I. Mondragn, S. M. Moschiar, M. M. Reboredo, A. Vázquez, Heat transfer for pultrusion of a modified acrylic/glass reinforced composite, *Polymer Composites* 23 (1) (2002) 21–27. doi:10.1002/pc.10408.
- [18] M. Yun, W. Lee, Analysis of bubble nucleation and growth in the pultrusion process of phenolic foam composites, *Composites Science and Technology* 68 (1) (2008). doi:10.1016/j.compscitech.2007.05.010.
- [19] M. S. Yun, W. I. Lee, Analysis of pulling force during pultrusion process of phenolic foam composites, *Composites Science and Technology* 68 (1) (2008) 140–146. doi:10.1016/j.compscitech.2007.05.032.
- [20] C.-H. Chen, I.-K. Chen, The unidirectional glass fiber reinforced furfuryl alcohol for pultrusion. II. Correlation of processing parameters for optimizing the process, *Journal of Applied Polymer Science* 119 (3) (2011) 1788–1796. doi:10.1002/app.32879.
- [21] S. Borges, C. Ferreira, J. Andrade, A. Prevedello, The influence of bath temperature on the properties of pultruded glass fiber reinforced rods, *Journal of Reinforced Plastics and Composites* 34 (15) (2015). doi:10.1177/0731684415587411.
- [22] C.-L. Chiang, C.-H. Chen, In situ pultrusion of vinyl ester/nano-mica matrix composites: Process feasibility and process parameters, *Journal of Reinforced Plastics and Composites* 35 (21) (2016) 1554–1565. doi:10.1177/0731684416659931.

- [23] I. Tena, M. Sarrionandia, J. Torre, J. Aurrekoetxea, The effect of process parameters on ultraviolet cured out of die bent pultrusion process, *Composites Part B: Engineering* 89 (2016) 9–17. doi:10.1016/j.compositesb.2015.11.027.
- [24] A. M. Fairuz, S. M. Sapuan, E. S. Zainudin, C. N. A. Jaafar, Effect of filler loading on mechanical properties of pultruded kenaf fibre reinforced vinyl ester composites, *Journal of Mechanical Engineering and Sciences* 10 (1) (2016) 1931–1942. doi:10.15282/jmes.10.1.2016.16.0184.
- [25] A. M. Fairuz, S. M. Sapuan, E. S. Zainudin, C. N. A. Jaafar, The effect of pulling speed on mechanical properties of pultruded kenaf fiber reinforced vinyl ester composites, *Journal of Vinyl and Additive Technology* 24 (2018) E13–E20. doi:10.1002/vnl.21552.
- [26] A. Safonov, M. Gusev, A. Saratov, A. Konstantinov, I. Sergeichev, S. Konev, S. Gusev, I. Akhatov, Modeling of cracking during pultrusion of large-size profiles, *Composite Structures* (2019) 111801doi:10.1016/j.compstruct.2019.111801.
- [27] F. Tucci, R. Bezerra, F. Rubino, P. Carlone, Multiphase flow simulation in injection pultrusion with variable properties, *Materials and Manufacturing Processes* (2020). doi:10.1080/10426914.2020.1711928.
- [28] F. Tucci, D. Larrea-Wachtendorff, G. Ferrari, P. Carlone, Pulling force analysis in injection pultrusion of glass/epoxy composites, *Materials and Manufacturing Processes* 0 (0) (2022) 1–12. doi:10.1080/10426914.2022.2049296.
- [29] C. D. Han, H. B. Chin, Development of a mathematical model for the pultrusion of unsaturated polyester resin, *Polymer Engineering Science* 28 (5) (1988) 321–332. doi:10.1002/pen.760280507.
- [30] H. Ng, I. Manas-Zloczower, Kinetic studies of a composite thermoset cure reaction—application in pultrusion simulations, *Polymer Engineering Science* 29 (5) (1989) 302–307. doi:10.1002/pen.760290507.
URL <https://www.scopus.com/inward/record.uri?eid=2-s2.0-0024620843&doi=10.1002%2Fpen.760290507&partnerID=40&md5=f7b025816e51e7cc01b894f82b51a04c>
- [31] L. Calabrese, A. Valenza, Effect of CTBN rubber inclusions on the curing kinetic of DGEBA-DGEBF epoxy resin, *European Polymer Journal* 39 (7) (2003) 1355–1363. doi:10.1016/S0014-3057(02)00390-7.
- [32] G. Liang, A. Garg, K. Chandrashekhara, V. Flanigan, S. Kapila, Cure characterization of pultruded soy-based composites, *Journal of Reinforced Plastics and Composites* 24 (14) (2005) 1509–1520. doi:10.1177/0731684405050387.
- [33] P. Badrinarayanan, Y. Lu, R. C. Larock, M. R. Kessler, Cure characterization of soybean oil-styrene-divinylbenzene thermosetting copolymers, *Journal of Applied Polymer Science* 113 (2) (2009) 1042–1049. doi:10.1002/app.29776.

- [34] Y.-W. Wang, B. Zhu, X.-M. Yuan, Y.-L. Liu, B. Liu, M. Zhang, H.-G. Liu, Investigation of facile strategy for eliminating internal cracks of pultruded carbon fiber composites, *Materials Research Express* 6 (12) (2019). doi:10.1088/2053-1591/ab448e.
- [35] I. Saenz-Dominguez, I. Tena, M. Sarrionandia, J. Torre, J. Aurrekoetxea, Effect of ultraviolet curing kinetics on the mechanical properties of out of die pultruded vinyl ester composites, *Composites Part A: Applied Science and Manufacturing* 109 (2018) 280–289. doi:10.1016/j.compositesa.2018.03.015.
- [36] S. C. Joshi, Y. C. Lam, Integrated approach for modelling cure and crystallization kinetics of different polymers in 3D pultrusion simulation, *Journal of Materials Processing Technology* 174 (1-3) (2006) 178–182. doi:10.1016/j.jmatprotec.2006.01.003.
- [37] R. B. Prime, C. Michalski, C. M. Neag, Kinetic analysis of a fast reacting thermoset system, *Thermochimica Acta* 429 (2) (2005) 213–217. doi:10.1016/j.tca.2004.11.029.
- [38] S. M. Moschiar, M. M. Reboredo, H. Larrondo, A. Vazquez, Pultrusion of epoxy matrix composites: Pulling force model and thermal stress analysis, *Polymer Composites* 17 (6) (1996) 850–858. doi:10.1002/pc.10678.
- [39] E. Barkanov, P. Akishin, N. L. Miazza, S. Galvez, ANSYS-based algorithms for a simulation of pultrusion processes, *Mechanics of Advanced Materials and Structures* 24 (5) (2017) 377–384. doi:10.1080/15376494.2016.1191096.
- [40] P. Carlone, G. Palazzo, R. Pasquino, Pultrusion manufacturing process development: Cure optimization by hybrid computational methods, *Computers and Mathematics with Applications* 53 (9) (2007) 1464–1471. doi:10.1016/j.camwa.2006.02.031.
- [41] Y. R. Chachad, J. A. Roux, J. G. Vaughan, E. Arafat, Three-Dimensional Characterization of Pultruded Fiberglass-Epoxy Composite Materials, *Journal of Reinforced Plastics and Composites* 14 (5) (1995) 495–512. doi:10.1177/073168449501400506.
- [42] R. Gorthala, J. A. Roux, J. G. Vaughan, Resin Flow, Cure and Heat Transfer Analysis for Pultrusion Process, *Journal of Composite Materials* 28 (6) (1994) 486–506. doi:10.1177/002199839402800601.
- [43] A. A. Safonov, Y. Suvorova, Optimization of the pultrusion process for a rod with a large diameter, *Journal of Machinery Manufacture and Reliability* 38 (6) (2009) 572–578. doi:10.3103/S1052618809060090.
- [44] C. M. Ma, C. Chen, The development of a mathematical model for the pultrusion of blocked polyurethane composites, *Journal of Applied Polymer Science* 50 (5) (1993) 759–764. doi:10.1002/app.1993.070500503.

- [45] Y.-Y. Sun, C.-H. Chen, Process feasibility and kinetic analysis of glass fiber-reinforced vinyl ester/nano-Al₂O₃ matrix composites for pultrusion, *Journal of Applied Polymer Science* 125 (SUPPL. 1) (2012) E429–E434. doi:10.1002/app.36495.
- [46] P. Akishin, E. Barkanov, N. Miazza, S. Galvez, Curing kinetic models of resins for microwave assisted pultrusion, *Key Engineering Materials* 721 KEM (2017) 92–96. doi:10.4028/www.scientific.net/KEM.721.92.
- [47] J. Wang, D. Kelly, W. Hillier, Finite Element Analysis of Temperature Induced Stresses and Deformations of Polymer Composite Components, *Journal of Composite Materials* 34 (17) (2000) 1456–1471. doi:10.1106/76G7-X9QM-C5JF-E4D5.
- [48] I. Baran, C. C. Tutum, J. H. Hattel, The Internal Stress Evaluation of Pultruded Blades for a Darrieus Wind Turbine, *Key Engineering Materials* 554-557 (2013) 2127–2137. doi:10.4028/www.scientific.net/KEM.554-557.2127.
- [49] I. Baran, C. C. Tutum, M. W. Nielsen, J. H. Hattel, Process induced residual stresses and distortions in pultrusion, *Composites Part B: Engineering* 51 (2013) 148–161. doi:10.1016/j.compositesb.2013.03.031.
- [50] I. Baran, R. Akkerman, J. H. Hattel, Modelling the pultrusion process of an industrial L-shaped composite profile, *Composite Structures* 118 (1) (2014) 37–48. doi:10.1016/j.compstruct.2014.07.018.
- [51] I. Baran, J. H. Hattel, R. Akkerman, Investigation of the spring-in of a pultruded l-shaped profile for various processing conditions and thicknesses, *Key Engineering Materials* 611-612 (2014) 273–279. doi:10.4028/www.scientific.net/KEM.611-612.273.
- [52] I. Baran, J. H. Hattel, R. Akkerman, Investigation of process induced warpage for pultrusion of a rectangular hollow profile, *Composites Part B: Engineering* 68 (2015) 365–374. doi:10.1016/j.compositesb.2014.07.032.
- [53] S. R. White, Y. K. Kim, Process-induced residual stress analysis of AS4/3501-6 composite material, *Mechanics of Composite Materials and Structures* 5 (2) (1998) 153–186. doi:10.1080/10759419808945897.
- [54] R. Hill, A self-consistent mechanics of composite materials, *Journal of the Mechanics and Physics of Solids* 13 (4) (1965) 213–222. doi:10.1016/0022-5096(65)90010-4.
- [55] G. L. Batch, C. W. Macosko, Heat transfer and cure in pultrusion: Model and experimental verification, *AIChE Journal* 39 (7) (1993) 1228–1241. doi:10.1002/aic.690390713.
- [56] I. Baran, J. H. Hattel, R. Akkerman, C. C. Tutum, Mechanical Modelling of Pultrusion Process: 2D and 3D Numerical Approaches, *Applied Composite Materials* 22 (1) (2014) 99–118. doi:10.1007/s10443-014-9394-3.

- [57] Y. Nasonov, A. Safonov, S. Gusev, I. Akhatov, Mathematical simulation the kinetics of polymerization of vinyl ester resin using in pultrusion, IOP Conference Series: Materials Science and Engineering 747 (2020) 12010. doi:10.1088/1757-899X/747/1/012010.
- [58] A. Johnston, An integrated model of the development of process-induced deformation in autoclave processing of composite structures, Ph.D. thesis (1997).
- [59] L. Khoun, T. Centea, P. Hubert, Characterization methodology of thermoset resins for the processing of composite materials - case study: CYCOM 890RTM epoxy resin, Journal of Composite Materials 44 (11) (2010) 1397–1415. doi:10.1177/0021998309353960.
- [60] D. J. O'Brien, S. R. White, Cure Kinetics, Gelation, and Glass Transition of a Bisphenol F Epoxide, Polymer Engineering and Science 43 (4) (2003) 863–874. doi:10.1002/pen.10071.
- [61] A. R. Plepys, R. J. Farris, Evolution of residual stresses in three-dimensionally constrained epoxy resins, Polymer 31 (10) (1990) 1932–1936. doi:10.1016/0032-3861(90)90019-U.
- [62] J. Svanberg, J. Holmberg, Prediction of shape distortions Part I. FE-implementation of a path dependent constitutive model, Composites Part A: Applied Science and Manufacturing 35 (6) (2004) 711–721. doi:10.1016/j.compositesa.2004.02.005.
- [63] T. A. Bogetti, J. Gillespie J.W., Process-Induced Stress and Deformation in Thick-Section Thermoset Composite Laminates, Journal of Composite Materials 26 (5) (1992) 626–660. doi:10.1177/002199839202600502.
- [64] I. Baran, Modelling the Pultrusion Process of Off Shore Wind Turbine Blades, Ph.D. thesis, Technical University of Denmark (2014).
- [65] S. W. Tsai, H. T. Hahn, Introduction to Composite Materials, New York, 1980. doi:10.1201/9780203750148.
- [66] D. B. Goetschel, D. W. Radford, Analytical development of through-thickness properties of composite laminates, Journal of Advanced Materials 28 (4) (1997) 37–46.
- [67] R. Akkerman, On the properties of quasi-isotropic laminates, Composites Part B:Engineering 33 (2) (2002) 133–140. doi:10.1016/S1359-8368(02)00002-1.
- [68] A. Johnston, R. Vaziri, A. Poursartip, A plane strain model for process-induced deformation of laminated composite structures, Journal of Composite Materials 35 (16) (2001) 1435–1469. doi:10.1106/YXEA-5MH9-76J5-BACK.
- [69] F. Awaja, B. Arhatari, K. Wiesauer, E. Leiss, D. Stifter, An investigation of the accelerated thermal degradation of different epoxy resin composites using

- X-ray microcomputed tomography and optical coherence tomography, *Polymer Degradation and Stability* 94 (10) (2009) 1814–1824. doi:10.1016/j.polymdegradstab.2009.06.005.
- [70] J. E. Sumerak, Pultrusion Process Troubleshooting, in: *Handbook of Troubleshooting Plastics Processes: A Practical Guide*, 2012. doi:10.1002/9781118511183.ch20.
- [71] A. N. Vedernikov, A. A. Safonov, S. A. Gusev, P. Carlone, F. Tucci, I. S. Akhatov, Spring-in experimental evaluation of L-shaped pultruded profiles, *IOP Conference Series: Materials Science and Engineering* 747 (2020) 012013. doi:10.1088/1757-899X/747/1/012013.
- [72] K.-T. Hsiao, S. Gangireddy, Investigation on the spring-in phenomenon of carbon nanofiber-glass fiber/polyester composites manufactured with vacuum assisted resin transfer molding, *Composites Part A: Applied Science and Manufacturing* 39 (5) (2008) 834–842. doi:10.1016/j.compositesa.2008.01.015.
- [73] T. Mahrholz, J. Stängle, M. Sinapius, Quantitation of the reinforcement effect of silica nanoparticles in epoxy resins used in liquid composite moulding processes, *Composites Part A: Applied Science and Manufacturing* 40 (3) (2009) 235–243. doi:10.1016/j.compositesa.2008.11.008.
- [74] W. Exner, R. Hein, T. Mahrholz, P. Wierach, H. P. Monner, M. Sinapius, Impact of nanoparticles on the process-induced distortions of carbon fiber reinforced plastics: An experimental and simulative approach, *Journal of Applied Polymer Science* 136 (5) (2019) 47031. doi:10.1002/app.47031.
- [75] M. Haider, P. Hubert, L. Lessard, Cure shrinkage characterization and modeling of a polyester resin containing low profile additives, *Composites Part A: Applied Science and Manufacturing* 38 (3) (2007) 994–1009. doi:10.1016/j.compositesa.2006.06.020.
- [76] K. Zhang, J. Hong, G. Cao, D. Zhan, Y. Tao, C. Cong, The kinetics of thermal dehydration of copper(II) acetate monohydrate in air, *Thermochimica Acta* 437 (1-2) (2005) 145–149. doi:10.1016/j.tca.2005.06.038.
- [77] C.-H. Zhang, H.-G. Wei, Y.-Y. Liu, H.-F. Tan, Z. Guo, Enhanced toughness and shape memory behaviors of toughened epoxy resin, *High Performance Polymers* 24 (8) (2012) 702–709. doi:10.1177/0954008312449846.
- [78] Y. Liu, F. Zhang, J. Leng, L. Wang, C. Cotton, B. Sun, T. W. Chou, Synergistic effect enhanced shape recovery behavior of metal-4D printed shape memory polymer hybrid composites (dec 2019). doi:10.1016/j.compositesb.2019.107536.
- [79] Q. Meng, J. Hu, A review of shape memory polymer composites and blends (nov 2009). doi:10.1016/j.compositesa.2009.08.011.

- [80] A. Basit, G. Lhostis, B. Durand, Investigation of the shape memory and actuation properties of different asymmetric smart polymer composites, *Advanced Composite Materials* (2020). doi:10.1080/09243046.2020.1836572.
- [81] Y. Naito, M. Nishikawa, M. Hojo, Effect of reinforcing layer on shape fixity and time-dependent deployment in shape-memory polymer textile composites, *Composites Part A: Applied Science and Manufacturing* 76 (2015) 316–325. doi:10.1016/j.compositesa.2015.06.011.
- [82] R. Brown, K. Singh, F. Khan, Fabrication and vibration characterization of electrically triggered shape memory polymer beams, *Polymer Testing* 61 (2017) 74–82. doi:10.1016/j.polymertesting.2017.05.015.
- [83] C.-Y. Lee, C.-C. Chen, T.-H. Yang, C.-J. Lin, Structural vibration control using a tunable hybrid shape memory material vibration absorber, *Journal of Intelligent Material Systems and Structures* 23 (15) (2012) 1725–1734. doi:10.1177/1045389X12451190.
- [84] J. Li, Q. Duan, E. Zhang, J. Wang, Applications of Shape Memory Polymers in Kinetic Buildings, *Advances in Materials Science and Engineering 2018* (2018) 1–13. doi:10.1155/2018/7453698.
- [85] I. Abavisani, O. Rezaifar, A. Kheyroddin, Multifunctional properties of shape memory materials in civil engineering applications: A state-of-the-art review, *Journal of Building Engineering* 44 (2021). doi:10.1016/j.jobbe.2021.102657.
- [86] M. Behl, K. Kratz, U. Noechel, T. Sauter, A. Lendlein, Temperature-memory polymer actuators, *Proceedings of the National Academy of Sciences of the United States of America* 110 (31) (2013) 12555–12559. doi:10.1073/pnas.1301895110.
- [87] M. F. Sá, J. R. Correia, N. Silvestre, A. M. Gomes, Transverse bending and in-plane shear behaviours of multicellular pultruded GFRP deck panels with snap-fit connections, *Thin-Walled Structures* 154 (2020) 106854. doi:10.1016/j.tws.2020.106854.
- [88] T. F. Starr, *Pultrusion for engineers*, 2000.
- [89] M. F. Sá, A. M. Gomes, J. R. Correia, N. Silvestre, Flexural Behavior of Pultruded GFRP Deck Panels with Snap-Fit Connections, *International Journal of Structural Stability and Dynamics* 18 (2) (2018). doi:10.1142/S0219455418500190.
- [90] M. H. Love, P. S. Zink, R. L. Stroud, D. R. Bye, S. Rizk, D. White, Demonstration of morphing technology through ground and wind tunnel tests, in: *Collection of Technical Papers - AIAA/ASME/ASCE/AHS/ASC Structures, Structural Dynamics and Materials Conference, Vol. 1*, American Institute of Aeronautics and Astronautics Inc., Waikiki, HI, 2007, pp. 337–348. doi:10.2514/6.2007-1729.

- [91] F. Li, Y. Liu, J. Leng, Progress of shape memory polymers and their composites in aerospace applications, *Smart Materials and Structures* 28 (10) (2019). doi:10.1088/1361-665X/ab3d5f.
- [92] X. Lan, Y. Liu, H. Lv, X. Wang, J. Leng, S. Du, Fiber reinforced shape-memory polymer composite and its application in a deployable hinge, *Smart Materials and Structures* 18 (2) (2009) 24002. doi:10.1088/0964-1726/18/2/024002.
- [93] Q. Ze, X. Kuang, S. Wu, J. Wong, S. M. Montgomery, R. Zhang, J. M. Kovitz, F. Yang, H. J. Qi, R. Zhao, Magnetic Shape Memory Polymers with Integrated Multifunctional Shape Manipulation, *Advanced Materials* 32 (4) (2020). doi:10.1002/adma.201906657.
- [94] M. Herath, J. A. Epaarachchi, M. M. Islam, W. Al-azzawi, J. Leng, F. Zhang, Structural performance and photothermal recovery of carbon fibre reinforced shape memory polymer, *Composites Science and Technology* 167 (2018) 206–214. doi:10.1016/j.compscitech.2018.07.042.
- [95] L. Santo, F. Quadrini, A. Accettura, W. Villadei, Shape memory composites for self-deployable structures in aerospace applications, in: *Procedia Engineering*, Vol. 88, Elsevier Ltd, 2014, pp. 42–47. doi:10.1016/j.proeng.2014.11.124.
- [96] E. Ruiz, F. Trochu, Multi-criteria thermal optimization in liquid composite molding to reduce processing stresses and cycle time, *Composites Part A: Applied Science and Manufacturing* 37 (6) (2006) 913–924. doi:10.1016/j.compositesa.2005.06.010.
- [97] G. Struzziero, J. J. E. Teuwen, A fully coupled thermo-mechanical analysis for the minimisation of spring-in and process time in ultra-thick components for wind turbine blades, *Composites Part A: Applied Science and Manufacturing* 139 (2020). doi:10.1016/j.compositesa.2020.106105.
- [98] K. Shaker, Y. Nawab, A. Saouab, Experimental and numerical investigation of reduction in shape distortion for angled composite parts, *International Journal of Material Forming* 13 (6) (2020) 897–906. doi:10.1007/s12289-019-01510-6.